Promising bio-active transition metal complexes with azo/imine functional O N S donor ligands: Synthesis, characterization and in vitro anticancer activity

Thesis

Submitted for the degree of

Doctor of Philosophy (Science)

by

AKASH DAS

DEPARTMENT OF CHEMISTRY
JADAVPUR UNIVERSITY, KOLKATA - 700 032
INDIA

MARCH-2024

Dr. T.K. Mondal, Ph. D.
Professor
Department of Chemistry
Inorganic Chemistry Section

JADAVPUR UNIVERSITY
Kolkata – 700 032, India
Telephone: 91-033-2457-2970
tapank.mondal@jadavpuruniversity.in

CERTIFICATE FROM THE SUPERVISOR(S)

This is to certify that the thesis entitled **"Promising bio-active transition metal complexes with azo/imine functional O N S donor ligands: Synthesis, characterization and in vitro anticancer activity"** submitted by **Mr. Akash Das**, M.Sc., who got his name registered on **16.03.2021** for the award of Ph.D. (Science) degree of Jadavpur University, is absolutely based upon his own work under the supervision of Dr. Tapan Kumar Mondal and that neither this thesis nor any part of it has been submitted for either any degree / diploma or any other academic award anywhere before.

14/03/2024

(Signature of the Supervisor(s) date with official seal

Dr. TAPAN KUMAR MONDAL
Professor
Department of Chemistry
Jadavpur University
Kolkata-700032

"If you are searching for that person who will change your life, take a look in the mirror."

~ Sandeep Maheshwari

Dedicated to

My Parents and Wife…

ACKNOWLEDGEMENTS

My research journey which commenced on 1st August, 2018, has come to an end through making me a better and more mature researcher as well as a human being. Throughout this journey, so many people had an enormous impact on my way of thinking that either directly or indirectly benefited me. I take this opportunity to express my deep sense of reverence and gratitude to my supervisor Dr. Tapan Kumar Mondal, Department of Chemistry, Jadavpur University, Kolkata - 700 032 for letting me to do research freely in his group. Without his consistent encouragement and inspiring guidance throughout the course of this work, I could not have completed my research journey. I am thankful to him for his valuable suggestions during the tenure of my work and for pursuing the entire thesis.

It is also a pleasure to me to express my gratitude to the faculty members of Department of Chemistry, Jadavpur University, including Prof. Kajal Krishna Rajak, Head, Department of Chemistry, Prof. Ashis Kumar Sarkar, Dean of Science, JU, Prof. Partha Roy, Section-In-Charge, Inorganic Chemistry Section and all other faculty members of Department of Chemistry, Jadavpur University. I am thankful to all the teaching as well as non-teaching staff members of chemistry department and university for their support in various aspects.

I also express my appreciation as well as gratefulness to all my former and present lab mates viz., Dr. Krishnendu Aich, Dr. Saswati Gharami, Dr. Puspendu Roy, Dr. Subrata Jana, Dr. Apurba Sau Mondal, Dr. Sujan Biswas, Dr. Samik Acharya, Dr. Chandan Kumar Manna, Dr. Lakshman Patra, Dr. Rahul Naskar, Mr. Biswajit Bera, Mr. Atanu Maji, Mr. Sandipan Mandal, Mr. Amitabh Biswas, Mr. Subrata Mandal, Mr. Arpan Halder, Mr. Chandrasekhar Mandi, Miss Moumita Ghosh and Mr. Wasim Akram for their constant help and support throughout my research journey. The best part of my research period will be the memories I have with them. The journey was made much smoother and full of enthusiasm by the mere presence of all of them.

I express my deepest gratitude to my M.Sc. project supervisor, Dr. Braja Gopal Bag, Professor, Vidyasagar University for initializing the spirit of research through me during my masters which ultimately led me to begin this research journey. I also express my thankfulness to Mr. Animesh Pradhan, Mr. Pradip Shit, Mr. Prabir Ghorai and some other helpful friends and relatives of mine to support me continuously during my research journey.

I am incredibly grateful to my wife, Mrs. Mampi Bhunia, for her unwavering love, support and understanding during my pursuit of Ph.D degree that made the completion of my thesis possible.

I want to express my gratitude to my mother-in-law Mrs. Shamoli Bhunia and father-in-law Mr. Chandan Bhunia for their moral supports. Finally, I am very much indebted as well as lucky enough to have Mr. Natendra Nath Das and Mrs. Annapurna Das as my parents for their unconditional love, support, teachings and blessings which brought me this far without any pressure. I would also like to thank my loving elder sisters Mrs. Munmun Das and Mrs. Aditi Das for their blessings, encouragement and moral support during my research work. I would like to sincerely thank each and every one of the people mentioned above for their unwavering support, encouragement and love which gave me the strength and perseverance to successfully finish my research journey.

Akash Das

(Akash Das) 14/03/24

Department of Chemistry

Jadavpur University

CONTENTS

PREFACE

My thesis work entitled **"Promising bio-active transition metal complexes with azo/imine functional O N S donor ligands: Synthesis, characterization and in vitro anticancer activity"** contains new design as well as the synthesis of several transition metal complexes with different O, N, S donor azo/imine ligands. The synthesized complexes have been thoroughly studied by UV-Vis, fluorescence and ^{1}H and HRMS methods. In addition, anti-cancer activity of the metal complexes was studied in different cancer cell line and theoretical studies will have also been undertaken to probe the electronic structures of the complexes. Interaction with DNA and BSA with the newly synthesized metal complexes has also been explored. This thesis consists of six chapters based on the synthesis, structure elucidation and potential anti-cancer activity of various transition metal complexes.

Chapter I represents a brief introduction on the a review of the azo/imine ligands containing O N S donor site and different transition metal complexes of Palladium(II), Platinum(II), Ruthenium(II), Rhenium(I). The anti-cancer activities of the metal complexes and their interactions with DNA and BSA have been described.

Chapter II deals with the synthesis and characterization of 5-fluorosalicylaldehyde-4(N)-substituted thiosemicarbazones ligands and their Pd(II) complexes. Structure of the complexes are confirmed by single crystal X-ray diffraction method. Electronic structure of the complexes is interpreted by DFT/ TDDFT computations. The ability of the complexes to bind with CT-DNA and bovine serum albumin (BSA) are investigated by UV-Vis method and fluorescence method.

Chapter III introduces the synthesis and thoroughly characterization of new Pd(II) and Pt(II) complexes with ONS donor azo-thioether pincer ligand. Electronic structure, solution spectrum and redox properties of the complexes are interpreted by DFT/TDDFT studies. The binding properties of the complexes toward calf thymus DNA (CT-DNA) and bovine serum albumin (BSA) are investigated with the help of absorption and fluorescence spectroscopy. *In vitro* antitumor activity of the synthesized complexes was tested on human liver (HepG2), colorectal (HCT116) and human lung (A549) cancer cell lines using MTT assay.

Chapter IV deals with the synthesis and characterization of two novel morpholine-based Pd(II) and Pt(II) complexes with N,N′ donor ligand. Electronic structure and solution spectrum of the complexes are interpreted by DFT/TDDFT studies. The investigation of the biological characteristics of the complexes have been carried out focusing on the binding

properties with calf-thymus DNA (CT-DNA) and the affinity toward bovine serum albumin (BSA) investigated using UV-Vis and fluorescence spectroscopy. Finally, MTT assay has been used to evaluate the cytotoxic activity of the complexes against triple negative breast cancer cell line (MDA-MB-231) and normal kidney cell line (HEK-293).

Chapter V describes the synthesis and characterization of two new cyclometallated ruthenium(II) carbonyl complexes via C(aryl)-S bond activation. The compounds' electronic structure and UV-Vis spectra have been clarified by DFT and TD-DFT computations. The binding ability of complexes with calf thymus DNA (CT-DNA) and Bovine Serum Albumin (BSA) have been explored by absorption and emission titration methods. In addition, the *in vitro* cytotoxicity of the ligands and complexes against human breast cancer cell line (MCF-7), human lung cancer cell line (A549), triple negative breast cancer cell line (MDA-MB-231) and gastric adenocarcinoma cell line (AGS) were investigated by using the MTT assay.

Chapter VI deals with the synthesis and characterization of two new Rhenium(I) tricarbonyl complexes with ONS donor azo-thioether ligands. Electronic structures and spectral properties of the complexes were interpreted by DFT and TDDFT calculations. The binding properties of the complexes toward calf thymus DNA (CT-DNA) and bovine serum albumin (BSA) are investigated with the help of absorption and fluorescence spectroscopy. *In vitro* cytotoxicity of the fabricated complexes was tested on human breast epithelial adenocarcinoma cell line (MCF-7) and human breast epithelial cell line (MCF-10A) using MTT assay.

In brief, this thesis accounts the chemistry of different transition metal complexes with azo/imine functional O N S donor ligands. I am happy to note that the work has been published in international journals (**List of Publications**).

In keeping with the general practice of reporting scientific observation, due acknowledgement has been made whenever the work described as based on the findings of other investigators. I must take the responsibility of any unintentional oversights and errors which might have crept in spite of due precautions.

Akash Das 14/03/24

(Akash Das)

Department of Chemistry

Jadavpur University

CHAPTER-I

INTRODUCTION

Promising bio-active transition metal complexes with azo/imine functional O N S donor ligands: Synthesis, characterization and in vitro anticancer activity

I.1. General Introduction

Transition metal-based drugs offer variety in the chemical modification of ligands to fine-tune their bio-activity.[1-4] Based on the variable oxidation states, wide range of coordination numbers of these complexes, careful operation of these parameters can lead to the design of new complexes with unique biological properties. Following the pivotal discovery of the cisplatin, as an effective metal-based anticancer agent, a number of related platinum compounds have been designed and evaluated as anti-cancer agents.[5-10] Besides cisplatin, platinum-based drugs such as oxaliplatin, carboplatin, nedaplatin, heptaplatin and lobaplatin have been approved as current chemotherapeutic agents (Fig.I.1).[11-15] These drugs are employed in the treatment of a number of tumours, including lung, colorectal, lymphomas, testicular, cervical, bladder, head and neck cancers.[16] Despite of its clinical achievement in the treatment of certain tumors, it has many unpleasant side effects such as nausea, nephrotoxicity, ototoxicity, tumor resistance, neurotoxicity, bone and back pain, weakness, blood clots, fatigue and hair loss.[17-20] These severe side effect caused by cisplatin and its analogues oxaliplatin, carboplatin, nedaplatin, heptaplatin and lobaplatin, offer an encouragement for the breakthrough of novel platinum-based complexes bearing multidentate ligands which are alternative to cisplatin with higher potency, higher cancer cell selectivity and lower resistance. Therefore, a noteworthy number of different platinum complexes were fabricated with the aim to prevail over the disadvantages of cisplatin.[21-24] To date, besides platinum-based compounds, other metals such as palladium, ruthenium and rhenium have also been evaluated as anticancer agents.[25-39] Some of the non-platinum-based compounds that have found their way in human clinical trials are shown in Fig. I.2.[40-42]

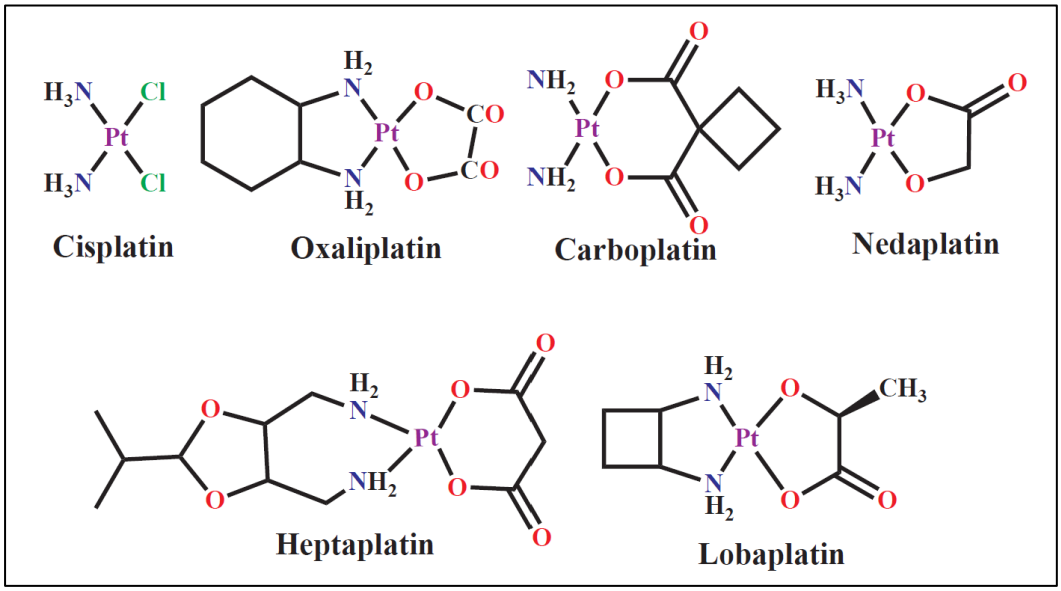

Fig. I.1. Platinum complexes currently being used in the treatment of cancer.

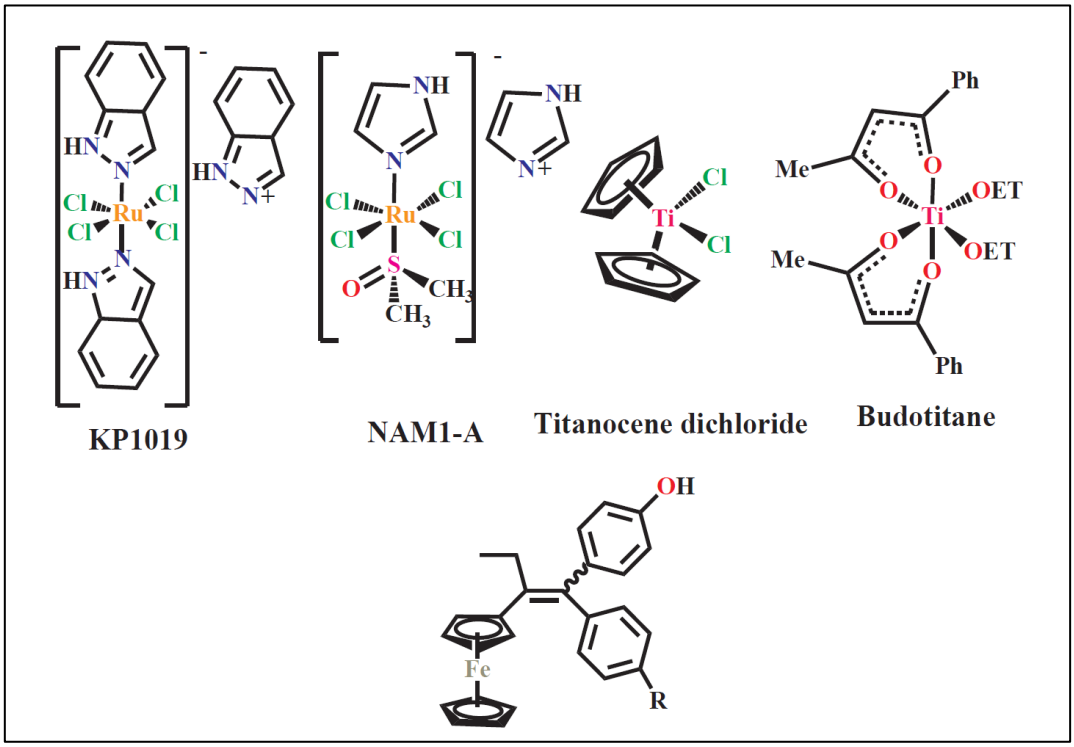

Fig. I.2. Non-Platinum based complexes currently undergoing clinical trials.

In this chapter, a discussion of the azo/imine functional ligands, their metal complexes and their general application is presented.

I.2. Transition Metals: Properties, coordination chemistry and potential applications

I.2.1. Palladium

palladium is a rare chemical element that is assigned the symbol Pd and the atomic number 46 and it belongs to 10th group and 5th period in modern periodic table. William Hyde Wollaston discovered the brilliant silvery-white palladium metal in 1803. He had given it the name palladium, from the Greek goddess of wisdom '*pallas*'. Catalytic converters use the maximum amount of palladium and its congener platinum to transform almost 90% of dangerous gasses from vehicle exhaust into less toxic substances. Palladium's oxidation states are 0, +1, +2, +4 and +6. The most common stable oxidation states are 0, +2 and +4. Six of the seven naturally occurring isotopes of palladium are stable: ^{102}Pd, ^{104}Pd, ^{105}Pd, ^{106}Pd, ^{108}Pd, ^{110}Pd. The most stable isotope is ^{106}Pd with 27.33% abundance. The catalytic preparation, utilization along with several others features of palladium complexes are elaborated in scheme I.1.

Palladium complexes have found extensive application in a range of catalytic processes involving C-C bond formation in diverse environments, such as carbon-hetero atom reactions, carbonylation, and allylic alkylation. Scheme I.1 displays a general overview of some of the most beneficial catalysts. When palladium metal is immersed in concentrated hydrochloric acid solution in presence of chlorine atmosphere, it generates chloropalladic acid (**1**) solution. Following the evaporation of this reddish-brown solution, palladium(II) chloride (**2**) is produced as a brown polymeric solid.[43] It is utilized in massive chemical manufacturing field as a carbonylation catalyst (Wacker-Hoechst process) for the transformation of ethylene to acetaldehyde, the formation of acetone from propene and in the synthesis of glycol derivatives.[44] Dichlorobis(acetonitrile)palladium(II), **3** is synthesized by the reaction using **2** in acetonitrile solution under refluxing condition to produce an orange/yellow crystalline solid. It serves as a hydro carboxylation catalyst and is employed in a number of cross-coupling processes, including Heck, Negishi, and Grignard.[45] Dichloro(bis(diphenylphosphino)ferrocene)palladium(II) dichloromethane (**4**) complex is synthesized by the reaction using **3** with the bis(diphenyl-phosphino)ferrocene in dichloromethane. It is employed in Buchwald-Hartwig, Stille, and Grignard coupling reactions as a catalyst.[46] Dichlorobis(tri-phenylphos-phine)palladium(II), **5** is prepared by reaction with triphenylphosphine in ethanol at 60°C temperature and a light yellow crystalline powder is produced in almost quantitative yield.[47,48] It serves as a catalyst for the carbonylation process that produces certain lactones and for the Sonogashira coupling of terminal alkynes with aryl halides.[49,50] Reaction of **2** with dibenzylideneacetone and sodium acetate in methanol at 60°C temperature produced tris(dibenzylideneacetone)dipalladium(0) (**6**). It is a highly useful catalyst for a wide range of carbon-carbon and carbon-heteroatom coupling processes. It is also utilized in specialized catalysis for Suzuki coupling of aryl chlorides with an Arduengo imidazolium salt to generate biphenyls. Another important complex, bis(tri-*tert*-butylphophine)palladium(0), **7** is synthesized by the reaction using **6** with tri-*tert*-butylphosphene in dimethylformamide solution to generate two sterically hindered phosphines (PBu^t_3) coordinated to palladium metal in the center in a linear fashion. These zero valent complex catalysts are used in the Negishi cross coupling of aryl and vinyl chlorides.[51]

Palladium powder dissolved in acetic acid reacts with nitric acid in the presence of refluxing conditions to produce palladium(II) acetate salt, **8**. It is employed as a catalyst to create substituted 1,6- and 1,7-dienes by the telomerization of butadiene.[52] The dichloro(1,5-cyclooctadiene)palladium(II) (**9**) complex is prepared by the reaction of **1** with 1,5-COD in

ethanol and is used as a catalyst to protect hydroxyl groups and also utilized in various organometallic coupling reactions.[53] Tetrakis(triphenylphosphine) palladium(0) (**10**) is a fascinating catalyst that can be utilized to catalyze sigmatropic rearrangements [3,3] and coupling reactions, especially the Sonogashira reaction.[54] The reaction of **2** with allyl chloride in methanol solvent in the presence of carbon monoxide has produced the significant catalyst π-allylpalladium(II), **11**. It finds extensive use in asymmetric alkylation, where the quaternary center formed by azolactone alkylation is transferred to a novel method utilized in the synthesis of sphingosines, an antifungal drug.[55-57]

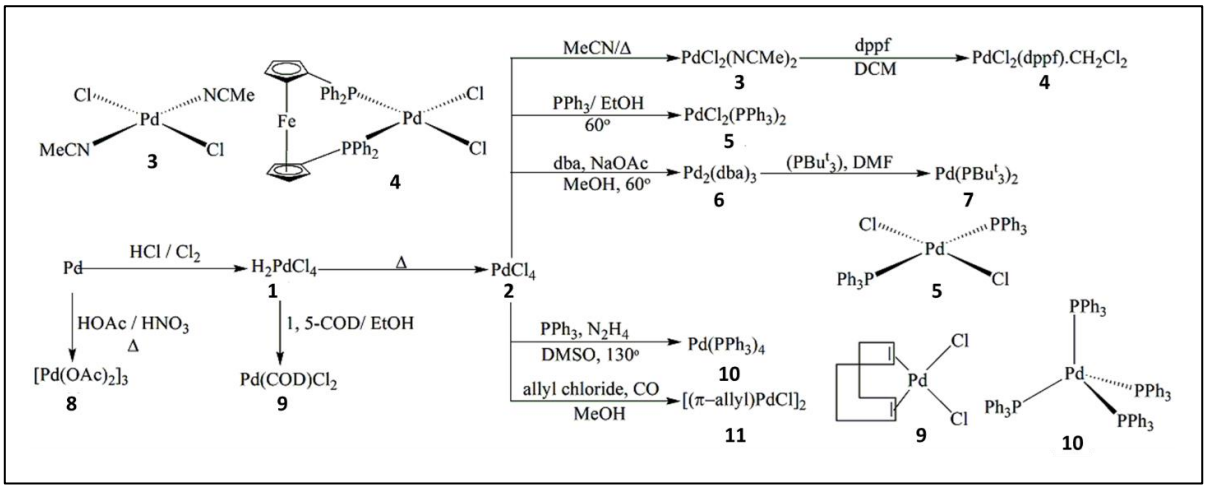

Scheme I.1. Preparation of palladium chemical products and their application

I.2.2. Platinum

This is the most valuable and rare transition platinum element with symbol Pt and atomic number 78 and it belongs to group 10th and 6th period in modern periodic table. Its name is derived from the Spanish term *platina*, means little silver. The platinum is a shiny, silvery-white metal when pure and it is also malleable and ductile. The term "malleable" means it can be pounded into a thin sheet and "ductile" means that it can be easily stretched into a wire. Oxidation state of platinum is +1, +2, +3, and +4. The most common stable oxidation states are +2 and +4. Sometimes platinum have an unambiguous +1 and +3 oxidation state and are stabilized by metal bonding in bimetallic or polymetallic species. Platinum has six naturally occurring isotopes ^{190}Pt, ^{192}Pt, ^{194}Pt, ^{195}Pt, ^{196}Pt and ^{198}Pt. The most stable isotope is ^{195}Pt with 33.83% abundance. Platinum is a metal that is widely used in jewelry, but it is also utilized as a catalyst to efficiently change engine emissions into less toxic waste products. The catalytic preparation, application along with several other uses of platinum complexes are explained in schemes I.2.

The hydrosilylation process used to synthesize silicone polymers and other similar compounds is the main use of the platinum complex. Its application in the functionalization of alkanes by C-H activation (Shilov activation), which creates methanol from methane, is another fascinating field.[58,59] The synthetic procedure of platinum complexes and their catalytic activity are established in scheme I.2. The platinum metal powder is immersed in aqua regia and then discharges nitrates to harvest chloroplatinic acid solution. This yellow/orange chloroplatinic acid solution can be crystallized by flash-cooling under liquid nitrogen atmosphere to generate yellow/orange hydrated crystalline solid of chloroplatinic acid **12**.[60] Then the chloroplatinic acid is treated with potassium chloride in water to produce potassium hexachloroplatinate, **13** as a yellow crystalline powder.[61,62] When it is treated with sulfur dioxide in hot water, potassium tetrachloroplatinate(II) salt (**14**) is produced.[63,64] It is used for Shilov activation, which at least initially works on C-H activation of alkane. The complex dichloro(1,5-cyclooctadiene)platinum(II) **15** is synthesized by the reaction of **14** with the addition of 1, 5 cyclooctadiene in isopropanol and the complex dichlorobis(diethyl-sulfide)-platinum(II), **16** is synthesized by inclusion of diethyl sulfide to an aqueous solution of **14**. The complex **15** is separated as a colorless crystalline solid, while **16** is isolated as a yellow crystalline powder. Both the complexes, **15** and **16** are used as hydrosilylation catalysts for industrial production of silicone polymers.[65-67] The Karstedt's catalyst, **17** is synthesized by treating divinyltetramethyldisiloxane in an inert solvent with **12** to produce the catalyst solution. This catalyst is widely employed to create cross-linked silicones, which are utilized in several applications like automotive gaskets and pressure-sensitive adhesives.[68]

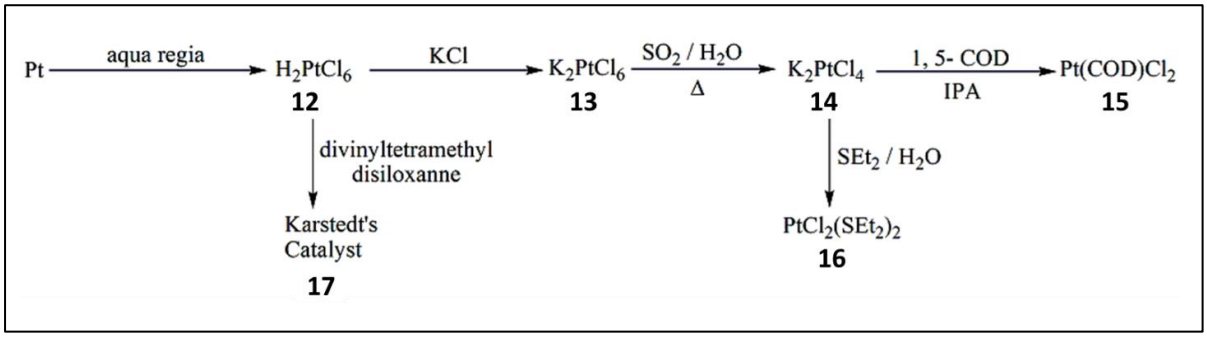

Scheme I.2. Synthesis of platinum complexes that demonstrate catalytic activity

I.2.3. Ruthenium

Ruthenium is a chemical element with symbol Ru and atomic number 44. Ruthenium constitutes the group 8 transition metals positioned in the second row of the periodic table. The German scientist Karl Karlovich Claus discovered the element in 1844 and named it after

his homeland, the Russian Empire (one of Russia's Latin names is Ruthenia). Ruthenium is exceedingly rare and is the 74th most abundant metal on earth found in platinum and other ores. The relative abundance is 7×10^{-3} %. Ruthenium complexes have special potential to operate as catalysts in a variety of organic transformation reactions with commercial applications because to ruthenium's broad range of oxidation states, from -2 to +8. On the other hand, this element's most stable oxidation states are +2 and +3. They are both essentially inactive, perhaps the latter more so than the former. This characteristic sets ruthenium apart from other elements in the periodic table and has been shown to be helpful in several single-electron transfer experiments. Ruthenium has 26 isotopes whose half-lives are known with mass numbers from 90 to 115. Of these 7 are stable: ^{96}Ru, ^{98}Ru, ^{99}Ru, ^{100}Ru, ^{101}Ru, ^{102}Ru, and ^{104}Ru. Naturally, with an abundance of 31.55%, ^{102}Ru is the most frequent isotope.

Ruthenium is finding a lot of new applications. The majority of this metal is utilized in the electronics sector for electrical connections and chip resistors. In the chemical industry, ruthenium oxide is used to coat the anodes of electrochemical cells that produce chlorine. In order to convert light energy into electrical energy, solar cells can employ molecules containing ruthenium. It is important to recognize that all ruthenium compounds are extremely hazardous and can cause cancer. The skin is highly stained by ruthenium compounds. Dietary ruthenium appears to be firmly stored in bones. Due to its extreme toxicity and volatility, ruthenium oxide, or RuO4, should be completely avoided.

Ruthenium complexes are widely employed in numerous organic transformation reactions, such as the transfer hydrogenation of ketones, oxidation of alcohols, olefin metathesis, and hydrogenation of alkenes. These reactions have been applied in a variety of application domains. The catalytic preparation, utilization and several other applications of ruthenium complexes are elaborated in schemes I.3 and I.4.

Ru(IV) oxide hydrate (**18**) is used as an ordinary beginning point for all value-added ruthenium chemical products. The binary ruthenium (IV) oxide as a hydrate, $RuO_2.xH_2O$, is precipitated by dissolving ruthenium metal powder in sodium hydroxide solution under a chlorine environment to create sodium ruthenate solution, which is then submerged in a moderate reducing agent (**18**).[69] $RuCl_3.xH_2O$ (**19**) is also an important primary synthetic precursor and widely used for the preparation of most of the ruthenium precursors. Concentrated hydrochloric acid is used to dissolve $RuO_2.xH_2O$. The resulting suspension mixture is refluxed and subsequently volume-concentrated to yield the hydrated ruthenium chloride, or $RuCl_3.xH_2O$ (**19**) salt, which is a crystalline solid that is black-brown and

hygroscopic. The ruthenium (III) chloride hydrate is useful for alkyne functionalization (such as the creation of vinyl carbamates with secondary amines, acetylene, and carbon dioxide) and can be used as an oxidation catalyst when NMO is present as a co-oxidant. It also acts as a catalyst for the metathesis polymerization of norbornene to form Norsorex in butanol solution.[70-72]

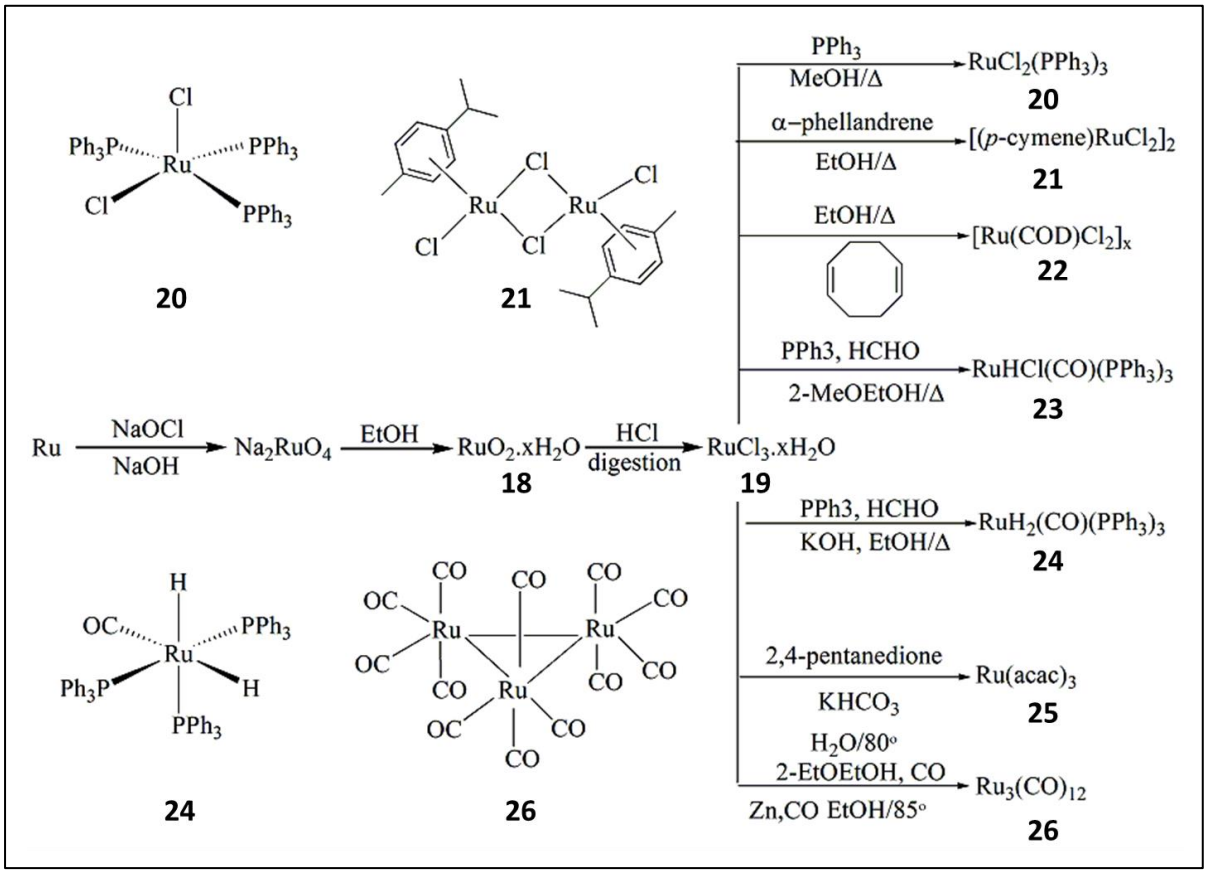

Scheme I.3. Fabrication of ruthenium chemical products having applications in catalysis

Dichlorotris(triphenylphosphine)ruthenium(II) (**20**) is also a appreciated synthetic precursor for the preparation of Ru(II) complexes with potential applications. It is prepared with reaction of $RuCl_3.xH_2O$ in presence of excess PPh_3 under refluxing condition in methanol.[73-81] It is a solid that has the color of chocolate and dissolves in organic solvents like benzene. The substance serves as a building block for further complexes, such as those involved in homogeneous catalysis. It is employed as a catalyst in reductions, cross-coupling, cyclization, and isomerization reactions as well as the oxidation of alcohols to aldehydes and ketones. In the Kharasch addition of chlorocarbons to alkenes, it is utilized.

It acts as a pre-catalyst in the hydrogenation of imines, ketones, carboxylic acids, nitro compounds, and alkenes. Using tert-butyl hydroperoxide, it catalyzes the oxidation of alkanes

to tertiary alcohols, amides to tert-butyldioxyamides, and tertiary amines to α-(tert-butyldioxyamides). The catalyst can oxidize alcohols to aldehydes or ketones by using oxygen, acetone, and other peroxides. Alcohols and amines can be easily N-alkylated by using dichlorotris(triphenylphosphine)ruthenium(II).

Dichloro(*p*-cymene)ruthenium(II) dimer (**21**) is also a good catalyst for transfer hydrogenations and is prepared by the dehydrogenative coordination of the proper cyclohexadiene with $RuCl_3.xH_2O$ under refluxing condition in ethanol.[82] It can arrange reactions in high enantiomeric excess when chiral ligands (e.g., BINAP: 2,2'-bis(diphenylphosphino)-1,1'-binaphthyl) are present. High quantitative yield dichloro(1,5-cyclooctadiene)ruthenium(II) oligomer (**22**) is produced by reacting 1,5-cyclooctadiene with $RuCl_3.xH_2O$ in an ethanol solution during refluxing.[83] The compound is used to create ruthenium-BINAP complexes as a catalyst precursor. Simple ketones can be asymmetrically hydrogenated using BINAP/diamine-Ru catalyst, whereas functionalized ketones can be hydrogenated asymmetrically using BINAP-Ru catalyst. Many medications, including the antimicrobial levofloxin, the antibiotic carbapenem, and the antipsychotic medicines, are made using these hydrogenations.

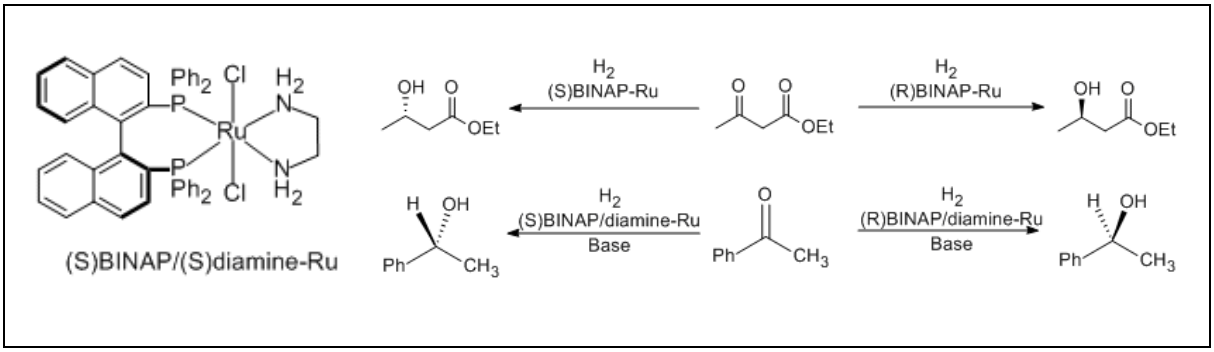

$Ru(H)(Cl)(CO)(PPh_3)_3$](**23**), an essential ruthenium carbonyl precursor, is created when excess PPh_3 reacts with $RuCl_3.xH_2O$ in the presence of formaldehyde while refluxing in 2-methoxyethanol.[84] It is used in the silylative coupling of vinyl alkyl ethers with vinyl silanes and has a broad variety of catalytic applications in the metathetical ring closure of silacycles. The dihydridocarbonyltris(triphenylphosphine)ruthenium(II) $[RuH_2(CO)(PPh_3)_3]$ (**24**) is produced in the same manner as that of complex **6** except that the reaction is carried out with base KOH under refluxing in ethanol solution. It has major application in the coupling of olefins to aromatic ketones via C-H bond activation.[85] The tris(2,4-pentanedionato)ruthenium (III), **25** is formed by the reaction of $RuCl_3.xH_2O$ with excess 2,4-pentanedione in hot H_2O

buffered with $KHCO_3$. It is utilized to demonstrate the catalytic utility of terpene and has vast applications in the sectors of materials science and electronic devices.[86-88] $Ru_3(CO)_{12}$ (**26**) is used as carbonylation catalyst and has application in acylate aromatic heterocycles via C-H bond activation under carbon monoxide atmosphere and has synthesized olefins to pyridyl ketones regiospecifically at the ortho position.[89-92] The chemical properties of $Ru_3(CO)_{12}$ are widely studied and the cluster can be converted to hundreds of derivatives. High pressures of CO convert the cluster to the monomeric ruthenium pentacarbonyl, which reverts back to the parent cluster upon standing. Bis(tricyclohexylphosphine)-3-methyl-2-butenylideneruthenium (IV) dichloride, **27** is synthesized using complex **22** in presence of PCy_3 under a hydrogen atmosphere to produce the intermediate η^2-H_2 complex which is then further treated with a propargyl chloride. In the process of olefin metathesis, the ruthenium carbene complex family includes the complex **27**. The ruthenium carbene community of olefin metathesis catalysts is referred to as "Grubbs Catalysts" because to Robert H. Grubbs' discovery of them.[93-95] These complexes have shown to be extremely useful in the production of chemical compounds and polymers. These catalysts have significant functional group acceptance, are less problematic to work with than previous molybdenum and tungsten complexes, and can catalyze almost any kind of olefin metathesis (such as ring-opening metathesis polymerization, ring-closing metathesis, acyclic diene metathesis polymerization, etc.) in a variety of solvents.[96] The complex bis(2-methylallyl)(1,5-cyclooctadiene)ruthenium(II), **28** is prepared by the reaction of **22** with the Grignard reagent at 0°C temperature and diligently isolated **28** as a lightly tanned thermally sensitive solid. It serves as a pre-catalyst when a chiral ligand is present, and PPG-Sipsy used it to create candoxatril, a cardiovascular medication that Pfizer promoted in the middle of the 1990s.[97,98]

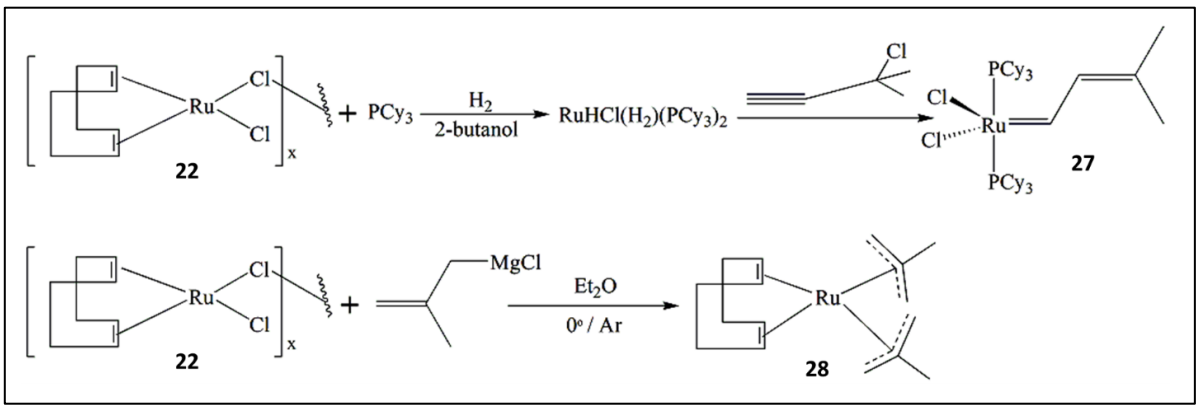

Scheme I.4. Formation of higher-value added ruthenium products that are used in catalysis

I.2.4. Rhenium

Rhenium belongs to period 6 and is the heaviest element in group 7. Nodaack et al. first discovered it in 1925 and later isolated from Molybdenite ores. Re is usually found in the Earth's crust in association with other metals, such as, Mo, Cu, Pd, Zn, Pt. Re isotopes are applied most prominently in the field of geology, cosmology and medicine.[99] Rhenium complexes have exhibited promising potential in catalysis. They can be used in oxygen-atom-transfer reaction, oxidation reaction, isomerization or etherification of allylic or propargylic alcohols, the Beckmann rearrangement of oximes, olefin metathesis etc[100], although commercial applications have been limited to date. The rich photophysical, photochemical, and redox properties of polypyridyl transition metal complexes make them more useful in a wide range of fields, including energy conversion[101,102], medicine[103], cellular imaging[104] and DNA sensing.[105] These metal complexes are useful because of their rich photophysical behavior, potential redox reactivity, and stability in a wide range of chemical conditions. Furthermore, these compounds' general synthetic exibility and modularity make it simple and systematic to modify these characteristics. Re complex of family fac-[$Re(CO)_3$(diimine)(L)] have been employed as probes in time-resolved infrared (TRIR) spectroscopy, where L is typically a cyclic imine or a halide. Vibrational modes which involve the tricarbonyl ligand set provide three unique and specific transition moments that are well removed energetically from those of organic carbonyl groups. These are the totally symmetric in-phase υ (CO) vibration which appears in ground state vibrational spectra near 2030 cm^{-1}, and the totally symmetric out-of-phase and equatorial asymmetric modes, which appear near 1920 cm^{-1}.[106] Elaborate photophysical and photochemical pathways can be elucidated by monitoring changes in the energies of these modes following electronic excitation of the complex.[107] Because the carbonyl ligand stretching frequencies are energetically isolated from most organic vibrational modes, these complexes are especially suitable for use in the study of biomolecular photophysics and redox chemistry. For example, by coordinating $ReI(CO)_3$(4,7-dimethyl-1,10-phenanthroline) to histidine 124 in Pseudomonas Aeruginosa azurin, researchers were able to follow the kinetics of charge transfer from the Re photooxidant to the Cu(I) center of the protein by observing changes in the vibrational frequencies of the Re CO ligands.[108,109] This work was based on an intervening aromatic residue such as tryptophan can serve as an intermediate in a multistep tunneling mechanism between the photooxidant and the Cu center, increasing the rate of charge transfer by several orders of magnitude. Similarly, early studies have appeared in which tricarbonyl Re complexes were used to trigger the oxidation of DNA.[110,111]

I.3. Polydentate ligands

In laboratories in the pharmaceutical, academic, and industrial sectors, efforts have been made from the start to synthesize novel and inventive ligand complexes for a variety of uses. In addition to controlling the metals, the ligands that form complexes with transition metal ions can also influence coordination number, coordination shape, and formal oxidation state.[112] The increased stability of metal-ligand complexes that these species provide to the metal site to which they are coupled has sparked interest in the production of polydentate ligand. The resultant metal-chelate complexes exhibit a greater degree of stability toward the circumstances than are not seen with comparable monodentate ligands.[113] The synthesis of unsymmetrical polydentate ligands that contain a number of electronically different donor sites has tremendous interest because the metal centre has variety of possible coordination environments.[114] When a ligand possesses both soft and hard donor moieties, it can partially dissociate, creating an empty coordination site at the metal that is "masked" in the ground state. This could result in some unusual behavior.[115] This phenomenon holds significant promise for application in catalysis since, during the catalytic cycles, the ligand does not entirely disappear from the metal's coordination sphere.

It is possible to responsively control the coordination at a particular metal center by varying the ligand's structure and the type of its donor sites. Thus, a substantial effect on the reactivity of the metal complexes should result from the existence of electrically distinct donor pieces inside the same metal scaffold. On the basis of Pearson's "hard-soft-acid-base" (HSAB) theorem, it is expected that soft late transition metals will bind more strongly to softer, more polarizable donor moieties and conversely harder less polarizable donor fragments will preferentially bind to the earlier metals.[116] For this reason, it is preferable to incorporate several electronically distinct donors into a single ligand framework, for example, a variety of softer donors like phosphines and thiols to contrast with more rigid oxygen and amine donors. Organochalcogen ligands typically exhibit larger trans influences than nitrogen donors, which in turn exhibit smaller trans influences than tertiary phosphines. By combining a range of donor atoms, the variations in their trans effects may be utilized in their ensuing complexes.[117] Most notably, the systematic change of the donor functionality results in a family of closely related ligands, which makes it possible to thoroughly examine the complete coordination capabilities of the resulting multidentate ligand family using metal centers.

I.3.1. Nitrogen donor ligands

The Classical or Werner's complexes where the metal binds to a heteroatom have been known since the early 19th century. These complexes are some of the simplest ligands and metal-ligand bonds. It was these types of complexes with which the research in coordination chemistry began. Although amine ligands have been extensively studied in coordination chemistry, they are not as common in organometallic chemistry. There are two main reasons for this: a) the N-H bond of the coordinated amine tends to be very reactive, and b) amines prefer class A metals and most organometallic chemistry focuses on class B metals which tend to coordinate only weakly. When amines do appear in organometallic chemistry it is most often with the borderline metals, there is less of a hard/soft mismatch. The coordination can be strengthened by replacing monodentate amines with polydentate ligands such as ethylenediamine, due to the chelate effect.[118]

Nitrogen donor ligands are available in the range from simple amines such as ethylenediamine, mentioned above, to pyridine ligands, such as 2,2'-bipyridine (bipy) and phenathroline (phen), oxazolines, porphyrins, and imines. Pyridine, imine and oxazoline based ligands are more common in organometallic chemistry as they are softer than amines.[119,120] In many cases the ligands are multidentate and include other heteroatoms such as phosphorus and oxygen. One famous class of N, O donor ligands are the salens, which have been used in both catalysis and coordination chemistry. The use of chiral amines leads to chiral salens suitable for asymmetric catalysis, e.g. the Jacobsen epoxidation.[121]

I.3.2. Oxygen/Sulphur containing ligands

There are many examples of sulphur and oxygen-based ligands and their applications are widespread in the literature. Comparatively, the harder oxygen donors, in paricular oxo-ethers, show stronger interactions with s-block and the earlier metals, most probably the best example of these donor ligands being those of crown ethers. Synthesis of the ligand with thioether donor centre in a chelated environment with additional N and O donors in acyclic/macrocyclic backbone is a fascinating field in coordination chemistry to develop good working models to account the role of metal ions in biological systems.

Many research groups are working for the synthesis of different sort of ligand containing N, S donor site to examine the role of metal ions in biological system, extraction of environmentally harmful heavy metal ions from common consumables. Several N_xS_y donor ligands have been designed where N belongs to aromatic nitrogenous systems like pyridine, imidazole, pyrazole, benzimidazole and their reactivity have been investigated with

different transition and non-transition metals.[122-126] There has been a considerable research interest to synthesize chemical analogues of the active site of metalloproteins and some of the bioactive molecules carry N, S donor centers. Synthesis of ligands with thioether donor center in a chelated environment with additional N and O donors in acyclic/macrocyclic platform is important in coordination chemistry to develop good working models.[127-128] In terms of their soft-hard donating ability, excited state and photophysical properties, generation of anticancer-platinum drugs with reduced nephrotoxicity etc. N_xS_y systems are attracting different fields of research.

I.3.3. Phosphorus donor ligands

Phosphines are regarded as σ-donors due to the lone pair on phosphorus that can be donated to the metal. The strength of σ-donation increases when the electron density on phosphorus has been increased through the use of electron-donating substituents on R. They can also act as π-acceptors (sometimes referred to as π-acids), with the σ^*-orbital of the P-R bonds playing the role of acceptor (Scheme I.5). Alkyl phosphines are the weakest π-acceptors, followed by aryl phosphines, then phosphites, with PF_3 being similar to CO.[129] Electron-withdrawing substituents on R favors π-back donation. Though it is complicated to separate out the σ-donor and π-acceptor properties of the phosphine by experimental methods, there have been numerous computational methods which can be applied.[130] These studies validate the fact that phosphines are both σ-donors and π-acceptors, with σ-bonding primarily arising from the lone pair of phosphorus, and π-bonding arising from the donation of electron density from the metal into an empty orbital of the ligand exhibiting phosphorus *3p* character.

Hofmann published a description of triethylphosphine platinum trichloride, the first phosphorus-metal combination, in 1857.[131] Since then, phosphines (PR_3) have become a traditional and versatile ligand class for transition metal complexes. In PR_3, the steric and electronic properties can be altered in a systematic and predictable fashion by varying R (R = aryl, alkyl), allowing for a wide range of ligand reactivity profiles to be accessed.[132]

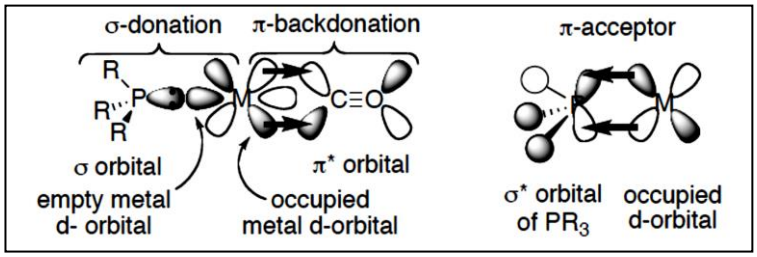

Scheme I.5. Phosphines as σ-donor and π-acceptor.

I.4. Schiff bases and their transition metal complexes

Schiff base ligands are synthesized from condensation of primary amines with carbonyl compounds and they were discovered by a German chemist, Nobel Prize winner Prof. Hugo Schiff in 1864.[133,134] Structurally, Schiff base ligands (also known as an imine or azomethine) are an analogue of an aldehyde or ketone in which carbonyl group (C=O) has been replaced by an imine or azomethine group.[135] Whereas the Schiff base ligands of aromatic aldehydes, which have an efficient conjugation mechanism, are more stable, those of aliphatic aldehydes are rather unstable and readily polymerize. Because they have the capacity to generate a variety of stable metal complexes, Schiff base ligands are crucial in the field of coordination chemistry.[136]

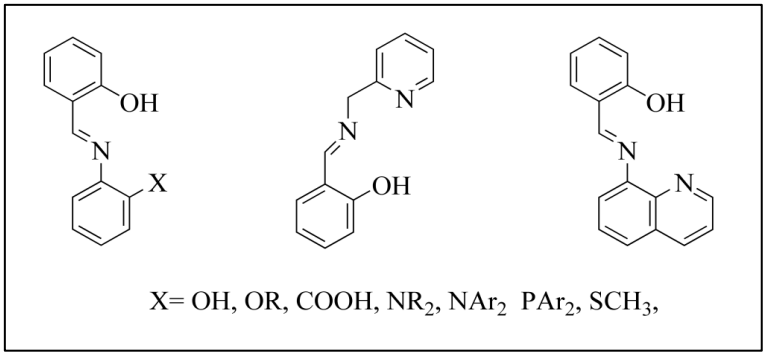

X= OH, OR, COOH, NR_2, NAr_2 PAr_2, SCH_3,

The Schiff base binds with heterocyclic compounds that contain heteroatoms like N, O, and S. In azomethine derivatives, the C=N linkage is essential for catalysts, as well as in a variety of biological systems, polymers, pigments, antifertility medications, and enzyme agents.[137] The presence of lone pair electron in sp^2 hybridized orbital of nitrogen atom of azomethine is of significant biological and chemical importance. The Schiff base ligands are excellent chelating agents; in most cases, stable complexes with different transition metals are more easily formed by bi- or tri-dentate ligands.[138] Schiff base ligands provide exceptional selectivity, sensitivity, and stability for a particular metal ion, making them useful as cation carriers in potentiometric sensors.[139] When hydrogenating olefins, the Schiff base complexes demonstrate catalytic characteristics. Because of their early accessibility and structural flexibility, schiff base metal chelates have remained crucial to stereochemical models in main group and transition metal coordination chemistry. Schiff bases with extra donor centers in the imine portion of the molecules and on the ligand's periphery produce a vast number of compounds with a variety of characteristics. Bioinorganic chemistry, material science, coordination polymers, and other fields have benefited greatly from the variation flexibility in both the aldehydic and amine parts, which can enhance multidimensional complexes.[140-142]

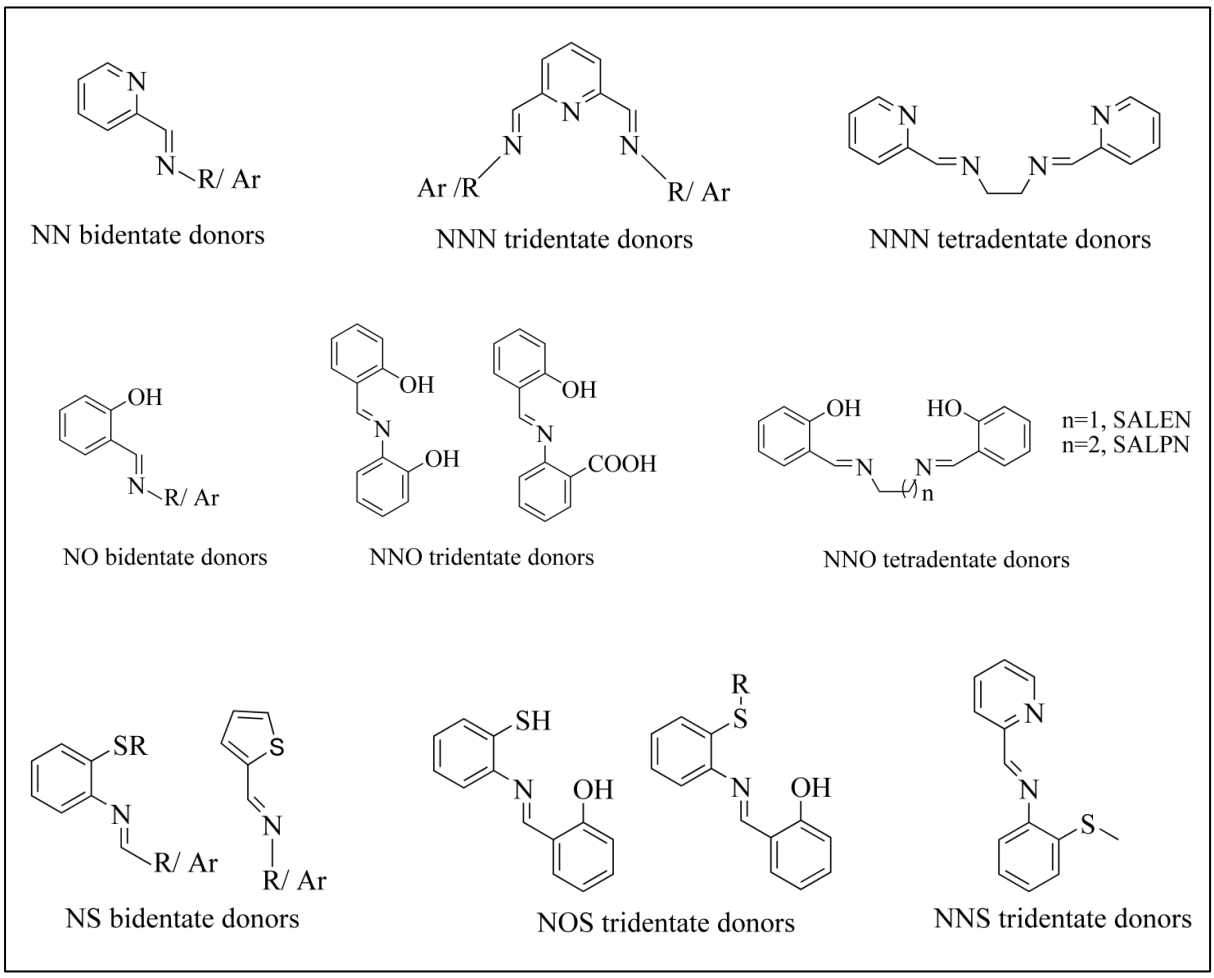

Scheme I.6. Some representative examples of Schiff base ligands.

I.5. Azo functionalized ligands and their transition metal complexes

Transition metal complexes with azo ligand coordination chemistry is a significant and intriguing area of study in chemistry. The coordination chemicals, which include azo ligands, are essential to industry, technology, and biological systems. The presence of the functional group azo group (-N=N-) distinguishes azo compounds. Because it has a low-lying azo centered anti-bonding pi-molecular orbital, the azo group is photochromic, redox responsive, pH sensitive, and stabilizes low valent metal oxidation states. It is also utilized as a metal ion indicator in complexometric titration and in textile industry dyes and pigments.[143,144] They have significant applications such as optical data storage, photo switching, and nonlinear optical materials. They also have outstanding thermal and optical characteristics and are highly colored. Inhibition of DNA, RNA, and protein synthesis, carcinogenesis, and biological activity against bacteria and fungus are only a few of the biological reactions they are engaged in.[145,146]

Due to the presence of mixed soft-hard donor character (O, N and S donor sites), azo compounds show versatile coordination behavior[147], diverse pharmacological properties[148] and optical and thermal properties. The remarkable chemical and physical features of azo-azomethine compound transition metal complexes have drawn attention. Metalized azomethines offer better thermal stability, simpler absorption wavelength adjustment, and more optical stability as compared to free ligands.[149]

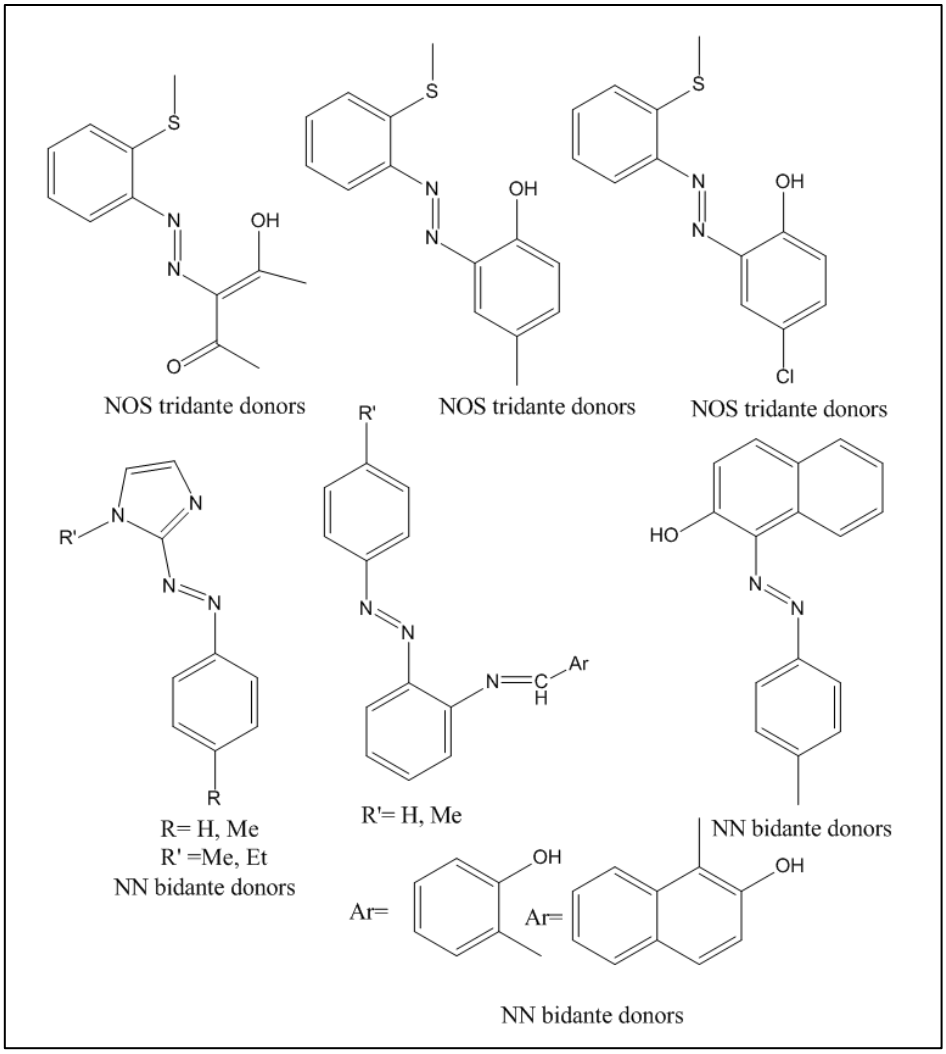

Scheme I.7. Some representative examples of azo ligands.

The complexes of azo metals are generally classified into two subcategories: those where the azo moiety is involved in bonding and those where it is not. The preceding one is based on azo compounds with donor functions like -OH, -NH2, -COOH, -SH, -SR etc. in a congenial position so as to form six or five membered chelates. Since the azo moiety is a poor donor in the absence of another donor group, it forms persistent chelates when it interacts with other strong donors such as OH, NH2, or C=O. The formation of azo moiety in an N-heterocycle

with C=N bond in a conjugated state generates azo heterocycle which bears this azoimine function. These classes of molecules are π-deficient and can be stabilized low valent metal redox state and exhibit metal to ligand charge transfer (MLCT) transitions.[150] The physical and chemical characteristics of azo compounds may be greatly altered by altering the ring size, amount of heteroatoms, substituents in the heterocyclic ring, and side arm to azo function; far larger modifications can be achieved by altering the heterocyclic portion. Most important changes have been received from replacing five membered N-heterocyclic by six-membered N-heterocyclic since six membered N-heterocycles being π-deficient are excellent π-acceptors while five-membered N-heterocycles are much poorer π-acceptors. Moreover, tridentate azo compounds are more stable than bidentate azo compounds.

I.6. Metal Carbonyl Complexes

The carbonyl group is one of the most common ligands in inorganic and organo-metallic chemistry. Carbon monoxide is the most common π acceptor ligand in organometallic chemistry. Homoleptic carbonyls (a complex only containing the carbonyl ligand) can be prepared for most of the d-block metals. Because it may absorb electron density from the metal center, the carbonyl ligand is able to stabilize low oxidation states at the metal center. Because of this, there has been a rapid development in the study of transition metal carbonyl (TMCC) donor–acceptor complexes.[151] It is evident from the previous findings that the complexation between CO and a transition metal M is carried out by two mechanisms.

1. A donor–acceptor σ-interaction 5σ(CO) → d(M), i.e. electron donation from the 5σ orbital to the unfilled M orbitals, leads to strengthening the C–O bond and an increase in the υ and k values.

2. A dative π-interaction dπ(M) → 2π*(CO), i.e. electron donation from the relevant filled metal d orbitals to the unfilled 2π* orbitals, results in weakening the C–O bond and a decrease in the υ and k values. Hence, the two oppositely directed interactions influence the carbonyl stretching frequency, υ and force constant, k; the latter being a more accurate measure of C–O bond strength.

It is evident that increasing electron density on M atom causes the deshielding of M-CO fragments carbonyl resonance and the chemical shifts δ reflect the electronic effects of groupings bonded to M.[152] Besides, the combination of these two interactions gives rise to the positive charge q+ on the carbonyl carbon. Metal carbonyl complexes have been evaluated as catalysts for a wide range of reactions, especially related to carbon mono-oxide utilization.[153]

Substitution of carbon mono-oxide ligand by various monodentate & polydentate ligands can be carried out using thermal and photochemical reactions.[154] The use of these chelates in biomolecule modeling, chemical and biological reactivity studies, and nuclear medicine has made coordination chemistry of transition metal carbonyl complexes with nitrogen, oxygen, and sulfur donor ligands the talk of chemists in recent years. Due to its ability to fluctuate in oxidation state from +II to +VIII, ruthenium-oriented oxidations among second-row transition metal ions offer a wide range of applications. The possible antitumor actions of some octahedral ruthenium and rhenium carbonyl complexes have drawn significant attention in the field of medical inorganic chemistry. Because of their low toxicity profile, ruthenium complexes also show promising pharmacological characteristics.[155]

The number of carbonyls and the variety of their reactions are enormous. In recent years increasing attention has been given to photochemical reaction. These derive from two main types of primary photo processes: (i) photoejection of a CO ligand. (ii) M-M bond scission. Virtually every metal carbonyl can undergo loss of one CO group to generate a reactive intermediate. The M-M bonds have a strongly absorbing $\sigma \rightarrow \sigma^*$ transition, the excitation of which will generate M(CO)x radicals. The photogeneration of $M(CO)_5$ from $M(CO)_6$, M=Cr, Mo, W, has been extensively studied.[156] In M-M bond photolysis process may often be accompanied by CO ejection, thus leading to more complex reaction[157], and also that species such as $(C_5H_5)_2Mo_2(CO)_4$ and $(C_5H_5)_2Fe_2(CO)_4$ as well as binary carbonyls such as $Mn_2(CO)_{10}$ can be photolyzed to metal -based radicals.

For M-CO units, nucleophilic assault at the carbon atom is a significant universal reaction. Reactions of this kind, particularly those involving H¬ or OH as the nucleophile, have been extensively researched because they serve as a model for reactions involving the water gas shift and other reactions involving CO in alcohols or water.

I.7. Cyclometalation

Scientist Trofimenko first introduced the term “cyclometallation”[158] to describe those reactions in which a ligand undergoes an intramolecular (or more rarely, intermolecular) metalation with formation of metal-carbon σ bond. Metalations of phenyl-substituted ligands have been most frequently described, and termed Ortho metalation, but the wider scope of these reactions are recognized as cyclometallation (Scheme I.8).[159] Cyclometallation has received considerable attention due to the probable representation of the mildest route for activating strong C-H and C-R bonds. Ever since, the first cyclometallated complex was synthesized, cyclometallation has been played an important part of organometallic chemistry

and several reviews covering the subject have been appeared. The first reported example of "C-H activation" by a transition metal complex is attributed to *Chatt*.[160] The cyclometallation reactions have been used for a long time and they constitute one of the most important parts of modern metalorganic chemistry. So far, the most of the cyclometallation reactions occurs via C–H bond activation, but examples of carbon-carbon, carbon-oxygen, and carbon-silicon bond activation (*i.e.* R = C, O, Si in Scheme I.9) are also known.

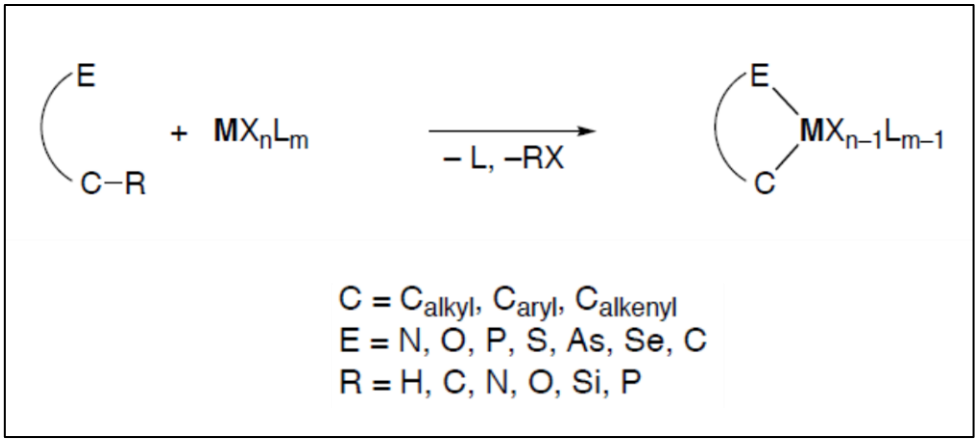

Scheme I.8. Cyclometallation by C-R bond activation, E = donor atom, M = transition metal, X = leaving group.

The chelation in cyclometallation supports the generally highly susceptible M-C bond which results in organometallic compounds with increased stability. This enhanced stability may have been relevant in the early discovery of the reaction and may have encouraged further developments, making cyclometallation one of the most convenient methods for creating a metal-carbon bond. Almost all transition metals have been successfully employed for cyclometallation. The platinum group metals Ru, Os, Rh, Ir, Pd and Pt have great attention, with palladium being the transition metal that has been studied in greatest detail. Hence, mechanistic data are particularly vast for cyclopalladation reactions. Scheme I.9. Cyclometallation, E = donor atom, M = transition metal, X = leaving group. Besides its genuine interest in the mechanism and scope of this fundamental bond-activation process, cyclometallation is a highly attractive and versatile synthetic method for creating organometallic entities, with wide application potential. Metallacycles have been successfully applied in traditional domains surrounding organic transformations and catalysis,[161] especially the catalytic activation of C-H bonds in un reactive alkanes,[162] and the stabilization of reactive intermediates.[163]

I.8. Theoretical calculations

Basic ideas behind DFT

Density functional theory (DFT) provides a powerful tool for computations of the quantum state of atoms, molecules and solids, and molecular dynamics. It has firmly established itself as the workhorse for electronic structure of matter-wave functions with density functional and quantum chemical systems, as well as atomic-level modeling of condensed matter phases.[164] Density functional theory techniques have made significant contributions to the theoretical explanation of charge distribution and associated features, such as chemical reactivity descriptors of chemical compounds.[165] However, DFT has made it possible for theoretical chemistry to precisely predict the structures and energetics of molecules and clusters throughout the past ten years. Thus, these reactivity descriptors that are derived directly from DFT calculations also deserve further attention at this time.

Significance of Density Functional Theory (DFT)

- The density functional theory (DFT) is presently the most successful (and also the most promising) approach to compute the electronic structure of matter and chemical reactivity.
- Its applicability ranges from atoms, molecules and solids to nuclei and quantum and classical fluids.
- In its original formulation, the density functional theory provides the ground state properties of a system, and the electron density plays a key role.
- DFT predicts a great variety of molecular properties: molecular structures, vibrational frequencies, atomization energies, ionization energies, electric and magnetic properties, reaction paths, etc.
- The original density functional theory has been generalized to deal with many different situations: spin polarized systems, multicomponent systems such as nuclei and electron hole droplets, free energy, superconductors with electronic pairing mechanisms, relativistic electrons, time-dependent phenomena and excited states, bosons, molecular dynamics, etc.

General Application Density Functional Theory (DFT)

- Total molecular energy calculation and study of tautomerisation
- Molecular Geometry optimization and to assign electronic structure

- Frequency calculation is done for vibrational mode and thermochemical analysis
- Spin density calculation and to explain EPR, magnetic and redox properties
- IRC (Intrinsic reaction coordinate) is done to follow the reaction path ways
- Scanning of potential energy surface.
- Potential energy surface
- To test the stability of wave functions
- Predicting and interpreting of other molecular properties and some common spectra

Time-dependent density function theory (TDDFT)

Overview

Time-dependent density functional theory) is a quantum mechanical theory used in physics and chemistry to investigate the properties and dynamics of many-body systems in the presence of time-dependent potentials, such as electric or magnetic fields. The effect of such fields on molecules and solids can be studied with TDDFT to extract features like excitation energies, frequency-dependent response properties, and photo absorption spectra.

The formal foundation of Time-dependent density function theory TDDFT is the Runge-Gross (RG) theorem (1984)[166] the time-dependent analogue of the Hohenberg-Kohn (HK) theorem (1964).[167] The RG theorem shows that, for a given initial wave function, there is a unique mapping between the time-dependent external potential of a system and its time-dependent density. This implies that the many-body wave function, depending upon 3*N* variables, is equivalent to the density, which depends upon only 3, and that all properties of a system can thus be determined from knowledge of the density alone. Unlike in DFT, there is no general minimization principle in time-dependent quantum mechanics. Consequently, the proof of the RG theorem is more involved than the HK theorem.

Given the RG theorem, the next step in developing a computationally useful method is to determine the fictitious non-interacting system which has the same density as the physical (interacting) system of interest. As in DFT, this is called the (time-dependent) Kohn-Sham system. This system is formally found as the stationary point of an action functional defined in the Keldysh formalism.[168]

The most popular application of TDDFT is in the calculation of the energies of excited states of isolated systems and, less commonly, solids. Such calculations are based on the fact that the linear response function - that is, how the electron density changes when the external potential changes - has poles at the exact excitation energies of a system. Such

calculations require, in addition to the exchange-correlation potential, the exchange-correlation kernel the functional derivative of the exchange-correlation potential with respect to the density.[169]

Utility of Time-dependent density functional theory

Time-dependent density functional theory TDDFT is an extension of density functional theory (DFT) and the conceptual and computational foundations are analogous - to show that the (time-dependent) wave function is equivalent to the (time-dependent) electronic density, and then to derive the effective potential of a fictitious non-interacting system which returns the same density as any given interacting system. Because the time-dependent effective potential at any given instant depends on the density value at all prior times, the problem of building such a system is more complicated for TDDFT. As such, the implementation of TDDFT involves developing time-dependent approximations later than DFT.

Basis set

A basis set in theoretical and computational chemistry is a set of functions (called basis functions) which are combined in linear combinations (generally as part of a quantum chemical calculation) to create molecular orbitals. In modern computational chemistry, quantum chemical calculations are typically performed using a finite set of basic functions. In these cases, the wave functions of the system in question are represented as vectors, the components of which correspond to coefficients in a linear combination of the basic functions in the basis set used.

Popular Software

- Gaussian Software Package (chemistry, Hartree-Fock, correlated approaches. current version: Gaussian09)
- Amsterdam Density Functional (ADF)
- Gamess-UK (chemistry, Hartree-Fock, DFT, correlated approaches)
- VASP (DFT, planewave, ultrasoft, PAW)
- ORCA
- Jaguar
- Turbomole
- Spartan

I.9. Physical measurements

(i) **Melting point determination:** Melting Point of the compounds was determined using a digital melting point apparatus.

(ii) **Elemental analysis:** Microanalytical data (C, H, N) were collected on a Series–II CHN-2400 CHNS/O elemental analyzer, Perkin Elmer, USA using the pure solid sample.

(iii) **FTIR spectra:** FTIR spectra were obtained on a Perkin Elmer; model RX–1(KBr disk, 4000–400 cm^{-1}) spectrometer with samples prepared as KBr pellets.

(iv) **UV-VIS spectra:** Absorption spectra were studied on a Perkin Elmer, Lambda 750 spectrophotometer using the solution of required concentration in acetonitrile. Solution will be kept in a quartz cell and absorption spectra will be recorded starting from visible to UV region.

(v) **Emission Measurements:** Emission properties were measured using Perkin Elmer LS 55 fluorescence spectrophotometer at room temperature (298 K).

(vi) **^{1}H NMR spectra:** ^{1}H NMR spectra were recorded by Bruker (AC) 300 MHz FTNMR spectrometer.

(vii) **Single crystal X-ray diffraction study:** Attempts were taken to obtain single crystals of the compounds by slow evaporation of solvent from solutions, or from the diffusion of another solvent into a solution of the compounds. Data were collected with an automated Bruker AXS Kappa equipped with an Apex-II CCD diffractometer with area detector using a graphite monochromated Mo-Kα radiation (λ = 0.71073 Å). X-ray data reduction, structure solution and refinement will be done by using SHELXS-97 and SHELXL-97 programs. The structures were solved by direct method.

(viii) **Mass Spectroscopic study:** ESI mass spectra were recorded on a micro mass Q-OF mass spectrometer.

(ix) **Electrochemical studies:** Electrochemical measurements were performed using computer-controlled CH-Instruments, Electrochemical workstation with Pt-disk milli electrode. All measurements were carried out in acetonitrile solution under dinitrogen environment at 298 K with reference to vs Ag/AgCl at 100 mV s^{-1} scan rate using Pt-bead working electrode and $[nBu_4N]ClO_4$ as supporting electrolyte. The reported potentials are uncorrected for junction potential.

I.10. Biological Activities

I.10.1. Antitumor and Cytotoxic activities

DNA is the main target of an antitumor agent while BSA acts as a carrier protein molecule in the blood stream for a variety of compounds including antitumor compounds. Therefore, interaction studies of metal complexes with DNA and proteins are very useful in order to design and ascertain the metal-based anticancer therapeutics.[170,171] Furthermore, proteins are admired as the major cellular target for antitumor drugs and the most carrier proteins in the blood stream is Human Serum Albumin (HSA). Since Bovine Serum Albumin (BSA) structure is homologous with HSA and owing to its easy accessibility and low cost, BSA is mostly used in biochemical and biophysical studies.[172-174]

I.10.2. Structure of DNA

DNA, or deoxyribonucleic acid, is the hereditary material in humans and almost all other organisms. In a person's body each cell has the same DNA. Most of the DNA molecules located in the cell nucleus are called nuclear DNA but a small amount of DNA can also be found in the mitochondria as mt-DNA. The information in DNA is stored as a code made up of four chemical bases: adenine (A), guanine (G), cytosine (C), and thymine (T). Human DNA consists of about 3 billion bases. More than 99% of these bases are the same in all people. The most widely accepted model for the structure of DNA molecule was proposed by Watson and Crick in 1953 for which he was awarded the Nobel Prize for Medicine in 1962. According to him the DNA molecule is a double helix (Fig. I.3). The molecule is formed by two anti-parallel polynucleotide strands which are spirally coiled round each other in a right-handed helix. The two strands are held together by hydrogen bonds. The double stranded helical molecule has alternated major and minor grooves. Each strand is a long polynucleotide of deoxyribonucleotides. The two strands are complementary to each other with regards to the arrangement of the bases in the two strands. Thus, in the double helix, purines and pyrimidines exist in base pairs, i.e., (A and T) and (G and C). As a result, if the base sequence of one strand of DNA is known, the base sequence of its complementary strand can be easily deduced. The backbone of the strand is formed by alternately arranged deoxyribose sugar and phosphate molecules which are joined by the phosphodiester linkages.
The DNA molecule that Watson and Crick described was in B form. However, DNA can exist in other forms also. A, B and Z forms have right-handed helix while Z form has left-handed helix. B is the major form that is found in the cell.

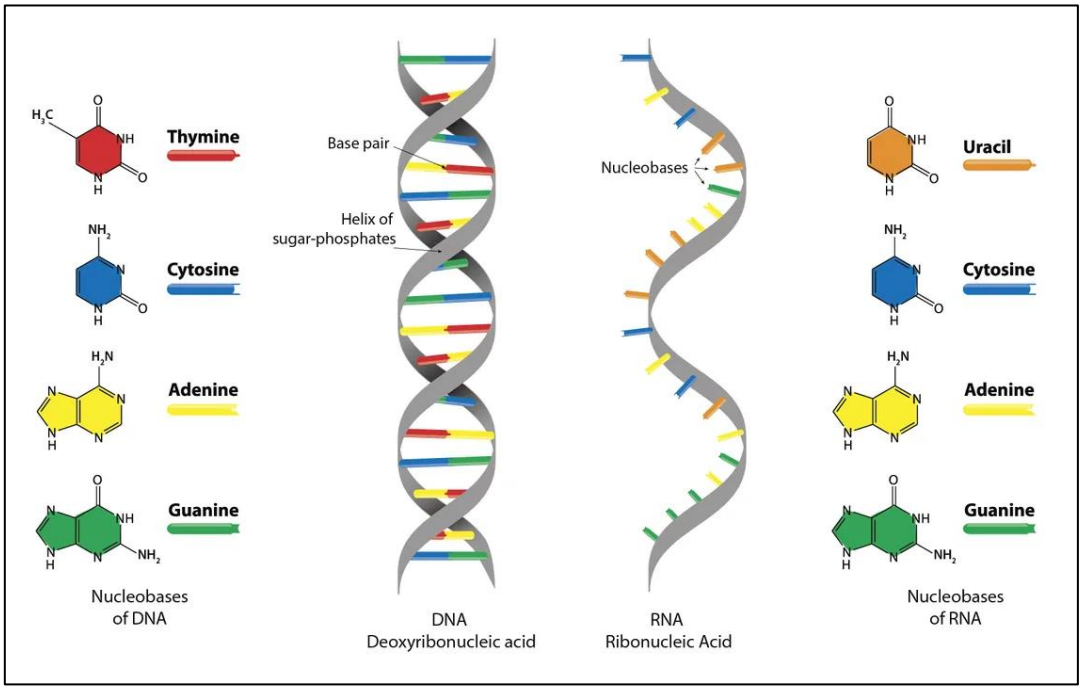

Fig. I.3. Structure of DNA.

I.10.3. DNA Binding Modes

DNA is an essential component of organisms' genetic makeup and the building block of gene expression. Small molecules can interact with DNA[175-177] through intercalative binding, groove binding, electrostatic binding/external binding (Fig. I.4). When tiny molecules or the medication intercalate into the non-polar interior of the DNA helix, intercalative binding occurs. When ligands of the proper size and chemical makeup fit themselves in between DNA base pairs, an aromatic group is stacked between the base pairs in this sort of binding. Since most of the ligands that are appropriate for intercalation are polycyclic, aromatic, and planar, they frequently function well as nucleic acid stains. Nowadays, there is a focus on creating and creating DNA strands since these compounds have the potential to be used as chemotherapeutics. In groove binding interactions, the bound molecule directly interacts with base pair edges in the major (G-C) or minor (A-T) grooves of the nucleic acids. The model groove binder, netropsin, is an antibiotic where intercalation is inhibited by methyl groups. Rarely do tiny molecules bind within the double helix's main groove. Electrostatic contact occurs between molecules that are positively charged. They interact electrostatically with the negatively charged phosphate backbone of the DNA molecule. Under physiological circumstances, electrostatic attraction is usually weak. This is the typical interaction of cations like Mg^{2+}.[178] The two most typical binding mechanisms are insertion into the minor groove and intercalation into the base pair stack at the double helix's core. Planar aromatic

rings in cationic compounds are commonly reported to exhibit intercalation. The positive charge could be on a substituent instead of in the ring structure. Under this binding mechanism, a binding pocket for the ligand must be created by the separation of two adjacent base pairs. Since this enables the molecule to modify its structure to follow the groove as it twists around the central axis of the helix, minor groove binders, on the other hand, typically have at least some flexibilities.[179,180] When binding in the minor groove as opposed to intercalative binding, significantly less DNA distortion is needed. Spectroscopy, UV-vis spectroscopy, fluorescence spectroscopy, circular dichroism (CD), and linear dichroism (LD) are often employed techniques to shed light on the binding patterns of tiny molecules.

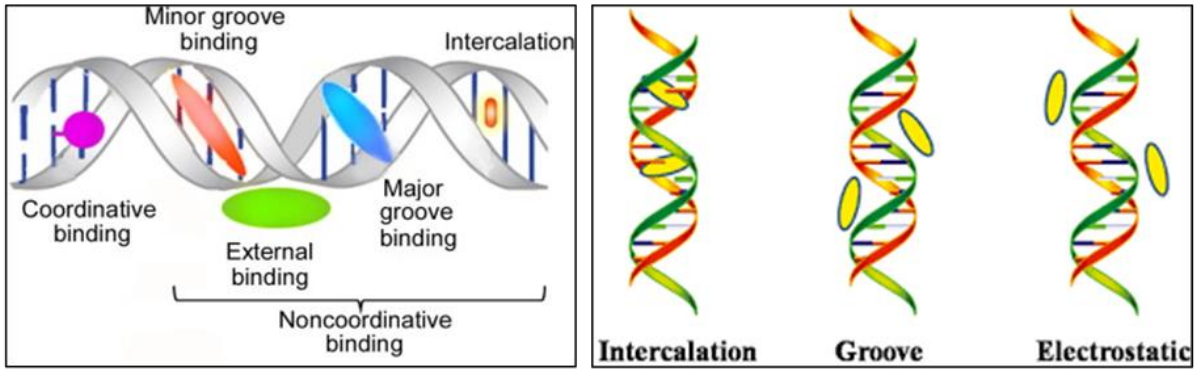

Fig. I.4. Binding modes of DNA.

The absorption maximum or peak extinction coefficient will frequently vary as a result of binding to DNA. However, this is not enough to identify a binding mode; instead, equilibrium binding constants can be found by analyzing the concentration dependence of any shifts that are noticed. Small fluorescent compounds can frequently take up energy from the bases of DNA and display changes in wavelength or quantum yield upon binding. UV light is used in these investigations to stimulate the DNA, and the ligand's fluorescence is sought after. The difference in the absorption of left- and right-handed circularly polarized light is measured by circular dichroism. The method of circular dichroism (CD) is helpful in determining the DNA-binding mode. CD is triggered when a ligand binds to the chiral DNA.[181,182] The binding mode, DNA sequence, and orientation of the ligand's transition dipole all affect the actual sign and strength of the produced CD signal. A groove binder touches a greater portion of the helix, often 4-6 base pairs, which is why intercalators frequently show lower intensity CD spectra in comparison to groove binders. Conversely, a basic intercalator only makes contact with two base pairs.

I.10.4. Transition metal complexes as chemical probes for DNA

The design of molecules that display strong binding affinity to DNA is a stimulating area of research. Such molecules can act as admirable chemotherapeutic reagents that exert their biological activity through interactions with DNA.[183-185] Interactions with DNA are not the only the factors that regulate the biological activity of these molecules, but their reactivity and selectivity are often correlated with their mode of binding with DNA. Therefore, the rational design of diverse DNA-targeted chemotherapeutic drugs and molecular probes for DNA depends critically on a deeper knowledge of the mechanisms that influence small molecules' interactions with DNA. As biological system probes, stable, inert compounds with active metal cores are very helpful.

The affinity and selectivity of metal complexes' binding to DNA have attracted a lot of attention. These studies' findings could be used to develop biotechnology tools and to treat chemotherapy. Extensive efforts have been made to comprehend the non-covalent interactions between metal complexes and DNA. We have investigated the palladium complexes' interactions with DNA by electrochemical and absorption spectroscopy investigations. Electronic absorption spectroscopy is one of the powerful techniques for probing metal ion DNA interactions.[186,187] The ‘hyperchromic’ effect and ‘hypochromic’ effect are spectral features of DNA concerning its double helix structure. ‘Hypochromism’ outcomes from the concentration of DNA in the helix axis as well as from the change in conformation on DNA, while ‘hyperchromism’ results from the structural damage of DNA.[188,189] The extent of hyperchromism suggests the strength of intercalative binding; on the other hand, either hyperchromism or hypochromism may result with metal complexes which bind non-intercalatively or electrostatically with DNA.[190,191] The electronic absorption titration of the complexes in 1:10 DMSO/buffer medium has been carried out in presence of increasing amounts of CT-DNA. When the amount of DNA is increased, the intensity of the charge transfer band is also changed, due to either hypochromism or hyperchromism. The intrinsic equilibrium binding constant (K_b) was estimated using the following Wolfe-Shimmer equation.[192]

$$\frac{[\mathrm{DNA}]}{(\varepsilon a - \varepsilon f)} = \frac{[\mathrm{DNA}]}{(\varepsilon b - \varepsilon f)} + \frac{1}{\mathrm{Kb}(\varepsilon b - \varepsilon f)}$$

Where, [DNA] is the concentration of CT-DNA and ε_a is the apparent extinction coefficient of the complex at a given DNA concentration, ε_f and ε_b are the extinction coefficients of the

complex in free solution and when fully bound to CT-DNA respectively. The plot of $[DNA]/(\varepsilon_a - \varepsilon_f)$ against $[DNA]$ will produce slope $1/(\varepsilon_b - \varepsilon_f)$ and intercept $1/K_b(\varepsilon_b - \varepsilon_f)$; K_b (M^{-1}) is the ratio of slope to intercept.

I.10.5. Albumin-binding properties of the compounds

Proteins are major targets for therapeutically active complexes. Bovine serum albumins (BSA) are frequently used in studies of the interactions with transition metal complexes and proteins because it is responsible for the transport of drugs in biological systems.[193,194] The binding ability of synthesized complexes with BSA protein were determined by employing UV-Vis and fluorescence spectroscopic techniques. The BSA stock solution was prepared using 500 mM phosphate buffer saline (PBS) at pH 7.4 and stored in the dark at 4°C for further use. The concentration of BSA was measured by taking absorbance at 280 nm in UV-Vis spectra (molar extinction coefficient 66,400 M-1 cm-1). The stock solution of complexes was prepared in DMSO medium and was suitably diluted with PBS whenever necessary. The absorption spectra were recorded at room temperature with constant concentration of BSA while varying the concentration of complex added to it.

UV-visible absorption measurement is a simple method to explore the structural changes and is useful to distinguish the type of quenching mechanism exist i.e. static or dynamic quenching mechanism. In the static quenching mechanism, a new complex is formed between BSA and the quencher in the ground state. Therefore, it will result in perturbation of the absorption spectrum of the fluorophore. But in the dynamic quenching mechanism, the fluorophore and quencher get in touch with each other during the transient existence of the excited state and therefore, no change is observed in the absorption spectrum of BSA.[195]

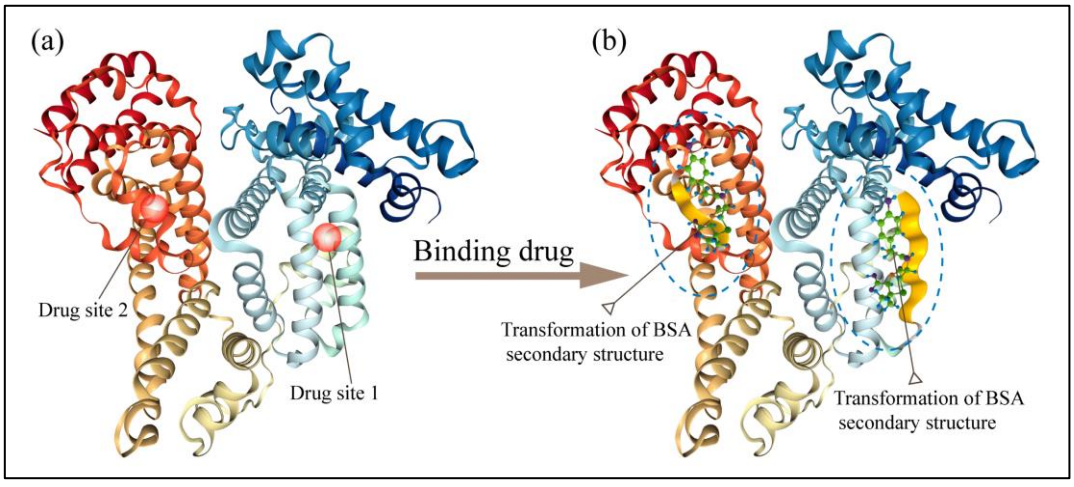

Figure I.5. Binding modes of BSA.

This hypsochromic shift corresponds to ground-state association between the complex and protein.[53] The apparent association constant (K_a) was calculated from the plot of $1/(A_{obs}-A_0)$ vs 1/[complex] by using the Benesi–Hildebrand equation.[196]

$$\frac{1}{A_{obs} - A_0} = \frac{1}{A_c - A_0} + \frac{1}{K_a(A_c - A_0)[complex]}$$

Where A_{obs} is the observed absorbance (at 280 nm) of the solution having various concentrations of the complex, A_0 and A_c are the absorbance of BSA only and of serum albumin with the complex.

Further, the binding constant and number of binding sites can be calculated by using following Scatchard equation.[197]

$$log\frac{(F_0 - F)}{F} = log\ K_b + nlog[complex]$$

Where K_b is the binding constant of synthesized compounds with BSA and n is the number of binding sites. The binding constant (K_b) and the binding sites (n) have been obtained from the plot of log $[(F_o-F)/F]$ versus log [complex].

I.11. Objectives and scope of the present work

Over the last few years, transition metal complexes that contain azo/imine functional O,N,S donor pincer ligands have attracted great attention and found important applications in various fields such as medicinal chemistry including antibacterial, antifungal, anticancer, antioxidant, antimalarial, antiviral activity. Pincer type complexes were designed and synthesized with various metal ions such as platinum, palladium, ruthenium and rhenium. Chelating behavior of ONS donor ligands with transition metals has been studied with the aim of gaining more information about their nature of coordination, structural and spectral features. Also, the coordination chemistry of transition metals with chelating ligands are widely studied because of their stability, chemical, biological, electrochemical activities and diversity in binding mode of the ligands to metal centre. Schiff bases are useful chelating ligands for metal ions, resulting in metal complexes with different physical and chemical properties and also azo compounds are found to have several health benefits, including cytotoxic, antitumor, antibacterial, antiviral, antifungal, and antiseptic properties. The

investigation of the interactions of biologically active compounds with DNA and BSA could provide very useful information on the structural features that determine the therapeutic effectiveness and pharmacological response of drugs.

Thus, the work presented in this thesis was carried out with the following objectives

- Design and synthesis of multidentate ligands incorporating azo/imine as functionality.
- Synthesis of transition metal complexes with azo/imine functional O, N, S donor ligands.
- Characterization of the synthesized metal complexes by spectroscopic techniques (NMR, FT-IR, UV-Vis etc).
- Structure determination by single crystal X-ray diffraction method.
- Exploration of binding ability of the complexes with DNA and BSA proteins by absorption and emission titration methods.
- Investigation of the metal complexes' in vitro anticancer activity against various human cancer cell lines.

I.12. References

1. P. Adão, S. Majumder, S. P. Dash, S. Roy, M. L. Kuznetsov, J. C. Pessoa, C. S. Gomes, M. R. Hardikar, E. R. Tiekink, R. Dinda, *Dalton Trans.*, 2018, **47**, 11358-11374.
2. J. Costa Pessoa, I. Tomaz, *Curr. Med. Chem.*, 2010, **17**, 3701-3738.
3. R. O. Omondi, S. O. Ojwach and D. Jaganyi, *Inorg. Chimica Acta*, 2020, **512**, 119883.
4. (a) S. Abdolmaleki, A. Aliabadi and S. Khaksar, *Coord. Chem. Rev.*, 2024, **501**, 215579; (b) S. Radisavljević and B. Petrović, *Fron. Chem.*, 2020, **8**, 379.
5. M. M. Milutinović, A. Rilak, I. Bratsos, O. Klisurić, M. Vraneš, N. Gligorijević, S. Radulović, Ž. D. Bugarčić, *J. Inorg. Biochem*., 2017, **169**, 1–12.
6. C. Riccardi, D. Capasso, G. M. Rozza, C. Platella, D. Montesarchio, S. Di Gaetano, T. Marzo, A. Pratesi, L. Messori, G. N. Roviello, *J. Inorg. Biochem*., 2020, **203**, 110868.
7. (a) Ö. Tarı, F. Gümüş, L. Açık, B. Aydın, *Bioorg. Chem*., 2017, **74**, 272–283; (b) R. O. Omondi, S. O. Ojwach and D. Jaganyi, *Inorg. Chimica Acta*, 2020, **512**, 119883.
8. Q. Wang, L. Yang, J. Wu, H. Wang, J. Song, X. Tang, *BioMetals*, 2017, **30**, 17–26.
9. D. Musumeci, C. Platella, C. Riccardi, A. Merlino, T. Marzo, L. Massai, L. Messori and D. Montesarchio, *Dalton Trans*., 2016, **45**, 8587–8600.
10. N. J. Patel, B. S. Bhatt, M. N. Patel, *Inorg. Chim. Acta*, 2019, **498**, 119130.
11. S. Dilruba, G.V. Kalayda, *Cancer Chemother. Pharmacol*., 2016, **77**, 1103–1124.
12. M. Fanelli, M. Formica, V. Fusi, L. Giorgi, M. Micheloni, P. Paoli, *Coord. Chem. Rev.*, 2016, **310**, 41–79.

13. S. Parveen, *Curr. Chin. Sci.*, 2022, **2**, 275-293.
14. T. Makovec, *Radiol Oncol.*, 2019, **53**, 148-158.
15. I. Ali, W. A. Wani, K. Saleem and A. Haque, *Curr Med Chem Anticancer Agents.*, 2013, **13**, 296-306.
16. S. Dasari and P. B. Tchounwou, 2014, **740**, 364-378.
17. A. Khan, R. Rashid, G. Murtaza, A. Zahra, *Trop. J. Pharm. Res*., 2014, **13**, 1169–1177.
18. P. Borst, S. Rottenberg, J. Jonkers, *Cell Cycle*, 2008, **7**, 1353–1359.
19. K. Barabas, R. Milner, D. Lurie, C. Adin, *Vet. Comp. Oncol.*, 2008, **6**, 1–18.
20. A. M. Florea and D. Büsselberg, *Cancers*, 2011, **3**, 1351-1371.
21. S. N. Mbugua, N. R. S. Sibuyi, L. W. Njenga, R. A. Odhiambo, S. O. Wandiga, M. Meyer, R. A. Lalancette and M. O. Onani, *ACS Omega*, 2020, **25**, 14942-14954.
22. E. Petruzzella, R. Sirota, I. Solazzo, V. Gandin and D. Gibson, *Chem. Sci*., 2018, **9**, 4299-4307.
23. T. C. Johnstone, K. Suntharalingam and J. Lippard, *Chem. Rev*., 2016, **116**, 3436-3486.
24. T. C. Johnstone, G. Y. Park and S. J. Lippard, *Cancer Res*., 2014, **34**, 471-476.
25. T. Storr, M. Merkel, G.X. Song-Zhao, L. E. Scott, D.E. Green, M.L. Bowen, K.H. Thompson, B. O. Patrick, H.J. Schugar, C. Orvig, *J. Am. Chem. Soc*., 2007, **129**, 7453–7463.
26. S. M. Meier-Menches, C. Gerner, W. Berger, C. G. Hartinger, B. K. Keppler, *Chem. Soc*., 2018, **47,** 909–928.
27. S. Gomez-Ruiz, D. Maksimović-Ivanić, S. Mijatović, G.N. Kaluđerović, *Bioinorg. Chem. Appl.*, 2012.
28. G. Gasser, I. Ott, N. Metzler-Nolte, *J. Med. Chem.*, 2011, **54**, 3–25.
29. A. Zianna, G. D. Geromichalos, A. G. Hatzidimitriou, E. Coutouli-Argyropoulou, M. Lalia-Kantouri, G. Psomas, *J. Inorg. Biochem*., 2019, **194**, 85–96.
30. F. Türker, C. Gürses, D. Barut Celepci, A. Aktaş, B. Ateş, Y. Gök, *Arch. Pharm*., 2019, **35**, 1900187.
31. H. Mansouri-Torshizi, S. Zareian-Jahromi, A. Ghahghaei, S. Shahraki, F. Khosravi, M. Heidari Majd, *J. Biomol. Struct. Dyn*., 2018, **36**, 2787–2806.
32. C. Riccardi, D. Musumeci, M. Trifuoggi, C. Irace, L. Paduano, D. Montesar, *Pharmaceuticals*, 2019, **12**, 146.
33. A. Bijelic, S. Theiner, B. K. Keppler, A. Rompel, *J. Med. Chem*., 2016, **59**, 5894–5903.
34. A. R. Kapdi and I. J. S. Fairlamb, *Chem. Soc. Rev*., 2014, **43**, 4751.
35. A. Garoufis, S. K. Hadjikakou and N. Hadjiliadis, *Coord. Chem. Rev.*, 2009, **253**, 1384.
36. M. D. Coskun, F. Ari, A. Y. Oral, M. Sarimahmut, H.M. Kutlu, V. T. Yilmaz and E. Ulukaya, *Bioorg. Med. Chem*., 2013, **21**, 4698.
37. J. Espino, E. Fernández-Delgado, S. Estirado, F. de la Cruz-Martinez, S. Villa-Carballar, E. Viñuelas-Zahínos, F. Luna-Giles and J. A. Pariente, *Sci. Rep.*, 2020, **10**, 1-16.

38. H. A. Rudbari, N. Kordestani, J. V. Cuevas-Vicario, M. Zhou, T. Efferth, I. Correia, T. Schirmeister, F. Barthels, M. Enamullah, A. R. Fernandes and N. Micale. *New J. Chem*., 2022, **46**, 6470-6483.
39. D. Simić, M. Zarić, I. Nikolić, R. Živković-Zarić, P. Čanović, A. Kočović, I. Radojević, I. Raković, S. Jovičić Milić, Đ. Petrović, D. Stojković, N. Vuković, M. Kačániová, M. Vukić and V. Jevtić, *Dalton Trans*., 2022, **51**, 1191-1205.
40. J. M. Rademaker-Lakhai, D. van den Bongard, D. Pluim, J. H. Beijnen and J. H. Schellens, *Clin. Cancer Res*., 2004, **10**, 3717-3727.
41. C. G. Hartinger, S. Zorbas-Seifried, M. A. Jakupec, B. Kynast, H. Zorbas and B. K. Keppler, *J. Inorg. Biochem.*, 2006, **100**, 891-904.
42. C. G. Hartinger, M. A. Jakupec, S. Zorbas-Seifried, M. Groessl, A. Egger, W. Berger, H. Zorbas, P. J. Dyson and B. K. Keppler, *Chem. Biodiversity*, 2008, **5**, 2140-2155.
43. J. P. Wolfe, S. Wagaw, J. F. Marcoux, S. L. Buchwald, *Acc. Chem. Res*., 1998, **31**, 805.
44. (a) P. H. Espeel, G. D. Peuter, M. C. Tielen, P. A. Jacobs, *J. Phys. Chem*., 1994, **98**, 11588; (b) M. Watanable, T. Yamamoto, M. Nishiyama, *Angew. chemie*., 2000, **112**, 2620; (c) M. Opanasenko, P. Stepnicka, J. Cejka, *RSC Adv*., 2014, **4**, 65137; (d) S. Paul, M. Islamc, M. Islam, *RSC Adv*., 2015, **5,** 42193.
45. (a) G. Ferguson, R. McCrindle, A. J. McAlees, M. Parvez, *Acta Cryst.*, 1982, **38**, 2679. (b) R. F. Heck, *J. Am. Chem. Soc*., 1963, **85**, 657. (c) R. F. Heck, *J. Am. Chem. Soc*., 1968, **90**, 313. (d) E. Negishi, L. Anastasia, *Chem. Rev*., 2003, **103**, 1979. (e) E. Negishi, *Acc. Chem. Res*., 1982, **15**, 340-348. (f) V. Grignard, *J. Ind. Eng. Chem*., 1917, **9**, 1142.
46. (a) J. F. Hartwig, *Acc. Chem. Res.*, 1998**,** **31**, 852; (b) J. F. Hartwig, *Inorg. Chem.*, 2007, **46**, 1936. (c) J. K. Stille, *Organometallics*, 1990, **9**, 3007. (d) J. K. Stille, R. Divakaruni, *J. Am. Chem. Soc.*, 1978, **100**, 1303.
47. J. Tsuji, I. Shimizu, I. Minami, Y. Ohashi, T. Sugiura, *J. Org. Chem*., 1985, **50**, 1523.
48. B. M. Trost, Z. Shi, *J. Am. Chem. Soc*., 1996, **118**, 3037.
49. K. Sonogashira, S. Takahashi, N. Hagihara, *Macromolecules*, 1977, **10,** 879.
50. A. C. Skapski, M. L. Smart, *Chem. Commun*., 1970, **8**, 658.
51. (a) R. Martin and S. L. Buchwald, *Acc. Chem. Res*., 2008, **41**, 1461; (b) B. M. Trost, M. Lautens, *J. Am. Chem. Soc*., 1985, **107,** 1781; (c) R. B. Bedford, C. S. J. Cazin and D. Holder, *Coord. Chem. Rev*., 2004, **248**, 2283.
52. R. Jackstell, A. Grotevendt, D. Michalik, L. E. Firdoussi, M. Beller, *J. Organometal. Chem*., 2007, **692**, 4737.
53. J. K. Stille, D. E. James, *J. Organometal. Chem.*, 1976, **108**, 401.
54. P. Fitton, E. A. Rick, *J. Organometal. Chem*., 1971, **28**, 287.
55. T. R. Hoye, C. J. Dinsmore, D. S. Johnson, P. F. Korkowski, *J. Org. Chem*., 1990, **55**, 4518.
56. Y. Tatsuno, T. Yoshida, S. Otsuka, *Inorg. Synth*., 1990, **28**, 342.

57. B. M. Trost, C. B. Lee, *J. Am. Chem. Soc*., 1998, **120**, 6818.
58. A. E. Shilov, G. B. Shulpin, Boston, 2000.
59. (a) Z. Xu, J. Oxgaard, W. Goddard, *Organometallics*, 2008, **27**, 3770-3773; (b) P. E. M. Siegbahn, R. H. Crabtre, *J. Am. Chem. Soc*., 1996, **118**, 4442-4450; (c) M. Lin, C. Shen, E. A. G. Zayas, A. Sen, *J. Am. Chem. Soc*., 2001, **123**, 1000-1001.
60. Handbook of Preparative Inorganic Chemistry, G. Brauer, NewYork, 1965, **2**, 1572.
61. S. W. Sparkst, P. D. Ellis, *J. Am. Chem. Soc*., 1986, **108**, 3215-3218.
62. J. M. Kinyanjui, R. H. Burr, J. G. Wagner, N. R. Wijeratne, D. W. Hatchett, *Macromolecules*, 2004, **37**, 8745-8753.
63. D. E. Schwab, J. V. Rund, *Inorg. Chem*., 1972, **11**, 499-503.
64. S. W. Sparks, P. D. Ellis, *J. Am. Chem. Soc*., 1986, **108**, 3215-3218.
65. T. M. Miller, G. M. Whitesides, *J. Am. Chem. Soc*., 1988, **110**, 3164-3170.
66. C. B. Anderson, B. J. Burreson, J. T. Michalowski, *J. Org. Chem.*, 1976, **41**, 1990-1994.
67. A. Singh, P.R. Sharp, O*rganometallics*, 2006, **25**, 678-683.
68. (a) F. Faglioni, M. Blanco, W. A. Goddard, D. Saunders, *J. Phys. Chem. B*, 2002, **106**, 1714-1721; (b) J. Stein, L. N. Lewis, Y. Gao, R. A. Scot, *J. Am. Chem. Soc*., 1999, **121**, 3693-3703; (c) Y. Motoyama, K. Kamo, H. Nagashima, *Org. Lett*., 2009, **11**, 1345-1348. (d) J. R. Sargent, W. P. Weber, *Macromolecules*, 1999, **32**, 2826-2829.
69. W. P. Griffith, The Chemistry of the Rarer Platinum Metals, London, 1967, **4**.
70. A. K. Singh, R. S. Varma, *Tetrahedron Lett*., 1992, **33**, 2307-2310.
71. B. Hartmann, J. P. Deprés, A. E. Greene, D. L. Friere, *Tetrahedron Lett*., 1993, **34**,1487-1490.
72. G. Z. Wang, J. E. Backvall, *J. Chem. Soc. Chem. Commun*., 1992, 337-339.
73. T. K. Meister, K. Riener, P. Gigler, J. Stohrer. W. A. Herrmann, F. E. Kühn, *ACS Catal*., 2016, **6**, 1274-1284.
74. T. Chihara, K. Tanaka, *J. Catal*., 1983, **80**, 97-105.
75. J. Holmes, C. M. Pask, C. E. Charlotte, *Dalton Trans*., 2016, **45**, 15818-15827.
76. S. Kamiguchi, K. Arai, K. Okumura, H. Iida, S. Nagashima, T. Chihara, *Appl. Catal. A*, 2015, **505**, 417-421.
77. S. Doherty, J. G. Knight, C. H. Smyth, R. W. Harrington, W. Clegg, *J. Org. Chem*., 2006, **71**, 9751-9764.
78. C. Michel, J. Zaffran, A. M. Ruppert, J. Matra-Michalska, M. Jedrzejczyk, J. Grams, P. Sautet, *Chem. Commun*., 2014, **50**, 12450-14453.
79. (a) M. A. Bennett, A. K. Smith, J. Chem. Soc. Dalton Trans. (1974) 233-241. (b) M. Baby, M. A. Esteruelas, E. Onate, *Organomet*., 2010, **29**, 6298-6307. (c) J. A. A. van den Tillaart, J. Leyrer, S. Eckhoff, E. S. Lox, *Appl. Catal*. 1996, **10**, 53-68.
80. R. Lalrempuia, M. Iglesias, V. Polo, P. J. S. Miguel, F. J. Fernandez-Alvarez, J. J. P. Torrente, L. A. Oro, *Angew. Chem*., 2012, **124**, 12996-13001.

81. (a) H. Charcosset, *Platin. Mrt. Rev*., 1979, **23**, 18-32; (b) K. D. Glusac, K. S. Schanze, Polymer Preprints **43** (2002) 87-91; (c) P. Charlesworth, *Platinum Metals Rev*., 1981, **25**, 106-112; (d) I. Shimizu, M. Tekawa, Y. Maruyama, A. Yamamoto, *Chem. Lett*., 1992, 1365-1372.
82. A. Albinati, H. Lehner, L. M. Venanzi and M. Wolfer, *Inorg. Chem*., 1987, **26**, 3933-3940.
83. H. Samouei, V. V. Grushin, *Organomet*., 2013, **32,** 4440-4443.
84. R. Noyori, M. Ohta, Y. Hisao, M. Kitamura, T. Ohta, H. Takaya, *J. Am. Chem. Soc*., 1986, **108**, 7117-7119.
85. S. V. Ley, J. Norman, W. P. Griffith, S. P. Marsden, *Synthesis*, 1994, 639-666.
86. N. Ahmad, J. J. Levison, S. D. Robinson, M. Uttley, *Inorg. Synth*., 1974, **15**, 48-51.
87. K. Wada, D. Izuhara, K. Yamada, M. Shiotsuki, T. Kondo. T. Mitsudo, *Chem. Commun*., 2001 1802–1803.
88. B. Marciniec, M. Kujawa, C. Pietraszuk, *Organomet*., 2000, **19**, 1677-1681.
89. S. Murai, F. Kakiuchi, S. Sekine; Y. Tanaka, A. Kamatani, M. Sonoda, N. Chatani, *Nature*, 1993, **366**, 529-531.
90. H. T. Teunissen, C. J. Elsevier, *Chem. Commun*., 1998, 1367-1368.
91. E. J. Moore, W. R. Pretzer, T. J. O'Connell, J. Harris, L. L. Bounty, L. Chou, S. Grimmer, *J. Am. Chem. Soc*., 1992, **114**, 5888-5890.
92. C. Landgrafe, W. S. Sheldrick, *Dalton Trans*., 1994, 1885-1893.
93. T. E. Wilhelm, T. R. Belderrain, S. N. Brown, R. H. Grubbs, *Organomet*., 1997, **16**, 3867-1369.
94. A. Furstner, *Angew. Chem. Int. Ed*., 2000, **39**, 3012-3015.
95. R. H. Grubbs, S. Chang, *Tetrahedron*, 1998, **54**, 4413-4450.
96. J. P. Genet, C. Pinel, S. Mallart, *Tetrahedron, Asym*., 1994, **5**, 665-674.
97. D. Oyama, T. Hamada, *Acta Cryst*., 2008, **64,** 442-447.
98. C. Nachtigal, S. Al-Gharabli, K. Eichele, E. Lindner, H. A. Mayer, *Organomet*., 2002, **21**, 105-112.
99. M. P. Doyle, M. S. Shankline, *Organomet*., 1994, **13**, 1081-1083.
100. M. J. Howard, M. D. Jones, M. S. Roberts, S. A. Taylor, *Catal. Today*, 1993, **18**, 325-327.
101. A. J. L. Pombeiro, M. F. C Guedes da Silva, R. H. Crabtree, *Encyclopedia of Inorg. Chem*., 2006.
102. C. C. Romão, *Encyclopedia of Inorg. Chem.*, 2006
103. (a) A. S. Polo, M. K. Itokazu, N. Y. Murakami Iha, *Coord. Chem. Rev*., 2004, **248**, 1343-1361; (b) A. Hagfeldt, G. Boschloo, L. Sun, L. Kloo, H. Pettersson, *Chem. Rev*., 2010, **110**, 6659-6663; (c) M. J. Clarke, *Coord. Chem. Rev*., 2003, **236**, 209-233.
104. (a) I. Eryazici, C. N Moorefield, G. R. Newkome, *Chem. Rev*., 2008, **108**, 1834-1895; (b) A. S. Abu-Surrah, M. Kettunen, *Curr. Med. Chem*., 2006, **13**, 1337-1357; (c) C. A. Puckett, J. K. Barton, *Bioorg. Med. Chem*., 2010, **18**, 3564-3569.

105. (a) L. Cosgrave, M. Devocelle, R. J. Forster, T. E. Keyes, *Chem. Commun*. 2010, **46**, 103-105; (b) M. R. Gill, J. Garcia-Lara, S. J. Foster, C. Smythe, G. Battaglia, J. A. Thomas, *Nature Chem.*, 2009, **1**, 662-667; (c) M. H. Lim, H. Song, E. D. Olmon, E. E. Dervan, J. K. Barton, *Inorg. Chem*., 2009, **48**, 5392-5397; (d) A. Marti, C. A. Puckett, J. Dyer, N. Stevens, S. Jockusch, J. K. Barton, N. J. J. Turro, *Am. Chem. Soc*., 2007, **129**, 8680-8681.
106. B. M. Zeglis, J. K. J. Barton, *Am. Chem. Soc*., 2006, **128**, 5654-5655.
107. (a) E. Ruba, J. R. Hart, J. K Barton, *Inorg. Chem*., 2004, **43**, 4570-4578; (b) A. Vlcek, *Organomet. Chem*., 2010, **29**, 73-114; (c) J. J. Turner, M. W. George, F. P. A. Johnson, J. R. Westwell, *Coord. Chem. Rev.,* 1993, **125**, 101-114; (d) M. W. George, J. J. Turner, *Coord. Chem. Rev*., 1998, **177**, 201-217; (e) J. Dyer, W. J. Blau, C. G. Coates, C. M. Creely, J. D. Gavey, M. W. George, J. A. Pho-tochem. *Photobiol. Sci.*, 2003, **2**, 542-554.
108. A. Vlcek, M. Busby, *Coord. Chem. Rev*., 2006, **250**, 755-1762.
109. C. Shih, A. K. Museth, M. Abrahamsson, J. R. Winkler, H. B. Gray, *Science*, 2008, **320**, 1760-1762.
110. A. M. Blanco-Rodriguez, A. J. Di Bilio, C. Shih, A. K. Museth, I. P. Clark, M. Towrie, A Cannizzo, J Sudhamsu, B. R. Crane, J. Sykora, J. R. Winkler, H. B. Gray, S. Zalis, and A. Vlcek, *Chem. Eur. J*., 2011, **17**, 5350-5361.
111. Q. Cao, C. M. Creely, E. S. Davies, J. Dyer, T. L. Easun, D. C. Grills, D. A. Mc-Govern, J. McMaster, J Pitchford, *Photochem. Photobiol. Sci*., 2011, **10**, 1355-1364.
112. (a) G. J. P. Britovsek, V. C. Gibson and D. F. Wass, *Angew. Chem. Int. Ed Engl*., 1999, **38**, 428; (b) R. E. Morris and L. Brammer, *Chem. Soc. Rev.*, 2017, **46**, 5444.
113. (a) P. Atkins, T. Overton, J. Rourke, M. Weller and F. Armstrong, Inorganic Chemistry 4th Ed. OUP, Oxford, 2006, 494. (b) A. E. Martell, R. D. Hancock and R. J. Motekaitis, *Coord. Chem. Rev*., 1994, **133**, 39.
114. X. Liu and J. Hamon, *Coord. Chem. Rev*., 2019, **389**, 94.
115. P. Braunstein and F. Naud, *Angew. Chem. Int. Ed.*, 2001, **40**, 680.
116. R. G. Pearson, *J. Am. Chem. Soc*., 1963, **85**, 3533.
117. T. G. Appleton, H. C. Clark, L. E. Manzer, *Coord Chem. Rev*., 1973, **10**, 335.
118. M. G. Gardiner, C. C. Ho, *Coord Chem. Rev.*, 2018**, 375**, 373.
119. (a) K. Buldurun, M. Ozdemir, *J. Mol. Struct*., 2020, **1202**, 127266; (b) M. Ramesh, G. Venkatachalam, *J. Organomet. Chem.*, 2019, **880**, 47.
120. H. A. McManus, P. J. Guiry, *Chem. Rev*., 2004, **104**, 4151.
121. E. M. McGarrigle, D. G. Gilheany, *Chem. Rev.*, 2005, **105**, 1563.
122. A. M. E. Geary, J. L. Yellowlees, A. L. Jack, D. H. I. Oswald, S. Parsons, N. Hirata, R. J. Durrant and N. Robertson, *Inorg. Chem*., 2005, **44**, 242.
123. X. Yang, F. Drepper, B. Wu, W. Sun, W. Haehnelb and C. Janiak, *Dalton Trans*., 2005, **2**, 256.

124. (a) X. Chen, P. Sun, B. Mo, C. Chen, and J. Peng, *J. Org. Chem*., 2021, **86,** 352; (b) J. Yu, J. Li, P. Wang, and J. Yu, *Angew. Chem*., 2019, **131**, 18309; (c) M. R. Malachonsk, M. Adams, N. Elia, A. L. Rheingold, R. S. Kelly, *Dalton Trans*., 1999, 2177.
125. (a) G. Cheng, Y. Weng, X. Yang, and X. Cui, *Org. Lett*., 2015, **17**, 3790; (b) P. Chakraborty, S. K. Chandra, A. Chakravorty, *Organomet.*, 1993, **12**, 4726; (c) S. Budagumpi and S. Endud, *Organomet*., 2013, **32**, 1537.
126. (a) K. E. Prosser, S. W. Chang, F. Saraci, P. H. Le, C. J. Walsby, *J. Inorg. Biochem*., 2017, **167**, 89; (b) A. K. Mahapatra, S. N. Dutta, S. Goswami, M. Mukherjee, A. K. Mukherjee, A. Mahapatra, *Inorg. Chem*., 1986, **25**, 1715; (c) N. Anbu, A. Dhakshinamoorthy, *J. Ind. Eng. Chem*., 2018, **65**, 120.
127. (a) A. Bhanja, R. Herchel, Z. Travnicek and D. Ray, *Inorg. Chem*., 2019, **58**, 12184; (b) R. Balamurugan, M. Palaniandaver, R. S. Gopalan, *Inorg. Chem*., 2001, **40**, 2246.
128. M. Kalita, P. Gogoi, P. Barman, B. Sarma, A. K. Buragohain, R. D. Kalita, *Polyhedron*, 2014, **74**, 93.
129. R. H. Crabtree, The Organometallic Chemistry of the Transition Metals, 2nd ed.; Wiley: New York, 1994, Chapter 4.
130. (a) M. P. Mitoraj, A. Michalak, *Inorg. Chem*., 2010, **49**, 578-582; (b) D. Woska, A. Prock, W. P. Giering, *Organometallics*, 2000, **19**, 4629.
131. (a) A. W. Hofmann, *Ann. Chem. Pharm*., 1857, **104**,1-39; (b) B. W. Malerbi, *Platinum Metal Rev.*, 1965, **9**, 47.
132. (a) J. Jover, N. Fey, J. N. Harvey, G. C. Lloyd-Jones, A. G. Orpen, G. J. J. Owen-Smith, P. Murray, D. R. J. Hose, R. Osborne, M. Purdie, *Organomet.*, 2010, **29**, 6245; (b) T. Sawano, Z. Lin, D. Boures, B. An, C. Wang and W. Lin, *J. Am. Chem. Soc*., 2016, **138**, 9783; (c) M. E. van der Boom and D. Milstein, *Chem. Rev*., 2003, **103,** 1759.
133. A. D. Garnovski, A. L. Nivorozhkin, V. I. Minkin, *Coord. Chem. Rev*., 1993, **126**, 1-69.
134. D. A. Atwood, *Coord. Chem. Rev*., 1997, **165**, 267-296.
135. H. Schiff, *Ann. Chem. Suppl*., 1864, **131**, 188-193.
136. (a) R. H. Holm, G. W. Evertt, A. Chakravorty, *Prog. Inorg. Chem*., 1966, **7**, 83-214; (b) S. R. Collinson, D. E. Fenton, *Coord. Chem. Rev*., 1996, **148**, 19-40; (c) A. D. Garnovski, A. L. Nivorozhkin, V. I. Minkin, *Coord. Chem. Rev*.,1993, **126**, 93-147; (d) P. Zalleno, S. Tamburini, G. A. Mazzocchin, *Coord. Chem. Rev.*, 1987, **77**, 165-273; (e) K. Dey, R. Bhowmik, S. Sarkar, *Synth. React. Inorg. Met. Org. Chem.*, 2002, **32**, 1393-1408; (f) K. Dey, R. K. Maity, *Indian J. Chem.*, 1976, **14**, 602-605.
137. (a) N. Raman, J. Joseph, A. Sakthivel, R. Jeyamurugan, *J. Chil. Chem. Soc*., 2009, **54**, 354-357; (b) F. Tuna, L. Patron, Y. Journaux, M. Andruch, *Rev. Roumaine Chemie*., 1997, **42**, 579-585; (c) V. Gutmann, G. Hampbel, *Montasch Chem.*, 1963, **94**, 830-833; (d) C. Marzano, M. Pellei,

S. Alidori, *J. Inorg. Biochem*., 2006, **100,** 299-304. (e) D. S. Chandel, K. K. Pande, *J. Indian Chem. Soc*., 1974, **51**, 684-687; (f) R. E. Winpenny, *Chem. Soc. Rev*., 1998, **27**, 447-452.

138. (a) A. Erkleban, *Inorg. Chem*., 2001, **40**, 208-213; (b) G. L. Choudhary, S. R. Prasad, A. Rahman, *J. Indian Chem. Soc*., 1997, **74**, 683-685.
139. A. S. Shawali, N. M. S. Harb, K.O. Badahdah, *J. Heterocylic Chem*., 1985, **22**, 1397-1403.
140. (a) Y. B. Dong, A. K. Zhang, J. P. Ma, R. Q. Huang, *Cryst. Growth Des*., 2005, **5**, 1857-1866; (b) K. S. Kumar, S. Ganguly, R. Veerasamy, *Eur. J. Med. Chem*., 2010, **45**, 5474-5479.
141. (a) V. K. Gupta, A. K. Singh, S. Mehtab, B. Gupta, *Anal. Chem. Acta*., 2006, **5**, 566-569; (b) O. W. Salawu, A. O. Abdulsalam, *J. Phy. Sci. & Inno*., 2011, **3**, 51-61; (c) E. Merino, *Chem. Soc. Rev.*, 2011, **40**, 3835-3853.
142. (a) S. Goswami, A. R. Chakravarty, A. Chakravorty, *Inorg. Chem*., 1981, **20**, 2246-2250; (b) S. Goswami, R. N. Mukherjee, A. Chakravorty, *Inorg. Chem*., 1983, **22**, 2825-2832.
143. (a) E. Merino, *Chem Soc Rev*., 2011, **40**, 3835-53; (b) K. Hunger, Industrial dyes: chemistry, properties, applications. Weinheim: VCH, 2003; (c) W. You, H. Y. Zhu, W. Huang, B. Hu, Y. Fan, X. Z. You, *Dalton Trans*, 2010, **39**, 7876-80.
144. H. S. Bhatti, S. Seshadri, *Color Technol.*, 2004, **12,** 151-55.
145. (a) H. Zollinger, Azo and Diazo Chemistry, Interscience, New York, 1961; (b) Z. M. Chen, Y. Q. Wu, D. H. Gu, F. X. Gan, *Dyes and Pigments*, 2008, **76**, 624-631; (c) M. Shivakumar, K. Pramanik, A. Chakravorty, *Inorg. Chem*., 2000, **39,** 4332-4338.
146. (a) W. Kohn, *Rev. Mod. Phys*., 1998, **71,** 1253-1266; (b) X. Su, S. Guang, H. Xu, J. Yang, Y. Song, *Dyes and Pigments*, 2010, **87**, 69-79; (c) G. Stork, G. P. Willard, *J. Am. Chem. Soc*., 1977, **99**, 7067-7068.
147. (a) H. Dinçalp, F. Toker, I. Durucasu, N. Avcıbas, S. Icli, *Dyes Pigment*, 2007, **75**, 11-24; (b) S, Roy, T. N. Mandal, A. K. Barik, S. Pal, S. Gupta, A. Hazra, *Polyhedron*, 2007, **26**, 2603-11.
148. D. Zhang, M. Zhang, Z. Liu, M. Yu, F. Li, T. Yi, *Tetrahedron Lett*., 2006, **47**, 7093-96.
149. (a) B. Wei, Y. Q. Wu, D. H. Gu, F. X. Gan, *Chin Phys Lett*., 2003, **20**, 1596-99; (b) F. X. Huang, Y. Q. Wu, D. H. Gu, F. X. Gan, *Chin Phys Lett.*, 2003, **20**, 2259-61.
150. M. Ucar, K. Polat, A. O. Solak, M. Toy, M. L. Aksu, *Dyes and Pigments*, 2010, **87**, 55-61.
151. D. M. P. Mingos, G. Wilkinson, F. G. A. Stone, E. W. Abel, *Organomet. Chem*., 1982, **3**, 1.
152. (a) M. Pagliaro, S. Campestrini, R. Ciriminna, *Chem. Soc. Rev*., 2005, **34**, 837-845; (b) G. M. Bodner, M. P. May, L. E. McKinney, *Inorg. Chem*., 1980, **19**, 1951.
153. (a) M. MuthuTamizh, K. Mereiter, K. Kirchner, R. Karvembu, *J. Organomet. Chem*., 2012, **700**, 194-201; (b) P. Suganthy, R. Prabhu, V. Sridevi, *Polyhedron*, 2015, **88**, 57-62.
154. (a) A. Cabeza, V. Riera, Y. Jeannin, D. Miguel, *Inorg. Chim. Acta*, 1990, **168**, 77-82; (b) T. Szymańska-Buzar, *Coord. Chem. Rev*., 2006, **250**, 976-990; (c) K. A. Azam, M.A.Hossain, M. B. Hursthouse, S. E. Kabir, K. A. Malik, H. Vahrenkamp, *J. Organomet. Chem.*, 1998, **555**, 285-292.

155. (a) M. J. Clarke, *Coord. Chem. Rev*., 2002, **232**, 69; (b) M. J. Clarke, F. Zhu, D. R. Frasca, *Chem. Rev*., 1999, **99**, 2511; (c) G. Mestroni, E. Alessio, G. Sava, S. Pacor, M. Coluccia, in: B.K., Keppler (Ed.), Metalcomplexes in Cancer chemotherapy, VCH, Weinheim, 1993, 157.
156. T. A. Seder, A.J. Quderkirk, E. Weitz, *J. Am. Chem. Soc*., 1985, **107,** 1432.
157. K. Yasufuku, H. Noda, J. Iwai, H. Ohtani, M. Hosino, T. Kobayashi, Organomet., 1985, **4**, 2174.
158. J. A. Smith, M. W. George, J. M. Kelly, *Coord. Chem. Rev*., 2011, **255,** 2666-2675.
159. S. Trofinenko, *J. Am. Chem. Soc.,* 1971, **93**, 1808; (b) S. Trofimenko, *Inorg. Chem*., 1973, **12**, 1215.
160. (a) F. Mohr, S. H. Priver, S. K. Bhargava, M. A. Bennet, *Coord. Chem. Rev*.,2006, **250**, 1851; (b) I. Omae, *Coord. Chem. Rev*., 2004, **248**, 995.
161. (a) A. C. Cope, R. W. Siekman, *J. Am. Chem. Soc.,* **87** (1965) 3272; (b) A. C. Cope, E. C. Friedrich, *J. Am. Chem. Soc*., 1968, **90**, 909; (c) I. Omae, *Chem. Rev.*,1979, **79**, 287; (d) M. I. Bruce, *Angew. Chem*., 1977, **89**, 75.
162. (a) M. Pfeffer, *Pure Appl. Chem*., 1992, **64**, 335; (b) J. Dupont, M. Pfeffer, J. Spencer, *Eur. J. Inorg. Chem.,* 2001, 1917; (c) J. T. Singleton, *Tetrahedron*, 2003, **59**, 1837; (d) R. B. Bedford, *Chem. Commun*., 2003, 1787; (e) I. P Beletskaya, A. V. Cheprakov, *J. Organomet. Chem*., 2004, **689**, 4055; (f) A. T. Normand, K. J. Cavell, *Eur. J. Inorg. Chem*., 2008, 2781; (g) N. Selander, K. J. Szabo, *Dalton Trans*., 2009, 6267.
163. (a) C. M. Jensen, *Chem. Commun*., 1999, 2443; (b) K. I. Goldberg, A. S. Goldman Eds. ACS Symposium Series 885; American Chemical Society: Washington, DC, 2004; (c) A. S. Goldman, A. H. Roy, Z. Huang, R. Ahuja, W. Schinski, M. Brookhart, *Science*, 2006, **312**, 257.
164. W. Kohn, *Rev. Mod. Phys*.,1998, **71**, 1253.
165. John Wiley & Sons, *Inc. J Comput Chem*., 1999, **20**, 129.
166. E. Runge, E. K. U. Gross, *Phys. Rev. Lett*., 1984, **52**, 997.
167. P. Hohenberg, W. Kohn, *Phys. Rev*., 1964, **136**, 864.
168. R.V. Leeuwen, *Phys. Rev. Lett*., 1998, **80**, 1280.
169. (a) M. E. Casida, C. Jamorski, F. Bohr, J. Guan, D. R. Salahub Washington, *D.C.: ACS Press*., 1996, 145; (b) M. Petersilka, U. J. Gossmann, and E. K. U. Gross, *Phys. Rev. Lett.*, 1996, **76**, 1212.
170. (a) J. Madureira, C. I. V. Ramos, M. Marques, C. Maia, B. D. Sousa, L. Campino, M. G. Santana-Marques and N. Farrell, *Inorg. Chem*., 2013, **52**, 8881-8894; (b) C. Icsel and V. T. Yilmaz, *DNA Cell Biol*., 2013, **32**, 165-172; (c) B. Onfelt, P. Lincoln and B. Nordén, *J. Am. Chem. Soc*., 2001, **123**, 3630.
171. (a) S. Banerjee, E. B. Veale, C.M. Phelan, S. A. Murphy, G.M. Tocci, L. J. Gillespie, D. O. Frimannsson, J. M. Kelly, T. Gunnlaugsson, *Chem. Soc. Rev*., 2013, **42**, 1601-1618; (b) L. Zarei, Z. Asadi, M. Dusek, V. Eigner, *J. Photochem., Photobiol. A*., 2019, **374**, 145-160.

172. D. Cocic, S. Jovanovic, S. Radisavljevic, J. Korzekwa, A. Scheurer, R. Puchta, D. Baskic, D. Todorovic, S. Popovic, S. Matic and B. Petrovic, *J. Inorg. Biochem*., 2018, **189**, 91-102.
173. N. Rajendiran and J. Thulasidhasan, Spectrochim, *Acta Part A Mol. Biomol. Spectrosc*., 2015, **144**, 183-191.
174. A. Divsalar, I. Zhila, A. A. Saboury, M. Nabiuni, M. Razmi and H. Mansuri-Torshizi, *J. Iran. Chem. Soc.*, 2013, **10**, 951-959.
175. W. D. Wilson, G. M. Blackburn, M. J. Gait, Nucleic acids in chemistry and biology. Oxford University Press, Oxford,1996, 329.
176. J. A. Mountzouris, L. H. Hurley, S. M. Hecht, Bioorganic chemistry: nucleicacids. Oxford University Press, New York, 1996, 288.
177. (a) J. A. Cowan, *Curr. Opin. Chem. Biol*., 2001, **5**, 634; (b) L. N. Ji, X. H. Zou, J. G. Liu, *Coord. Chem. Rev.*, 2001, **216**, 513.
178. (a) H. Mei, J. Barton, *J. Am. Chem. Soc*., 1986, **108**, 7414; (b) J. Kelly, A.Tossi, D. McComell, *Nucl. Acids. Res.*, 1985, **13**, 6017.
179. B. H. Geierstanger, D. E. Wemmer, R. Annu, *Biophys. Biomol. Struct.*, 1995, **24**, 463.
180. B. A. Armitage, *Top Curr Chem*., 2005, **253,** 55.
181. R. Lyng, A. Rodger, B. Nordén, *Biopolymers*, 1991, **31**, 1709.
182. R. Lyng, A. Rodger, B. Nordén, *Biopolymers*, 1992, **32**, 1201.
183. (a) B. J. Pages, D. L. Ang, E. P. Wright, J. R. Aldrich-Wright, *Dalton Trans*., 2015, **44,** 3505; (b) H. Liu, P. J. Sadler, *Acc. Chem. Res*., 2011, **44**, 349.
184. (a) M. Lazoua, A. Tarushia, P. Gritzapisb, G. Psomas, *J. Inorg. Biochem*., 2020, **206,** 111019; (b) E. Moradinia, M. Mansournia, Z. Aramesh-Boroujeni, A. Bordba, *Appl Organo. Chem.*, 2019, **33**, 4893.
185. (a) N. Vamsikrishna, S. Daravath, N. Ganji, N. Pasha, Shivaraj, *Inorg. Chem. Commun*., 2020, **113**, 107767; (b) M. Lazoua, A. Tarushia, P.Gritzapisb, G. Psomasa, *J. Inorg. Biochem.*, 2020, **206**, 111019.
186. Q. Wang, Z. Y. Yang, G. F. Qi, D. D. Qin, *Eur. J. Med. Chem.*, 2009, **44**, 2425.
187. X. H. Zou, B. H. Ye, H. Li, J. G. Liu, Y. Xiong, L. N. Ji, J. Chem. Soc., *Dalton Trans.*,1999 1423.
188. F. Q. Liu, Q. X. Wang, K. Jiao, F.F. Jian, G. Y. Liu, R. X. Li, *Inorg. Chim. Acta*., 2006, **359**, 1524.
189. D. Lawrence, V. G. Vaidyanathan, B. Unni Nair, *J. Inorg. Biochem*., 2006, **100,** 1244.
190. E. C. Long, J. K. Barton, *Acc. Chem. Res.*, 1990, **23**, 271.
191. S. Tabassum, I. U. H. Bhat, *Chem. Pharm. Bull*., 2010, **58**, 318.
192. A. Wolfe, G. H. Shimer, T. Meehan, *Biochemistry*., 1987, **26**, 6392.
193. F. Dimiza, F. Perdih, V. Tangoulis, I. Turel, D. P. Kessissoglou and G. Psomas, *J. Inorg. Biochem*., 2011, **105**, 476–489.

194. F. Samari, B. Hemmateenejad, M. Shamsipur, M. Rashidi and H. Samouei, *Inorg. Chem*., 2012, **51**, 3454–3464.

195. (a) P. R. Callis, *J. Mol. Struct*., 2014, **1077**, 14-21; (b) A. Sharma, J. Enderlein and M. Kumbhakar, *J. Phys. Chem. Lett*., 2017, **8**, 5821-5826.

196. M. A. Jhonsi, A. Kathiravan, R. Renganathan and M. S. A. El-Sadek, *J. Nanosci. Nanotechnol*., 2011, **3**, 125-130.

197. W. C. Galley, M. Bouvier, S. D. Clas, G. R. Brown and L. E. St-Pierre, *Biopolymers*, 1988, **27**, 79-86.

CHAPTER-II

Synthesis, characterization, X-ray structure, DFT computation and DNA/Protein binding of Pd(II) complexes containing N-substituted thiosemicarbazones

Abstract

The variable chelating behavior of 5-fluorosalicylaldehyde-4(N)-substituted thiosemicarbazones were explored by reacting with equimolar amount of $[PdCl_2(PPh_3)_2]$. The synthesized complexes were thoroughly characterized by various analytical, spectroscopic techniques (mass, ^{1}H-NMR, absorption, IR). The molecular structure of the complexes **1** and **2** were characterized by single crystal X-ray diffraction studies which revealed that the ligand H_2L^1 is coordinated to Pd(II) as uninegative bidentate N, S donor ligand in the complex **1** by forming a five-member chelate ring. However, the ligand H_2L^2 bound to palladium in complex **2** as binegative tridentate ONS donor by forming six and five member rings. From this study, it was found that the substitution on terminal 4(N)-nitrogen may have an influence on the chelating ability of thiosemicarbazone. The presence of hydrogen bonding in complex **1** might be responsible for preventing the coordination of phenolic oxygen to the metal ion. The interactions of complexes with calf thymus DNA (CT-DNA) have been evaluated by absorption and ethidium bromide (EB) competitive studies which revealed that complexes could interact with CT-DNA through intercalation. Further, the interactions of the complexes with bovine serum albumin (BSA) were also investigated using UV-visible, fluorescence and synchronous fluorescence spectroscopic methods, which showed that the complexes could bind strongly with BSA.

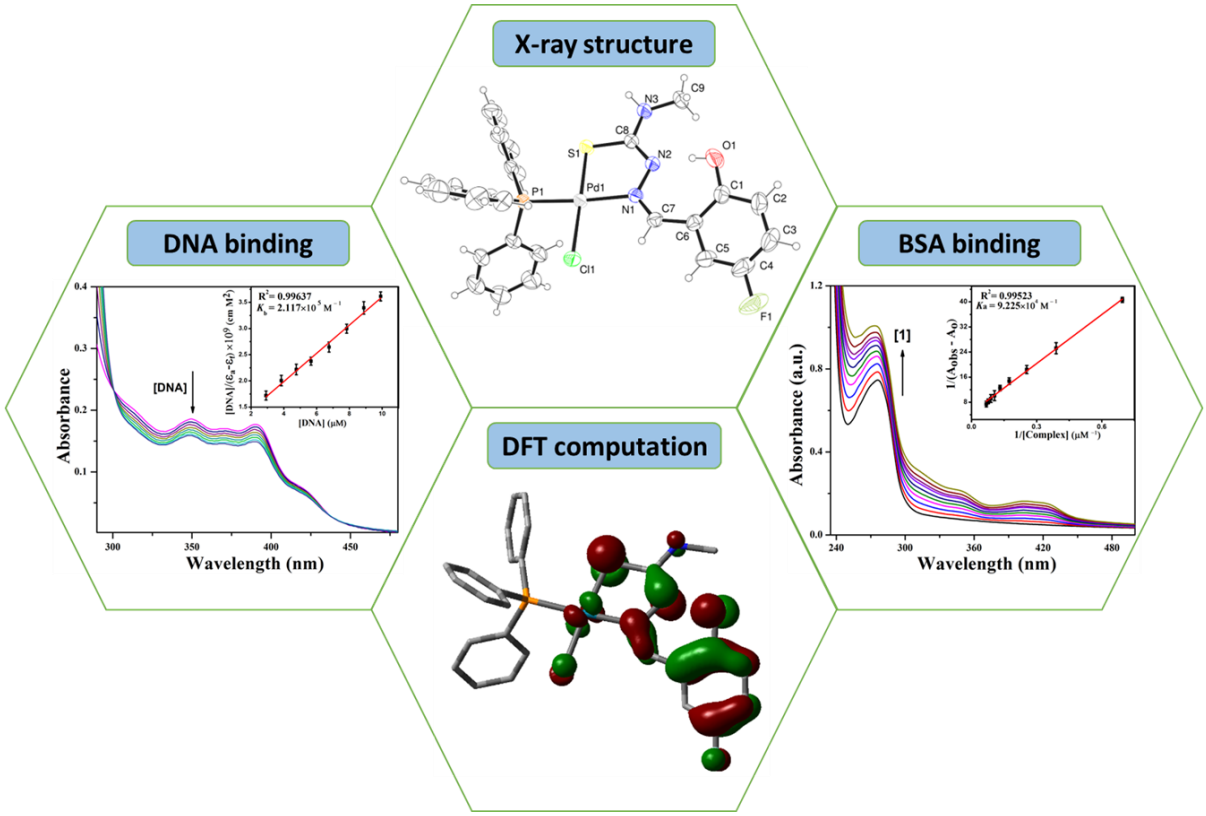

II.1. Introduction

Nowadays, cancer is one of the most important human health concerns in the world, which claims numerous deaths each year and is on the increase worldwide.[1,2] A majority of drugs used for the treatment of cancer today are not cancer cell specific and are potently toxic against normal cells also. This has opened up a new and active area of research in bioinorganic medicinal chemistry. In this regard, cisplatin, carboplatin, and oxaliplatin are well-known metal-based drugs and are widely used to treat solid tumors.[3,4] However, they have some limitations due to resistance over a period of time and severe side effects in causing nausea and the failure of kidney and liver, which are typical of heavy metal toxicity.[5] Hence, attempts have been made extensively to replace these drugs with more-efficient, less toxic, and target-specific noncovalent DNA binding anticancer drugs. Since palladium(II) complexes are good alternative candidates for metal organic antitumor drugs due to their structural and thermodynamic similarities to platinum(II) complexes, a number of palladium(II) thiosemicarbazone complexes have been synthesised and examined for their potential as antitumor agents.[6] In this area, palladium(II) complexes of 4(N)-substituted thiosemicarbazones have attracted considerable attention and many of them showed remarkable cytotoxic activity.[7-9]

Among the sulfur family, thiosemicarbazones are unique and multifaceted ligands that hold a variety of flexible donor sets and are proficient of coordinating to the metal ion through the sulfur and one of the hydrazinic nitrogen atoms (N1 or N2), leading to the formation of either a five or a four member chelate ring.[10,11] The versatility of the thiosemicarbazone ligands for binding to the metal ion has been well documented. Besides the enormous structural diversity exhibited by the metal complexes, they have a wide range of biological properties such as antitumor, antibacterial, antiviral, antifungal, and insulin mimetic properties.[12-14]

Synthesis of new metal complexes with structural design and properties analogous to anticancer agents is one of the most productive areas of coordination chemistry. The fact that DNA and protein biomolecules are electron-rich and metal ions electron-deficient compels one to believe to have strong interactions between metal ions and biomolecules. Therefore, the study of the binding properties of metal complexes with DNA and protein is of great significance for the design of new drugs and their application.[15] Depending on the nature of the metal and ligands, the complexes can bind to the DNA via the following three non-covalent modes: intercalation, groove binding interaction and electrostatic interaction between negatively charged DNA phosphate residue and positively charged species.[16] Additionally, the study on interaction of proteins with metal complex is very helpful as it

could offer information to examine the therapeutic efficiency and pharmacological response of drugs. Furthermore, proteins are venerated as the major cellular target for antitumor drugs and the most carrier proteins in the blood stream is Human Serum Albumin (HSA). Since Bovine Serum Albumin (BSA) structure is homologous with Human Serum Albumin (HSA) and due to its easy availability and low price, BSA is typically used in biochemical and biophysical studies.[17-20]

With the above facts in mind, new palladium(II) complexes containing 4(N)-substituted thiosemicarbazones have been synthesized and characterized by using various spectroscopic techniques like NMR, IR, Mass and UV-Vis. The crystal structures of the synthesized complexes have been determined by X-ray crystallography. DFT and TD-DFT calculations were accomplished to elucidate the electronic structure and UV-Vis spectra of the complexes. The investigation of the biological properties of the complexes have been carried out focusing on the binding properties with calf thymus DNA (CT-DNA) and competitive binding studies with ethidium bromide (EB). Also, the interaction of the complexes with BSA were studied to determine their binding mode.

II.2. Experimental

II.2.1. Materials and methods

4(N)-methylthiosemicarbazide, 4(N)-phenylthiosemicarbazide, 5-fluorosalicylaldehyde and $PdCl_2$ were purchased from Sigma-Aldrich. Solvents were available from commercial sources and used without further purification. Ethidium bromide (EB), Tri(hydroxylmethyl) aminomethane (Tris-HCl), calf thymus DNA(CT-DNA) and bovine serum albumin (BSA) were obtained from Sigma Aldrich chemical company. The ligands and the starting complex, $[PdCl_2(PPh_3)_2]$ were synthesized according to the standard literature procedures.[21]

Elemental analyses (C, H, N) were performed on a 2400 Series-II CHN analyzer, Perkin Elmer, USA. Waters (Xevo G2 Q-TOF) mass spectrometer was used to record mass spectra of the ligand and complexes. Infrared spectra of the ligands and the metal complexes were recorded in the range of 4000-400 cm^{-1} using a RX-1 PerkinElmer spectrometer from KBr pellets. ^{1}H-NMR spectra of ligand and complexes were recorded in DMSO with TMS as the internal standard on a Bruker (AC) 300 MHz FT-NMR spectrometer. The electronic spectra of the complexes were recorded using PerkinElmer Lambda 750 spectrophoto-meter. The emission spectra were recorded by using Shimadzu RF-6000 fluorescence spectrophotometer at room temperature (298 K).

II.2.2. Syntheses

II.2.2.1. Synthesis of the ligand [H_2-Fsal-mtsc] (H_2L^1)

4(N)-methylhiosemicarbazide (0.09 g, 0.856 mmol) was dissolved in 20 mL of acetonitrile with continuous stirring and it was gently heated for a period of 30 min. To this, acetonitrile solution (10 mL) of 5-fluorosalicylaldehyde (0.12 g, 0.856 mmol) was added and the mixture was refluxed by stirring for 4 h. The reaction mixture was then cooled and was used for complex formation reactions. Yield 0.145 g (75%).

Anal. Calc. for $C_9H_{10}FN_3OS$: C,47.57; H,4.44; N,18.49. Found: C, 47.42; H, 4.35; N, 18.36. IR (KBr, cm^{-1}): 3376 υ(O-H); 3238, 3135 υ(N-H); 3032, 2942 υ(C-H); 1559 υ(C=N). ^{1}H NMR (300 MHz, DMSO-d_6, ppm): 11.49 (s, 1H, OH), 9.93 (s, 1H, NHCS), 8.57 (s, 1H, NHCH3), 8.31 (s, 1H, CH=N), 7.88-6.84 (m, 3H, aromatic), 3.01 (d, 3H, CH3). HRMS: calculated for $C_9H_{10}FN_3OS$ $[M+H]^+$ (m/z): 228.0607; found: 228.1616.

II.2.2.2. Synthesis of the ligand [H_2-Fsal-ptsc] (H_2L^2)

The ligand [H_2-Fsal-ptsc] was prepared from 4(N)-phenyl thio- semicarbazide (0.14 g, 0.856 mmol) and 5- fluorosalicylaldehyde. (0.12 g, 0.856 mmol). Yield 0.191 g (77%).

Anal. Calc. for $C_{14}H_{12}FN_3OS$: C, 58.12; H, 4.18; N, 14.52. Found: C, 58.02; H, 4.05; N, 14.42. IR (KBr, cm^{-1}): 3383 υ(O-H); 3231, 3114 υ(N-H); 3032, 2950 υ(C-H); 1566 υ(C=N). ^{1}H NMR (300 MHz, DMSO-d_6, ppm): 11.48 (s, 1H, OH), 9.85 (s, 1H, NHCS), 9.24 (s, 1H, NHPh), 8.32 (s, 1H, CH=N), 7.73-6.92 (m, 8H, aromatic). HRMS: calculated for $C_{14}H_{12}FN_3OS$ $[M+H]^+$ (m/z): 290.0763; found: 290.0602.

II.2.2.3. Synthesis of Pd(II) complex, [Pd(H-Fsal-mtsc)Cl(PPh_3)] (1)

A solution of [$PdCl_2(PPh_3)_2$] (0.100 g, 0.142 mmol) in 20ml of acetonitrile was added to the ligand, H_2-Fsal-mtsc (0.032 g, 0.142 mmol). The mixture was refluxed for 6 h during which period an orange-colored precipitate was formed. The reaction mixture was then cooled to room temperature and the solid compound was filtered. The single crystals of complex **1** grown from methanol/DMSO through slow evaporation were found to be suitable for X-ray diffraction. The yield was, 0.071 g, 79%.

Anal. Calc. for $C_{27}H_{24}ClFN_3OPPdS$: C, 51.44; H, 3.84; N, 6.67. Found: C, 51.31; H, 3.75; N, 6.55. IR (KBr, cm^{-1}): 3341 υ(O-H); 3252 υ(N-H); 3046, 2956 υ(C-H); 1592 υ(C=N). ^{1}H NMR (300 MHz, DMSO-d_6, ppm): 11.32 (s, 1H, OH), 8.71 (s, 1H, $NHCH_3$), 8.44 (s, 1H, CH=N), 7.69-6.90 (m, aromatic), 2.76 (d, 3H, CH3). HRMS: calculated for $C_{27}H_{24}ClFN_3OPPdS$ $[M-Cl]^+$ (m/z): 594.0397; found: 594.0493.

II.2.2.4. Synthesis of Pd(II) complex, [Pd(Fsal-mtsc)(PPh$_3$)] (2)

It was prepared as described for complex **1** by the reaction of [$PdCl_2(PPh_3)_2$] (0.100 g, 0.142 mmol) with ligand, H_2-Fsal-ptsc (0.041 g, 0.142 mmol). An orange-colored precipitate formed was filtered. The single crystals of complex **2** grown from methanol/DMSO were found to be suitable for X-ray diffraction. The yield was, 0.075 g, 81%.

Anal. Calc. for $C_{32}H_{25}FN_3OPPdS$: C, 58.59; H, 3.84; N, 6.41. Found: C, 58.45; H, 3.74; N, 6.32. IR (KBr, cm^{-1}): 3273 υ(N-H); 3059, 3018 υ(C-H); 1587 υ(C=N). ^{1}H NMR (300 MHz, DMSO-d_6, ppm): 9.40 (s, 1H, NHPh), 8.62 (s, 1H, CH=N), 7.72-6.92 (m, aromatic). HRMS: calculated for $C_{32}H_{25}FN_3OPPdS$ $[M+H]^+$ (m/z): 656.0553; found: 656.0293.

II.2.3. Single crystal X-ray diffraction studies

Single crystal data of complex **1** and **2** were collected at 293K on an automated Bruker AXS D8 Quest CMOS diffractometer using graphite monochromated Mo-Kα (λ=0.71073Å) radiation by the ω scan method. The structures were solved by direct method using the SHELX-2016 and refined by full-matrix least-squares methods on F^2. All the data were adjusted for Lorentz and polarization effects and multi-scan absorption corrections were applied using SHELXTL program package.[22] All non-hydrogen atoms were refined with anisotropic thermal parameters. The hydrogen atoms bound to carbon were placed in idealized positions and were set riding on the parent atom.

II.2.4. Computational method

All geometry optimization and energy computations were performed using density functional theory (DFT) with the B3LYP level of theory.[23] LanL2DZ[24] basis set with effective core potential was employed for Pd atom while for the other elements the basis set 6-31G(d)[25] were considered for calculations. The vibrational frequency calculations were performed to ensure that the optimized geometries represented the local minimum on the potential energy surface and there were only positive Eigen values. Gaussian09 program package[26] was employed to visualize geometry optimized structures and to calculate the minimum energy structure. The calculated electronic density contour plots for frontier molecular orbitals were plotted by using the GaussView, Version 5 visualization program. Solvent effects play an important role in the electronic structure of the complexes. On the basis of the optimized ground state geometries, the absorption spectra in DMSO were calculated by time-dependent density functional theory (TD-DFT)[27] using the conductor-like polarizable continuum model (CPCM)[28]. The fractional contributions of various groups to each molecular orbital were calculated using GaussSum.[29]

II.2.5. DNA binding studies

II.2.5.1. Absorption spectroscopic studies

The DNA binding ability of complex **1** and **2** has been evaluated by absorption as well as emission spectroscopy. The interaction of the complex with CT-DNA was performed by using Tris-HCl buffer solution having pH 7.2. The concentration of CT-DNA was determined from its absorption intensity at 260 nm by employing an extinction coefficient of 6600 $M^{-1}cm^{-1}$. The UV absorbance at 260 and 280 nm of the CT-DNA solution gave a ratio in the range of 1.8 to 1.9, indicating that the DNA was satisfactorily free from protein molecules. The absorption spectra of the complexes at a constant concentration were recorded in presence of different concentrations of CT-DNA and a noteworthy change in absorption values was observed.[30]

II.2.5.2. Ethidium bromide displacement experiments

The competitive binding interactions of the complexes were examined by fluorescence spectroscopy method in order to find out whether the compound can displace EB from its EB-CT-DNA system.[31] The CT-DNA-EB complex was initially prepared by adding 15 μM EB and 30 μM CT-DNA in Tris-HCl/NaCl buffer solution (pH 7.4). Ethidium bromide (EB) displacement experiments were done by successive addition of complexes into the Tris-HCl buffer solution of EB-CT-DNA complex. After successive addition of the metal complexes, the change in fluorescence intensity at 612 nm were monitored (ex. wavelength 540 nm).

II.2.6. Protein binding studies

Bovine serum albumins (BSA) are frequently used in studies of the interactions with complexes and proteins because it is responsible for the transport of drugs in biological systems.[32,33] The binding ability of complexes with BSA protein were determined by employing UV-Vis and fluorescence spectroscopic techniques. The BSA stock solution was prepared using 500 mM phosphate buffer saline (PBS) at pH 7.4 and stored in the dark at 4°C for further use. The concentration of BSA was measured by taking absorbance at 280 nm in UV-Vis spectra (molar extinction coefficient 66,400 M^{-1} cm^{-1}). The stock solution of complexes was prepared in DMSO medium and was suitably diluted with PBS whenever necessary. The absorption spectra were recorded at room temperature with constant concentration of BSA (9 μM) while varying the concentration of complex added to it. In fluorescence experiment, tryptophan fluorescence of BSA was recorded in the range 290-450 nm at an excitation wavelength of 280 nm. Quenching of emission intensity at ~336 nm for BSA was monitored with successive addition of complex.

II.3. Results and discussion

II.3.1. Synthesis and spectra

The new palladium(II) complexes were synthesized by reacting 4(N)-substituted 5-fluorosalicylaldehyde thiosemicarbazone ligands (H_2L^1/ H_2L^2) with equimolar amount of $[PdCl_2(PPh_3)_2]$ in acetonitrile (Scheme II.1). The ligands and complexes were characterized by IR, UV-visible and H NMR spectroscopic techniques and the structure of **1** and **2** were confirmed by single crystal X-ray diffraction studies.

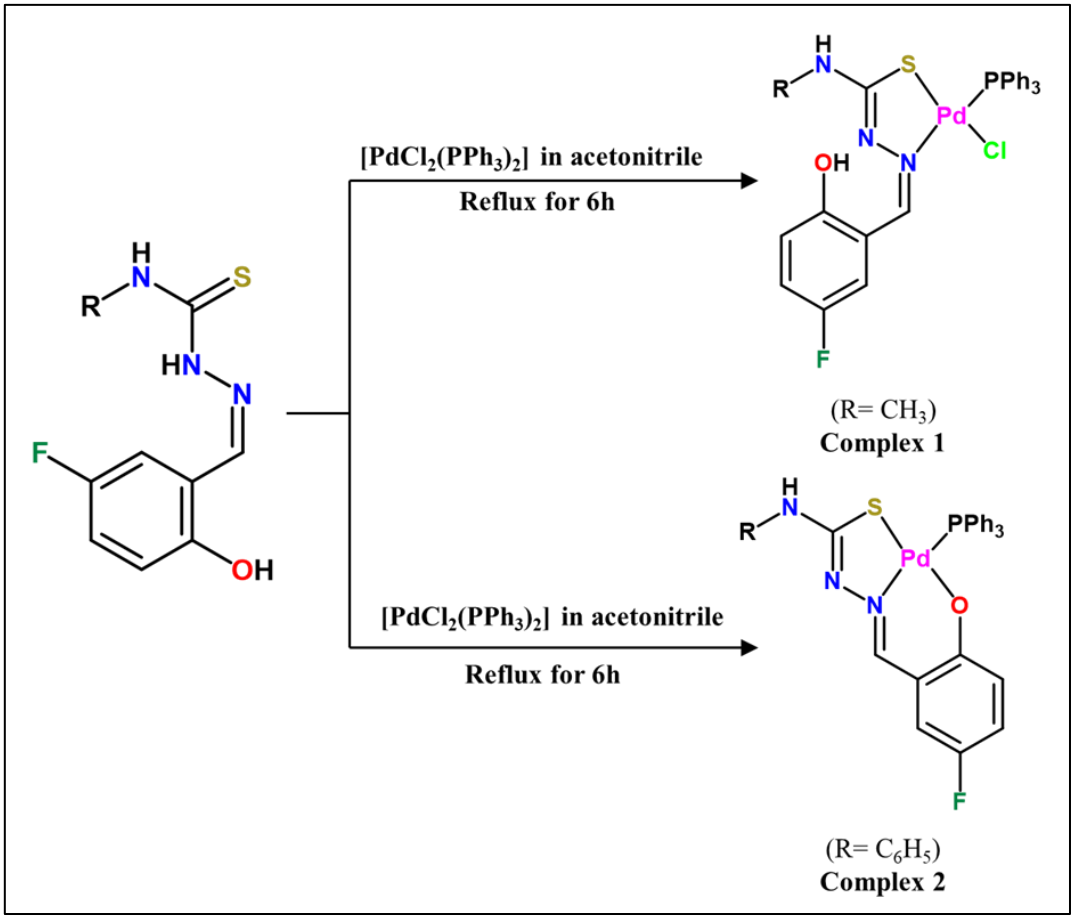

Scheme II.1. Synthetic scheme for complex **1** and complex **2**

The Fourier transform infrared (FT-IR) spectra provide promising indications regarding the involvement of coordination sites of the ligand in chelation with metal. A band in the region 3376-3383 cm^{-1} due to a hydrogen bonded –OH group in the free ligands was not observed in the IR spectra of complex **2**. This indicates that the phenolic oxygen is deprotonated and coordinated to metal in the complex **2**. However, the υ(O-H) stretching frequency found at 3341 cm^{-1} for the complex **1** indicated the non-participation of phenolic oxygen in coordination to the palladium ion (Fig. II.1 and Fig. II.2). A strong vibration observed at 1559–1566 cm^{-1} in the ligands corresponding to υ(C=N) was shifted to 1587–1592 cm^{-1} in the complexes indicating the participation of azomethine nitrogen in bonding.[21]

The ^{1}H-NMR spectra of ligands and their corresponding Pd(II) complexes were recorded in DMSO and are shown in Fig. II.3 – Fig.II.6. In the spectra of free ligands, a singlet appeared at 9.93-9.85 ppm corresponding to N(2)H proton, which disappeared in the complexes, confirming deprotonation followed by coordination of thiolate sulfur to palladium which results in the formation of a five membered chelate ring. In spectra of free ligands, a sharp singlet corresponding to the phenolic -OH group has appeared at 11.49-11.48 ppm. In the spectra of complex **1** the appearance of a singlet at 11.32 ppm indicated the nonparticipation of phenolic oxygen from coordination. But the same singlet peak has completely disappeared in complex **2**, confirming the involvement of phenolic oxygen in coordination.[8] In the spectra the complexes, a multiplet appeared in the region of 7.72-6.90 ppm due to aromatic protons of the ligands and triphenylphosphine. The ligands had a singlet for azomethine (-CH=N-) proton at 8.31-8.32 ppm, however in spectra of the complexes, this proton signal shifted downfield region (at 8.44-8.62 ppm) due to azomethine nitrogen coordination. The signals corresponding to the terminal -NH proton of the complexes was observed as a sharp singlet at 9.40-8.71 ppm. In addition, H_2L^1 and complex **1** showed a doublet at 2.76 ppm for the terminal -CH3 protons. Mass spectrum of complex **1** shows m/z peak corresponding to $[M-Cl]^+$ at 594.0493 (Fig. II.9) while complex **2** exhibits m/z peak corresponds to $[M+H]^+$ at 656.0553 (Fig. II.10).

Absorption spectra of complexes **1** and **2** were taken in DMSO (Fig. II.11). The solution spectrum of complex **1** exhibit moderately intense energy band at 390 nm along with a shoulder band at 419 nm. In addition, high energy bands appeared at 370, 349 and 302 nm. Absorption spectra of complex **2** exhibit low energy peaks at 412 nm along with a shoulder band at 428 nm and high energy bands appeared at 346 nm and 318 nm.

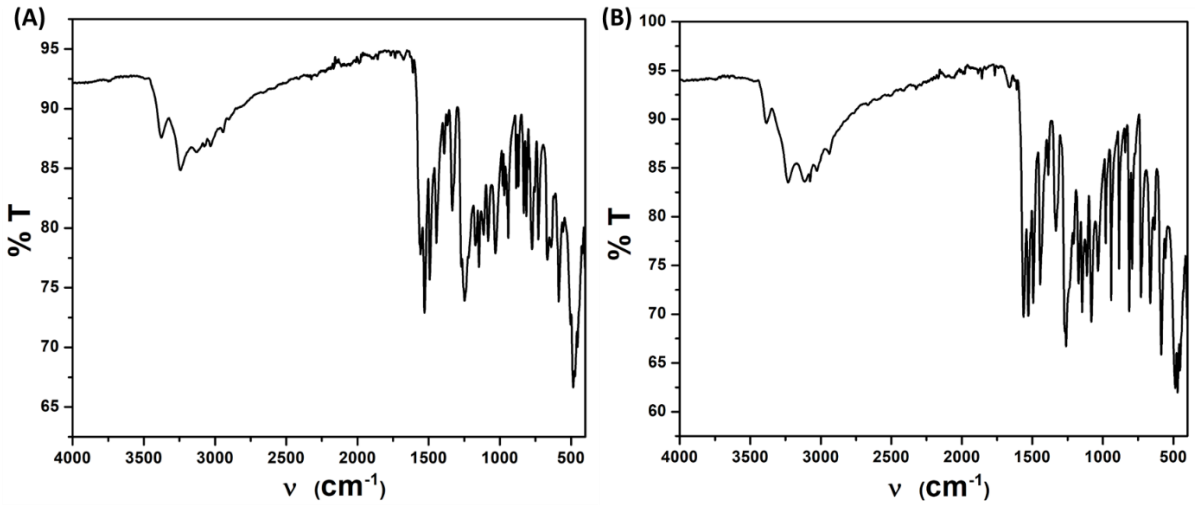

Fig. II.1. IR spectrum of ligand H_2L^1 (A) and ligand H_2L^2 (B)

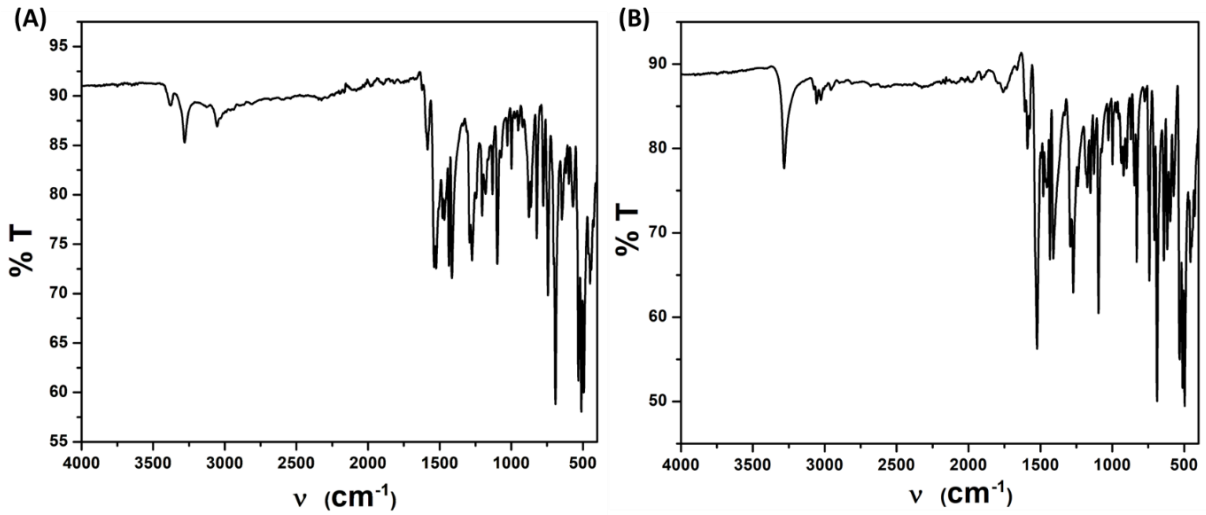

Fig. II.2. IR spectrum of complex **1** (A) and complex **2** (B)

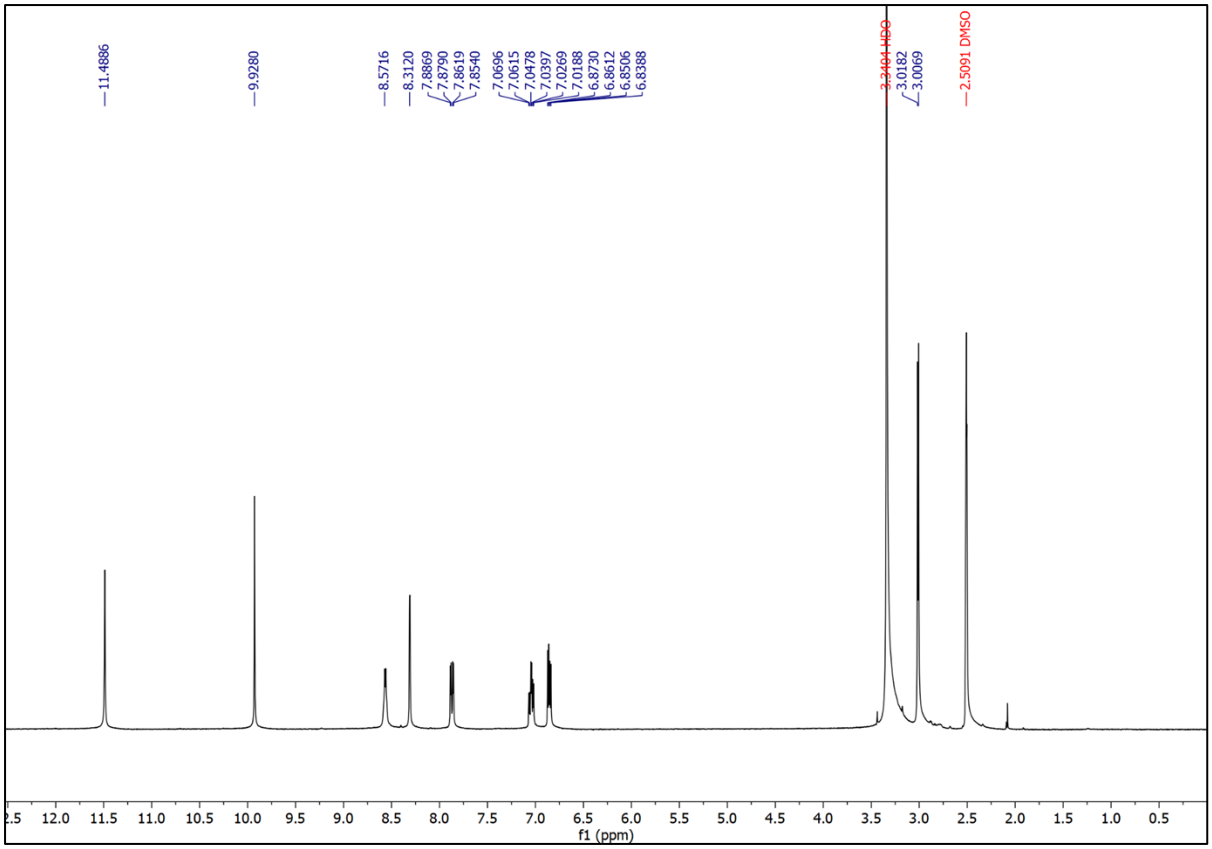

Fig. II.3. ^{1}H-NMR spectrum of ligand H_2L^1 in DMSO-d_6

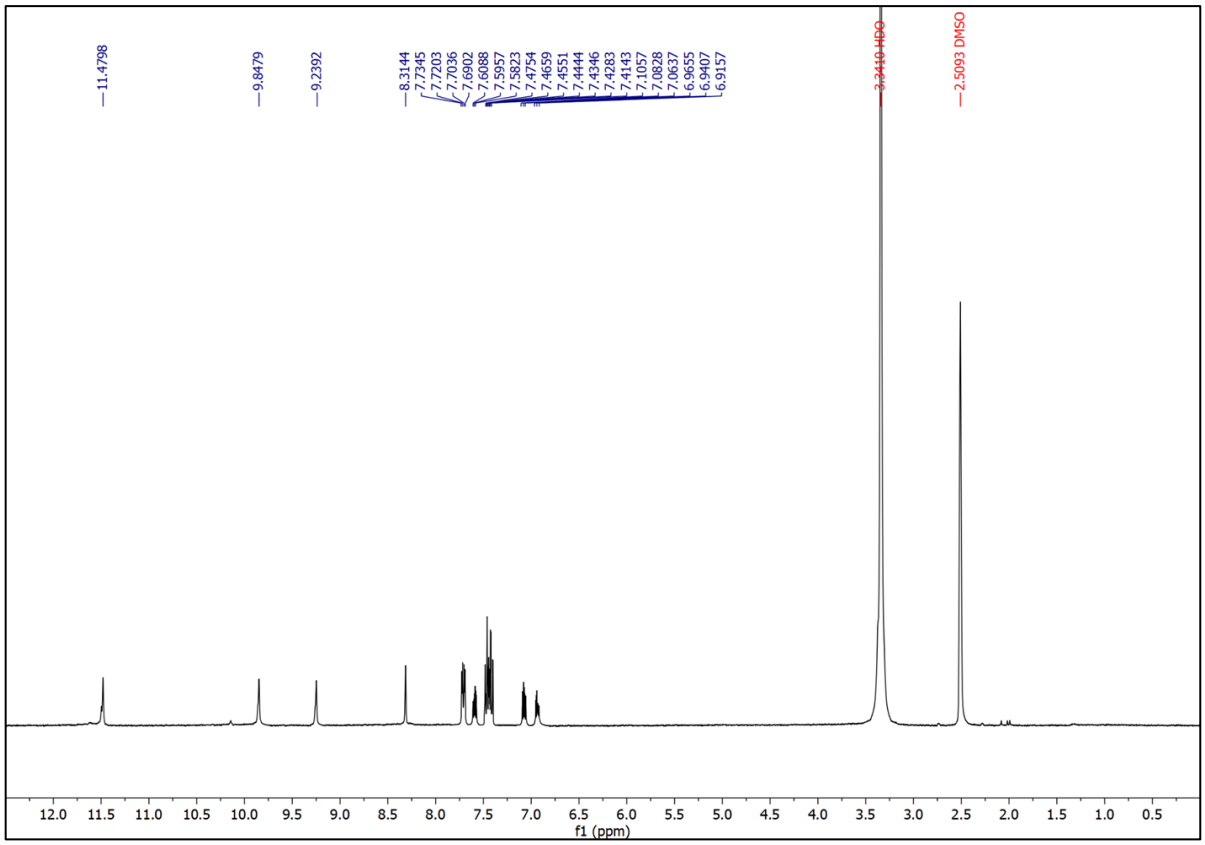

Fig. II.4. ^{1}H-NMR spectrum of ligand H_2L^2 in DMSO-d_6

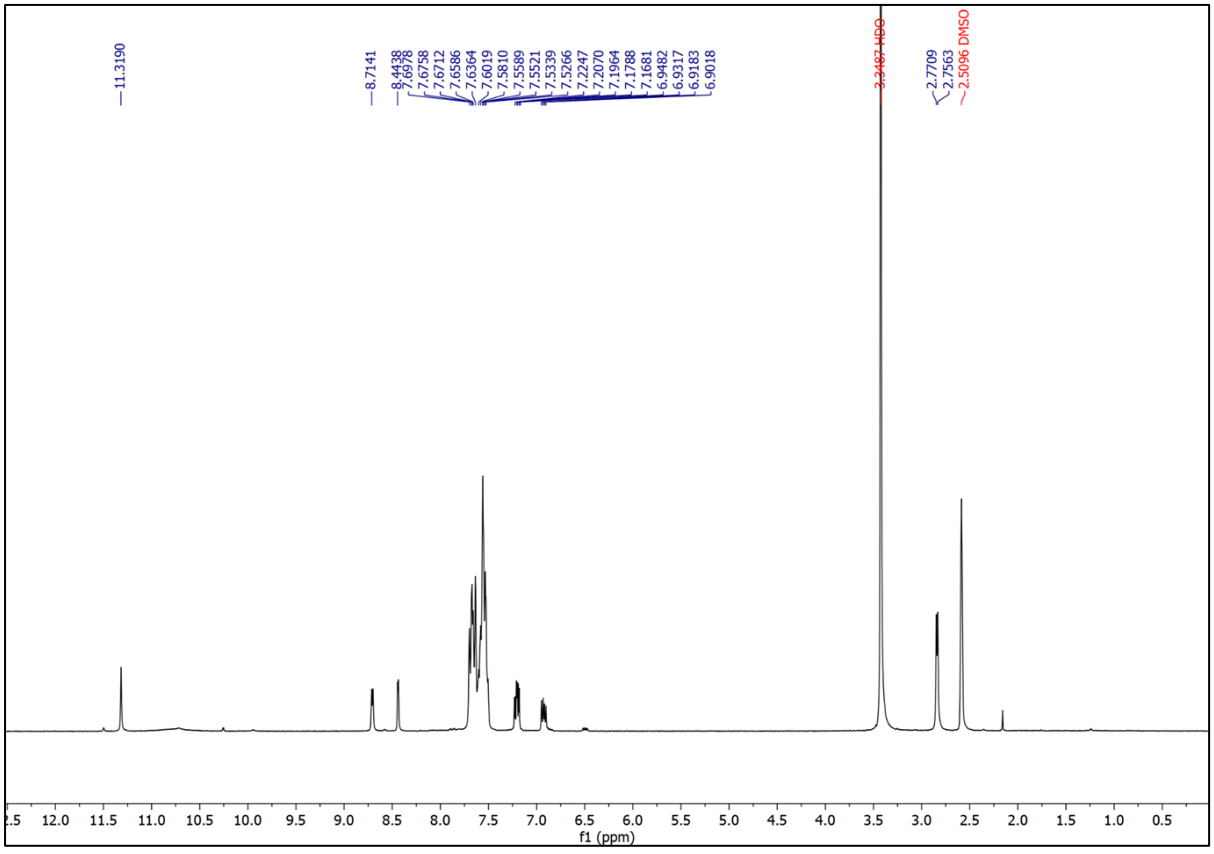

Fig. II.5. ^{1}H-NMR spectrum of complex **1** in DMSO-d_6

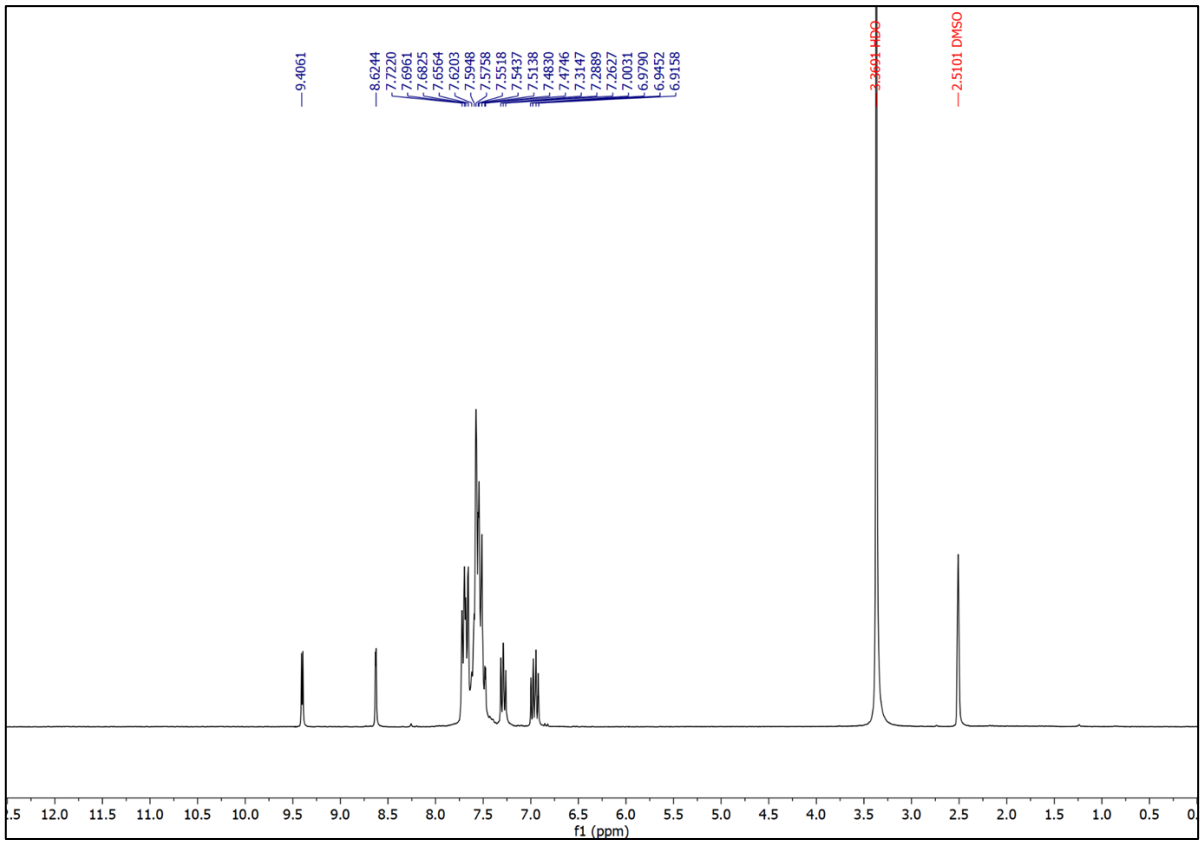

Fig. II.6. ^{1}H-NMR spectrum of complex **2** in DMSO-d_6

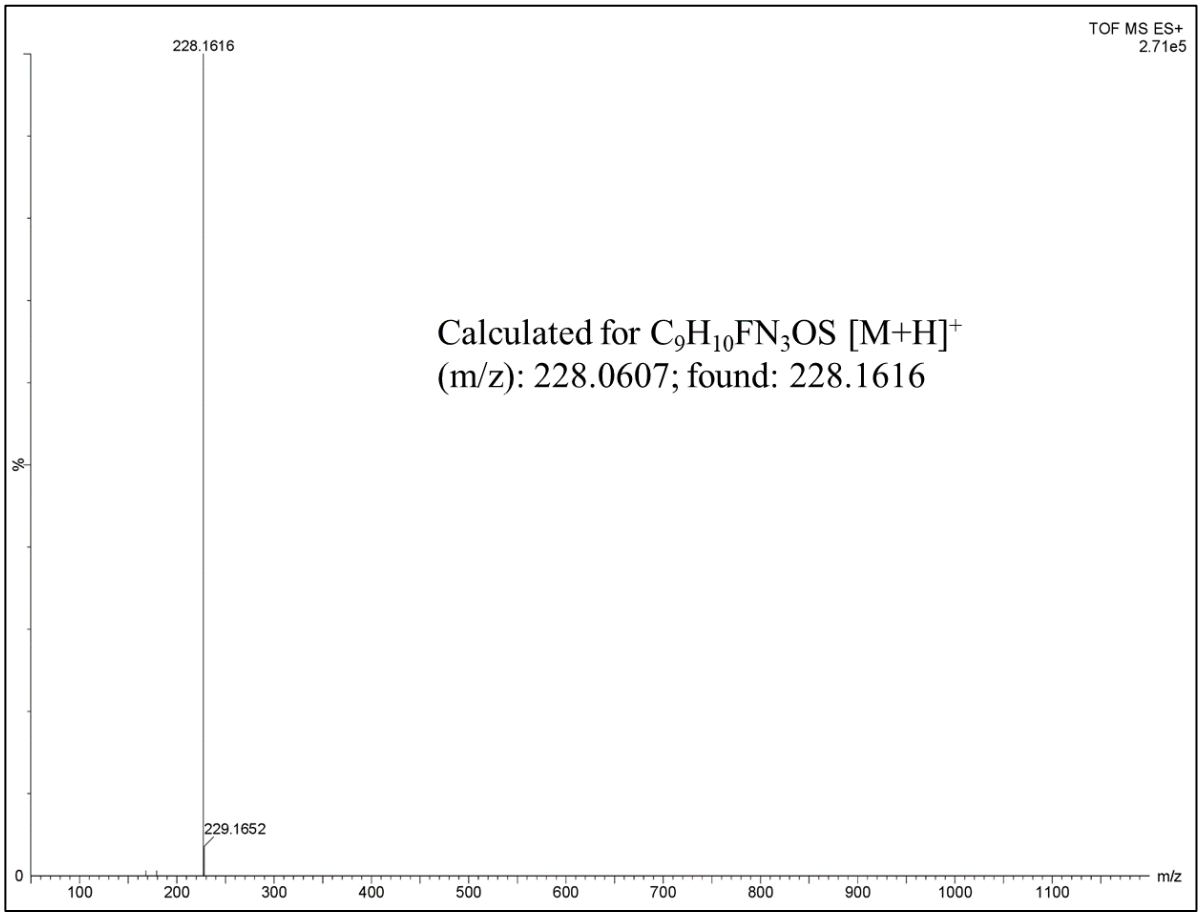

Fig.II.7. HRMS spectrum of ligand H_2L^1

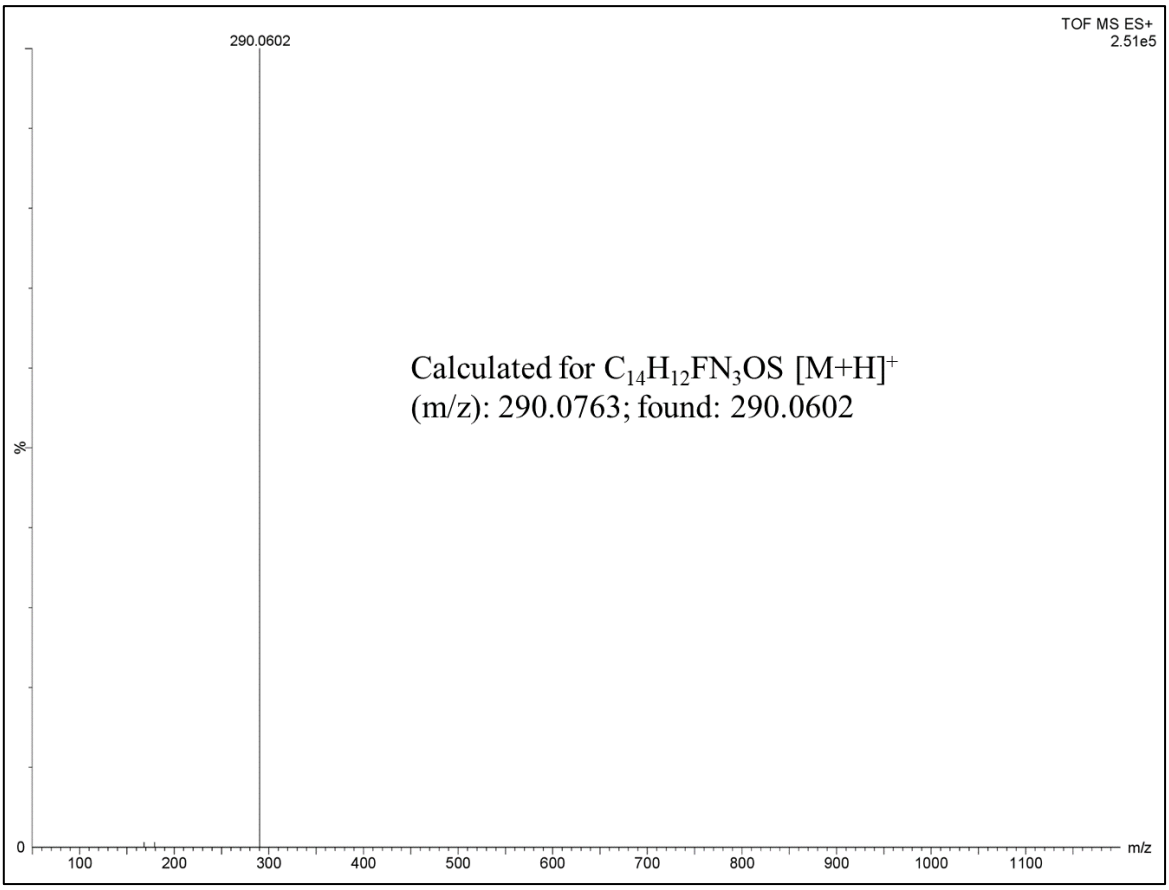

Fig.II.8. HRMS spectrum of ligand H_2L^2

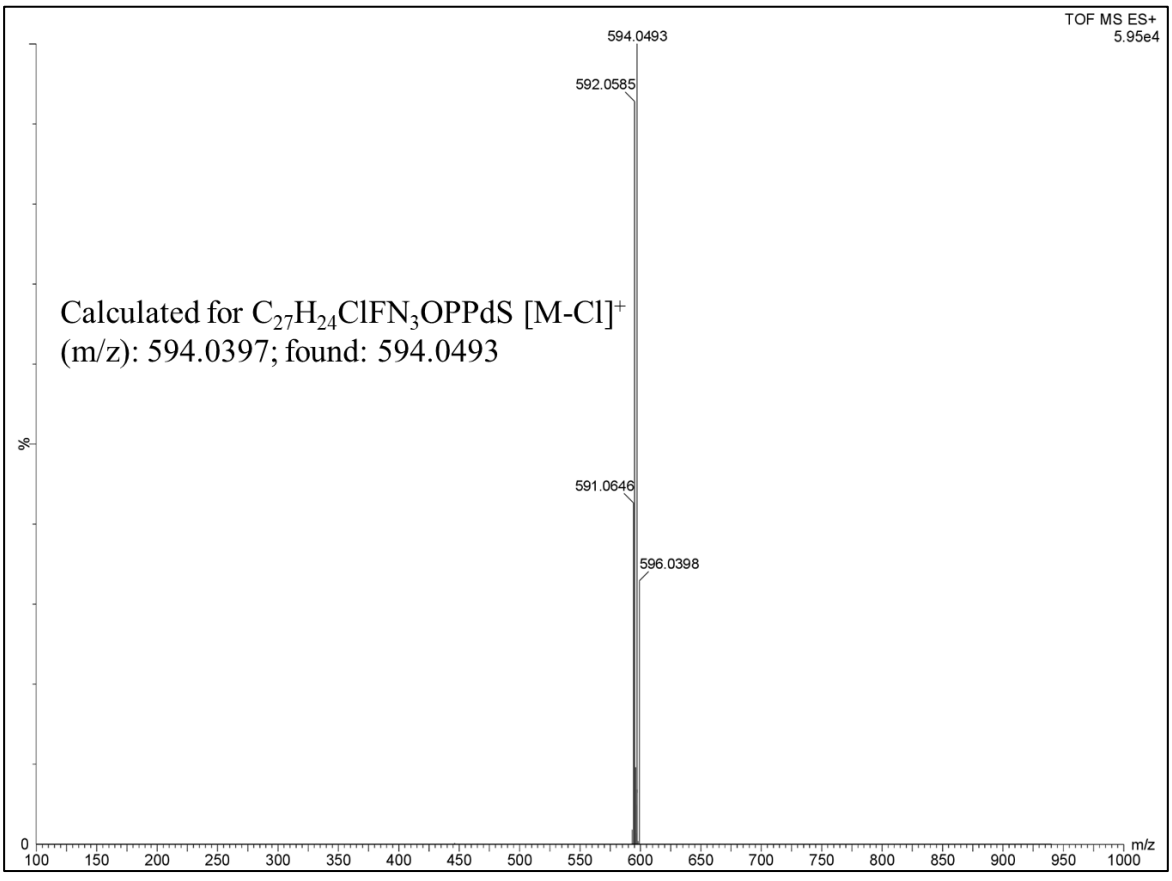

Fig.II.9. HRMS spectrum of complex **1**

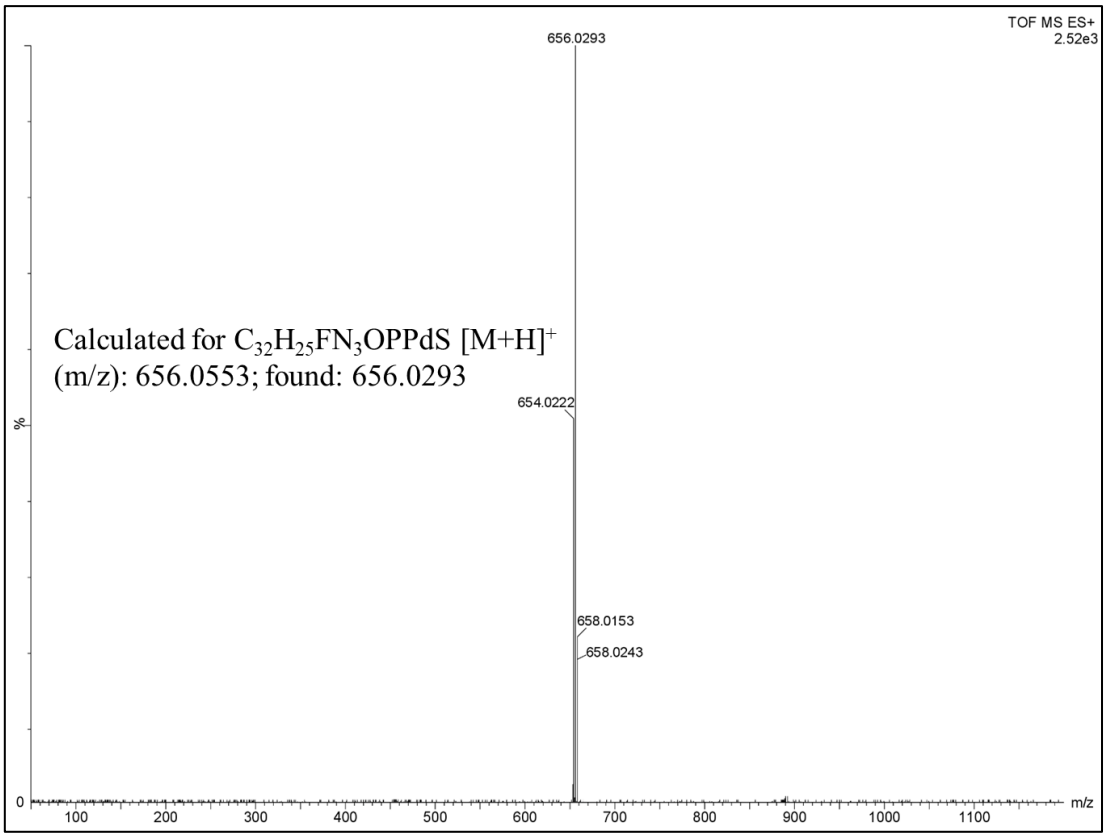

Fig.II.10. HRMS spectrum of complex **2**

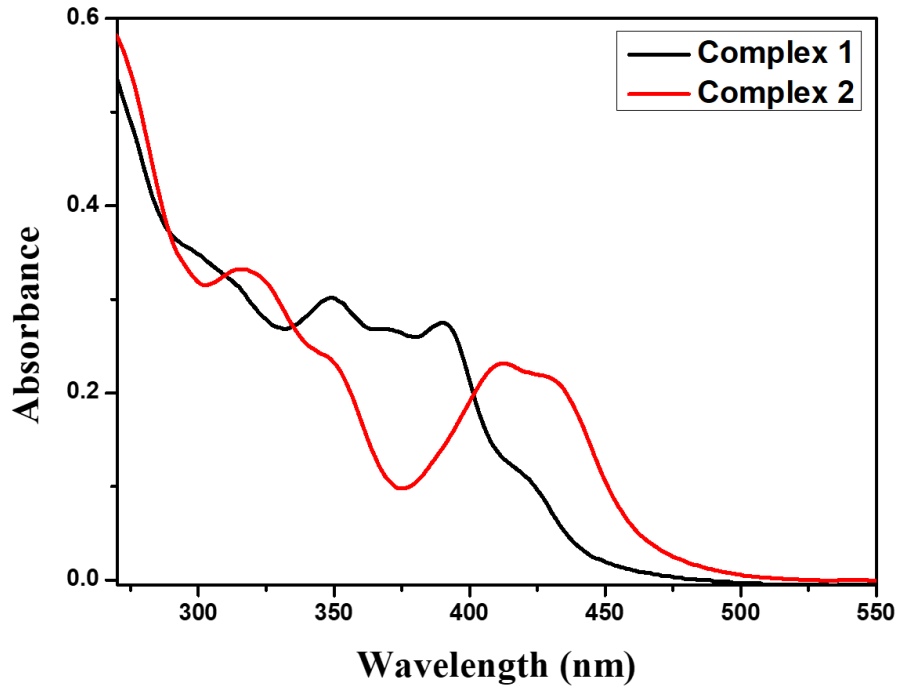

Fig. II.11. UV-Vis spectra of Complex **1** and **2** in DMSO

II.3.2. Crystallographic study

The molecular structures of complexes **1** and **2** have been determined by the single crystal X-ray diffraction method to predict the coordination mode of ligands. The single-crystal X-ray

studies revealed that the complex **1** is crystallized in a monoclinic crystal system with the space group P 21/c, whereas the complexes **2** crystallized in the triclinic system with the space group *P-1*. The ORTEP view along with the atomic numbering scheme of the complexes **1** and **2** are shown in Fig. II.12. Relevant crystallographic data and details of structure refinements for the complexes are summarized in Table II.1. Selected inter atomic bond lengths and bond angles are listed in Table II.2. In the complexes **1**, the Pd(II) ion is coordinated to the mono basic bidentate ligand through the thiolate sulfur atom [Pd1-S1, 2.2392(6) Å] and the imine nitrogen atom [Pd1-N1, 2.1118(19) Å] by forming a five membered ring with a bite angle N(1)-Pd(1)-S(1) of 84.00(5)^{o}. The remaining binding sites are occupied by one chlorine atom [Pd1-Cl1, 2.3470(6) Å] and the triphenylphosphine unit [Pd1-P1, 2.2501(6) Å]. The cis-angles N1-Pd1-S1, N1-Pd1-Cl1, P1-Pd1-Cl1 and S1-Pd1-P1 are found to be 84.00(5)^{o}, 96.94(6)^{o}, 87.90(2)^{o} and 91.17(2)^{o} respectively, while the two trans-angles N1-Pd1-P1 and S1–Pd1–Cl1 are 175.16(5)^{o} and 179.01(2)^{o} respectively. The cis and trans-angles are in significant deviation from their respective idealistic values of 90^{o} and 180^{o}, suggesting significant distortion in the square planar geometry of the complex. In the complexes **2**, the Pd(II) ion is coordinated to the negatively charged tridentate ligand through the thiolate sulfur atom [Pd1-S1, 2.2456(12) Å], phenolic oxygen atom [Pd1-O1, 2.009(3) Å] and the imine nitrogen atom [Pd1-N1, 2.007(3) Å] by forming a five and six membered chelate rings with a bite angle N1-Pd1-S1 of 84.00(10)^{o} and O1-Pd1-N1 of 92.35(14)^{o}. The remaining binding site is occupied by the triphenylphosphine unit [Pd1-P1, 2.2836(12) Å]. The two trans-angles N1-Pd1-P1 and S1-Pd1-O1 are 177.74(11)^{o} and 176.34(10)^{o}, which deviate considerably from the ideal angle of 180◦ causing significant distortion in the square planar geometry the complex.

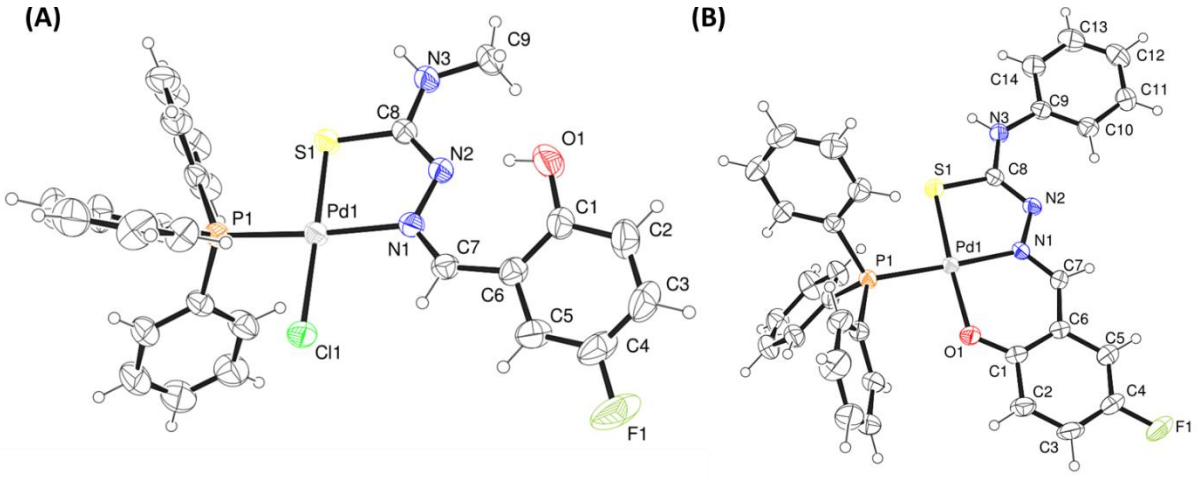

Fig. II.12. ORTEP plots with 35% ellipsoidal probability of complex **1** (A) and **2** (B)

Table II.1. Crystallographic data and refinement parameters of complex **1** and **2**

Complex	Complex **1**	Complex **2**
Formula	C27 H24 Cl F N3 O P Pd S	C34 H31 F N3 O2 P Pd S2
Formula Weight	630.37	734.11
Crystal System	*monoclinic*	*triclinic*
Space group	$P\ 2_1/c$	$P\ \bar{1}$
a, b, c [Å]	12.6549(7), 19.6241(11), 12.0433(7)	10.7511(3), 12.3684(4), 14.5484(4)
α [°]	90	114.8430(10)
β [°]	113.289(2)	105.0530(10)
γ [°]	90	95.4720(10)
V [$Å^3$]	2747.2(3)	1648.50(8)
Z	4	2
D(calc) [g/cm^3]	1.524	1.479
Mu(MoKa)[mm^{-1}]	0.939	0.779
F(000)	1272	748
Temperature (K)	293(2)	293(2)
Radiation [Å]	0.71073	0.71073
θ(Min-Max) [°]	2.113- 27.117	1.825- 27.222
Dataset (h; k; l)	-16 to 16, -25 to 25, -15 to 15	-13 to 13, -15 to 15, -18 to 18
R, wR_2	0.0307, 0.0721	0.0629, 0.1100
Goodness of fit(S)	1.051	1.191

Table II.2. Selected X-ray and calculated bond distances and angles of complexes **1** and **2**

Complex **1**			Complex **2**		
Bonds(Å)	X-ray	Calc.	Bonds(Å)	X-ray	Calc.
Pd1-N1	2.1118(19)	2.13658	Pd1-N1	2.007(3)	2.04594
Pd1-S1	2.2392(6)	2.31252	Pd1-S1	2.2456(12)	2.30798
Pd1-P1	2.2501(6)	2.31713	Pd1-P1	2.2836(12)	2.34443
Pd1-Cl1	2.3470(6)	2.38279	Pd1-O1	2.009(3)	2.03348
N1-C7	1.286(3)	1.30154	N1-C7	1.285(5)	1.30565
N1-N2	1.398(3)	1.38050	N1-N2	1.409(5)	1.38131

Angles (°)					
N1-Pd1-S1	84.00(5)	82.55235	N1-Pd1-S1	84.00(10)	83.31420
N1-Pd1-P1	175.16(5)	177.49192	N1-Pd1-P1	177.74(11)	177.49452
S1-Pd1-P1	91.17(2)	94.97979	S1-Pd1-P1	93.75(4)	94.76242
N1-Pd1-Cl1	96.94(6)	94.71171	N1-Pd1-O1	92.35(14)	92.71536
S1-Pd1-Cl1	179.01(2)	176.57012	S1-Pd1-O1	176.34(10)	175.92889
P1-Pd1-Cl1	87.90(2)	87.77068	P1-Pd1-O1	89.91(10)	89.23153

II.3.3. DFT and TDDFT calculations

The geometry of the complexes **1** and **2** were optimized in singlet ground state by DFT/B3LYP method to recognize the electronic structure of the complexes. The calculated geometric parameters are reasonably well reproducing the X-ray crystal structures data. Contour plots of selected molecular orbitals for both the complexes **1** and **2** are shown in Fig. II.13 and Fig. II.14 respectively. Energy and compositions of selected molecular orbitals are given in Table II.3 and Table II.4 respectively. For complex **1,** the higher energy occupied molecular orbital (HOMO) has 90% contribution of ligand and the low-lying virtual orbital, LUMO has 42% contribution of dπ(Pd) orbitals and 32% contribution of ligand π*orbitals. For complex **2**, HOMO has 94% contribution of ligand while LUMO has 42% contribution of dπ(Pd) orbitals and 41% contribution of ligand π*orbital (Table II.5). The HOMO to LUMO energy gap in the complexes is found to be 3.11 eV and 3.20 eV for **1** and **2** respectively.

UV-Vis absorption bands of the complexes are interpreted by TDDFT calculations using B3LYP/CPCM method in DMSO. Calculated vertical electronic transitions are summarized in Table II.5. For complex **1**, the calculated low energy transition at 428 nm (f = 0.0188) corresponds to the HOMO-3 $\rightarrow$ LUMO transition ($\lambda_{expt.}$ = 419 nm) having mixed XLCT and XMCT character. The experimentally observed peak at 390 nm corresponds to HOMO-4 $\rightarrow$ LUMO transition (367 nm, f = 0.1466) having MLCT character. For complex **2** the lower energy experimental band at 412 nm and 428 nm correspond to the HOMO-2 $\rightarrow$ LUMO+1 transition at 412 nm (f = 0.324) having ILCT character. Similarly, the experimental observed band at 346 nm correspond to the HOMO-1 $\rightarrow$ LUMO+1 transition at 343 nm (f = 0.134) having ILCT character. The high energy band at 318 nm correspond to mixed LMCT and ILCT character.

Table II.3. Energy and % of composition of some selected molecular orbitals of complex **1**

MO	Energy	% of composition			
		Pd	Ligand	Cl	PPh_3
LUMO+5	-0.5	08	02	00	90
LUMO+4	-0.61	03	01	00	96
LUMO+3	-0.78	02	02	01	95
LUMO+2	-1.0	00	02	00	97
LUMO+1	-1.54	03	93	00	03
LUMO	-2.38	42	32	11	15
HOMO	-5.49	06	90	03	00
HOMO-1	-5.81	21	65	13	01
HOMO-2	-6.21	06	92	02	00
HOMO-3	-6.48	20	18	54	07
HOMO-4	-6.49	63	08	09	21
HOMO-5	-6.76	05	27	32	35
HOMO-6	-6.88	05	21	23	52
HOMO-7	-7.03	00	01	00	99
HOMO-8	-7.11	03	10	11	76
HOMO-9	-7.14	09	14	11	65
HOMO-10	-7.24	12	29	05	54

Table II.4. Energy and % of composition of some selected molecular orbitals of complex **2**

MO	Energy	% of composition		
		Pd	Ligand	PPh_3
LUMO+5	-0.43	07	04	89
LUMO+4	-0.65	05	01	94
LUMO+3	-0.84	02	02	96
LUMO+2	-1.08	00	01	99
LUMO+1	-1.4	02	96	01
LUMO	-1.74	42	41	17
HOMO	-4.94	05	94	00
HOMO-1	-5.57	09	90	00
HOMO-2	-5.67	08	91	01
HOMO-3	-6.44	69	23	09
HOMO-4	-6.56	11	60	29
HOMO-5	-6.62	01	99	00
HOMO-6	-6.73	15	84	01
HOMO-7	-6.83	07	27	66
HOMO-8	-7.09	03	06	91
HOMO-9	-7.13	04	06	90
HOMO-10	-7.23	05	03	92

Table II.5. Vertical electronic transition calculated by TDDFT/CPCM method of complexes **1** and **2**

Comp	λ (nm)	E (eV)	Osc. Strength (f)	Key excitations	Character	$\lambda_{expt.}$ (nm)
1	428.05	2.8965	0.0188	(56%)HOMO-3→LUMO	XLCT/ XMCT	419 (sh.)
	367.57	3.3731	0.1466	(29%)HOMO-4→LUMO	MLCT	390
	364.77	3.3989	0.2789	(75%)HOMO→LUMO+1	ILCT	370
	321.01	3.8623	0.1554	(35%)HOMO-4→LUMO	MLCT	349
	301.34	4.1145	0.2156	(74%)HOMO-2→LUMO+1	ILCT	302
2	412.94	3.0025	0.3243	(83%)HOMO-2→LUMO+1	ILCT	428 (sh) 412
	343.85	3.6057	0.1341	(47%)HOMO-1→LUMO+1	ILCT	346
	331.82	3.7365	0.1898	(52%)HOMO-1→LUMO+1	ILCT	
	322.05	3.8499	0.1751	(39%)HOMO-4→LUMO	LMCT/ ILCT	318

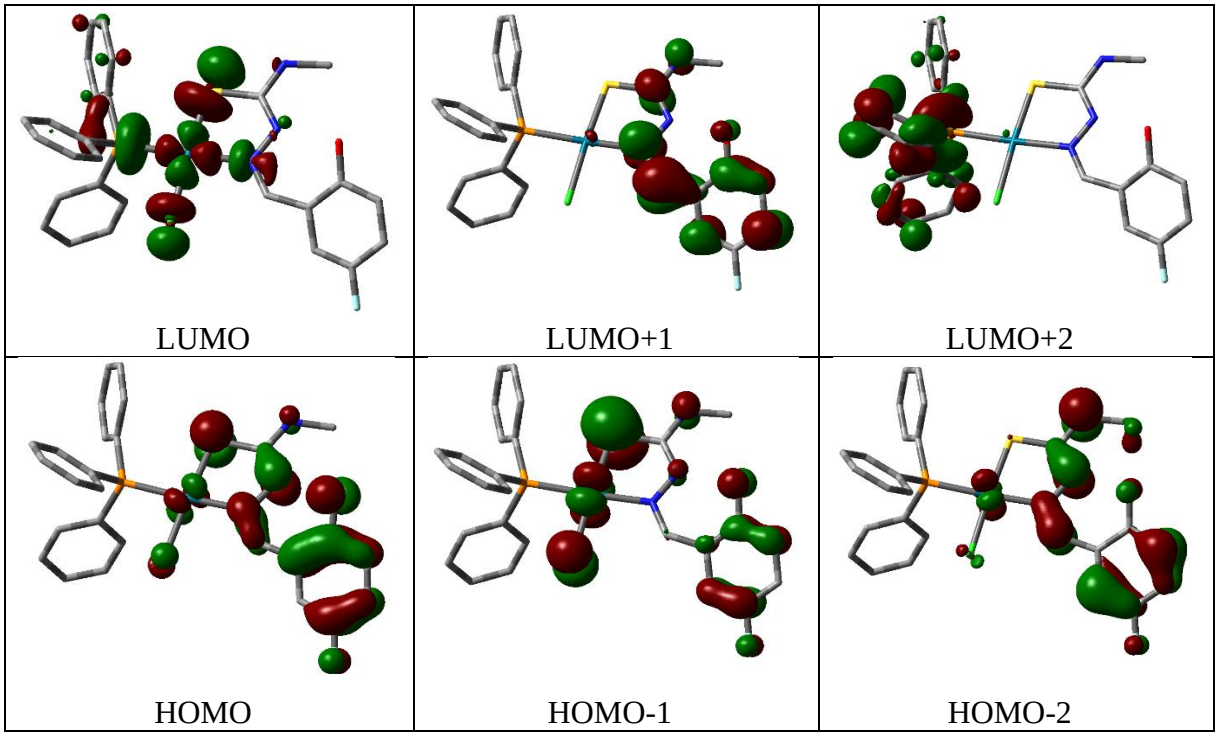

Fig. II.13. Contour plots of some selected molecular orbital of complex **1**

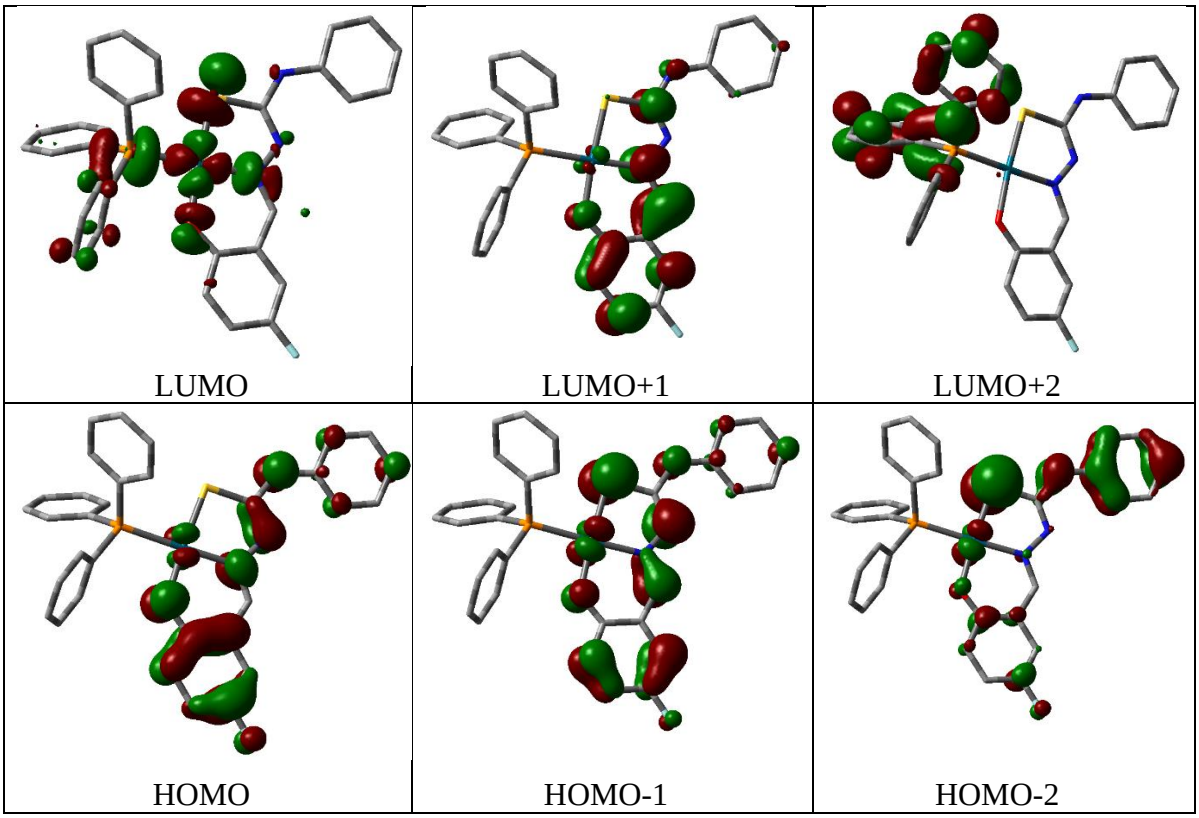

Fig. II.14. Contour plots of some selected molecular orbital of complex **2**

II.3.4. DNA binding studies

II.3.4.1. Absorption spectral studies

Electronic absorption spectroscopy is one of the most common techniques used for investigating the mode of binding between the metal complexes and DNA.[34,35] In general, the metal complexes binding to DNA through intercalation results in hypochromism with or without a small red or blue shift, since the intercalative mode involves in a strong stacking interaction between the planar aromatic chromophore and the base pairs of DNA.[36-38] The representative absorption spectra of the complexes in the absence and presence of CT-DNA are shown in Fig. II.15. It is seen from the spectra that, as the concentration of DNA is gradually increased, a significant hypochromism was observed. These results indicated that the complexes bind to the DNA helix via intercalation. The intrinsic binding constant (K_b) which offers an approximation of magnitude of the binding strength, was determined by plotting [DNA]/($\varepsilon_a - \varepsilon_f$) vs. [DNA] from the spectral titration data using the Wolfe-Shimer equation (Eq. II.1).[39]

$$\frac{[DNA]}{(\varepsilon a - \varepsilon f)} = \frac{[DNA]}{(\varepsilon b - \varepsilon f)} + \frac{1}{Kb(\varepsilon b - \varepsilon f)} \qquad \text{(Eq.II.1)}$$

where [DNA] is the concentration of CT-DNA and ε_a is the apparent extinction coefficient value found by calculating A(observed)/[complex], ε_f and ε_b are the extinction coefficients of the complex in free solution and when it is fully bound to CT-DNA respectively. ε_f was determined from the calibration curve of the isolated metal complex following Beer's law. The plot of $[DNA]/(\varepsilon_a - \varepsilon_f)$ *vs.* [DNA] give a straight line with $1/(\varepsilon_b - \varepsilon_f)$ and $1/[K_b(\varepsilon_b - \varepsilon_f)]$ as slope and intercept, respectively. The values of K_b were calculated from the ratio of the slope to the intercept. The intrinsic binding constant (K_b) values are shown in Table II.6. The K_b values are found to be $2.117(\pm0.097)\times10^5\ M^{-1}$ and $1.941(\pm0.092)\times10^5\ M^{-1}$ for complexes **1** and **2** respectively. These values are very much similar to the reported values of binding constants for other complexes towards CT-DNA.[40-43]

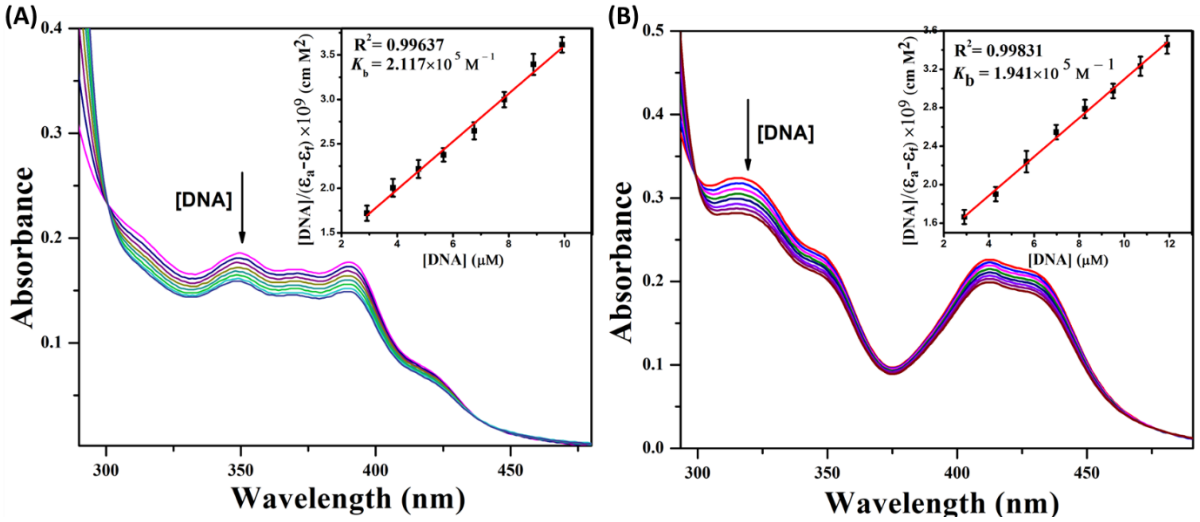

Fig. II.15. Change in absorption spectra of the complex **1** (A) and **2** (B) in Tris–HCl/NaCl buffer with the gradual addition of CT-DNA. Inset: Plot of $[DNA]/(\varepsilon_a - \varepsilon_f)$ vs. [DNA].

II.3.4.2. Ethidium bromide (EB) displacement experiment

Ethidium bromide displacement experiments were carried out in order to confirm the binding mode and compare their binding affinities. EB is a planar, cationic dye and it is widely used as a sensitive fluorescence probe for native DNA. In general, EB emits intense fluorescent light in the presence of DNA due to its strong intercalation between the adjacent DNA base pairs.[44] Hence, the EB displacement technique can provide indirect evidence for the DNA binding mode. The displacement technique is based on the decrease of fluorescence resulting from the displacement of EB from a DNA sequence by a quencher and the quenching is due to the reduction of the number of binding sites on the DNA that is available to the EB.[45,46] The emission spectra of the EB-CT-DNA system with increasing the concentration of the Pd(II) complexes are shown in Fig. II.16. From the observed decrease in the fluorescence

intensity, it has been inferred that the EB molecules are displaced from their DNA binding sites and are replaced by the complexes under investigation. The fluorescence quenching is explained by the Stern–Volmer equation (Eq. II.2).[47]

$$F_0/F = 1 + K_{sv}[Q] \qquad \text{(Eq. II.2)}$$

Where F_0 and F are the fluorescence intensities of the CT-DNA solutions in the absence and presence of the complex, respectively. K_{sv} is the Stern–Volmer quenching constant and [Q] is the concentration of complex. The K_{sv} values are obtained as a slope from the plot of F_0/F versus [Q] (Fig. II.16 inset) and are found to be 7.551(±0.220)×10^4 M^{-1} and 7.145(±0.209) ×10^4 M^{-1} for **1** and **2**, respectively.

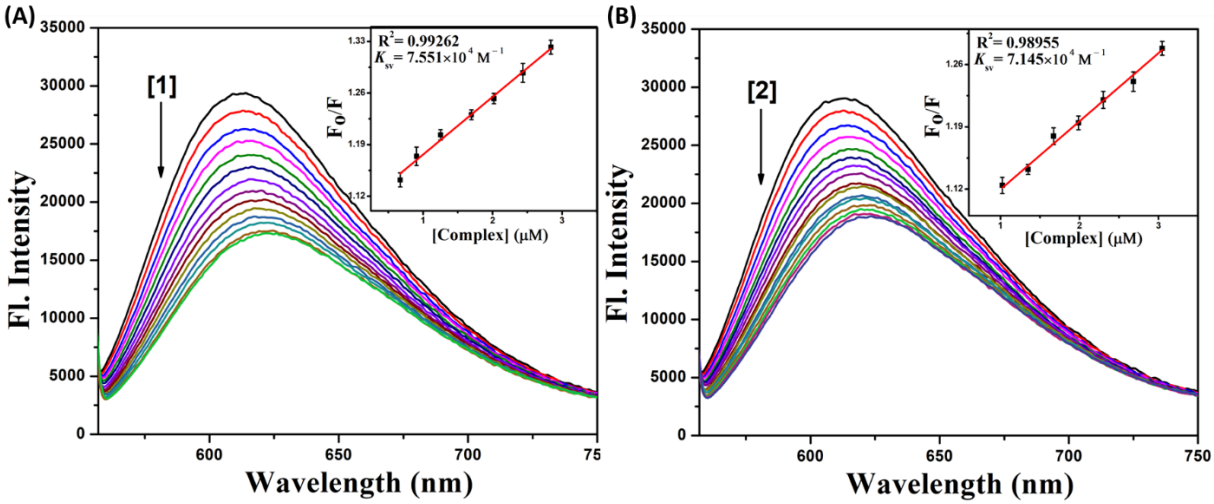

Fig. II.16. Emission spectra (λ_{ex} = 540 nm) of EB-CT-DNA in presence of increasing concentrations of the complex **1** (A) and **2** (B). Inset: Plots of emission intensity F_0/F vs. [complex].

Table II.6. CT-DNA-binding constants (K_b), Gibbs free energies (ΔG), Stern-Volmer constants (K_{SV}) of complexes **1** and **2**.

Compound	UV Method	Fluorescence Method
	K_b (×10^5) (M^{-1})	K_{sv} (×10^4) (M^{-1})
EB-CT- DNA + 1	2.117 ± 0.097	7.551 ± 0.220
EB-CT- DNA + 2	1.941 ± 0.092	7.145 ± 0.209

II.3.5. Protein binding studies

II.3.5.1. Electronic absorption titration

Electronic absorption spectra of BSA (9 μM in PBS at pH 7.4) was recorded in the range of 230-500 nm in presence of different concentration of the complex which is shown in the Fig. III.17. BSA has a characteristic absorption band at 280 nm. Successive addition of complex to the BSA solution exhibited that the absorption intensity of BSA enhanced and was a small blue shift in the wavelength for both the complexes. This hypsochromic shift corresponds to ground-state association between the complex and protein.[48-50] The apparent association constant (K_a) was calculated from the plot of $1/(A_{obs}-A_0)$ vs 1/[complex] (Fig. II.17 inset) adopting the following equation (Eq. II.3).

$$\frac{1}{A_{obs}-A_0} = \frac{1}{A_c-A_0} + \frac{1}{K_a(A_c-A_0)[complex]} \qquad \text{(Eq. II.3)}$$

Where A_{obs} is the observed absorbance (at 280 nm) of the solution having various concentrations of the complex, A_0 and A_c are the absorbance of BSA only and of serum albumin with the complex. The calculated value of apparent association constant (K_a) for the complexes **1** and **2** are 9.225(±0.208)×10^4 M^{-1} and 8.242(±0.228)×10^4 M^{-1} respectively and these values are comparable to reported value.[40-42]

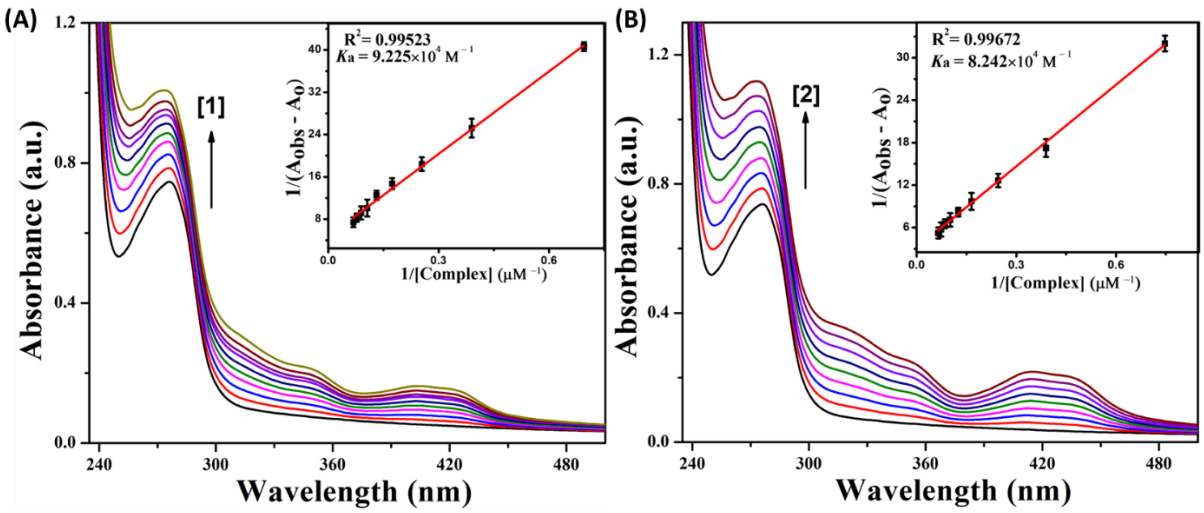

Fig. II.17. Change in absorption spectra of BSA with the gradual addition of complex **1** (A) and complex **2** (B). Inset: Plot of $1/(A_{obs}-A_0)$ vs 1/[complex].

II.3.5.2. Fluorescence quenching studies

The BSA-complex interactions were also examined by fluorescence spectral titration method. Complex is non-fluorescent in DMSO solution. But upon excitation at 280 nm, an aqueous

solution (9 μM, pH 7.4 PBS buffer) of BSA exhibits a strong fluorescence at 336 nm. The effect of the complexes on the fluorescence emission spectrum of BSA is shown in Fig. III.18. Successive addition of the complex to the solution of BSA results a significant decreased in fluorescence intensity of BSA at 336nm with a blue shift. This decrease in emission intensity with a prominent blue shift in maximum emission wavelength of BSA was noticed with an increase in quencher concentration, indicating the associative interaction between the BSA and quenchers.[51-53] The observed blue shift is mainly due to the fact that the active site in the protein is buried in a hydrophobic environment.

The fluorescence quenching mechanisms are generally classified as either static quenching or dynamic quenching. Static quenching usually results to the formation of a complex between the quencher and the fluorophore in the ground state whereas in dynamic quenching the fluorophore and the quencher interact with each other in the excited state. To study the quenching process, fluorescence quenching data were analysed using the Stern–Volmer equation (Eq. II.2). The Stern-Volmer quenching constant values (K_{sv}) calculated from the plot of F_0/F vs [Q] (Fig. II.18 inset) in respect to complexes **1** and **2** were found to be $9.757(\pm0.267)\times10^4$ M^{-1} and $7.425(\pm0.205)\times10^4$ M^{-1}. The high K_{sv} values indicate that complexes show good fluorescence quenching ability. Furthermore, the quenching rate constant (Kq) of the complexes were found to be in the range of $9.757–7.425 \times 10^{12}$ M^{-1} s^{-1}, following the equation $K\text{q} = K_{sv}/\tau_o$ (τ_o refers to the lifetime of the fluorophore without the quencher with an average value of 10^{-8} s). Since the obtained Kq value is greater than the value suggested in dynamic quenching (2×10^{10} M^{-1} s^{-1}), the preferred quenching process is static through the formation of a complex.[54]

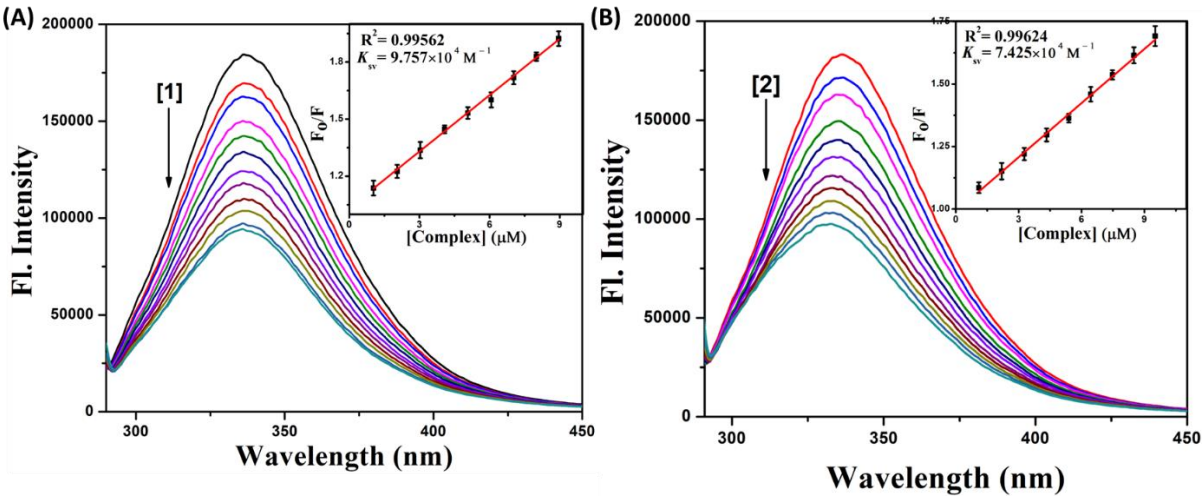

Fig. II.18. Emission spectra (λ_{ex} = 280 nm) of BSA in presence of increasing concentration of the complex **1** (A) and **2** (B). Inset: Plots of emission intensity F_0/F vs. [complex].

II.3.5.3. Binding constant and binding sites

Further, the binding constant and number of binding sites can be calculated by using following Scatchard equation (Eq. II.4).

$$log\frac{(F_0-F)}{F} = log\ K_b + nlog[complex] \qquad \text{(Eq. II.4)}$$

Where K_b is the binding constant of synthesized compounds with BSA and n is the number of binding sites. The binding constant (K_b) and the binding sites (n) have been obtained from the plot of log [(F_o-F)/F] versus log [complex] (Fig. II.19). Based on the plot, calculated values of binding constant (K_b) for the complexes **1** and **2** are 2.251(±0.063)×10^5 M^{-1} and 1.145(±0.045)×10^5 M^{-1} and binding sites (n) are 0.957(±0.021) and 1.102(±0.020) respectively. The binding constant (K_b) values suggested that the complexes have strong binding affinity with the serum albumins. The obtained binding site values n (~1) strongly supported the existence of single binding site in BSA protein.

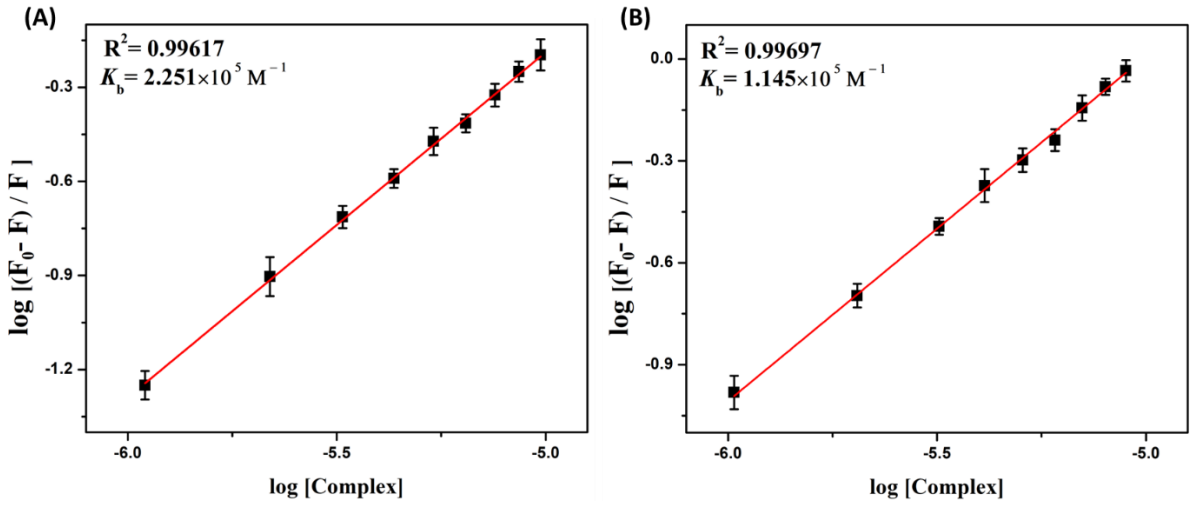

Fig. II.19. Plot of log [(F_o-F)/F] versus log [complex] of complex **1** (A) and complex **2** (B).

Table II.7. Protein apparent association constant (K_a), binding constant (K_b), quenching constant (K_{sv}) and number of binding sites (n) for complexes **1** and **2.**

Compound	UV Method	Fluorescence Method		
	K_a (×10^4) (M^{-1})	K_b (×10^5) (M^{-1})	K_{sv} (×10^4) (M^{-1})	n
BSA + 1	9.225 ± 0.208	2.251 ± 0.063	9.757 ± 0.267	0.957 ± 0.021
BSA + 2	8.242 ± 0.228	1.145 ± 0.045	7.425 ± 0.205	1.102 ± 0.020

II.3.5.4. Synchronous fluorescence spectroscopic studies

With an aim to investigate in detail the structural changes that occurred to BSA upon the addition of complexes, synchronous fluorescence spectra of BSA were also measured before and after the addition of complexes. Results from such studies usually provide reasonable information on the molecular microenvironment particularly in the vicinity of the fluorophore functional groups.[55] Because of the presence of tyrosine, tryptophan, and phenylalanine residues, the BSA has fluorescence properties and hence spectroscopic methods are usually applied to study the conformation of the serum protein. In synchronous fluorescence spectroscopy, according to Miller,[56] the difference between the excitation and emission wavelengths ($\Delta\lambda = \lambda_{em} - \lambda_{ex}$) indicates the nature of the chromophores in the spectra. If the $\Delta\lambda$ value is 15 nm, the synchronous fluorescence spectra of BSA are characteristics of tyrosine residue, whereas the larger $\Delta\lambda$ value of 60 nm is characteristics of tryptophan residue. The synchronous fluorescence spectra of BSA upon the addition of complexes recorded at $\Delta\lambda$ = 15 nm and $\Delta\lambda$ = 60 nm are shown in Fig. II.20 and Fig. II.21 respectively. In the synchronous fluorescence spectra of BSA at $\Delta\lambda$ = 15, the addition of the complexes to the solution of BSA results in a small decrease in the fluorescence intensity of BSA at 301 nm. But, for $\Delta\lambda$ = 60, the addition of the complexes to the solution of BSA results in a significant decrease in the fluorescence intensity of BSA at 343 nm accompanied by a blue shift. It suggested that the interaction of complexes with BSA affects the conformation of the tryptophan micro-region.[57-60] It additionally points out that the hydrophobicity around tryptophan residues is strengthened. The hydrophobicity observed in fluorescence and synchronous measurements confirmed the effective binding of the complexes with the BSA.

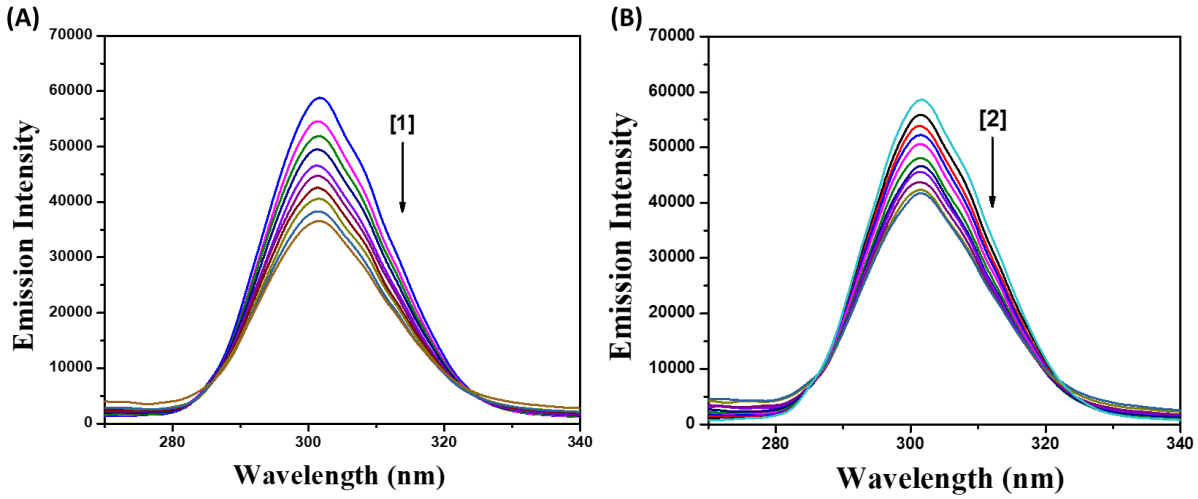

Fig. II.20. The synchronous spectra of BSA in the presence of increasing amounts of the complex **1** (A) and **2** (B) at a wavelength difference of $\Delta\lambda$ = 15 nm. The arrow shows the emission intensity changes upon an increase in the concentration of the complexes.

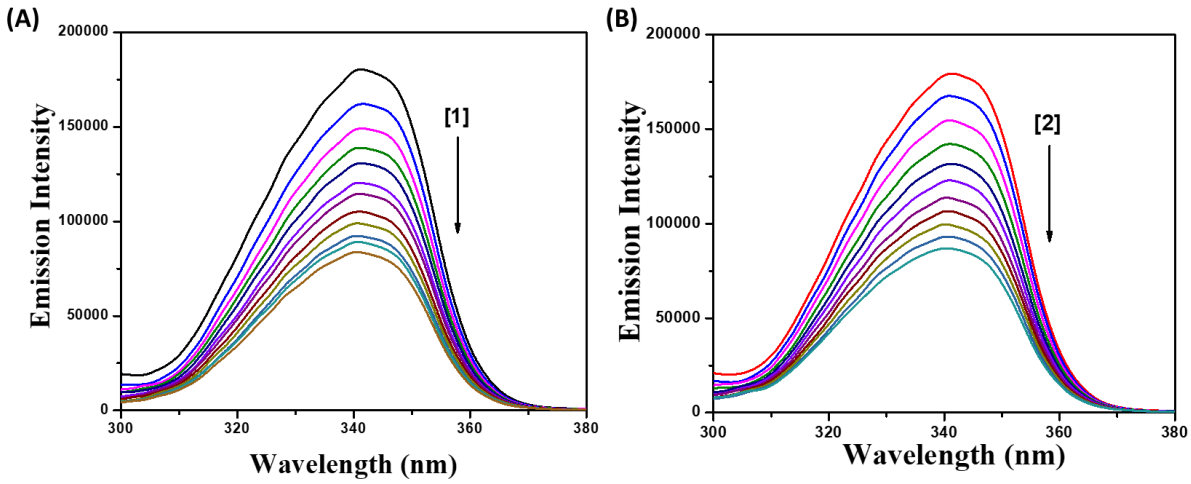

Fig. II.21. The synchronous spectra of BSA in the presence of increasing amounts of the complex **1** (A) and **2** (B) at a wavelength difference of $\Delta\lambda$ = 60 nm. The arrow shows the emission intensity changes upon an increase in the concentration of the complexes.

II.4. Conclusions

Various N-substituted thiosemicarbazones containing 5- fluorosalicylaldehyde were reacted with $[PdCl_2(PPh_3)_2]$. The molecular structures of complexes have been confirmed by single-crystal X-ray diffraction studies, which revealed that, the N-methyl substituted thiosemicarbazone ligand coordinates to palladium in a monobasic bidentate (NS) manner via imine nitrogen atom and thiolate sulfur atom. Whereas, the N-phenyl substituted thiosemicarbazone ligand coordinated in a dibasic tridentate (ONS) manner via phenolic oxygen atom, imine nitrogen atom and thiolate sulfur atom. Further, the interaction of the complexes with DNA and proteins were investigated by employing absorption and emission spectroscopy. From the results, it is observed that the complexes significantly bind to the DNA and the protein. Among the complexes, complex **1** exhibited better binding affinity over the DNA and proteins.

II.5. References

1. C. de Martel, D. Georges, F. Bray, J. Ferlay and G. M. Clifford, *Lancet Glob. Health.*, 2020, **8**, 180-190.
2. H. Sung, J. Ferlay, R. L. Siegel, M. Laversanne, I. Soerjomataram, A. Jemal and F. Bray, *Ca Cancer J. Clin.*, 2021, **71**, 209-249.
3. D. Cirri, F. Bartoli, A. Pratesi, E. Baglini, E. Barresi and T. Marzo, *Biomedicines*, 2021, **9**, 504.
4. (a) N. V. Loginova, H. I. Harbatsevich, N. P. Osipovich, G. A. Ksendzova, T. V. Koval' chuk and G. I. Polozov, Curr., *Med. Chem.*, 2020, **27**, 5213-5249; (b) L. Kelland, *Nat. Rev. Cancer*, 2007, **7**, 573-584

5. (a) A. S. Jadon, P. Bhadauriya and M. Sharma, *J drug deliv. ther.*, 2019, **9**, 673-677; (b) A. M. Florea and D. Büsselberg, *Cancers*, 2011, **3**, 1351-1371; (c) S. Ghosh, *Bioorg. Chem.*, 2019, **88**, 102925.
6. J. Haribabu, M. M. Tamizh, C. Balachandran, Y. Arun, N. S. Bhuvanesh, A. Endo and R. Karvembu, *New J. Chem.*, 2018, **42**, 10818-10832
7. E. Ramachandran, D. Senthil Raja, N. P. Rath and K. Natarajan, *Inorg. Chem.*, 2013, **52**, 1504-1514.
8. R. Prabhakaran, P. Kalaivani, P. Poornima, F. Dallemer, R. Huang, V. V. Padma and K. Natarajan, *Bioorg. Med. Chem.*, 2013, **21**, 6742-6752.
9. (a) D. Anu, P. Naveen, T. Devendhiran, S. Shyamsivappan, K. Kumarasamy, M. C. Lin, C. S. Frampton and M. V. Kaveri, *J. Coord. Chem.*, 2021, **74**, 3153-3169; (b) E. Ramachandran, D. S. Raja, N. S. Bhuvanesh and K. Natarajan, *Dalton Trans.*, 2012, **41**, 13308-13323.
10. F. Cortezon-Tamarit, K. Song, N. Kuganathan, R. L. Arrowsmith, S. R. Mota Merelo de Aguiar, P. A. Waghorn, A. Brookfield, M. Shanmugam, D. Collison, H. Ge and G. Kociok-Kohn, *ACS omega*, 2023, **8**, 16047-16079.
11. B. S. Yüksel, *J. Mol. Struct.*, 2021, **1229**, 129617.
12. E. J. Siddiqui, I. Azad, A. R. Khan and T. Khan, *J. drug deliv. ther.*, 2019, **9**, 689-703.
13. S. E. Jamal, A. Iqbal, K. Abdul Rahman and K. Tahmeena, *J. Drug Deliv. Ther.*, 2019, **9**, 689-703.
14. I. A. Mir, Q. U. Ain, T. Qadir, A. Q. Malik, S. Jan, S. Shahverdi and S. A. Nabi, *J. Mol. Struct.*, 2023, 136216.
15. (a) J. Madureira, C. I. V. Ramos, M. Marques, C. Maia, B. D. Sousa, L. Campino, M. G. Santana-Marques and N. Farrell, *Inorg. Chem.*, 2013, **52**, 8881-8894; (b) C. Icsel and V. T. Yilmaz, *DNA Cell Biol.*, 2013, **32**, 165-172; (c) B. Onfelt, P. Lincoln and B. Nordén, *J. Am. Chem. Soc.*, 2001, **123**, 3630.
16. (a) S. Banerjee, E.B. Veale, C.M. Phelan, S.A. Murphy, G.M. Tocci, L.J. Gillespie, D. O. Frimannsson, J. M. Kelly, T. Gunnlaugsson, *Chem. Soc. Rev.*, 2013, **42**, 1601-1618; (b) L. Zarei, Z. Asadi, M. Dusek, V. Eigner, *J. Photochem., Photobiol. A.*, 2019, **374**, 145-160.
17. D. Cocic, S. Jovanovic, S. Radisavljevic, J. Korzekwa, A. Scheurer, R. Puchta, D. Baskic, D. Todorovic, S. Popovic, S. Matic and B. Petrovic, *J. Inorg. Biochem.*, 2018, **189**, 91-102.
18. N. Rajendiran and J. Thulasidhasan, *Spectrochim, Acta Part A Mol. Biomol. Spectrosc.*, 2015, **144**, 183-191.
19. T. Peters, *Serum Albumin,* 1985, **37**, 161-245.
20. A. Divsalar, I. Zhila, A. A. Saboury, M. Nabiuni, M. Razmi and H. Mansuri-Torshizi, *J. Iran. Chem. Soc.*, 2013, **10**, 951-959.
21. P. Kalaivani, R. Prabhakaran, E. Ramachandran, F. Dallemer, G. Paramaguru, R. Renganathan, P. Poornima, V. V. Padma and K. Natarajan, *Dalton Trans.*, 2012, **41**, 2486-2499.

22. (a) G.M. Sheldrick, *Acta Cryst*., 2008, **A64**, 112-122; (b) G.M. Sheldrick, *Acta Cryst.*, 2015, **C71**, 3-8.
23. (a) A. D. Becke, *J. Chem. Phys*., 1993, **98**, 5648-5652; (b) C. Lee, W. Yang and R. G. Parr, *Phys. Rev. B: Condens. Matter Mater. Phys.*, 1988, **37**, 785-789.
24. (a) P. J. Hay and W. R. Wadt, *J. Chem. Phys*., 1985, **82**, 270-283; (b) W. R. Wadt and P. J. Hay, *J. Chem. Phys.*, 1985, **82**, 284-298; (c) P. J. Hay and W. R. Wadt, *J. Chem. Phys.*, 1985, **82**, 299-310.
25. (a) R. Ditchfield, W. J.Hehre and J.A. Pople, *J. Chem. Phys.*, 1971, **54**, 724; (b) W. Hehre, J. R. Ditchfield and J. A. Pople, *J. Chem. Phys*., 1972, **56**, 2257.
26. M. J. Frisch, G. W. Trucks, H. B. Schlegel, G. E. Scuseria, M. A. Robb, J. R. Cheeseman, G. Scalmani, V. Barone, B. Mennucci, G. A. Petersson, H. Nakatsuji, M. Caricato, X. Li, H. P. Hratchian, A. F. Izmaylov, J. Bloino, G. Zheng, J. L. Sonnenberg, M. Hada, M. Ehara, K. Toyota, R. Fukuda, J. Hasegawa, M. Ishida, T. Nakajima, Y. Honda, O. Kitao, H. Nakai, T. Vreven, J. A. Montgomery, Jr., J. E. Peralta, F. Ogliaro, M. Bearpark, J. J. Heyd, E. Brothers, K. N. Kudin, V. N. Staroverov, R. Kobayashi, J. Normand, K. Raghavachari, A. Rendell, J. C. Burant, S. S. Iyengar, J. Tomasi, M. Cossi, N. Rega, J. M. Millam, M. Klene, J. E. Knox, J. B. Cross, V. Bakken, C. Adamo, J. Jaramillo, R. Gomperts, R. E. Stratmann, O. Yazyev, A. J. Austin, R. Cammi, C. Pomelli, J. W. Ochterski, R. L. Martin, K. Morokuma, V. G. Zakrzewski, G. A. Voth, P. Salvador, J. J. Dannenberg, S. Dapprich, A. D. Daniels, O¨. Farkas, J. B. Foresman, J. V. Ortiz, J. Cioslowski and D. J. Fox, Gaussian 09, Revision D.01, Gaussian, Inc., Wallingford CT, 2009.
27. (a) R. Bauernschmitt and R. Ahlrichs, *Chem. Phys. Lett.*, 1996, **256**, 454-464; (b) R. E. Stratmann, G. E. Scuseria and M. J. Frisch, *J. Chem. Phys.*, 1998, **109**, 8218; (c) M. E. Casida, C. Jamorski, K. C. Casida and D. R. Salahub, *J. Chem. Phys.*, 1998, **108**, 4439-4449.
28. (a) V. Barone and M. Cossi, *J. Phys. Chem.* A, 1998, **102**, 1995-2001; (b) M. Cossi and V. Barone, *J. Chem. Phys.*, 2001, **115**, 4708-4717; (c) M. Cossi, N. Rega, G. Scalmani and V. Barone, *J. Comput. Chem.*, 2003, **24**, 669-681.
29. N. M. O'Boyle, A. L. Tenderholt, K. M. Langner, *J. Comput. Chem.*, 2008, **29**, 839-845.
30. (a) K. M. Prabhu Kumar, B. C. Vasantha Kumar, P. R. Kumar, R. J. Butcher, H. K. Vivek, P. A. Suchetan, H. D. Revanasiddappa and S. Foro, *Appl. Organomet. Chem.*, 2020, **34,** 5634; (b) M. Sirajuddin, S. Ali and A. Badshah, *J. Photochem. Photobiol.*, B, 2013, **124**, 1-19.
31. (a) M. Feizi-Dehnayebi, E. Dehghanian and H. Mansouri-Torshizi, *Spectrochim. Acta A Mol. Biomol. Spectrosc.*, 2021, **249**, 119215; (b) M. Dustkami and H. Mansouri-Torshizi, *Int. J. Biol. Macromol.*, 2017, **99**, 319-334.
32. F. Dimiza, F. Perdih, V. Tangoulis, I. Turel, D. P. Kessissoglou and G. Psomas, *J. Inorg. Biochem.*, 2011, **105**, 476–489.
33. F. Samari, B. Hemmateenejad, M. Shamsipur, M. Rashidi and H. Samouei, *Inorg. Chem*., 2012, **51**, 3454–3464.

34. K. P. Thakor, M. V. Lunagariya, B. S. Bhatt and M. N. Patel, *Lumin.*, 2019, **34**, 113-124.
35. A. A. Sharfalddin, A. H. Emwas, M. Jaremko and M. A. Hussien, *Appl. Organomet. Chem.*, 2021, **35**, 6041.
36. (a) Q. Zhang, J. Liu, H. Chao, G. Xue and L. Ji, *J. Inorg. Biochem.*, 2001, **83**, 49; (b) A. Tarushi, E. Polatoglou, J. Kljun, I. Turel, G. Psomas and D. P. Kessissoglou, *Dalton Trans*., 2011, **40**, 9461; (c) I. Mitra, S. Mukhaerjee, B. Misini, P. Das, S. Dasgupta, W. Linert and S. C. Moi, *New J. Chem.*, 2018, **42**, 2574-2589.
37. J. Sochacka, M. Pacholczyk, M. Jeleń, B. Morak-Młodawska and K. Pluta, *Spectrochim Acta A Mol. Biomol.*, 2021, **262**, 120105.
38. Z. Asadi, E. Haddadi and M. Sedaghat, *J. Photochem. Photobiol., A*, 2017, **337**, 140-150.
39. A. Wolfe, G. H. Shimer and T. Meehan, *Biochemistry*, 1987, **26**, 6392.
40. F. Darabi, H. Hadadzadeh, J. Simpson and A. Shahpiri, *New J. Chem*., 2016, **40**, 9081-9097.
41. M. Saeidifar, H. Mirzaei, N. A. Nasab and H. Mansouri-Torshizi, *J. Mol. Struct.*, 2017, **1148**, 339-346.
42. E. Gao, L. Liu, M. Zhu, Y. Huang, F. Guan, X. Gao, M. Zhang, L. Wang, W. Zhang and Y. Sun, *Inorg. Chem.*, 2011, **50**, 4732-4741.
43. A. Ramezanpour, K. Karami, M. Kharaziha, M. Zakariazadeh, J. Lipkowski, A. Shahpiri, N. Azizi and M. Namazian, *Polyhedron*, 2021, **206**, 115333.
44. J. Tan, B. Wang and L. Zhu, *Bioorg. Med. Chem.*, 2009, **17**, 614-620.
45. M. M. V. Ramana, R. Betkar, A. Nimkar, P. Ranade, B. Mundhe and S. Pardeshi, *J. Photochem. Photobiol.*, 2015, **151**, 194-200.
46. D. P. Heller and C. L. Greenstock, *Biophys. Chem.*, 1994, **50**, 305-312.
47. O. Stern and M. Volmer, Z. *Phys.*, 1919, **20**, 183–188.
48. (a) K. Jeyalakshmi, J. Haribabu, C. Balachandran, N. S. P. Bhuvanesh, N. Emi and R. Karvembu, *New J. Chem*., 2017, **41**, 2672-2686. (b) K. Karami, S. Hashemi, J. Lipkowski, F. Mardani, A. A. Momtazi-borojeni and Z. M. Lighvan, *Appl. Organomet. Chem*., 2017, **31**, e3740; (c) X. F. Zhao, Y. Ouyang, Y. Z. Liu, Q. J. Su, H. Tian, C. -Z. Xie and J. Y. Xu, *New J. Chem*., 2014, **38**, 955-965.
49. M. G. Khrenova, A. V. Nemukhin and V. G. Tsirelson, *Chem. Phys.*, 2019, **522**, 32-38.
50. M. Wanko, M. Hoffmann, P. Strodel, A. Koslowski, W. Thiel, F. Neese, T. Frauenheim and M. Elstner, *J. Phys. Chem. B.*, 2005, **109**, 3606-3615.
51. Y. J. Hu, Y. Liu, J.-B. Wang, X. H. Xiao and S. S. Qu, *J. Pharm. Biomed. Anal*., 2004, **36**, 915-919.
52. N. K. Das, L. Pawar, N. Kumar and S. Mukherjee, *Chem. Phys. Lett.*, 2015, **635**, 50-55.
53. X. Pan, R. Liu, P. Qin, L. Wang and X. Zhao, *J. Lumin.*, 2010, **130**, 611-617.
54. (a) M. Z. Hoffman, F. Bolletta, L. Moggi and G. L. Hug, *J. Phys. Chem. A*, 1989, **18**, 219-543; (b) S. Deepa and A. K. Mishra, *J. Pharm. Biomed. Anal*., 2005, **38**, 556-563.
55. D. Senthil Raja, N. S. P. Bhuvanesh and K. Natarajan, *Dalton Trans*., 2012, **41**, 4365–4377.

56. J. N. Miller, *Proc. Anal. Div. Chem. Soc*., 1979, **16**, 203–208.
57. F. Shiri, M. Rahimi-Nasrabadi, F. Ahmadi and H. Ehrlich, *Spectrochim. Acta A Mol. Biomol.*, 2018, **203**, 510-521.
58. M. S. Ali, M. T. Rehman, H. A. Al-Lohedan and M. F. Alajmi, *J. Spectrosc.*, 2023.
59. M. Shinde, K. Kale, K. Kumar and D. Ottoor, *Lumin.*, 2021, **36**, 129-141.
60. M. Manjushree and H. D. Revanasiddappa, *Spectrochim. Acta A Mol. Biomol.*, 2019, **209**, 264-273.

CHAPTER-III

New palladium(II) and platinum(II) complexes with ONS donor azo-thioether pincer ligand: Synthesis, characterization, protein binding study and in vitro cytotoxicity

Abstract

New Pd(II) and Pt(II) complexes, [Pd(L)Cl] (**1**) and [Pt(L)Cl] (**2**) with O,N,S donor azo-thioether pincer ligand (HL) are synthesized and thoroughly characterized by spectroscopic techniques. X-ray structures of the complexes revealed the distorted square planar geometry around the central metal ions. Electronic structures and spectral properties are interpreted by DFT and TDDFT calculations. Interaction of the complexes with CT-DNA and BSA proteins are studied by absorption and fluorescence methods. Fluorescence titration revealed that the complexes strongly quench DNA bound ethidium bromide (EB) as well as the intrinsic fluorescence of BSA protein through static quenching. High binding constants (K_b) obtained from the DNA binding studies promoted the in-vitro cytotoxicity assay of complexes on various human cancer cell lines (colon cancer cell line HCT116, lung cancer cell line A549 and liver cancer cell line HepG2). The half maximal inhibitory concentration (IC_{50}) of complexes **1** and **2** are found to be less compare to cisplatin.

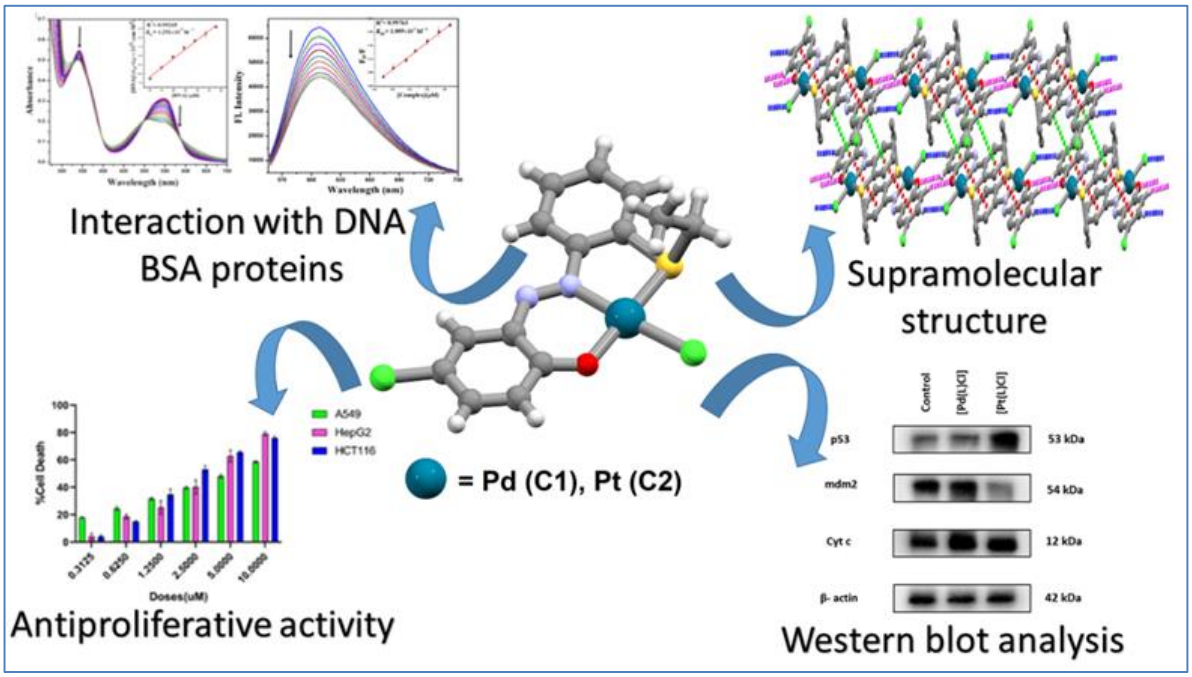

III.1. Introduction

Cancer is undoubtedly one of the foremost health concerns in our society and serves as a principal target in the field of medicinal chemistry.[1] While searching for antitumor drugs among metal complexes, the invention of cisplatin occurred during the period from 1960 to 1970. Cisplatin is one of the most potent chemotherapy drugs extensively used for cancer treatment.[2,3] Despite of its clinical accomplishment for the past 40 years in the treatment of certain tumors, it has many disagreeable side effects such as nausea, nephrotoxicity, ototoxicity, tumor resistance, neurotoxicity, bone and back pain, weakness, blood clots, fatigue and hair loss.[4] These severe side effect caused by cisplatin and its analogues carboplatin and oxaliplatin, offer an incentive for the breakthrough of novel platinum based complexes bearing multidentate ligands which are alternative to cisplatin with higher potency, higher cancer cell selectivity and lower resistance. Therefore, a noteworthy number of different platinum complexes were fabricated with the aim to prevail over the disadvantages of cisplatin.[5-8] Also due to the similarity between the coordination geometry of Pd(II) and Pt(II), non-platinum metal based compounds such as palladium(II) complexes are being used for cancer treatment. Thus the design of new palladium based anti-cancer drugs is very vital for effectual and proficient use as chemotherapic agents.[9-14] However, a disadvantage of the palladium-based drugs is the fact that the aquation and ligand-exchange rates of Pd(II) complexes are about 10^5 times faster than those of the Pt(II) analogues.[15] The higher reactivity of Pd(II) could avert the metal based drugs to reach their target DNA by favouring interactions with other donor species present in the blood stream, boosting their toxicity and deteriorating their therapeutic potential. Thus, in order to fabricate an improved and competitive palladium complex based anticancer agents, a fitting choice of ligands is of the essence.[16-17] The coordinated ligands play a significant role in anticancer activity of metal containing antitumor drugs as they can adjust key parameters such as reactivity and lipophilicity. In Recent time, several Pd(II) complexes were designed and studied against various types of cancer cells and some of them demonstrate highly capable biological activity *in vitro* which is most notably preferable than cisplatin.[18-24]

Azo compounds are intriguing substances that have demonstrated a variety of applications, including food technology, analytical chemistry, as colorants, as corrosion inhibitors, and in the dyeing or textile industry. Aside from their typical coloring role, azo compounds have been found to have several health benefits, including cytotoxic, antitumor, antibacterial, antiviral, antifungal, and antiseptic properties.[25] They have the potential to be employed as drug carriers, either as a 'cargo' that entraps therapeutic molecules or as a

prodrug strategy. As seen in colon-targeted drug delivery, the medication is discharged by external or internal triggers in the area of interest.[26] Because they are biodegradable, low toxic, redox active, and generally resemble the structure of active sites in proteins, they have been widely employed to create Pt group transition metal complexes.[27]

It is well known that DNA is the main target of an antitumor agent while BSA acts as a carrier protein molecule in the blood stream for a variety of compounds including antitumor compounds. Therefore, interaction studies of metal complexes with DNA and proteins are very useful in order to design and ascertain the metal-based anticancer therapeutics.[28] Depending on the nature of the metal and ligand, the complexes can bind to the DNA through the following ways (i) electrostatic interaction between negatively charged DNA phosphate residue and positively charged species, (ii) intercalation with base pairs and (iii) major and minor groove binding interaction via hydrogen bonding and van der Waals interaction forces.[29] Additionally, the study on interaction of proteins with metal complex is very constructive as it could offer information to scrutinize the therapeutic efficiency and pharmacological response of drugs. Furthermore, proteins are admired as the major cellular target for antitumor drugs and the most carrier proteins in the blood stream is Human Serum Albumin (HSA). Since Bovine Serum Albumin (BSA) structure is homologous with HSA and owing to its easy accessibility and low cost, BSA is mostly used in biochemical and biophysical studies.[30-33]

In this paper we have synthesized Pd(II) and Pt(II) complexes (Scheme III.1) having general formula, [Pd(L)Cl] (**1)** and [Pt(L)Cl] (**2)** with ONS donor azo-thioether ligand (HL) and characterized both of them by using various spectroscopic techniques like NMR, IR, Mass, UV-Vis as well as single crystal X-ray diffraction study. Finally, the binding properties of these complexes toward calf thymus DNA (CT-DNA) and bovine serum albumin (BSA) are investigated with the help of absorption and fluorescence spectroscopy. In vitro antitumor activity of these synthesized complexes were tested on human liver (HepG2), colorectal (HCT116) and human lung (A549) cancer cell lines using MTT assay (MTT is 3-(4,5-dimethylthiazol-2-yl)-2,5-diphenyltetrazolium bromide). To determine selective effect of complexes, they were treated on cancer cells as well as normal PBMC cells under the same experimental conditions. The Pd(II) and Pt(II) complexes to induce apoptosis of tumor cell (HCT116) were tested by flow cytometric analysis of Annexin V-FITC/PI double staining assay. DFT and TD-DFT calculations were accomplished to elucidate the electronic structure and UV-Vis spectra of the complexes.

III.2. Experimental

III.2.1. Materials and methods

4-Chlorophenol, 2-aminothiophenol, $Na_2[PdCl_4]$ and $Pt(SEt_2)_2Cl_2$ were purchased from Sigma-Aldrich. Solvents were available from commercial sources and used without further purification. Ethidium bromide (EB), calf thymus DNA(CT-DNA) and bovine serum albumin(BSA) were obtained from Sigma Aldrich chemical company. 4-Chloro-2-((2-(ethylthio)phenyl)diazenyl)phenol (HL) was prepared following the reported method.[34] A549, HepG2 and HCT116 cells were procured from National Centre for Cell Science, Pune, India. MTT (Cat.No. 19265) was purchased from USB Corporation, Cleaveland, US. DMEM (Cat.No. 12800082) and Penicillin-Streptomycin (Cat.No. 15140122) was brought from Thermo Fisher Scientific, US. FBS (Cat.No.10270106) was purchased from Invitrogen, US. Annexin v-FITC/PI kit (Cat.No. V13242) was brought from Invitrogen, Formally Thermo Fisher Scientific, US. JC1(Cat. No. 420200) was purchased from Calbiochem, Sigma Aldrich, US. Primary antibodies of p53 (Cat.No. sc-393031), mdm2 (Cat.No. sc-965) and Cyt C (Cat.No. sc-13156) were brought from Santa Cruz Biotechnology, Inc., US and primary antibodies for Bax (Cat.No. 5023T), Bcl2 (Cat.No. 3498T) and β-actin (Cat.No. 3700S) were obtained from Cell signalling Technology, US. All the secondary antibodies were brought from Santa Cruz Biotechnology, Inc., US. DAPI (Cat.No. D9542) was purchased from Sigma Aldrich, US.

Elemental analyses (C, H, N) were carried out by a 2400 Series-II CHN analyzer, Perkin Elmer, USA. Waters (Xevo G2 Q-TOF) mass spectrometer was used to record mass spectra of the ligand and complexes. IR spectra (4000–400 cm^{-1}) were recorded on a RX-1 PerkinElmer spectrometer using KBr pellets technique. ^{1}H-NMR spectra were recorded in $CDCl_3$ solution on a Bruker (AC) 300 MHz FT-NMR spectrometer and TMS was used as the internal standard. PerkinElmer Lambda 750 spectrophotometer was used for study the binding interactions of complexes with CT-DNA and BSA. The emission spectra were recorded by using Shimadzu RF-6000 fluorescence spectrophotometer at room temperature (298 K). Cyclic voltammetric experiments were performed using a CHI Electrochemical workstation. A platinum wire working electrode, a platinum wire auxiliary electrode and Ag/AgCl reference electrode were used in a standard three-electrode configuration using $[n\text{-}Bu_4N][ClO_4]$ as supporting electrolyte with solute concentration ~10^{-3} M and scan rate of 50 mV s^{-1}.

III.2.2. Syntheses

III.2.2.1. Synthesis of Pd(II) complex, [Pd(L)Cl] (1)

At first, 0.058 g (0.2 mmol) $Na_2[PdCl_4]$ was dissolved in 10 mL acetonitrile. To this solution, a 10 mL acetonitrile solution of previously synthesized HL (0.058 g, 0.2 mmol) was added and refluxed for 6 h. The initial orange color changed to deep red. After slow evaporation of the solvents for a week, deep red single crystals suitable for X-ray structure analysis were formed. The yield was, 0.070 g, 81%.

Anal. Calc. for $C_{14}H_{12}Cl_2N_2OPdS$: C, 38.78; H, 2.79; N, 6.46. Found: C, 38.57; H, 2.62; N, 6.35. IR (KBr, cm^{-1}): 3062, 2958, 2922 υ(C-H); 1380 υ(N=N); 774 υ(C-S). ^1H NMR (300 MHz, $CDCl_3$): δ 8.39 (d, J=8 Hz, 1H), 7.82 (s,1H), 7.71-7.44 (m, 4H), 7.27 (d, J = 9.3 Hz, 1H), 3.52-3.19 (m, 2H), 1.50 (t, J=7.1Hz, 3H). HRMS: calculated for $C_{14}H_{12}Cl_2N_2OPdS$ $[M+Na]^+$ (m/z): 456.6328; found: 456.6211. UV-Vis (in CH_3CN), λ_{max} (ε, M^{-1} cm^{-1}): 550 (12302), 520 (sh.), 372 (sh.), 338 (18162). E_{pa}: 1.68 V; $E_{1/2}$: −1.02 V (ΔE = 165 mV).

III.2.2.2. Synthesis of Pt(II) complex, [Pt(L)Cl] (2)

0.047 g (0.105mmol) $Pt(SEt_2)_2Cl_2$ was dissolved in 10 mL acetonitrile. To it 0.030 g (0.105 mmol) ligand, HL solution in 10 mL acetonitrile was added. The reaction mixture was then refluxed for 7 h. As a result of this reaction, a red coloured solution appeared which was filtered and evaporated to dryness. A deep red coloured solid product appeared and single red colored crystals of the complex was obtained by slow diffusion of n-hexane into DCM solution. The yield was, 0.046 g, 84%.

Anal. Calc. for $C_{14}H_{12}Cl_2N_2OPtS$: C, 32.19; H, 2.32; N, 5.36. Found: C, 32.05; H, 2.21; N, 5.15. IR (KBr, cm^{-1}): 3069, 2958, 2929 υ(C-H); 1390 υ(N=N); 767 υ(C-S). ^1H NMR (300 MHz, $CDCl_3$): δ 8.51 (d, J=9.7 Hz, 1H), 7.98 (s, 1H), 7.78-7.56 (m, 4H), 7.29 (d, J = 9.3 Hz, 1H), 3.50-3.24 (m, 2H), 1.32 (t, J= 7.2Hz, 3H). HRMS: calculated for $C_{14}H_{12}Cl_2N_2OPtS$ $[M+Na]^+$ (m/z): 545.2968; found: 545.2924. UV-Vis (in CH_3CN), λ_{max} (ε, M^{-1} cm^{-1}): 557 (15077), 374 (sh.), 343 (23742). E_{pa}: 1.62 V; $E_{1/2}$: −1.05 V (ΔE = 155 mV).

III.2.3. Crystal structure determination and refinement:

Crystallographic data collections were performed with an automated Bruker AXS D8 Quest CMOS diffractometer using graphite monochromated Mo-Kα (λ=0.71073Å) radiation by the ω scan method. The structures were solved by direct method and refinements were carried out by full-matrix least-squares techniques on F^2 using the SHELX-2016. All the data were corrected for Lorentz and polarization effects and multi-scan absorption corrections were

applied using SHELXTL program package.[35] Anisotropic displacement parameters included for all non-hydrogen atoms, while all hydrogen atoms were placed geometrically and refined by using riding model. Crystallographic data and refinement parameters are given in Table III.1.

Table III.1. Crystallographic data and refinement parameters of **1** and **2**

Formula	$C_{14}H_{12}Cl_2N_2OPdS$	C28H24Cl4N4O2Pt2S2
Formula Weight	433.62	1044.61
Crystal System	*triclinic*	*triclinic*
Space group	$P\bar{1}$	$P\bar{1}$
a, b, c [Å]	7.4987(6), 9.4330(7), 11.6092(9)	10.1219(11), 12.2233(13), 13.6071(15)
α	101.126(2)	109.453(3)
β	103.873(2)	95.228(3)
γ	98.613(2)	96.489(3)
V [$Å^3$]	765.50(10)	1562.3(3)
Z	2	2
D(calc) [g/cm^3]	1.881	2.221
Mu(MoKa) [/mm]	1.695	9.455
F(000)	428	984
Temperature (K)	293(2)	293(2)
Radiation [Å]	0.71073	0.71073
θ(Min-Max) [°]	2.554- 27.217	1.943- 27.542
Dataset (h; k; l)	-9 to 9, -12 to 12, -14 to 14	-13 to 13, -15 to 15, -17 to 17
R, wR_2	0.0278, 0.0748	0.0249, 0.0595
Goodness of fit(S)	1.094	1.023
CCDC No.	2178572	2178573

III.2.4. Computational method

Geometries of the complexes in native (**1**/**2**) as well as one electron oxidized ($\mathbf{1}^+$/$\mathbf{2}^+$) and reduced ($\mathbf{1}^-$/$\mathbf{2}^-$) states were optimized by DFT/B3LYP method.[36] LanL2DZ[37] basis set with effective core potential was employed for palladium and platinum metal atoms while for the

other elements the basis set 6-31G(d)[38] were considered for calculations. Vibrational frequency calculations were performed to ensure that the optimized geometries represented the local minimum on the potential energy surface and only positive Eigen values were obtained. All computations were performed using Gaussian09 program package[39] with the aid of the GaussView, Version 5 visualization program. The time-dependent density functional theory (TD-DFT)[40] method was carried out for the characterization of electronic transition. In the TDDFT simulations, acetonitrile was use as a solvent to mimic the experimental conditions and absorption properties in acetonitrile solvent were calculated using the conductor-like polarizable continuum model (CPCM)[41]. GaussSum[42] was used to calculate the fractional contributions of various groups to each molecular orbital.

III.2.5. DNA-binding studies

DNA is the most like target site for the metal based anticancer drugs. In order to understand the antitumor properties of these palladium and platinum-based complexes, it is necessary to analyze the binding abilities of complexes with CT DNA using Absorption and emission spectroscopy.[43]

III.2.5.1. UV–Vis titration

The interactions of complexes **1** and **2** with CT DNA were studied using UV-Vis spectroscopy. The binding experiments involving CT DNA were performed at room temperature in Tris–HCl/ NaCl buffer solution (pH=7.4). The concentration of CT DNA was determined spectro-photometrically by employing an extinction coefficient of 6600 $M^{-1}cm^{-1}$ at 260 nm using Lambert-Beer law. The absorbance ratio at 260 nm and 280 nm was measured and found to be in the range of 1.8 to 1.9, indicating that the DNA was sufficiently free of protein. The absorption spectra of the complexes at a constant concentration were recorded in presence of varying concentrations of CT DNA. After each addition of CT DNA solutions, it was allowed to equilibrate for 5 min before collecting the absorption spectra and added stepwise until a saturation state was achieved.

III.2.5.2. Competitive study with EB by fluorescence method

The complexes showed no fluorescence at room temperature in solution or in the presence of DNA, and hence, their binding with DNA could not be directly predicted through the emission spectral studies. The extent of quenching of fluorescence due to EB bound to DNA (EB-CT-DNA) is used to predict the binding of the complexes to CT-DNA. This competitive

binding study of the complexes (**1/2**) with EB were carried out by the fluorescence method in order to understand the efficiency of displacement of EB from EB-CT-DNA system by the complexes. The EB-CT-DNA complex was initially prepared by mixing of 15 μM EB and 30 μM CT-DNA in Tris– HCl/NaCl buffer solution at pH 7.40. The fluorescence spectra of EB bound to CT DNA at 608 nm was obtained at an excited wavelength of 540 nm. The intercalating effect of both the complexes with the EB-CT-DNA were studied by gradual addition of the complex solution into the solution of EB-CT-DNA.

III.2.6. Protein binding studies

Proteins are major targets for therapeutically active complexes. Bovine serum albumins (BSA) are frequently used in studies of the interactions with transition metal complexes and proteins because it is responsible for the transport of drugs in biological systems.[44,45] The binding ability of synthesized complexes with BSA protein were determined by employing UV-Vis and fluorescence spectroscopic techniques. The BSA stock solution was prepared using 500 mM phosphate buffer saline (PBS) at pH 7.4 and stored in the dark at 4°C for further use. The concentration of BSA was measured by taking absorbance at 280 nm in UV-Vis spectra (molar extinction coefficient 66,400 M^{-1} cm^{-1}). The stock solution of complexes were prepared in DMSO medium and was suitably diluted with PBS whenever necessary. The absorption spectra were recorded at room temperature with constant concentration of BSA (10 μM) while varying the concentration of complex added to it. In fluorescence experiment, tryptophan fluorescence of BSA was recorded in the range 290–450 nm at an excitation wavelength of 280 nm using a slit width of 5 nm. Quenching of emission intensity at ~336 nm for BSA was monitored with subsequent addition of metal complex.

III.2.7. Biological Studies

III.2.7.1. Cell viability assay

The cell viability was analysed by MTT (3-(4,5-dimethylthiazol-2yl)-2,5-diphenyltetrazolium bromide) assay. First, 1×10^6 number of cells were seeded in each well into 96-well plates and the cells were allowed to attach for 24 h. Following those various concentrations of [Pd(L)Cl] (**1**) and [Pt(L)Cl] (**2**), were added to the wells with at least three replicates and kept for 24 h. This is followed by removal of medium and addition of fresh medium containing (1mg/ml) MTT. The plates were then incubated for 4 h. The MTT containing medium is then removed and the purple formazan crystals were then dissolved by an addition of 100 μL dimethyl

sulfoxide (DMSO). Finally, the absorbance was determined by a microplate reader at a wavelength of 595 nm. Then, Cell viability was calculated as follows:

$$\%\ of\ cell\ viability = \frac{(Absorbance\ of\ control - Absorbance\ of\ sample)}{Absorbance\ of\ Control} \times 100$$

III.2.7.2. Analysis of ROS generation using DCF-DA assay

$1x10^6$ HCT 116 Cells were seeded and treated with complexes **1** and **2** for about 24 h followed by the cells were harvested by centrifugation and trypsinisation. The pellets were resuspended in 0.1µM DCFDA solution for 25 mins at 37°C. Then, the cells were washed and the pellets were resuspended in 1x PBS. Immediately after that the cells were analysed at excitation-emission wavelengths of 485/530nm using flowcytometry (BD FACSAria™, BD Biosciences, San Jose, CA, USA).

III.2.7.3. Analysis of Mitochondrial membrane potential using flowcytometry

JC1 (1, 1', 3, 3'-tetraethyl-5, 5', 6, 6'- tetrachloroimidacarbocyanine iodide) was used to analyse Mitochondrial membrane potential (MMP). It is a lipophilic dye with cationic nature. Briefly, $1x10^6$ HCT 116 cells were seeded per well in 6 well plates. Cells were then treated with Pd and Pt complexes for 24 h. Untreated cells were used as control. After exposure to [Pd(L)Cl] (**1**) and [Pt(L)Cl] (**2**), 1 µM JC-1 was added to each well and kept for 20 mins at room temperature. This was followed by washing and the cells were analysed using flowcytometry (BD FACSAria™, BD BioSciences, San Jose, CA, USA).

III.2.7.4. Flow cytometric analysis of apoptosis

HCT 116 Cells were seeded and kept for 24 h. This was followed by treatment with Pd and Pt complexes for 24 h by dual staining with recombinant FITC-conjugated Annexin V and PI followed by flowcytometry, Cellular apoptosis was then analysed by using the Annexin V-FITC Apoptosis Detection kit (Becton-Dickinson, USA) according to the manufacturer's instructions. Data analysis was performed using CellQuest software.

III.2.7.5. Analysis of protein expression via Confocal Microscopy

1×10^6 number of HCT 116 Cells were seeded in 60mm culture dishes containing coverslips and treated with **1** and **2** for 24 h. 4% formalin was used to fix the cells followed by washing

with 1xPBS. Then the cells were permeabilized using permeabilization buffer. The cells were then exposed to blocking buffer followed by treatment with primary antibody for BAX, p53 and Bcl2 and kept overnight at 4°C. Later, it was exposed to Fluorescent-dye conjugated secondary antibodies and followed by mounting on slides and observed under Confocal Microscope.

III.2.7.6. Western Blot analysis of cellular protein expression

Cells were seeded and treated with Pd and Pt complexes (**1/2**). Then, washed with PBS and lysed using RIPA buffer supplemented with protease inhibitor cocktail. This was followed by quantification of protein Micro BCA Protein Assay kit (Thermo Scientific). Equal amount (20 µg) of proteins were loaded on to wells and separated by 10% SDS-PAGE gels and transferred to PVDF (polyvinylidene difluoride) membranes. Then the membrane was blocked using 5% skim milk in TBST containing 0.1% Tween 20, followed by incubation with primary antibodies at 4 °C overnight. After that the membranes were washed and incubated with HRP (horseradish proxidase)-conjugated secondary antibodies at room temperature for 1 h. The target proteins were visualized using chemiluminescence.

III.2.7.8. Cell Cycle Analysis using flow cytometry:

The cells (1×10^5) were seeded in 6 well plates and treated with complexes **1** and **2**. Cells were then trypsinised and centrifuged and washed in cold PBS twice. Fixation of cells was done using ice-cold ethanol (70% w/w) and then incubated in PBS containing 0.1%, Triton X-100, 0.1% sodium citrate, RNase A (50 µg/ml; Fermentas), and PI (50 µg/ml; Sigma) at 4 °C for 25 mins. The percent of calculated cells in the sub-G0, G1, S, and G2/M phases were analysed by flow cytometry (BD FACSCalibur flow cytometer, USA).

III.3. Results and discussion

III.3.1. Synthesis and spectra

The palladium(II) complex, [Pd(L)Cl] (**1**) was synthesized by the reaction of ligand, HL with Na_2PdCl_4 in 1:1 molar ratio under refluxing condition in acetonitrile. Similarly, the platinum(II) complex, [Pt(L)Cl] (**2**) was synthesized by the reaction of $Pt(SEt_2)_2Cl_2$ with HL (Scheme III.1).

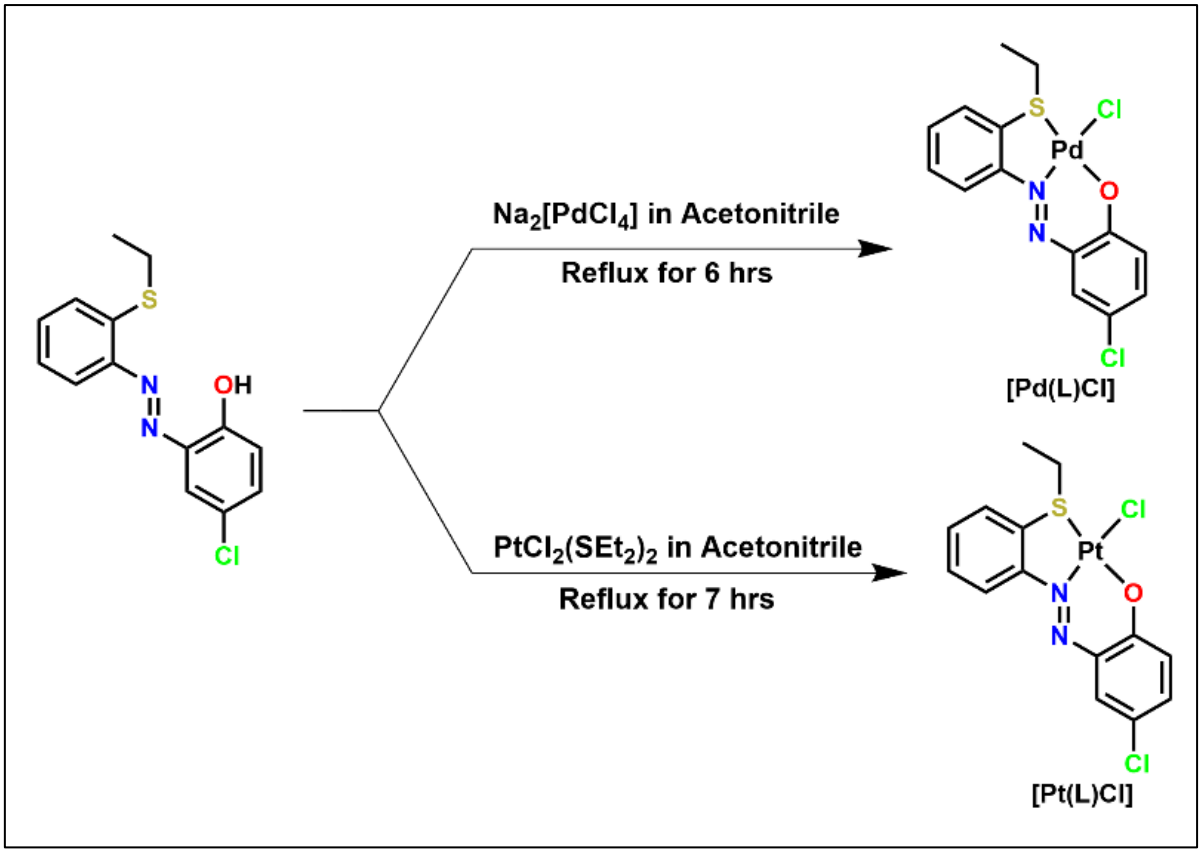

Scheme III.1. Synthetic scheme for [Pd(L)Cl] (**1**) and [Pt(L)Cl] (**2**)

The complexes were thoroughly characterized by spectroscopic techniques. IR spectra of the complexes exhibit υ(N=N) stretching peak at 1380-1390 cm^{-1} (Fig. III.6), which is lower than the υ(N=N) stretching of the free ligand (1449 cm^{-1}) (Fig. III.5). The significant shift of υ(N=N) stretching in the complexes supports the dπ(Pd/Pt)→π*(N=N) back donation.[46] ^{1}H NMR spectra of the complexes, the peak at 12.68 ppm correspond to O-H proton of the free ligand disappeared along with significantly downfield shifting of $-SCH_2$ proton signals which also suggest the coordination of ligand to the metal ions through phenolic-O and thioether-S (Fig. III.1 and Fig. III.2). The $–CH_2$ protons of $–CH_2CH_3$ moiety appear as multiplate at 3.52-3.19 ppm probably because of the two different type (diastereotopic) of $–CH_2$ protons. Mass spectrum of [Pd(L)Cl] (1) shows m/z peak corresponding to $[M+Na]^+$ at 456.6211 (Fig. III.3) while [Pt(L)Cl] (2) exhibits m/z peak corresponds to $[M+Na]^+$ at 545.2924 (Fig. III.4).

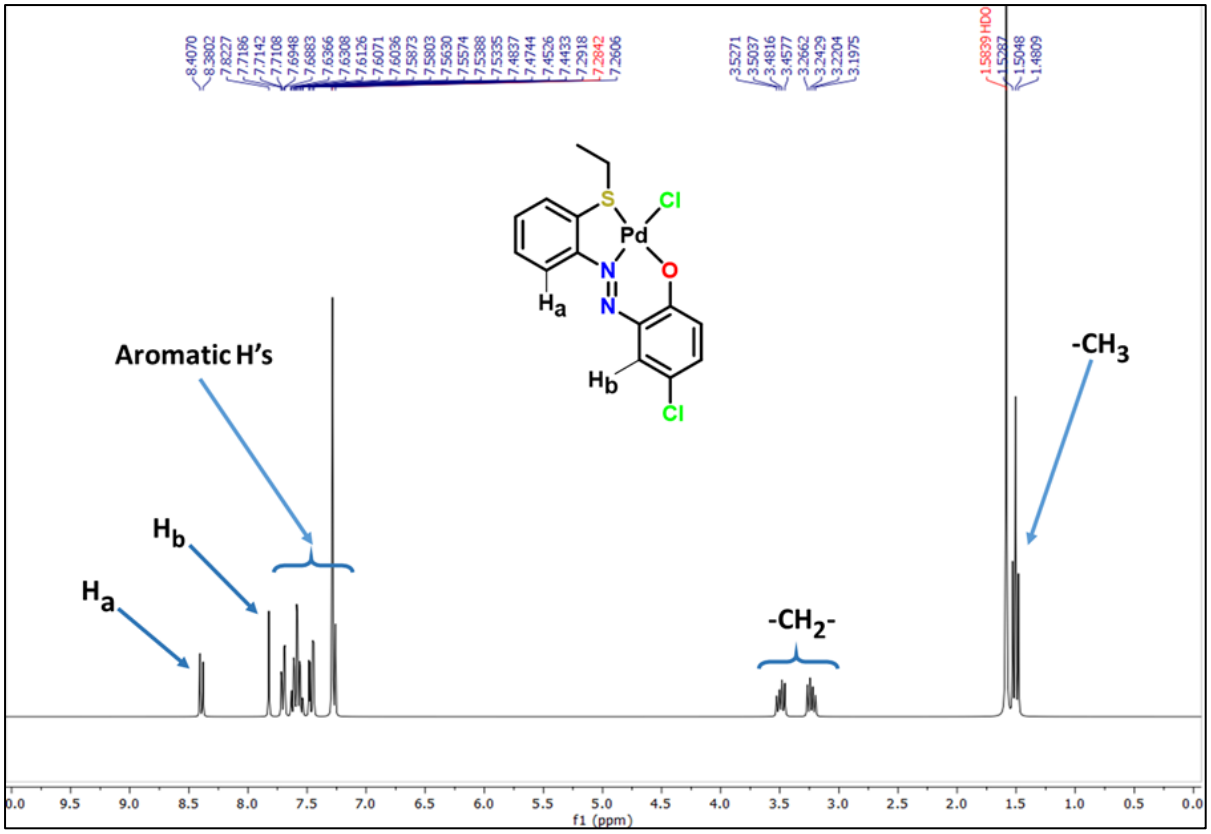

Fig. III.1. ^{1}H-NMR spectrum of [Pd(L)Cl] (**1**) in $CDCl_3$

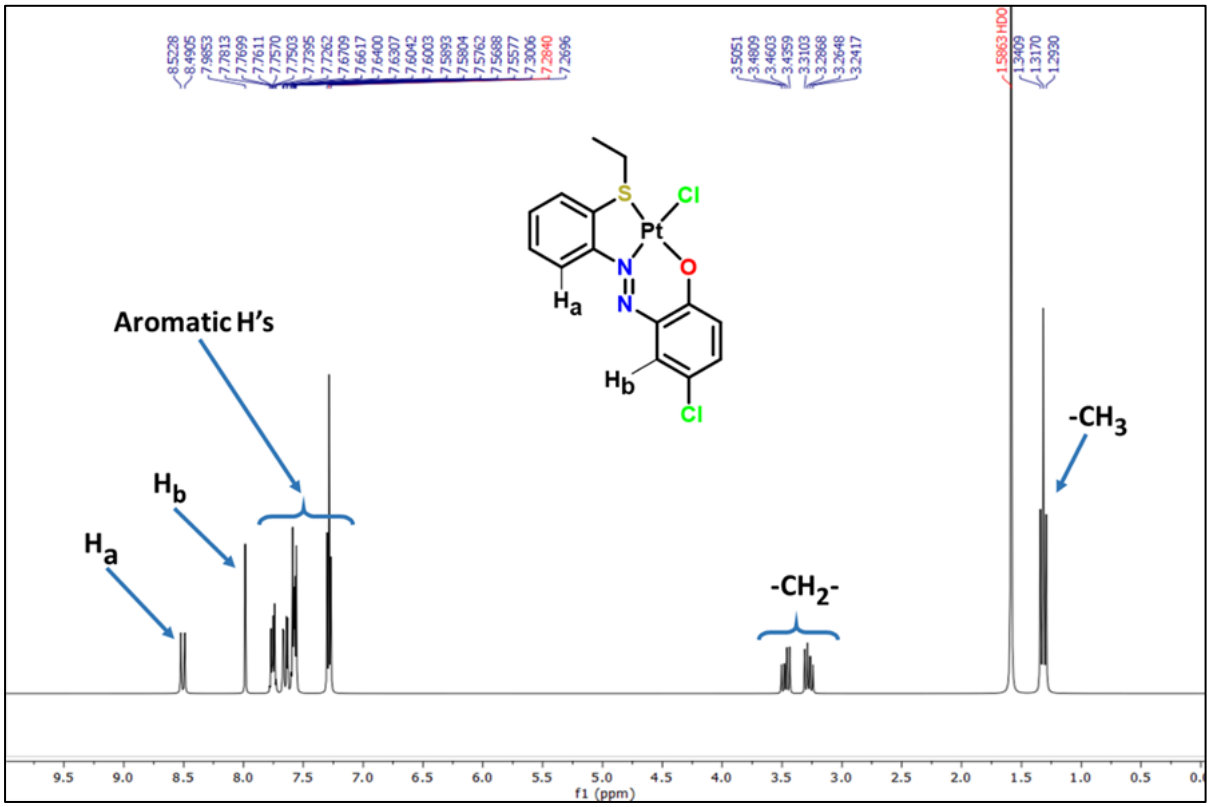

Fig. III.2. ^{1}H-NMR spectrum of [Pt(L)Cl] (**2**) in $CDCl_3$

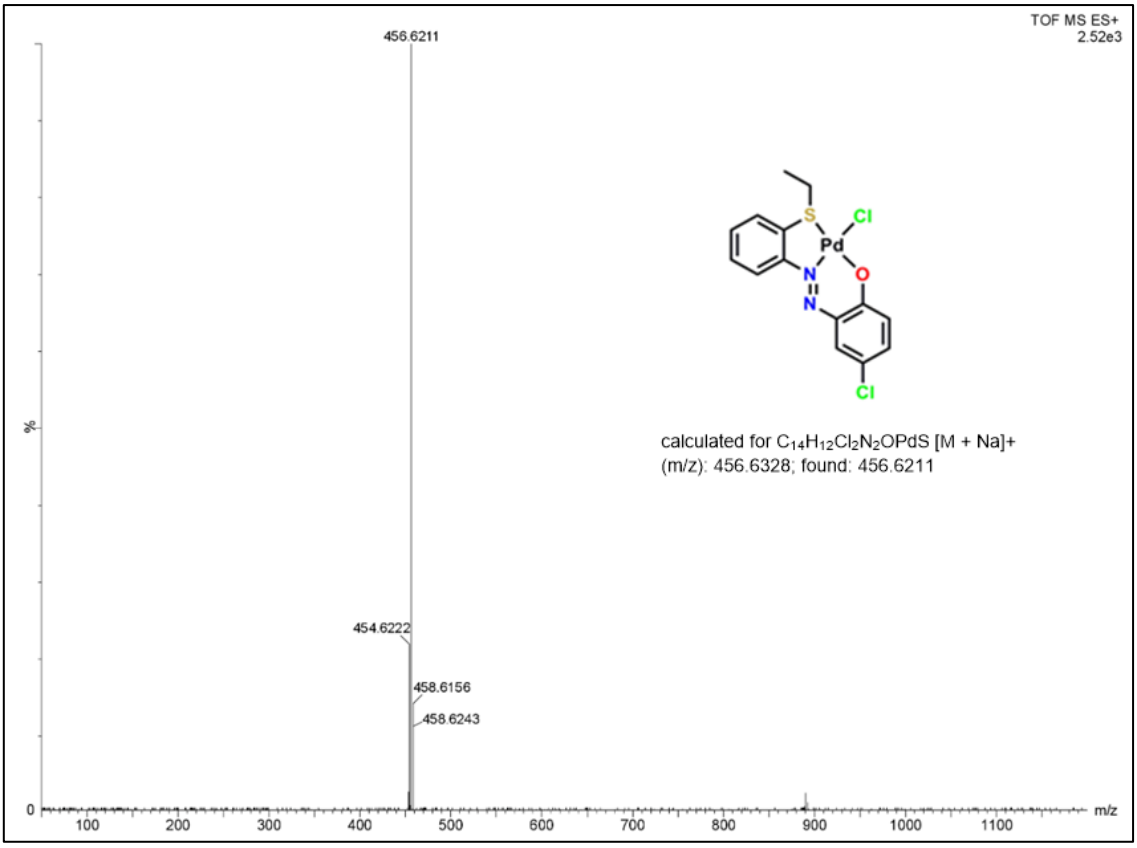

Fig.III.3. HRMS spectrum of complex **1**

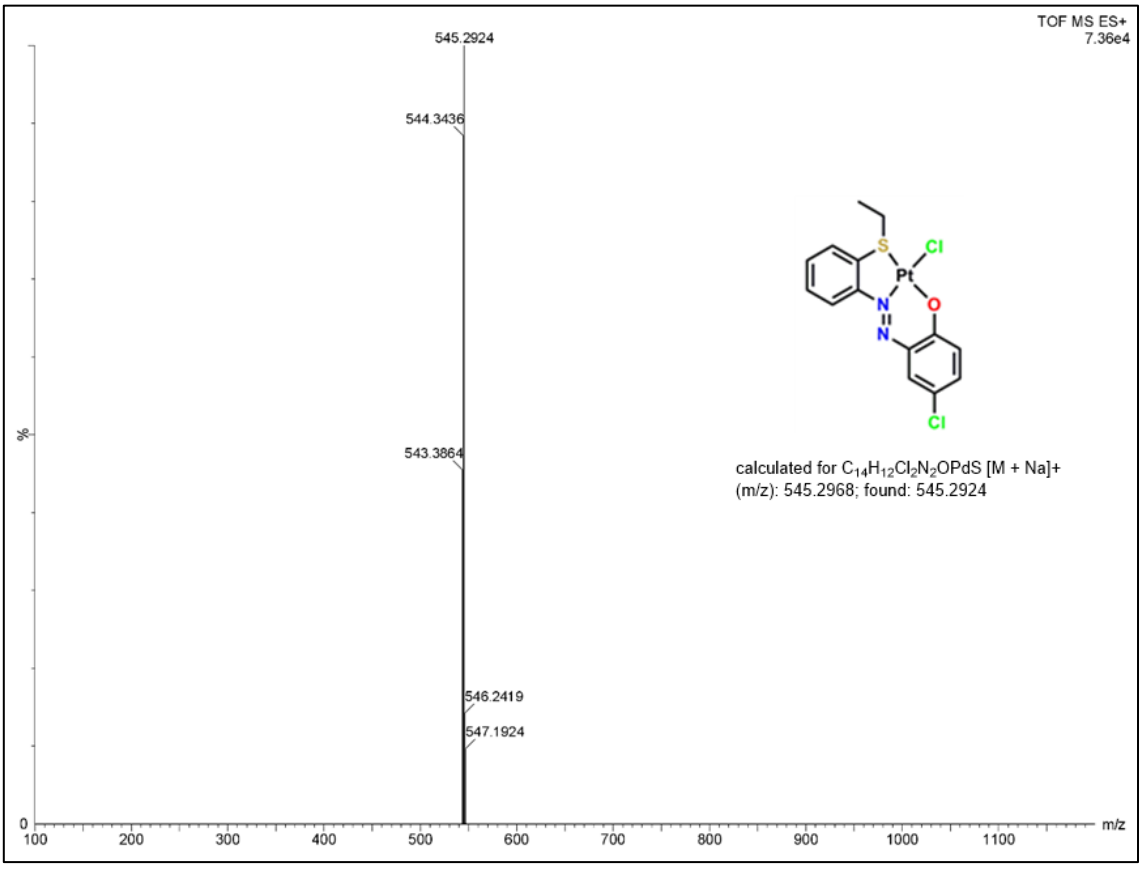

Fig. III.4. HRMS spectrum of complex **2**

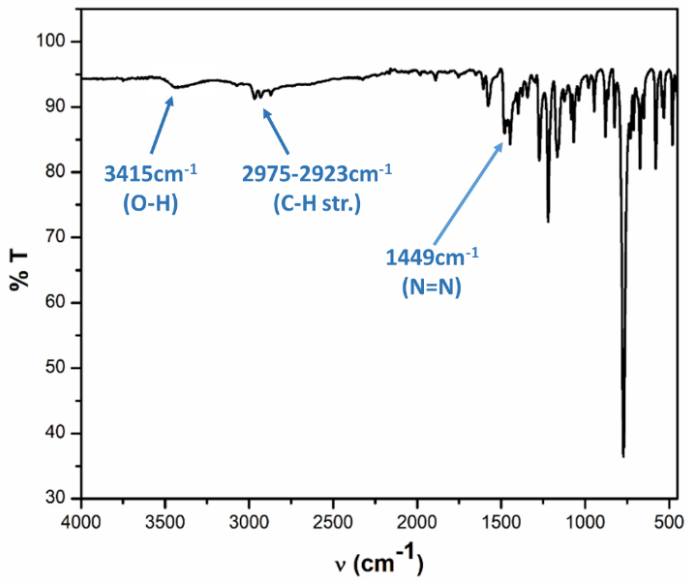

Fig. III.5. IR spectrum of free HL

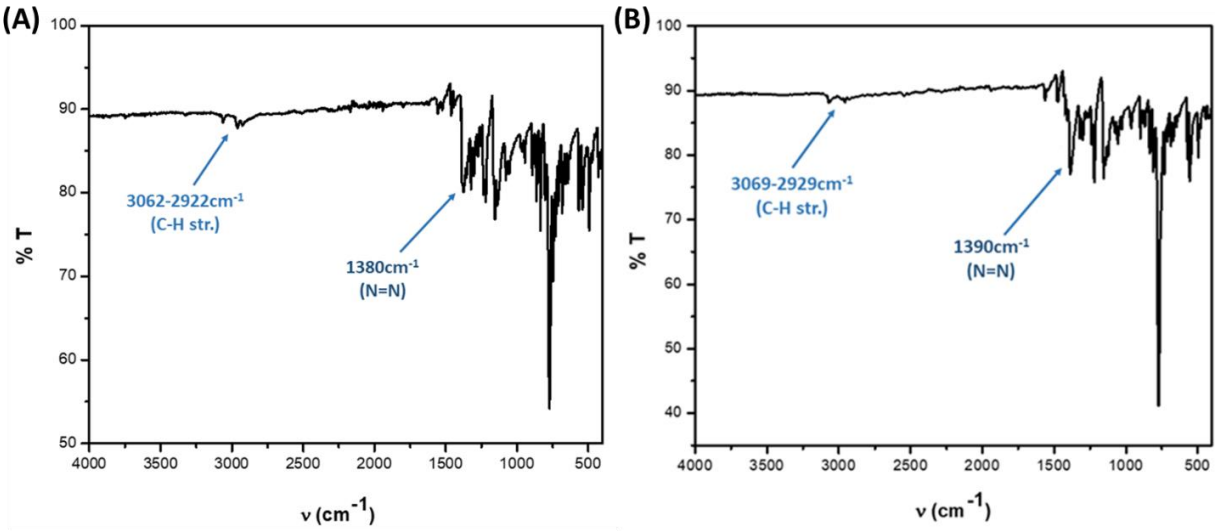

Fig. III.6. IR spectrum of complex **1** (A) and complex **2** (B)

Absorption spectra of complexes **1** and **2** were taken in acetonitrile. The solution spectrum of complex **1** exhibit moderately intense low energy band at 550 nm (ε, 12302 $M^{-1}cm^{-1}$) along with a shoulder band at 520 nm. Absorption spectrum of complex **2** exhibit low energy peaks at 557 nm (ε, 15077 $M^{-1}cm^{-1}$). High energy bands appeared at 374 nm (sh.) and 343 nm (ε, 23742 $M^{-1}cm^{-1}$) (Fig. III.7).

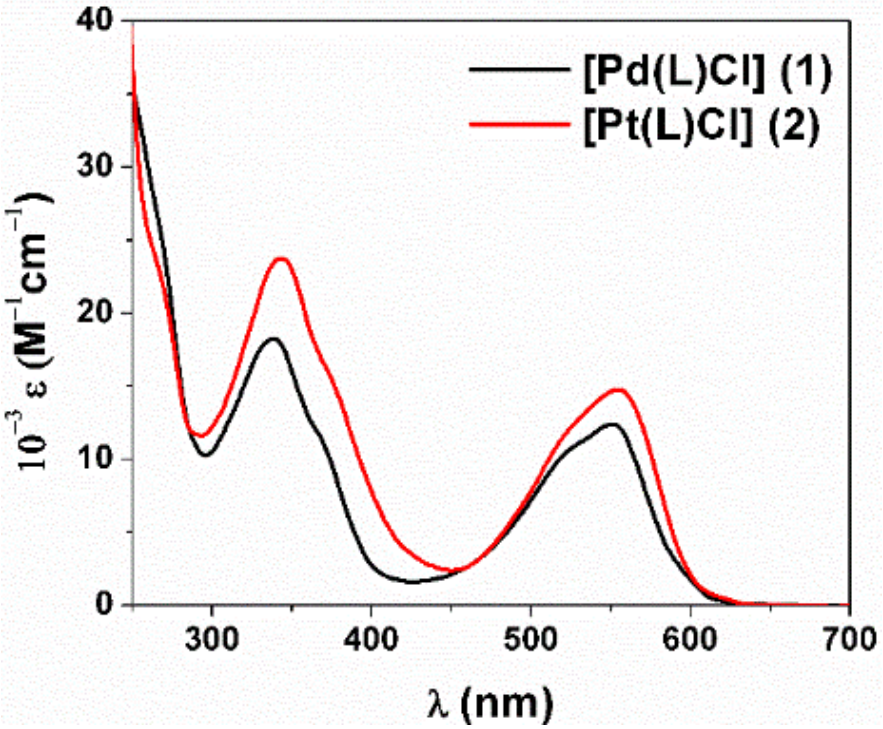

Fig. III.7. UV-Vis spectra of [Pd(L)Cl] (**1**) and [Pt(L)Cl] (**2**) in acetonitrile

III.3.2. Crystallographic study

The molecular structures of complexes have been established by the single crystal X-ray diffraction method. The single crystal X-ray diffraction study reveals that both the complexes are crystallized in a triclinic crystal system with the space group $\overline{P}1$. The ORTEP plots of the complexes **1** and **2** along with the atom numbering scheme are shown in Fig. III.8. Selected inter atomic bond lengths and bond angles of the complexes are summarized in Table III.2. The bond parameters of the complexes suggest a slightly distorted square planar geometry around the metal atoms. The O,N,S pincer type of ligand coordinated with central metal ions through phenolic O, azo-N and thioether-S atoms by forming five- and six- membered chelate rings. The azo bond distances (N1-N2) are found to be 1.270(3) Å and 1.283(5) Å in **1** and **2** respectively. In complex **1**, the cis-angles N1-Pd1-O1, N1-Pd1-S1, O1-Pd1-Cl1 and S1-Pd1-Cl1 are found to be 93.06(8)^o, 87.71(6)^o, 90.84(5)^o and 88.41(3)^o respectively while the two trans-angles O1-Pd1-S1 and N1-Pd1-Cl1 are 178.54(6)^o and 175.99(6)^o respectively. In complex **2**, the cis-angles N1-Pt1-O1, N1-Pt1-S1, O1-Pt1-Cl1 and S1-Pt1-Cl1 are found to be 93.37(13)^o, 87.64(10)^o, 89.14(9)^o and 89.96(4)^o respectively while the two trans-angles O1-Pt1-S1 and N1-Pt1-Cl1 are 177.71(9)^o and 176.21(10)^o respectively. The cis and trans-angles are in significant deviation from their respective idealistic values of 90^o and 180^o, suggesting significant distortion in the square planar geometry of the two complexes. The Pd-N(azo)

[Pd1-N1, 1.979(2) Å], Pd-O(phenolic) [Pd1-O1, 1.9960(18) Å] and Pd-S(thioether) [Pd1-S1, 2.2401(6) Å] bond lengths in complex **1** and Pt-N(azo) [Pt1-N1, 1.966(3) Å], Pt-O(phenolic) [Pt1-O1, 2.000(3) Å] and Pt-S(thioether) [Pt1-S1, 2.2316(12) Å] bond lengths in complex **2** were found to be similar to the reported values.[47]

Table III.2. Selected X-ray and calculated bond distances and angles of complexes **1** and **2.**

	[Pd(L)Cl] (**1**)		[Pt(L)Cl] (**2**)	
Bonds(Å)	X-ray	Calc.	X-ray	Calc.
Pd1–N1	1.979(2)	2.017	1.966(3)	2.00813
Pd1–O1	1.9960(18)	2.018	2.000(3)	2.02230
Pd1–S1	2.2401(6)	2.301	2.2316(12)	2.29275
Pd1–Cl1	2.3106(7)	2.341	2.3126(11)	2.35894
Cl2–C4	1.738(3)	1.756	1.745(5)	1.75638
S1–C12	1.771(3)	1.797	1.774(5)	1.79677
S1–C13	1.821(3)	1.857	1.824(5)	1.85930
O1–C1	1.291(3)	1.285	1.306(5)	1.29344
N1–N2	1.270(3)	1.277	1.283(5)	1.27865
N1–C7	1.448(3)	1.431	1.444(5)	1.43421
Angles (°)				
N1–Pd1–O1	93.06(8)	92.058	93.37(13)	92.52811
N1–Pd1–S1	87.71(6)	86.946	87.64(10)	87.05536
O1–Pd1–S1	178.54(6)	177.927	177.71(9)	178.30795
N1–Pd1–C1	175.99(6)	176.199	176.21(10)	177.60868
O1–Pd1–Cl1	90.84(5)	91.046	89.14(9)	89.26697
S1–Pd1–Cl1	88.41(3)	90.019	89.96(4)	91.19538
C12–S1–C13	102.64(12)	103.691	103.1(2)	103.55565
C12–S1–Pd1	98.10(9)	97.325	98.38(15)	97.60226
C13–S1–Pd1	106.66(9)	107.014	108.44(16)	107.83721
N2–N1–Pd1	127.66(16)	127.164	128.1(3)	127.33641

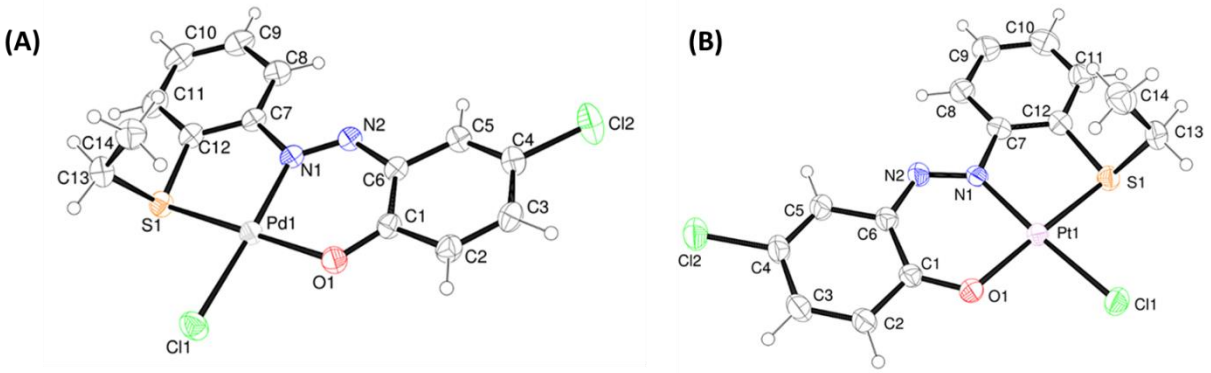

Fig. III.8. ORTEP plots with 35% ellipsoidal probability of complexes **1** (A) and **2** (B)

The interesting feature of crystal structures of **1** and **2** is the formation of 1D-supramoleculare architecture by intramolecular π…π, O…H and Cl…H hydrogen bonding interactions as shown in Fig. III.9 and Fig. III.10 respectively. In the crystal structure of **1**, strong π…π interactions are observed between the adjacent phenyl rings (Cg(3) and Cg(4)) Cg(3): C1-C2-C3-C4-C5-C6 and Cg(4): C7-C8-C9-C10-C11-C12) of the coordinating ligands with Cg…Cg distances of 3.5981(16) Å (symmetry: 1-X, 1-Y, 1-Z) and 3.9424(16) Å (symmetry: 2-X, 1-Y, 1-Z). In addition, weak O…H and Cl…H hydrogen bonding interactions having hydrogen bond distances of 2.82 Å and 2.78 Å respectively are observed (Fig. III.9). Crystal structure of **2** forms 1D-supramolecular structure by hydrogen bond interactions between the bared O (O1) and Cl (Cl1 and Cl2) atoms and H atoms of adjacent coordinating ligand with O1…H2, Cl1…H3 and Cl2…H5 distances of 2.64 Å, 2.71 Å and 2.86 Å respectively (Fig. III.10).

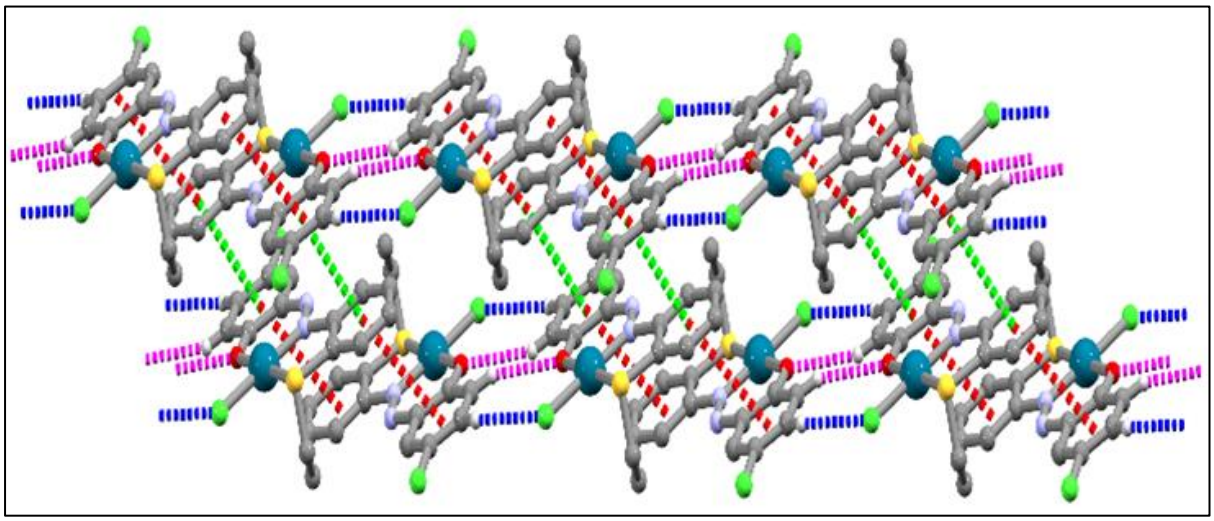

Fig. III.9. 1D supramolecular structure of **1** formed by Cl…H (●●●), O…H (●●●) hydrogen bonding interactions and π…π (●●●) interactions.

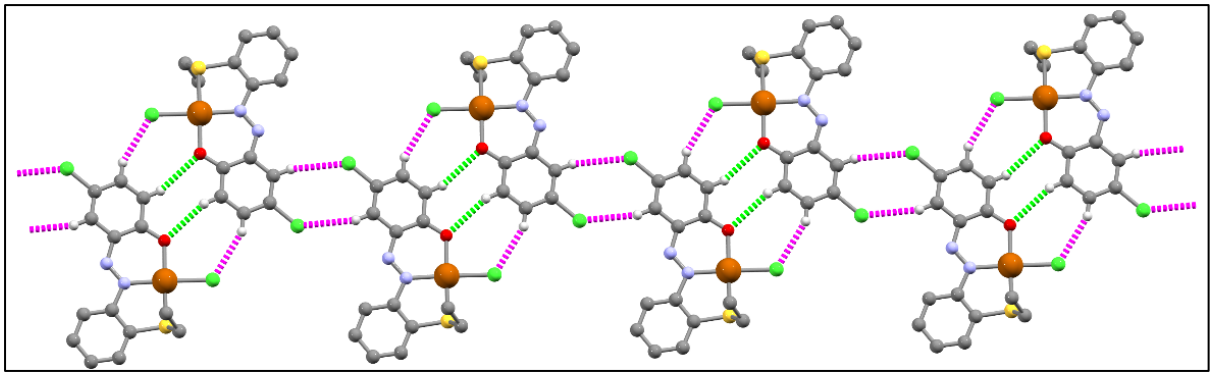

Fig. III.10. 1-D supramolecular structure of **2** formed by Cl…H (●●●) and O…H (●●●) bonding interactions.

III.3.3. DFT and TDDFT calculations

The geometry of the complexes **1** and **2** were optimized in singlet ground state by DFT/B3LYP method to understand the electronic structure of the complexes. The calculated geometric parameters are reasonably well reproducing the X-ray crystal structures data. Contour plots of selected molecular orbitals for both the complexes **1** and **2** are shown in Fig. III.11 and Fig. III.12 respectively. Energy and compositions of selected molecular orbitals are given in Table III.3 and Table III.4 respectively. For complex **1,** the higher energy occupied molecular orbital (HOMO) has 80% contribution of ligand and the low-lying virtual orbital, LUMO has 97% contribution of ligand and for complex **2**, HOMO has 70% contribution of ligand and 17% contribution of dπ(Pt) orbitals while LUMO has 95% contribution of ligand π^* orbital [ESI, †Table **S**4]. The HOMO to LUMO energy gap in the complexes is found to be 2.85 eV and 2.80 eV for **1** and **2** respectively.

UV-Vis absorption bands of the complexes are interpreted by TDDFT calculations using B3LYP/CPCM method in acetonitrile. Calculated vertical electronic transitions are summarized in Table III.5. For complex **1**, the calculated low energy transition at 536 nm (f = 0.1505) corresponds to the HOMO → LUMO transition ($\lambda_{expt.}$ = 550 nm) having intra-ligand charge transfer (ILCT) character. The shoulder peak at 520 nm corresponds to HOMO → LUMO+1 transition (507 nm, f = 0.018) having mixed LMCT and ILCT character. The experimentally observed shoulder peak at 372 nm corresponds to mixed halogen to ligand charge transfer (XLCT) and MLCT character. In addition, an intense sharp band at 338 nm correspond to ILCT transition. For complex **2** the lower energy experimental band at 557 nm (ε = 15077 $M^{-1}cm^{-1}$) correspond to the HOMO → LUMO transition at 544 nm having ILCT character along with reduced contribution of MLCT transition. Similarly, the experimental

shoulder band at 374 nm correspond to mixed XLCT and MLCT character. The sharp intense band at 343 nm correspond to mixed ILCT character.

Table III.3. Energy and % of composition of some selected molecular orbitals of complex **1**

MO	Energy (eV)	% Composition		
		Pd	L	Cl
LUMO+5	-0.04	83	17	0
LUMO+4	-0.21	01	99	0
LUMO+3	-0.66	01	99	0
LUMO+2	-1.44	03	97	03
LUMO+1	-2.28	47	39	14
LUMO	-3.03	03	97	03
HOMO	-5.88	10	80	10
HOMO-1	-6.55	17	20	63
HOMO-2	-6.57	16	10	74
HOMO-3	-7.02	75	14	11
HOMO-4	-7.11	05	85	09
HOMO-5	-7.32	12	66	22
HOMO-6	-7.54	31	64	05
HOMO-7	-7.86	34	65	01
HOMO-8	-8.18	20	73	07
HOMO-9	-8.37	19	64	17
HOMO-10	-8.47	41	49	09

Table III.4. Energy and % of composition of some selected molecular orbitals of complex **2**

MO	Energy (eV)	% Composition		
		Pt	L	Cl
LUMO+5	-0.04	51	48	01
LUMO+4	-0.23	01	99	0
LUMO+3	-0.68	01	99	0
LUMO+2	-1.46	06	93	01
LUMO+1	-1.50	44	45	11
LUMO	-3.01	05	95	0
HOMO	-5.81	17	70	13
HOMO-1	-6.49	22	35	42
HOMO-2	-6.55	21	07	72
HOMO-3	-6.96	90	07	03
HOMO-4	-7.12	13	76	11
HOMO-5	-7.36	25	65	09
HOMO-6	-7.48	18	57	25
HOMO-7	-7.82	17	80	02

HOMO-8	-8.16	20	69	11
HOMO-9	-8.42	28	53	19
HOMO-10	-8.48	26	61	13

Table III.5. Vertical electronic transition calculated by TDDFT/CPCM method of complexes **1** and **2**

Compd.	λ (nm)	E (eV)	Osc. Strength (f)	Key excitations	Character	$\lambda_{expt.}$ (nm) (ε, $M^{-1}cm^{-1}$)
1	535.9	2.3134	0.1505	(84%)HOMO→LUMO	ILCT	550 (12302)
	507.5	2.4429	0.0180	(82%)HOMO→LUMO+1	LMCT/ ILCT	520 (sh.)
	368.5	3.3643	0.0861	(67%)HOMO-1→LUMO	XLCT/ MLCT	372 (sh.)
	348.4	3.5586	0.2497	(67%)HOMO-4→LUMO	ILCT	338 (18162)
	340.8	3.6383	0.0893	(66%)HOMO-5→LUMO	ILCT	
2	544.1	2.2786	0.1444	(96%)HOMO→LUMO	ILCT/ MLCT	557 (15077)
	382.1	3.2452	0.0589	(72%)HOMO-1→LUMO	XLCT/ MLCT	374 (sh.)
	353.0	3.5123	0.2993	(78%)HOMO-4→LUMO	ILCT	343 (23742)
	336.1	3.6893	0.1345	(75%)HOMO-5→LUMO	ILCT	

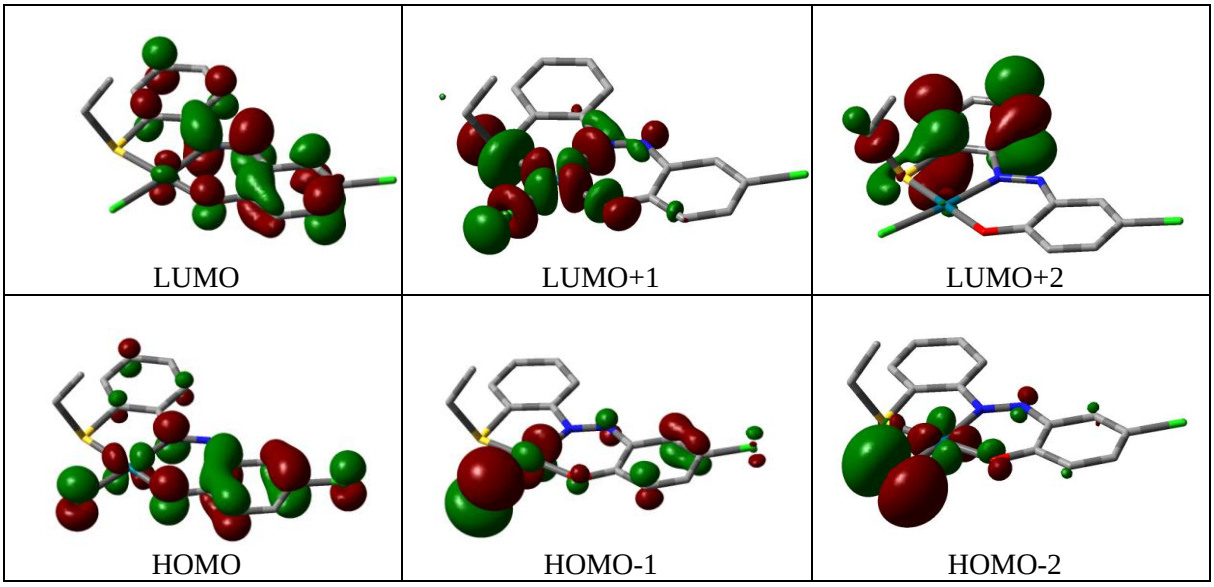

Fig. III.11. Contour plots of some selected molecular orbital of Pd(II) complex (**1**)

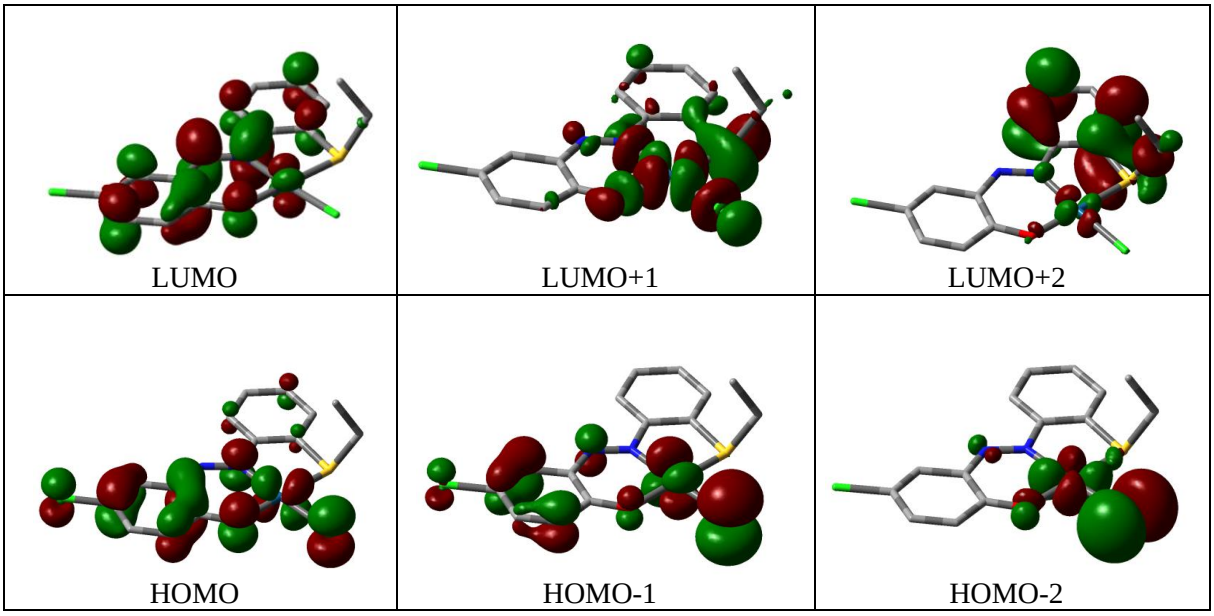

Fig. III.12. Contour plots of some selected molecular orbital of **Pt(II)** complex (**2**)

III.3.4. Cyclic voltammetry

Electrochemical behaviour of the complexes **1** and **2** were investigated by cyclic voltammetry (CV) in presence of $[nBu_4N][ClO_4]$ in acetonitrile. Complexes (**1/2)** exhibit one irreversible oxidation peak at 1.62-1.68 V along with one quasi-reversible reduction couple at -(1.02-1.05) V (ΔE = 155-165 mV) positive and negative to the reference electrode respectively (Ag/AgCl) in the potential range -2.0 to 2.0 V (Fig. III.13). The irreversible oxidation for the complexes may be assigned as Pd(II)/Pd(IV) or Pt(II)/Pt(IV) oxidation or the oxidation of phenolate moiety to form the phenoxyl radical. DFT calculations clearly show that the HOMOs of the complexes have 70-80% ligand contribution, predominantly concentrated on the phenolate moiety and negligible contribution of dπ(Pd/Pt) orbitals. Moreover, the calculated spin density of the oxidized species ($\mathbf{1}^+/\mathbf{2}^+$) predominantly concentrated on the phenolate moiety and has negligible contribution of the metals (Fig. III.14). So, the oxidation of the complexes is assigned as the oxidation of the phenolate moiety to form the phenoxyl radical. Moreover, the LUMOs of the complexes have 95-97% ligand character with a major contribution of π*(N=N) orbital. Similarly, calculated spin density of $\mathbf{1}^-/\mathbf{2}^-$ is mainly concentrated on the ligand with maximum contribution of azo moiety (Fig. III.15). Therefore, the reduction of the complex is assigned as the reduction of azo (N=N) bond to form azo anion radical ($L/L^{\bullet-}$).

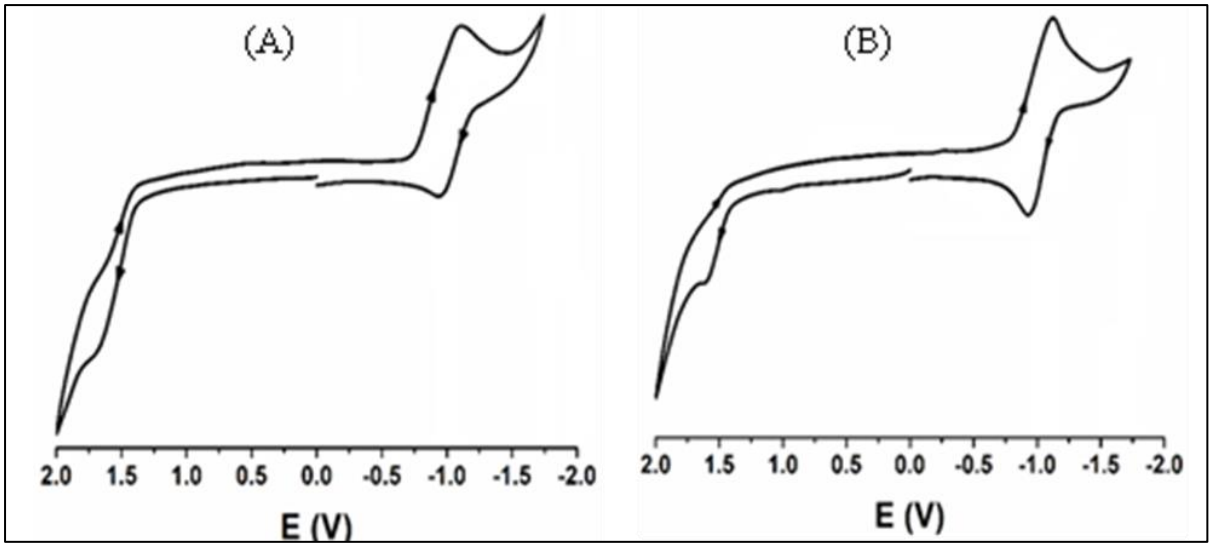

Fig. III.13. Cyclic voltammogram of complexes **1** (A) and **2** (B) in acetonitrile.

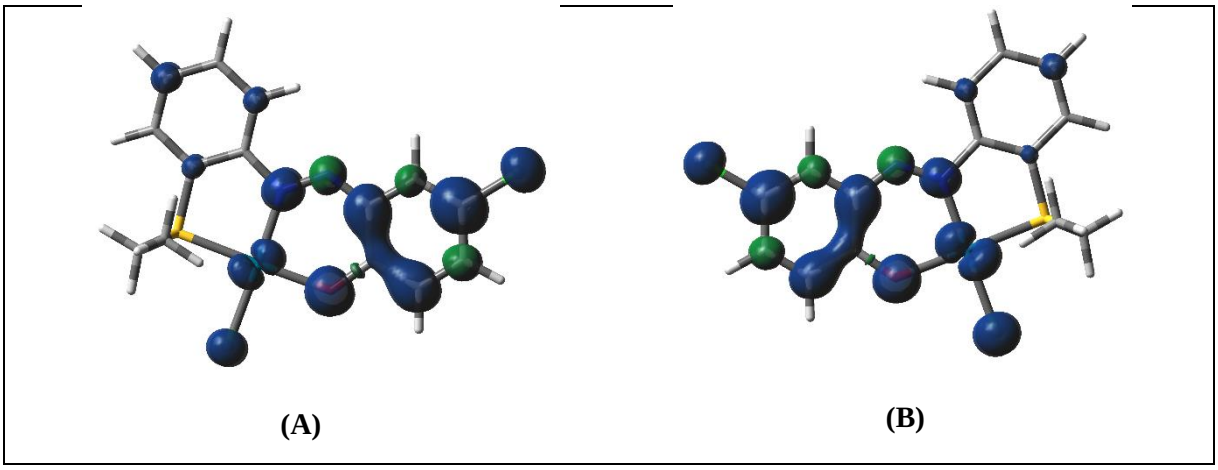

Fig. III.14. Spin density plots of (A) $\mathbf{1}^{+}$ and (B) $\mathbf{2}^{+}$

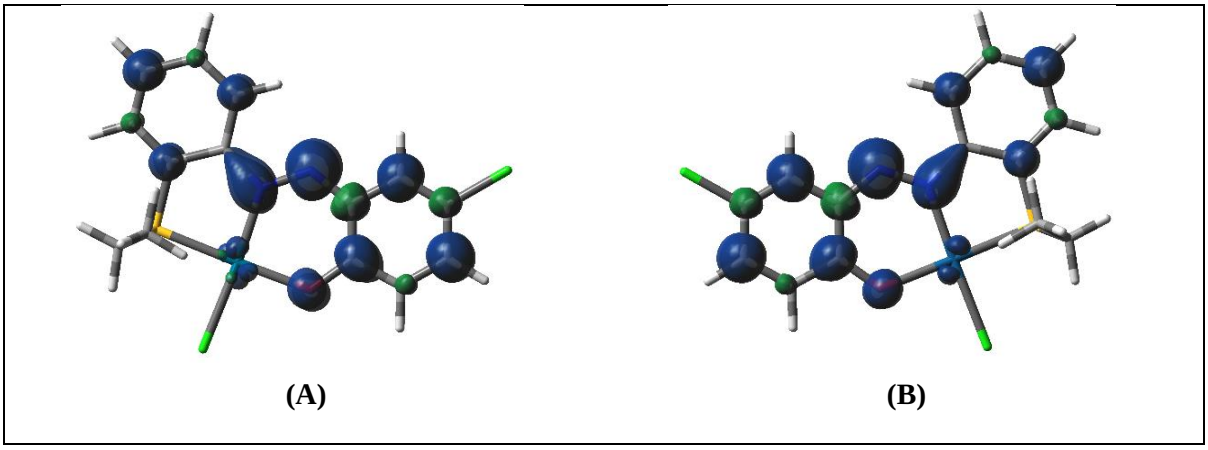

Fig. III.15. Spin density plots of (A) $\mathbf{1}^{-}$ and (B) $\mathbf{2}^{-}$

III.3.5. DNA binding studies

III.3.5.1. UV-vis method

The binding mode and strength of the complexes with CT-DNA were investigated by using the UV-Vis method. UV-Vis titration is a very well-known method used to monitor the interaction of a compound with DNA. The UV-Vis absorption spectra were significantly affected by the gradual addition of DNA, confirming the formation of the new complex adduct with double helical CT DNA. The significant hypochromic shift in the absorption maxima and a significant shift in wavelength was observed along with the increasing concentration of DNA (Fig. III.16). The observed hypochromic shift suggests that the complexes are likely bound to CT-DNA via intercalative mode.[48] The intrinsic binding constant (K_b) which offers an approximation of magnitude of the binding strength, was determined by plotting [DNA]/($\varepsilon_a - \varepsilon_f$) vs. [DNA] from the spectral titration data using the Wolfe-Shimer equation (Eq. III.1).[49]

$$\frac{[DNA]}{(\varepsilon a - \varepsilon f)} = \frac{[DNA]}{(\varepsilon b - \varepsilon f)} + \frac{1}{Kb(\varepsilon b - \varepsilon f)} \qquad \text{(Eq.III.1)}$$

where [DNA] is the concentration of CT-DNA and ε_a is the apparent extinction coefficient value found by calculating A(observed)/[complex], ε_f and ε_b are the extinction coefficients of the complex in free solution and when it is fully bound to CT-DNA respectively. ε_f was determined from the calibration curve of the isolated metal complex following Beer's law. K_b is the equilibrium binding constant in M^{-1}. The plot of [DNA]/($\varepsilon_a - \varepsilon_f$) *vs.* [DNA] give a straight line with $1/(\varepsilon_b - \varepsilon_f)$ and $1/[K_b(\varepsilon_b - \varepsilon_f)]$ as slope and intercept, respectively. The values of K_b were calculated from the ratio of the slope to the intercept. The intrinsic binding constant (K_b) values are shown in Table III.6. The K_b values are found to be $1.292(\pm0.058)\times10^5\ M^{-1}$ and $1.874(\pm0.091)\times10^5\ M^{-1}$ for complexes **1** and **2** respectively. These values are very much comparable to the reported values of binding constants for other complexes towards CT DNA.[50]

The stability of the complex DNA adducts were revealed by the binding constant values while a measure of the spontaneity of a complex towards DNA binding was given by using Eq. (Eq. III.2).

$$\Delta G = - RT \ln K_b \qquad \text{(Eq. III.2)}$$

The free energies for the complexes (listed in Table III.6) were negative which indicated the spontaneity of compound-DNA interaction.

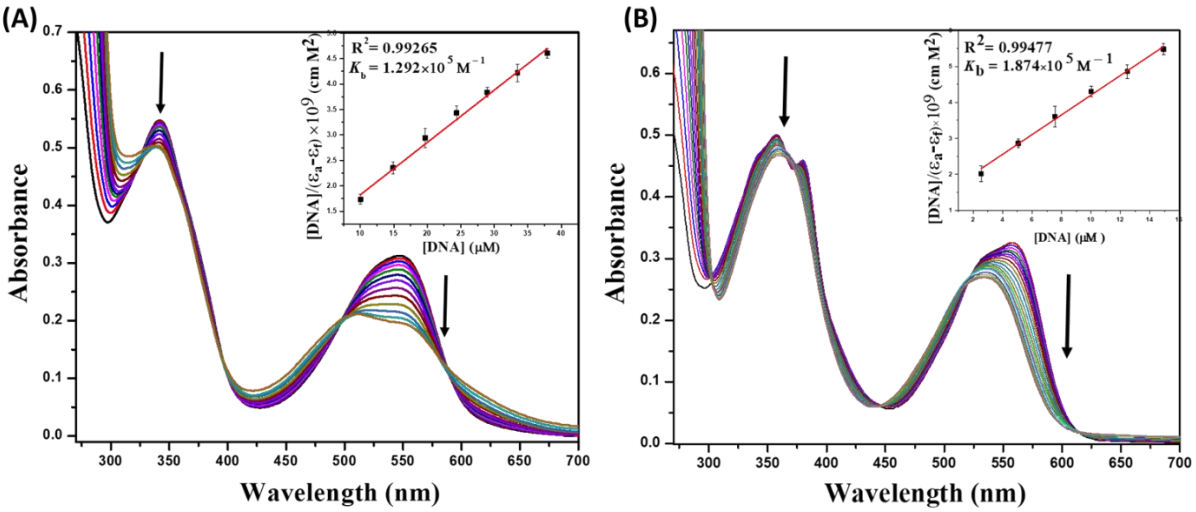

Fig. III.16. Change in absorption spectra of the complexes **1** (A) and **2** (B) in Tris–HCl/NaCl buffer with the gradual addition of CT DNA. Inset: Plot of [DNA]/($\varepsilon_a - \varepsilon_f$) vs. [DNA].

III.3.5.2. Fluorescence studies of Competitive DNA binding

The fluorescence method is an effective way to study the interaction of metal complex with CT-DNA. In this purpose, Ethidium bromide (EB) is a common fluorescent probe that used to bind with DNA. An enhancement of fluorescence intensity is observed due to the intercalation of EB into CT-DNA.[51] When metal complex intercalates into DNA it leads to a decrease in fluorescence intensity due to the replacement of EB from the EB-CT-DNA system (Fig. III.17). Herein, the addition of complexes to CT DNA pre-treated with EB causes a significant amount of decease in emission intensities, indicating that the complexes compete with EB for the binding sites of DNA. The fluorescence quenching is explained by the Stern–Volmer equation (Eq. III.3).[52]

$$F_0/F = 1 + K_{sv}[Q] \qquad \text{(Eq. III.3)}$$

Where F_0 and F are the fluorescence intensities of the CT DNA solutions in the absence and presence of the complex, respectively. K_{sv} is the Stern–Volmer quenching constant and [Q] is the concentration of complex. The K_{sv} values are obtained as a slope from the plot of F_0/F versus [Q] (Fig. III.17 inset) and are found to be $1.009(\pm0.020)\times10^5$ M^{-1} and $1.197(\pm0.029)\times10^5$ M^{-1} for **1** and **2**, respectively.

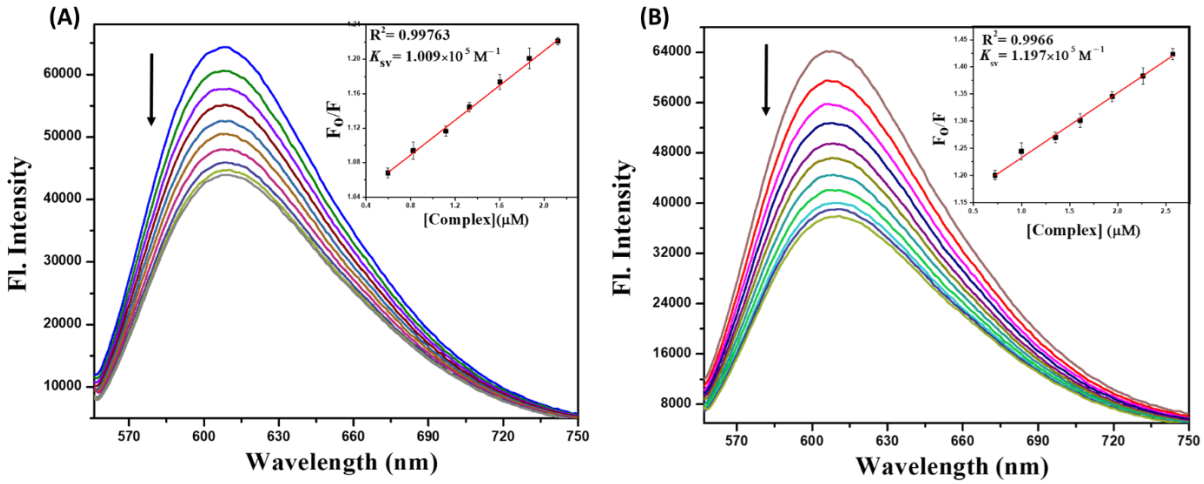

Fig. III.17. Emission spectra (λ_{ex} = 540 nm) of EB–CT DNA in presence of increasing concentrations of the complexes **1** (A) and **2** (B). Inset: Plots of emission intensity F_0/F vs. [complex].

Table III.6. CT-DNA-binding constants (K_b), Gibbs free energies (ΔG), Stern-Volmer constants (K_{SV}) of complexes **1** and **2**.

Compound	UV Method		Fluorescence Method
	K_b (×10^5) (M^{-1})	ΔG (KJ.mol^{-1})	K_{sv} (×10^5) (M^{-1})
EB-CT- DNA + 1	1.292 ± 0.058	-29.158	1.009 ± 0.020
EB-CT- DNA + 2	1.874 ± 0.091	-30.146	1.197 ± 0.029

III.3.6. Protein binding studies

III.3.6.1. Electronic absorption titration

Electronic absorption spectra of BSA (10 μM in PBS at pH 7.4) was recorded in the range of 240-450 nm in presence of different concentration of the complex which is shown in the Fig. III.18. BSA has a characteristic absorption band at 280 nm. Gradual addition of complex to the BSA solution showed that the absorption intensity of BSA enhanced and was a small blue shift in the wavelength for all the complexes. This hypsochromic shift corresponds to ground-state association between the complex and protein.[53] The apparent association constant (K_a) was calculated from the plot of $1/(A_{obs}-A_0)$ vs 1/[complex] (Fig. III.18 inset) adopting the following equation (Eq. III.4).

$$\frac{1}{A_{obs}-A_0} = \frac{1}{A_c-A_0} + \frac{1}{K_a(A_c-A_0)[complex]} \qquad \text{(Eq. III.4)}$$

Where A_{obs} is the observed absorbance (at 280 nm) of the solution having various concentrations of the complex, A_0 and A_c are the absorbance of BSA only and of serum albumin with the complex. The calculated value of apparent association constant (K_a) for the complexes **1** and **2** are 4.522(±0.108)×10^4 M^{-1} and 5.628(±0.128)×10^4 M^{-1} respectively and these values are comparable to reported value.[50]

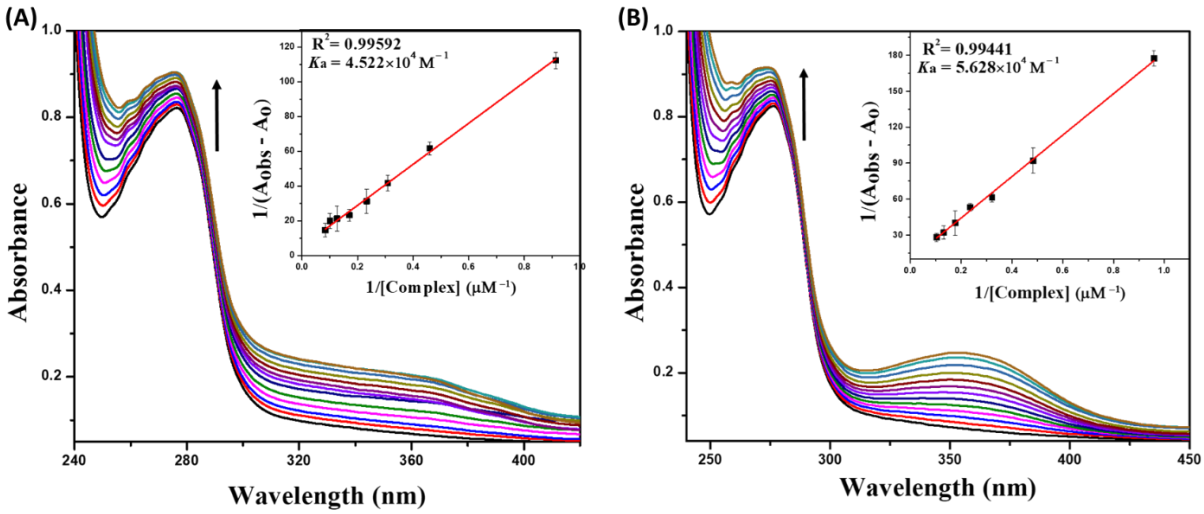

Fig. III.18. Change in absorption spectra of BSA with the gradual addition of complex **1** (A) and complex **2** (B). Inset: Plot of 1/(A_{obs}-A_0) vs 1/[complex].

III.3.6.2. Fluorescence quenching studies

The BSA-complex interactions were also studied by fluorescence spectral titration technique. Complex is non-fluorescent in DMSO solution. But upon excitation at 280 nm, an aqueous solution (10 μM, pH 7.4 PBS buffer) of BSA exhibits a strong fluorescence at 336 nm. The effect of the compounds on the fluorescence emission spectrum of BSA is shown in Fig. III.19. Addition of the above compounds to the solution of BSA results in a significant decreased in fluorescence intensity of BSA at 336nm, up to 59.6% and 63.7% of the initial fluorescence intensity of BSA accompanied by a blue shift of 2 nm and 6 nm for complexes **1** and **2** respectively. This decrease in emission intensity with a prominent blue shift in maximum emission wavelength of BSA was noticed with an increase in quencher concentration, indicating the associative interaction between the BSA and quenchers.[54] The observed blue shift is mainly due to the fact that the active site in the protein is buried in a hydrophobic environment.

The fluorescence quenching mechanisms are usually classified as either static or dynamic quenching. Static quenching usually results to the formation of a complex between the

quencher and the fluorophore in the ground state, whereas in dynamic quenching the fluorophore and the quencher interact with each other in the excited state. To study the quenching process, fluorescence quenching data were analysed using the Stern–Volmer equation (Eq. III.3). The Stern-Volmer quenching constant values (K_{sv}) calculated from the plot of F_0/F vs [Q] (Fig. III.19 inset) in respect to complexes **1** and **2** were found to be $1.947(\pm0.067)\times10^4$ M^{-1} and $3.549(\pm0.125)\times10^4$ M^{-1}. The high K_{sv} values indicate that complexes exhibit good fluorescence quenching ability. Furthermore, the quenching rate constant (Kq) of the complexes were found to be in the range of $1.947–3.549 \times 10^{12}$ M^{-1} s^{-1}, following the equation $K\text{q} = K_{sv}/\tau_o$ (τ_o refers to the lifetime of the fluorophore without the quencher with an average value of 10^{-8} s). Since the obtained Kq value is greater than the value suggested in dynamic quenching (2×10^{10} M^{-1} s^{-1}), the preferred quenching process is static through the formation of a complex.[55]

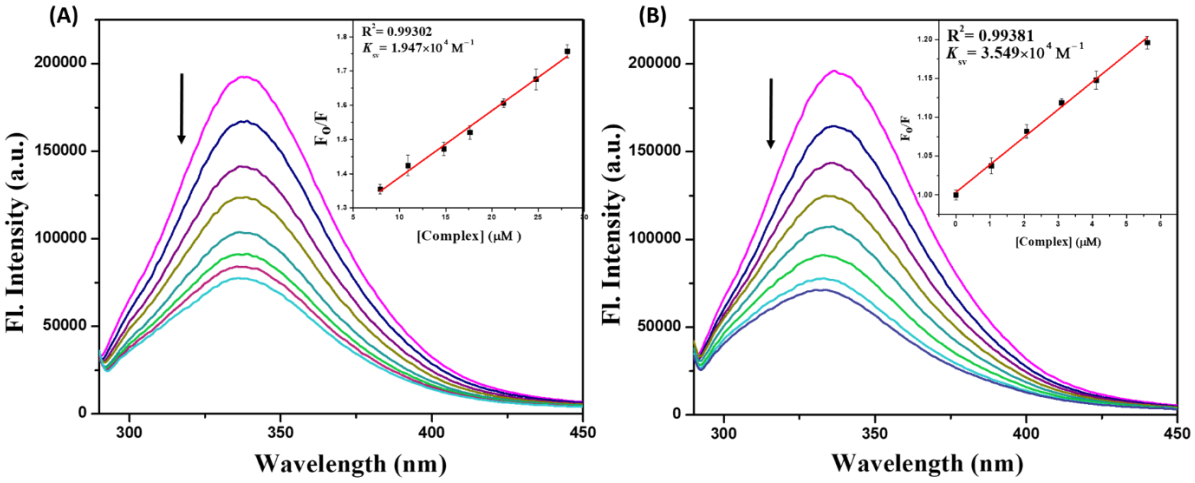

Fig. III.19. Emission spectra (λ_{ex} = 280 nm) of BSA in presence of increasing concentration of the complexes **1** (A) and **2** (B). Inset: Plots of emission intensity F_0/F vs. [complex].

III.3.6.3. Binding constant and binding sites

Further, the binding constant and number of binding sites can be calculated by using following Scatchard equation (Eq. III.5).

$$log\frac{(F_0-F)}{F} = log\ K_b + nlog[complex] \qquad \text{(Eq. III.5)}$$

Where K_b is the binding constant of synthesized compounds with BSA and n is the number of binding sites. The binding constant (K_b) and the binding sites (n) have been obtained from the plot of log [(F_o-F)/F] versus log [complex] (Fig. III.20). Based on the plot, calculated values

of binding constant (K_b) for the complexes **1** and **2** are 2.141(±0.059)×10^4 M^{-1} and 3.422(±0.095)×10^4 M^{-1} and binding sites (n) are 0.917(±0.022) and 1.005(±0.023) respectively. The binding constant (K_b) values suggested that the synthesized complexes have strong binding affinity with the serum albumins. The obtained binding site values n (~1) strongly supported the existence of single binding site in BSA protein.

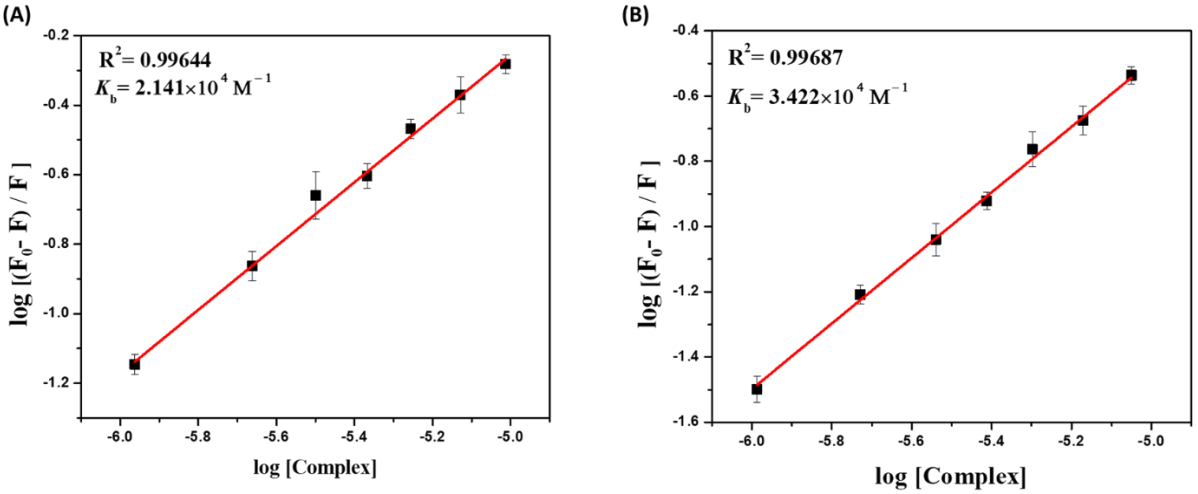

Fig. III.20. Plot of log [(F_o-F)/F] versus log [complex] of complex **1** (A) and complex **2** (B).

Table III.7. Protein apparent association constant (K_a), binding constant (K_b), quenching constant (K_{sv}) and number of binding sites (n) for complexes **1** and **2**

Comp.	UV Method	Fluorescence Method		
	K_a (×10^4) (M^{-1})	K_b (×10^4) (M^{-1})	K_{sv} (×10^4) (M^{-1})	n
BSA + 1	4.522 ± 0.108	2.141 ± 0.059	1.947 ± 0.067	0.917 ± 0.022
BSA + 2	5.628 ± 0.128	3.422 ± 0.095	3.549 ± 0.125	1.005 ± 0.023

III.3.6.4. Synchronous fluorescence spectroscopic studies

A synchronous fluorescence spectroscopic study was used to obtain information about the molecular microenvironment, particularly in the vicinity of the fluorophore moieties of BSA.[56] According to Miller,[57] in synchronous fluorescence spectroscopy the difference between the excitation and emission wavelengths ($\Delta\lambda = \lambda_{em} - \lambda_{ex}$) indicates the nature of the chromophores in the spectra. If the $\Delta\lambda$ value is 15 nm, the synchronous fluorescence spectra of BSA are characteristics of tyrosine residue, whereas the larger $\Delta\lambda$ value of 60 nm is characteristics of tryptophan residue. The maximum emission wavelength of tryptophan and tyrosine residues in the protein molecule are related to the polarity of their surroundings,

changes of the maximum emission wavelengths can reflect changes of protein conformation. The synchronous fluorescence spectra of BSA with various concentrations of complexes recorded at $\Delta\lambda$ = 15 nm and $\Delta\lambda$ = 60 nm are shown in Fig. III.21 and III.22 respectively. In the synchronous fluorescence spectra of BSA at $\Delta\lambda$ = 15, the addition of the complexes to the solution of BSA results in a small decrease in the fluorescence intensity of BSA at 301 nm, up to 37% and 39% of the initial fluorescence intensity of BSA for the complex **1** and **2** respectively, with no shift in their emission wavelength maxima. But, at the same time, in the case of the synchronous fluorescence spectra of BSA at $\Delta\lambda$ = 60, the addition of the complexes to the solution of BSA results in a significant decrease in the fluorescence intensity of BSA at 343 nm, up to 61% and 66% of the initial fluorescence intensity of BSA accompanied by a blue shift of 4 and 5 nm for the complex **1** and **2** respectively. The spectral studies clearly suggested that the fluorescence intensities of both the tryptophan and tyrosine were decreased but the emission wavelength of the tryptophan residues is blue shifted with increasing concentration of the complexes. At the same time, there is no change in the emission wavelength of tyrosine. It suggested that the interaction of complexes with BSA affects the conformation of the tryptophan micro-region. It also indicated that the hydrophobicity around tryptophan residues is strengthened. The hydrophobicity observed in fluorescence and synchronous measurements confirmed the effective binding of all the complexes with the BSA. Hence, the strong interaction of these complexes with BSA suggested that the complexes may be fit for anticancer studies.

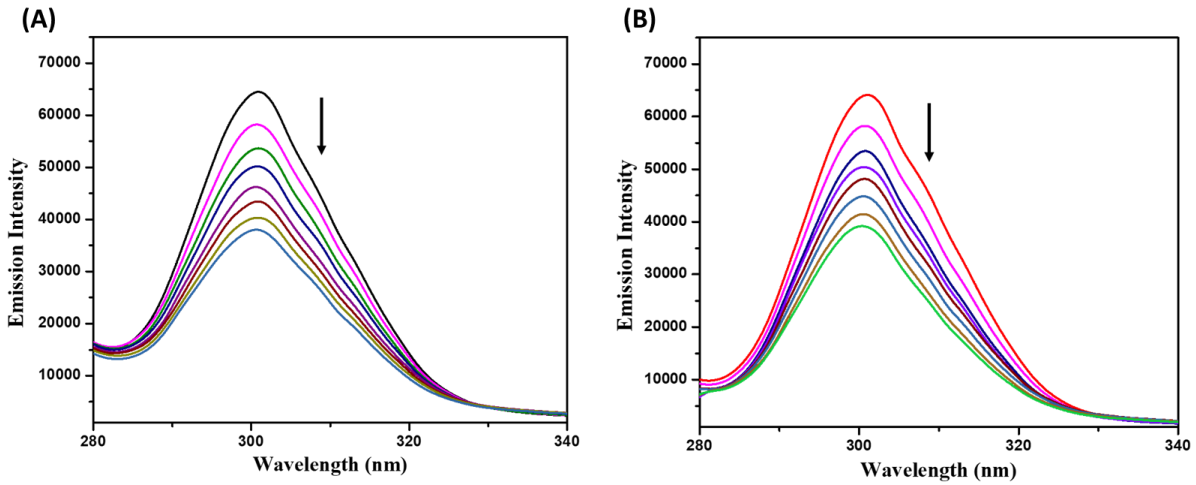

Fig. III.21. The synchronous spectra of BSA in the presence of increasing amounts of the complexes **1** (A) and **2** (B) at a wavelength difference of $\Delta\lambda$ = 15 nm. The arrow shows the emission intensity changes upon an increase in the concentration of the complexes.

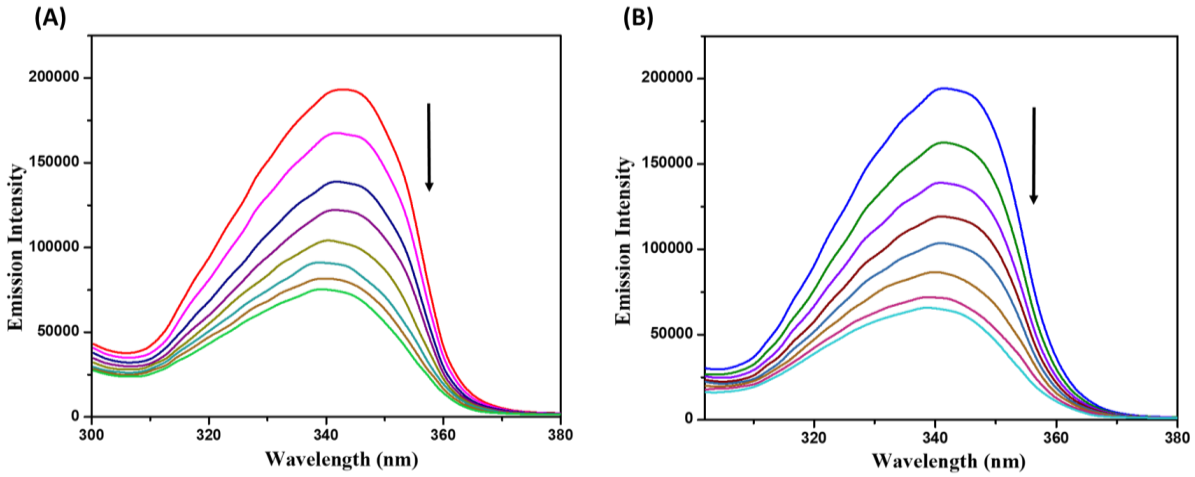

Fig. III.22. The synchronous spectra of BSA in the presence of increasing amounts of the complexes **1** (A) and **2** (B) at a wavelength difference of $\Delta\lambda$ = 60 nm. The arrow shows the emission intensity changes upon an increase in the concentration of the complexes.

III.3.7. In vitro Cytotoxicity Study

III.3.7.1. Cell viability assay:

Cell viability was studied using MTT assay on three different human cancer cell lines (HepG2, HCT 116, and A549). IC_{50} values of the complexes are tabulated in Table III.8. Both the complexes have showed different degree of cytotoxicity (Fig. III.23 and III.25) asserting their efficacy in an order of HCT 116> HepG2> A549 using cisplatin and doxorubicin (Dox) as positive controls.[58] Hence, HCT 116 cells have chosen for further study. Moreover, HL and normal PBMC cells (human peripheral blood mononuclear cells) have showed significantly higher IC_{50} values on all three cell types than other two compounds (Fig. III.24).

Table III.8. IC_{50} values (in μM) of HL, [Pd(L)Cl] (**1**) and [Pt(L)Cl] (**2**) against various cancer and normal cell lines.

Compds.	A549	HepG2	HCT116	PBMC
HL	>200	>200	>200	>200
1	5.14±0.03	4.28±0.20	4.06±0.08	>200
2	3.53±0.09	3.48±0.09	3.29±0.12	>200
Cisplatin	11.7±0.62	12.3±0.50	7.8±0.26	>200
Dox	4.60±0.12	0.75±0.31	4.72±0.04	>200

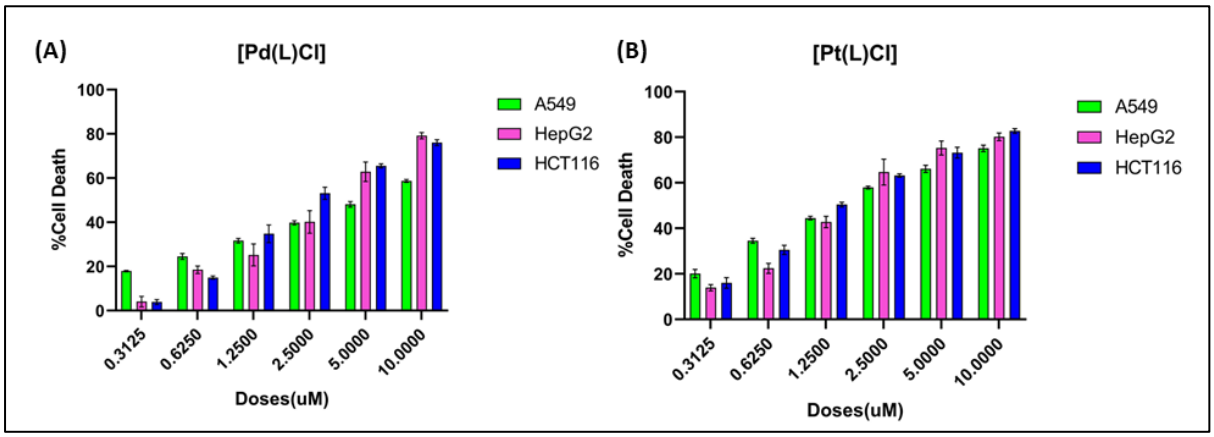

Fig. III.23. Assessment of cell viability using MTT. Viability of A549, HepG2 and HCT116 cells were assessed by treating different doses of [Pd(L)Cl] (**1**) (A) and [Pt(L)Cl] (**2**) (B).

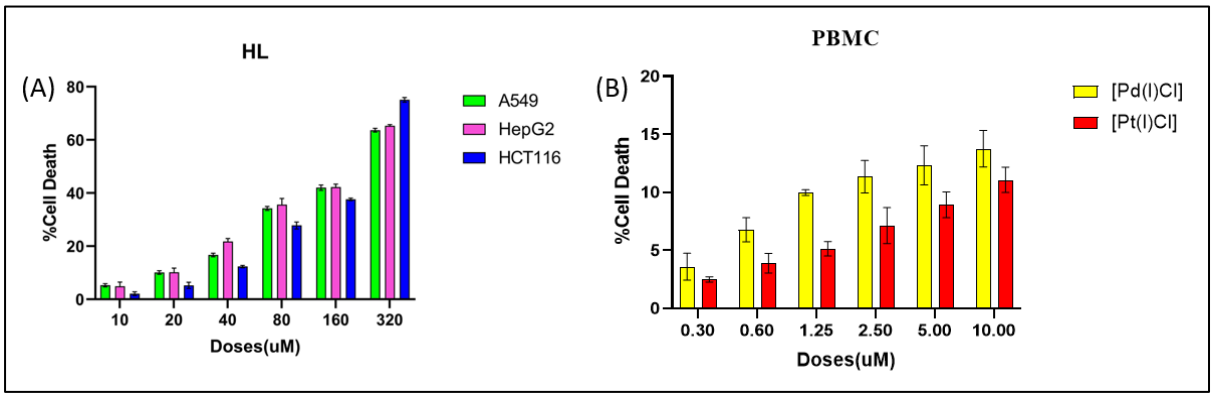

Fig. III.24. (A) Viability of A549, HepG2 and HCT116 cells were assessed by treating different doses of HL, (B) The effects of [Pd(L)Cl] (**1**) and [Pt(L)Cl] (**2**) in peripheral blood mononuclear cells (PBMCs).

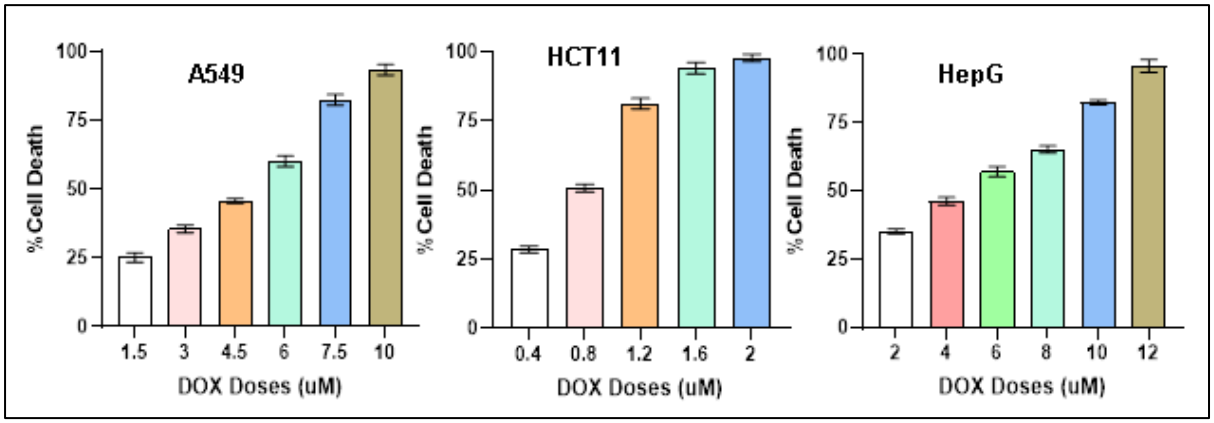

Fig. III.25. Viability of A549, HepG2 and HCT116 cells were assessed by treating different doses of Doxorubicin (Dox).

III.3.7.2. Analysis of ROS generation using DCF-DA assay

Flowcytometric analysis of Reactive Oxygen Species (ROS) indicated significant increase in intracellular ROS following treatment with [Pt(L)Cl] (**2**) due to increased DCFDA fluorescence, compared to [Pd(L)Cl] (**1**) and control (Fig. III.26). More appropriately, administration of **2** had increased generation of intracellular ROS by 8.19-fold and 1.43-fold than Control and complex **1** respectively.[59, 60]

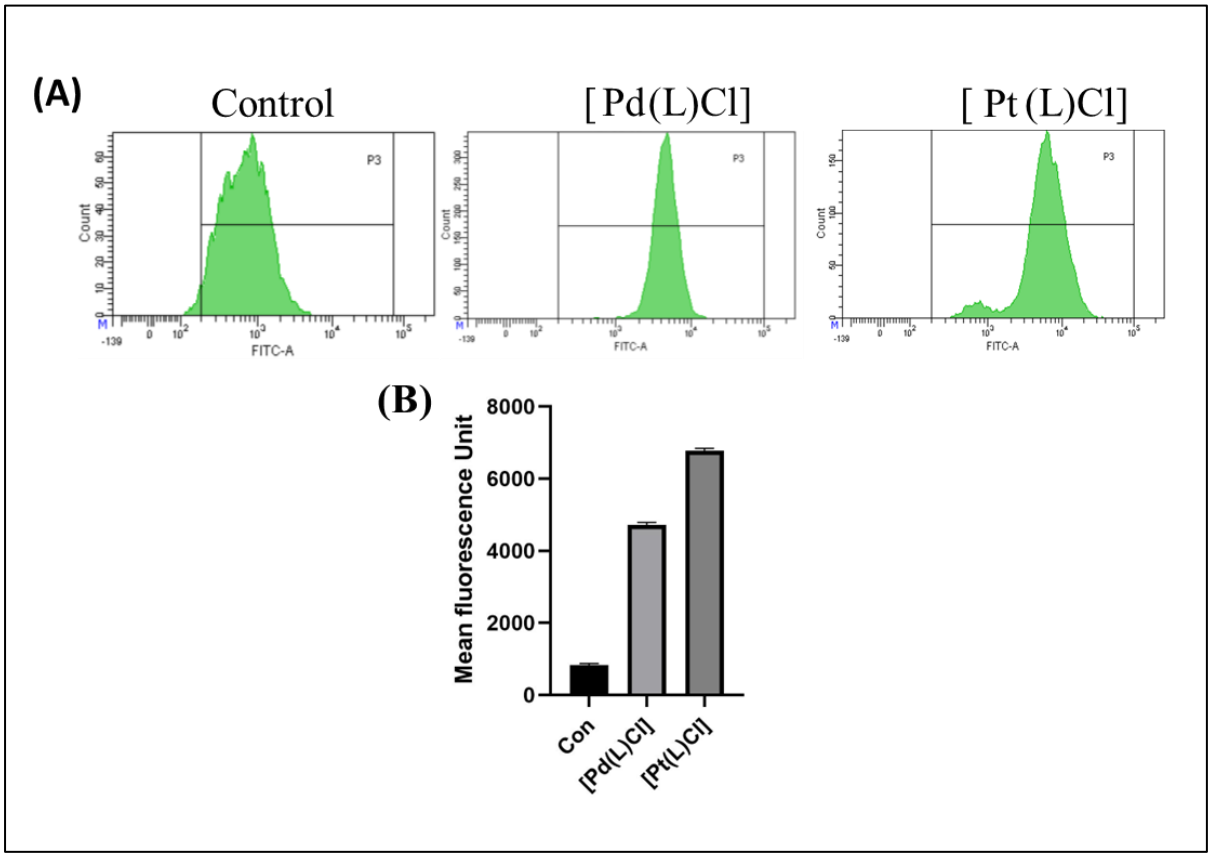

Fig. III.26. Changes in intracellular ROS following treatment with [Pd(L)Cl] (**1**) and [Pt(L)Cl] (**2**). (A) Intracellular ROS was measured using flowcytometry. (B) Comparison of DCFDA fluorescence in mean fluorescence unit.

III.3.7.3. Analysis of Mitochondrial membrane potential using flowcytometry– JC1 staining

Mitochondrial membrane potential (MMP) is used as an indicator of function of mitochondria. Dysfunction of mitochondria can lead to loss of MMP.[61, 62] Flow cytometry analysis of JC-1 staining demonstrated a significantly decreased fluorescence intensity in [Pt(L)Cl] (**2**) treated cells compared to [Pd(L)Cl] (**1**) treated cells and control cells suggesting an enhanced capability of Pt-complex to cause mitochondrial dysfunction than Pd-complex (Fig. III.27).

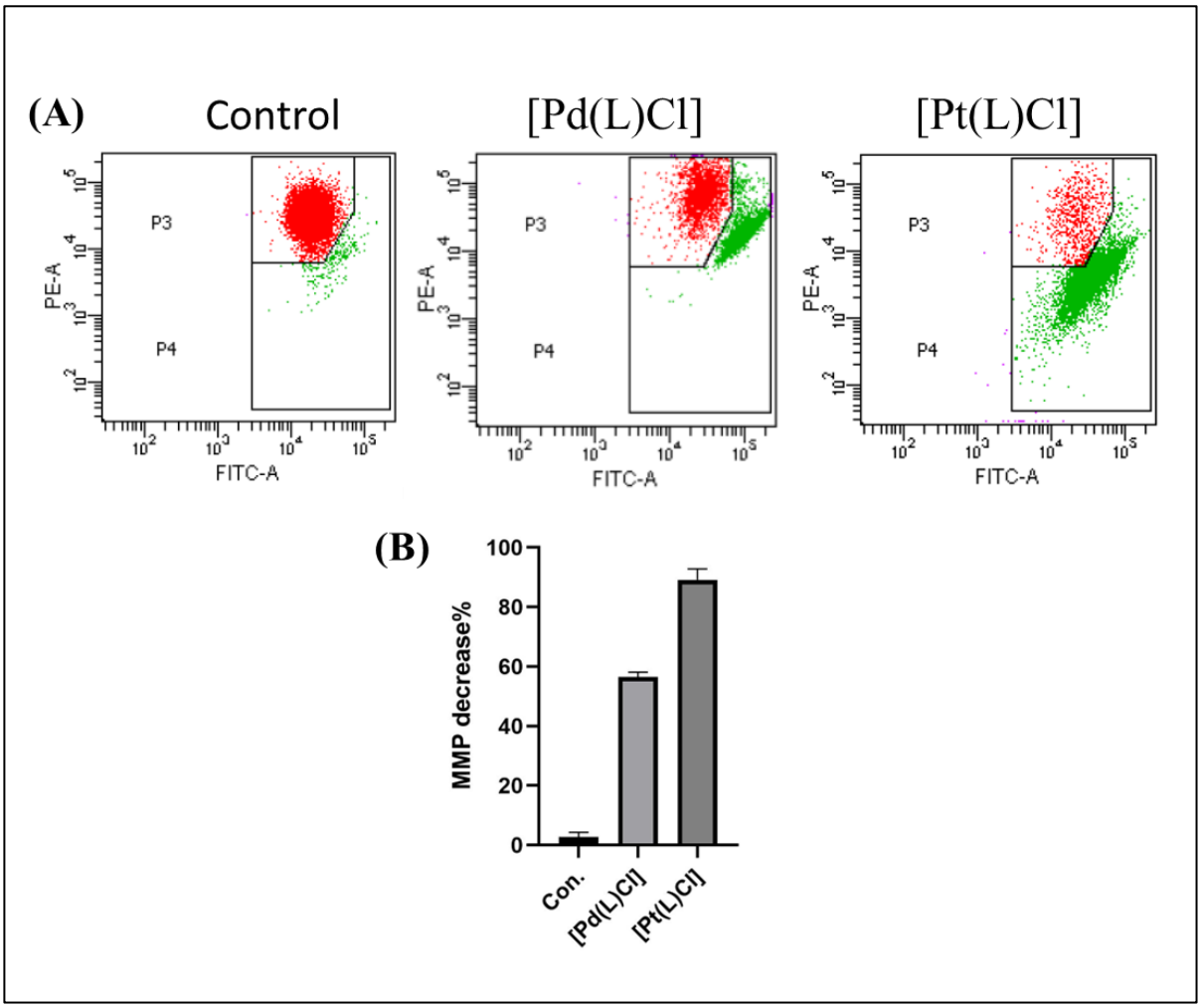

Fig. III.27. Effect of [Pd(L)Cl] (**1**) and [Pt(L)Cl] (**2**) on Mitochondrial membrane potential (MMP). (A) JC1 fluorescence in HCT116 Cells and (B) comparison of decrease in MMP.

III.3.7.4. Flowcytometric analysis of apoptosis

Flowcytometric analysis of apoptosis in HCT 116 cells were done using Annexin V/PI double staining assay.[63-66] Flowcytometric data showed that cells exposed to [Pt(L)Cl] (**2**) have shown significant increase in Late Apoptotic population (35.5%) than Necrotic (30.7%) population after 24 h exposure than [Pd(L)Cl] (**1**) which showed significantly higher rate of necrotic cell population (i.e.,46.2% Necrotic and 25.5% late apoptotic cell population) (Fig. III.28). However, untreated cells did not show significant apoptosis or necrosis. Thus, the results demonstrated a higher apoptotic potential of Pt-complex compared to Pd-complex.

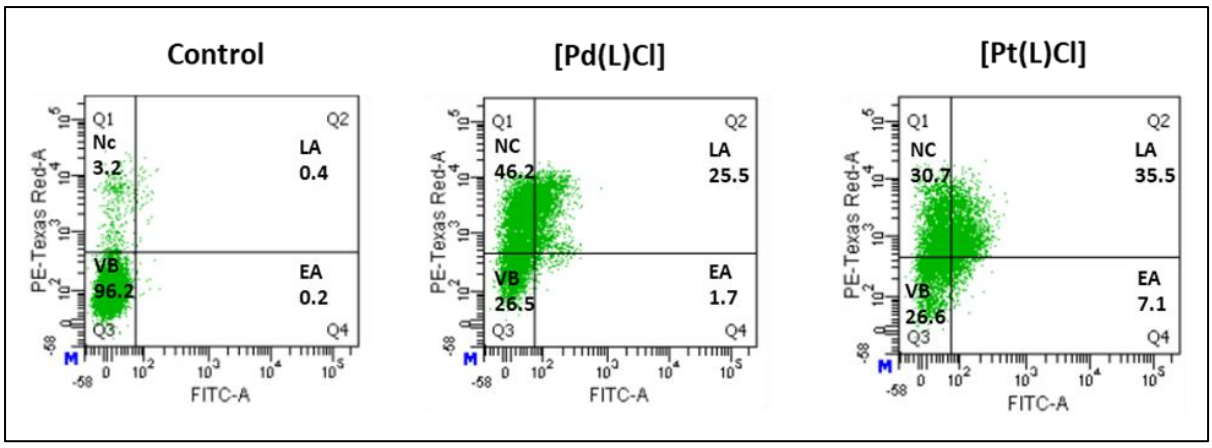

Fig. III.28. Role of [Pd(L)Cl] (**1**) and [Pt(L)Cl] (**2**) in apoptosis. Annexin V-FITC/PI was used to analysed apoptosis. HCT116 cells was treated with complex **1** and complex **2** and observed for apoptosis using flowcytometry.

III.3.7.5. Analysis of protein expression via confocal microscopy

Confocal Microscopic analysis showed decreased level of antiapoptotic protein bcl2 and increased expression of BAX (proapoptotic protein) and P53 in case of [Pt(L)Cl] (**2**) treated cells than [Pd(L)Cl] (**1**) and controlled cells signifying dominance of **1** over **2** in causing cellular apoptosis (Fig. III.29).[67]

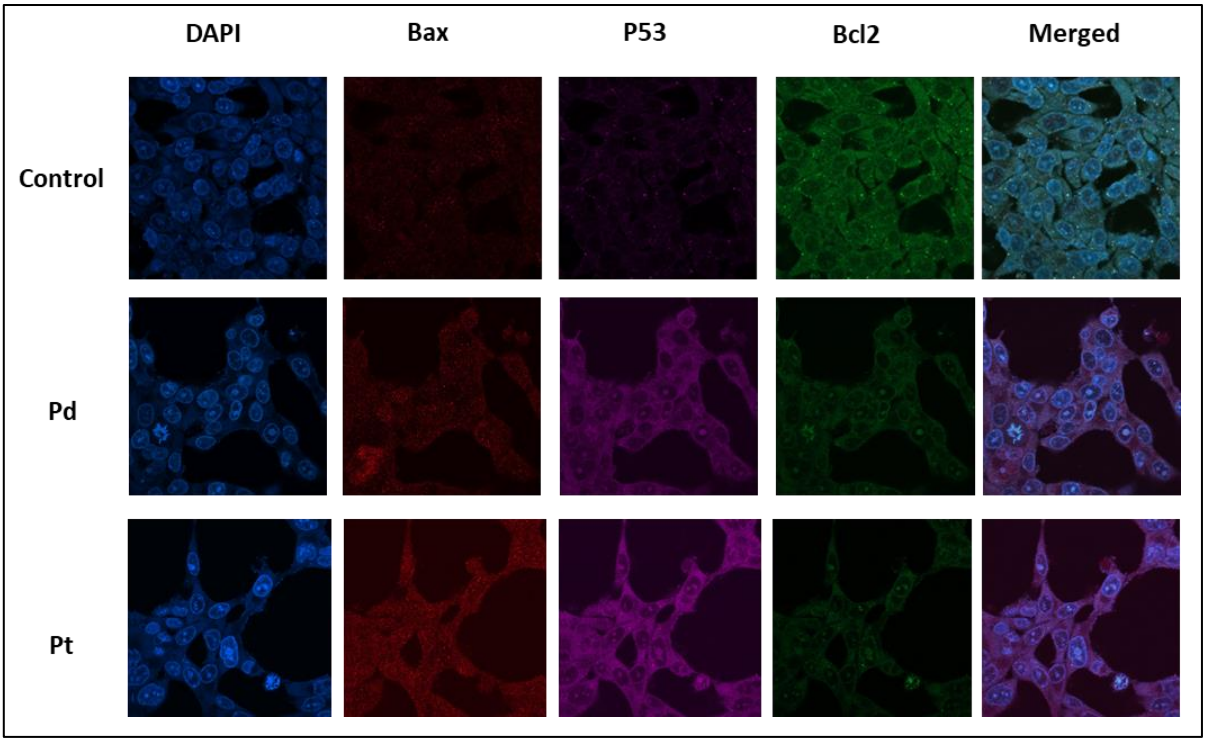

Fig. III.29. Pd(L)Cl] (**1**) and [Pt(L)Cl] (**2**) altered expression of pro and anti- apoptotic proteins. HCT116 Cells was treated with different compounds and changes observed under confocal microscopy.

III.3.7.6. Western Blot analysis of cellular protein expression

P53 act as a tumor suppressor and MDM2 function as an inhibitory protein of p53 regulating its expression via proteasomal degradation. Western blot analysis suggested significantly increased level of p53 and decreased expression of MDM2 in [Pt(L)Cl] (**2**) treated cells compared to [Pd(L)Cl] (**1**) and control cells (Fig. III.30). Cyt C releases from inner mitochondrial membrane during apoptosis and a key protein of intrinsic pathway of apoptosis.[68-70] Significantly, increased level of Cyt C in **2** treated cells is attributed to greater apoptotic potential of **2** than **1**.

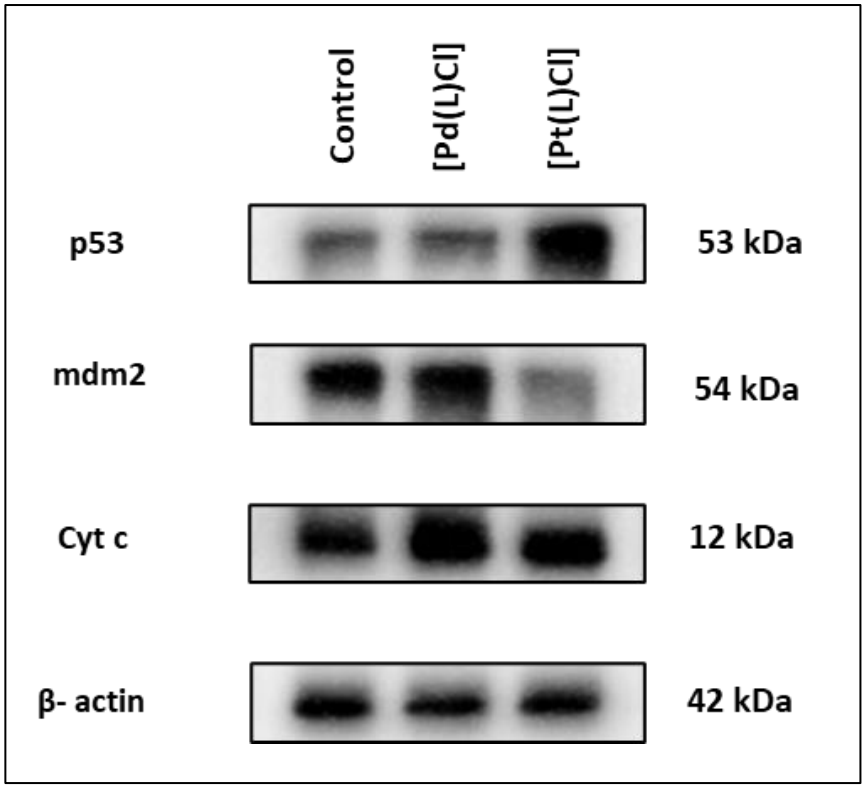

Fig. III.30. Western blot analysis of key regulatory proteins of apoptosis. p53, mdm2 and CytC expression levels were analysed following treatment with complexes **1** and **2**.

III.3.7.7. Analysis of Cell Cycle using Flowcytometry

After treatment of cells with complexes **1** and **2**, for 24 h samples were collected and analysed by flow cytometry assay for determining of cell cycle phase. Our results indicated that treatment with both complexes **1** and **2** caused an increase in G1 and S phase cell population compared with the control group suggesting possible arrest at G1/S phase.[71-73] Also, treatment with Pt-complex had significantly greater effect than Pd-complex in this scenario (Fig. III.31).

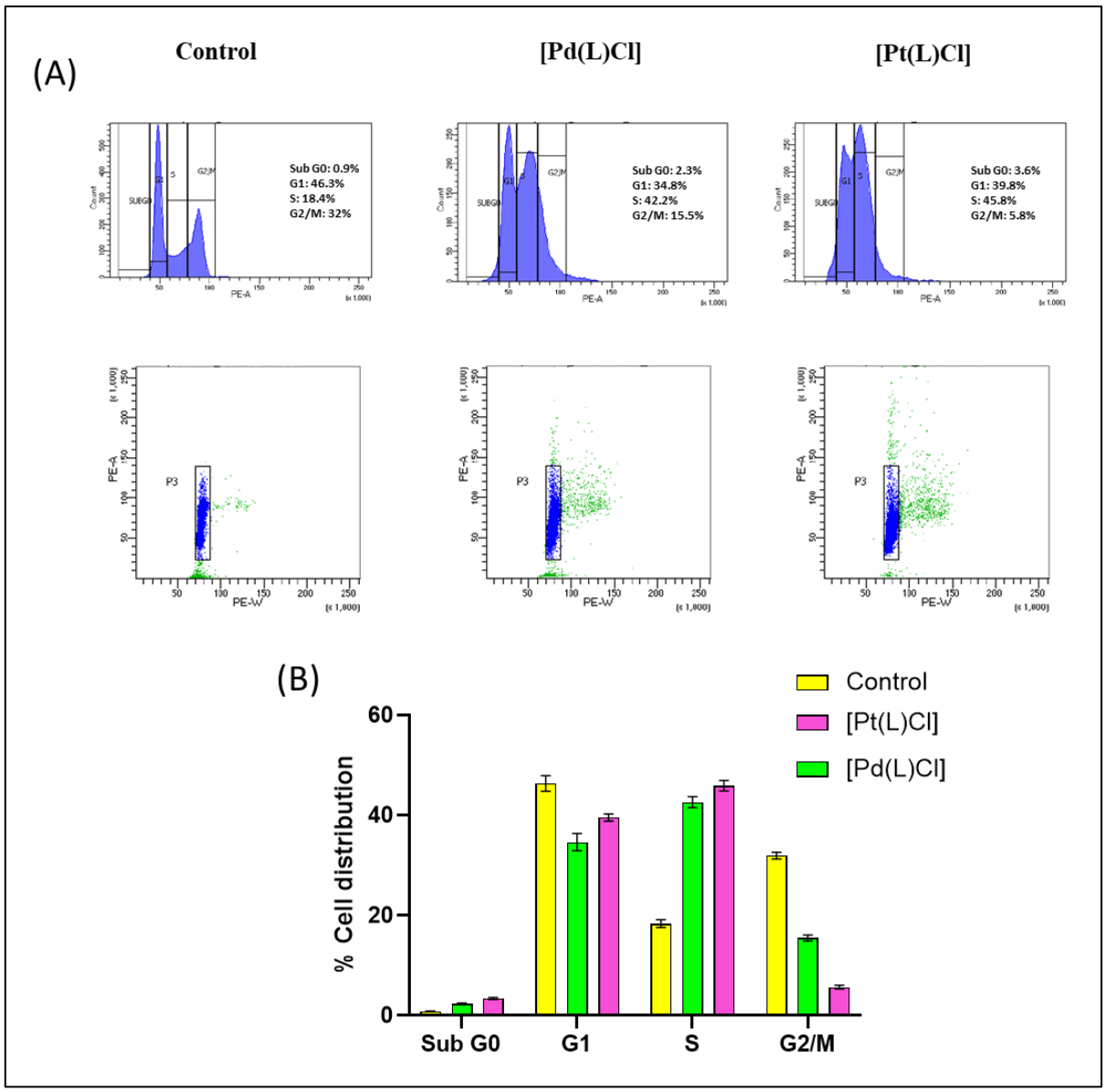

Fig. III.31. Analysis of cell cycle. (A) Flowcytometric analysis of distribution of HCT116 cells at different stages of cell cycle following **1** and **2** administrations. (B) Bar diagram representing cell population at different stages of cell cycle.

III.4. Conclusions

The new palladium(II) and platinum(II) complexes, [Pd(L)Cl] (**1**) and [Pt(L)Cl] (**2**) with ONS donor azo-thioether ligands (HL) were successfully synthesized and characterized. X-ray structures reveal that the geometries of these complexes are slightly distorted from regular square planar geometry around the metal center. The interaction of CT DNA with both the complexes were investigated by employing the UV–Vis method and binding constant values suggest that the complexes strongly bind with CT DNA. Competitive binding

titrations with ethidium bromide (EB) by the fluorescence titration method reveal that the complexes efficiently displace EB from the EB–DNA system. Also, both the complexes showed a good binding affinity to BSA with relatively high binding constants. The antiproliferative activity of the complexes showed that Pt(II) complex **2** is more potent than Pd(II) complex **1** in HCT116, HepG2 and A549 cell lines. Apoptotic analysis by annexin-V/FITC-PI binding assay shows that the percentage of apoptotic and total dead cells is significantly higher in Pt(II) complex **2** than that of Pd(II) complex **1.** From the MTT assay data, it is concluded that the synthesized complexes exhibited higher cytotoxic potency towards cancer cell lines than the widely used as anti-cancer drugs cisplatin and doxorubicin (Dox). Thus, our synthesized Pd(II) and Pt(II) complexes under study deserve further investigation on their in vivo antitumor activities, which can enable them to serve as an ideal anticancer drugs capable of targeting tumor cells having no adverse effect on the normal cells.

III.5. References

1. H. Sung, J. Ferlay, R. L. Siegel, M. Laversanne, I. Soerjomataram, A. Jemal and F. Bray, *Ca Cancer J. Clin.*, 2021, **71**, 209-249.
2. N. V. Loginova, H. I. Harbatsevich, N. P. Osipovich, G. A. Ksendzova, T. V. Koval' chuk and G. I. Polozov, Curr., *Med. Chem.*, 2020, **27**, 5213-5249
3. L. Kelland, *Nat. Rev. Cancer*, 2007, **7**, 573-584
4. A. M. Florea and D. Büsselberg, *Cancers*, 2011, **3**, 1351-1371.
5. S. N. Mbugua, N. R. S. Sibuyi, L. W. Njenga, R. A. Odhiambo, S. O. Wandiga, M. Meyer, R. A. Lalancette and M. O. Onani, *ACS Omega*, 2020, **25**, 14942-14954.
6. E. Petruzzella, R. Sirota, I. Solazzo, V. Gandin and D. Gibson, *Chem. Sci*, 2018, **9**, 4299-4307.
7. T. C. Johnstone, K. Suntharalingam and J. Lippard, *Chem. Rev.*, 2016, **116**, 3436-3486.
8. T. C. Johnstone, G. Y. Park and S. J. Lippard, *Cancer Res.*, 2014, **34**, 471-476.
9. A. R. Kapdi and I. J. S. Fairlamb, *Chem. Soc. Rev.*, 2014, **43**, 4751.
10. A. Garoufis, S. K. Hadjikakou and N. Hadjiliadis, *Coord. Chem. Rev*., 2009, **253**, 1384.
11. M. D. Coskun, F. Ari, A. Y. Oral, M. Sarimahmut, H.M. Kutlu, V. T. Yilmaz and E. Ulukaya, *Bioorg. Med. Chem*., 2013, **21**, 4698.
12. J. Espino, E. Fernández-Delgado, S. Estirado, F. de la Cruz-Martinez, S. Villa-Carballar, E. Viñuelas-Zahínos, F. Luna-Giles and J. A. Pariente, *Sci. Rep.*, 2020, **10**, 1-16.
13. H. A. Rudbari, N. Kordestani, J. V. Cuevas-Vicario, M. Zhou, T. Efferth, I. Correia, T. Schirmeister, F. Barthels, M. Enamullah, A. R. Fernandes and N. Micale. *New J. Chem.*, 2022, **46**, 6470-6483.

14. D. Simić, M. Zarić, I. Nikolić, R. Živković-Zarić, P. Čanović, A. Kočović, I. Radojević, I. Raković, S. Jovičić Milić, Đ. Petrović, D. Stojković, N. Vuković, M.Kačániová, M. Vukić and V. Jevtić, *Dalton Trans.*, 2022, **51**, 1191-1205.
15. Ž. D. Bugarčić, J. Bogojeski and R. van Eldik, *Coord. Chem. Rev.*, 2015, **292**, 91-106.
16. D. Aguila, E. Escribano, S. Speed, D. Talancon, L. Yerman and S. Alvarez, *Dalton Trans*., 2009, **33**, 6610-6625.
17. A. L. Gavrilova and B. Bosnich, *Chem. Rev*., 2004, **104**, 349-383
18. A. Eskandari, A. Kundu, A. Johnson, S. Karmakar, S. Ghosh and K. Suntharalingam, *Dalton Trans.*, 2020, **49**, 4211-4215.
19. M. N. Alam and F. Huq, *Coord. Chem. Rev.*, 2016, **316**, 36-67.
20. T. Lazarević, A. Rilak and Ž. D. Bugarčić, *Eur. J. Med. Chem.*, 2017, **142**, 8-31.
21. H. H. Repich, V. V. Orysyk, L. G. Palchykovska, S. I. Orysyk, Y. L. Zborovskii, O. V. Vasylchenko, O. V. Storozhuk, A. A. Biluk, V. V. Nikulina, L. V. Garmanchuk, V. I. Pekhnyo and M. V. Vovk, *J. Inorg. Biochem.*, 2017, **168**, 98-106.
22. A. Garoufis, S. K. Hadjikakou and N. Hadjiliadis, *Coord. Chem. Rev*., 2009, **253**, 1384-1397
23. B. B. Zmejkovski, A. Savic, J. Poljarevic, N. Pantelic, N. A. Elovic, S. Radulovic, G. N. Kaluderovic and T. J. Sabo, *Polyhedron*, 2014, **80**, 106-111.
24. S. Halder, S. M. Peng, G.-H. Lee, T. Chatterjee, A. Mukherjee, S. Dutta, U. Sanyal and S. Bhattacharya, *New J. Chem*., 2008, **32**, 105-114.
25. W. H. Mahmoud, F. N. Sayed and G. G. Mohamed, *Appl. Organomet. Chem.*, 2016, **30**, 959-973.
26. W. Ha, X. B. Zhao, W. H. Zhao, J. J. Tang and Y. P. Shi, *J. Mater. Chem. B*, 2021, **9**, 3200-3209.
27. I. de la Cueva-Alique, L. Muñoz-Moreno, E. de la Torre-Rubio, A. M. Bajo, L. Gude, T. Cuenca and E. Royo, *Dalton Trans.*, 2019, **48**, 14279-14293.
28. (a) J. Madureira, C. I. V. Ramos, M. Marques, C. Maia, B. D. Sousa, L. Campino, M. G. Santana-Marques and N. Farrell, *Inorg. Chem.*, 2013, **52**, 8881-8894; (b) C. Icsel and V. T. Yilmaz, *DNA Cell Biol*., 2013, **32**, 165-172; (c) B. Onfelt, P. Lincoln and B. Nordén, *J. Am. Chem. Soc*., 2001, **123**, 3630.
29. (a) S. Banerjee, E. B. Veale, C.M. Phelan, S. A. Murphy, G.M. Tocci, L. J. Gillespie, D. O. Frimannsson, J. M. Kelly, T. Gunnlaugsson, *Chem. Soc. Rev*., 2013, **42**, 1601-1618; (b) L. Zarei, Z. Asadi, M. Dusek, V. Eigner, *J. Photochem., Photobiol. A.*, 2019, **374**, 145-160.
30. D. Cocic, S. Jovanovic, S. Radisavljevic, J. Korzekwa, A. Scheurer, R. Puchta, D. Baskic, D. Todorovic, S. Popovic, S. Matic and B. Petrovic, *J. Inorg. Biochem*., 2018, **189**, 91-102.
31. N. Rajendiran and J. Thulasidhasan, *Spectrochim, Acta Part A Mol. Biomol. Spectrosc*., 2015, **144**, 183-191.
32. T. Peters, *Serum Albumin*, 1985, **37**, 161-245.

33. A. Divsalar, I. Zhila, A. A. Saboury, M. Nabiuni, M. Razmi and H. Mansuri-Torshizi, *J. Iran. Chem. Soc*., 2013, **10**, 951-959.
34. P. Roy, A. S. Mondal, A. K. Pramanik and T. K. Mondal, *J. Organomet. Chem.*, 2017, **828**, 1-9.
35. (a) G. M. Sheldrick, *Acta Cryst*., 2008, **A64**, 112-122; (b) G. M. Sheldrick, *Acta Cryst.*, 2015, **C71**, 3-8.
36. (a) A. D. Becke, *J. Chem. Phys.*, 1993, **98**, 5648-5652;(b) C. Lee, W. Yang and R. G. Parr, *Phys. Rev. B: Condens. Matter Mater. Phys.*, 1988, **37**, 785-789.
37. (a) P. J. Hay and W. R. Wadt, *J. Chem. Phys.*, 1985, **82**, 270-283; (b) W. R. Wadt and P. J. Hay, *J. Chem. Phys.*, 1985, **82**, 284-298; (c) P. J. Hay and W. R. Wadt, *J. Chem. Phys.*, 1985, **82**, 299-310.
38. (a) R. Ditchfield, W. J.Hehre and J.A. Pople, *J. Chem. Phys.*,1971, **54**, 724; (b) W. Hehre, J. R. Ditchfield and J. A. Pople, *J. Chem. Phys*.,1972, **56**, 2257.
39. M. J. Frisch, G. W. Trucks, H. B. Schlegel, G. E. Scuseria, M. A. Robb, J. R. Cheeseman, G. Scalmani, V. Barone, B. Mennucci, G. A. Petersson, H. Nakatsuji, M. Caricato, X. Li, H. P. Hratchian, A. F. Izmaylov, J. Bloino, G. Zheng, J. L. Sonnenberg, M. Hada, M. Ehara, K. Toyota, R. Fukuda, J. Hasegawa, M. Ishida, T. Nakajima, Y. Honda, O. Kitao, H. Nakai, T. Vreven, J. A. Montgomery, Jr., J. E. Peralta, F. Ogliaro, M. Bearpark, J. J. Heyd, E. Brothers, K. N. Kudin, V. N. Staroverov, R. Kobayashi, J. Normand, K. Raghavachari, A. Rendell, J. C. Burant, S. S. Iyengar, J. Tomasi, M. Cossi, N. Rega, J. M. Millam, M. Klene, J. E. Knox, J. B. Cross, V. Bakken, C. Adamo, J. Jaramillo, R. Gomperts, R. E. Stratmann, O. Yazyev, A. J. Austin, R. Cammi, C. Pomelli, J. W. Ochterski, R. L. Martin, K. Morokuma, V. G. Zakrzewski, G. A. Voth, P. Salvador, J. J. Dannenberg, S. Dapprich, A. D. Daniels, O¨. Farkas, J. B. Foresman, J. V. Ortiz, J. Cioslowski and D. J. Fox, Gaussian 09, Revision D.01, Gaussian, Inc., Wallingford CT, 2009.
40. (a) R. Bauernschmitt and R. Ahlrichs, *Chem. Phys. Lett.*, 1996, **256**, 454-464;(b) R. E. Stratmann, G. E. Scuseria and M. J. Frisch, *J. Chem. Phys.*, 1998, **109**, 8218; (c) M. E. Casida, C. Jamorski, K. C. Casida and D. R. Salahub, *J. Chem. Phys.*, 1998, **108**, 4439-4449.
41. (a) V. Barone and M. Cossi, *J. Phys. Chem.* A, 1998, **102**, 1995-2001; (b) M. Cossi and V. Barone, *J. Chem. Phys.*, 2001, **115**, 4708-4717; (c) M. Cossi, N. Rega, G. Scalmani and V. Barone, *J. Comput. Chem.*, 2003, **24**, 669-681.
42. N. M. O'Boyle, A. L. Tenderholt, K. M. Langner, *J. Comput. Chem.*, 2008, **29**, 839-845.
43. M. Sirajuddin, S. Ali and A. Badshah, *J. Photochem. Photobiol.*, B, 2013, **124**, 1-19.
44. F. Dimiza, F. Perdih, V. Tangoulis, I. Turel, D. P. Kessissoglou and G. Psomas, *J. Inorg. Biochem.*, 2011, **105**, 476–489.
45. F. Samari, B. Hemmateenejad, M. Shamsipur, M. Rashidi and H. Samouei, *Inorg. Chem*., 2012, **51**, 3454–3464.

46. (a) A. K. Pramanik, D. Sarkar and T. K. Mondal, *Polyhedron*, 2015, **102**, 32-40. (b) S. Jana, A. K. Pramanik, C. K. Manna and T. K. Mondal, *Polyhedron*, 2015, **150**, 118-125.
47. (a) P. Pattanayak, S. P. Parua, D. Patra, C. -K. Lai, P. Brandao, V. Felix and S. Chattopadhyay, *Inorg. Chim. Acta*, 2015, **429**, 122-131; (b) S. Biswas, A. K. Pramanik and T. K. Mondal, *J. Mol. Struct*., 2015, **1088**, 28-33; (c) D. Anu, P. Naveen, N.P. Rath and M. Kaveri, *J. Mol. Struct.*, 2020, **1206**, 127703; (d) S. A. Elsayed, H. E. Badr, A. di Biase, A. M. El-Hendawy, *J. Inorg. Biochem*., 2021, **223**, 111549.
48. (a) Q. Zhang, J. Liu, H. Chao, G. Xue and L. Ji, *J. Inorg. Biochem.*, 2001, **83**, 49; (b) A. Tarushi, E. Polatoglou, J. Kljun, I. Turel, G. Psomas and D. P. Kessissoglou, *Dalton Trans*., 2011, **40**, 9461; (c) I. Mitra, S. Mukhaerjee, B. Misini, P. Das, S. Dasgupta, W. Linert and S. C. Moi, *New J. Chem.*, 2018, **42**, 2574-2589.
49. A. Wolfe, G. H. Shimer and T. Meehan, *Biochemistry*, 1987, **26**, 6392.
50. F. Darabi, H. Hadadzadeh, J. Simpson and A. Shahpiri, *New J. Chem*., 2016, **40**, 9081-9097.
51. R. R. Monaco, J. Biomol., *Struct. Dyn*., 2007, **25**, 119-125.
52. O. Stern and M. Volmer, Z. *Phys*., 1919, **20**, 183–188.
53. (a) K. Jeyalakshmi, J. Haribabu, C. Balachandran, N. S. P. Bhuvanesh, N. Emi and R. Karvembu, *New J. Chem*., 2017, **41**, 2672-2686; (b) K. Karami, S. Hashemi, J. Lipkowski, F. Mardani, A. A. Momtazi-borojeni and Z. M. Lighvan, *Appl. Organomet. Chem*., 2017, **31**, 3740; (c) X. F. Zhao, Y. Ouyang, Y. Z. Liu, Q. J. Su, H. Tian, C. Z. Xie and J. Y. Xu, *New J. Chem*., 2014, **38**, 955-965.
54. Y. J. Hu, Y. Liu, J.B. Wang, X.H. Xiao and S. S. Qu, *J. Pharm. Biomed. Anal*., 2004, **36**, 915-919.
55. S. Deepa and A. K. Mishra, *J. Pharm. Biomed. Anal*., 2005, **38**, 556–563.
56. D. Senthil Raja, N. S. P. Bhuvanesh and K. Natarajan, *Dalton Trans*., 2012, **41**, 4365–4377.
57. J. N. Miller, *Proc. Anal. Div. Chem. Soc*., 1979, **16**, 203–208.
58. (a) S. Rubino, R. Busà, A. Attanzio, R. Alduina, V. Di Stefano, M. A. Girasolo, S. Orecchio and L. Tesoriere, *Bioorg. Med. Chem*., 2017, **25**, 2378-2386; (b) N. Miklášová, E. Fischer-Fodor, P. Lönnecke, C. I. Tomuleasa, P. Virag, M. P. Schrepler, R. Mikláš, L. S. Dumitrescu and E. Hey-Hawkins, *Eur. J. Med. Chem.*, 2012, **49**, 41-47; (c) S. Rubino, V. Di Stefano, A. Attanzio, L. Tesoriere, M. A. Girasolo, F. Nicolò, G. Bruno, S. Orecchio and G.C. Stocco, *Inorg. Chim. Acta*, 2014, **418**, 112-118; (d) L. Masaryk, P. Zoufalý, K. Słoczyńska, E. Zahradniková, D. Milde, P. Koczurkiewicz-Adamczyk and P. Štarha, *Inorg. Chim. Acta*, 2022, **536**, 120891; (e) L. Niu, G. Ren, T. Hou, X. Shen and D. Zhu, *Inorg. Chem. Commun.*, 2021, **130**, 108737.
59. A. Brozovic, A. Ambriović-Ristov and M. Osmak, *Crit. Rev. Toxicol.*, 2010, **40**, 347-359.
60. Y. Li, Z. Gu, C. Zhang, S. Li, L. Zhang, G. Zhou, S. Wang and J. Zhang, *Eur. J. Med. Chem.*, 2018, **144**, 662-671.

61. F. A. Serrano, A. L. Matsuo, P. T. Monteforte, A. Bechara, S. S. Smaili, D. P. Santana and T. Rodrigues, *BMC cancer*, 2011, **11**, 1-16.
62. M. J. Hosseini, I. Jafarian, S. Farahani, R. Khodadadi, S. H. Tagavi, P. Naserzadeh, A. Mohammadi-Bardbori and N. Arghavanifard, *Metallomics*, 2016, **8**, 252-259.
63. S. H Lee, X. W. Meng, K. S. Flatten, D. A. Loegering and S. H. Kaufmann, *Cell Death & Differentiation*, 2013, **20**, 64-76.
64. G. Zhang, V. Gurtu, S. R. Kain and G. Yan, *BioTechniques*, 1997, **23**, 525-531.
65. V. Turinetto and C. Giachino, *Nucleic Acids Res.*, 2015, **43**, 2489-2498.
66. M. D. Coskun, F. Ari, A. Y. Oral, M. Sarimahmut, H. M. Kutlu, V. T. Yilmaz and E. Ulukaya, *Bioorganic & medicinal chemistry*, 2013, **21**, 4698-4705.
67. J. Haribabu, M. M. Tamizh, C. Balachandran, Y. Arun, N. S. Bhuvanesh, A. Endo and R. Karvembu, *New J. Chem.*, 2018, **42**, 10818-10832.
68. R. Li, P. Zatloukalova, P. Muller, M. Gil-Mir, S. Kote, S. Wilkinson, A. J. Kemp, L. Hernychova, Y. Wang, K. L. Ball and K. Tao, *Cell. Mol. Biol. Lett.*, 2020, **25**, 1-21.
69. D. D. Fang, Q. Tang, Y. Kong, Q. Wang, J. Gu, X. Fang, P. Zou, T. Rong, J. Wang, D. Yang and Y. Zhai, *J. Immunother. Cancer*., 2019, **7**, 1-16.
70. Z. Cao, N. Kon, Y. Liu, W. Xu, J. Wen, H. Yao, M. Zhang, Z. Wu, X. Yan, W. G. Zhu and W. Gu, *Sci. Adv.*, 2021, **7**, 4148.
71. N. Sanchez, M. Gallagher, N. Lao, C. Gallagher, C. Clarke, P. Doolan, S. Aherne, A. Blanco, P. Meleady, M. Clynes and N. Barron, *PloS one*, 2013, **8**, 65671.
72. A. B. Niculescu III, X. Chen, M. Smeets, L. Hengst, C. Prives and S. I. Reed, *Mol. Cell. Biol.*, 1998, **18**, 629-643.
73. O. Kacar, B. Cevatemre, I. Hatipoglu, N. Arda, E. Ulukaya, V. T. Yilmaz and C. Acilan, *Bioorg. Med. Chem.*, 2017, **25**, 1770-1777.

CHAPTER-IV

Development of Anticancer Activity of Morpholine Based Pd(II) and Pt(II) Complexes: Synthesis, Characterization, DNA/BSA Binding and Biological Evaluation

Abstract

In the hunt for prospective new metal-based anticancer drugs, two novel morpholine-based Pd(II) and Pt(II) complexes, [Pd(**MPMA**)Cl_2] (**1**) and [Pt(**MPMA**)Cl_2] (**2**), with N,N′ donor ligand (**MPMA**), are synthesized and comprehensively studied using spectroscopic techniques. Single crystal X-ray diffraction examination revealed the deformed square planar geometry of the complexes' crystal formations. To strengthen and validate the experimental results, a theoretical method based on optimization structures, the HOMO-LUMO energy gap, global reactivity parameters, and time-dependent density functional theory was used. The DNA binding properties of the complexes are explored by employing UV-vis, fluorescence spectral methods and also viscosity measurements which indicate that these complexes can bind to DNA covalently and non-covalently. Furthermore, the complexes' interactions with bovine serum albumin (BSA) were examined using a range of spectroscopic techniques. The changes in the microenvironmental and structural properties of BSA are monitored by a synchronous and 3D fluorescence study. The anticancer potential of these complexes was studied preliminarily by using MTT assay against triple negative breast cancer cell line (MDA-MB-231) and normal kidney cell line (HEK-293). Complex **2**, compared to complex **1**, was found to be more efficient and highly toxic toward MDA-MB-231 cancer cells.

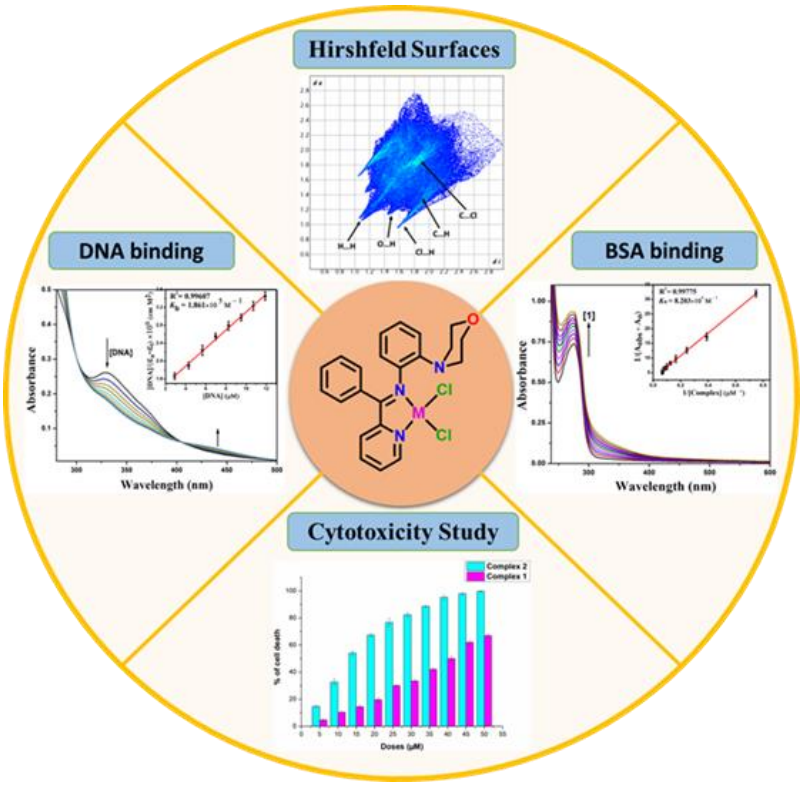

IV.1. Introduction

Inorganic medicinal chemistry is a discipline of inducing importance in both therapeutic and diagnostic medicine.[1] The innovation and advancement of the anti-tumour drugs based on platinum metal posed a major role in the area of inorganic medicinal chemistry.[2] Among these drugs, Cisplatin is one of the most effective chemotherapy drugs that is vastly utilized for cancer treatment.[3,4] Although it is clinically successful for the treatment of certain tumors, it has countless unpleasant side effects such asnausea, neurotoxicity, ototoxicity, nephrontoxi-city, tumor resistance.[5] These drawbacks have motivated the fabrication of better platinum based anticancer drugs whose structure and mode of action vary from that of cisplatin. Thus, a significant number of diverse platinum complexes were fabricated with the intend to overcome the shortcomings of cisplatin.[6-9]

Furthermore, there is a budding curiosity in the search for novel non-platinum metal based compounds for use in cancer treatment.[10] Recently, Pd(II) complexes have been investigated thoroughly enough as a substitute to Pt(II) complexes as anticancer agents owing to their comparable coordination geometry and chemistry. So the design and fabrication of new palladium based anti-cancer drugs is very essential for effective and capable application as chemotherapic agents.[11-14] Even though Pt(II) and Pd(II) complexes have analogous chemical properties, the latter is much more labile towards aquation, resulting in very reactive species that are incapable of reaching their target biomolecules in the cancer cells.[15] In order to surmount this, the use of strongly coordinated nitrogen ligands and the appropriate leaving groups has been explored to acquire less reactive Pd(II) complexes with capable anticancer activity.[16]

The coordinated ligands play a noteworthy part in anticancer activity of metal containing antitumor drugs as they can regulate key parameters like reactivity and lipophilicity. Schiff bases are valuable chelating ligands for metal ions, resulting in complexes with different physical and chemical properties.[17] Thus, the metal complexes of Schiff bases have been broadly designed and studied for biomedical applications, such as antitumor, antibacterial, anti-inflammatory and antifungal activities.[18]

DNA is the major biological target for anticancer drugs while BSA performs as a carrier protein molecule in the blood stream for various compounds. So the design and fabrication of DNA targeting metal-based anticancer agents with probable cytotoxicity have attained significance in recent years.[19,20] Metal complexes including aromatic ligands are reported to demonstrate a dual-function mode of action, in which DNA binding takes place via both coordination with the metal centre, and non-covalent interaction such as intercalation

with the DNA base pairs, along with π-π aromatic interactions between the double helix and the aromatic components of the metal complex.[21,22] Further, some metal complexes with bulky ligands are displayed to act as DNA groove binders.[23]

Furthermore, the study on interaction of proteins with metal complex is very beneficial as it could offer information to analyse the therapeutic effectiveness and pharmacological response of drugs. Also, proteins are well-accepted as the main cellular target for antitumor drugs and the most carrier proteins in the blood stream are Human Serum Albumin (HSA). Bovine Serum Albumin (BSA) structure is homologous with HSA and due to its effortless and simple accessibility and low cost, BSA is the mostly useful in biochemical and biophysical studies.[24-26]

In this paper we have synthesized Pd(II) and Pt(II) complexes (Scheme IV.1) having general formula, [Pd(MPMA)Cl_2] (**1**) and [Pt(MPMA)Cl_2] (**2**) and characterized both of them by using various spectroscopic techniques like NMR, IR, Mass, UV-Vis as well as single crystal X-ray diffraction study. The structural optimization, calculated energy difference of HOMO-LUMO, calculated different reactivity descriptors and TD-DFT analysis were executed by the application of DFT study to acquire an insight into the electronic structure of the complexes about the reactivity and structural property. The investigation of the biological characteristics of these complexes have been carried out focusing on the binding properties with calf-thymus DNA (CT-DNA) and the affinity toward bovine serum albumin (BSA) investigated using UV-Vis and fluorescence spectroscopy. Finally, MTT assay has been used to evaluate the cytotoxic activity of the complexes against triple negative breast cancer cell line (MDA-MB-231) and normal kidney cell line (HEK-293). The Pd(II) and Pt(II) complexes to induce apoptosis of tumor cell (MDA-MB-231) were tested by flow cytometric analysis of Annexin V-FITC/PI double staining assay.

IV.2. Experimental

IV.2.1. Materials and methods

2-benzoylpyridine, 2-morpholinoaniline, $Na_2[PdCl_4]$ and $Pt(SEt_2)_2Cl_2$ were purchased from Sigma-Aldrich. Solvents were available from commercial sources and used without further purification. Tri(hydroxylmethyl)aminomethane (Tris-HCl), Ethidium bromide (EB), calf thymus DNA(CT-DNA) and bovine serum albumin (BSA) were obtained from Sigma Aldrich chemical company.

Elemental analyses (C, H, N) were performed on a 2400 Series-II CHN analyzer, Perkin Elmer, USA. Waters (Xevo G2 Q-TOF) mass spectrometer was used to record mass

spectra of the ligand and complexes. IR spectra were run as KBr pellets on a RX-1 PerkinElmer spectrometer in the 4000–400 cm^{-1} region. ^{1}H-NMR spectra of ligand and complexes were recorded in $CDCl_3$ with TMS as the internal standard on a Bruker (AC) 300 MHz FT-NMR spectrometer. PerkinElmer Lambda 750 spectrophotometer was used for study the binding interactions of complexes with CT-DNA and BSA. The emission spectra were recorded by using Shimadzu RF-6000 fluorescence spectrophotometer at room temperature (298 K). Viscometric measurements were performed using an Ostwald viscometer placing it in a thermostated water bath at 25^0C and flow time was measured with a digital stopwatch. Circular dichroism (CD) studies were made on a JASCO spectropolarimeter (model J815, Jasco International Co., Japan) equipped with a thermalprogrammer (model PFD-425L/15) and temperature controller using a 1cm path length rectangular quartz cuvette.

IV.2.2. Preparation of ligand and complexes

IV.2.2.1. Synthesis of the ligand (MPMA)

2-benzoylpyridine (0.031 g, 0.169 mmol) and 2-morpholinoaniline (0.03g, 0.169 mmol) were mixed in 20 mL acetonitrile and then stirred and refluxed for 4h. The reaction mixture was then cooled and was used for complex formation reactions. Yield 0.055 g (95%).

Anal. Calc. for $C_{22}H_{21}N_3O$: C, 76.94; H, 6.16; N, 12.24; O, 4.66. Found: C, 76.72; H, 6.01; N, 12.24; O, 4.47. IR (KBr, cm^{-1}): 3061, 2963, 2901 υ(C-H); 1661 υ(C=N). ^{1}H NMR (300 MHz, $CDCl_3$): δ (ppm) 8.75 (d, J=6.4 Hz, 1H), 8.11-8.05 (m, 3H), 7.95-7.90 (m, 1H), 7.65-7.48 (m, 4H), 7.04-6.94 (m, 2H), 6.80-6.75 (m, 2H), 3.87 (t, J=4.6Hz, 4H), 2.94 (t, J=4.6Hz, 4H). HRMS: calculated for $C_{22}H_{21}N_3O$ $[M+H]^+$ (m/z): 344.1763; found: 344.1912.

IV.2.2.2. Synthesis of Pd(II) complex, [Pd(MPMA)Cl_2] (1)

An acetonitrile solution (10ml) of $Na_2[PdCl_4]$ (0.049 g, 0.169mmol) was slowly added to the Schiff base ligand MPMA (0.058 g, 0.169 mmol) in 10ml acetonitrile and refluxed for 6h. The color of the solution changed to orange. The solvent was slowly evaporated to dryness and the obtained residue was washed with diethylether to yield an orange solid [Pd(MPMA)Cl_2]. The complex was recrystallized by slow diffusion of n-hexane into saturated solution of the complex in dichloromethane. The yield was, 0.076 g, 86%.

Anal. Calc. for $C_{22}H_{21}Cl_2N_3OPd$: C, 50.74; H, 4.06; N, 8.07. Found: C, 50.57; H, 3.89; N, 7.93. IR (KBr, cm^{-1}): 3066, 2990, 2942 υ(C-H); 1593 υ(C=N). ^{1}H NMR (300 MHz, $CDCl_3$): δ (ppm) 9.66 (d, J=6.6 Hz, 1H), 8.12-8.06 (m,1H), 7.83-7.78 (m, 1H), 7.52-7.39 (m, 6H), 7.16-7.10 (m, 2H), 7.08 (d, J=7.4Hz, 1H), 6.96-6.75 (m, 1H), 3.78-3.73 (m, 6H), 2.38-

2.32 (m, 2H). HRMS: calculated for $C_{22}H_{21}Cl_2N_3OPd$ $[M-Cl]^+$ (m/z): 484.0408; found: 484.0493.

IV.2.2.3. Synthesis of Pt(II) complex, [Pt(MPMA)Cl_2] (2)

The complex **2** was prepared by the same procedure as used for complex 1, with $Pt(SEt_2)_2Cl_2$ (0.075 g, 0.169mmol) and MPMA (0.058 g, 0.169mmol). The yield was, 0.086 g, 83%.

Anal. Calc. for $C_{22}H_{21}Cl_2N_3OPt$: C, 43.36; H, 3.47; N, 6.90. Found: C, 43.18; H, 3.37; N, 6.85. IR (KBr, cm^{-1}): 3053, 2984, 2950 υ(C-H); 1597 υ(C=N). ^1H NMR (300 MHz, $CDCl_3$): δ (ppm) 10.08 (d, J=6.6 Hz, 1H), 8.19-8.13 (m,1H), 7.87-7.82 (m, 1H), 7.56-7.37 (m, 6H), 7.19-7.15 (m, 2H), 6.93 (d, J=7.9Hz, 1H), 6.81-6.78 (m, 1H), 3.72-3.62 (m, 6H), 2.30-2.24 (m, 2H). HRMS: calculated for $C_{22}H_{21}Cl_2N_3OPt$ $[M-Cl]^+$ (m/z): 573.1021; found: 573.1051.

IV.2.3. Single crystal X-ray diffraction studies

Single crystal data of complex **1** and **2** were collected at 293K on an automated Bruker AXS D8 Quest CMOS diffractometer using graphite monochromated Mo-Kα (λ=0.71073Å) radiation by the ω scan method. The structures were solved by direct method using the SHELX-2016 and refined by full-matrix least-squares methods on F^2. All the data were adjusted for Lorentz and polarization effects and multi-scan absorption corrections were applied using SHELXTL program package.[27] All non-hydrogen atoms were refined with anisotropic thermal parameters. The hydrogen atoms bound to carbon were placed in idealized positions and were set riding on the parent atom.

IV.2.4. Computational method

All geometry optimization and energy computations were performed using density functional theory (DFT) with the B3LYP level of theory.[28] LanL2DZ[29] basis set with effective core potential was employed for Pd and Pt atoms while for the other elements the basis set 6-31G(d)[30] were considered for calculations. The vibrational frequency calculations were performed to ensure that the optimized geometries represented the local minimum on the potential energy surface and there were only positive Eigen values. Gaussian09 program package[31] was employed to visualize geometry optimized structures and to calculate the minimum energy structure. The calculated electronic density contour plots for frontier molecular orbitals were plotted by using the GaussView, Version 5 visualization program. Solvent effects play an important role in the electronic structure of the complexes. On the

basis of the optimized ground state geometries, the absorption spectra in DMSO were calculated by time-dependent density functional theory (TD-DFT)[32] using the conductor-like polarizable continuum model (CPCM).[33] The fractional contributions of various groups to each molecular orbital were calculated using GaussSum.[34]

IV.2.5. Hirshfeld Surface Analysis

In order to visualize the intermolecular interactions, prevailing in the crystal, Molecular Hirshfeld surfaces (HS)[35] and the associated 2D-fingerprint[36] plots of complex **1** and **2** were calculated using Crystal Explorer 17.5 software.[37] Bond lengths to hydrogen atoms were automatically set to standard values, while the structural input CIF. files of the crystals **1** and **2** were read into the software for calculations. For each point on the Hirshfeld isosurface, two distances *d*e, the distance from the point to the nearest nucleus external to the surface and *d*i, the distance to the nearest nucleus internal to the surface, are defined. The normalized contact distance (d_{norm}) based on *d*e and di is given by following equation (Eq. IV.1).

$$d_{norm} = \frac{(d_i - r_i^{vdw})}{r_i^{vdw}} + \frac{(d_e - r_e^{vdw})}{r_e^{vdw}} \qquad \text{(Eq. IV.1)}$$

where, r_i^{vdw} and r_e^{vdw} are the van der Waals radii of the atoms. The value of d_{norm} is negative or positive depending on intermolecular contacts being shorter or longer than the van der Waals separations.

Graphical plots of the molecular Hirshfeld surfaces mapped with d_{norm} uses a red-white-blue colour scheme, where bright red spots highlight shorter contacts, white areas represent contacts around the van der Waals separation, and blue regions are devoid of close contacts. To visualize the molecular moiety, transparent mapped surfaces are usually shown. For a given crystal structure and set of spherical atomic electron densities, the Hirshfeld surface is unique and thus it suggests the possibility of gaining additional insight into the intermolecular interaction of molecular crystals. 2D Fingerprint plot resolved into different contacts contributed to the total Hirshfeld surface area of the complex **1** and complex **2**.

IV.2.6. DNA binding studies

IV.2.6.1. Absorption spectroscopic studies

The DNA binding ability of complex **1** and **2** has been evaluated by absorption as well as emission spectroscopy. The interaction of the complex with CT-DNA was performed by using Tris-HCl buffer solution having pH 7.2. The concentration of CT-DNA was determined

from its absorption intensity at 260nm by employing an extinction coefficient of 6600 $M^{-1}cm^{-1}$. [38] The UV absorbance at 260 and 280 nm of the CT-DNA solution gave a ratio in the range of 1.8 to 1.9, indicating that the DNA was satisfactorily free from protein molecules. The absorption spectra of the complexes at a constant concentration were recorded in presence of different concentrations of CT-DNA and a noteworthy change in absorption values was observed.

IV.2.6.2. Ethidium bromide displacement experiments

The competitive binding interactions of the complexes were investigated by fluorescence spectroscopy method in order to find out whether the compound can displace EB from its CT-DNA-EB system. The CT-DNA-EB complex was initially prepared by adding 15 μM EB and 30 μM CT-DNA in Tris– HCl/NaCl buffer solution (pH = 7.4). Ethidium bromide (EB) displacement experiments were done by successive addition of the complexes into the Tris-HCl buffer solution of CT-DNA-EB complex.[39] After successive addition of the metal complexes, the change in fluorescence intensity at 612 nm were monitored (excitation wavelength 540 nm).

IV.2.6.3. DNA viscosity measurements

The viscosity of the CT-DNA solutions (32.5μM) was measured in the presence of increasing amounts of the complexes using an Ostwald viscometer placing it in a thermostated water bath at 25.0 °C. Flow time was measured with a digital stopwatch and each sample was measured three times, then the average flow time was calculated. Viscosity values were calculated from the observed flow time of DNA-containing solutions (t) corrected for the flow time of buffer alone (t_0), $\eta = (t - t_0)/ t_0$. The data is reported as $(\eta / \eta_0)^{1/3}$ versus the ratio of the concentration of the complex to CT-DNA (R = [compound]/[CT-DNA]), where η is the viscosity of CT-DNA in the presence of the compound and η_0 is the viscosity of CT-DNA solution alone.[40]

IV.2.7.1. Protein binding studies

BSA (bovine serum albumin) is the most abundant plasma protein present in the circulatory system, which plays a vital role for the distribution and transportation of metal ions, hormones, nutrients, and drug molecules to the specific organs or tissues in the body.[41] The binding ability of complexes with BSA was performed with the help of UV-Vis spectroscopic titration and fluorescence emission quenching methods. The BSA stock solution was

prepared using 500 mM phosphate buffer saline (PBS) at pH 7.4 and stored in the dark at 4°C for further use. The concentration of BSA was measured by taking absorbance at 280 nm in UV-Vis spectra (molar extinction coefficient 66,400 M^{-1} cm^{-1}).[42] The stock solution of complexes was prepared in DMSO medium. The absorption spectra of BSA (10 μM) were recorded after gradual addition of complexes at room temperature for calculation of binding constants and binding modes. In fluorescence experiment, tryptophan fluorescence of BSA was recorded in the range 290-450 nm at an excitation wavelength of 280 nm using a slit width of 5 nm. Quenching of emission intensity at ~336 nm for BSA was monitored with subsequent addition of metal complex. The synchronous fluorescence spectra were also captured in the same instrument in the range of 270-380 nm by scanning the excitation and emission monochromators simultaneously. Different wavelength interval ($\Delta\lambda = \lambda_{em} - \lambda_{ex}$) of $\Delta\lambda$ = 15 nm and $\Delta\lambda$ = 60 nm were set to study the spectrum behavior of tyrosine (Tyr) and tryptophan (Trp) residues of BSA. 3D fluorescence spectroscopy is used to know about the fluorescence of chromophore and also the conformational changes of protein macromolecules by measuring the change of fluorescence intensity in the presence of complexes. The 3D fluorescence spectra of BSA (6 μM) with and without the complex **1** and **2** were recorded in the wavelength range of 200-400 nm for excitation and 200-500 nm for emission.

IV.2.7.2. Circular dichroism measurements

Circular dichroism (CD) spectra were obtained employing JASCO (J-815) spectropolarimeter at 298 K using a quartz cuvette of 1 cm cell path length. The spectra were recorded in far UV region (200–245 nm) for BSA in presence and absence of copper complexes **1** and **2**. Concentration of BSA was kept constant at 1 μM while varying the concentration of added complexes **1** and **2**. The CD results were expressed in terms of the mean residual ellipticity (MRE) in deg cm^2 $dmol^{-1}$ according to the following equation (Eq. IV.2).[43]

$$MRE = \frac{Observed\ CD\ (mdeg)}{10 C_p n l} \qquad \text{(Eq. IV.2)}$$

Here, C_p represents the molar concentration of the protein, n stands for the number of amino acid residues (583 for BSA) and l is the path length of the cell (1 cm). The α-helical (%) contents of the free and bound BSA were calculated from the mean MRE values at 208 nm using the following equation (Eq. IV.3).[44]

$$\alpha - helix\ (\%) = \frac{[-MRE_{208} - 4000]}{[33000 - 4000]} \times 100 \qquad \text{(Eq. IV.3)}$$

MRE_{208} is the MRE value observed at 208 nm, 4000 is the MRE of the β-form and random coil conformation at 208 nm, and 33000 is the MRE value of a pure α-helix at 208 nm.

IV.2.7.3. Förster Resonance Energy Transfer (FRET)

The value of R_0 was calculated using the following equation (Eq. IV.4).

$$R_0 = 0.2018\left\{[K^2\Phi_D\eta^{-4}J(\lambda)]^{1/6}\right\}\text{Å} \qquad \text{(Eq. IV.4)}$$

where the orientation factor between the emission dipole of the donor and the absorption dipole of the acceptor κ^2 is taken as 2/3, the fluorescence quantum yield of the donor ϕ_D is 0.118, the refractive index of the medium (η) is 1.33, and $J(\lambda)$ is the extent of spectral overlap of donor (BSA) emission and the acceptor (complex) absorption spectra.[45] The value of $J(\lambda)$ can be calculated using the equation (Eq. IV.5).[46]

$$J(\lambda) = \int_0^\infty \bar{I}_D(\lambda)\varepsilon_A(\lambda)\lambda^4 d\lambda \quad M^{-1}cm^{-1}nm^4 \qquad \text{(Eq. IV.5)}$$

Where, $\bar{I}_D(\lambda)$ denotes the normalized fluorescence emission of the donor BSA at the wavelength λ, and $\varepsilon_A(\lambda)$ represents the molar extinction coefficient of the acceptor metal complex at the wavelength λ.

IV.2.8. Biological Studies

IV.2.8.1. Cell Culture

The MDA-MB-231 cell line, derived from human triple-negative breast cancer, was obtained from ATCC (American Type Culture Collection) in Manassas, USA. The cells were cultured in DMEM (Dulbecco's Modified Eagle Medium) supplemented with 10% heat-inactivated fetal bovine serum (FBS) from GibcoTM, USA, and 1% Pen-Strep (penicillin-streptomycin) from GibcoTM, USA. The culture was maintained in a 37°C incubator with 5% CO2.When the cells reached 75-80% confluence, they were harvested using a PBS-based solution containing 0.25% trypsin and 0.52 mM EDTA. This trypsin-EDTA solution facilitates detachment of the cells from the culture dish. Subsequently, the cells were seeded at the desired density and allowed to re-equilibrate for one day before initiating the experiment. This procedure ensures that the cells are in an optimal state for experimentation by maintaining their growth phase and overall viability.

IV.2.8.2. Cytotoxicity assay

To assess cell viability, an MTT assay was performed.[47] For the initial screening experiment, MDA-MB-231 cells were seeded at a density of 10,000 cells per well in a 96-well plate and incubated. Afterward, the cells were treated with varying concentrations of the complex (0, 5, 10, 15, 20, 25, 30, 35, 40, 45, and 50 μM) for 24 hours. Following the 24-hour treatment period, the cells were washed with PBS. Subsequently, an MTT solution from Sigma Aldrich, USA, was added to each well, and the plate was placed in an incubator for 4 hours to allow the formation of formazan salt. After incubation, the formazan salt was dissolved using DMSO, and the absorbance was measured at 595 nm using an ELISA reader (Emax, Molecular Devices, USA). Cell proliferation was determined based on the intensity of absorbance. Cell viability was calculated using the formula:

$$\text{Cell viability (\%)} = (OD_{control} - OD_{sample}) / OD_{control} \times 100.$$

Here, $OD_{control}$ represents the absorbance of untreated cells, and OD_{sample} represents the absorbance of treated cells. The experiments were conducted multiple times to ensure reliable results.

IV.2.8.3. Quantification of Apoptosis Using Flow Cytometry

To analyze apoptosis and necrosis, flow cytometry was employed using the Dead Cell Apoptosis Kits with Annexin V from Invitrogen™, USA.[48] Treated cells at a concentration of 1×10^6 were harvested and stained with Annexin-V-FITC for 30 minutes, along with propidium iodide (PI), following the manufacturer's instructions. Flow cytometry analysis was performed using a BD LSRFortessa instrument located in San Jose, CA, USA. The percentages of viable cells, as well as apoptotic (early and late) and necrotic cells, were determined based on the staining patterns obtained. These experiments were conducted multiple times to ensure the reliability and consistency of the results.

IV.2.8.4. Measurement of Mitochondrial Membrane Potential Using Flow Cytometry

After the treatment, the cells were incubated with JC-1, a cationic carbocyanine dye (5,5′,6,6′-tetrachloro-1,1′,3,3′-tetraethylbenzimidazolylcarbocyanine iodide) from Invitrogen™, USA. The incubation was performed according to the manufacturer's instructions. JC-1 is known for its potential-dependent accumulation in mitochondria and its ability to exhibit a fluorescence emission shift from green (525 nm) to red (590 nm).

Following the incubation period, flow cytometry analysis was conducted to assess the cells based on the fluorescence of JC-1. The fluorescence change allows for the determination of the percentage of hyperpolarized and depolarized mitochondria by evaluating the resultant fluorescence of JC-1 monomers and aggregates.[49] These experiments were conducted multiple times to ensure the reliability and reproducibility of the results.

IV.2.8.5. Determination of Intracellular ROS (iROS)

Mitochondria are known as the primary source of reactive oxygen species (ROS) accumulation in mammalian cells. ROS accumulation plays a crucial role in stimulating apoptosis in various cell types. In order to estimate intracellular ROS levels, the treated cells were incubated with 10 mM H2DCFH-DA (2′, 7′-dichlorofluorescein diacetate) from Invitrogen™, USA. This incubation was performed at 37 °C for 30 minutes prior to analysis using flow cytometry. Flow cytometry analysis was conducted using a BD LSR Fortessa instrument from Becton Dickinson, located in Franklin Lakes, NJ, USA.[50,51] The increment in DCF (dichlorofluorescein) fluorescence directly reflects the generation of ROS within the cells. The mean fluorescence intensity of DCF was used to represent the level of ROS generated. These experiments were repeated multiple times to ensure the accuracy and consistency of the results.

IV.2.8.6. Confocal Microscopy

Confocal microscopy was utilized to observe the expression of apoptotic markers including p53, p21, Caspase-3, Caspase-9, Cytochrome C, and BCL-2 in both control and treated MDA-MB-231 cells. The experimental procedure involved the following steps: The cells were washed twice with 0.01 M PBS (Phosphate Buffered Saline). Following the washes, the cells were fixed with a 4% Paraformaldehyde solution in PBS and incubated at room temperature for 15 minutes. A blocking solution containing 1% BSA (Bovine Serum Albumin) was then applied to the cells, and they were incubated for 1 hour. Subsequently, the cells were permeabilized with 0.3% Triton X-100 in PBS. After permeabilization, the cells were incubated overnight at 4 °C with specific primary antibodies targeting Caspase-3, Caspase-9, Cytochrome C, BCL-2, p53, and p21. These primary antibodies were obtained from CST, USA. The cells were then washed and incubated with secondary antibodies conjugated with fluorophores (anti-mouse/rabbit/goat Alexa Fluor-555, Alexa Fluor-647, and Alexa Fluor-488) obtained from CST, USA. This incubation lasted for 4 hours. Following the secondary antibody incubation, the cells were counterstained with DAPI (4',6-diamidino-2-

phenylindole) for 5 minutes and mounted using Fluorescent Mounting Media, Aqueous from Sigma, USA.[52,53] Confocal laser scanning microscopy (ZEISS LSM-980, Germany) was employed to visualize the stained cells, and the acquired images were analyzed using ZEN lite 3.4 Blue edition software. These experiments were conducted multiple times to ensure consistency and validity of the findings.

IV.3. Results and discussion

IV.3.1. Synthesis and formulation

A novel morpholine based ligand and its corresponding Pd(II) and Pt(II) complexes were synthesized as shown in scheme IV.1. The ligand (MPMA) was synthesized by standard Schiff base condensation reaction of 2-benzoylpyridine with 2-morpholinoaniline under refluxed for 4h. The Pd(II) complex, $[Pd(MPMA)Cl_2]$ (**1**) was synthesized by the reaction of ligand, MPMA with Na_2PdCl_4 in 1:1 molar ratio under refluxing condition in acetonitrile. Similarly, the Pt(II) complex, $[Pt(MPMA)Cl_2]$ (**2**) was synthesized by the reaction of $Pt(SEt_2)_2Cl_2$ with MPMA. The complexes were thoroughly characterized by several spectroscopic techniques such as IR, UV-Vis, ^{1}H NMR and ESI mass spectrometry. Their structures were confirmed by single crystal X-ray crystallography.

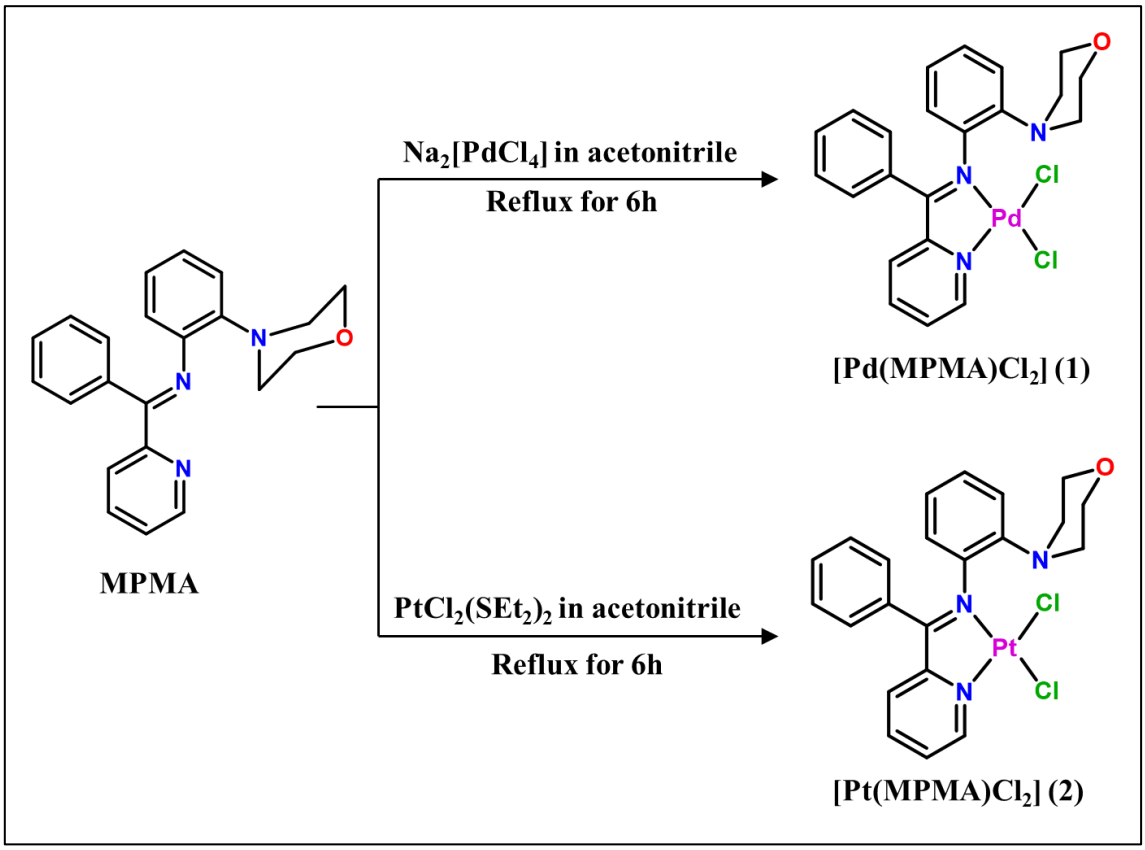

Scheme IV.1. Synthetic scheme for $[Pd(MPMA)Cl_2]$ (**1**) and $[Pt(MPMA)Cl_2]$ (**2**).

IV.3.2. Spectral characterization

The Fourier transform infrared (FT-IR) spectra provide promising indications regarding the involvement of coordination sites of the ligand in chelation with metal. The infrared spectrum of the Schiff base ligand (MPMA) exhibits a characteristic peak at 1661 cm^{-1} (Fig. IV.1), which was attributed to the imine (C=N) stretching vibrations. After complexation, a redshift occurred for the imine (C=N) stretching in chelated ligand (1593 cm^{-1} and 1597 cm^{-1} for complexes **1** and **2** respectively), suggesting the coordination of Schiff-N to the metal (Fig. IV.2).[54,55] The ^{1}H-NMR spectra of ligand and the complexes **1** and **2** were recorded in $CDCl_3$ and are shown in Fig. IV.3, Fig. IV.4 and Fig. IV.5 respectively. In ^{1}H-NMR spectra of complexes, the proton ortho to the coordinated pyridyl-N appeared as a doublet in the downfield region (δ 9.66-10.08 ppm) compared to the free ligand (δ 8.75 ppm), this downfield shift is because of the coordination of pyridyl-N to the metal.[55] This arises from an σ effect based on electron donation to metal ions via the pyridyl nitrogen lone pair and confirms the coordination of ligand to the metal ions through pyridyl-N. The others aromatic protons and aliphatic protons are observed in the complexes in the region of δ 8.19-6.75 ppm and δ 3.78-2.24 ppm respectively. Mass spectrum of $[Pd(MPMA)Cl_2]$ (**1**) shows m/z peak corresponding to $[M\text{-}Cl]^+$ at 484.0493 (Fig. IV.7) while $[Pt(MPMA)Cl_2]$ (**2**) exhibits m/z peak corresponds to $[M\text{-}Cl]^+$ at 573.1061 (Fig. IV.8).

The UV-Vis spectra of complexes **1** and **2** were obtained in DMSO in the range of 250-500nm (Fig. IV.9). The solution spectrum of complex **1** exhibit peak at 330 nm along with a shoulder at 372 nm. Absorption spectrum of complex **2** exhibit low energy peaks at 431 nm (with a shoulder band at 408 nm) along with a high energy band appeared at 359 nm.

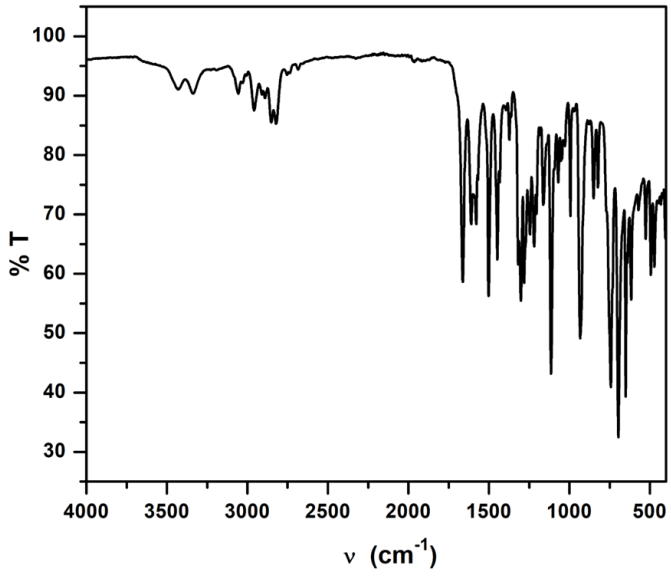

Fig. IV.1. IR spectrum of free ligand MPMA.

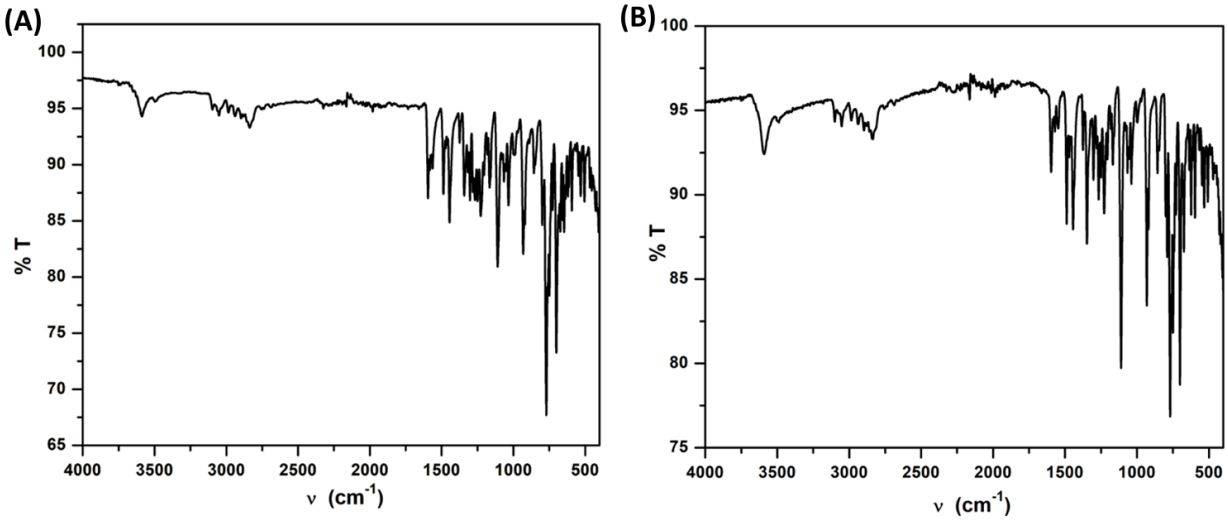

Fig. IV.2. IR spectrum of complex **1 (**A) and complex **2** (B).

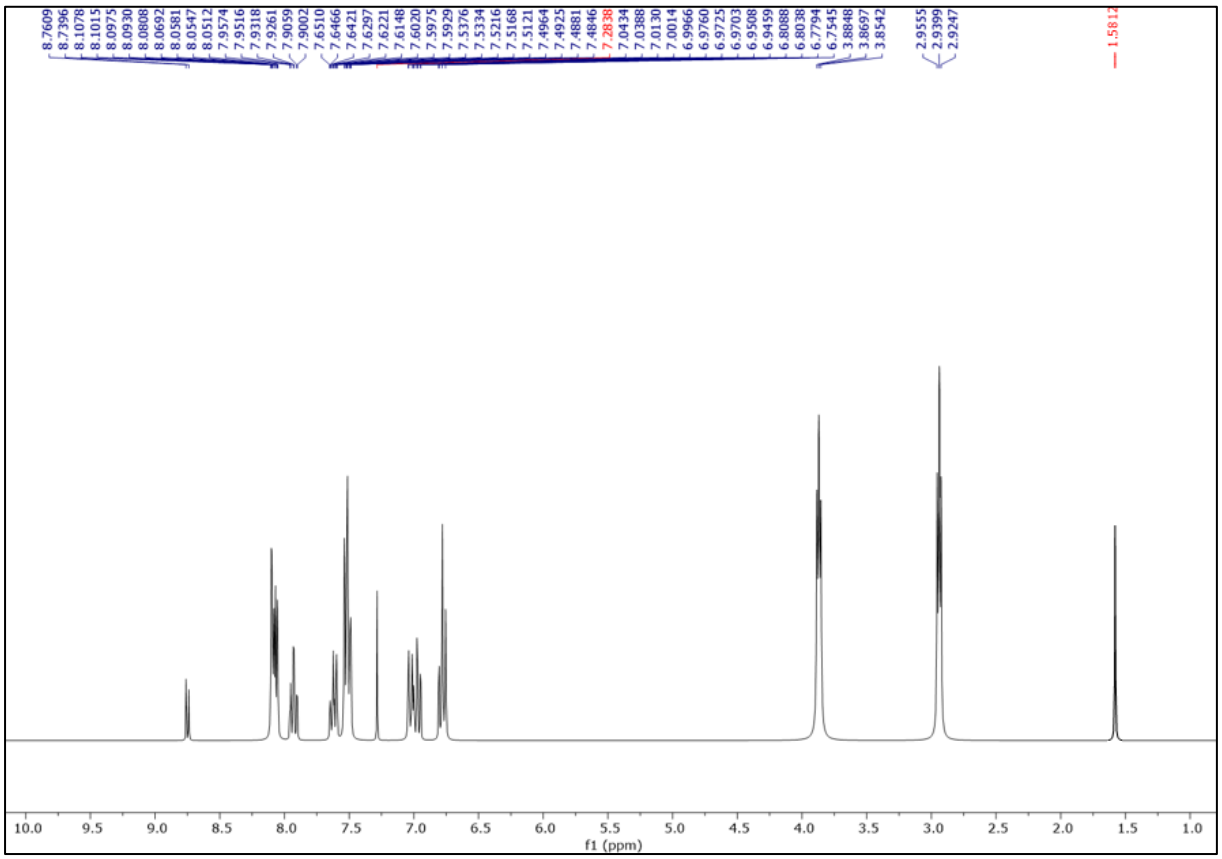

Fig. IV.3. ^{1}H-NMR spectrum of ligand MPMA in $CDCl_3$

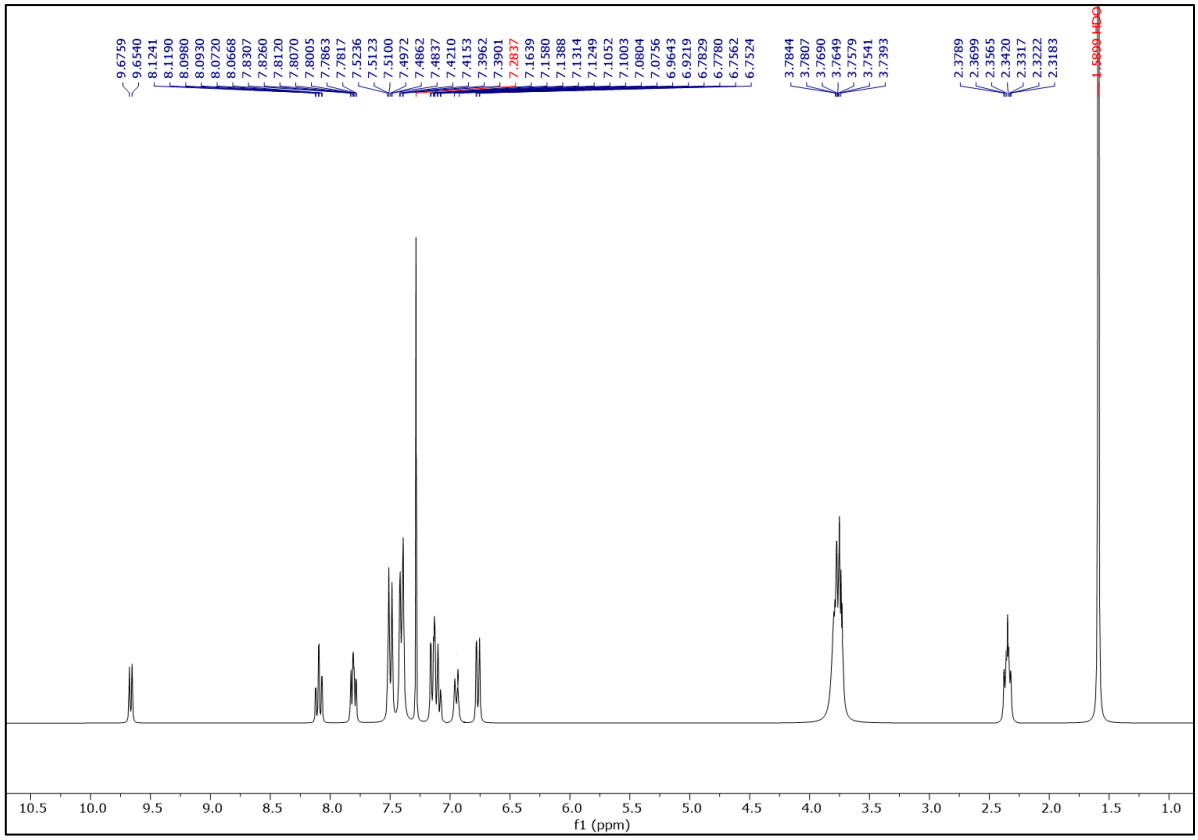

Fig. IV.4. ^{1}H-NMR spectrum of [Pd(MPMA)Cl_2] (**1**) in $CDCl_3$

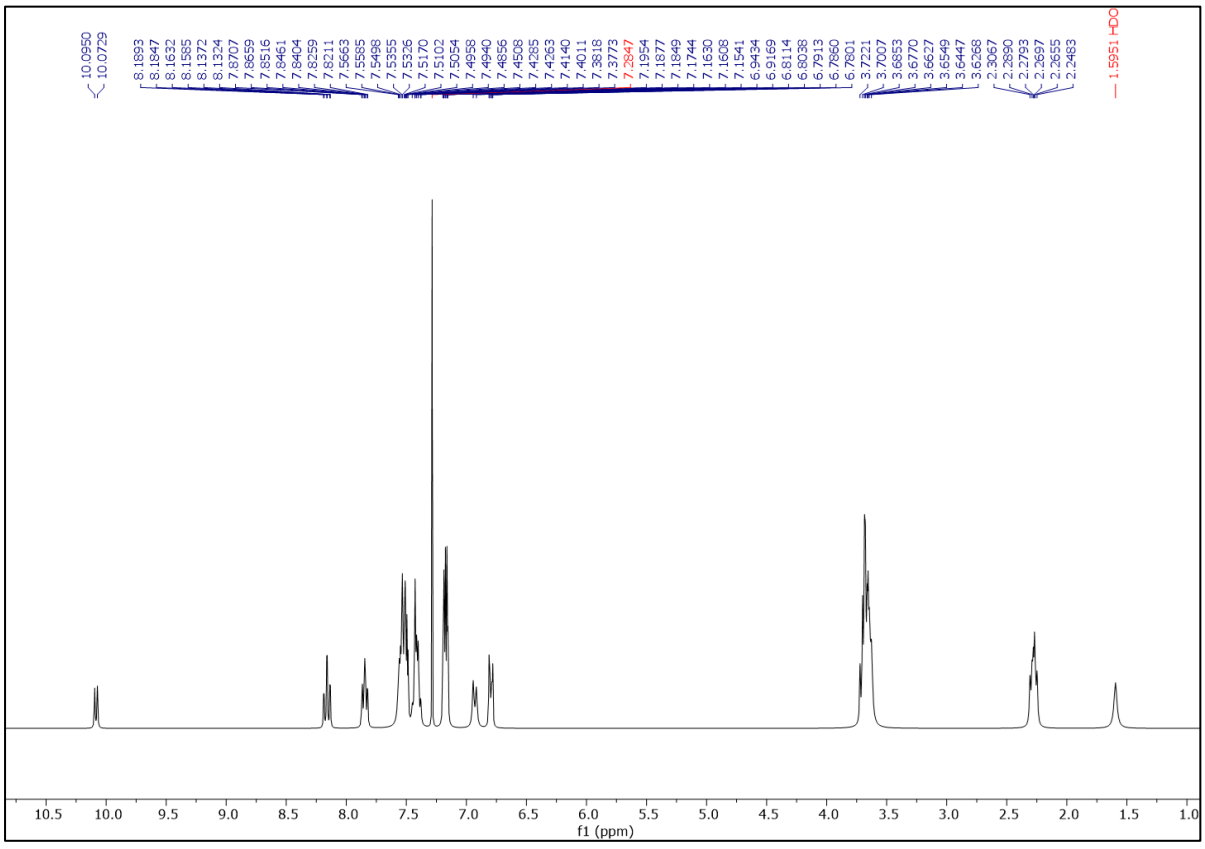

Fig. IV.5. ^{1}H-NMR spectrum of [Pt(MPMA)Cl_2] (**2**) in $CDCl_3$

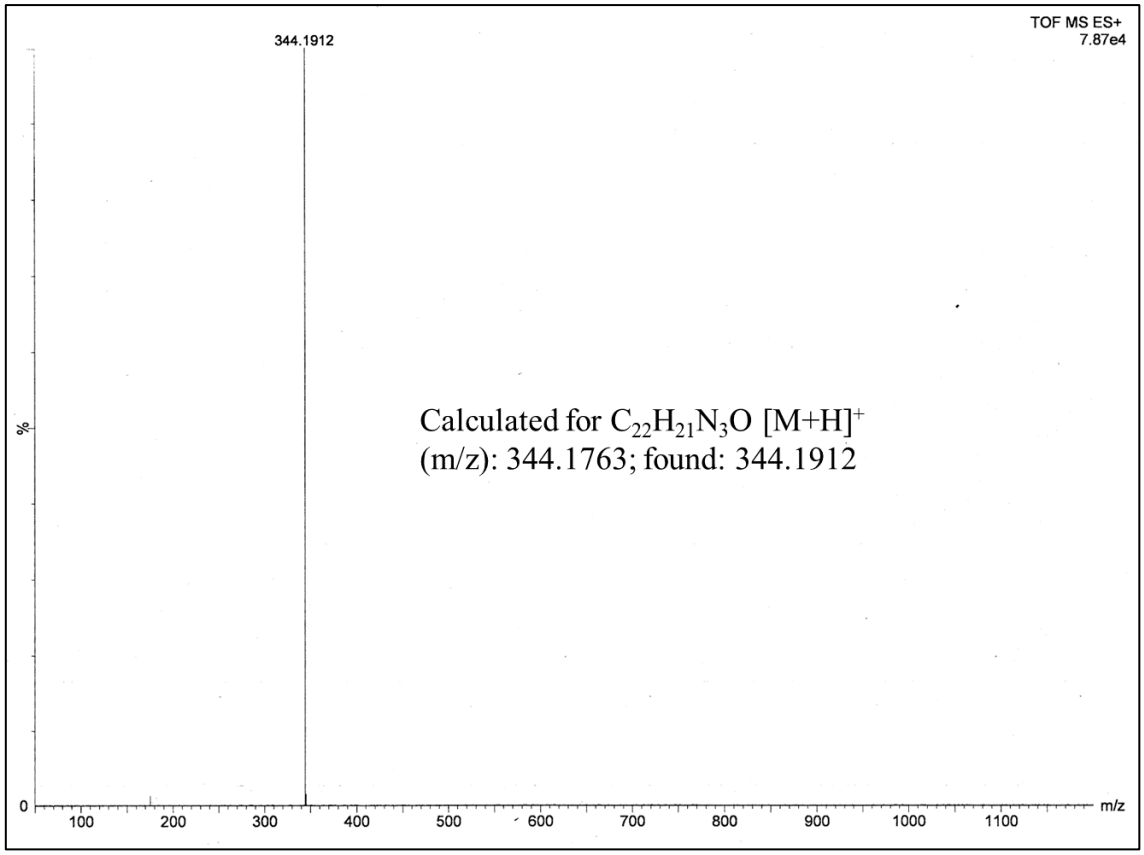

Fig. IV.6. HRMS spectrum of ligand (MPMA)

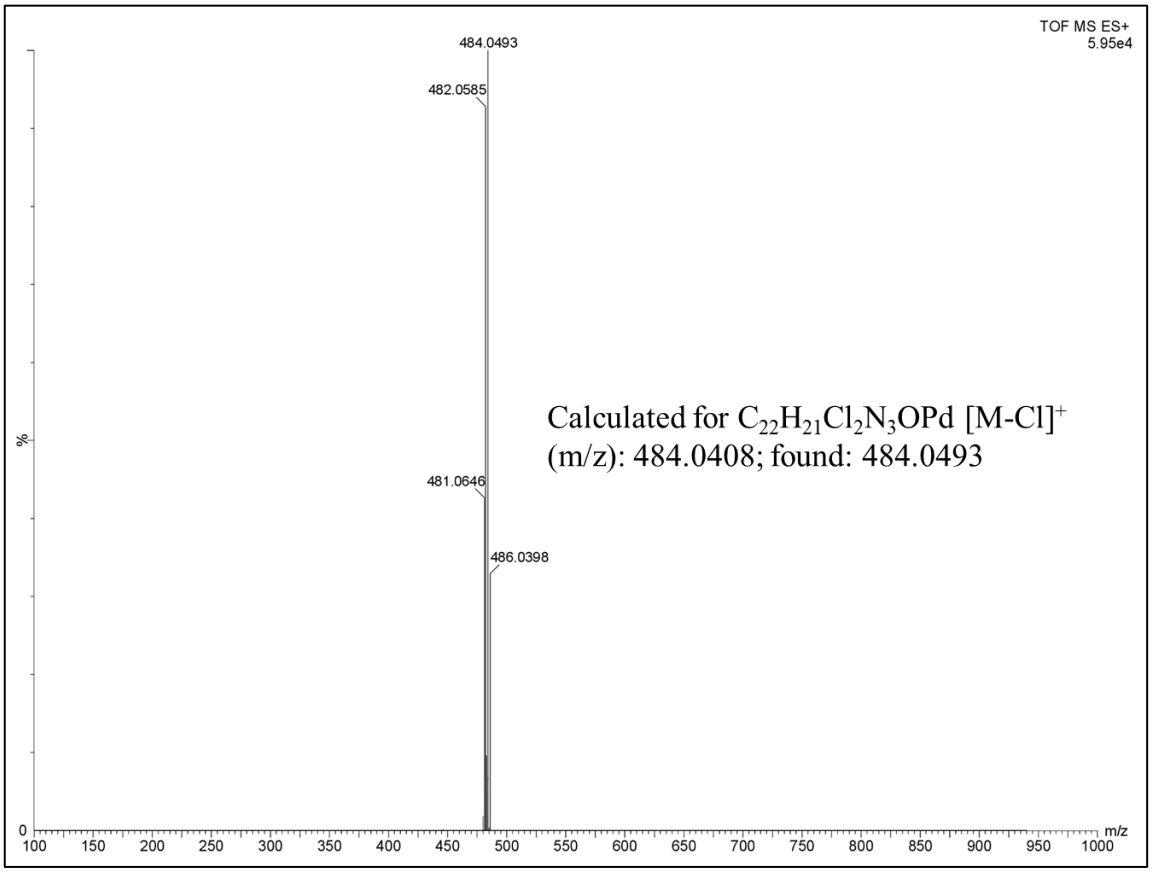

Fig. IV.7. HRMS spectrum of [Pd(MPMA)Cl_2] (**1**)

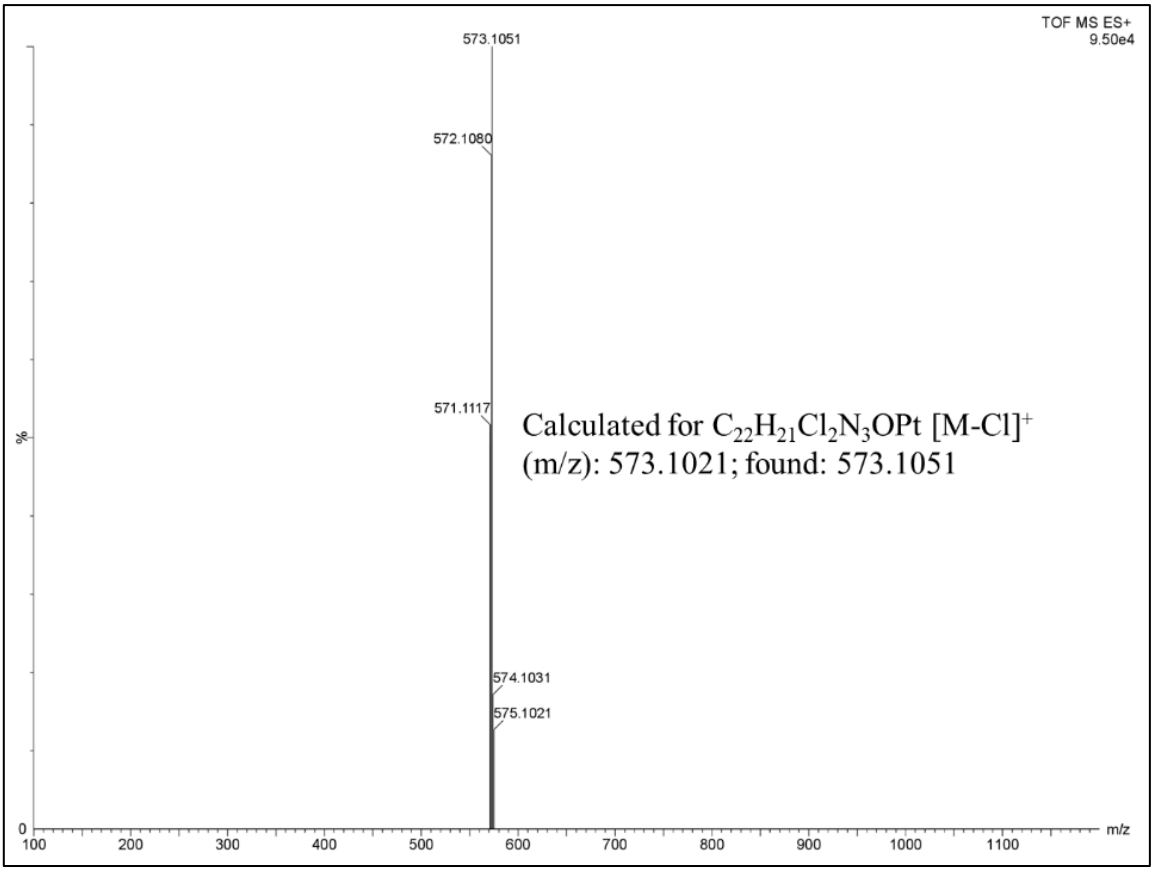

Fig. IV.8. HRMS spectrum of [Pt(MPMA)Cl_2] (**2**)

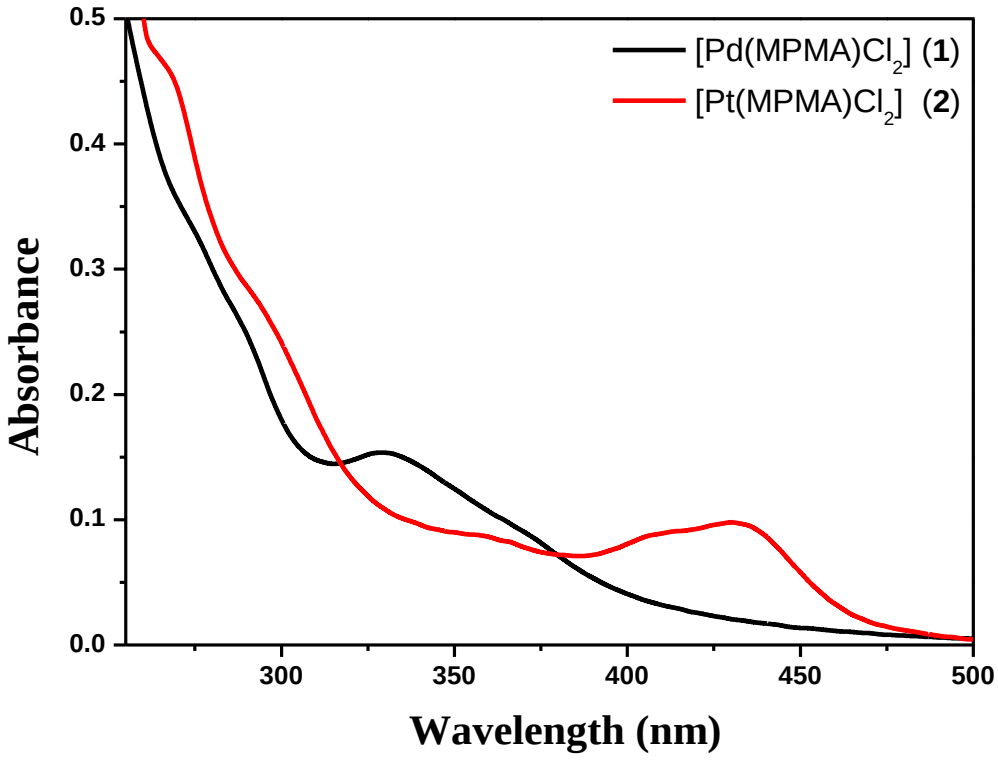

Fig. IV.9. UV-Vis spectra of [Pd(MPMA)Cl_2] (**1**) and [Pt(MPMA)Cl_2] (**2**)

IV.3.3. Crystallographic study

The molecular structures of complexes **1** and **2** have been determined by the single crystal X-ray diffraction method to predict the coordination mode of MPMA ligand. The X-ray crystal structure revealed that both the complexes are crystallized in a triclinic crystal system with the space group $\bar{P}1$. The ORTEP view along with the atomic numbering scheme of the complexes **1** and **2** are shown in Fig. IV.10. Relevant crystallographic data and details of structure refinements for the complexes are summarized in Table IV.1. Selected inter atomic bond lengths and bond angles are listed in Table IV.2. In complex **1**, the coordination geometry around Pd(II) ion can be described as distorted square planar, the Pd(II) ion was attached to the bidentate N, N donor MPMA in such a way that a five membered ring was formed and the remaining sites were occupied by two chlorine atoms originating from Na_2PdCl_4. The cis-angles N1-Pd1-N2, N1-Pd1-Cl2, N2-Pd1-Cl1 and Cl1-Pd1-Cl2 are found to be 80.13(8)^o, 95.43(6)^o, 94.31(6)^o and 90.13(3)^o respectively while the two trans-angles N1-Pd1-Cl1 and N2-Pd1-Cl2 are 174.43(6)^o and 175.23(6)^o respectively.

In complex **2** the coordination geometry of the Pt(II) ion was distorted square planar, composed of two nitrogen atoms from MPMA and two chlorine atoms originating from $Pt(SEt_2)_2Cl_2$. The cis-angles N1-Pt1-N2, N1-Pt1-Cl2, N2-Pt1-Cl1 and Cl1-Pt1-Cl2 are found to be 79.97(14)^o, 95.92(11)^o, 94.98(11)^o and 89.13(5)^o respectively while the two trans-angles N1-Pt1-Cl1 and N2-Pt1-Cl2 are 174.94(10)^o and 175.65(10)^o respectively. The cis and trans-angles are in significant deviation from their respective idealistic values of 90^o and 180^o, suggesting significant distortion in the square planar geometry of the two complexes. The Pt–N(pyridyl) bond length [Pt1-N1, 2.013(3) Å] is shorter compared to Pd–N(pyridyl) bond length [Pd1-N1, 2.0225(19) Å], indicating strong interaction of Pt(II) with pyridyl-N in complex **2**. Similarly, the Pt–N(imine) bond distance [Pt1-N2, 2.006(4) Å] in Complex **2** was significantly shorter compared to the Pd–N(imine) bond distance [Pd1-N2, 2.0263(19) Å] in Complex **1**. Moreover, the M–N(pyridyl) and M–N(imine) (M = Pd/Pt) bond distances are well corroborated with the reported values.[55,56] Pd1–Cl1 and Pd1–Cl2 bond distances are found to be 2.2726(7) Å and 2.2975(7) Å, respectively, in Complex **1**, while for the complex **2**, the Pt1–Cl1 and Pt1–Cl2 bond distance are found to be 2.2811(11) Å and 2.3033(13) Å, which is in good agreement with that reported for palladium and platinum complexes.[55,57]

Table IV.1. Crystallographic data and refinement parameters of complexes **1** and **2**

Complex	[Pd(MPMA)Cl_2]	[Pt(MPMA)Cl_2]
Formula	$C_{23}H_{23}Cl_4N_3OPd$	$C_{23}H_{23}Cl_4N_3OPt$
Formula Weight	605.64	694.33
Crystal System	*Triclinic*	*T1riclinic*
Space group	$P\bar{1}$	$P\bar{1}$
a, b, c [Å]	9.4749(7), 10.6338(8), 13.2782(10)	9.5037(12), 10.6433(13), 13.2099(16)
α [°]	78.000(2)	77.852(4)
β [°]	84.267(2)	84.384(3)
γ [°]	73.951(2)	74.300(3)
V [$Å^3$]	1256.32(16)	1256.3(3)
Z	2	2
D(calc) [g/cm^3]	1.601	1.835
Mu(MoKa)[mm^{-1}]	1.185	6.031
F(000)	608	672
Temperature (K)	293(2)	293(2)
Radiation [Å]	0.71073	0.71073
θ(Min-Max) [°]	2.029- 27.135	2.025- 27.184
Dataset (h; k; l)	-12 to 12, -13 to 13, -17 to 17	-12 to 12, -13 to 13, -16 to 16
R, wR_2	0.0294, 0.0592	0.0363, 0.0851
Goodness of fit(S)	1.062	1.096

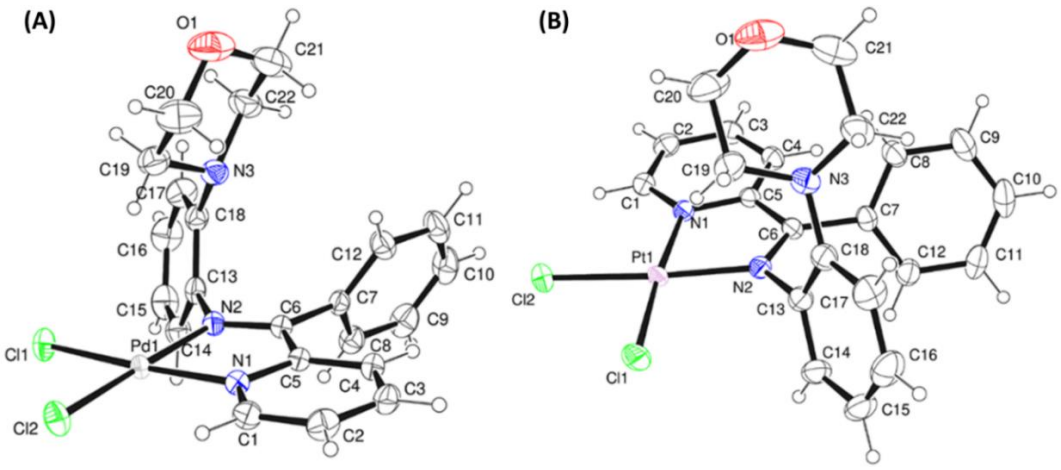

Fig. IV.10. ORTEP plot of complex **1** (A) and complex **2** (B) with 35% ellipsoidal probability.

Table IV.2. Selected X-ray and calculated bond distances and angles of complexes **1** and **2.**

[Pd(MPMA)Cl_2]			[Pt(MPMA)Cl_2]		
Bonds(Å)	X-ray	Calc.	Bonds(Å)	X-ray	Calc.
Pd1-N1	2.0225(19)	2.07252	Pt1-N1	2.013(3)	2.04977
Pd1-N2	2.0263(19)	2.08665	Pt1-N2	2.006(4)	2.05383
Pd1-Cl1	2.2726(7)	2.30283	Pt1-Cl1	2.2811(11)	2.32567
Pd1-Cl2	2.2975(7)	2.31596	Pt1-Cl2	2.3033(13)	2.33785
N1-C5	1.361(3)	1.36119	N1-C5	1.366(5)	1.36627
N2-C6	1.291(3)	1.30166	N2-C6	1.302(5)	1.30864
Angles (°)					
N1-Pd1-N2	80.13(8)	78.76130	N1-Pt1-N2	79.97(14)	78.92278
N1-Pd1-Cl1	174.43(6)	174.68931	N1-Pt1-Cl1	174.94(10)	175.36778
N2-Pd1-Cl1	94.31(6)	95.94466	N2-Pt1-Cl1	94.98(11)	96.44875
N1-Pd1-Cl2	95.43(6)	94.13484	N1-Pt1-Cl2	95.92(11)	94.66456
N2-Pd1-Cl2	175.23(6)	172.85590	N2-Pt1-Cl2	175.65(10)	173.57239
Cl1-Pd1-Cl2	90.13(3)	91.16416	Cl1-Pt1-Cl2	89.13(5)	89.96518

IV.3.4. DFT and TDDFT calculations

Density functional theory (DFT) study was utilized as a theoretical approach to perceive a proper idea about the structural properties of the molecules.[58] DFT calculation was implemented for the structural optimization, HOMO-LUMO energy calculation of the complexes, which are relevant for their structural, bonding mode and biochemical activity.[59] Calculated bond distances and bond angles of the complexes are summarized in Table IV.2, ESI†. The calculated geometric parameters are reasonably well reproducing the X-ray crystal structures data. Contour plots of selected molecular orbitals for both the complexes **1** and **2** are shown in Fig. IV.11. and Fig. IV.12. respectively. Energy and compositions of selected molecular orbitals are given in Table IV.3 and Table IV.4. The HOMO and LUMO energies were used to calculate global reactivity parameters such as ionisation potential (I), electron affinity (A), electronegativity (χ), chemical hardness (η), chemical potential (μ) and electrophilicity index (ω).[60] All the calculated reactivity parameters are listed in Table IV.5. The calculated energy gaps between the HOMO and LUMO are 2.78 eV and 2.74 eV for Complex **1** and **2** respectively. The calculated HOMO-LUMO energy gaps of the complexes are significantly smaller than the free ligand (Fig. IV.13), thereby suggesting that the complexes are kinetically more reactive towards receptor biomacromolecules like DNA and BSA compared to the free ligand.

The theoretical TD-DFT study is a convenient simulation technique which is used to correlate and equate the simulated absorbance properties of the complexes with the experimental UV-Vis spectrum.[61] The UV-Vis spectrum of the complex **1** shows an absorption band with λ_{max} at 330 nm which is very close to TD-DFT simulated peak at around 336 nm, corresponding to the HOMO-8 → LUMO transition (Fig. IV.14 A). The complex **2** exhibits the electronic spectrum with λ_{max} at 431 and 359 nm, which are very close to TD-DFT simulated peak positions 402 and 353 nm (Fig. IV.14 B). These peaks correspond to the HOMO-2 → LUMO transition and HOMO-8 → LUMO transition respectively. The corresponding energy of important peaks, the oscillator strength, and the major transition are listed in Table IV.6.

Table IV.3. Energy and % of composition of some selected molecular orbitals of complex **1.**

MO	Energy	% of composition		
		Pd	MPMA	Cl
LUMO+5	-0.27	02	98	00
LUMO+4	-0.89	01	99	00
LUMO+3	-1.15	02	97	01
LUMO+2	-1.81	02	98	00
LUMO+1	-2.11	46	24	30
LUMO	-3.1	05	93	01
HOMO	-5.88	05	84	11
HOMO-1	-6.02	23	15	62
HOMO-2	-6.11	15	07	79
HOMO-3	-6.31	31	10	59
HOMO-4	-6.36	14	05	81
HOMO-5	-6.6	75	14	11
HOMO-6	-6.85	08	81	11
HOMO-7	-7.01	02	96	02
HOMO-8	-7.5	02	98	01
HOMO-9	-7.68	21	63	16
HOMO-10	-7.7	01	98	02

Table IV.4. Energy and % of composition of some selected molecular orbitals of complex **2.**

MO	Energy	% of composition		
		Pt	MPMA	Cl
LUMO+5	-0.25	05	94	01
LUMO+4	-0.87	02	98	00
LUMO+3	-1.04	14	77	08
LUMO+2	-1.45	31	51	19
LUMO+1	-1.81	02	97	00
LUMO	-3.1	08	89	02
HOMO	-5.84	21	45	33
HOMO-1	-5.96	18	53	29
HOMO-2	-6.1	24	07	69
HOMO-3	-6.21	36	16	47
HOMO-4	-6.43	09	12	79
HOMO-5	-6.58	87	07	06
HOMO-6	-6.89	03	85	12
HOMO-7	-7.01	03	93	04
HOMO-8	-7.49	02	97	01
HOMO-9	-7.66	16	67	17
HOMO-10	-7.69	07	85	08

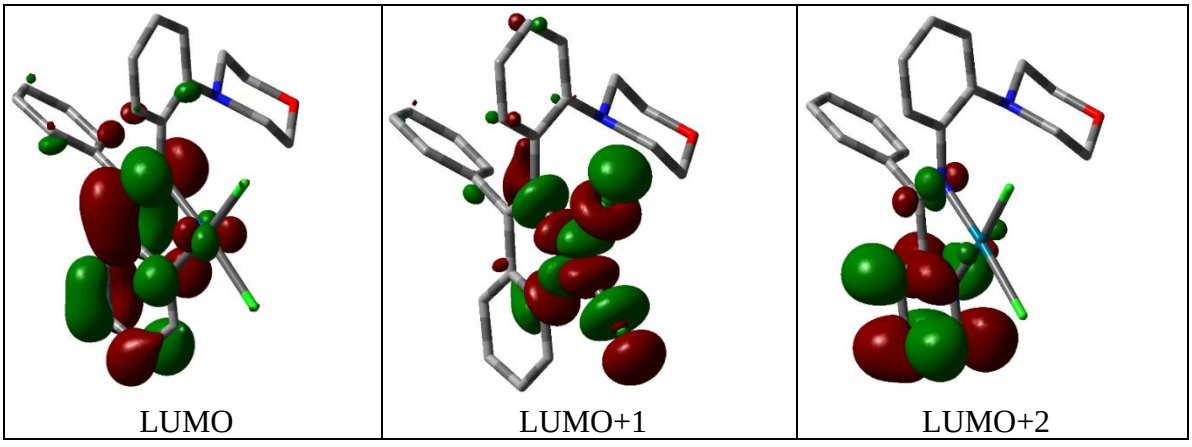

LUMO | LUMO+1 | LUMO+2

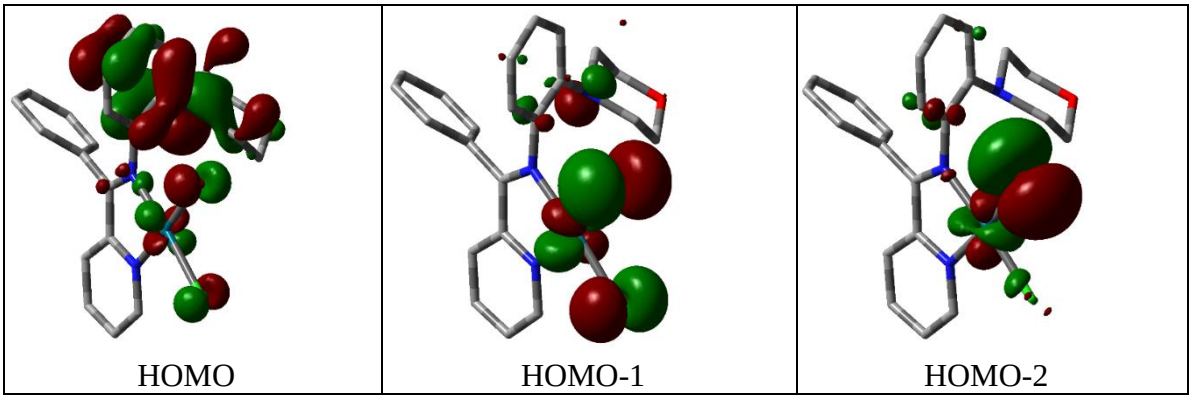

Fig. IV.11. Contour plots of some selected molecular orbital of Pd(II) complex (**1**).

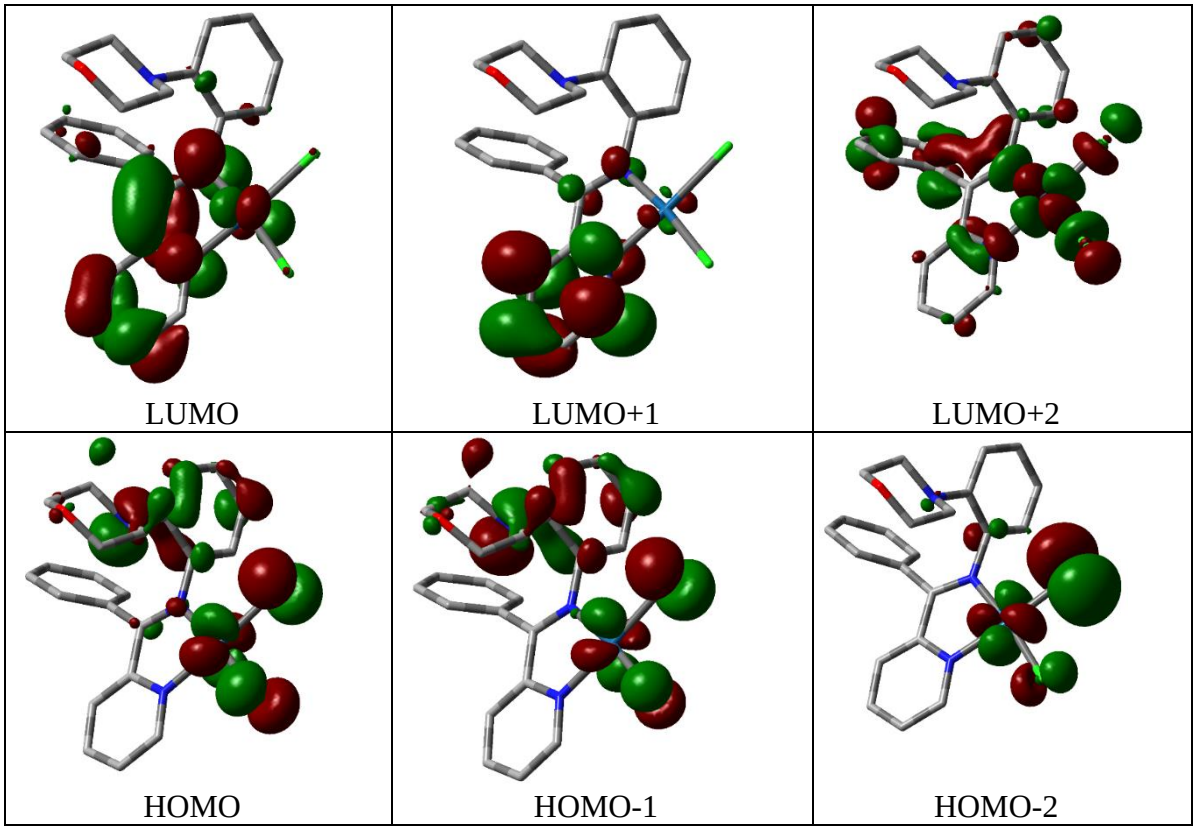

Fig. IV.12. Contour plots of some selected molecular orbital of Pt(II) complex (**2**).

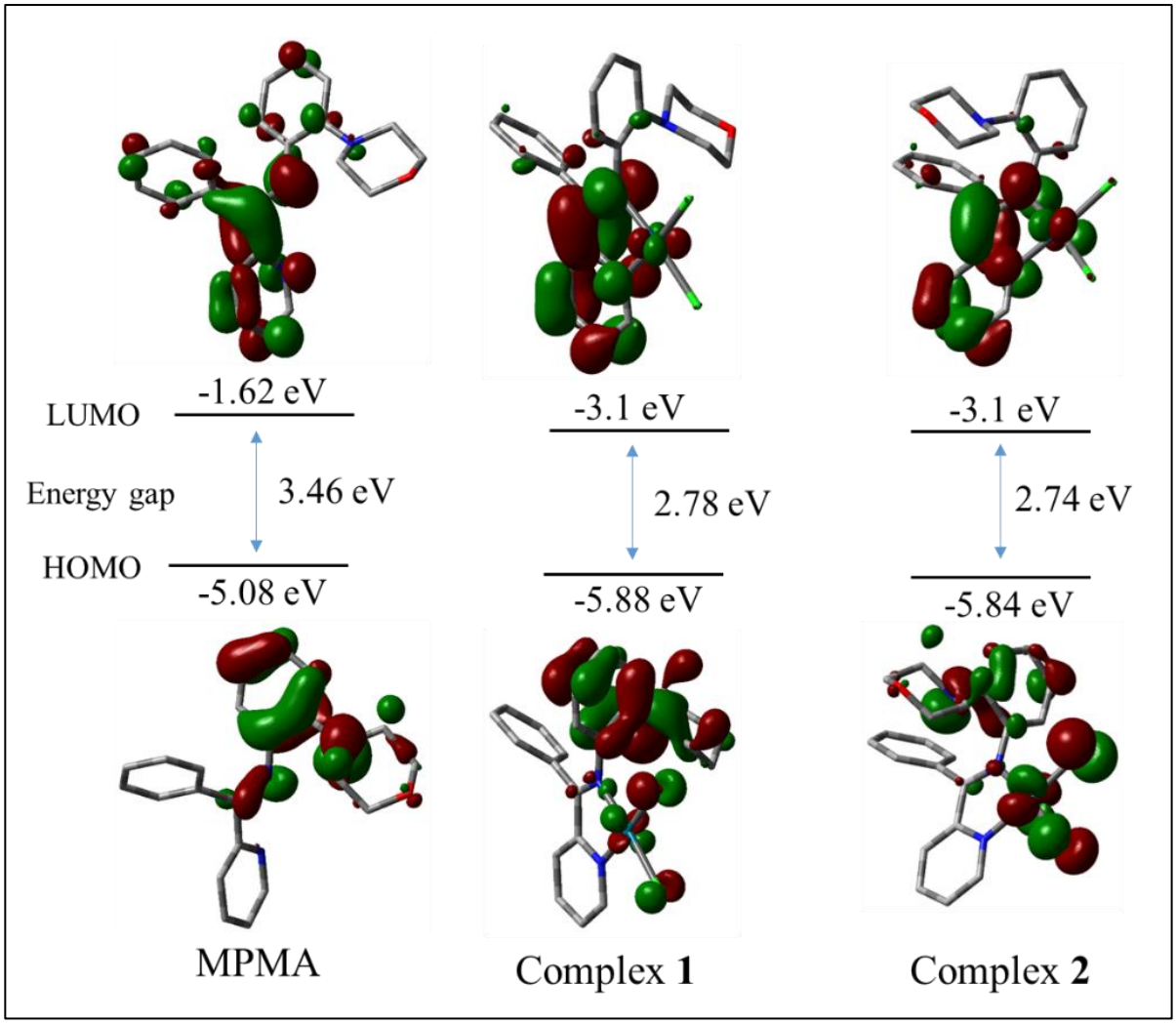

Fig. IV.13. Frontier molecular orbitals of ligand and complexes **1**, **2** and their HOMO–LUMO energy gaps.

Table IV.5. Global reactivity descriptors for complex **1** and **2**.

S. No.	Physical property	Formula used	Complex **1**	Complex **2**
1	Ionization Potential (I)	$I = -E_{HOMO}$	5.88 eV	5.84 eV
2	Electron Affinity (A)	$A = -E_{LUMO}$	3.1 eV	3.1 eV
3	Electronegativity (χ)	$\chi = (I+A)/2$	4.49 eV	4.47 eV
4	Chemical Hardness (η)	$\eta = (I-A)$	2.78	2.74
5	Chemical Potential (μ)	$\mu = -(I+A)/2$	-4.49	-4.47
6	Chemical Softness (S)	$S = 1/\eta$	0.719	0.729
7	Electrophilicity Index (ω)	$\omega = \mu^2/2\eta$	3.626	3.646

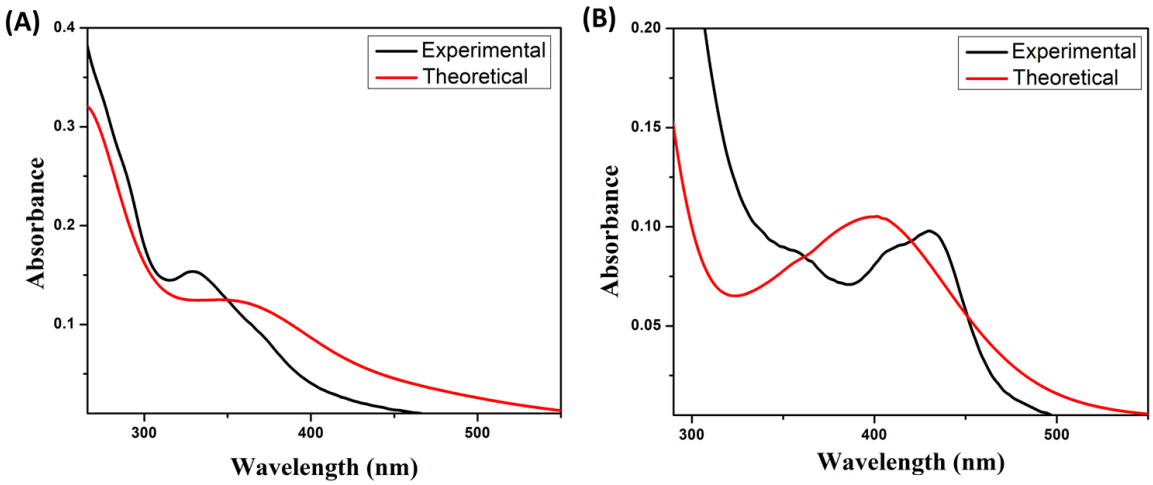

Fig. IV.14. Experimental (black) and TD-DFT simulated (red) UV-Vis spectra of complexes **1** (A) and **2** (B).

Table IV.6. Vertical electronic transition calculated by TDDFT/CPCM method of complexes **1** and **2.**

Comp.	λ (nm)	E (eV)	Osc. Strength (f)	Key excitations	Character	$\lambda_{expt.}$ (nm)
1	360.12	3.3864	0.0509	(39%)HOMO-4→LUMO	MLCT/ XLCT	372 (sh.)
	336.17	3.6881	0.0422	(93%)HOMO-8→LUMO	ILCT	330
2	402.28	3.0592	0.0997	(45%)HOMO-2→LUMO	XLCT/ MLCT	431 408 (sh.)
	353.27	3.6544	0.0409	(96%)HOMO-8→LUMO	ILCT	359

IV.3.5. Molecular Electrostatic Potential (MEP)

The molecular electrostatic potential (MEP) prediction is a theoretical useful technique used to depict the visual understanding of molecular shape, electron density, relative polarity, electrophilic-nucleophilic sites and molecular interaction. The molecular electrostatic potential (MEP) surface was computed at the B3LYP/6-31G(d) level from optimized geometry to predict the reactive sites in the metal complexes. Different colours are used to indicate different electrostatic potential values at the surface. The red-orange, green and blue colour represents the zone of most negative electrostatic potential, zero electrostatic potential and most positive electrostatic potential respectively. The magnitude of electrostatic potential increase in order as red < orange < yellow < green < cyan < blue.[62] The negative regions (red) and the positive regions (blue) of MEP correspond to the nucleophilic and the electrophilic nature respectively. The colour code of MEP maps for complex **1** and **2** are shown in Fig. IV.15. The negative electrostatic potential regions are mainly located around the electronegative oxygen and chloride atoms, while positive electrostatic potential areas are

not visible on the MEP surface of both the complexes. Overall, neutral green regions are prevailing in both the complexes originating from carbon atom skeletons. The intermolecular interactions of the complexes with DNA and BSA can be anticipated entered on the regional potential molecular behaviour and the location of the active sites.

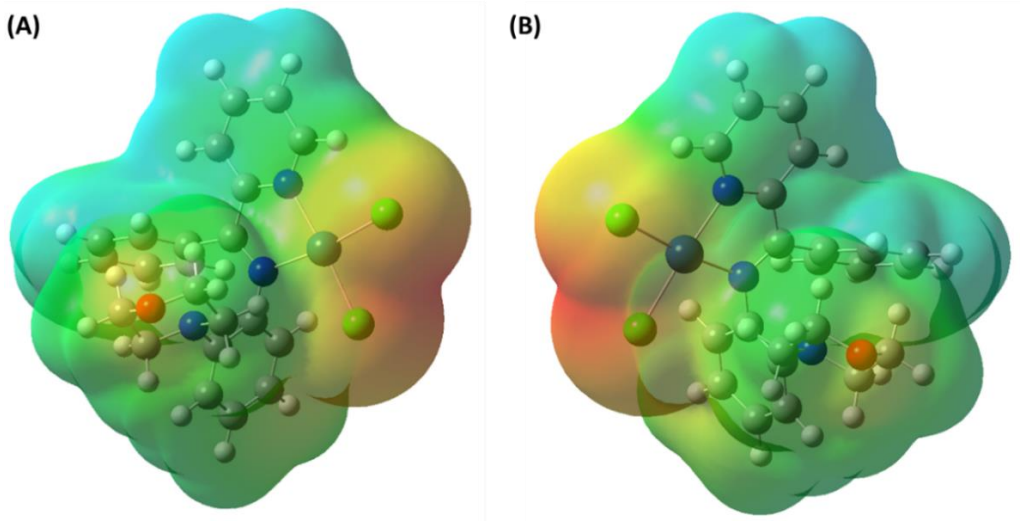

Fig. IV.15. Molecular electrostatic potential map for complex **1** (A) and for complex **2** (B).

IV.3.6. Hirshfeld surface (HS) analysis

Hirshfeld surface analysis is very appreciated in order to explore the packing modes and intermolecular interactions in the molecular crystals.[63] The HS of complexes **1** and **2** mapped over d_{norm} (in the range of -0.05 to 1.2Å), shape index (range of -1.0 to 1.0 Å), and curvedness (range of -4.0 to 4.0 Å) are shown in Fig. IV.16. The Hirshfeld surface plotted over d_{norm} can be utilized to exhibit strong H-bonding as well as H-bonding interactions using diverse colors.[64] This surface contains three colors, red, white, and blue. Among them, the red color signifies the interatomic contacts for which the distance between the atoms is less than the sum of van der Waals radii of the atoms involved. The blue regions designate the distance between the atoms which is greater than the sum of the van der Waals radii of the atoms involved. A white spot is found to be present on the HS if the distance between the atoms is identical to the sum of van der Waals radii of the atoms involved. The occurrence of π···π interactions in the titled compounds is confirmed by the adjacent red and blue triangles over the shape-index of the HS. Hirshfeld surface mapped on a curvedness map specifies the planar arrangement of the molecules.

All the available contacts are summarized in a 2D fingerprint plot as distinct spikes (Fig. IV.17 to Fig. IV20). All of the possible interactions (H···H, H···C/C···H, H···Cl/Cl···H, H···O/O···H, C···Cl/Cl···C, N···Cl/Cl···N) in the complexes and their respective contributions to the total HS can be highlighted by the fingerprint plot's decomposition. The H···H contacts

are primary in the complexes and the relative contributions are found to be 47.2% for both the complexes. This is in accord with the high amount of hydrogen atoms in the structure.

	d_{norm}	Shape index	Curvedness
1	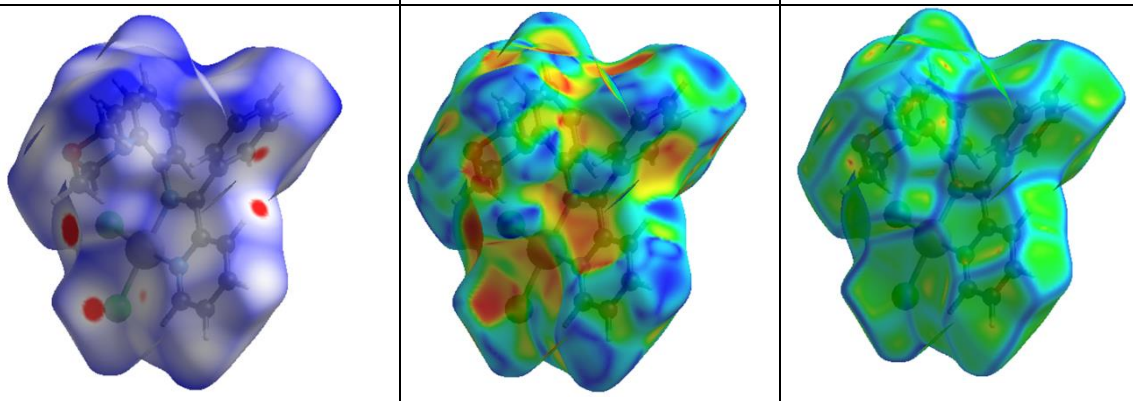		
2	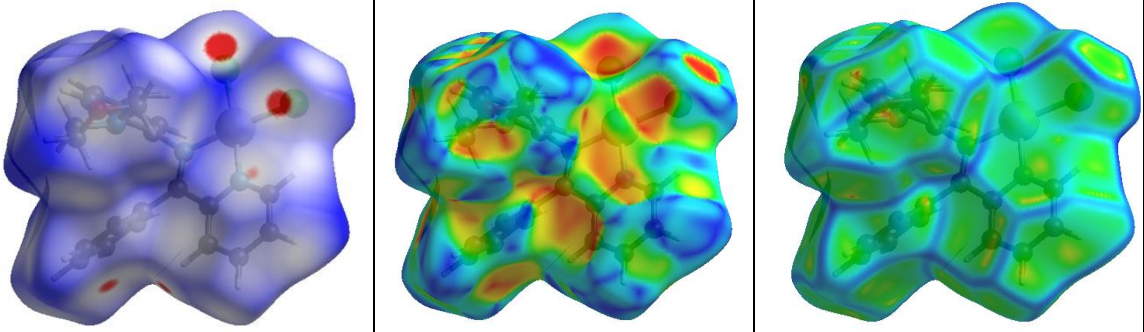		

Fig. IV.16. Hirshfeld surfaces mapped with dnorm (left side), shape index (middle) and curvedness (right side).

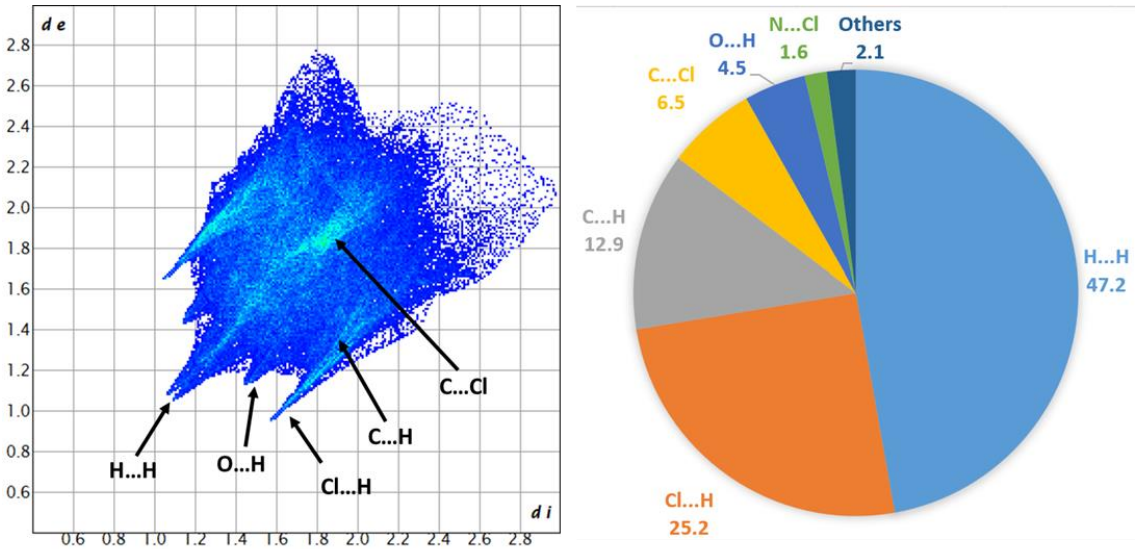

Fig. IV.17. 2D-Fingerprint plot (full) and relative contributions of various intermolecular interactions to the Hirshfeld surface area of complex **1**.

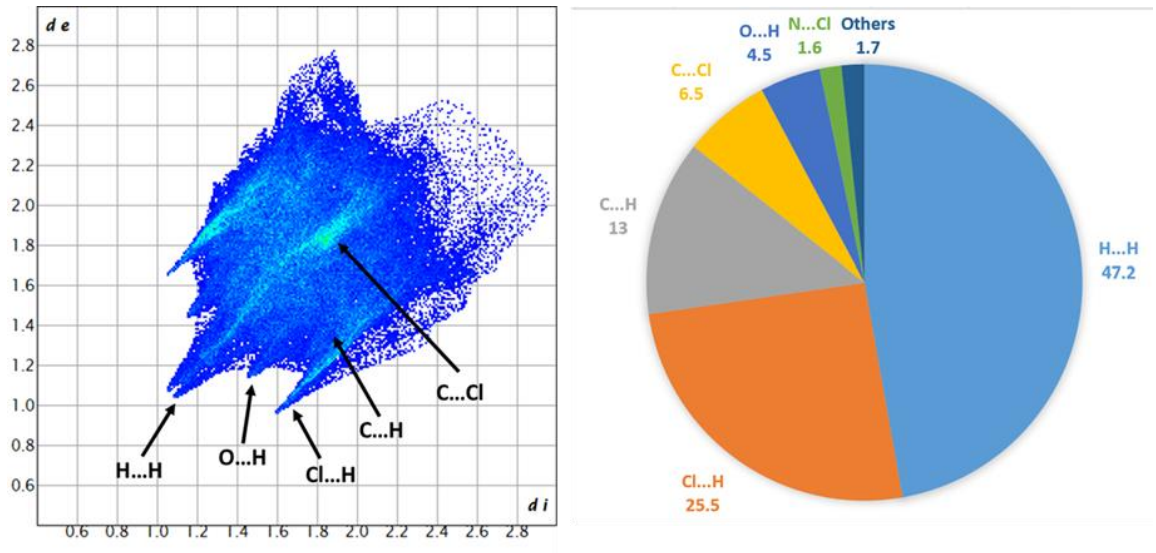

Fig. IV.18. 2D-Fingerprint plot (full) and relative contributions of various intermolecular interactions to the Hirshfeld surface area of complex **2**.

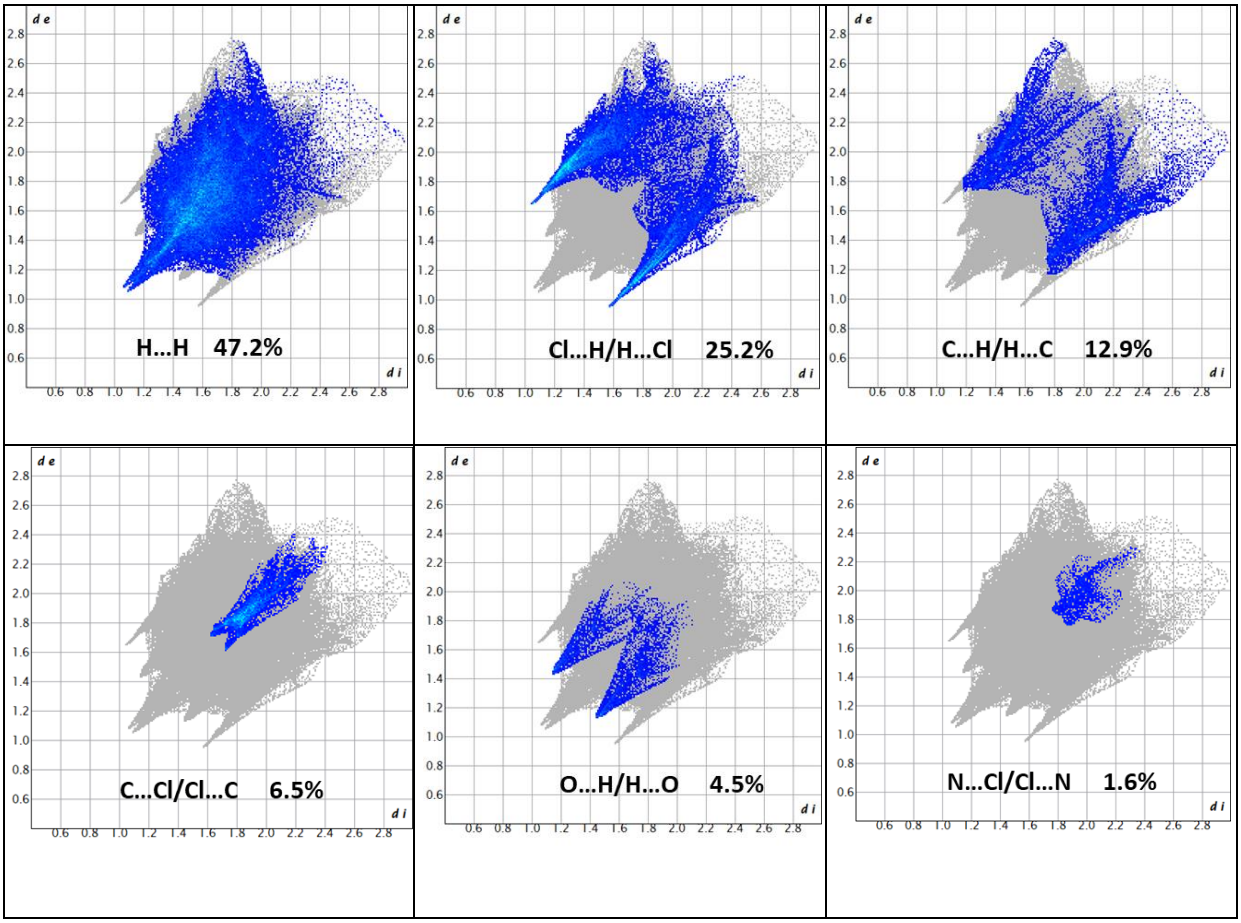

Fig. IV.19. 2D Fingerprint plot resolved into different contacts contributed to the total Hirshfeld surface area of the complex **1**.

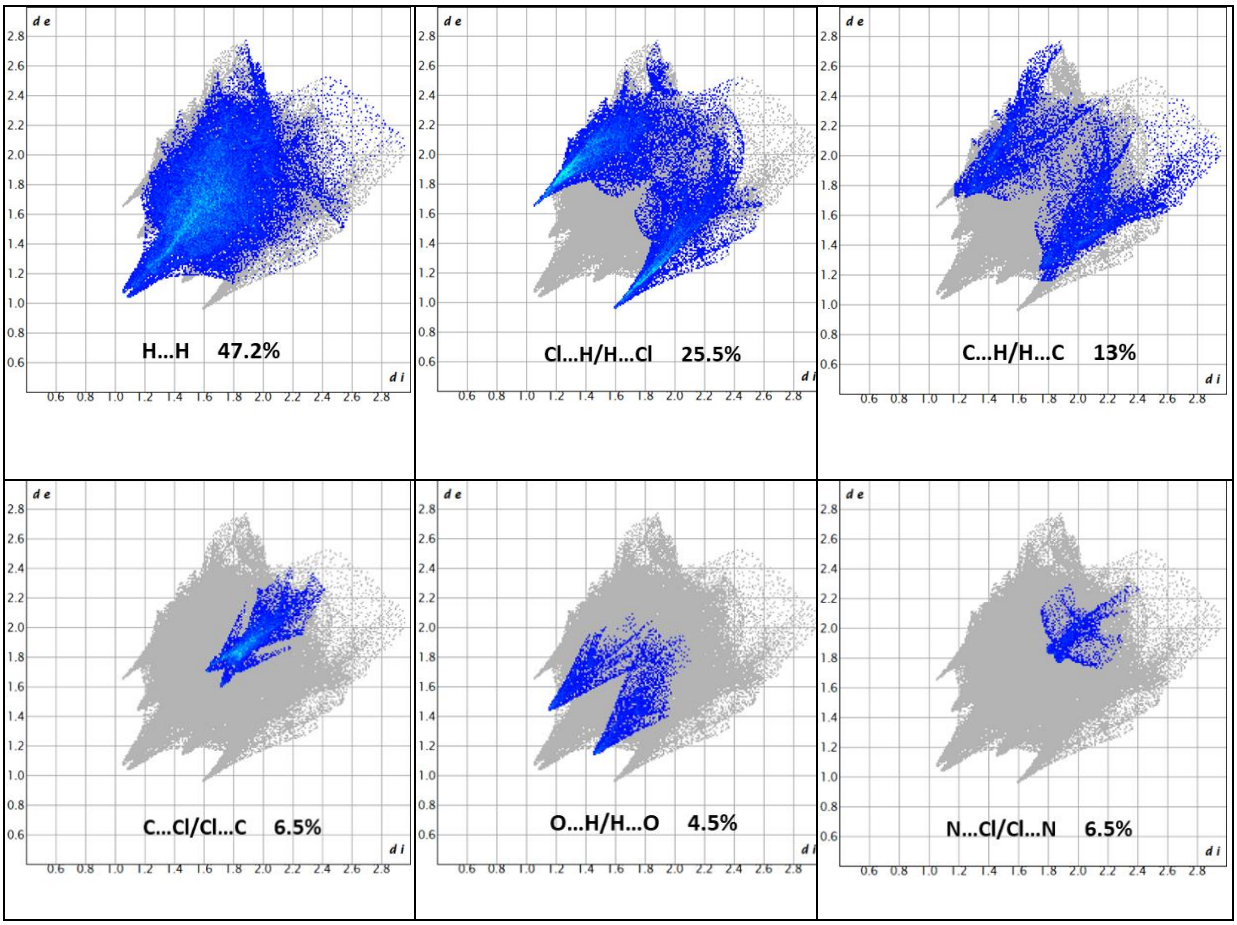

Fig. IV.20. 2D Fingerprint plot resolved into different contacts contributed to the total Hirshfeld surface area of the complex **2**.

IV.3.7. DNA binding studies

The major target of the antitumor drugs is DNA. The DNA-drug interaction gives information about the mutation of genes, replication and transcription.[66] Therefore, it is of great importance to understand DNA binding properties of potential anticancer agents. In general, transition metal complexes can bind to DNA via both covalent (replacement of a labile ligand of the complex by a nitrogen base of DNA, e.g., guanine N7) and/or non-covalent (intercalation, electrostatic or groove binding) interactions.

IV.3.7.1. UV-vis method

The application of electronic absorption spectroscopy is one of the most universally employed methods for the determination of the binding modes and the binding extent of metal complexes with DNA. The absorption intensity of complexes may decrease (hypochromism) or increase (hyperchromism) with a slight increase in the absorption wavelength (bathochromism) upon the addition of DNA. The intercalation results in

hypochromism with a small red/blue shift of the CT-band.[67] Otherwise, the hyperchromic shift might be assigned to the electrostatic and non-intercalative interactions.[68] On the other hand, the covalent interaction occurs via the exchange of the labile ligand of the complex, for example, by a nitrogen base of DNA e.g. guanine N7.[69]

The absorption spectra of complexes **1**–**2** (~30 μM) in 1:10 DMSO/buffer medium were obtained in the range of 270-600 nm in presence of increasing amounts of CT-DNA which are shown in the Fig. IV.21. The electronic absorption spectrum of **1** and **2** exhibited two absorption bands at ~330 nm and ~431 nm, which were assigned to intra ligand charge transfer (ILCT) or metal to ligand charge transfer (MLCT). Both the bands suffered from significant hypochromism along with a minor hypsochromic shift as a result of the progressive addition of CT-DNA, indicating an intercalative interaction between the complex's aromatic chromophore and the DNA base pairs. The addition of successive amounts of DNA to the solution of complex **1** resulted in appearance of an isosbestic point at 405 nm and 299 nm (Fig. IV.21). Similar spectral pattern was also obtained upon the addition of increasing amounts of CT-DNA to complex **2**. Observation of the isosbestic point was also reported for the Pd(II) and Zn(II) complexes of the phosphonium Schiff-base ligand.[70] This suggests a covalent interaction via the loss of the chloride ion(s) due to the development of an isosbestic point. This compares well with the mechanism of the action of cis-platin. Another indirect evidence for it comes from the substitution kinetic data of complexes **1** and **2**, which were previously described. So, we may propose that our synthesized complexes could interact with DNA in a bifunctional mode, including covalent binding to the nucleobases and non-covalent intercalation. The dual-function mode of action was reported for other Pt(II) complexes in which the electron-rich DNA binds covalently to the electron-deficient metal centre and non-covalently via the intercalation mode.[71]

The intrinsic equilibrium binding constant (K_b) was estimated using the following Wolfe-Shimmer equation (Eq. IV.6).[72]

$$\frac{[DNA]}{\varepsilon_a - \varepsilon_f} = \frac{[DNA]}{\varepsilon_b - \varepsilon_f} + \frac{1}{K_b(\varepsilon_b - \varepsilon_f)} \qquad \text{(Eq. IV.6)}$$

Where, [DNA] is the concentration of CT-DNA and ε_a is the apparent extinction coefficient of the complex at a given DNA concentration, ε_f and ε_b are the extinction coefficients of the complex in free solution and when fully bound to CT-DNA respectively. The plot of $[DNA]/(\varepsilon_a - \varepsilon_f)$ against $[DNA]$ will produce slope $1/(\varepsilon_b - \varepsilon_f)$ and intercept $1/K_b(\varepsilon_b - \varepsilon_f)$; K_b (M^{-1}) is the ratio of slope to intercept. The K_b values of complex **1** [(1.861 ±

0.07) × 10^5 M^{-1}] and complex **2** [(2.817 ± 0.05) × 10^5 M^{-1}] indicate that all the complexes strongly intercalated with DNA. Even though the electronic absorption tests revealed that the chemicals can bind to DNA by intercalation, the binding mode required to be demonstrated through additional experiments.

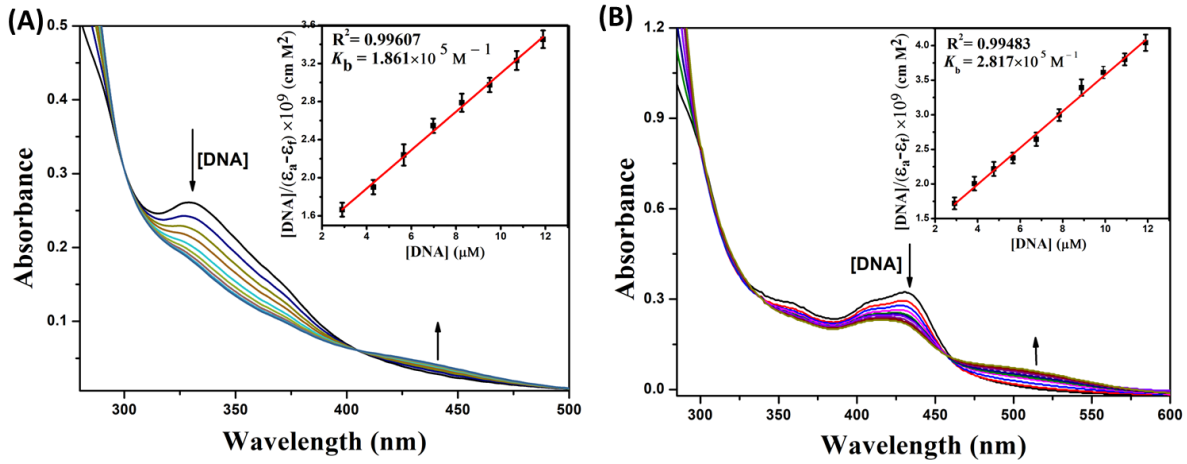

Fig. IV.21. Change in absorption spectra of the complexes **1** (A) and **2** (B) in Tris–HCl/NaCl buffer with the gradual addition of CT-DNA. Inset: Plot of [DNA]/(ε_a – ε_f) vs. [DNA].

IV.3.7.2. Ethidium bromide (EB) displacement experiment

An ethidium bromide (EB) fluorescence displacement experiment was executed to confirm the intercalative mode of the binding between the complexes and CT-DNA. EB is a planar cationic dye that is extensively used as a sensitive fluorescence probe for DNA. In presence of DNA, EB emits deep fluorescent light due to the strong intercalation between adjacent DNA base pairs. The displacement technique depends on diminishing fluorescence resulting from the displacement of EB from the DNA sequence by a quencher. The quenching is the result of the reduction of the number of binding sites on the DNA which are available to EB. Hence the method offers indirect verification for an intercalative binding mode.[73] The degree of fluorescence quenching may further be utilized to establish the extent of binding between the quencher and DNA. Herein, the addition of complexes to CT-DNA pre-treated with EB results in a noteworthy amount of decease in emission intensities with a red shift thereby demonstrating that the complexes compete with EB for the binding sites of DNA (Fig. IV.22). Quenching data were analyzed according to the following Stern-Volmer equation (Eq. IV.7).[74]

$$\frac{F_0}{F} = 1 + K_{sv}[Q] \qquad \text{(Eq. IV.7)}$$

Where F_0 and F are the fluorescence intensities of the CT-DNA solutions in the absence and presence of the complexes, respectively. K_{sv} is the Stern-Volmer quenching constant and [Q] is the concentration of complex. The K_{sv} values are obtained from the slope of the plot of F_0/F versus [Q] (Fig. IV.22 inset) and are found to be $(2.309\pm0.06)\times10^5$ M^{-1} and $(2.435\pm0.04)\times10^5$ M^{-1} for **1** and **2** respectively.

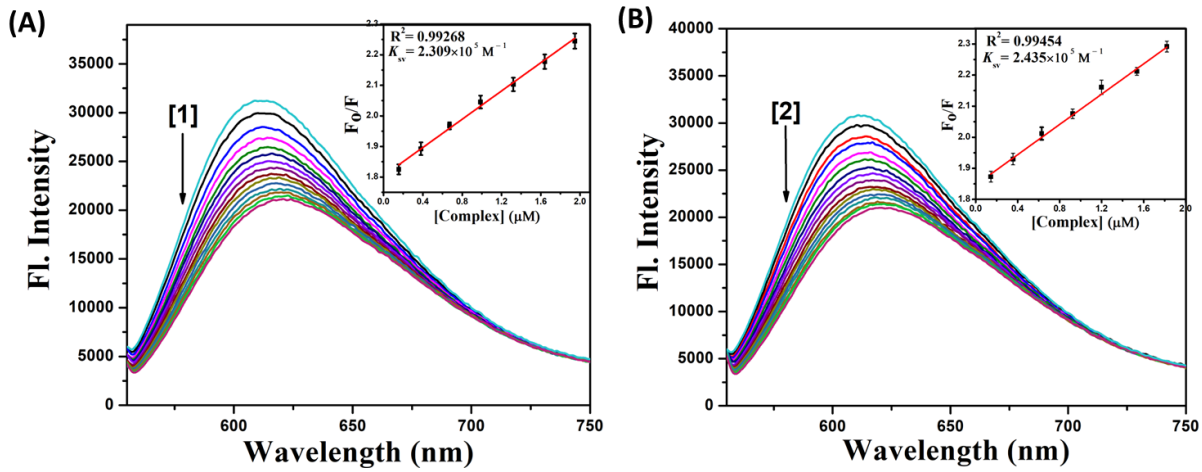

Fig. IV.22. Emission spectra (λ_{ex} = 540 nm) of EB-CT-DNA in presence of increasing concentrations of the complexes **1** (A) and **2** (B). Inset: Plots of emission intensity F_0/F vs. [complex].

Table IV.7. Binding constants (K_b) and Stern-Volmer constants (K_{SV}) values for the interaction of complexes **1** and **2** with CT-DNA.

Compound	UV Method	Fluorescence Method
	K_b ($\times10^5$) (M^{-1})	K_{sv} ($\times10^5$) (M^{-1})
EB-CT-DNA + 1	1.861±0.07	2.309 ± 0.06
EB-CT-DNA + 2	2.817±0.05	2.435 ± 0.04

IV.3.7.3. Viscosity Measurements

Viscosity measurements are considered as one of the least vague and most significant tests of a DNA binding study in solution. This technique is sensitive to changes in length of DNA and provides strong verification for the DNA binding mode of complexes. As base pairs are detached to accommodate the binding of complexes, lengthening of DNA helix occurs on intercalation thereby leading to an increase in DNA viscosity.[75] In contrast, electrostatic or groove binders do not hinder the CT-DNA structure and do not considerably modify the viscosity of the CT-DNA solution.[76] The effects of the complexes on the viscosity of CT-DNA are revealed in the (Fig. IV.23). The values of $(\eta / \eta_0)^{1/3}$ were plotted against R (R =

[complex]/[CT-DNA]), where η and η_0 are the relative viscosities of DNA in presence and absence of the complex respectively. The viscosity of CT-DNA enhanced gradually with the increase of the complexes, much like the usual intercalator EB[77] and the ability of the complexes to increase the viscosity of DNA follows the order EB > **2** > **1**. The results from the viscosity experiments validate the intercalation of the complexes into the DNA base pairs, as already established via absorption and fluorescence spectroscopic studies.

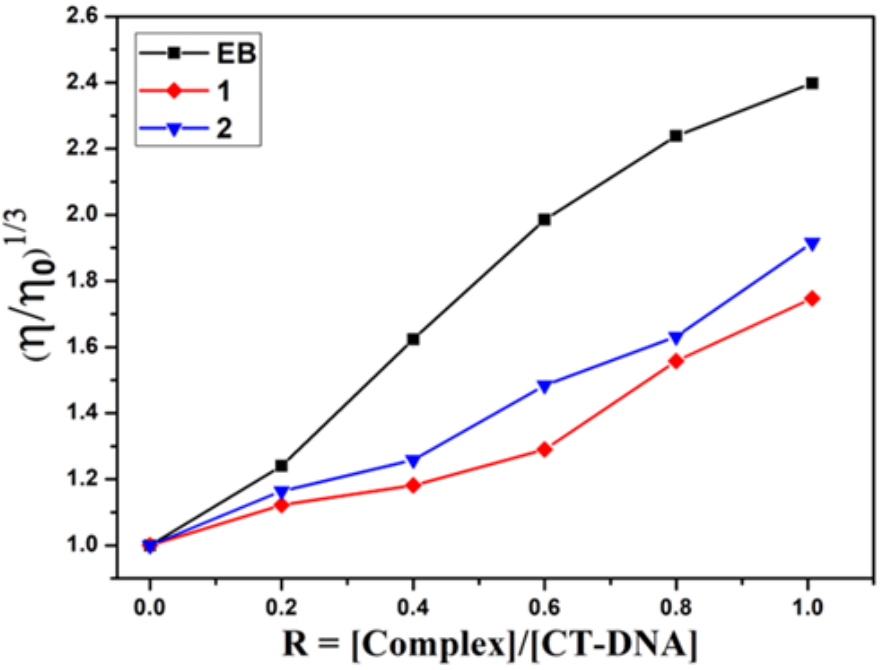

Fig. IV.23. Relative viscosity of CT-DNA interacting with complexes **1**, **2** and EB.

IV.3.8. Protein binding studies

The interactions of drugs with mostly plasma proteins with serum albumin are very essential to study. The reason behind this is that binding these proteins may result into a loss or an enhancement of the biological properties of the drugs or offer paths for drug transportation. Here bovine serum albumin (BSA) was utilized as a significant and relatable model to explore the binding affinity and interaction mechanism of the metal complex.[78]

IV.3.8.1. Absorption spectral studies

UV-Vis absorption spectroscopy is a valuable technique to discriminate between static and dynamic quenching based on the absorption spectra of BSA in the presence of the complexes. Dynamic quenching is a procedure in which the fluorophore and the quencher come into contact through the transient existence of the excited state whereas static quenching refers to the fluorophore-quencher complex formation in the ground state.[79] Electronic absorption

spectra of BSA (10 μM in PBS at pH 7.4) were recorded in the range of 240-600 nm in presence of different concentration of complex which is shown in the Fig. IV.24. BSA has a characteristic absorption band at 280 nm. From absorption spectra of BSA, it is obvious that the absorption intensity of BSA steadily increases along with the blue shift in the wavelength signifying static type of fluorophore–quencher mechanism between BSA and complexes.[80] The apparent association constants (K_a) for the interaction of complexes with BSA were calculated using the Benesi–Hildebrand equation (Eq. IV.8).

$$\frac{1}{A_{obs}-A_0} = \frac{1}{A_c-A_0} + \frac{1}{K_a(A_c-A_0)[complex]} \qquad \text{(Eq. IV.8)}$$

Where A_{obs} is the observed absorbance (at 280 nm) of the solution having various concentrations of the complex, A_0 and A_c are the absorbance of BSA only and of BSA with the complex. The apparent association constants (K_a) were calculated from the plot of $1/(A_{obs}-A_0)$ vs 1/[complex] (Fig. IV.24 inset) and were found to be $(8.203\pm0.40)\times10^4$ M^{-1} and $(9.134\pm0.34)\times10^4$ M^{-1} for the complexes **1** and **2** respectively. These values are comparable to reported value.[81]

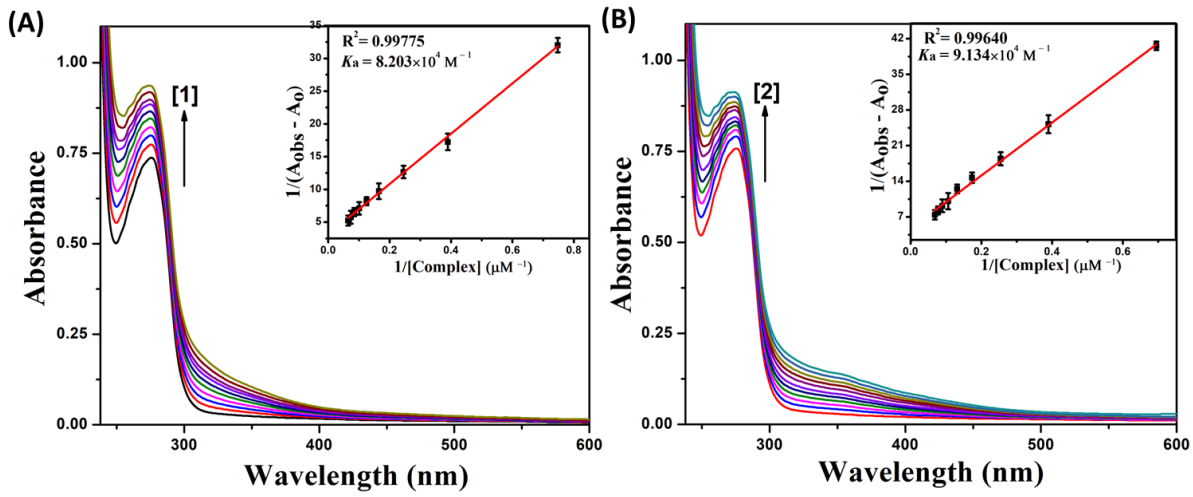

Fig. IV.24. Change in absorption spectra of BSA with the gradual addition of complex **1** (A) and complex **2** (B). Inset: Plot of $1/(A_{obs}-A_0)$ vs 1/[complex].

IV.3.8.2. Fluorescence quenching studies

The fluorescence spectrum of BSA was observed and studied thoroughly upon the incremental addition of the complex in order to attain more information on the binding of the complexes with BSA. Although BSA contains three fluorophores, i.e., tryptophan, tyrosine and phenylalanine, the intrinsic fluorescence of BSA is primarily due to tryptophan solely. As

phenyl alanine has a very low quantum yield and the fluorescence of tyrosine is nearly totally quenched if it is ionized or in close proximity to an amino group, a carbonyl group or a tryptophan residue, only tryptophan is responsible for the fluorescence quenching. Alterations in the emission spectra of tryptophan are familiar in response to protein conformational transitions, subunit associations, substrate binding or denaturation. The interaction between the metal complexes and BSA was assessed by recording the fluorescence emission spectra of BSA with and without the metal complex (Fig. IV.25). A progressive decrease in the fluorescence intensity was observed along with a small blue shift on increasing the concentration of complexes. It is chiefly due to the active site in the protein which is buried in a hydrophobic environment.[82] These results suggested a definite interaction of the complexes with the BSA protein.

The linear Stern–Volmer equation (Eq. IV.7) is generally employed to describe the quenching mechanism between the complex and BSA. The Stern-Volmer quenching constant values (K_{sv}) calculated from the plot of F_0/F vs [Q] (Fig. IV.25 inset) in respect to complexes **1** and **2** were found to be $(7.217\pm0.37)\times10^4$ M^{-1} and $(9.867\pm0.33)\times10^4$ M^{-1}. The high K_{sv} values signify that complexes demonstrate good fluorescence quenching ability. Moreover, the quenching rate constant (K_q) of the complexes were found to be in the range of 7.217–9.867 $\times 10^{12}$ M^{-1} s^{-1}, following the equation $Kq = K_{sv}/\tau_o$ (τ_o refers to the lifetime of the fluorophore without the quencher with an average value of 10^{-8} s). Since the obtained Kq value is greater than the value suggested in dynamic quenching (2×10^{10} M^{-1} s^{-1}), the preferred quenching process is static through the formation of a complex.[83]

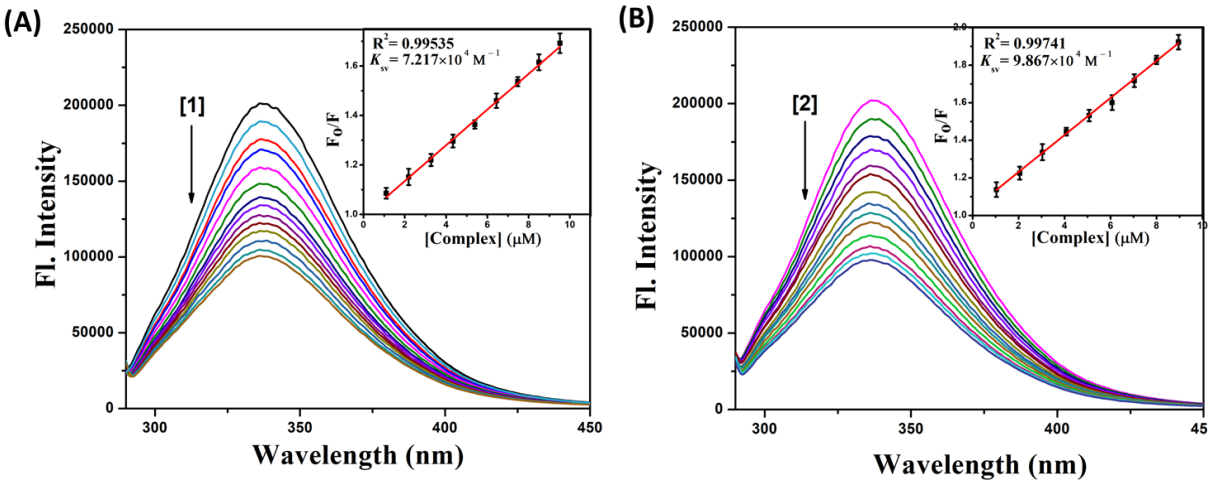

Fig. IV.25. Emission spectra (λ_{ex} = 280 nm) of BSA in presence of increasing concentrations of the complexes **1** (A) and **2** (B). Inset: Plots of emission intensity F_0/F vs. [complex].

IV.3.8.3. Binding constant and binding sites

Base on the Scatchard equation (Eq. IV.9), the binding constant and the number of binding sites can be determined.

$$log\frac{(F_0-F)}{F} = log\ K_b + nlog[complex] \qquad \text{(Eq. IV.9)}$$

Where K_b is the binding constant of complex with BSA and n is the number of binding sites. The binding constant (K_b) and the binding sites (n) have been obtained from the intercept and slope of the curve of log [(F_o-F)/F] versus log [complex] (Fig. IV.26). Based on the plot, calculated values of binding constant (K_b) for the complexes **1** and **2** are (1.204±0.05)×10^5 M^{-1} and (2.065±0.09)×10^5 M^{-1} and binding sites (n) are (1.014±0.04) and (1.100±0.03) respectively. The binding constant (K_b) values clearly recommended that the fabricated complexes have powerful binding affinity with the serum albumins. The obtained binding site values n (~1) evidently displays the existence of a single binding site on BSA protein for the complex.

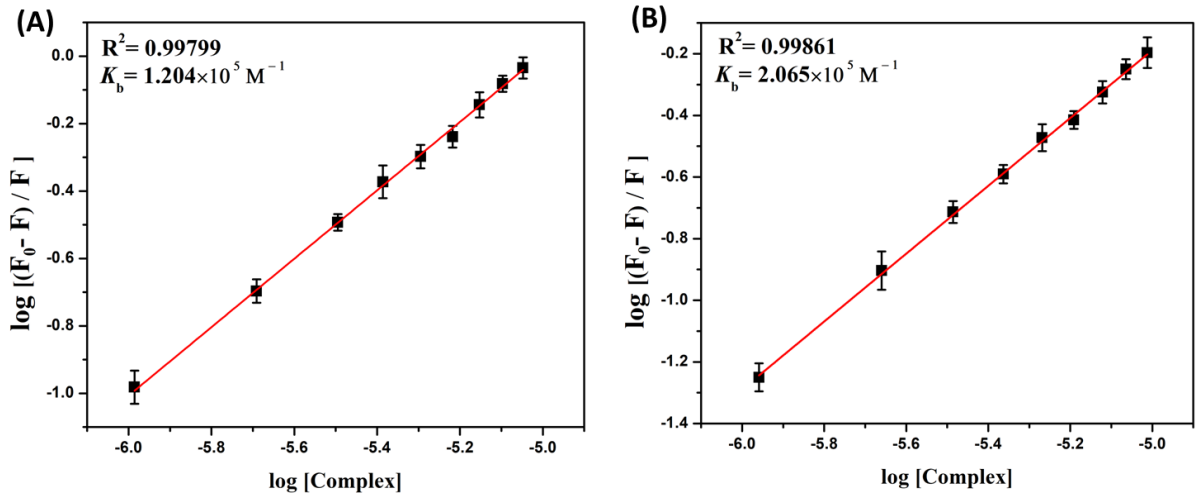

Fig. IV.26. Plot of log [(F_o-F)/F] versus log [complex] of complex **1** (A) and complex **2** (B)

Table IV.8. Protein apparent association constant (K_a), binding constant (K_b), quenching constant (K_{sv}) and number of binding sites (n) for the interaction of complexes **1** and **2** with BSA.

Compound	UV Method	Fluorescence Method		
	K_a (×10^4) (M^{-1})	K_b (×10^5) (M^{-1})	K_{sv} (×10^4) (M^{-1})	n
BSA + 1	8.203 ± 0.40	1.204 ± 0.05	7.217 ± 0.37	1.014 ± 0.04
BSA + 2	9.134 ± 0.34	2.065 ± 0.09	9.867 ± 0.33	1.100 ± 0.03

IV.3.8.4. Synchronous fluorescence spectroscopic studies

The synchronous fluorescence spectra can provide information about the conformational change of the protein molecular microenvironment, specifically in the locality of the fluorophore moieties of BSA.[84] From the point of view of Miller,[85] in synchronous fluorescence spectroscopy, the difference between the excitation and emission wavelengths ($\Delta\lambda = \lambda_{em} - \lambda_{ex}$) designates to the nature of the chromophores in the spectra. If the $\Delta\lambda$ value is 15 nm, the synchronous fluorescence spectra of BSA are characteristics of tyrosine residue, whereas the larger $\Delta\lambda$ value of 60 nm is characteristics of tryptophan residue.[86] The maximum emission wavelength of tryptophan and tyrosine residues in the protein molecule are related to the polarity of their surroundings, changes of the maximum emission wavelengths can reflect changes of protein conformation. The synchronous fluorescence spectra of BSA upon the addition of complexes recorded at $\Delta\lambda$ = 15 nm and $\Delta\lambda$ = 60 nm are shown in Fig. IV.27 and Fig. IV.28 respectively. In the synchronous fluorescence spectra of BSA at $\Delta\lambda$ = 15, the addition of the complexes to the solution of BSA results in a minute decrease in the fluorescence intensity of BSA at 301 nm. But, the synchronous fluorescence spectra of BSA at $\Delta\lambda$ = 60, the addition of the complexes to the solution of BSA causes a noteworthy decrease in the fluorescence intensity of BSA at 343 nm along with a small blue shift. It discloses that the binding around the tryptophan residues was toughened. The results plainly point towards that both the complexes bind to the active sites of the protein and brought a conformational change in the secondary structure of the protein thereby making them potential molecules for biological applications.

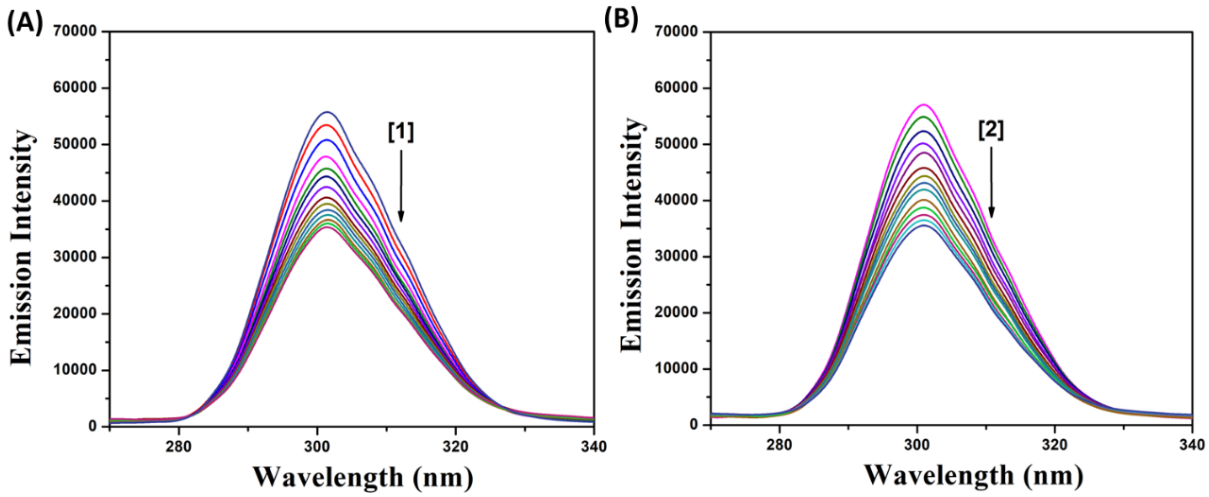

Fig. IV.27. The synchronous spectra of BSA in the presence of increasing amounts of the complexes **1** (A) and **2** (B) at a wavelength difference of $\Delta\lambda$ = 15 nm. The arrow shows the emission intensity changes upon an increase in the concentration of the complexes.

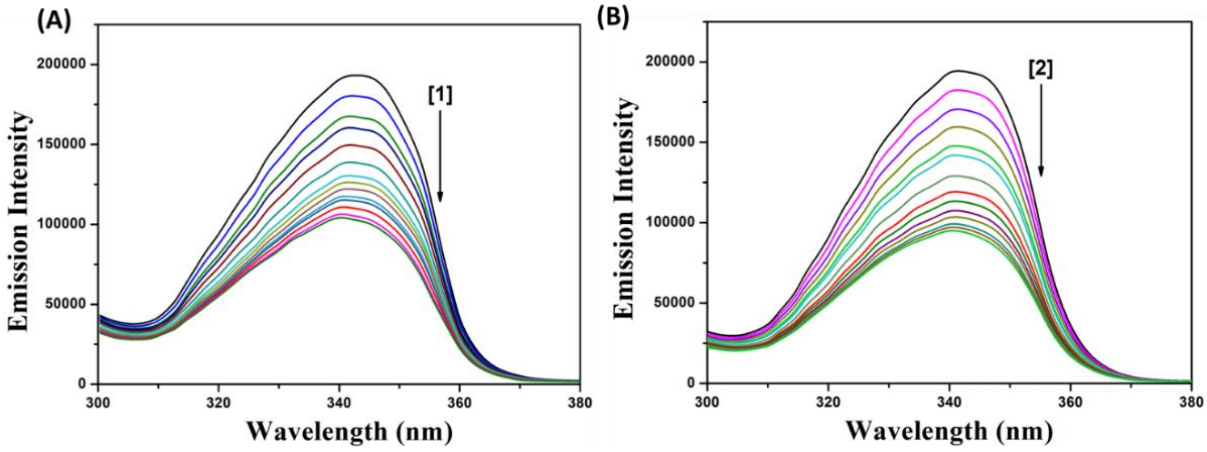

Fig. IV.28. The synchronous spectra of BSA in the presence of increasing amounts of the complexes **1** (A) and **2** (B) at a wavelength difference of $\Delta\lambda$ = 60 nm. The arrow shows the emission intensity changes upon an increase in the concentration of the complexes.

IV.3.8.5. Three-dimensional fluorescence spectra analysis

The study of conformational changes of BSA by three-dimensional fluorescence spectra is a commanding technique for binding interactions with BSA. The alterations noticed in 3D emission spectra and their related contour diagrams of BSA in the absence and presence of complexes are given in Fig. IV.29. The first-order Rayleigh scattering peak ($\lambda_{em} = \lambda_{ex}$) and second-order Rayleigh scattering peak ($\lambda_{em} = 2\lambda_{ex}$) are referred to as peak 'c' and 'd' respectively. The very strong peak 'a' depict the spectral behavior of the Trp and Tyr residues in proteins while another peak 'b' mainly shows the properties of the polypeptide backbone structures.[87] The emission intensity of Rayleigh scattering peak enhanced upon addition of the complex to BSA. This is owing to the formation of fluorophore-quencher complex between BSA and complexes which increased the diameter of the macromolecule and enlarged the scattering effect. But the fluorescence intensity of peak 'a' and 'b' went down noticeably in the presence of complexes. This result disclosed that the binding of the complexes to BSA induced molecular microenvironment and conformational changes in protein.

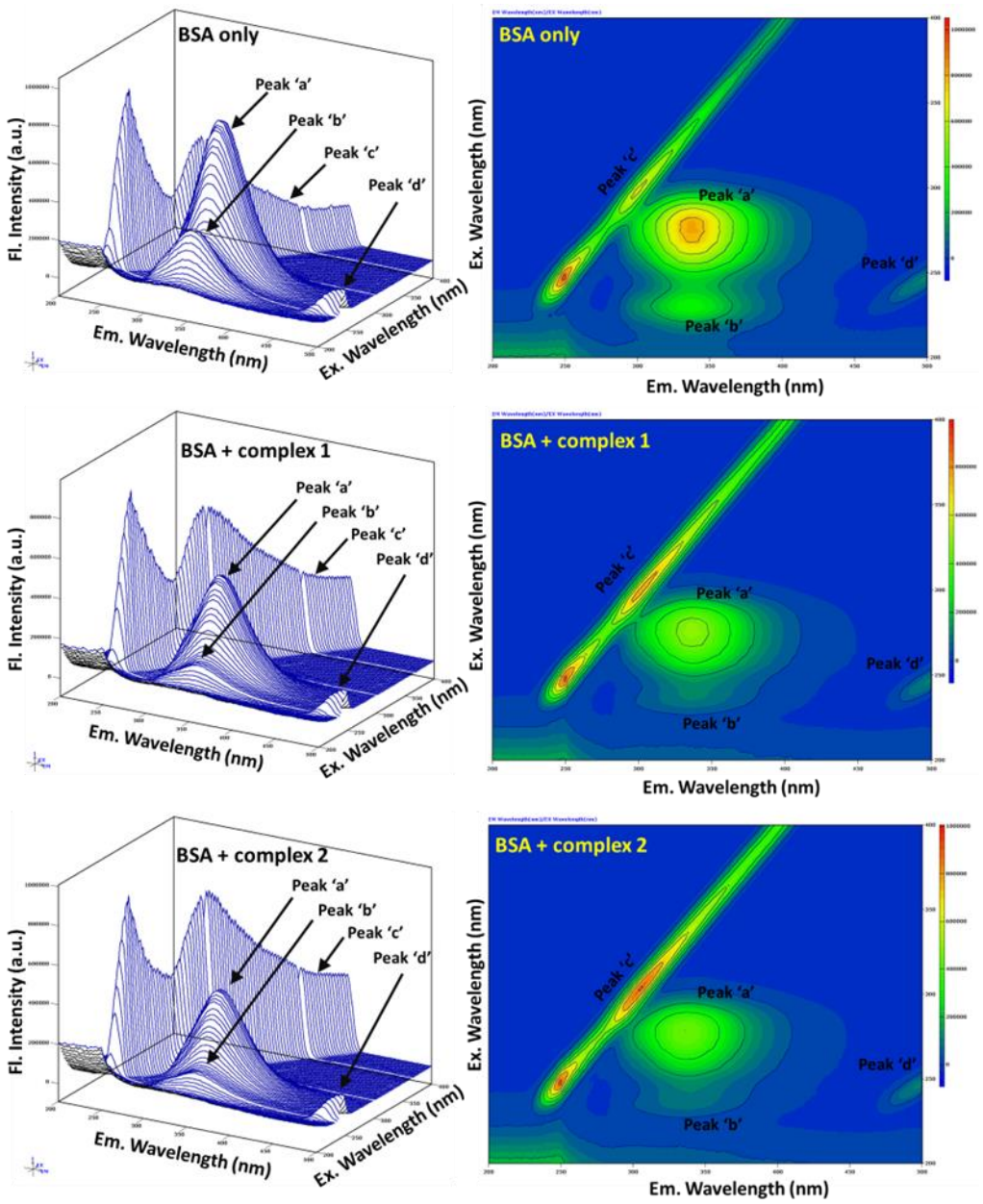

Fig. IV.29. Three-dimensional fluorescence spectra of BSA in the absence and presence of complexes **1** and **2.**

IV.3.8.6. Transfer of energy from BSA to the complexes

Förster resonance energy transfer (FRET) is a non-radiative spectroscopic method that can be implemented to observe the closeness and relative orientation of the fluorophores.[88] FRET is also utilized to quantify the distance dependent energy transfer efficiency (*E*) between the donor and acceptor. The effectual energy transfer from a protein residue (donor) to a complex (acceptor) happens whenever the overlap between the fluorescence emission spectrum of the donor and the UV-Vis absorption spectrum of the acceptor is adequate. The energy transfer efficiency (*E*) can be attained using the following equation (Eq. IV.10).[89]

$$E = \frac{R_0^6}{R_0^6 + r^6} = 1 - \frac{F}{F_0} \qquad \text{(Eq. IV.10)}$$

where F and F_0 denote the fluorescence intensity of BSA in presence and absence of the complexes, r is the acceptor-donor distance and R_0 is the critical distance when the transfer efficiency is 50%. The $J(\lambda)$ value can be determined by integrating the overlapped segment of the normalized donor emission spectrum of BSA with the molar extinction coefficient spectrum of acceptor complexes as displayed in Fig. IV.30 (yellow shaded area for complex **1** and **2** respectively). All values of FRET parameters were obtained from Eq. IV.4, IV.5 and IV.10 and are summarized in Table IV.9.

The donor-acceptor distance (r) should be on the order of 2-8 nm for productive energy transfer between BSA and complexes. The statistics (r = 3.73–4.12 nm) visibly point towards that energy transfer is greatly viable for complex **1** and **2**. Moreover, the r value follows the relationship $0.5R_0 < r < 1.5R_0$, which confirms the occurrence of static quenching interactions between BSA and complexes.[90] The findings also specify that the effectiveness of energy transfer (E) for complexes follows the pattern complex **2** > complex **1**.

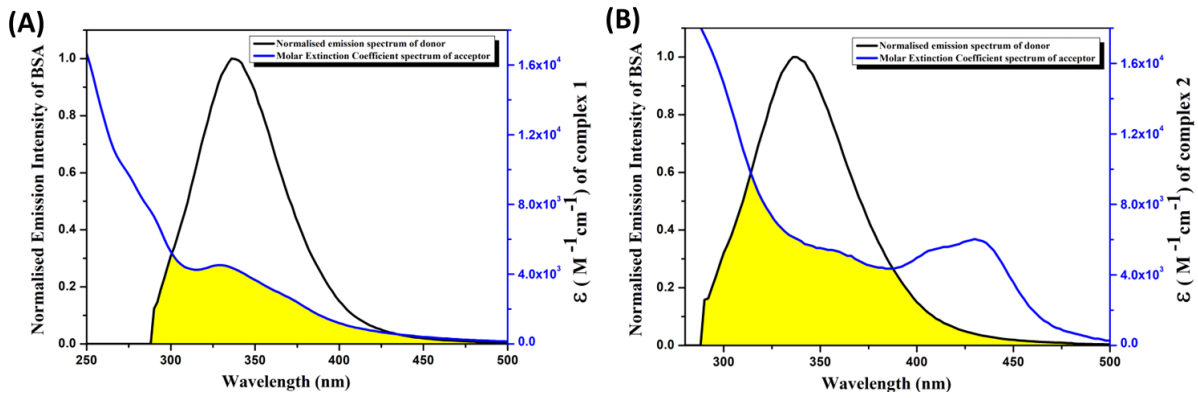

Fig. IV.30. Spectral overlap (yellow shaded area) of the normalized emission spectrum of BSA in PBS buffer (donor) with the molar extinction coefficient of complex **1** (A) and **2** (B) (acceptor) in DMSO.

Table IV.9. Parameters obtained from energy transfer between BSA and complexes **1** and **2**.

Complex	$J(\lambda)$ ($M^{-1}cm^{-1}nm^4$)	R_0 (nm)	E	r (nm)
1	1.67×10^{15}	3.74	0.5025	3.73
2	3.10×10^{15}	4.17	0.5197	4.12

IV.3.8.7. Circular dichroism spectral measurement

Circular dichroism (CD) experiments were executed at room temperature in order to determine whether complexes **1** and **2** can trigger a conformational change in BSA protein. CD is a commanding technique for exploring changes in protein secondary structures during protein-drug interaction.[91] Hence, the CD spectra of BSA with or without complexes were recorded. At physiological pH, free BSA shows two strong negative bands in the far UV region at 208 nm (π-π^* transition) and 219 nm (n-π^* transition), which are characteristic of the α-helical structure of BSA.[92] As the intermolecular forces responsible for sustaining the secondary structures can be rehabilitated and activate a conformational change of the protein, such bands are considered to be vastly sensitive to the binding of drugs. Thus, individual addition of complexes **1** and **2** to BSA solution in diverse molar ratios resulted in a decrease in these negative band intensities without any noteworthy shifting of the peaks. Fig. IV.31 illustrate the CD spectra of BSA at physiological pH and in numerous molar ratios of protein to drug (1 : 0, 1 : 1, 1 : 3, 1 : 5). These results visibly recommend that the binding of our fabricated complexes with BSAs directed to an alteration in the secondary structure of these proteins.[93] The observed results were denoted in terms of mean residue ellipticity (MRE at 208 nm deg cm^2 $dmol^{-1}$) (Eq. IV.2).

The α-helix content of BSA for different BSA : complex ratios are 55.72% (1 : 0); 49.18% for **1** and 48.01% for **2** (1 : 1); 47.26% for **1** and 43.99% for **2** (1 : 3); 45.24% for **1** and 42.26% for **2** (1:5). The calculated results displayed a decrease of α-helix content from the native BSA. It was obvious that both of the complexes altered the shape of BSA and decreased the stability of the α-helix. The impact of complex **2** on BSA conformation was stronger than the complex **1** under identical circumstances.

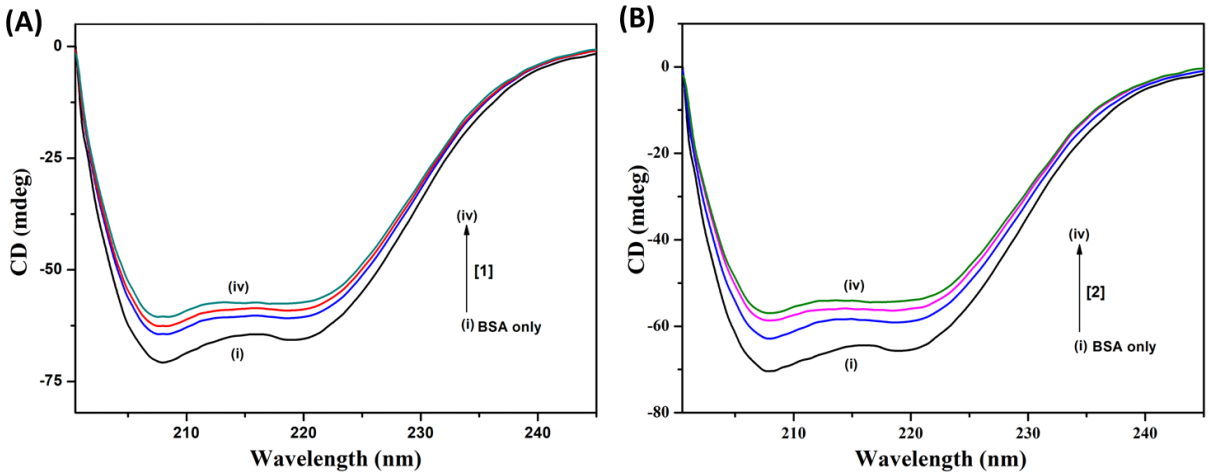

Fig. IV.31. CD spectrum of BSA with different molar ratios of complex **1** (A) and **2** (B).

IV.3.9. *In-vitro* Cytotoxicity Study

IV.3.9.1. Cell viability assay

Our study aimed to investigate the cytotoxic effects of the synthesized complexes, on MDA-MB-231 triple negative breast cancer cells. We conducted the MTT assay to assess cell viability after treating MDA-MB-231 cells with different concentrations (0, 5, 10, 15, 20, 25, 30, 35, 40, 45, 50 μM) of the complexes for 24 hours. The results [Fig. IV.32 (A)] demonstrated a significant cytotoxicity of complex **2**, as evidenced by a notable decrease in cell viability. The IC50 value for complex **2** was determined to be 15 ± 2.02 μM, indicating its potency in inducing cell death. In contrast, complex **1** exhibited a higher IC50 value of 40 ± 2.08 μM, suggesting a comparatively lower efficacy. Additionally, we compared the Cytotoxicity of complex **2** with that of the chemotherapeutic drug 5-fluorouracil, used as a positive control.[94] The IC50 value for 5-fluorouracil was found to be 10.15 ± 2.22 μg/mL. Furthermore, complex **1** and **2** demonstrated significantly lower toxicity towards normal HEK-293 cells when compared to MDA-MB-231 cells [Fig. IV.32 (B)]. These results highlight the potential of complex **2** as a promising candidate for further investigation in the treatment of breast cancer.

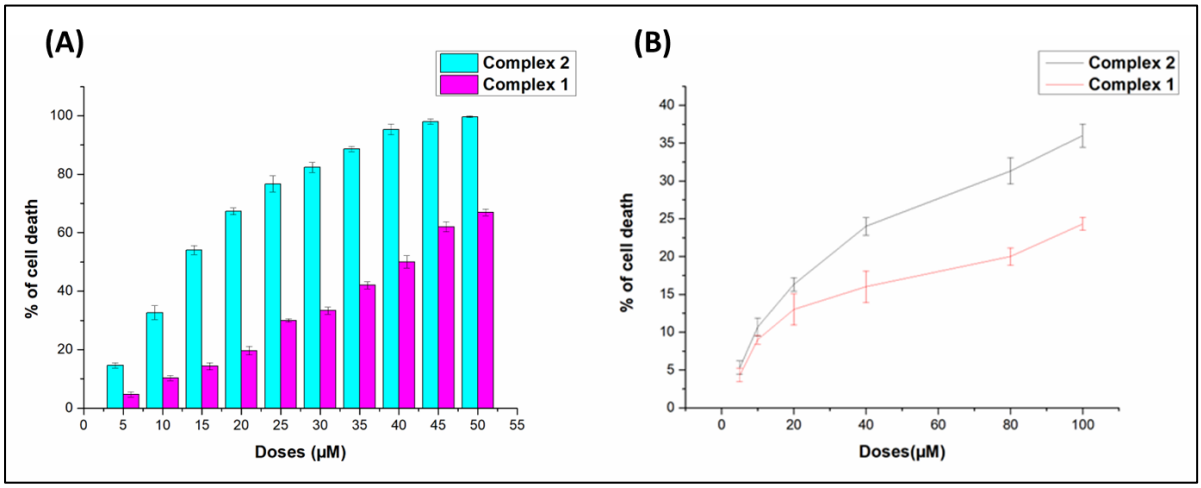

Fig. IV.32. Assessment of cell viability using MTT. Viability of MDA-MB-231 (A) and HEK-293 (B) cells were assesses by treating different doses of complexes **1** and **2.**

IV.3.9.2. Analysis of ROS generation using DCF-DA assay

The generation of reactive oxygen species (ROS) has been implicated in apoptosis-induced cell death and the subsequent damage to cellular components such as proteins, nucleic acids, lipids, membranes, and organelles. In our study, we employed 2′,7′-dichlorodihydrofluorescein diacetate (H2DCFDA) to estimate intracellular ROS levels.[95] Under normal conditions, H2DCFDA is a non-fluorescent molecule. However, in the presence of ROS, H2DCFDA is

oxidized to 2′,7′-dichlorofluorescein (DCF), which exhibits strong fluorescence. By utilizing flow cytometry, we quantified the fluorescence intensity of DCF and observed a concentration-dependent increase in ROS levels. This indicates that the treatment with complex **2** induces the generation of ROS in a dose-dependent manner (Fig. IV.33). These findings suggest a potential involvement of ROS in the cytotoxic effects of complex **2** and its role in apoptotic cell death.

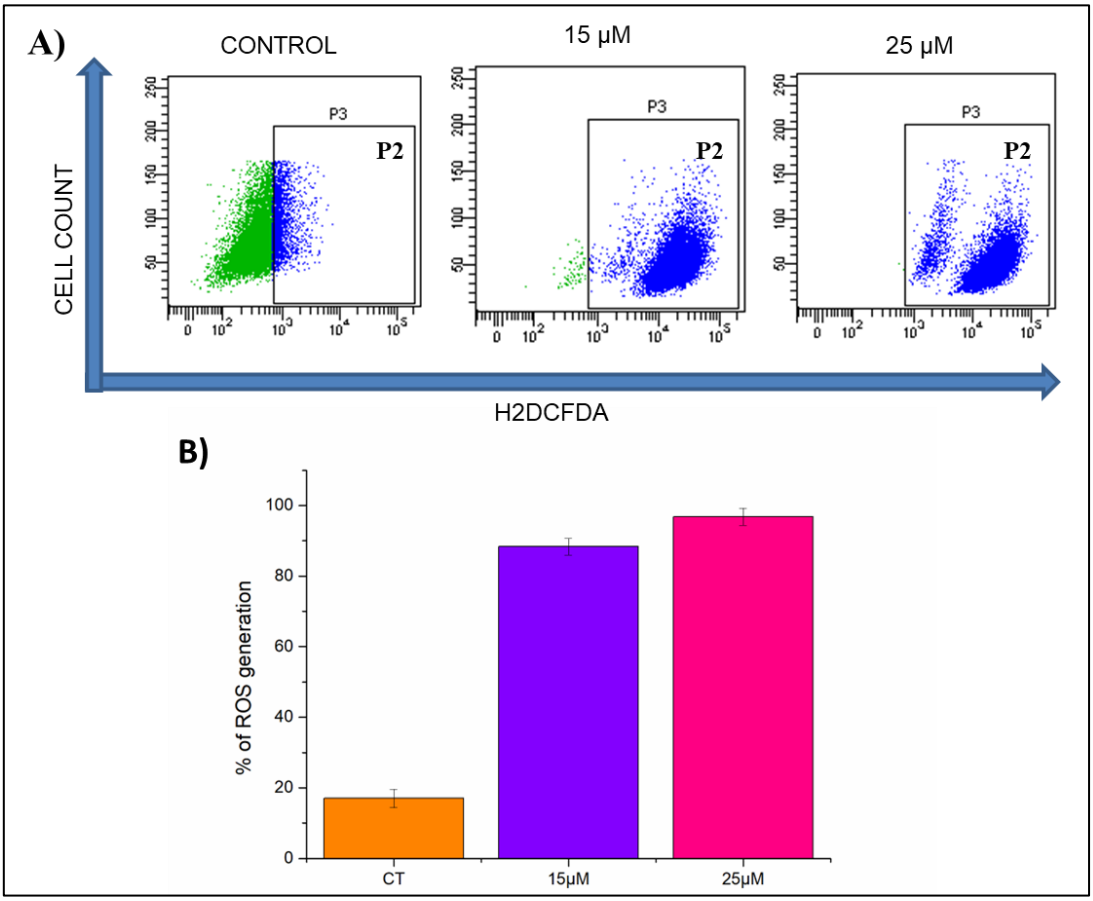

Fig. IV.33. Determination of ROS generation upon treatment of complex **2** on MDA-MB-231 triple negative breast cancer cell. (A) Intracellular ROS were measured using flow cytometry. (B) Comparison of DCFDA positive cell population.

IV.3.9.3. Flow cytometric analysis of apoptosis

To determine whether the cytotoxic effects of complexes were directly associated with apoptosis or necrosis, we conducted flow cytometry analysis using Annexin-V-FITC/Propidium Iodide (PI) staining. This assay allowed us to assess the exposed amount of phosphatidylserine on the outer membrane of cells, a characteristic feature of apoptotic cells.[96] Our results demonstrated a concentration-dependent increase in the percentage of apoptotic cells, both in the early apoptotic (EA) and late apoptotic (LA) stages, following treatment with complex **2**. Specifically, at a concentration of 15 uM, we observed 13.3% EA

and 24.8% LA cells, while at 25 uM, the percentages increased to 50.9% EA and 4.6% LA, compared to the control group (5.5% EA and 6% LA) (Fig. IV.34). These findings strongly suggest that the cytotoxic effects of complex **2** are primarily mediated through apoptosis rather than necrosis. Thus, our flow cytometry analysis using Annexin-V-FITC/PI staining provides evidence that complex **2** induces cell death in a concentration-dependent manner, predominantly through apoptosis. These results further support the cytotoxicity of complex **2** and its potential as a promising agent for targeting MDA-MB-231 triple negative breast cancer cells.

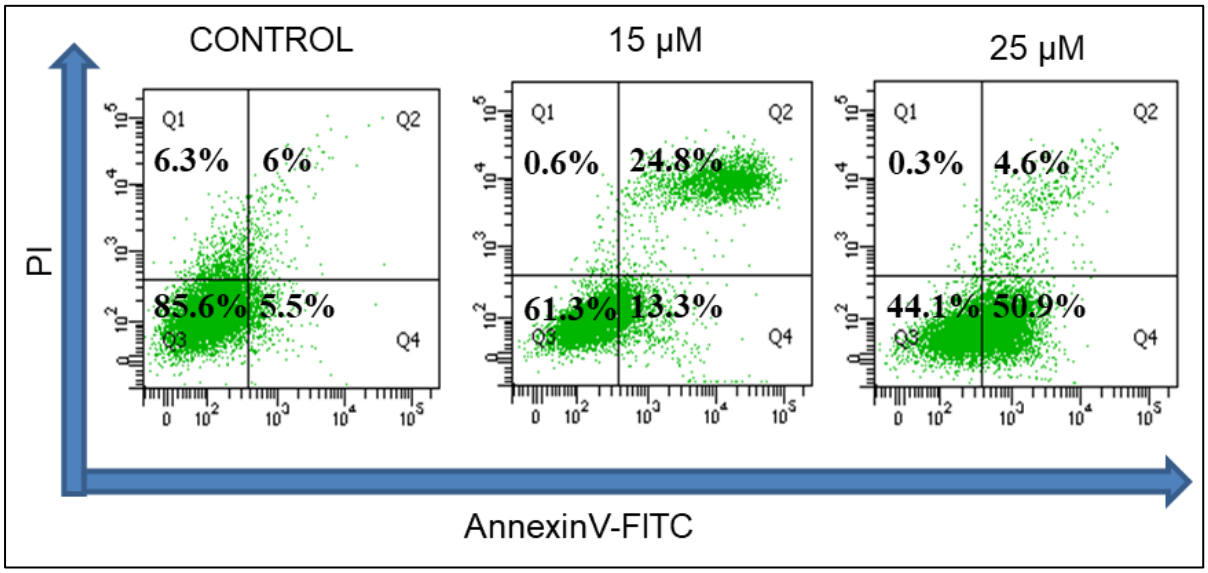

Fig. IV.34. Determination of apoptosis using Annexin V-FITC/ PI upon treatment of different concentration of complex **2**.

IV.3.9.4. Analysis of Mitochondrial membrane potential using flow cytometry

Apoptosis, a programmed cell death process, can be initiated through either the mitochondrial-dependent (intrinsic) pathway or the mitochondrial-independent (extrinsic) pathway, or a combination of both. Mitochondria, known as the powerhouses of the cell due to their role in ATP synthesis,[97] play a crucial role in regulating apoptosis.[98] We investigated the involvement of the mitochondrial-dependent pathway in complex **2** induced apoptosis in MDA-MB-231 cells. As a key event in apoptosis, we assessed the loss of mitochondrial membrane potential and examined the changes in the axis of pro- and anti-apoptotic proteins.[99] Our findings revealed a significant concentration-dependent increase in the loss of mitochondrial membrane potential following complex **2** treatment (30.9% for 15uM, 73.3% for 25uM, and 3.4% for control) (Fig. IV.35). This increase in mitochondrial membrane potential loss was accompanied by the enlargement of mitochondrial membrane pores, as evidenced by the elevated levels of JC1 green fluorescence intensity observed in complex **2**

treated cells. Additionally, we observed a distinct decrease in Bcl2 expression compared to the control cells, as indicated by fluorescence analysis from confocal images. Notably, the introduction of complex **2** into the cells resulted in increased ROS levels, concomitant with a decrease in Bcl2 expression. These various apoptotic stimuli led to the release of Cytochrome C from the mitochondria into the cytosol, where it plays a major role in caspase activation and subsequent cell death. The release of Cytochrome C initiates a cascade of events involving caspases, a family of proteases responsible for triggering apoptosis by cleaving specific enzymes. Our study demonstrated a concentration-dependent increase in caspase-3 and caspase-9 activity, further supporting the involvement of complex **2** in inducing apoptosis in MDA-MB-231 cells. Overall, our findings highlight the activation of the mitochondrial-dependent pathway in complex 2-induced apoptosis, characterized by the loss of mitochondrial membrane potential, altered expression of pro- and anti-apoptotic proteins, release of Cytochrome C, and subsequent caspase activation.[100] These results contribute to a better understanding of the mechanistic basis of complex 2-induced cytotoxicity in MDA-MB-231 triple-negative breast cancer cells.

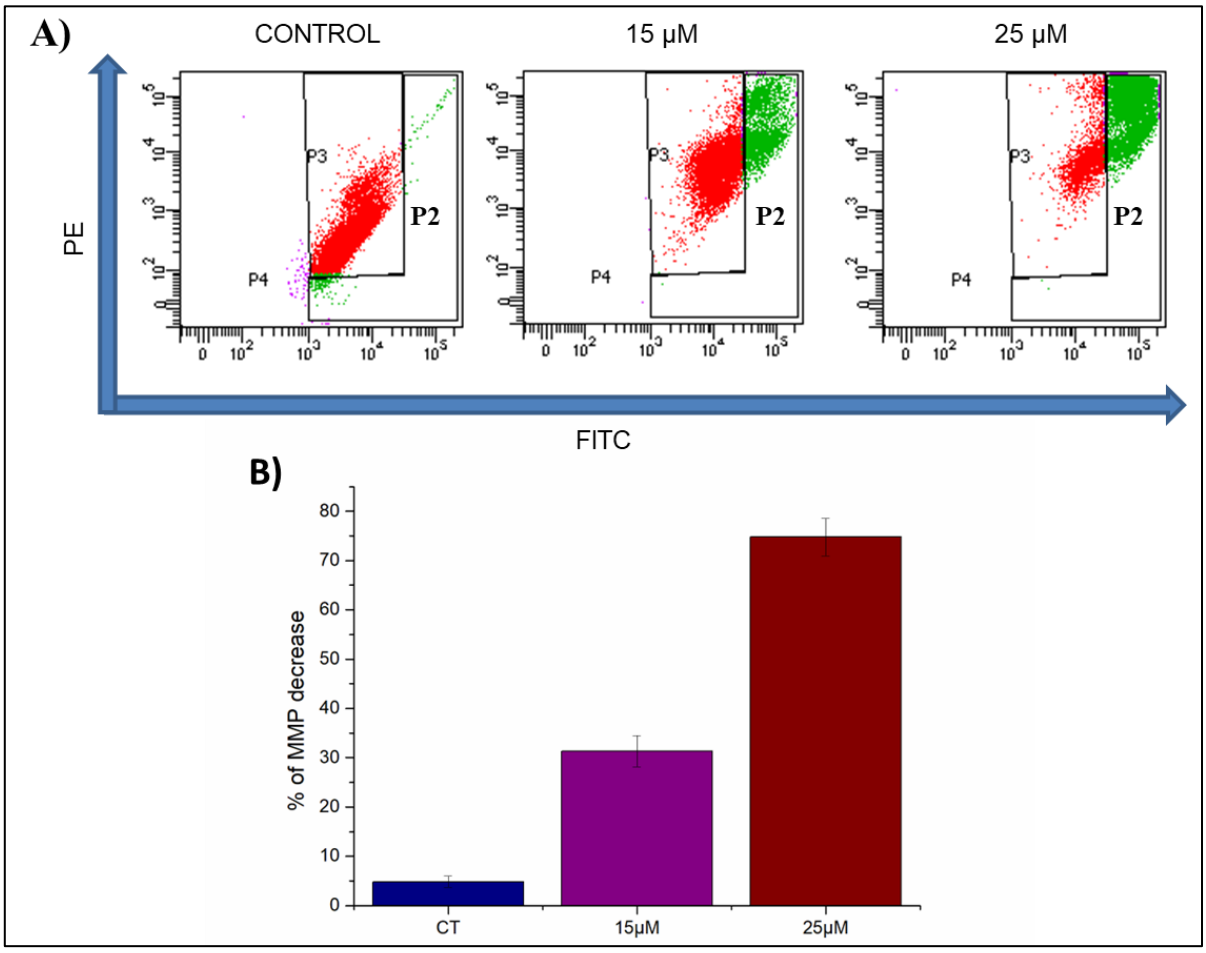

Fig. IV.35. Effect of complex 2 on Mitochondrial membrane potential (MMP). **(A)** JC1 Fluorescence measurement in MDA-MB-231 cells. **(B)** Comparison of MMP decrease.

IV.3.9.4. Evaluation of apoptotic markers protein through confocal microscopy

In the regulation of the mitochondrial-dependent apoptosis pathway, an essential redox-assisted transcription factor called p53 (tumor suppressor protein) plays a critical role.[101] Phosphorylation of p53 serves as a key mediator of mitochondrial-dependent apoptosis.[102] This post-translational modification of p53 enhances its ability to regulate the expression of proapoptotic members of the Bcl2 family proteins through transcriptional control. The phosphorylation of p53 targets specific sites on the protein, resulting in its activation and subsequent modulation of gene expression. This activated form of p53 exerts its regulatory influence on the proapoptotic members of the Bcl2 family, which are pivotal regulators of apoptosis. By controlling the transcription of these genes, phosphorylated p53 promotes the induction of apoptosis through the mitochondrial-dependent pathway.[103] The enhanced phosphorylation of p53 serves as a crucial step in the apoptotic response (Fig. IV.36), amplifying the apoptotic signals and facilitating the activation of downstream effectors involved in mitochondrial-dependent apoptosis. Through its role as a redox-assisted transcription factor, p53 contributes to the orchestration of a finely regulated apoptotic program by coordinating the expression of key apoptotic regulators. The involvement of p53 in the regulation of mitochondrial-dependent apoptosis underscores its significance as a tumor suppressor protein and its pivotal role in maintaining cellular homeostasis. The interplay between p53, mitochondrial function, and the apoptotic machinery represents an important axis in cellular responses to various apoptotic stimuli, including the induction of apoptosis by complex **2**. Understanding the intricate mechanisms governing p53-mediated apoptosis provides valuable insights into the complex processes underlying cancer biology and potential therapeutic strategies.

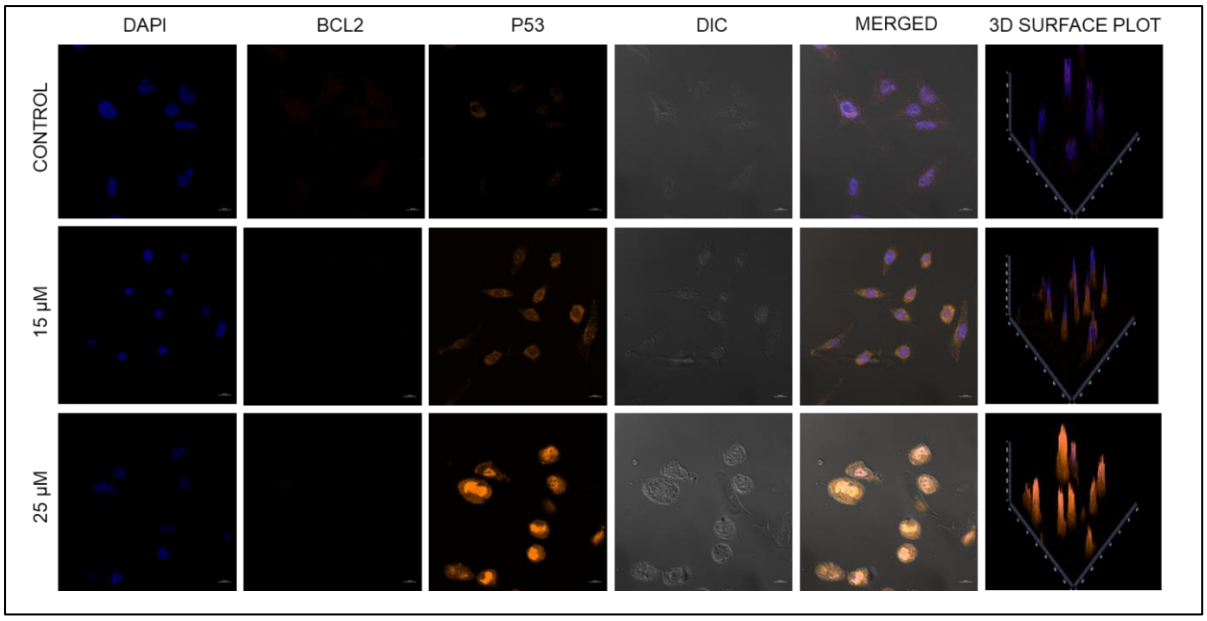

Fig. IV.36. Immunofluorescence images showing the expression of BCL2 and P53 pro and anti-apoptotic protein. DAPI was used for nuclear staining.

Caspases, a family of proteases, play a crucial role in the initiation and execution of apoptosis.[104] They are responsible for cleaving specific target proteins and enzymes, leading to the controlled dismantling of the cell. Caspase activation is a key event in the apoptotic process, and one of the upstream triggers for caspase activation is the release of cytochrome c (Fig. IV.37) from the mitochondria.[105]

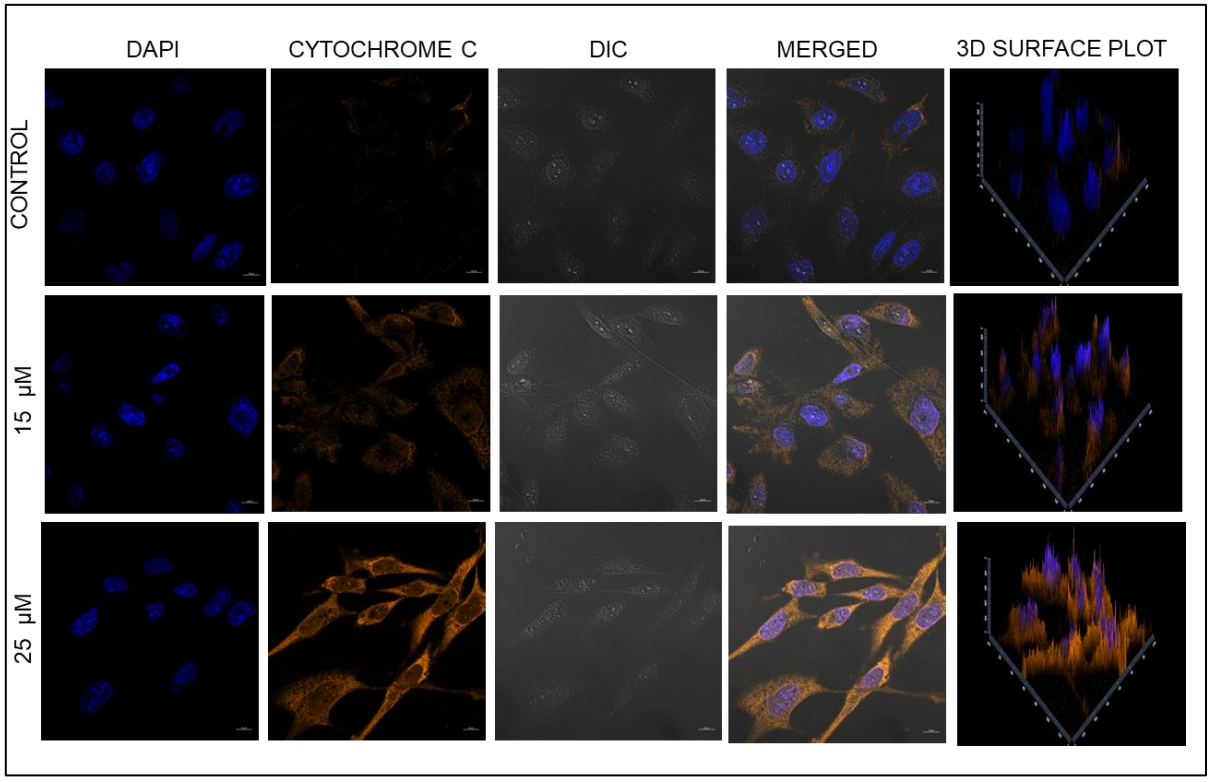

Fig. IV.37. Immunofluorescence images showing the expression of Cytochrome C and P21. DAPI was used for nuclear staining.

In our study, we observed a gradual increase in the levels of caspase-3 and caspase-9 in a concentration-dependent manner upon treatment with Pt(II) complex. This indicates that complex **2** induces the activation of caspases, specifically caspase-3 and caspase-9, in MDA-MB-231 breast cancer cells (Fig. IV.38). The upregulation of cytochrome c, which we previously observed due to the increased mitochondrial membrane potential loss induced by complex **2**, likely contributes to the activation of caspases and the initiation of apoptosis.

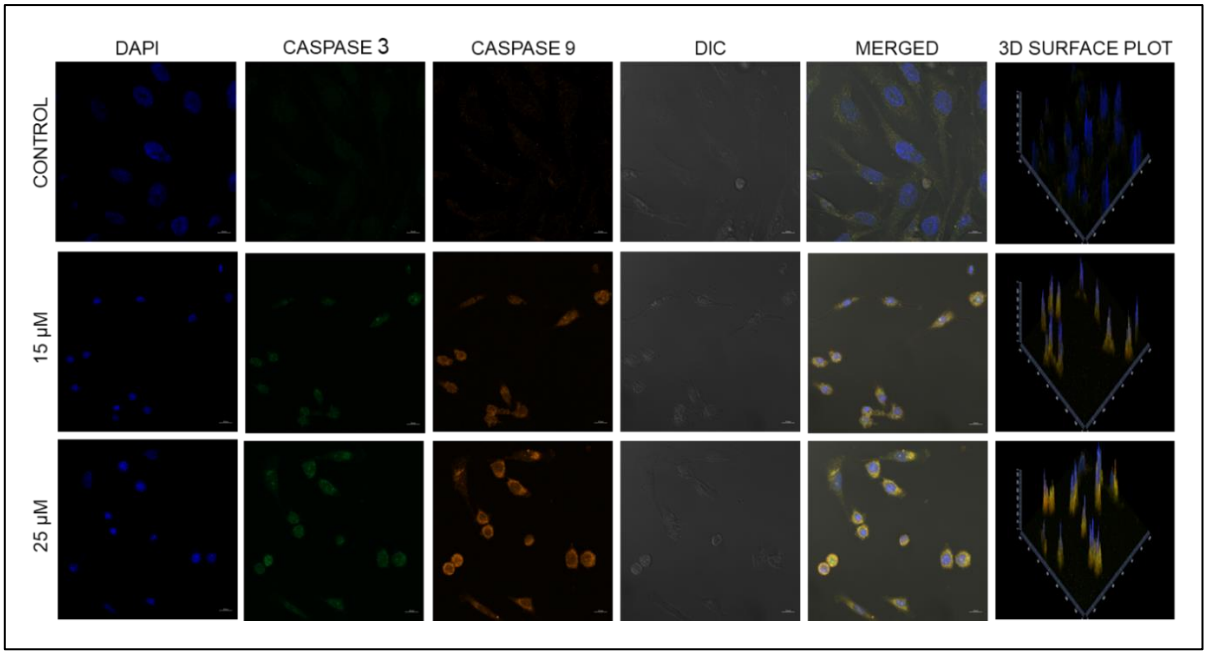

Fig. IV.38. Immunofluorescence images showing the expression of Caspase 3 and Caspase 9.

Furthermore, the confirmation of complex-induced cell death via apoptosis is supported by the evaluation of P53 and Bcl2 protein expression. As mentioned earlier, phosphorylated p53 plays a role in regulating the mitochondrial-dependent apoptosis pathway,[106] and its upregulation can promote the expression of proapoptotic members of the Bcl2 family. In our study, we observed a decrease in Bcl2 expression in complex 2-treated cells compared to control cells, indicating a shift towards a proapoptotic state.

The combined evidence of increased caspase-3 and caspase-9 activity, along with the modulation of P53 and Bcl2 protein expression, strongly supports the conclusion that complex **2** induces cell death in MDA-MB-231 cells through apoptosis. These findings provide valuable insights into the molecular mechanisms underlying the cytotoxic effects of complex **2** and its potential as a therapeutic agent for triple-negative breast cancer.

IV.4. Conclusions

The new palladium(II) and platinum(II) complexes, [Pd(MPMA)Cl_2] (**1**) and [Pt(MPMA)Cl_2] (**2**) with N,N donor Schiff base ligand (MPMA) were effectively fabricated and thoroughly characterized by several spectroscopy methods. X-ray structures reveal that the geometries of these complexes are slightly distorted from regular square planar geometry around the metal centre. The theoretical investigation on their structural optimization, HOMO-LUMO energy and calculated different reactivity descriptors by the DFT study provide an overview of their stability and reactivity. The electrophilicity index of complex **2** shows a little bit higher value

suggesting a higher affinity toward DNA and BSA. The molecular electrostatic potential (MEP) surface of the complexes evidently portrays the reactive region accessible for interactions. Further the interaction of CT DNA with both the complexes were investigated by employing the UV-visible method and binding constant values suggest that the complexes strongly bind with CT DNA. Here, the complex **2** shows more binding affinity to DNA than complex **1**. Additionally, binding abilities of the complexes with BSA also monitored by absorption and fluorescence spectroscopy and revealed the presence of static quenching. Moreover, the complexes were assessed for their primary in- vitro anticancer activities against triple negative breast cancer cell line (MDA-MB-231) and normal kidney cell line (HEK-293). Complex **2** exhibited potent anticancer activity against MDA-MB-231 cancer cell lines better than complex **1**. The major chemical and biological discoveries of this study have established the fact that the complexes can certainly display activity in human cancer cells in vitro in a practical range of concentrations signifying that these complexes are very capable candidates as antitumor reagents. Additional studies are necessary to evaluate their pharmacological properties in vivo and explain the authentic mechanism of their biological activity.

IV.5. References

1. (a) J. Karges, R.W. Stokes and S. M. Cohen, *Trends Chem.*, 2021, **3**, 523-534; (b) R. Lengacher, A. Marlin, D. Śmiłowicz and E. Boros, *Chem. Soc. Rev.*, 2022, **51**, 7715-7731; (c) H. Sung, J. Ferlay, R. L. Siegel, M. Laversanne, I. Soerjomataram, A. Jemal and F. Bray, *Ca Cancer J. Clin.*, 2021, **71**, 209-249.
2. B. Tylkowski, R. Jastrząb and A. Odani, *Phys. Sci. Rev.*, 2018, **3**, 20160007.
3. (a) A. Brown, S. Kumar and P. B. Tchounwou, *J. Cancer Ther.*, 2019, **11**; (b) S. Ghosh, *Bioorg. Chem.*, 2019, **88,** 102925.
4. S. Dasari and P. B. Tchounwou, *Eur. J. Pharmacol.*, 2014, **740**, 364-378.
5. A. M. Florea and D. Büsselberg, *Cancers*, 2011, **3**, 1351-1371.
6. S. N. Mbugua, N. R. S. Sibuyi, L. W. Njenga, R. A. Odhiambo, S. O. Wandiga, M. Meyer, R. A. Lalancette and M. O. Onani, *ACS Omega*, 2020, **25**, 14942-14954.
7. E. Petruzzella, R. Sirota, I. Solazzo, V. Gandin and D. Gibson, *Chem. Sci*, 2018, **9**, 4299-4307.
8. T. C. Johnstone, K. Suntharalingam and J. Lippard, *Chem. Rev.*, 2016, **116**, 3436-3486.
9. T. C. Johnstone, G. Y. Park and S. J. Lippard, *Cancer Res.*, 2014, **34**, 471-476.

10. (a) Y. Gou, G. Huang, J. Li, F. Yang and H. Liang, *Coord. Chem. Rev.*, 2021, **441**, 213975; (b) M. G. Ferraro, M. Piccolo, G. Misso, R. Santamaria and C. Irace, *Pharm.*, 2022, **14**, 954.
11. (a) A. R. Kapdi and I. J. S. Fairlamb, *Chem. Soc. Rev.*, 2014, **43**, 4751; (b) A. Garoufis, S. K. Hadjikakou and N. Hadjiliadis, *Coord. Chem. Rev.*, 2009, **253**, 1384.
12. M. D. Coskun, F. Ari, A. Y. Oral, M. Sarimahmut, H.M. Kutlu, V. T. Yilmaz and E. Ulukaya, *Bioorg. Med. Chem*., 2013, **21**, 4698.
13. J. Espino, E. Fernández-Delgado, S. Estirado, F. de la Cruz-Martinez, S. Villa-Carballar, E. Viñuelas-Zahínos, F. Luna-Giles and J. A. Pariente, *Sci. Rep.*, 2020, **10**, 1-16.
14. (a) H. A. Rudbari, N. Kordestani, J. V. Cuevas-Vicario, M. Zhou, T. Efferth, I. Correia, T. Schirmeister, F. Barthels, M. Enamullah, A. R. Fernandes and N. Micale. *New J. Chem.*, 2022, **46**, 6470-6483; (b) D. Simić, M. Zarić, I. Nikolić, R. Živković-Zarić, P. Čanović, A. Kočović, I. Radojević, I. Raković, S. Jovičić Milić, Đ. Petrović, D. Stojković, N. Vuković, M.Kačániová, M. Vukić and V. Jevtić, *Dalton Trans.*, 2022, **51**, 1191-1205.
15. Ž. D. Bugarčić, J. Bogojeski and R. van Eldik, *Coord. Chem. Rev.*, 2015, **292**, 91-106.
16. (a) I. de la Cueva-Alique, E. de la Torre-Rubio, L. Muñoz-Moreno, A. Calvo-Jareño, A. Pérez-Redondo, L. Gude, T. Cuenca and E. Royo, *Dalton Trans.*, 2022, **51**, 12812-12828; (b) M. Vojtek, M. P. Marques, I. M. Ferreira, H. Mota-Filipe and C. Diniz, *Drug Discov. Today*, 2019, **24**,1044-1058; (c) Y. G. Sun, D. Sun, W. Yu, M. C. Zhu, F. Ding, Y. N. Liu, E. J. Gao, S. J. Wang, G. Xiong, I. Dragutan and V. Dragutan, *Dalton Trans.*, 2013, **42**, 3957-3967.
17. (a) F. M. Ibrahim and S. M. Abdalhadi, *Al-Nahrain j. sci.*, 2021, **24**, 1-10; (b) D. T. Sakhare, *Int. j. adv. eng. res. sci.*, 2020, **6**, 1538-1544; (c) A. Ali, M. Pervaiz, Z. Saeed, U. Younas, R. Bashir, S. Ullah, S. M. Bukhari, F. Ali, S. Jelani, A. Rashid and A. Adnan, *Inorg. Chem. Commun.*, 2022, **145**, 109903.
18. (a) M. N. Uddin, S. S. Ahmed and S. R. Alam, *J. Coord. Chem.*, 2020, **73**, 3109-3149; (b) N. V. Loginova, H. I. Harbatsevich, N. P. Osipovich, G. A. Ksendzova, T. V. Koval'chuk and G. I. Polozov, *Curr. Med. Chem.*, 2020, **27**, 5213-5249.
19. J. Madureira, C. I. V. Ramos, M. Marques, C. Maia, B. D. Sousa, L. Campino, M. G. Santana-Marques and N. Farrell, *Inorg. Chem*., 2013, **52**, 8881-8894.
20. (a) C. Icsel and V. T. Yilmaz, *DNA Cell Biol*., 2013, **32**, 165-172; (b) B. Onfelt, P. Lincoln and B. Nordén, *J. Am. Chem. Soc*., 2001, **123**, 3630.
21. (a) A. M. Mansour and O. R. Shehab, *Dalton Trans.*, 2018, **47**, 3459-3468; (b) A. Zianna, G. D. Geromichalos, A. Pekou, A. G. Hatzidimitriou, E. Coutouli-Argyro poulou, M. Lalia-Kantouri, A. A. Pantazaki and G. Psomas, *J. Inorg. Biochem.*, 2019, **199**, 110792.
22. N. Joksimović, N. Janković, J. Petronijević, D. Baskić, S. Popovic, D. Todorović, M. Zarić, O. Klisurić, M. Vraneš, A. Tot and Z. Bugarčić, *Med. Chem.*, 2020, **16**, 78-92.

23. N. Shahabadi, F. Shiri and R. Khodarahmi, *J. Mol. Liq.*, 2022, **345**, 117904.
24. D. Cocic, S. Jovanovic, S. Radisavljevic, J. Korzekwa, A. Scheurer, R. Puchta, D. Baskic, D. Todorovic, S. Popovic, S. Matic and B. Petrovic, *J. Inorg. Biochem*., 2018, **189**, 91-102.
25. (a) N. Rajendiran and J. Thulasidhasan, *Spectrochim, Acta Part A Mol. Biomol. Spectrosc*., 2015, **144**, 183-191; (b) T. Peters, *Serum Albumin*, 1985, **37**, 161-245.
26. A. Divsalar, I. Zhila, A. A. Saboury, M. Nabiuni, M. Razmi and H. Mansuri-Torshizi, *J. Iran. Chem. Soc*., 2013, **10**, 951-959.
27. (a) G.M. Sheldrick, *Acta Cryst*., 2008, **A64**, 112-122; (b) G.M. Sheldrick, *Acta Cryst*., 2015, **C71**, 3-8.
28. (a) A. D. Becke, *J. Chem. Phys*., 1993, **98**, 5648-5652; (b) C. Lee, W. Yang and R. G. Parr, *Phys. Rev. B: Condens. Matter Mater. Phys*., 1988, **37**, 785-789.
29. (a) P. J. Hay and W. R. Wadt, *J. Chem. Phys*., 1985, **82**, 270-283; (b) W. R. Wadt and P. J. Hay, *J. Chem. Phys*., 1985, **82**, 284-298; (c) P. J. Hay and W. R. Wadt, *J. Chem. Phys*., 1985, **82**, 299-310.
30. (a) R. Ditchfield, W. J.Hehre and J.A. Pople, *J. Chem. Phys*.,1971, **54**, 724; (b) W. Hehre, J. R. Ditchfield and J. A. Pople, *J. Chem. Phys*., 1972, **56**, 2257.
31. M. J. Frisch, G. W. Trucks, H. B. Schlegel, G. E. Scuseria, M. A. Robb, J. R. Cheeseman, G. Scalmani, V. Barone, B. Mennucci, G. A. Petersson, H. Nakatsuji, M. Caricato, X. Li, H. P. Hratchian, A. F. Izmaylov, J. Bloino, G. Zheng, J. L. Sonnenberg, M. Hada, M. Ehara, K. Toyota, R. Fukuda, J. Hasegawa, M. Ishida, T. Nakajima, Y. Honda, O. Kitao, H. Nakai, T. Vreven, J. A. Montgomery, Jr., J. E. Peralta, F. Ogliaro, M. Bearpark, J. J. Heyd, E. Brothers, K. N. Kudin, V. N. Staroverov, R. Kobayashi, J. Normand, K. Raghavachari, A. Rendell, J. C. Burant, S. S. Iyengar, J. Tomasi, M. Cossi, N. Rega, J. M. Millam, M. Klene, J. E. Knox, J. B. Cross, V. Bakken, C. Adamo, J. Jaramillo, R. Gomperts, R. E. Stratmann, O. Yazyev, A. J. Austin, R. Cammi, C. Pomelli, J. W. Ochterski, R. L. Martin, K. Morokuma, V. G. Zakrzewski, G. A. Voth, P. Salvador, J. J. Dannenberg, S. Dapprich, A. D. Daniels, O¨. Farkas, J. B. Foresman, J. V. Ortiz, J. Cioslowski and D. J. Fox, Gaussian 09, Revision D.01, Gaussian, Inc., Wallingford CT, 2009.
32. (a) R. Bauernschmitt and R. Ahlrichs, *Chem. Phys. Lett*., 1996, **256**, 454-464; (b) R. E. Stratmann, G. E. Scuseria and M. J. Frisch, *J. Chem. Phys*., 1998, **109**, 8218; (c) M. E. Casida, C. Jamorski, K. C. Casida and D. R. Salahub, *J. Chem. Phys*., 1998, **108**, 4439-4449.
33. (a) V. Barone and M. Cossi, *J. Phys. Chem. A*, 1998, **102**, 1995-2001; (b) M. Cossi and V. Barone, *J. Chem. Phys*., 2001, **115**, 4708-4717; (c) M. Cossi, N. Rega, G. Scalmani and V. Barone, *J. Comput. Chem*., 2003, **24**, 669-681.
34. N. M. O'Boyle, A. L. Tenderholt, K. M. Langner, *J. Comput. Chem*., 2008, **29**, 839-845.
35. (a) M. A. Spackman and D. Jayatilaka, *Cryst. Eng. Comm*., 2009, **11**, 19-32; (b) F. L. Hirshfeld, *Theor. Chem. Acc*.,1977, **44**, 129-138; (c) H. F. Clausen, M. S. Chevallier, M.A.

Spackman and B. B. Iversen, *New J. Chem*., 2010, **34**, 193-199.

36. (a) A. L. Rohl, M. Moret, W. Kaminsky, K. Claborn, J. J. McKinnon and B. Kahr, *Cryst. Growth Des*., 2008, **8**, 4517-4525; (b) A. Parkin, G. Barr, W. Dong, C. J. Gilmore, D. Jayatilaka, J. J. McKinnon, M. A. Spackman and C. C. Wilson, *Cryst. Eng. Comm.*, 2007, **9**, 648-652; (c) M. A. Spackman and J. J. McKinnon, *Cryst. Eng. Comm.*, 2002, **4**, 378-392.
37. (a) C. F. Mackenzie, P. R. Spackman, D. Jayatilaka and M. A. Spackman, *IUCrJ*, 2017, **4**, 575-587; (b) P. R. Spackman, M. J. Turner, J. J. McKinnon, S. K. Wolff, D. J. Grimwood, D. Jayatilaka and M. A. Spackman, *J. Appl. Crystallogr*., 2021, **54**, 1006-1011.
38. M. Sirajuddin, S. Ali and A. Badshah, *J. Photochem. Photobiol.*, B, 2013, **124**, 1-19.
39. S. Dasari and A. K. Patra, *Dalton Trans*., 2015, **44**, 19844-19855.
40. (a) M. Kumar, G. Kumar, N. K. Mogha, R. Jain, F. Hussain and D. T. Masram, *Spectrochim. Acta*, 2019, **212**, 94–104; (b) M. Kumar, N. K. Mogha, G. Kumar, F. Hussain and D. T. Masram, *Inorg. Chim. Acta*, 2019, **490**, 144–154.
41. (a) F. Kratz, *J Control Release*., 2008, **132**, 171-183; (b) B. Demoro, R. F. De Almeida, F. Marques, C. P. Matos, L. Otero, J. C. Pessoa, I. Santos, A. Rodríguez, V. Moreno, J. Lorenzo and D. Gambino, *Dalton Trans*., 2013, **42**, 7131-7146; (c) V. D. Suryawanshi, L. S. Walekar, A. H. Gore, P. V. Anbhule and G. B. Kolekar, *J. Pharm. Anal*., 2016, **6**, 56–63.
42. S. Tunç, A. Çetinkaya and O. Duman, *J. Photochem. Photobiol. B: Biol*., 2013, **120**, 59-65.
43. (a) M. Kumar, G. Kumar, K. M. dadure and D. T. Masram, *New J. Chem*., 2019, **43**,15462–15481; (b) S. Afrin, Y. Rahman, M. Alhaji Isa, S. Ahmed, M. Tabish, *J. Biomol. Struct. Dyn*., 2020, **38**, 1375-1387.
44. H. Gao, L. Lei, J. Liu, Q. Kong, X. Chen and Z. Hu, J. *Photochem. Photobiol*., A, 2004, **167**, 213–221.
45. A. Banerjee, M. Mohanty, S. Lima, R. Samanta, E. Garribba, T. Sasamori and R. Dinda, *New J. Chem*., 2020, **44**, 10946-10963.
46. S. U. Parsekar, P. Velankanni, S. Sridhar, P. Haldar, N. A. Mate, A. Banerjee, P. K. Sudhadevi Antharjanam, A. P. Koley and M. Kumar, *Dalton Trans*., 2020, **49**, 2947-2965.
47. T. Mosmann, *J. Immunol. Methods*, 1983, **65**, 55-63.
48. S. K. Dey, D. Bose, A. Hazra, S. Naskar, A. Nandy, R. N. Munda, S. Das, N. Chatterjee, N. B. Mondal, S. Banerjee and K. D. Saha, *PLoS One*, 2013, **8**, 58055.
49. A. Nandy, S. K. Dey, S. Das, R. N. Munda, J. Dinda and K. D. Saha, *Mol. Cancer*, 2014, **13**, 1-14
50. A. J. Lambert and M. D. Brand, *Biochem. J.*, 2004, **382**, 511-517.
51. T. M. Paravicini and C. G. Sobey, *Clin. Exp. Pharmacol. Physiol.*, 2003, **30**, 855-859.
52. S. Hamada and S. Fujita, *Histochem. Cell Biol.* 1983, **79**, 219-226.
53. J. C. Kern and J. P. Kehrer, *Chem. Biol. Interact.*, 2002, **139**, 79-95.

54. S. Biswas, C. K. Manna, R. Naskar, A. Das and T. K. Mondal, *Inorganica Chim. Acta*, 2021, **515**, 120096;
55. B. Bera, S. Mondal, S. Gharami, R. Naskar, K. D. Saha and T. K. Mondal, *New J. Chem.*, 2022, **46**, 11277-11285.
56. (a) J. A. Alvarez-Herna´ndez, N. Andrade-Lo´pez, J. G. Alvarado-Rodrı´guez, S. Gonza´lez-Montiel, L. A. Za´rate- Herna´ndez and J. Cruz-Borbolla, *Polyhedron*, 2022, **214**, 115635; (b) S. Biswas, P. Roy and T. K. Mondal, *J. Mol. Struct.*, 2017, **1142**, 110–115; (c) D. Qiu, Y. Guo, H. Wang, X. Bao, Y. Feng, Q. Huang, J. Zeng and G. Qiu, *Inorg. Chem. Commun*., 2011, **14**, 1520–1524.
57. (a) E. Ferna´ndez-Delgado, F. de la Cruz-Martı´nez, C. Gala´n, L. Franco, J. Espino, E. Vin˜uelas-Zahı´nos, F. Luna-Giles and I. Bejarano, *J. Inorg. Biochem*., 2020, **202**, 110870; (b) E. Ferna´ndez-Delgado, S. Estirado, J. Espino, E. Vin˜uelas-Zahı´nos, F. Luna-Giles, A. B.-R. Moratinos and J. A. Pariente, *J. Inorg. Biochem*., 2022, **227**, 111688.
58. (a) I. B. Obot, D. D. Macdonald and Z. M. Gasem, *Corros. Sci*., 2015, **99**, 1-30: (b) D. K. Verma, R. Aslam, J. Aslam, M. A. Quraishi, E. E. Ebenso and C. Verma, *J. Mol. Struct*., 2021, **1236**, 130294.
59. A. Thamarai, R. Vadamalar, M. Raja, S. Muthu, B. Narayana, P. Ramesh, R. Raj Muhamed, S. Sevvanthi and S. Aayisha, *Spectrochim. Acta A Mol. Biomol. Spectrosc.*, 2020**, 226**, 117609.
60. (a) V. Choudhary, A. Bhatt, D. Dash and N. Sharma, *J. Comput. Chem.*, 2019, **40**, 2354-2363; (b) M. Miar, A. Shiroudi, K. Pourshamsian, A. R. Oliaey and F. Hatamjafari, *J. Chem. Res*., 2021, **45**, 147-158.
61. A. G. Martynov, J. Mack, A. K. May, T. Nyokong, Y. G. Gorbunova and A. Y. Tsivadze, *ACS omega*, 2019, **4**, 7265-7284.
62. (a) M. S. A. Abdel-Mottaleb and S. N. Ali, *Int. J. Photoenergy*, 2016; (b) M. K. Chaudhary, A. Srivastava, K. K. Singh, P. Tandon and B. D. Joshi, *Comput Theor Chem.*, 2020, **1191**, 113031; (c) M. Feizi-Dehnayebi, E. Dehghanian and H. Mansouri-Torshizi, *J. Mol. Struct.*, 2021, **1240**, 130535.
63. (a) P. R. Spackman, M. J. Turner, J. J. McKinnon, S. K. Wolff, D. J. Grimwood, D. Jayatilaka and M. A. Spackman, *J. Appl. Crystallogr.*, 2021, **54**, 1006-1011; (b) S. L. Tan, M. M. Jotani and E. R. Tiekink, *Acta Crystallogr. E: Crystallogr.*, 2019, **75**, 308-318.
64. (a) A. Fatima, G. Khanum, A. Sharma, K. Garima, S. Savita, I. Verma, N. Siddiqui and S. Javed, *J. Mol. Struct.*, 2022, **1249**, 131571; (b) A. Fatima, M. Singh, N. Agarwal, I. Verma, R. J. Butcher, N. Siddiqui and S. Javed, *J. Mol. Liq.*, 2021, **343**, 117549.
65. (a) G. Lente, I. Fábián and A. J. Poë, *New J. Chem.*, 2005, **29**, 759-760; (b) T. Yamamoto, S. Wakabayashi and K. Osakada, *J. Organomet. Chem.*, 1992, **428**, 223-237.
66. (a) R. Mishra, A. Kumar, R. Chandra and D. Kumar, *Int J. Sci. Technol. Soc.*, 2017, **3**, 11-27.; (b) M. Misiak F. Mantegazza and G. L. Beretta, *Curr. Pharm. Des.*, 2016, **22**, 6596-6611.

67. (a) Q. L. Zhang, J. G. Liu, H. Chao, G. Q. Xue and L. N. Ji, *J. Inorg. Biochem*., 2001, **83**, 49-55; (b) Z. C. Liu, B. D. Wang, B. Li, Q. Wang, Z. Y. Yang, T. R. Li and Y. Li, *Eur. J. Med. Chem*., 2010, **45**, 5353.
68. (a) M. Hong, G. Chang, R. Li and M. Niu, *New J. Chem*., 2016, **40**, 7889-7900; (b) L. Tjioe, A. Meininger, T. Joshi, L. Spiccia and B. Graham, *Inorg. Chem*., 2011, **50**, 4327-4339.
69. O. Novakova, J. Kasparkova, O. Vrana, P. M. van Vliet, J. Reedijk and V. brabec, *Biochemistry*, 1995, **34**, 12369-12378.
70. (a) A. M. Mansour and O. R. Shehab, *Dalton Trans.*, 2018, **47**, 3459-3468; (b) Z. Mandegani, Z. Asadi, M. Asadi, H. R. Karbalaei-Heidari and B. Rastegari, *Dalton Trans*., 2016, **45**, 6592-6611.
71. (a) A. H. Wang, J. Nathans, G. van der Marel, J. H. van Boom and A. Rich, *Nature*, 1978, **276**, 471; (b) Z. Ma, J. R. Choudhury, M. W. Wright, C. S. Day, G. Saluta, G. L. Kucera and U. Bierbach, *J. Med. Chem*., 2008, **51**, 7574; (c) K. R. Barnes and S. J. Lippard, *Metal ions in biological systems*, 2004, **42**, 143-177.
72. A. Wolfe, G. H. Shimer Jr and T. Meehan, *Biochem*., 1987, **26**, 6392-6396.
73. (a) S. Wongsuwan, J. Chatwichien, W. Sirisaksoontorn, K. Chainok, A. Songsasen and R. Chotima, *New J. Chem.*, 2023, **47**, 10624-10637; (b) A. Das, M. Saha, S. Mandal, S. Das, K. D. Saha and T. K. Mondal, *New J. Chem*., 2023, **47**, 4931-4943.
74. (a) J. R. Lakowicz, springer, 2006; (b) D. J. Desilets, P. T. Kissinger, F. E. Lytle, *Anal. Chem.*, 1987, **59**, 1244-1246.
75. (a) L. Haque, S. Bhuiya, R. Tiwari, A. B. Pradhan and S. Das, *RSC Adv*., 2016, **6**, 83551-83562: (b) Y. Wang, G. Lin, J. Hong, T. Lu, L. Li, N. Okabe and M. Odoko, *Inorganica Chim. Acta*, 2009, **362**, 377-384; (c) M. Kumar, G. Kumar, N. K. Mogha, R. Jain, F. Hussain and D. T. Masram, *Acta A Mol. Biomol. Spectrosc*., 2019, **212**, 94-104; (d) M. Kumar, N. K. Mogha, G. Kumar, F. Hussain and D. T. Masram, *Inorganica Chim. Acta*, 2019. **490**, 144-154.
76. (a) A. B. Pradhan, L. Haque, S. Bhuiya and S. Das, *RSC Adv.*, 2015, **5**, 10219-10230; (b) A. B. Pradhan, L. Haque, S. Bhuiya, A. Ganguly and S. Das, *J. Phys. Chem.*, B 2015, **119**, 6916-6929.
77. (a) S. De, S. R. Chaudhuri, A. Panda, G. R. Jadhav, R. S. Kumar, P. Manohar, N. Ramesh, A. Mondal, A. Moorthy, S. Banerjee and P. Paira, *New J. Chem.*, 2019, **43**, 3291-3302; (b) K. Nagaraj and S. Arunachalam, *Int. J. Biol. Macromol*., 2013, **62**, 273-280.
78. (a) G. Lambrinidis, T. Vallianatou and A. Tsantili-Kakoulidou, *Adv. Drug Deliv. Rev*., 2015, **86**, 27-45; (b) Y. Yuan, S. Chang, Z. Zhang, Z. Li, S. Li, P. Xie, W. P. Yau, H. Lin, W. Cai, Y. Zhang and X. Xiang, *Chemom. Intell. Lab. Syst.*, 2020, **199**, 103962; (c) N. A. Kratochwil, W. Huber, F. Müller, M. Kansy and P. R. Gerber, *Biochem. Pharmacol*., 2002, **64**, 1355-1374.
79. (a) P. R. Callis, *J. Mol. Struct*., 2014, **1077**, 14-21; (b) A. Sharma, J. Enderlein and M. Kumbhakar, *J. Phys. Chem. Lett*., 2017, **8**, 5821-5826.

80. (a) K. Jeyalakshmi, J. Haribabu, C. Balachandran, N. S. P. Bhuvanesh, N. Emi and R. Karvembu, *New J. Chem*., 2017, **41**, 2672-2686. (b) K. Karami, S. Hashemi, J. Lipkowski, F. Mardani, A. A. Momtazi-borojeni and Z. M. Lighvan, *Appl. Organomet. Chem*., 2017, **31**, 3740; (c) X. F. Zhao, Y. Ouyang, Y. Z. Liu, Q. J. Su, H. Tian, C. Z. Xie and J. Y. Xu, *New J. Chem*., 2014, **38**, 955-965.
81. (a) N. Biswas, S. Khanra, A. Sarkar, S. Bhattacharjee, D. P. Mandal, A. Chaudhuri, S. Chakraborty and C. R. Choudhury, *New J. Chem.*, 2017, **41**, 12996-13011; (b) K. Karami, M. Alinaghi, Z. Amirghofran, J. Lipkowski and A. A. Momtazi-borojeni, *New J. Chem.*, 2018. **42**,574-586.
82. (a) K. Karami, S. Hashemi, J. Lipkowski, F. Mardani, A. A. Momtazi-borojeni and Z. M. Lighvan, *Appl. Organomet. Chem.*, 2017, **31**, 3740; (b) D. G. Isom, C. A. Castañeda, B. R. Cannon, P. D. Velu and B. García-Moreno, *Proc. Natl. Acad. Sci.*, 2010, **107**, 16096-16100.
83. (a) Y. Xiang and F. Wu, *Spectrochim. Acta A Mol. Biomol. Spectrosc*., 2010, **77**, 430-436: (b) P. Acharya, R. Maity, A. Kuila, T. Maity, S. Maity, N. Sepay and B. C. Samanta, *Appl. Organomet. Chem*., 2022, **36**, 6640.
84. D. S. Raja, N. S. Bhuvanesh and K. Natarajan, *Dalton Trans*., 2012, **41**, 4365-4377.
85. J. N. Miller, *J. Pharm. Biomed. Anal*., 1983, **1**, 525-535.
86. M. Makarska-Bialokoz and A. Lipke, *J. Mol. Liq*., 2019, **276**, 595-604.
87. (a) S. Mukhopadhyay, R. K. Gupta, R. P. Paitandi, N. K. Rana, G. Sharma, B. Koch, L. K. Rana, M. S. Hundal and D. S. Pandey, *Organomet*., 2015, **34**, 4491-4506; (b) F. F. Tian, F. L. Jiang, X. L. Han, C. Xiang, Y. S. Ge, J. H. Li, Y. Zhang, R. Li, X. L. Ding and Y. Liu, *Phys. Chem. B*., 2010, **114**, 14842-14853.
88. J. R. Lakowicz, Principles of Fluorescence Spectroscopy, 3rd edition, 2006.
89. A. Banerjee, M. Mohanty, S. Lima, R. Samanta, E. Garribba, T. Sasamori and R. Dinda, *New J. Chem*., 2020, **44**, 10946-10963.
90. (a) G. Sahu, A. Banerjee, R. Samanta, M. Mohanty, S. Lima, E. R. Tiekink and R. Dinda, *Inorg. Chem*., 2021, **60**, 15291-15309; (b) T. A. Wani, A. H. Bakheit, S. Zargar, M. A. Hamidaddin and I. A. Darwish, *PLoS One*., 2017, **12**, 0176015; (c) F. Jalilehvand, A. E. Garcia, P. Niksirat, Y. Z. Finfrock and B. S. Gelfand, *J. Inorg. Biochem*., 2021, **224**, 111556.
91. (a) M. Kumar, G. Kumar and D. T. Masram, *New J. Chem*., 2020, **44**, 8595-8613; (b) Z. Chen, S. Zhang, Z. Zhu and Y. Zhang, *New J. Chem*., 2017, **41**, 6340-6348.
92. (a) Z. Tian, L. Tian, M. Shi, S. Zhao, S. Guo, W. Luo, C. Wang and Z. Tian, *J. Photochem. Photobiol. B, Biol*., 2020, **209**, 111917; (b) A. Precupas, A. R. Leonties, A. Neacsu, R. Sandu and V. T. Popa, *New J. Chem.*, 2019, **43**, 3891-3898.
93. X. Long, Y. F. Zeng, Y. Liu, Y. Liu, T. Li, L. Liao and Y. Guo, *RSC Adv*., 2018, **8**, 31201-31212.
94. P. Bhanja, S. Mishra, K. Manna, K. D. Saha and A. Bhaumik, ACS omega, 2018, **3**, 529-535.

95. Y. Zhang, M. Luo, Y. Zu, Y. Fu, C. Gu, W. Wang, L. Yao, and T. Efferth, *Chem. Biol. Interact.*, 2012, **199**, 129-136.
96. P. Bhanja, S. Mishra, K. Manna, A. Mallick, K. Das Saha and A. Bhaumik, *ACS Appl. Mater. Interfaces.*, 2017, **9**, 31411-31423.
97. (a) A. Mallick, P. More, S. Ghosh, R. Chippalkatti, B. A. Chopade, M. Lahiri and S. Basu, *ACS Appl. Mater. Interfaces.*, 2015, **7**, 7584-7598; (b) B. Liu, Y. Chen and D. K. S. Clair, *Free Radic. Biol. Med.*, 2008, **44**, 1529-1535; (c) S. Wisnovsky, E. K. Lei, S. R. Jean and S. O. Kelley, *Cell Chem. Biol.*, 2016, **23**, 917-927; (d) A. Ashkenazi, *Cytokine Growth Factor Rev.*, 2008, **19**, 325-331.
98. J. D. Ly, D. R. Grubb and A. Lawen, *Apoptosis*, 2003, **8,** 115-128.
99. E. Gottlieb, S. M. Armour, M. H. Harris and C. B. Thompson, *Cell Death Differ.*, 2003, **10**, 709-717.
100. A. Eckert, U. Keil, C. A. Marques, A. Bonert, C. Frey, K. Schüssel and W. E. Müller, *Biochem. Pharmacol.*, 2003, **66**, 1627-1634.
101. S. Jamil, I. Lam, M. Majd, S. H. Tsai, V. Duronio, *Cancer Cell Int.*, 2015, **15**, 1-11.
102. M. S. Sheikh and A. J. Fornace Jr, *J. Cell. Physiol.*, 2000, **182**, 171-181.
103. K. Ito, T. Nakazato, K. Yamato, Y. Miyakawa, T. Yamada, N. Hozumi, K. Segawa, Y. Ikeda and M. Kizaki, *Cancer Res.*, 2004, **64**, 1071-1078.
104. G. M. Cohen, *Biochem. J.*, 1997, **326**, 1-16.
105. J. L. Franklin, *Antioxid. Redox Signal.*, 2011, **14**, 1437-1448.
106. C. S. Boyd and E. Cadenas, 2002, 411-423.

CHAPTER-V

Synthesis of Ru(II) cyclometallated complexes via C(aryl)-S bond activation: X-ray structure, DNA/BSA protein binding and antiproliferative activity

Abstract

As a contribution to the development of new ruthenium complexes with pharmacologically interesting properties, two new cyclometallated ruthenium(II) carbonyl complexes of the general formula $[Ru(L^1/L^2)(CO)(PPh_3)_2]$ (**1/2**) were synthesized and characterized by analytical and spectral techniques (IR, UV/visible, 1H NMR and ESI-MS). The crystal structures of complexes (**1** and **2)** were confirmed by X-ray crystallography, which indicated CNO tridentate coordination of the ligands through C(aryl)–S bond activation. Electronic structures and spectral properties of complexes **1** and **2** were interpreted by DFT and TDDFT calculations. The binding ability of the Ru(II) complexes with calf thymus DNA (CT DNA) and Bovine Serum Albumin (BSA) have been explored by absorption and emission titration methods. Good binding affinity with DNA was observed with intercalative binding mode, which was further confirmed by EB displacement and viscosity measurement studies. The BSA protein binding studies have been monitored by quenching of tryptophan and tyrosine residues in the presence of complexes and the quenching mechanism was found to be static. Synchronous and 3D fluorescence spectroscopy studies were carried out to validate the micro environmental changes in BSA. In addition, the in vitro cytotoxicity of the ligands and complexes against human breast cancer cell line (MCF-7), human lung cancer cell line (A549), triple negative breast cancer cell line (MDA-MB-231) and gastric adenocarcinoma cell line (AGS) were investigated by using the MTT assay and IC_{50} values of the complexes towards MCF-7 cell lines were found to be even less compare to cisplatin.

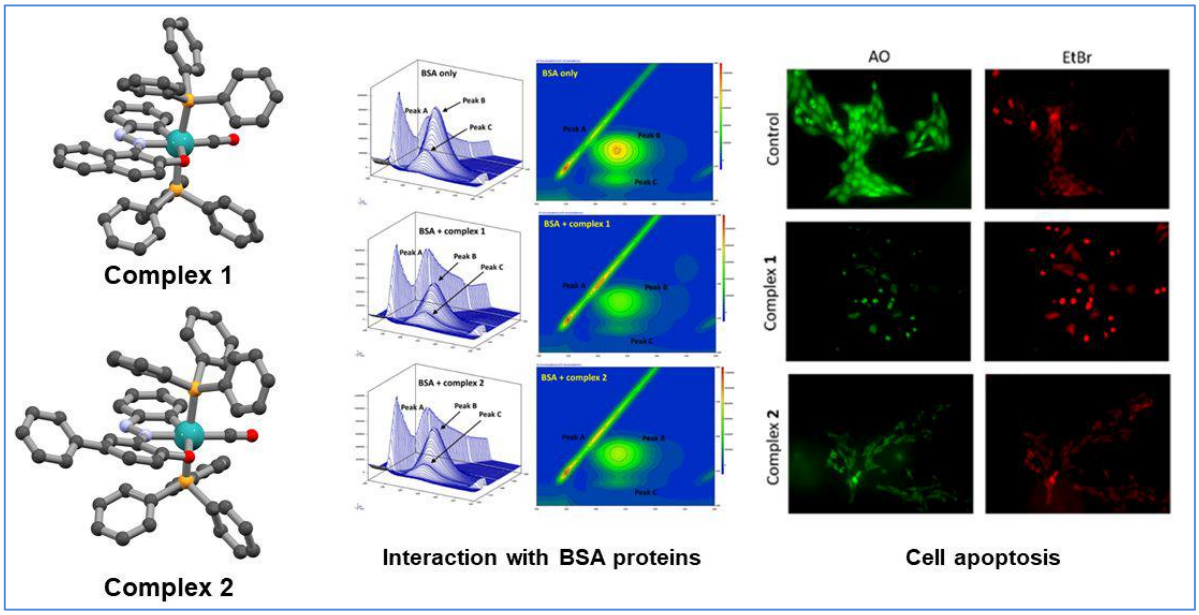

V.1. Introduction

Despite tremendous breakthroughs in the previous fifty years, cancer remains one of the major causes of mortality worldwide.[1,2] Chemotherapy, the administration of cytotoxic chemical agents, remains the most common cancer treatment methods, along with surgical excision and radiotherapy.[3-5] Rosenberg's serendipitous discovery of cisplatin as a powerful anticancer agent in 1965, and subsequent clearance for clinical usage, propelled chemotherapy to the forefront of cancer treatment for common tumours such as testicular, ovarian, colorectal etc.[6-8] Additionally, this has sparked interest in the creation of numerous generations of platin medications, including carboplatin,[9] oxaliplatin[10] and nedaplatin[11] which are now widely accepted in clinical settings. Although cis-platin and its analogues have been the mainstay of therapeutic medications for cancer therapy globally, these FDA-approved Pt(II) drugs face significant challenges due to their significant, inescapable adverse effects, including nephrotoxicity, hair loss, blood clots, high toxicity and multi-drug resistance.[12-15] So, an urgency for the development of some alternative drugs that can address the aforementioned flaws, comes into picture. Ruthenium (II/III)-based anticancer medicines have emerged as appealing alternatives to Pt(II)-based anticancer agents over the years.[16] Some of the significant developments in this field include the beginning of clinical trials for NAMI-A ([ImH][trans-RuCl4(DMSO-S)(Im)], where Im = imidazole and DMSO-S = sulphur bound dimethylsulfoxide, and KP1019 ([IndH][trans-RuCl4(Ind)2] as Ru(III)-based anticancer drug candidates.[17-20] However, NAMI-A's low therapeutic index and KP1019's poor solubility precluded its entry into phase II clinical studies.[21-23] Nonetheless, this early achievement spurred a lot of interest in Ru(II/III) complexes as viable chemotherapeutics, laying a new road map in the field of anti-cancer metallodrugs beyond Pt(II) complexes. Ru-based complexes are endowed with rich physiochemical and biological properties. Ruthenium complexes (a) may form a variety of rigid geometries with tuneable Ru (II/III) redox states and optimum ligand exchange rates, (b) have low toxicity and high selectivity towards proliferative cells, (c) are active against some cisplatin resistant cell lines, (d) can emulate iron in binding to some biological molecules (like transferring albumin in the blood stream), all of which makes it easier to deliver drugs to cancer cells with minimal drug efflux and negative effects. Moreover, photodynamic treatment (PDT) and photoactivated chemotherapy (PACT) use Ru(II) complexes as efficient photosensitizers to enable spatiotemporal control over traditional chemotherapy.[24-27] Cycloruthenated compounds with distinctive photophysical and electrochemical properties, have become an incredibly adaptable class of molecules in recent years, showing applications in organic synthesis,

catalysis, photochemistry, biological and pharmaceutical chemistry.[28] Furthermore, ruthenacycles have been discovered to show promising anticancer properties.[29] Ruthenium arene complexes are highly effective for a variety of cancer types (breast, colon and pancreatic cancer cells).[30,31] The hydrophilic metal core and the hydrophobic arene moiety give these complexes their amphiphilic characteristics. RAPTA-C and RAED are two such lead Ru(II)-arene anticancer medicines that are at an advanced level of preclinical research.[32]

Aromatic azo compounds are one-of-a-kind and multifarious ligands that can coordinate various transition metals and have a variety of flexible donors of combined hard/soft oxygen/nitrogen-sulfur atoms. Apart from their traditional colouring function, azo compounds have also been reported to have cytotoxic, anticancer, antibacterial, antiviral, antifungal, and antiseptic activities.[33] They have been used frequently to make ruthenium complexes because they are biodegradable, low toxic, redox active, and generally resemble the structure of active sites in proteins.[34] One important intracellular target for cancer therapy is DNA, which these complexes can interact with covalently or non-covalently. They can also cause DNA hydrolysis or oxidative cleavage. Consequently, for bettering therapeutic design, understanding compound-DNA interactions is crucial.[35, 36] Moreover, the interaction of metal complexes with albumins may offer valuable structural data that impacts how well a drug works therapeutically. Antitumor medicines are frequently delivered to cellular targets through proteins. Bovine serum albumin (BSA) is a desirable macromolecule used mostly in biophysical and biochemical research among serum albumins due to structural homology with human serum albumin and remarkable ligand-binding characteristics.[37-39]

With this background in mind, aromatic azo ligands have been employed to synthesis two novel cyclometallated ruthenium(II) carbonyl complexes with the general formula trans-[Ru(L^1/L^2)(CO)(PPh_3)$_2$] (**1/2**). The aryl-C, azo-N, and phenolato-O donor systems of CNO pincer ligands are of highly effective in stabilizing the core ruthenium metal. When cyclometallates with pincer-like CXY-donor ligands are formed, the metal is chelated through the two heteroatoms (X and Y = O or N) first, followed by C-S bond activation of the dangling aliphatic arm. All the complexes are fully characterized using various spectroscopic techniques and single crystal X-ray diffraction study. The compounds' electronic structure and UV-Vis spectra have been clarified by DFT and TD-DFT computations. The metal complexes show admirable binding interaction with biomolecules DNA and BSA, promisingly higher than that of the free ligands suggesting the encouraging role of ruthenium metal in complex-biomolecule interaction. The MTT assay has been used to assess the complexes' in vitro anticancer activity against the human breast cancer cell line (MCF-7), the

human lung cancer cell line (A549), and the triple negative breast cancer cell line (MDA-MB-231). In the same experimental setup, complexes were supplied to both cancer cells and the normal healthy noncancerous cell line to investigate their selective effects. Acridine orange/ethidium bromide (AO/EB) staining assay and Hoechst staining have been used in morphological examination under fluorescence microscopes.

V.2. Experimental

V.2.1. Materials and methods

All the reagents and solvents were purchased of highest commercial grade and used without any further purification. 4-phenylphenol, 2-naphthol, 2-(methylthio)aniline, 2-(ethylthio)aniline and $RuCl_3$. $3H_2O$ were purchased from Sigma-Aldrich. The metal precursor [$RuHCl(CO)(PPh_3)_3$] was prepared according to the published procedure.[40] Tris–HCl buffer, phosphate buffer saline (PBS), Ethidium bromide (EB), calf thymus DNA (CT-DNA) and bovine serum albumin (BSA) were obtained from Sigma Aldrich chemical company. Doubly distilled water was used to prepare buffers. Human breast cancer cell line MCF 7, human lung cancer cell line A549, triple negative breast cancer cell line MDA-MB-231 and gastric adenocarcinoma cell line AGS were bought from National Center for Cell Science, Pune, India. Crystal violet solution or Gram's crystal violet and 3-(4, 5-Dimethylthiazol-2-yl)-2, 5-diphenyl tetrazolium bromide (MTT) were purchased from MERCK. Minimal Essential Media Earl's (MEM) and Fetal Bovine Serum (FBS) were obtained from Gibco Life Technologies, USA. 1% penicillin/streptomycin and Trypsin-EDTA were purchased from Invitrogen. Hoechst 33258 was purchased from Sigma-Aldrich, Acridine Orange was purchased from Sigma-Aldrich and Ethidium Bromide was purchased from HIMEDIA.

Elemental analyses (C, H, N) were carried out by a 2400 Series-II CHN analyzer, Perkin Elmer, USA. Waters (Xevo G2 Q-TOF) mass spectrometer was used to record mass spectra of the ligand and complexes. Infrared spectra were recorded as KBr pellets using a Perkin-Elmer FT-IR spectrophotometer in the range 4000-400 cm^{-1}. ^{1}H-NMR spectra were recorded on a Bruker (AC) 300 MHz FT-NMR spectrometer using $CDCl_3$ as a solvent and TMS as an internal reference. PerkinElmer Lambda 750 spectrophotometer was used for study the binding interactions of complexes with CT-DNA and BSA. The emission spectra were recorded by using Shimadzu RF-6000 fluorescence spectrophotometer at room temperature (298 K). Geometry optimization by the density functional theory (DFT) method was performed using the GAUSSIAN09 (B3LYP/LanL2DZ) package.

V.2.2. Preparation of ligands and complexes

V.2.2.1. Synthesis of (E)-1-((2-(ethylthio)phenyl)diazenyl)naphthalen-2-ol (HL^1-SEt)

A solution of 2-(ethylthio)aniline (2.16 g, 0.014 mol) in 1:1 HCl (10 mL) was cooled in an ice bath and an ice cold $NaNO_2$ (1.159 g in 10 mL water) solution was added to this ice cold aniline solution dropwise at 0-5^{0}C under stirring condition. Then it was added to an ice-cold solution of Na_2CO_3 (6 g in 25 mL) and 2-naphthol (2.016 g, 0.014 mol) with vigorous stirring and a red precipitate of crude product was obtained. The crude product was collected by filtration, washed thoroughly with water and then finally dried over $CaCl_2$. The dry mass was dissolved in minimum volume of CH_2Cl_2 and was purified by column chromatographic separation on silica gel (mesh 60–120). A red band of HL^1-SEt was eluted by 30% (v/v) ethyl acetate-petroleum ether mixture. Evaporation of solvent under reduced pressure yielded the pure HL^1-SEt. The yield was, 3.280 g, 76%.

Anal. Calc. for $C_{18}H_{16}N_2OS$: C, 70.10; H, 5.23; N, 9.08. Found: C, 71.75; H, 5.02; N, 8.92. IR (KBr, cm^{-1}): 3421 υ(O-H); 3062, 2973, 2929 υ(C-H); 1480 υ(N=N). ^{1}H NMR (300 MHz, $CDCl_3$): δ 12.85 (s, 1H), 8.54 (d, 1H, *J* = 6.2 Hz), 8.09 (d, 1H, *J* = 6.2 Hz), 7.69 (d, 1H, *J* = 7.1 Hz), 7.57-7.20 (m, 6H), 6.84 (d, 1H, *J* = 7.1 Hz), 2.96 (q, 2H, *J* = 5.5 Hz), 1.31 (t, 3H, *J* = 5.5 Hz). HRMS: calculated for $C_{18}H_{16}N_2OS$ $[M+Na]^+$ (m/z): 331.0881; found: 331.1300.

V.2.2.2. Synthesis of 3-((2-(methylthio)phenyl)diazenyl)-[1,1'-biphenyl]-4-ol(HL^2-SMe)

A very similar method was followed to synthesize the following ligand. The ligand HL^2-SMe was synthesized by diazocoupling reaction between 2-(methylthio)aniline (2.01 g, 0.014 mol) and 4-phenylphenol (2.38 g, 0.014 mol). Yield obtained was 3.23g (72%).

Anal. Calc. for $C_{19}H_{16}N_2OS$: C, 71.22; H, 5.03; N, 8.74. Found: C, 71.02; H, 4.93; N, 8.55. IR (KBr, cm^{-1}): 3416 υ(O-H); 3057, 2960, 2923 υ(C-H); 1458 υ(N=N). ^{1}H NMR (300 MHz, $CDCl_3$): δ 12.72 (s, 1H), 8.25 (s, 1H), 7.91 (d, 1H, *J* = 8.8 Hz), 7.69-7.26 (m, 9H), 7.17 (d, 1H, *J* = 8.6 Hz), 2.60 (s, 3H). HRMS: calculated for $C_{19}H_{16}N_2OS$ $[M+Na]^+$ (m/z): 343.0881; found: 342.9886.

V.2.2.3. Synthesis of Ru(II) complex, $[Ru(L^1)(CO)(PPh_3)_2]$ (1)

A solution of $[RuHCl(CO)(PPh_3)_3]$ (0.102 g, 0.107 mmol) in 20 ml of acetonitrile was refluxed with an equimolar quantity of the ligand HL^1-SEt (0.033 g, 0.107 mmol) for 8 h. The resulting deep green coloured solution was concentrated. It was subjected to thin layer chromatography where two spots were identified and isolated by column chromatography using silica gel (mesh 60-120). The first green coloured band was eluted by 20% (V/V) ethyl

acetate-petroleum ether solvent mixture. Again, the solvent was removed under reduced pressure and the pure complex **1** was obtained as a green solid which was crystallized from dichloromethane and methanol mixture to yield green transparent needle like crystals suitable for X-ray analysis. Yield was, 0.078 g, 81.2%.

Anal. Calc. for $C_{53}H_{40}N_2O_2P_2Ru$: C, 70.74; H, 4.48; N, 3.11. Found: C, 70.31; H, 4.23; N, 2.98. IR (KBr, cm^{-1}): 3055, 2919, 2855 υ(C-H); 1923 υ(CO); 1436 υ(N=N). ^{1}H NMR (300 MHz, $CDCl_3$): δ 8.13 (d, 1H, *J* = 6.1 Hz), 8.01 (d, 1H, *J* = 4.9 Hz), 7.86-7.23 (m, 37H), 7.11 (d, 1H, *J* = 7.6 Hz). HRMS: calculated for $C_{53}H_{40}N_2O_2P_2Ru$ $[M+H]^+$ (m/z): 901.1687; found: 901.1806. UV-Vis (in DMSO), λ_{max} (ε, M^{-1} cm^{-1}): 656 (5248), 432 (8854), 364 (10196).

V.2.2.4. Synthesis of Ru(II) complex, $[Ru(L^2)(CO)(PPh_3)_2]$ (2)

Complex **2** was synthesized by a similar method like complex **1** using HL^2-SMe as a ligand. Finally needle shape transparent green colour crystal was obtained. The yield was, 0.083 g, 84%.

Anal. Calc. for $C_{55}H_{42}N_2O_2P_2Ru$: C, 71.34; H, 4.57; N, 3.03. Found: C, 71.12; H, 4.41; N, 2.91. IR (KBr, cm^{-1}): 3057, 2923, 2860 υ(C-H); 1904 υ(CO); 1429 υ(N=N). ^{1}H NMR (300 MHz, $CDCl_3$): δ 8.01 (s, 1H), 7.84 (m, 1H), 7.73-7.19 (m, 40H). HRMS: calculated for $C_{55}H_{42}N_2O_2P_2Ru$ $[M]^+$ (m/z): 926.1765; found: 926.0455. UV-Vis (in DMSO), λ_{max} (ε, M^{-1} cm^{-1}): 682 (4419), 434 (3828), 319 (22914).

V.2.3. Crystal structure determination and refinement

The crystal data collections for complexes **1** and **2** were performed at room temperature with an automated Bruker AXS D8 Quest CMOS diffractometer using graphite monochromated Mo-Kα radiation (λ=0.71073Å). Reflection data were recorded using the ω and φ scans with frame width of 0.5^o scan technique. The structures were solved by direct methods and refined using the full-matrix least-squares techniques on F^2 with SHELX-2016. All the data were corrected for Lorentz and polarization effects and multi-scan absorption corrections were applied using SHELXTL program package.[41] All non-hydrogen atoms were located and refined with anisotropic thermal parameters. H-atoms attached to carbon were included as a fixed contribution and were geometrically calculated and refined by using riding model. Crystallographic data for ruthenium(II) complexes and structure refinement parameters are given in Table V.1.

Table V.1. Crystallographic data and refinement parameters of complexes **1** and **2.**

Complex	$[Ru(L^1)(CO)(PPh_3)_2]$ (**1**)	$[Ru(L^2)(CO)(PPh_3)_2]$ (**2**)
Formula	C53 H40 N2 O2 P2 Ru	C55 H42 N2 O2 P2 Ru
Formula Weight	899.88	925.91
Crystal System	*monoclinic*	*triclinic*
Space group	*C m*	*P -1*
a, b, c [Å]	18.2738(15), 15.3551(11), 9.8021(7)	10.5463(8), 12.0634(9), 17.8689(14)
α	90	76.220(2)
β	120.739(2)	86.297(2)
γ	90	86.034(2)
V [$Å^3$]	2364.0(3)	2199.9(3)
Z	2	2
D(calc) [g/cm^3]	1.264	1.398
Mu(MoKa) [/mm]	0.440	0.475
F(000)	924	952
Temperature (K)	293(2)	293(2)
Radiation [Å]	0.71073	0.71073
θ(Min-Max) [°]	2.417- 26.685	1.858- 26.420
Dataset (h; k; l)	-23 to 23, -19 to 19, -12 to 12	-13 to 13, -15 to 15, -22 to 22
R, wR_2	0.0343, 0.0643	0.0487, 0.1035
Goodness of fit(S)	1.066	1.149
CCDC No.	2262838	2262839

V.2.4. Computational method

Full geometry optimizations of the complexes were carried out using the DFT method at the Becke's three parameter hybrid exchange functional (B3LYP) level of theory.[42] The ruthenium metal atom was described using the Lee-Yang-Parr nonlocal correlation functional (LanL2DZ)[43] basis set while the other elements were described using the basis set 6-31G(d)[44]. Harmonic vibrational frequency calculations were performed to ensure that the optimized geometries represented the local minimum on the potential energy surface and only positive Eigen values were obtained. All the theoretical calculations were performed using Gaussian09 program package[45] with the aid of the GaussView, Version 5 visualization

program. Electronic transitions were computed using the time-dependent density functional theory (TD-DFT)[46] formalism and solvent effect was simulated using the conductor-like polarizable continuum model (CPCM)[47]. GaussSum[48] was used to calculate the fractional contributions of various groups to each molecular orbital.

V.2.5. DNA-binding studies

V.2.5.1. UV–Vis titration

The interactions of complexes **1** and **2** with CT-DNA were studied using UV-Vis spectroscopy. The DNA-binding experiments were performed at room temperature in Tris–HCl/50mM NaCl buffer solution (pH=7.4).[49] The concentration of CT-DNA was determined spectro-photometrically by employing an extinction coefficient of 6600 $M^{-1}cm^{-1}$ at 260 nm using Lambert-Beer law. It was stored at 4°C and used within one week. The stock solution of the complexes **1** and **2** were prepared in 1:10 DMSO /buffer medium and was suitably diluted with Tris buffer whenever necessary. This low DMSO percentage added to the DNA solution should not interfere with the nucleic acid. The absorption titration was performed by using a fixed complex concentration to which increments of the DNA stock solution were added. After each addition, the solution was stirred homogeneously and let to equilibrate for 2 min before collecting the absorption profile.

V.2.5.2. Competitive study with EB by fluorescence method

In order to know the exact mode of binding of the synthesized complexes with CT-DNA, fluorescence quenching experiments of ethidium bromide (EB)–DNA complex were carried out by gradual addition of the ruthenium(II) complexes into the solution of EB-CT-DNA.[50] The EB-CT-DNA complex was initially prepared by mixing of 15 μM EB and 30 μM CT-DNA in Tris– HCl/NaCl buffer solution (pH 7.40). The emission was recorded at 556–750 nm. The fluorescence spectra in the fluorimeter were obtained at an excitation wavelength of 540 nm and an emission wavelength of 608 nm.

V.2.5.3. DNA viscosity measurements

The viscosity of the CT-DNA solutions (35.8μM) was measured in the presence of increasing amounts of the complexes using an Ostwald viscometer placing it in a thermostated water bath at 25.0 °C. Flow time was measured with a digital stopwatch and each sample was measured three times, then the average flow time was calculated. Viscosity values were calculated from the observed flow time of DNA-containing solutions (t) corrected for the

flow time of buffer alone (t_0), $\eta = t - t_0$. The data is reported as $(\eta / \eta_0)^{1/3}$ versus the ratio of the concentration of the compound to CT-DNA (R = [compound]/[CT-DNA]), where η is the viscosity of CT-DNA in the presence of the compound and η_0 is the viscosity of CT-DNA solution alone.[51]

V.2.6. Protein binding studies

Proteins are major targets for therapeutically active complexes. Serum albumins are the most abundant proteins in the blood plasma which transport ions to cells and tissues.[52] Therefore, serum albumin can act as an important carrier for metallodrug delivery. Since Bovine Serum Albumin (BSA) structure is homologous with human serum albumin, BSA is mostly used in biochemical and biophysical studies.

The binding interaction between BSA and complexes were deciphered by employing UV-Vis and fluorescence methods. A stock solution of BSA was prepared using 500 mM phosphate buffer saline (PBS) at pH 7.4 and stored in the dark at 4°C for further use. BSA concentration was measured by taking absorbance at 280 nm in UV-Vis spectra (molar extinction coefficient 66,400 $dm^3\ mol^{-1}\ cm^{-1}$).[24] The stock solution of complexes **1** and **2** were prepared in DMSO medium. For recording UV-Vis spectra, BSA-concentration was kept constant (10 μM) while varying the concentration of the complexes added to it. In fluorescence experiment, tryptophan fluorescence of BSA was recorded in the range 290-500 nm at an excitation wavelength of 280 nm using a slit width of 10 nm. Quenching of emission intensity at ~336 nm for BSA was monitored with subsequent addition of metal complex. The synchronous fluorescence spectra were also captured in the same instrument in the range of 255-400nm by scanning the excitation and emission monochromators simultaneously. Different wavelength interval ($\Delta\lambda = \lambda_{em} - \lambda_{ex}$) of $\Delta\lambda$ = 15 nm and $\Delta\lambda$ = 60 nm were set to study the spectrum behavior of tyrosine (Tyr) and tryptophan (Trp) residues of BSA. For three-dimensional (3D) fluorescence spectroscopy, the excitation (λ_{ex}) and emission (λ_{em}) wavelength was scanned (at a speed of 6000 nm/min) in the range 200-400 nm and 200-500 nm, respectively with 2 nm interval and a slit width of 10 nm. BSA (6 μM) with and without the complex **1** and **2** were subjected to 3D fluorescence spectroscopy to produce the 3D spectra and related contour maps.

V.2.7. Biological Studies

V.2.7.1. Cell Culture

Human breast cancer cell line MCF-7, human lung cancer cell line A549, triple negative breast cancer cell line MDA-MB-231, and gastric adenocarcinoma cell line AGS, were bought from the National Center for Cell Science in Pune, India, and kept in MEM media containing Earle's salts (for MCF 7 and WRL68), DMEM high glucose medium (for A549 and MDAMB231) and RPMI 1640 medium (for AGS) with 10 % Fetal Bovine Serum (FBS) supplements (Gibco). All of the cell lines were maintained in a 37°C humidified incubator with a 5 % CO_2 environment. Early passage numbers were used for all tests.

V.2.7.2. Cell Viability Assay

The cell viability was analyzed by MTT (3-(4,5-Dimethylthiazol-2-yl)-2,5-diphenyl tetrazolium bromide) assay in different cell lines. A 96-well plate with 1×10^3 cells per well was initially treated for 24 hours at 37 °C with escalating concentrations of ligands, cisplatin (12.5 µM to 200 µM) and Ru(II) complexes (6.25 µM to 100 µM). Each well was then filled with 25 µl of MTT solution (5 mg/ml in PBS) and incubated for 3 hours at 37°C. 100µl of DMSO: Methanol was added to each well and the absorbance was measured at 570 nm in a Spectramax i3X microtitre plate reader. The IC_{50} value was determined using CompuSyn software.

V.2.7.3. Colony Formation Assay

In six-well plates, approximately 500 cells of MCF 7 cell line were plated and then they were incubated at 37°C for 24 hours. The cells were then exposed to ligands, Ru(II) complexes. This was followed by washing with 1X PBS and fixing with methanol. The generated colonies were stained with crystal violet for 15 minutes. Colonies, defined as more than 50 cells, were counted using Olympus CKX41, an inverted bright field microscope with a 4X objective magnification.

V.2.7.4. Statistical analysis

Each experiment was carried out in triplicate, and the typical data are shown as mean values with standard deviations. To assess the main differences between the control and each treated group, one-way analysis of variance (ANOVA) and post hoc comparisons was done with the use of the Turkey test. P value of 0.05 or less was regarded as statistically significant. The software used for analysis of all the tests was Graph Pad Prism 8.0.1.

V.3. Results and discussion

V.3.1. Synthesis and characterization

The synthetic route employed for the preparation of the new cyclometallated ruthenium (II) carbonyl complexes is described in Scheme V.1. The novel complexes **1** and **2** were prepared via refluxing the equimolar amount of ligand [HL^1-SEt / HL^2-SMe] with the Ru(II) precursor [$RuHCl(CO)(PPh_3)_3$]. Both the ligands and complexes were fully characterized by using various spectroscopic techniques and the structures of complexes **1** and **2** were confirmed by single crystal X-ray crystallographic studies.

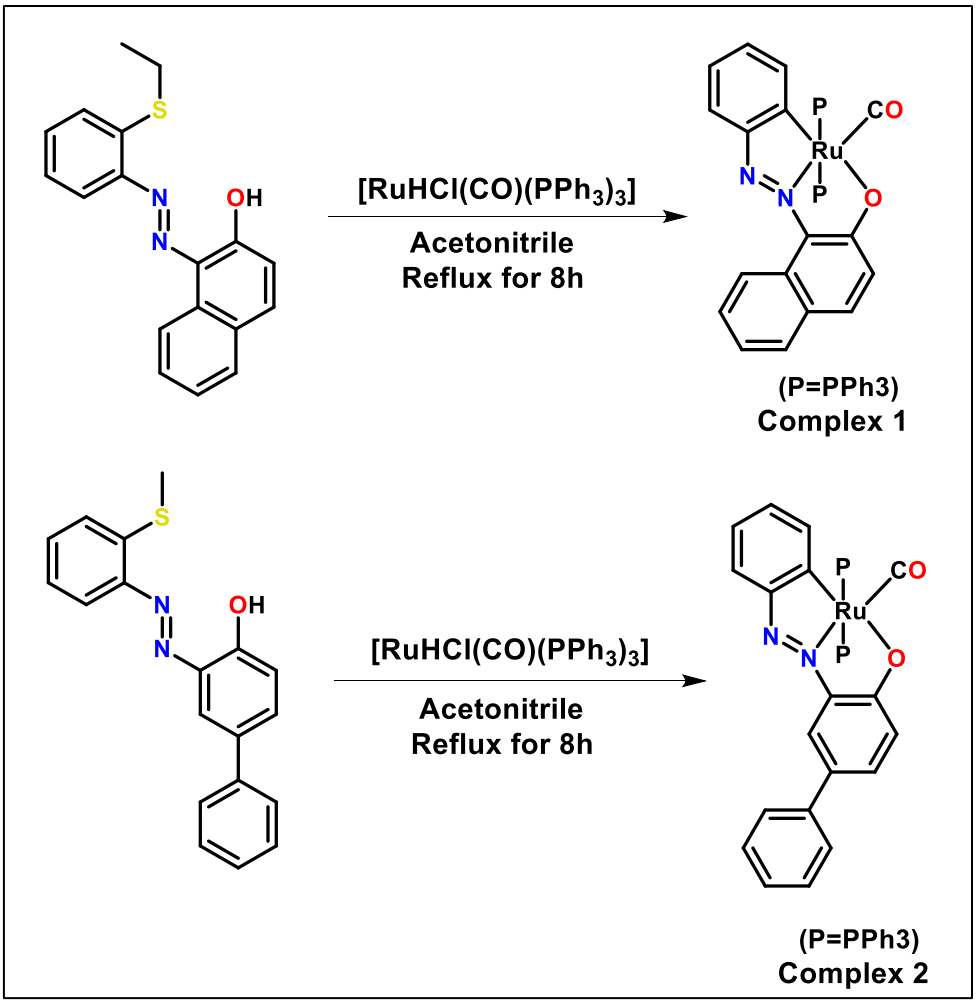

Scheme V.1. Synthetic scheme for complex **1** and complex **2.**

IR spectra of the free ligands exhibit υ(N=N) stretching frequency at 1480-1458 cm^{-1} (Fig. V.1), which is shifted to lower frequency (1436-1429cm^{-1}) upon complexation with the Ru(II) ion in the complexes, (Fig. V.2). The significant shift of υ(N=N) stretching in the complexes supports the dπ(Ru)→π*(N=N) back donation.[53] In the complexes **1** and **2**, terminally coordinated carbonyl group appear as a strong band in the region 1923-1904 cm^{-1}.

The presence of triphenyl phosphine group is confirmed by the υ(Ru-P) stretching in the range of 512-515 cm^{-1} and υ(P-C) stretching in the range of 1095-1086 cm^{-1}.[54,55] ^1H NMR spectra of the complexes, the peak at 12.85-12.72 ppm correspond to O-H proton of the free ligands (Fig. V.3 and Fig. V.4) disappeared which suggest the coordination of ligand to the metal ions through phenolic-O. All the expected proton signals of the ligands including aromatic protons are resolved except S-CH_2CH_3/ S-CH_3 peaks, which suggest the C-S bond cleavage in the complexes (Fig. V.5 and Fig. V.6). A series of overlapping multiplet signals appeared in the region 7.86-7.19 ppm correspond to the protons of coordinated triphenylphosphine along with azo-thiophenolato ligand in the complex. Mass spectrum of [Ru(L^1)(CO)(PPh_3)$_2$] (**1**) shows m/z peak corresponding to $[M+H]^+$ at 901.1806 (Fig. V.9) while [Ru(L^2)(CO)(PPh_3)$_2$] (**2**) exhibits m/z peak corresponds to $[M]^+$ at 926.0455 (Fig. V.10).

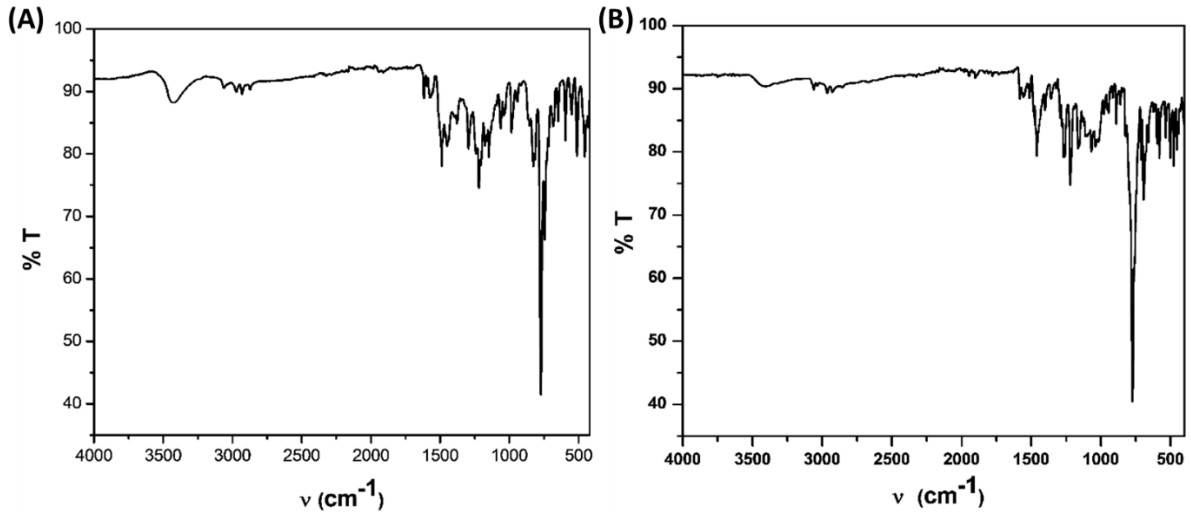

Fig. V.1. IR spectrum of ligand HL^1-SEt (A) and ligand HL^2-SMe (B).

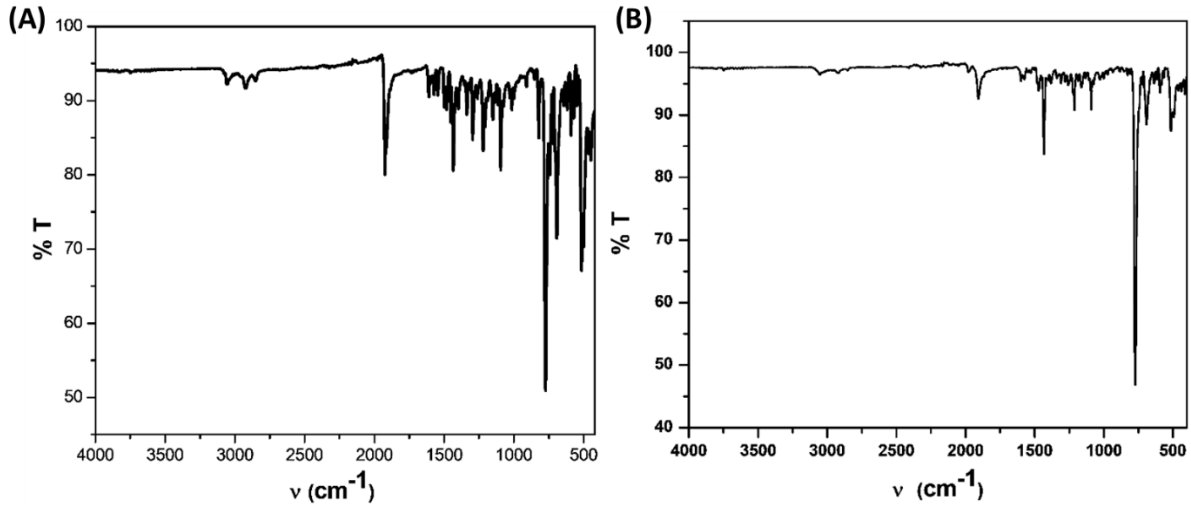

Fig. V.2. IR spectrum of complex **1** (A) and complex **2** (B).

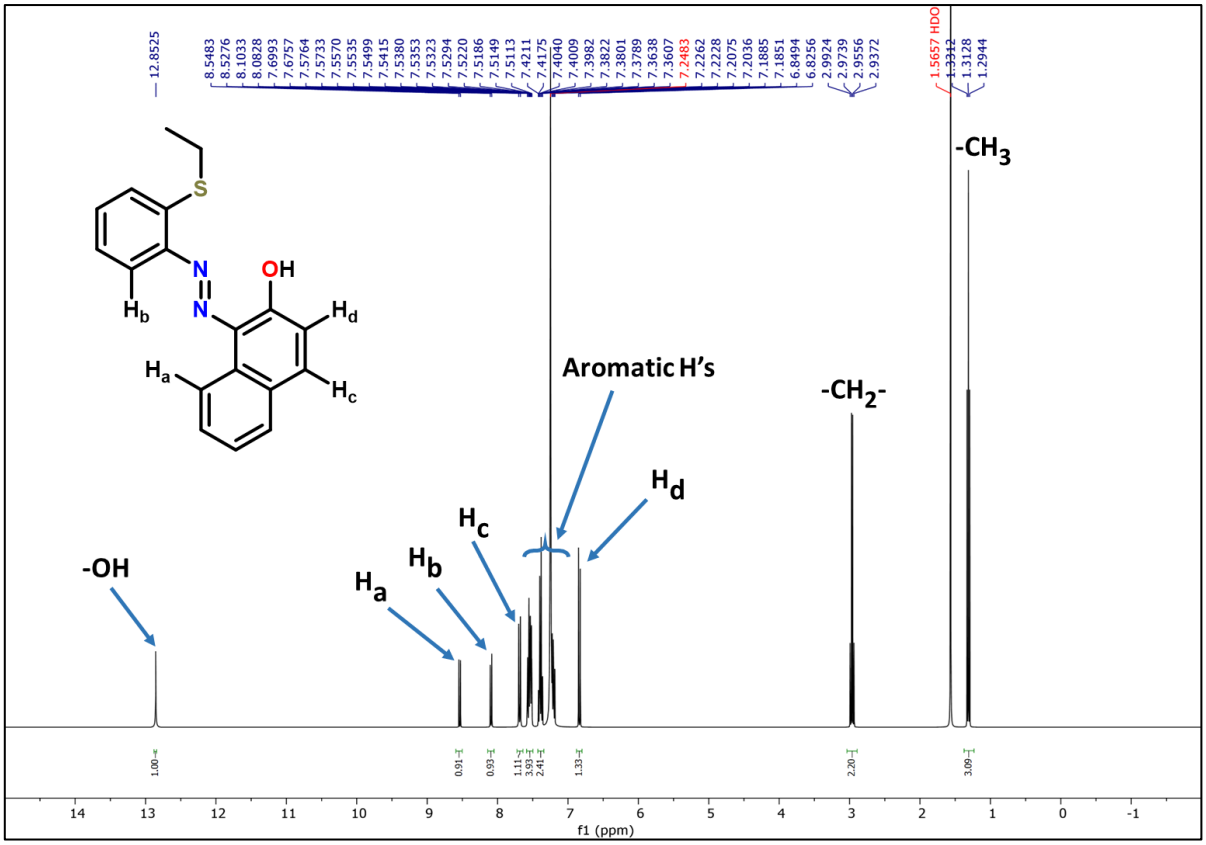

Fig. V.3. ^{1}H-NMR spectrum of ligand HL^{1}-SEt in $CDCl_3$

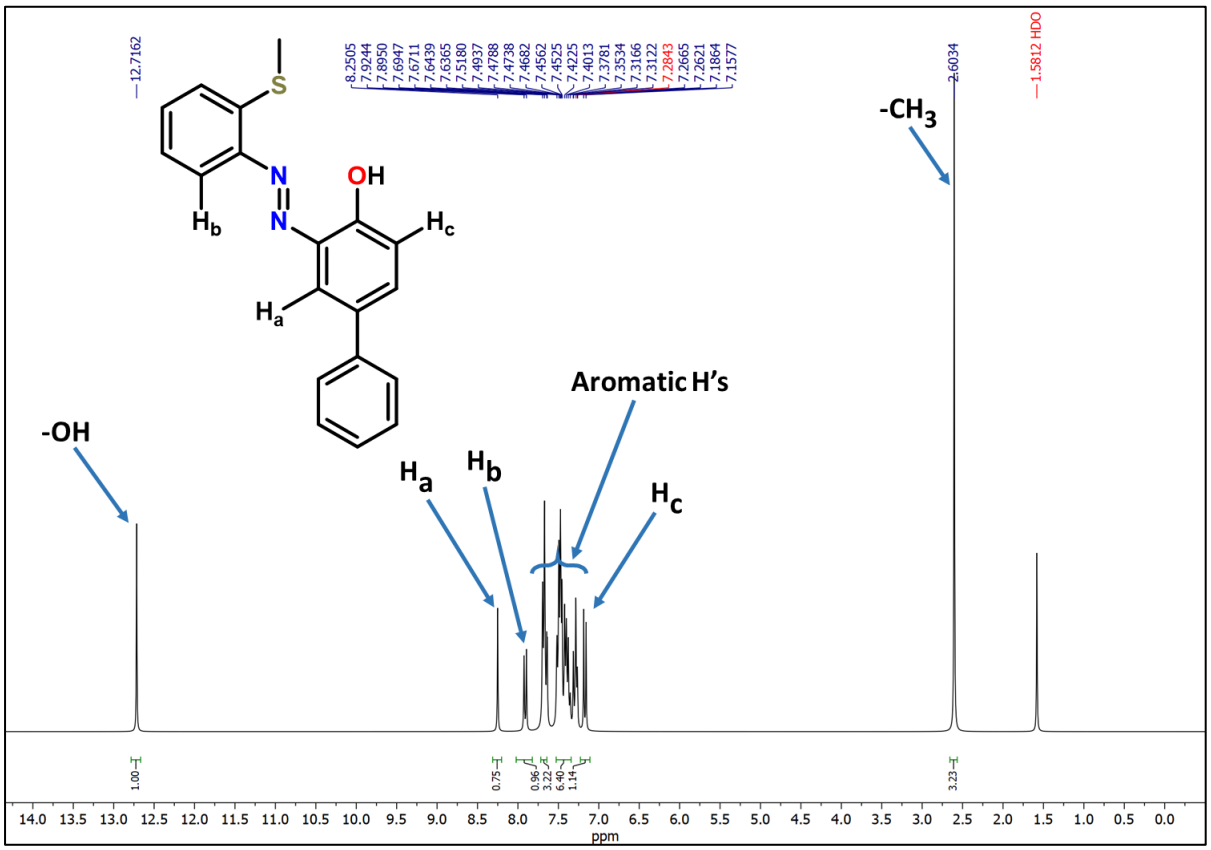

Fig. V.4. ^{1}H-NMR spectrum of ligand HL^{2}-SMe in $CDCl_3$

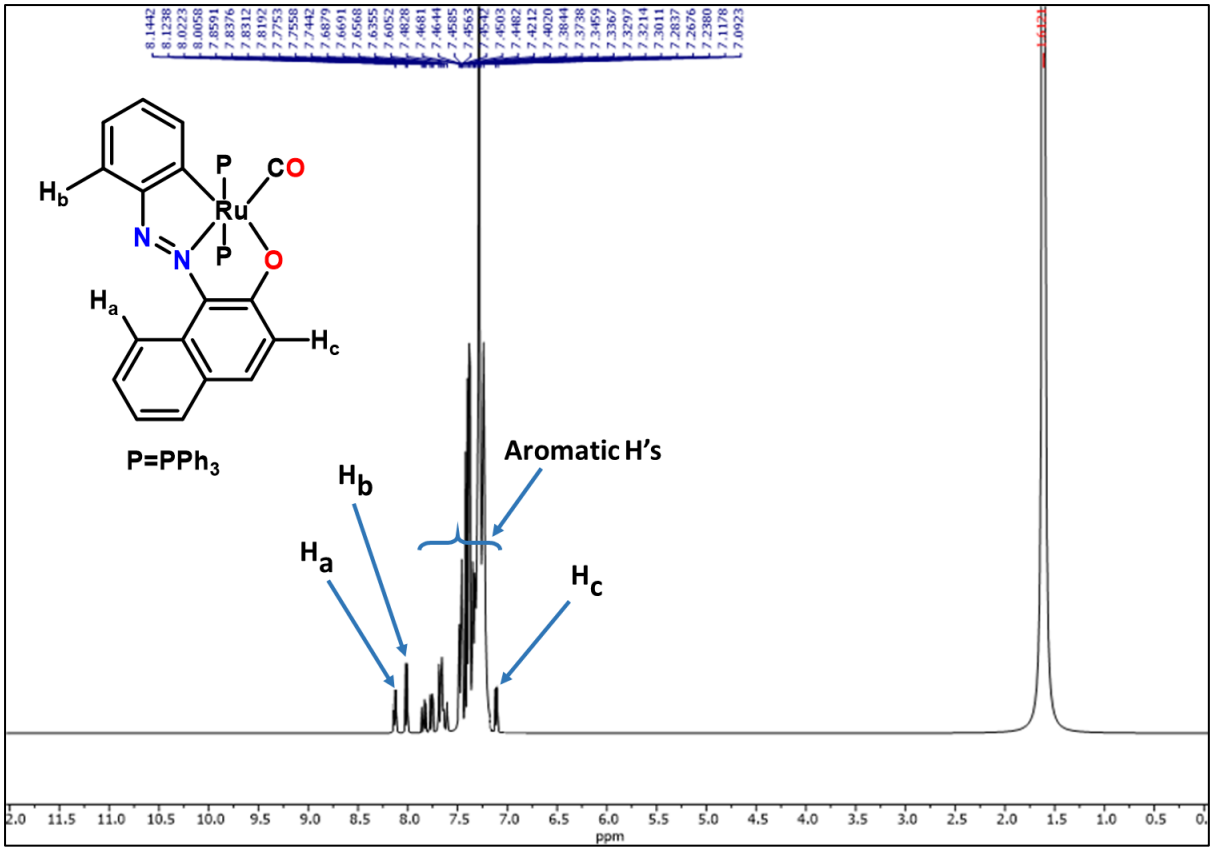

Fig. V.5. ^{1}H-NMR spectrum of [Ru(L^{1})(CO)(PPh_3)$_2$] (**1**) complex in $CDCl_3$

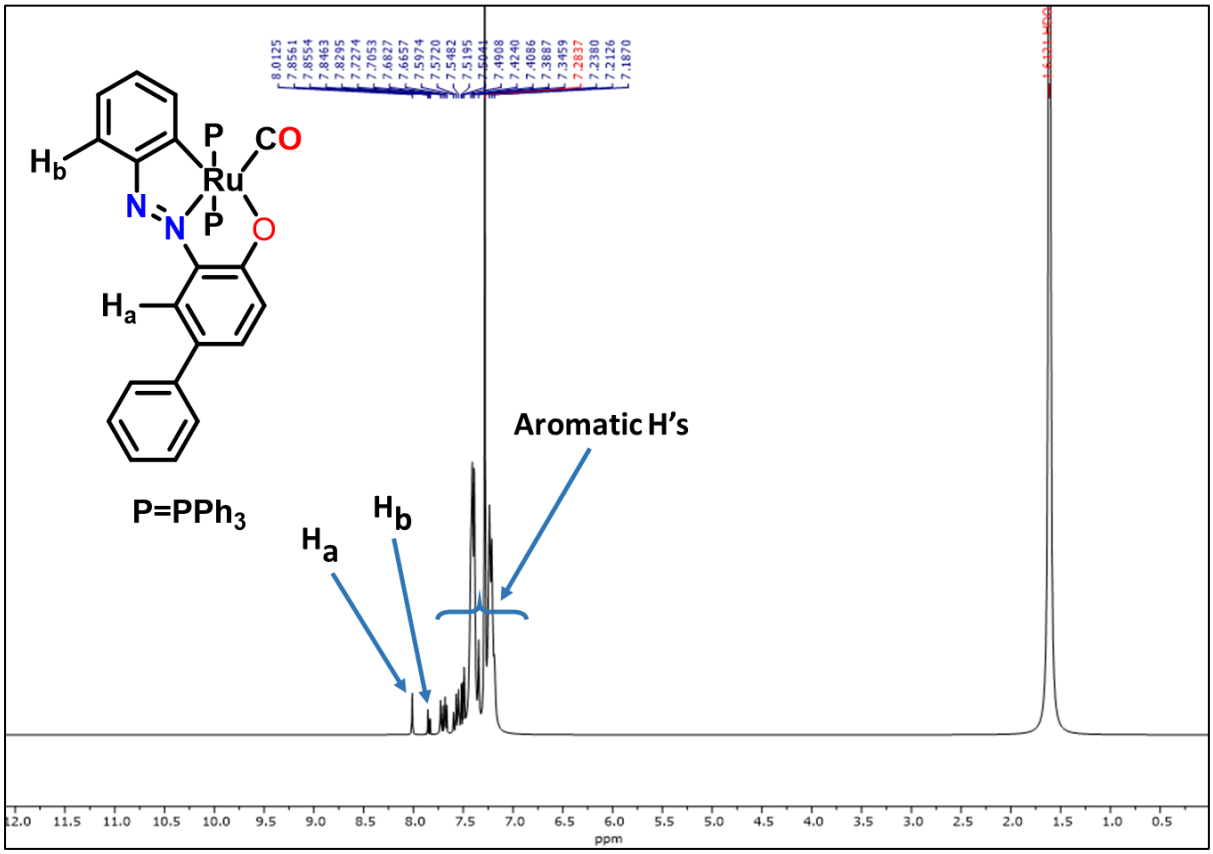

Fig. V.6. ^{1}H-NMR spectrum of [Ru(L^{2})(CO)(PPh_3)$_2$] (**2**) complex in $CDCl_3$

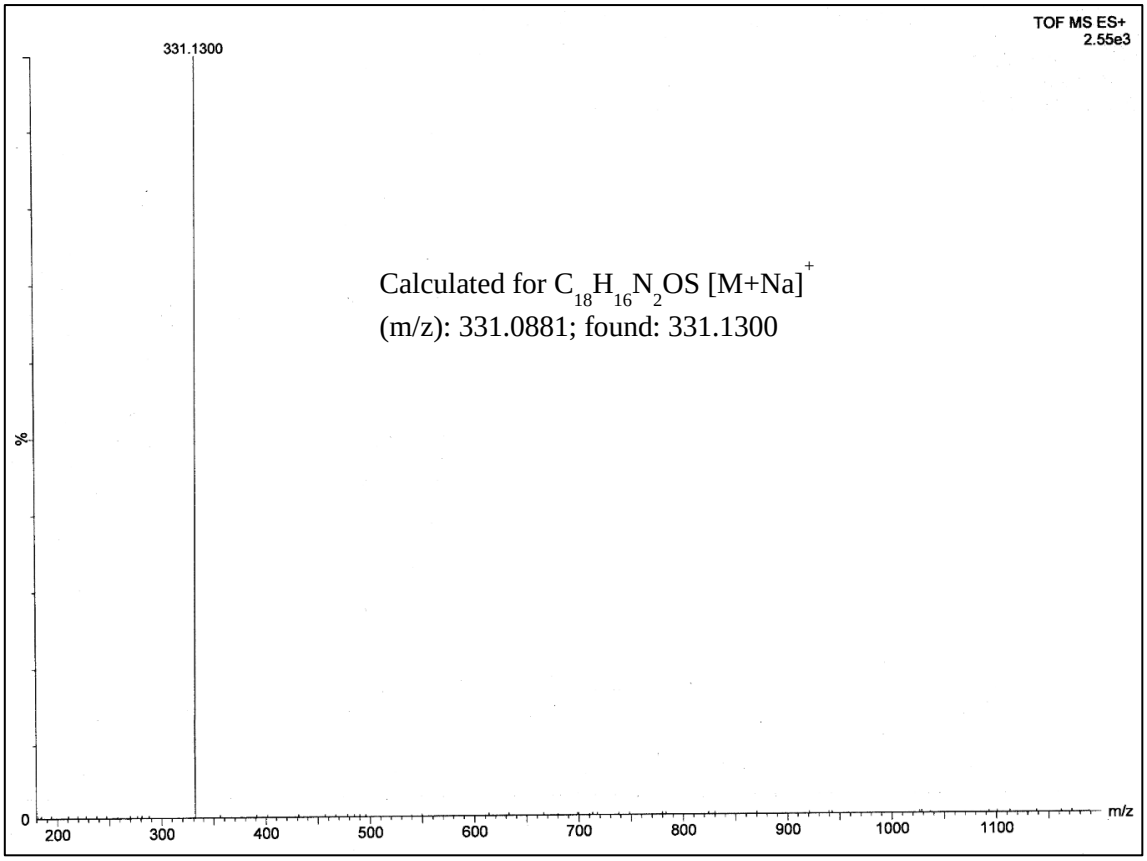

Fig. V.7. HRMS of ligand HL^1-SEt.

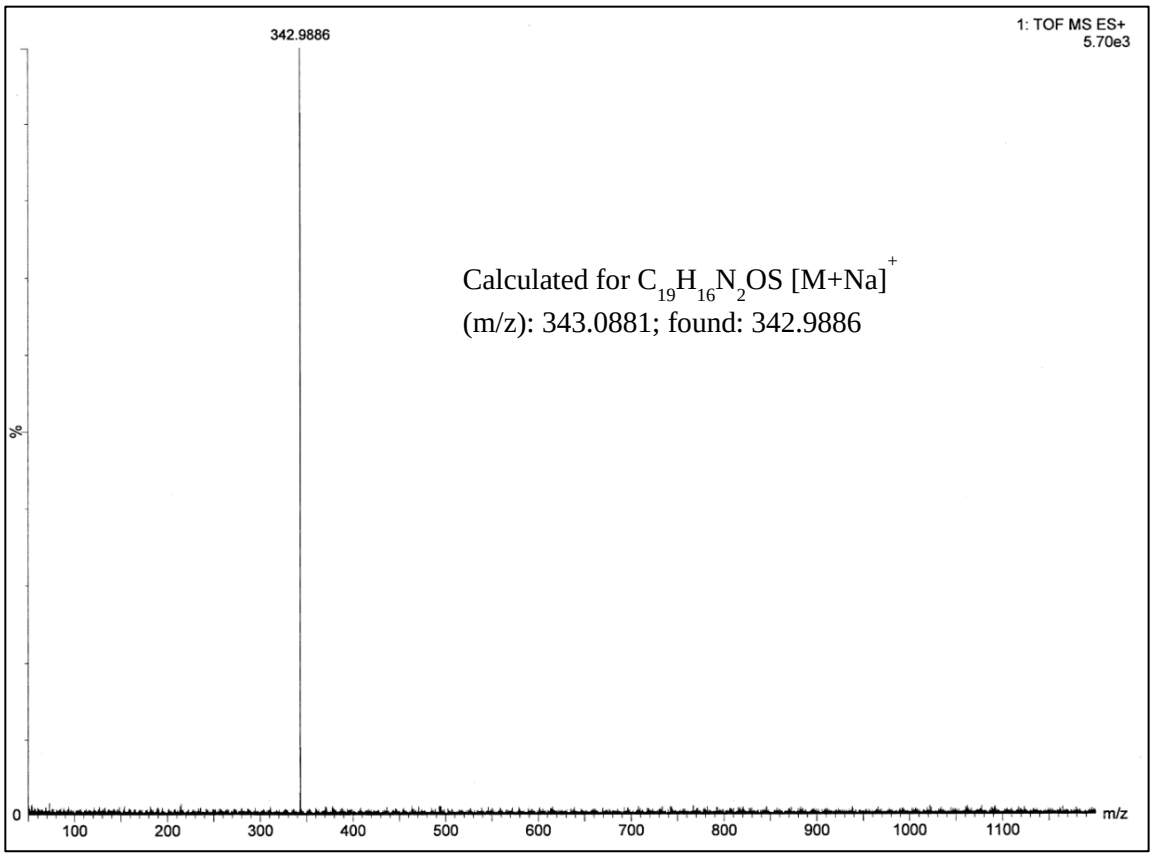

Fig. V.8. HRMS of ligand HL^2-SMe.

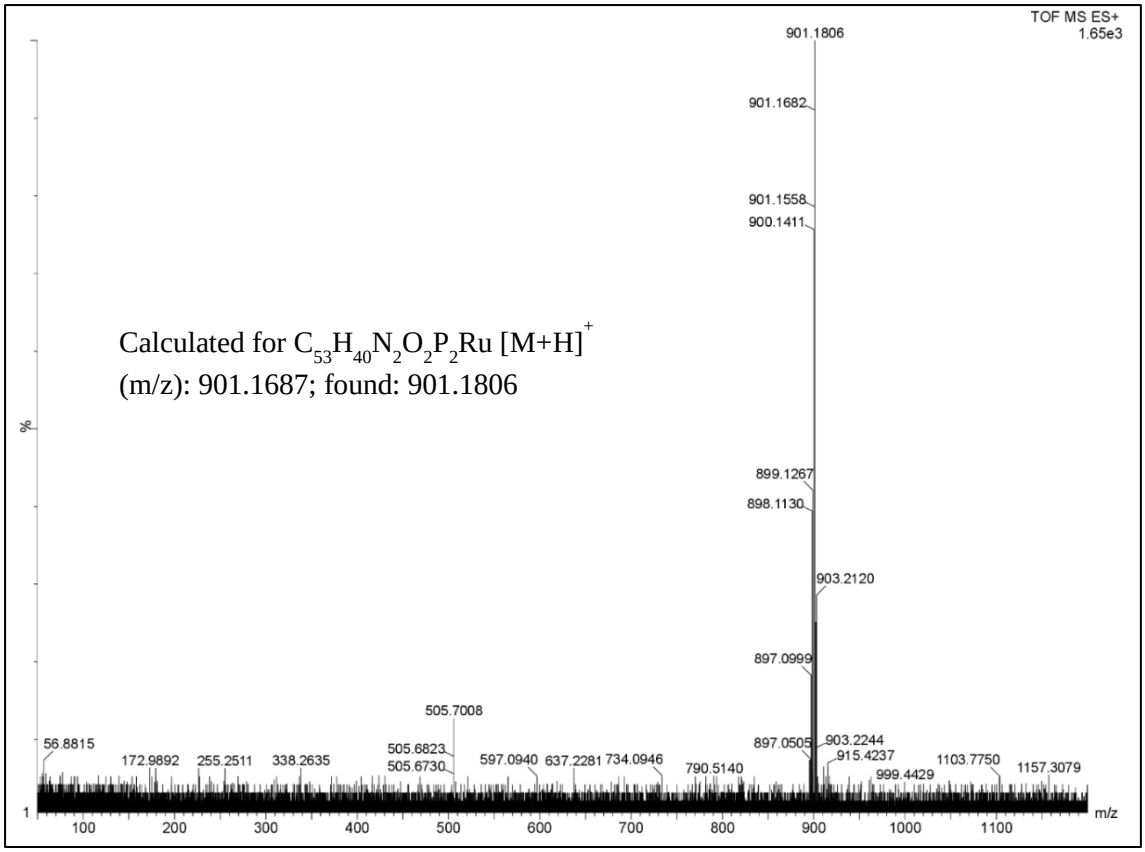

Fig. V.9. HRMS of $[Ru(L^1)(CO)(PPh_3)_2]$ (**1**) complex.

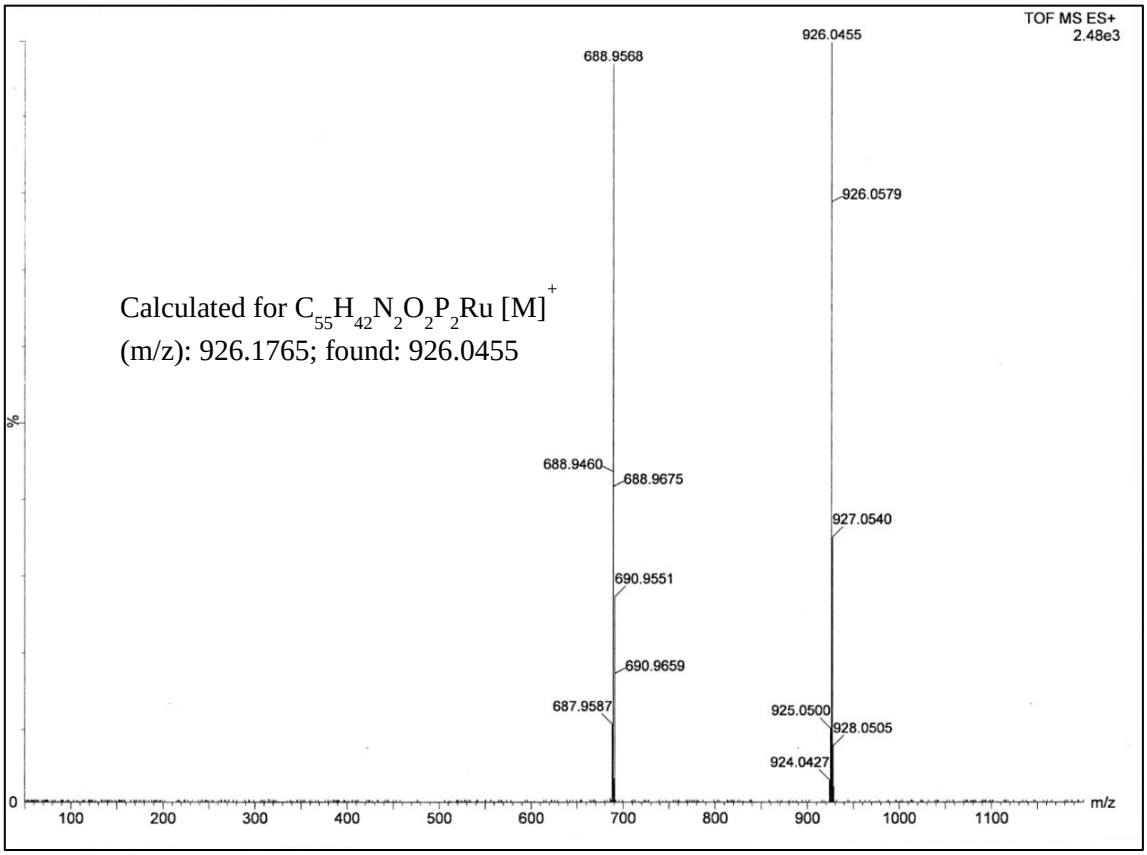

Fig. V.10. HRMS of $[Ru(L^2)(CO)(PPh_3)_2]$ (**2**) complex.

Absorption spectra of complexes **1** and **2** were taken in DMSO (Fig. V.11). The solution spectrum of complex **1** exhibit moderately intense low energy band at 656 nm (ε, 5248 $M^{-1}cm^{-1}$). In addition, high energy bands appeared at 432 (ε, 8854 $M^{-1}cm^{-1}$) and 364 nm (ε, 10196 $M^{-1}cm^{-1}$). Electronic spectra of complex **2** exhibit low energy peaks at 682 nm (ε, 4419 $M^{-1}cm^{-1}$) and high energy bands appeared at 434 nm (ε, 3828 $M^{-1}cm^{-1}$) and 319 nm (ε, 22914 $M^{-1}cm^{-1}$).

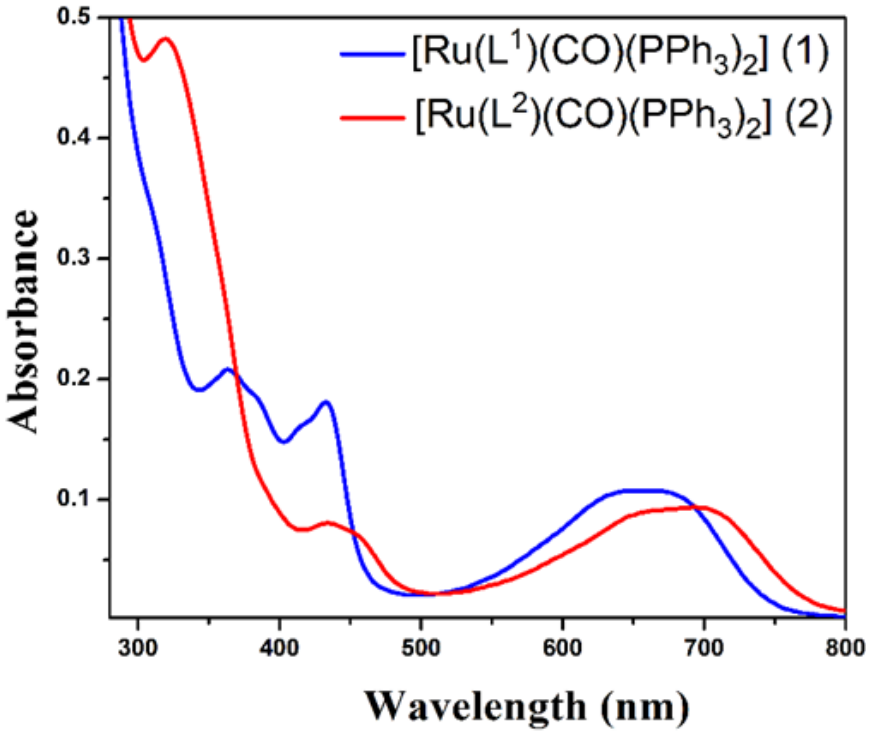

Fig. V.11. UV-Vis spectra of complex **1** and complex **2** in DMSO.

V.3.2. Crystallographic study

The molecular structures of the complexes (**1** and **2**) have been established by the single crystal X-ray diffraction method. The single crystal X-ray diffraction study reveals that the crystal of complex **1** belong to the monoclinic system with *Cm* space group and the crystal of the complex **2** belong to the triclinic system with $\bar{P}1$ space group. The ORTEP plots of the complexes **1** and **2** along with the atomic numbering scheme are shown in Fig. V.12. The summary of the data collection and the refinement parameters have been given in Table V.1. Selected inter atomic bond lengths and bond angles of the complexes are summarized in Table V.2. The bond parameters of the complexes suggest a distorted octahedral geometry around the metal atoms. In the complexes, the modified chelating ligands coordinated to the ruthenium ion through phenolic-O, azo-N and aryl-C atoms, forming two five member

chelate rings with a bite angle N(1)-Ru(1)-O(1) of 77.3(2)^{o} , C(1)-Ru(1)-N(1) of 77.9(3)^{o} for complex **1** and a bite angle N(1)-Ru(1)-O(2) of 77.93(10)^{o}, C(2)-Ru(1)-N(1) of 77.84(13)^{o} for complex **2** respectively. The fourth position is occupied by the carbon atom of the carbonyl group to form a CNOC square plane. The carbonyl group occupied the site trans to the N(1), which is confirmed from the bond angle C(17)-Ru(1)-N(1) of 171.6(3)^{o} for complex **1** and C(1)-Ru(1)-N(1) of 178.12(14)^{o} for complex **2**. The remaining two axial coordination sites of each complex are occupied by phosphorous atoms of triphenylphosphine, which are mutually trans to each other with Ru(1)-P(1) and Ru(1)-P(2) distances of 2.3827(10) Å and 2.3842(10) Å for complex **1**, 2.3781(9) Å and 2.3797(9) Å for complex 2 and are slightly bent towards the carbonyl group due to steric requirements of somewhat bulky chelating ligand. This effect caused a significant deviation from a linear trans arrangement, which is confirmed from the bond angles C(17)-Ru(1)-P(1) of 88.54(4)^{o} for complex **1** and C(1)-Ru(1)-P(1) of 87.59(10)^{o} for complex **2** are smaller than bond angle N(1)-Ru(1)-P(1) of 92.11(4) for complex **1** and N(1)-Ru(1)-P(1) of 90.99(8) for complex **2**. The bond distances of Ru(1)-P(1) and Ru(1)-P(2) are comparatively longer than that of the other four basal planar bonds, such as Ru(1)-N(azo) [2.037-2.069 Å], Ru(1)-C(aryl) [2.046-2.054 Å], Ru(1)-O(phenolic) [2.192-2.250 Å] and Ru(1)-C(CO) [1.853-1.933 Å]. The lengthening of the Ru-P bonds is due to the strong trans influence of bulky PPh_3 ligands. The observed bond distances of complexes **1** and **2** such as Ru-P, Ru-O, Ru-N and Ru-C and bond angles are found to be similar to the other reported triphenylphosphine containing ruthenium complexes.[56,57] The azo bond distances (N1-N2) are found to be 1.274(7) Å and 1.274(4) Å in **1** and **2** respectively.[58]

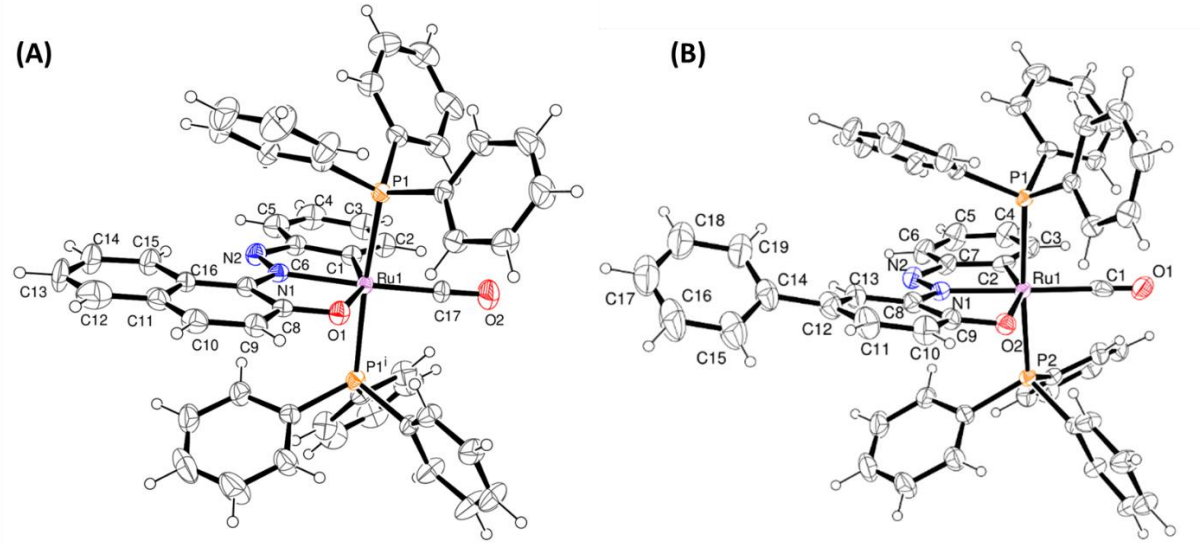

Fig. V.12. ORTEP plots with 35% ellipsoidal probability of complexes **1** (A) and **2** (B).

Table V.2. Selected X-ray and calculated bond distances (Å) and angles (°) of complexes.

1			**2**		
Bonds(Å)	X-ray	Calc.	Bonds(Å)	X-ray	Calc.
Ru(1)- C(17)	1.853(7)	1.861	Ru(1)- C(2)	2.054(4)	2.058
Ru(1)- C(1)	2.046(6)	2.055	Ru(1)- C(1)	1.933(5)	1.866
Ru(1)- N(1)	2.069(6)	2.107	Ru(1)- N(1)	2.037(3)	2.085
Ru(1)- O(1)	2.192(4)	2.216	Ru(1)- O(2)	2.250(2)	2.238
Ru(1)- P(1)	2.3827(10)	2.438	Ru(1)- P(1)	2.3781(9)	2.439
N(1)-N(2)	1.274(7)	1.284	N(1)-N(2)	1.274(4)	1.277
O(2)-C(17)	1.151(8)	1.142	O(1)-C(1)	1.004(4)	1.114
Angles (°)					
C(17)-Ru(1)-C(1)	93.7(3)	97.970	C(1)-Ru(1)-C(2)	103.39(17)	98.747
C(17)-Ru(1)-N(1)	171.6(3)	175.729	C(1)-Ru(1)-N(1)	178.12(14)	175.736
C(1)-Ru(1)-N(1)	77.9(3)	77.759	C(2)-Ru(1)-N(1)	77.84(13)	76.989
C(17)-Ru(1)-O(1)	111.1(3)	108.598	C(1)-Ru(1)-O(2)	100.86(14)	107.993
C(1)-Ru(1)-O(1)	155.20(19)	153.431	C(2)-Ru(1)-O(2)	155.75(13)	153.257
N(1)-Ru(1)-O(1)	77.3(2)	75.671	N(1)-Ru(1)-O(2)	77.93(10)	76.270
C(17)-Ru(1)-P(1)	88.54(4)	88.296	C(1)-Ru(1)-P(1)	87.59(10)	88.536
C(1)-Ru(1)-P(1)	94.59(3)	92.849	C(2)-Ru(1)-P(1)	90.13(10)	92.780
N(1)-Ru(1)-P(1)	92.11(4)	91.896	N(1)-Ru(1)-P(1)	90.99(8)	91.567
O(1)-Ru(1)-P(1)	86.33(4)	88.041	O(2)-Ru(1)-P(1)	91.25(6)	88.248

V.3.3. DFT and TDDFT calculations

The Full geometry of the complexes **1** and **2** were optimized by DFT method in singlet ground state using the B3LYP correlation functional. Calculated bond distances and bond angles of the complexes are summarized in Table V.2. The calculated geometric parameters are reasonably well reproducing the X-ray crystal structures data. The contour plots of selected molecular orbitals for both the complexes **1** and **2** are given in Fig. V.13 and Fig. V.14 respectively. Energy and % of compositions of selected molecular orbitals are summarized in Table V.3 and Table V.4 respectively. For complex **1,** the higher energy occupied molecular orbital (HOMO) has 82% contribution of ligand along with 17% contribution of dπ(Ru) orbital and the low lying virtual orbital, LUMO has 92% contribution of ligand and for complex **2**, HOMO has 83% contribution of ligand and 15% contribution of

dπ(Ru) orbitals while LUMO has 90% contribution of ligand π* orbital. The HOMO to LUMO energy gaps is found to be 2.63 eV and 2.35 eV for **1** and **2** respectively.

UV-Vis absorption bands of the complexes are interpreted by TDDFT calculations using B3LYP/CPCM method in DMSO. Calculated vertical electronic transitions are shown in Table V.5. For complex **1**, the calculated low energy transition at 613 nm (*f* = 0.1216) corresponds to the HOMO → LUMO transition ($\lambda_{expt.}$ = 656 nm) having mixed ILCT and MLCT character. The moderately intense transition at 405 nm (HOMO-1 → LUMO transition, f=0.1986) corresponds to the experimentally observed peak at 432 having mixed MLCT and ILCT character. The high energy experimental band at 364 nm correspond to the ILCT character. For complex **2** the lower energy experimental band at 682 nm (ε = 4419 $M^{-1}cm^{-1}$) correspond to the HOMO → LUMO transition at 638 nm having mixed MLCT and ILCT character. The experimentally observed peak at 434 nm is well corroborated with the calculated transition at 427 nm corresponds to HOMO-1 → LUMO transitions having mixed ILCT and MLCT character. The high energy band at 319 nm corresponds to ILCT character.

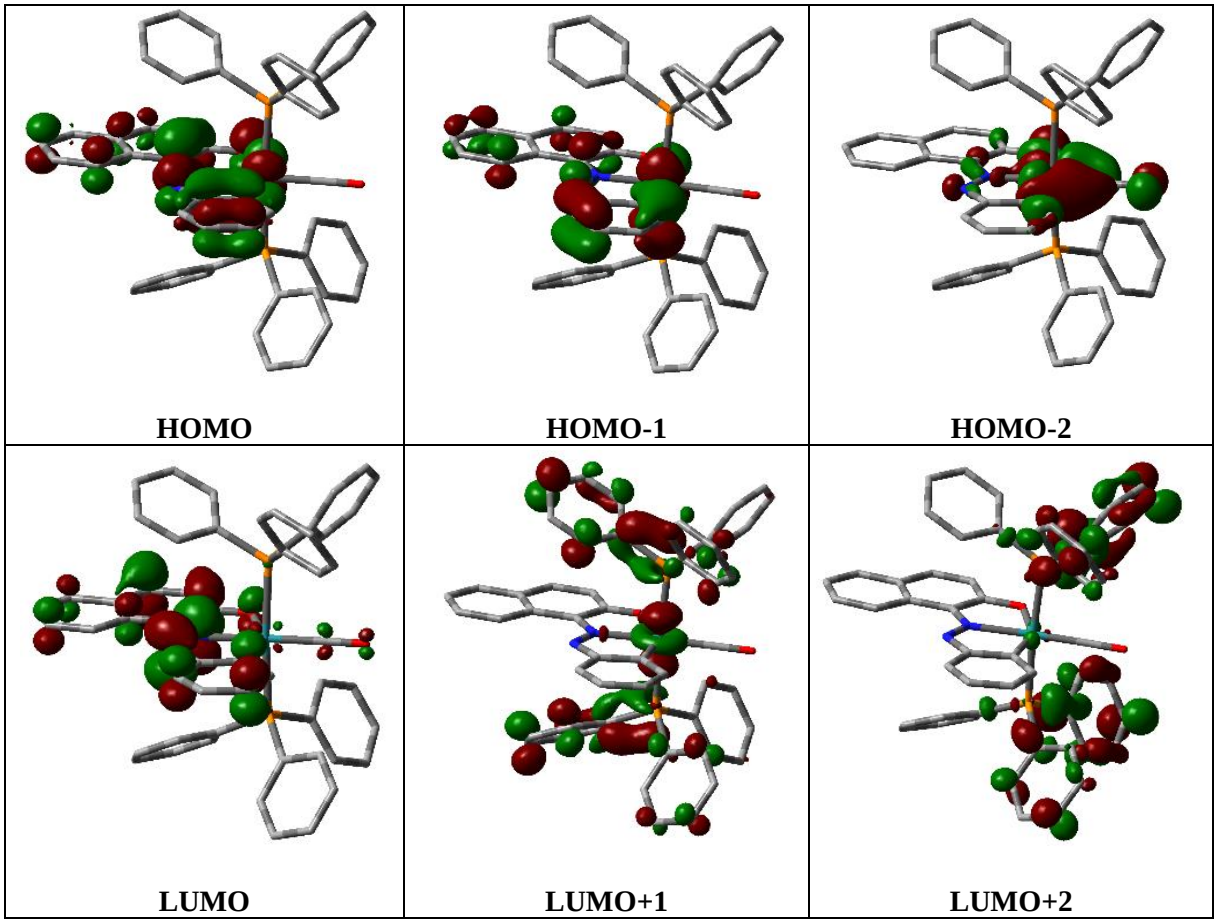

Fig. V.13. Contour plots of some selected molecular orbital of complex **1.**

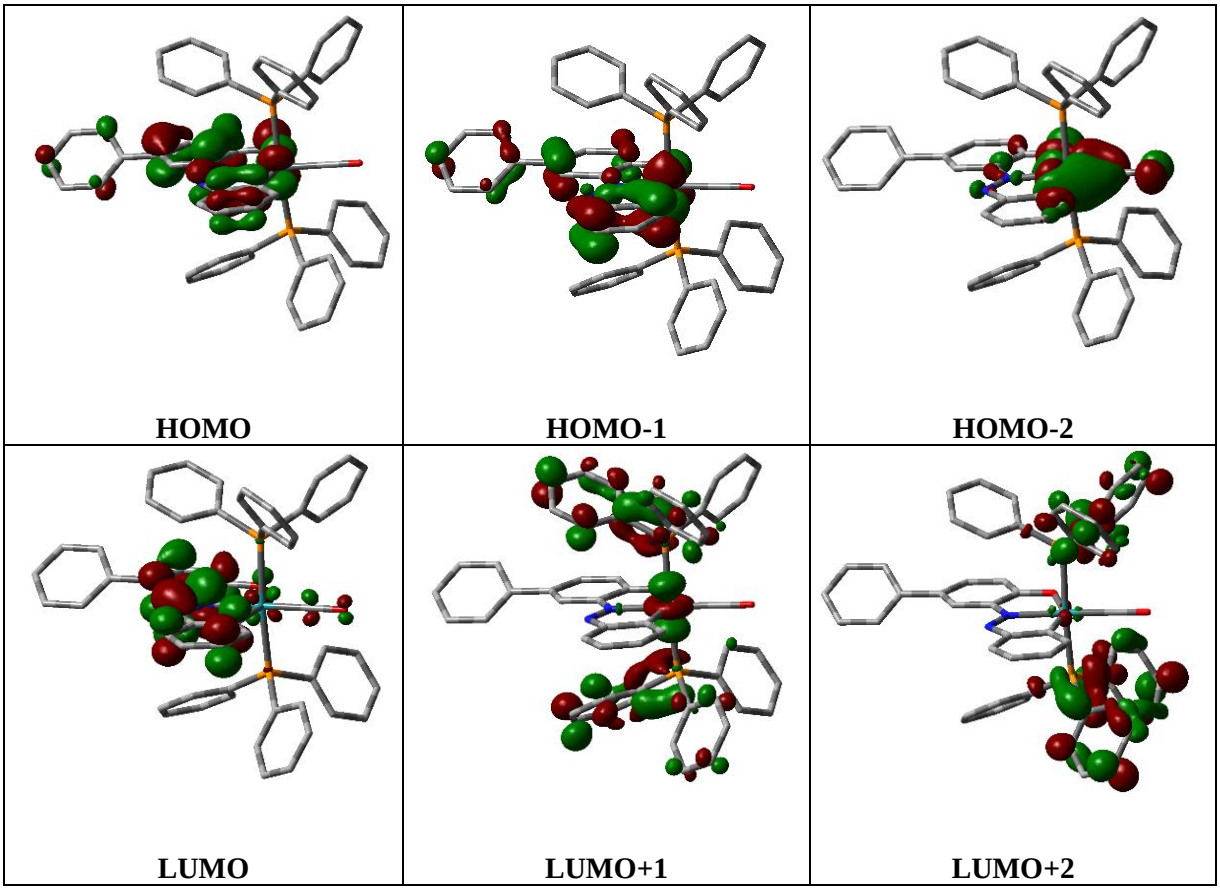

Fig. V.14. Contour plots of some selected molecular orbital of complex **2.**

Table V.3. Energy and % of composition of some selected molecular orbitals of complex **1.**

MO	Energy	% Composition			
		Ru	L^1	CO	PPh3
LUMO+5	-0.47	02	09	01	88
LUMO+4	-0.49	03	00	00	97
LUMO+3	-0.59	00	03	02	95
LUMO+2	-0.64	03	00	00	96
LUMO+1	-0.87	19	02	01	78
LUMO	-1.83	03	92	02	03
HOMO	-4.46	17	82	00	01
HOMO-1	-5.45	29	66	00	06
HOMO-2	-5.56	52	30	16	02
HOMO-3	-5.74	01	89	00	10
HOMO-4	-6.06	26	47	03	25

HOMO-5	-6.24	04	35	01	59
HOMO-6	-6.47	09	75	04	13
HOMO-7	-6.58	23	33	01	43
HOMO-8	-6.63	30	21	03	45
HOMO-9	-6.68	02	02	00	96
HOMO-10	-6.72	04	05	01	90

Table V.4. Energy and % of composition of some selected molecular orbitals of complex **2.**

MO	Energy	% Composition			
		Ru	L^2	CO	PPh3
LUMO+5	-0.50	03	03	01	93
LUMO+4	-0.52	02	00	00	97
LUMO+3	-0.63	00	02	02	97
LUMO+2	-0.68	03	00	00	96
LUMO+1	-0.92	19	02	01	77
LUMO	-1.92	04	90	03	03
HOMO	-4.51	15	83	00	02
HOMO-1	-5.48	28	66	00	06
HOMO-2	-5.61	51	31	15	02
HOMO-3	-5.84	09	86	01	04
HOMO-4	-6.13	15	24	00	61
HOMO-5	-6.44	16	40	03	42
HOMO-6	-6.48	00	99	00	01
HOMO-7	-6.61	30	50	05	16
HOMO-8	-6.68	06	26	01	67
HOMO-9	-6.70	09	18	00	72
HOMO-10	-6.72	01	11	01	87

Table V.5. Vertical electronic transition calculated by TDDFT/CPCM method of complexes **1** and **2.**

Compd.	λ (nm)	E (eV)	Osc. Strength (f)	Key excitations	Character	$\lambda_{expt.}$ (nm) (ε, $M^{-1}cm^{-1}$)
1	613.06	2.0224	0.1216	(94%)HOMO→LUMO	ILCT/MLCT	656 (5248)
	405.29	3.0592	0.1986	(92%)HOMO-1→LUMO	ILCT/MLCT	432 (8854)
	374.31	3.3123	0.1473	(93%)HOMO-3→LUMO	ILCT	364 (10196)
	332.91	3.7355	0.0633	(80%)HOMO-5→LUMO	ILCT	
2	637.97	1.9434	0.1192	(95%)HOMO→LUMO	ILCT/MLCT	682 (4419)
	427.45	2.9005	0.0524	(90%)HOMO-1→LUMO	ILCT/MLCT	434 (3828)
	370.20	3.3491	0.0543	(72%)HOMO-3→LUMO	ILCT	
	329.05	3.7680	0.1119	(70%)HOMO-6→LUMO	ILCT	319 (22914)

V.3.4. DNA binding studies

V.3.4.1. UV-Vis method

The interactions between metal complexes and CT-DNA were monitored by using the UV-Vis method, where the spectral changes in the absorbance were captured upon addition of CT-DNA to a fixed concentration of the Ru(II) complexes. The spectral titration curves showed a hypochromic shift with the increasing concentration of CT-DNA (Fig. V.15). The magnitude of the shift depends on the strength of interaction between metal complexes and CT-DNA. The intrinsic DNA binding constant (K_b) was determined by plotting [DNA]/($\varepsilon_a - \varepsilon_f$) vs. [DNA] from the spectral titration data using the Wolfe-Shimer equation (Eq. V.1).[59]

$$\frac{[DNA]}{(\varepsilon_a - \varepsilon_f)} = \frac{[DNA]}{(\varepsilon_b - \varepsilon_f)} + \frac{1}{K_b(\varepsilon_b - \varepsilon_f)} \qquad \text{(Eq. V.1)}$$

Where [DNA] is the concentration of DNA in the base pairs and ε_a is the apparent extinction coefficient observed for the complex, ε_f corresponds to the extinction coefficient of the complex in its free form and ε_b refers to the extinction coefficient of the complex when it is fully bound to CT-DNA. The plot of [DNA]/($\varepsilon_a - \varepsilon_f$) *vs.* [DNA] give a straight line with $1/(\varepsilon_b - \varepsilon_f)$ and $1/[K_b(\varepsilon_b - \varepsilon_f)]$ as slope and intercept, respectively. The ratio of the slope to the intercept from the linear fit give the value of the intrinsic binding constant (K_b). The K_b values are found to be $5.887(\pm0.12)\times10^5\ M^{-1}$ and $4.494(\pm0.16)\times10^5\ M^{-1}$ for complexes **1** and **2** respectively. These value are very much comparable to the reported values of binding constants for other complexes towards CT-DNA.[60] The significant hypochromic shift in

absorbance and the magnitude of calculated binding constants suggest that the Ru(II) complexes are likely bound to CT-DNA via intercalative mode.[61-63]

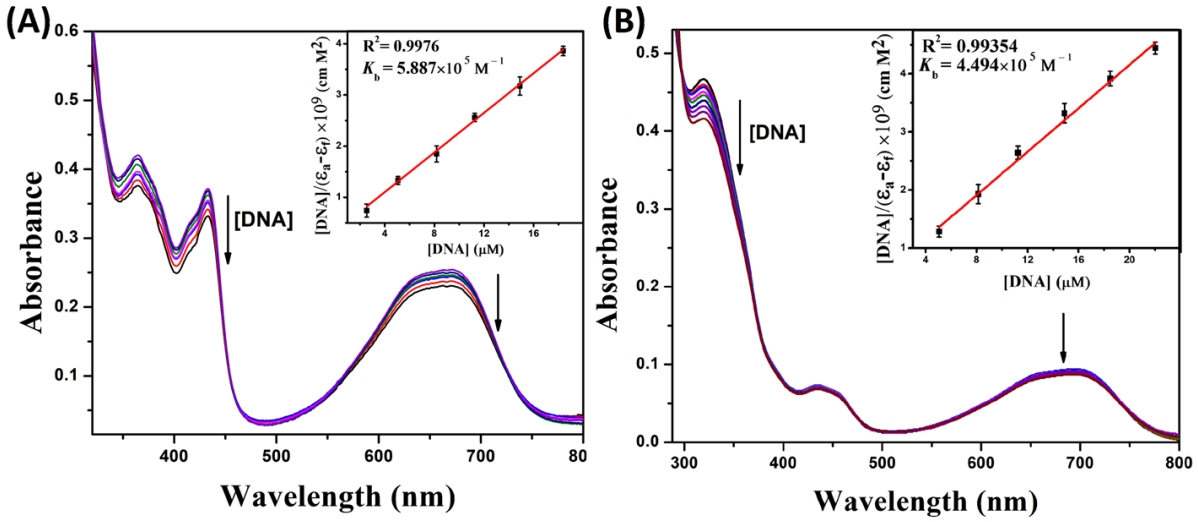

Fig. V.15. Change in absorption spectra of the complexes **1** (A) and **2** (B) in Tris–HCl/NaCl buffer with the gradual addition of CT DNA. Inset: Plot of [DNA]/($\varepsilon_b - \varepsilon_f$) vs. [DNA].

V.3.4.2. Fluorescence studies of Competitive DNA binding

The competitive binding experiments were carried out on the EB-CT-DNA system by varying the concentrations of the complexes to get further information about the binding mode of compounds with DNA. Ethidium bromide (EB) is a well-known DNA intercalator, which does not show fluorescence in its free-state, however, in presence of CT-DNA, it shows strong fluorescence as it is intercalated between the adjacent DNA base pairs. The addition of Ru(II) complexes to the EB–CT-DNA system caused a decrease in fluorescence intensity of about 39% and 35% with a red shift of 2-3 nm for the complexes **1** and **2** respectively (Fig. V.16). The observed quenching of DNA–EB fluorescence in the presence of the complexes suggested that they displace EB from the DNA double helix. The fluorescence quenching is explained by the Stern–Volmer equation (Eq. V.2).[64]

$$F_0/F = 1 + K_{sv}[Q] \qquad \text{(Eq. V.2)}$$

Where F_0 and F are the fluorescence intensities in the absence and presence of the complex, respectively. K_{sv} is the Stern–Volmer quenching constant and [Q] is the concentration of complex. The K_{sv} values are obtained with a slope from the plot of F_0/F versus [Q] (Fig. V.16 inset) and are found to be $8.748(\pm0.20)\times10^4$ M^{-1} and $6.740(\pm0.14)\times10^4$ M^{-1} for **1** and **2**

respectively. The quenching and binding constants of the Ru(II) complexes suggested that the interaction of the synthesized complexes with CT-DNA should be of intercalation.[65]

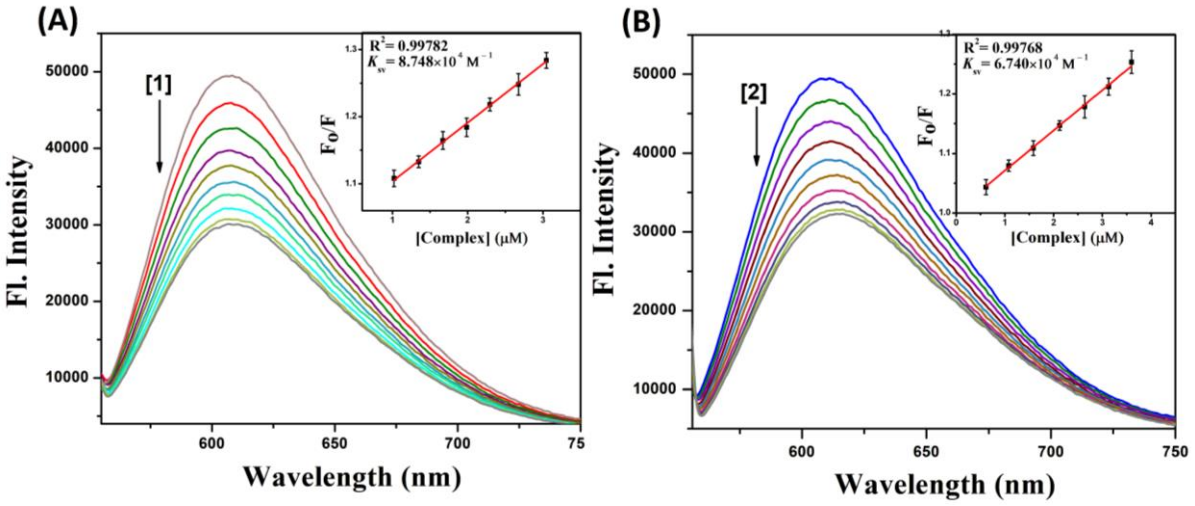

Fig. V.16. Emission spectra (λ_{ex} = 540 nm) of EB–CT-DNA in presence of increasing concentrations of the complexes **1** (A) and **2** (B). Inset: Plots of emission intensity F_0/F vs. [complex].

Table V.6. Binding constants (K_b) and Stern-Volmer constant (K_{SV}) values for the interaction of complexes **1** and **2** with CT-DNA.

Compound	UV Method	Fluorescence Method
	K_b ($\times 10^5$) (M^{-1})	K_{sv} ($\times 10^4$) (M^{-1})
DNA-EtBr + 1	5.887 ± 0.12	8.748 ± 0.20
DNA-EtBr + 2	4.494 ± 0.16	6.740 ± 0.14

V.3.4.3. Mode of binding: Viscometric analysis

Viscometric measurements were made to look into the binding manner of interaction between complexes **1** and **2** with CT-DNA. The least confusing way for determining how a tiny chemical interacts with nucleic acids is this hydrodynamic research.[66] The DNA helix will stretch as a result of a classical intercalator's insertion or accommodation into the DNA base pairs, which causes the double helix to unwind and ultimately increases viscosity.[67] Contrarily, electrostatic or groove binders don't interfere with the CT-DNA structure and don't significantly change the viscosity of the CT-DNA solution.[68]The specific viscosities of DNA with and without the complexes are η and η_0, respectively, and are significantly increased by a traditional DNA intercalator like EB.[69] In Fig. V.17, a plot of plot of $(\eta / \eta_0)^{1/3}$ against R (R = [complex]/[CT-DNA]) depicts the effects of complexes **1** and **2** on the viscosity of CT-DNA.

The relative viscosity of DNA solutions steadily rises with the addition of the ruthenium (II) complexes **1** and **2,** much like the conventional intercalator EB. This finding leads us to the conclusion that intercalative binding, not groove or electrostatic binding, is the preferred method for the complexes **1** and **2** to bind CT-DNA. The viscometric data show the complexes' DNA intercalation potentials in the trend EB > **1** > **2**, which precisely matches the results of our spectrometric DNA titration, as previously mentioned. As a result, the viscosity values are compatible with the spectral experiment results.

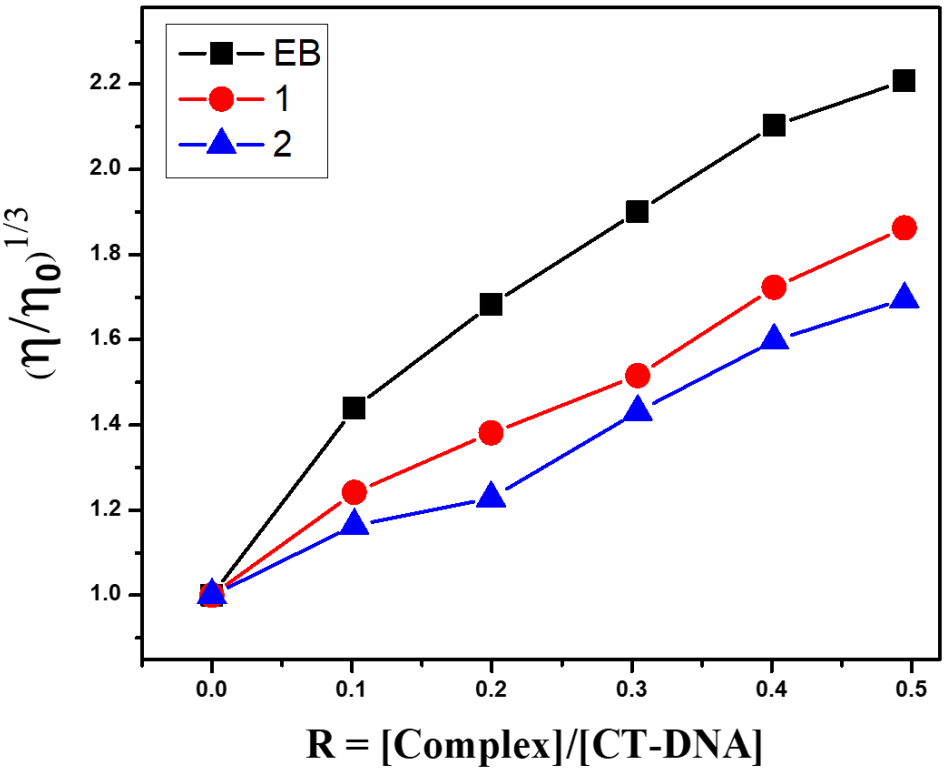

Fig. V.17. Relative viscosity of CT-DNA interacting with Ru(II) complexes **1**, **2** and EB.

V.3.5. Protein binding studies

V.3.5.1. Electronic absorption titration

UV-visible absorption measurement is a simple method to explore the structural changes and is useful to distinguish the type of quenching mechanism exist i.e. static or dynamic quenching mechanism. In the static quenching mechanism, a new complex is formed between BSA and the quencher in the ground state. Therefore, it will result in perturbation of the absorption spectrum of the fluorophore. But in the dynamic quenching mechanism, the fluorophore and quencher get in touch with each other during the transient existence of the excited state and therefore, no change is observed in the absorption spectrum of BSA. Electronic absorption spectra of BSA (10 μM in PBS at pH 7.4) were recorded in the range of

240-400 nm in presence of different concentration of complex which is shown in the Fig. V.18. BSA has a characteristic absorption band at 280 nm. From Fig. V.18 it is clear that the absorption intensity gradually increases with a small blue shift in the presence of complex, indicating a static interaction between BSA and the complexes. The apparent association constant (K_a) was calculated from the plot of $1/(A_{obs}-A_0)$ vs 1/[complex] (Fig. V.18 inset) adopting the following equation (Eq. V.3).

$$\frac{1}{A_{obs}-A_0} = \frac{1}{A_c-A_0} + \frac{1}{K_a(A_c-A_0)[complex]} \qquad \text{(Eq. V.3)}$$

Where A_{obs} is the observed absorbance (at 280 nm) of the solution taking various concentrations of the complex, A_0 and A_c are the absorbance of BSA only and the absorbance of serum albumin with the complex. The calculated value of apparent association constant (K_a) is $10.211(\pm0.24)\times10^4$ M^{-1} and $6.922(\pm0.15)\times10^4$ M^{-1} for the complexes **1** and **2** respectively and these values are comparable to reported value.[60, 65, 70]

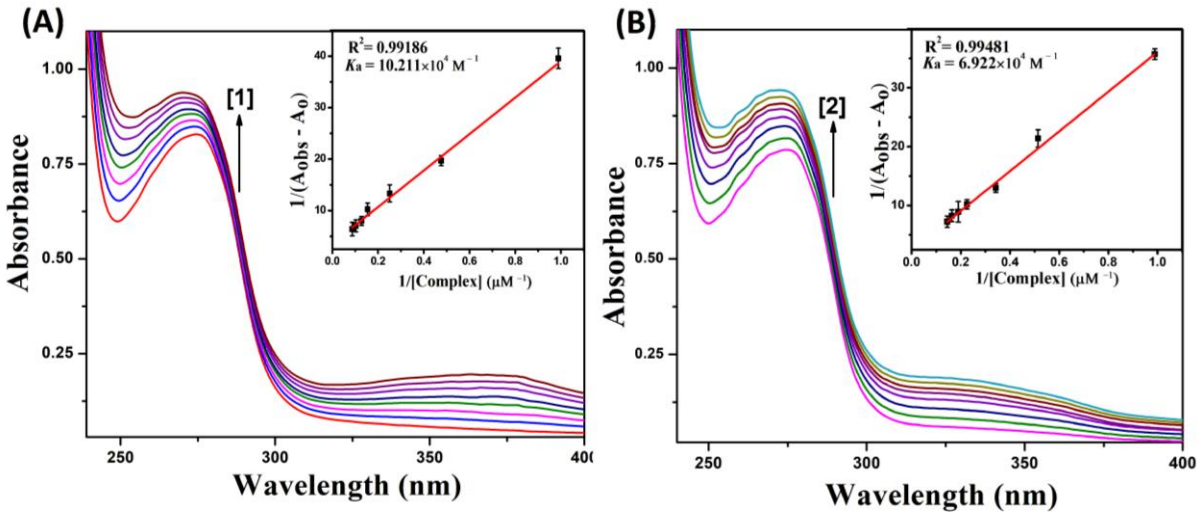

Fig. V.18. Change in absorption spectra of BSA with the gradual addition of complex **1** (A) and complex **2** (B). Inset: Plot of $1/(A_{obs}-A_0)$ vs 1/[complex].

V.3.5.2. Fluorescence quenching studies

In order to determine the protein binding affinity of the complexes, tryptophan quenching experiments were carried out upon the gradual addition of the complexes. Though BSA contains three fluorophores, namely tryptophan, tyrosine and phenylalanine, the emission spectra of BSA exhibit an intense fluorescence emission maximum at 336 nm, due to the tryptophan residues alone, because phenyl alanine has a very low quantum yield and the

fluorescence of tyrosine is completely quenched if it is ionized or near a tryptophan residue. The fluorescence emission spectra of BSA solution were recorded in the range of 290-450nm (λ_{ex} = 280nm), with various concentration of the complexes which are shown in Fig. V.19. Addition of the Ru(II) complexes to the solution of BSA results in a significant decreased in fluorescence intensity with a blue shift of 4-3 nm for complexes **1** and **2** respectively. The observed blue shift is mainly due to the fact that the active site in protein is buried in a hydrophobic environment. It suggested that some associative interaction is taking place between the complexes and BSA protein.[71]

The Stern-Volmer equation was employed to investigate fluorescence quenching data in order to study the quenching process (Eq. V.2). The Stern-Volmer quenching constant values (K_{sv}) obtained from the plot of F_0/F vs [Q] (Fig. V.19 inset) were found to be 6.853(±0.18)×10^4 M^{-1} and 4.629(±0.07)×10^4 M^{-1} corresponding to complexes **1** and **2** respectively. From the K_{sv} values, it is seen that complexes exhibited a good fluorescence quenching ability. Furthermore, the quenching rate constant (K_q) calculated from K_{sv} and τ_o using the equation $Kq = K_{sv}/\tau_o$ (τ_o refers to the lifetime of the fluorophore without the quencher with an average value of 10^{-8} s) were found to be in the range of 6.85–4.62 × 10^{12} M^{-1} s^{-1} for complexes **1** and **2** respectively. These values are higher than the maximum possible value for dynamic quenching (2 × 10^{10} M^{-1} s^{-1}), suggesting the involvement of static quenching mechanism in this process.[72]

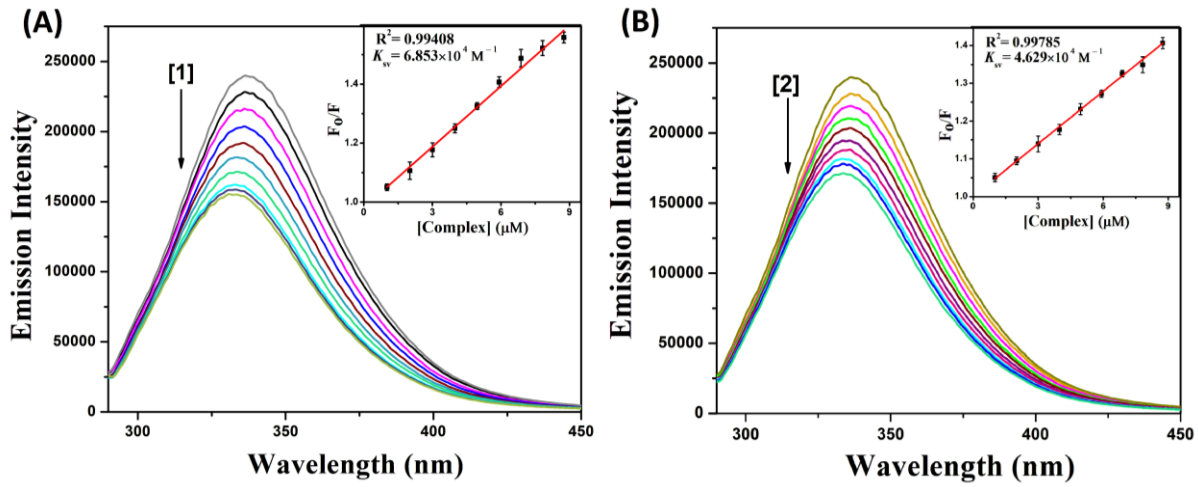

Fig. V.19. Emission spectra (λ_{ex} = 280 nm) of BSA in presence of increasing concentrations of the complexes **1** (A) and **2** (B). Inset: Plots of emission intensity F_0/F vs. [complex].

V.3.5.3. Binding constant and binding sites

Further, the binding constant (K_b) and number of binding sites (n) in static quenching can be calculated by using following Scatchard equation (Eq. V.4).

$$log\,\frac{(F_0-F)}{F} = log\,K_b + nlog[complex] \qquad \text{(Eq. V.4)}$$

Where F_0 and F are the fluorescence intensities in the absence and presence of the complex. The values of binding constant (K_b) and the binding sites (n) are given in Table V.7, which obtained from the plot of log [(F_o-F)/F] versus log [complex] (Fig. V.20). Based on the plot, calculated values of K_b for the complexes **1** and **2** are 4.103(±0.11)×10^5 M^{-1} and 1.444(±0.07)×10^5 M^{-1} and n are 1.15(±0.03) and 1.05(±0.01) respectively. These high binding constant (K_b) values confirm the existence of strong interactions between BSA protein and Ru(II) complexes, which is essential for transport of the complexes through the biological systems. The obtained n value is approximate to 1, strongly suggesting the complexes are bound to BSA protein via one binding site.

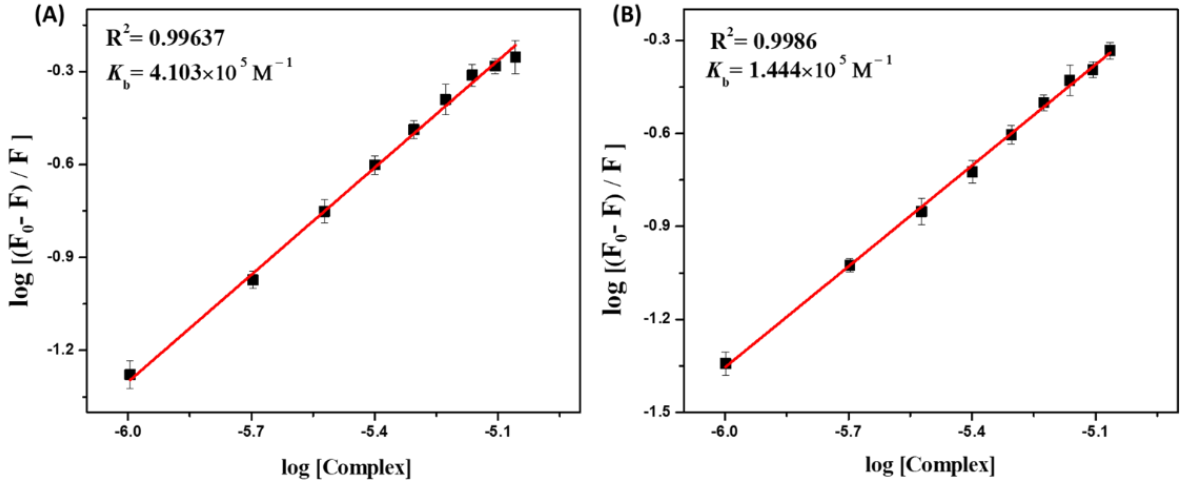

Fig. V.20. Plot of log [(F_o-F)/F] versus log [complex] of complexes **1** (A) and **2** (B).

Table V.7. Protein apparent association constant (K_a), binding constant (K_b), quenching constant (K_{sv}) and number of binding sites (n) for the interaction of complexes **1** and **2** with BSA.

Compound	UV Method	Fluorescence Method		
	K_a (×10^4) (M^{-1})	K_b (×10^5) (M^{-1})	K_{sv} (×10^4) (M^{-1})	n
BSA + 1	10.211 ± 0.24	4.103 ± 0.11	6.853 ± 0.18	1.15 ± 0.03
BSA + 2	6.922 ± 0.15	1.444 ± 0.07	4.629 ± 0.07	1.05 ± 0.01

V.3.5.4. Synchronous fluorescence spectroscopic studies

The conformational changes of the protein molecular environment in the vicinity of the fluorophore functional groups have been investigated by synchronous fluorescence spectroscopy. The fluorescence of BSA is mainly due to the tryptophan and tyrosine residues.[73] According to Miller,[74] the difference between the excitation and emission wavelengths ($\Delta\lambda = \lambda_{em} - \lambda_{ex}$) indicates the nature of the chromophores in the spectra. A lower $\Delta\lambda$ value such as 15 nm is characteristics of the tyrosine residue, while a larger $\Delta\lambda$ value such as 60 nm is characteristics of tryptophan residue. The synchronous fluorescence spectra of BSA with various concentrations of complexes recorded at $\Delta\lambda$ = 15 nm and $\Delta\lambda$ = 60 nm are shown in Fig. V.21 and Fig. V.22 respectively. In the synchronous fluorescence spectra of BSA at $\Delta\lambda$ = 15, addition of the complexes to the solution of BSA results in a small decrease in the fluorescence intensity of BSA at 302 nm. But, at the same time, in the case of the synchronous fluorescence spectra of BSA at $\Delta\lambda$ = 60, addition of the complexes to the solution of BSA results in a significant decrease along with a blue shift of the fluorescence intensity of BSA at 343 nm. Therefore, the synchronous fluorescence spectral studies suggested that the fluorescence intensity of both the tryptophan and tyrosine residues were affected by increasing the concentration of the complexes but a significant decrease along with a blue shift of the fluorescence intensity of tryptophan residues has been observed. At the same time, there is no change in the emission wavelength of tyrosine. These results confirmed that the interaction of the complexes with BSA protein affects the conformation of tryptophan much more than the tyrosine micro region. Hence, the strong interaction of these complexes with BSA suggested that the complexes can easily be stored in protein and can be fit for anticancer studies.

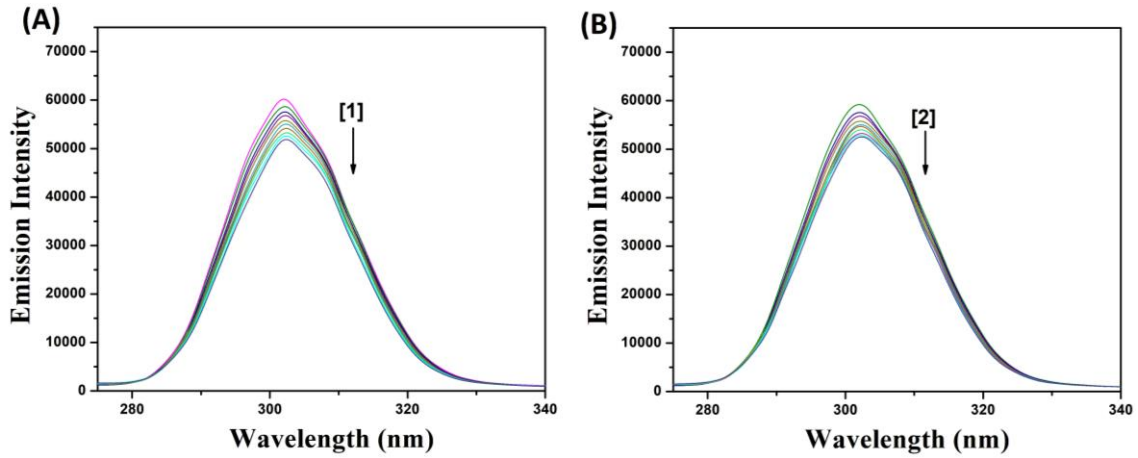

Fig. V.21. The synchronous spectra of BSA in the presence of increasing amounts of the complexes **1** (A) and **2** (B) at a wavelength difference of $\Delta\lambda$ = 15 nm. The arrow shows the emission intensity changes upon an increase in the concentration of the complexes.

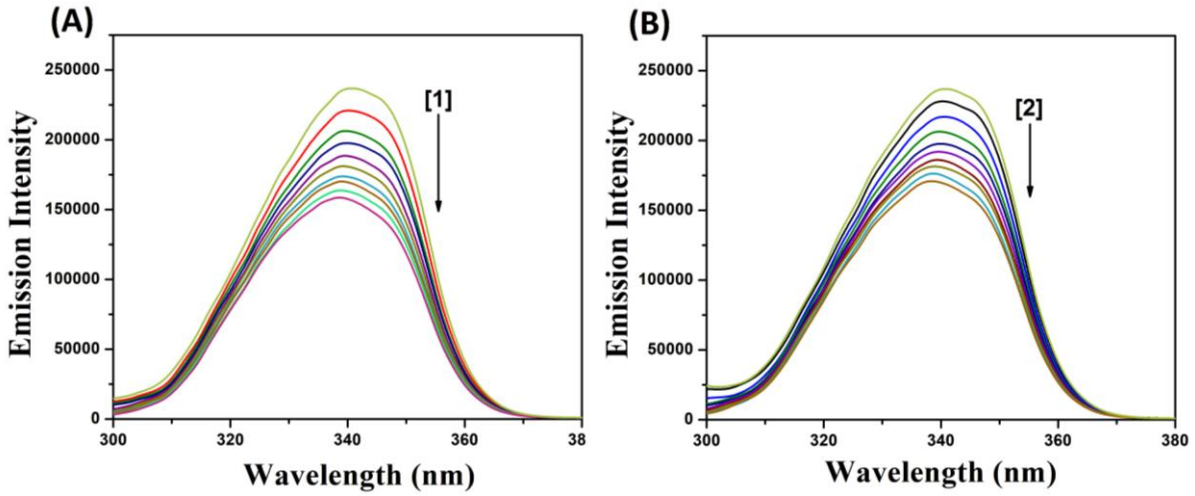

Fig. V.22. The synchronous spectra of BSA in the presence of increasing amounts of the complexes **1** (A) and **2** (B) at a wavelength difference of $\Delta\lambda$ = 60 nm. The arrow shows the emission intensity changes upon an increase in the concentration of the complexes.

V.3.5.5 Three-dimensional fluorescence spectra analysis

To investigate the micro environmental change in BSA during interaction with the ruthenium complexes, three-dimensional fluorescence spectroscopic studies have been performed. The changes observed in 3D emission spectra and contour lines of BSA in the absence and presence of complexes are given in Fig. V.23.

The 3D fluorescence spectra of BSA exhibit three characteristics peaks which are marked as peak A, B and C. Peak A denotes the Rayleigh scattering peak ($\lambda_{em} = \lambda_{ex}$), whereas peak B mainly reveals the spectral behavior of Trp and Tyr residues of proteins and another peak C mainly exhibits the fluorescence emission characteristic of the polypeptide backbone structures.[75,76] The emission intensity of Rayleigh scattering peak increased upon adding the complex to BSA. This is due to the formation of fluorophore-quencher complex between BSA and ruthenium complexes which increased the diameter of the macromolecule and enhanced the scattering effect. The fluorescence intensity of peak B and peak C were found to decrease after the addition of complexes, indicating that there was interaction between complexes and BSA proteins. The intensity changes of peak B and C revealed that the molecular microenvironment and conformational changes of BSA protein occurred after interaction with ruthenium complexes.

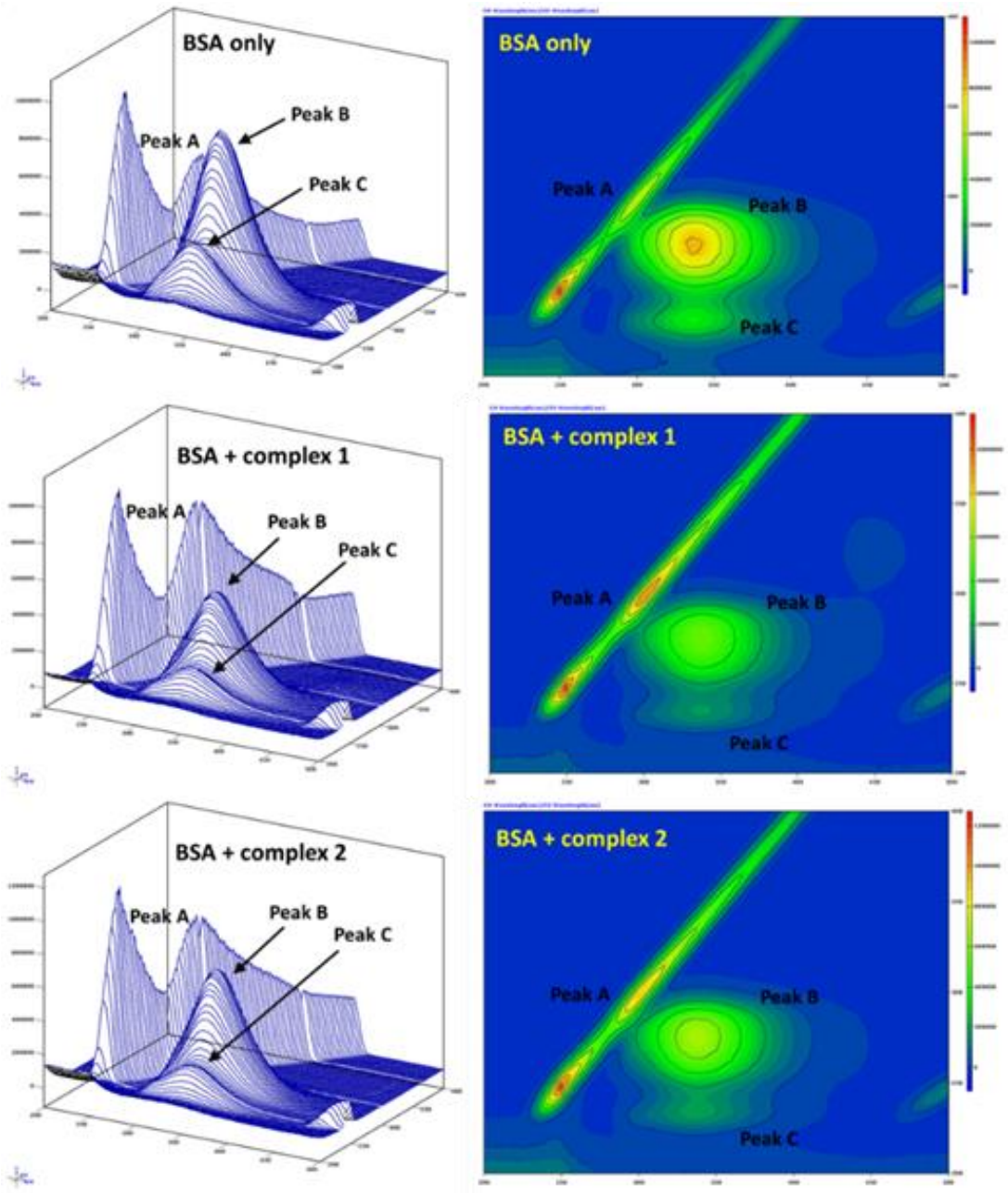

Fig. V.23. Three-dimensional fluorescence spectra of BSA in the absence and presence of ruthenium (II) complexes **1** and **2.**

V.3.6. In vitro antiproliferative studies

V.3.6.1 Cell viability assay

Cell viability was studied using MTT assay on different cancer cell lines (MCF-7, A549, MDA-MB-231 and AGS). The IC_{50} values of the ligands as well as complexes were tabulated in Table V.8. After 24 h of incubation, it was shown that complex **1** and **2** were the most potent inhibitors of MCF-7 cell growth and proliferation compared to other cell lines (Fig. V.25). Therefore, MCF-7 cells were utilized in subsequent investigations.[77] When tested on

the normal hepatic cell line WRL68, both the complexes showed significantly high IC_{50} values (>55 μM) compare to MCF-7 (5.1-6.3 μM) and A549 (21.3-36.2 μM) cell lines. Most importantly the IC_{50} values of complexes **1** and **2** are found to be less compare to cisplatin (14.2 μM) towards MCF-7 cells.

Table V.8. IC_{50} values (in μM) of ligands and their respective complexes against various cancer and normal cell lines.

Cell lines	MCF-7	A549	MDAMB231	AGS	WRL68
Compounds	IC_{50} of compounds (μM)				
HL^1-SEt	97.9±2.3	105.3±1.3	118.3±1.1	145.2±2.1	110.1±2.3
HL^2-SMe	122.5±1.7	112.4±1.6	124.2±1.3	151.2±1.6	130.1±1.5
Complex 1	5.1±1.2	36.2±1.5	65.3±1.2	42.1±3.1	55.3±1.4
Complex 2	6.3±3.1	21.3±3.2	53.2±1.3	51.1±1.4	57.8±2.4
Cisplatin	14.2±1.6	15.2±2.8	90.8±2.1	27.1±2.3	40.0±2.1

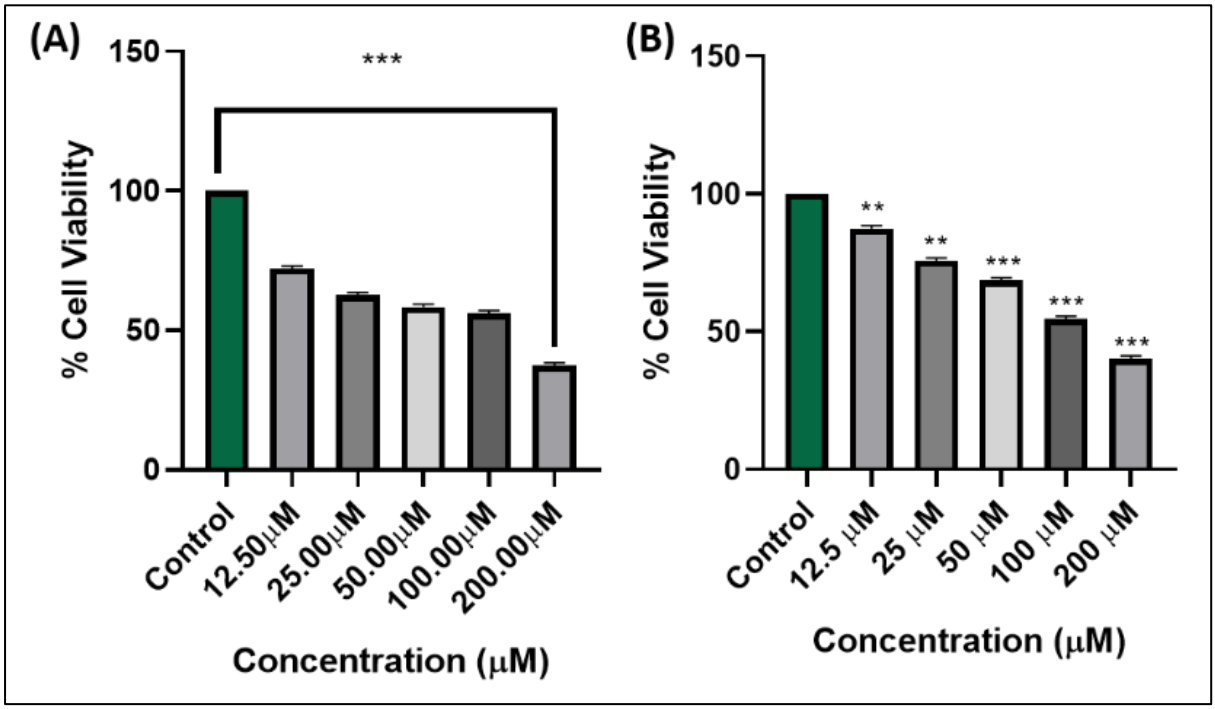

Fig. V.24. Percentage cell viability measured for HL^1-SEt (A) and HL^2-SMe (B) against MCF-7.

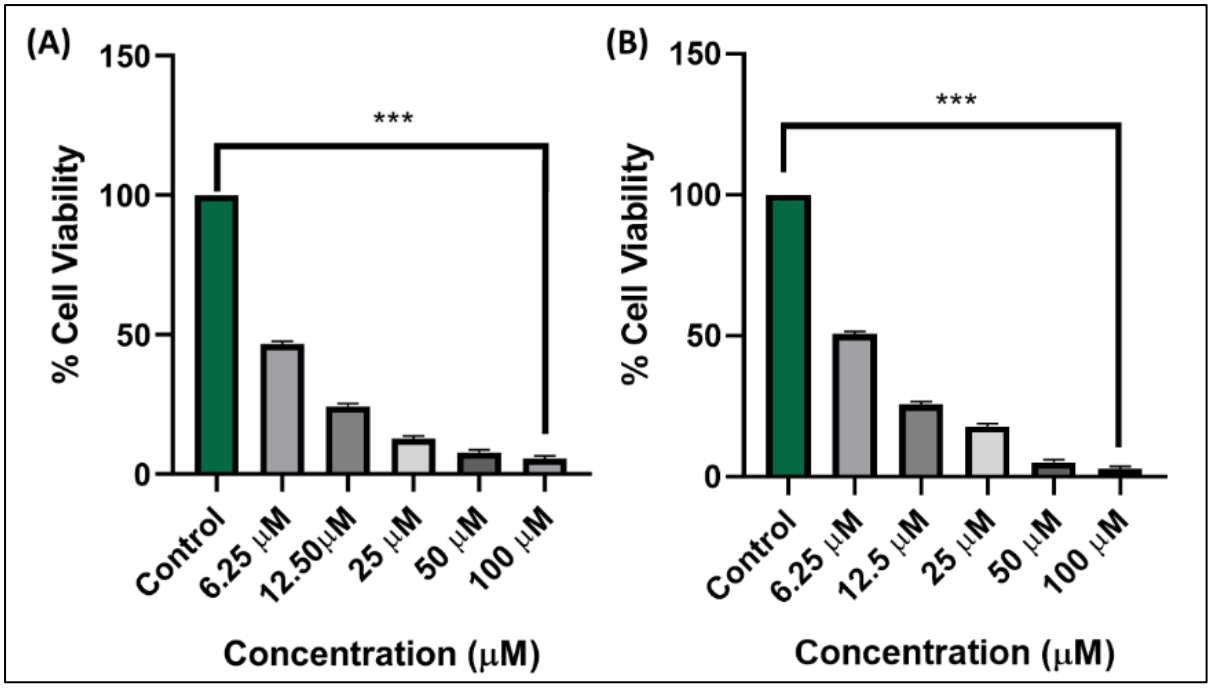

Fig. V.25. Percentage cell viability measured for complexes **1** (A) and **2** (B) against MCF-7.

V.3.6.2. Colony formation assay

For 24 h, MCF-7 was treated with various concentrations of ligands as well as their respective complexes.[78] At 4X magnification, the cells were observed in a bright field. The numbers and sizes of the colony were examined, and a significant decrease was found for both complexes compared to ligands and controls (Fig. V.26).

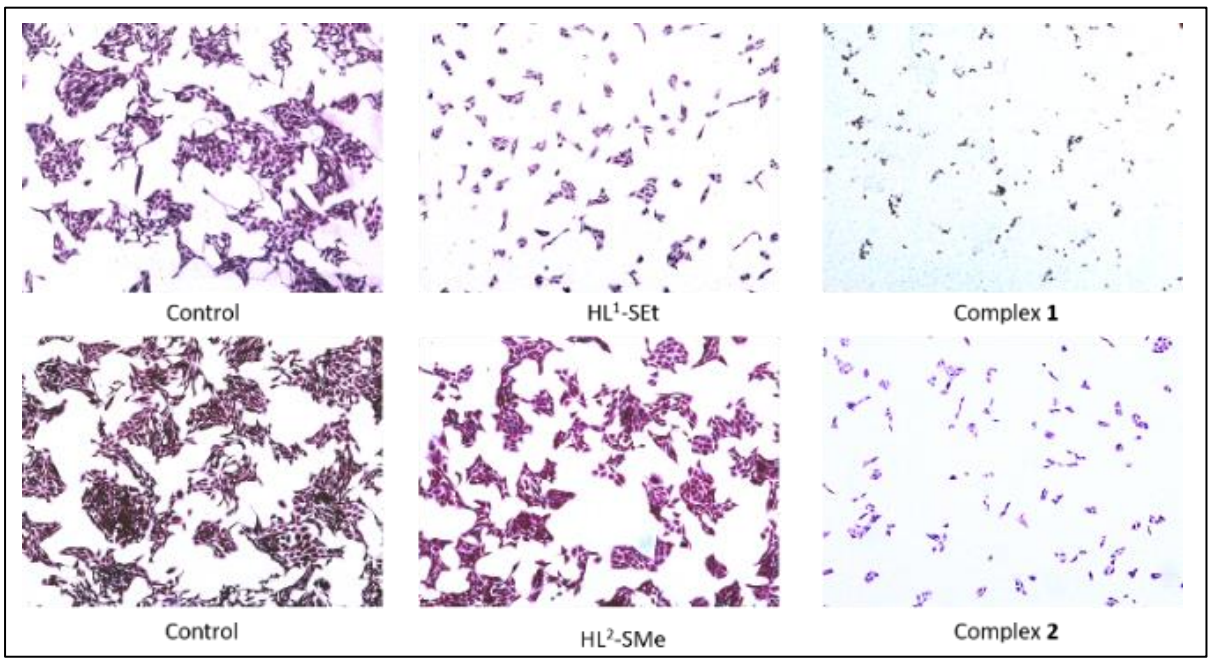

Fig. V.26. Colony formation of AGS cell lines after treatment of ligands and their respective complexes **1** and **2** for 24 h.

V.3.6.3. Hoechst assay

Hoechst Staining Assay, which is sensitive to DNA, was used to investigate the anti-cancer effect of the complex **1** and **2** on breast cancer cells in more detail.[79] After 24 hours of exposure to both ruthenium complexes, MCF-7 cells showed changes in their nucleus morphology (Fig. V.27). In the treated cells, there were blatant signs of nuclear fragmentation which indicated the occurrence of cellular apoptosis along with nucleus shrinkage, cytoplasmic vacuolation, blebbing, and chromatin condensation. In contrast, in the untreated control, the nucleus had a distinct shape, appeared blue, and had no morphological alterations. These findings demonstrated the substantial apoptosis-inducing potential of complexes **1** and **2**.

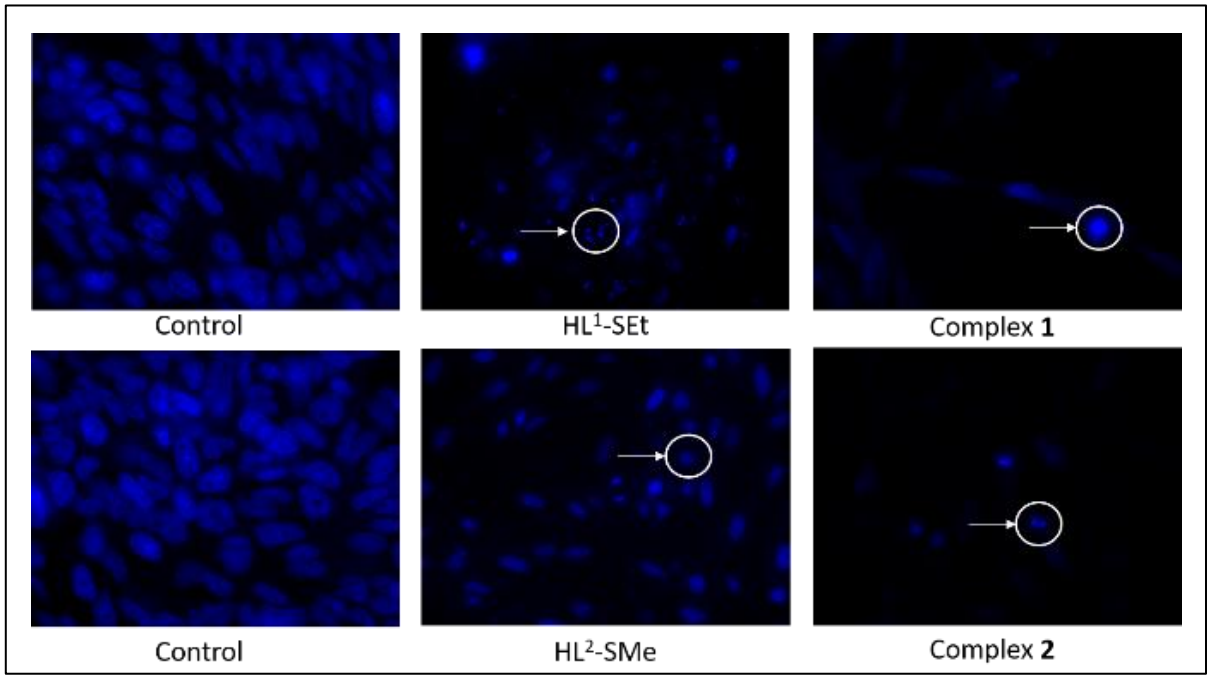

Fig. V.27. Nuclear staining of MCF-7 breast cancer cells using Hoechst 33258 staining. Untreated control shows uniformly stained nucleus. Whereas after 24 hrs treatment with ligands along with their respective complexes there were visible nuclear fragmentation and condensation with an apoptotic morphology. The results were prominent in the cells treated with the complexes than their respective ligands.

V.3.6.4. AO/EB staining

An established method for determining the frequency of cellular apoptosis, which is distinguished by different alterations in cellular morphology and DNA fragmentation, is AO/EB staining.[80-82] Green staining of viable cells with ordered cellular structure shows no evidence of apoptosis. While cells that stain red suggest cellular death combined with

chromatin condensation or fragmentation, cells that retain a yellow stain are indicative of early apoptosis where the cell membrane is intact but there is clear commencement of DNA fragmentation. MCF-7 cells displayed an increase in red/orange staining after being exposed to selective dose of the complex **1** and **2**, which is a clear sign of apoptosis and is characterized by nuclear morphological distortion, membrane blebbing, fragmentation, and shrinkage (Fig. V.28).

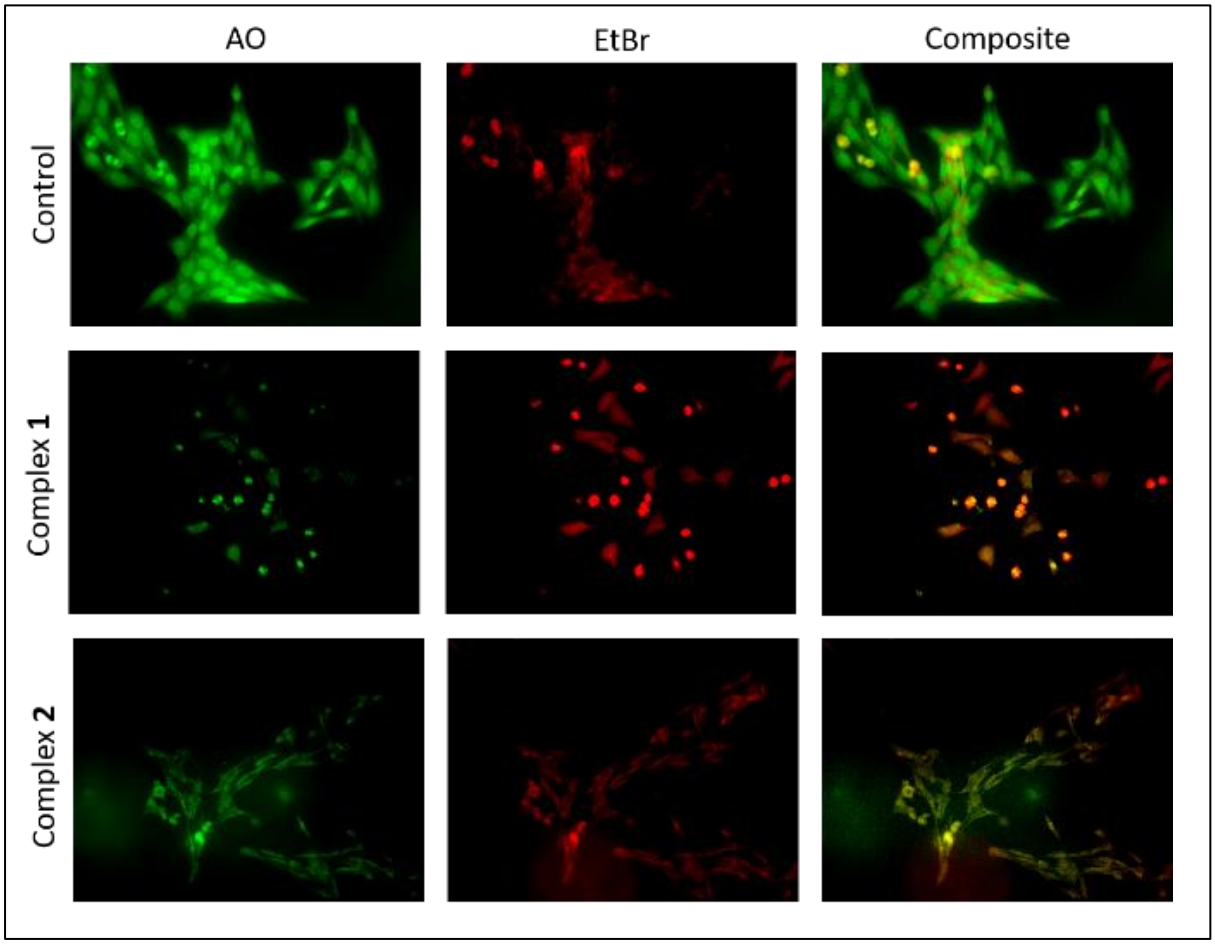

Fig. V.28. Acridine Orange/ EtBr staining with the MCF-7 Cells. The negative control group shows the normal nucleus located at the center. Cells treated with Complex **2** shows early apoptosis with nucleus stained with Acridine orange whereas cells upon 24 hrs exposure to Complex **1** showed orange/red fluorescence due to the uptake of EtBr stain. This nucleus is a typical representation of a late apoptotic cell.

V.4. Conclusions

Two new cyclometallated ruthenium(II) carbonyl complexes of the general formula $[Ru(L^1/L^2)(CO)(PPh_3)_2]$ (**1**/**2**) were synthesized and characterized by analytical and spectral techniques (IR, UV/visible, 1H NMR and ESI-MS). The crystal structures of complexes (**1** and **2)** were confirmed by X-ray crystallography, which indicated CNO tridentate

coordination of the ligands through C(aryl)–S bond activation. The XRD study also reveals the presence of a distorted octahedral geometry around the ruthenium(II) ion. DFT calculations were used to determine the structural parameters of the complexes that are in good agreement with X-ray analysis. Also, TD-DFT generated electronic transitions were in good agreement with the experimentally resolved UV-vis spectra of the complexes. The DNA binding ability of the complexes examined by absorption and fluorescence spectral techniques revealed an intercalative interaction between complexes and CT-DNA. Further, binding abilities of the complexes with BSA also monitored by absorption and fluorescence spectroscopy revealed the presence of static quenching and the results of synchronous and 3D fluorescence spectroscopic studies indicated that the complexes bound with BSA protein in both tyrosine and tryptophan residues and change the secondary structure of the BSA protein. The *in vitro* antiproliferative activities of the complexes showed that complex **1** is more potent than complex **2** in MCF-7 cell line. From the MTT assay data, it is concluded that the synthesized complexes exhibited higher cytotoxic potency than the widely used clinical chemotherapeutic agent cisplatin against MCF-7. Morphological analysis was performed using fluorescence microscope by AO/EB staining assay, which showed that complexes were able to prompt the cell death of the human breast cancer cells (MCF-7) through apoptosis. On the basis of the reported results, our synthesized cyclometallated ruthenium (II) complexes can be further investigated using in vivo models, since they represent promising candidates for anticancer applications.

V.5. References

1. H. Sung, J. Ferlay, R. L. Siegel, M. Laversanne, I. Soerjomataram, A. Jemal and F. Bray, *Ca Cancer J. Clin.*, 2021, **71**, 209-249.
2. H. Nagai, and Y.H. Kim, *J. Thorac. Dis.*, 2017, **9**, 448.
3. P. G. Corrie, *Medicine*, 2011, **39**, 717-722.
4. K. Bukowski, M. Kciuk, and R. Kontek, *Int. J. Mol. Sci.*, 2020, **21**, 3233.
5. I. Bratsos, T. Gianferrara, E. Alessio, C. G. Hartinger, M. A. Jakupec and B. K. Keppler, *Bioorg. Med. Chem.*, 2011, 151-174.
6. P. F. Iqbal, M. A. Malik, and W. A. Wani, *World J. Pharm. Pharm. Sci*., 2018, **7**, 654-664.
7. R. M. G. Rajapakse and S. P. Dunuweera, *Int. J. Clin. Oncol. Cancer Res*., 2017, **2**, 65-74.
8. N. V. Loginova, H. I. Harbatsevich, N. P. Osipovich, G. A. Ksendzova, T. V. Koval'chuk and G. I. Polozov, Curr., *Med. Chem.*, 2020, **27**, 5213-5249
9. A. J. Wagstaff, A. Ward, P. Benfield and R. C. Heel, *Drugs*, 1989, **37**, 162-190.

10. E. Raymond, S. Chaney, A. Taamma and E. Cvitkovic, *Ann. Oncol*., 1998, **9**, 1053-1071.
11. M. Shimada, H. Itamochi and J. Kigawa, *Cancer Manage. Res.*, 2013, **5**, 67.
12. A. M. Florea and D. Büsselberg, *Cancers*, 2011, **3**, 1351-1371.
13. R. Siegel, D. Naishadham and A. Jemal, *Ca-Cancer J. Clin.*, 2013, **63**, 11–30.
14. T. T. H. Fong, C. N. Lok, C. Y.-S. Chung, Y. M. E. Fung, P. K. Chow, P. K. Wan and C. M. Che, *Angew. Chem., Int. Ed*., 2016, **55**, 11935-11939.
15. H. Huang, P. Zhang, Y. Chen, K. Qiu, C. Jin, L. Ji and H. Chao, *Dalton Trans*., 2016, **45**, 13135.
16. C. S. Allardyce and P. J. Dyson, *Platinum Metals Rev*., 2001, **45**, 62-69
17. S. Thota, D. A. Rodrigues, D. C. Crans and E. J. Barreiro, *J. Med. Chem*., 2018, **61**, 5805–5821.
18. A. Bergamo, C. Gaiddon, J. Schellens, J. Beijnen and G. Sava, *J. Inorg. Biochem*., 2012, **106**, 90-99.
19. P.-S. Kuhn, V. Pichler, A. Roller, M. Hejl, M. Jakupec, W. Kandioller and B. Keppler, *Dalton Trans*., 2015, **44**, 659-668.
20. S. W. Chang, A. R. Lewis, K. E. Prosser, J. R. Thompson, M. Gladkikh, M. B. Bally, J. J. Warren and C. J. Walsby, *Inorg. Chem*., 2016, **55**, 4850-4863.
21. J. M. Rademaker-Lakhai, D. van den Bongard, D. Pluim, J. H. Beijnen and J. H. Schellens, *Clin. Cancer Res*., 2004, **10**, 3717-3727.
22. C. G. Hartinger, S. Zorbas-Seifried, M. A. Jakupec, B. Kynast, H. Zorbas and B. K. Keppler, *J. Inorg. Biochem*., 2006, **100**, 891-904.
23. C. G. Hartinger, M. A. Jakupec, S. Zorbas-Seifried, M. Groessl, A. Egger, W. Berger, H. Zorbas, P. J. Dyson and B. K. Keppler, *Chem. Biodiversity*, 2008, **5**, 2140-2155.
24. D. A. Smithen, H. Yin, M. H. R. Beh, M. Hetu, T. S. Cameron, S. A. McFarland and A. Thompson, *Inorg. Chem*., 2017, **56**, 4121-4132.
25. Y. Chen, W. Lei, G. Jiang, Y. Hou, C. Li, B. Zhang, Q. Zhou and X. Wang, *Dalton Trans.*, 2014, **43**, 15375-15384.
26. C. Imberti, P. Zhang, H. Huang and P. J. Sadler, *Angew. Chem.*, 2020, **59**, 61-73.
27. Y. Chen, L. Bai, P. Zhang, H. Zhao and Q. Zhou, *Molecules*, 2021, **26**, 5679.
28. (a) T. Bessho, E. Yoneda, J. H. Yum, M. Guglielmi, I. Tavernelli, H. Imai, U. Rothlisberger, M. K. Nazeeruddin and M. J. Grcatzel, *J. Am. Chem. Soc*., 2009, **131**, 5930-5934; (b) P. G. Bomben, K. C. D. Robson, P. A. Sedach and C. P. Berlinguette, *Inorg. Chem*., 2009, **48**, 9631-9643; (c) B. D. Koivisto, K. C. D. Robson and C. P. Berlinguette, *Inorg. Chem*., 2009, **48**, 9644-9652.
29. (a) C. Gaidon, P. Jeannequin, P. Bischoff, M. Pfeffer, C. J. P. Sirlin and Loeffler, *J. Pharmacol. Exp. Ther*., 2005, **315**, 1403-1411; (b) L. Leyva, C. Sirlin, L. Rubio, C. Franco, R. L. Lagadec, J. Spencer, P. Bischoff, J. Gaidon, C. P. Loeffler and M. Pfeffer,

Eur. J. Inorg. Chem., 2007, **19**, 3055-3066; (c) L. Leyva, F. Malek, S. Benzina, J. M. Denis, J. Gueulette, P. Dufour, C. Gaiddon, J. P. Loeffler, C. Sirlin, M. Pfeffer and P. Bischoff, *Lett. Drug Des. Discovery*, 2008, **5**, 1-6; (d) X. Meng, M. L. Leyva, M. Jenny, I. Gross, S. Benosman, B. Fricker, S. Harlepp, P. Hebraud, A. Boos, P. Wlosik, P. Bischoff, C. Sirlin, M. Pfeffer, J. P. Loeffler and C. Gaiddon, *Cancer Res*., 2009, **69**, 5458–5466; (e) J. Ruiz, C. Vicente, C. De Haro and D. Bautista, *Dalton Trans*., 2009, **26**, 5071-5073.

30. (a) Y. K. Yan, M. Melchart, A. Habtemariam and P. J. Sadler, *Chem. Commun*., 2005, **38**, 4764-4776. (b) P. C. Bruijnincx and P. J. Sadler, *Curr. Opin. Chem. Biol*., 2008, **12**, 197–206. (c) F. Wang, A. Habtemariam, E. P. van der Geer, R. Ferna´ndez, M. Melchart, R. J. Deeth, R. Aird, S. Guichard, F. P. Fabbiani and P. Lozano-Casal, *Proc. Natl. Acad. Sci. U. S. A*., 2005, **102**, 18269-18274.
31. (a) S. W. Magennis, A. Habtemariam, O. Novakova, J. B. Henry, S. Meier, S. Parsons, I. D. Oswald, V. Brabec and P. J. Sadler, *Inorg. Chem*., 2007, **46**, 5059-5068. (b) F. Wang, J. Xu, A. Habtemariam, J. Bella and P. J. Sadler, *J. Am. Chem. Soc*., 2005, **127**, 17734-17743.
32. (a) A. Weiss, R. H. Berndsen, M. Dubois, C. Müller, R. Schibli, A. W. Griffioen, P. J. Dyson and P. Nowak-Sliwinska, *Chem. Sci*., 2014, **5**, 4742-4748. (b) M. Rausch, P. J. Dyson and P. Nowak-Sliwinska, *Adv. Ther*., 2019, **2**, 1900042.
33. W. H. Mahmoud, F. N. Sayed and G. G. Mohamed, *Appl. Organomet. Chem.*, 2016, **30**, 959-973.
34. E. Villemin, Y. C. Ong, C. M. Thomas and G. Gasser, *Nat. Rev. Chem*., 2019, **3**, 261-282.
35. (a) J. Madureira, C. I. V. Ramos, M. Marques, C. Maia, B. D. Sousa, L. Campino, M. G. Santana-Marques and N. Farrell, *Inorg. Chem*., 2013, **52**, 8881-8894; (b) C. S. Devi, P. Nagababu, S. Natarajan, N. Deepika, P. V. Reddy, N. Veerababu, S. S. Singh and S. Satyanarayana, *Eur. J. Med. Chem.*, 2014, **72**, 160-169; (c) B. Onfelt, P. Lincoln and B. Nordén, *J. Am. Chem. Soc*., 2001, **123**, 3630.
36. (a) S. Banerjee, E.B. Veale, C.M. Phelan, S.A. Murphy, G.M. Tocci, L.J. Gillespie, D.O. Frimannsson, J.M. Kelly, T. Gunnlaugsson, *Chem. Soc. Rev*., 2013, **42**, 1601-1618; (b) D. Obitz, R. G. Miller and N. Metzler-Nolte, *Dalton Trans.*, 2021, **50**, 13768-13777.
37. F. Macii and T. Biver, *J. Inorg. Biochem*., 2021, **216**, 111305.
38. E. N. Hoogenboezem and C. L. Duvall, *Adv. Drug Deliv. Rev.*, 2018, **130**, 73-89.
39. V. P. Torchilin, and A. N. Lukyanov, *Drug Discov. Today*, 2003, **8**, 259-266.
40. N. Ahmed, J. J. Levision, S. D. Robinson and M. F. Uttley, *Inorg. Synth*., 1974, **15**, 45-64.
41. (a) G.M. Sheldrick, *Acta Cryst*., 2008, **A64**, 112-122; (b) G.M. Sheldrick, *Acta Cryst.*, 2015, **C71**, 3-8.
42. (a) A. D. Becke, *J. Chem. Phys.*, 1993, **98**, 5648-5652;(b) C. Lee, W. Yang and R. G. Parr, *Phys. Rev. B: Condens. Matter Mater. Phys.*, 1988, **37**, 785-789.

43. (a) P. J. Hay and W. R. Wadt, *J. Chem. Phys.*, 1985, **82**, 270-283; (b) W. R. Wadt and P. J. Hay, *J. Chem. Phys.*, 1985, **82**, 284-298; (c) P. J. Hay and W. R. Wadt, *J. Chem. Phys.*, 1985, **82**, 299-310.
44. (a) R. Ditchfield, W. J.Hehre and J.A. Pople, *J. Chem. Phys.*,1971, **54**, 724; (b) W. Hehre, J. R. Ditchfield and J. A. Pople, *J. Chem. Phys*.,1972, **56**, 2257.
45. M. J. Frisch, G. W. Trucks, H. B. Schlegel, G. E. Scuseria, M. A. Robb, J. R. Cheeseman, G. Scalmani, V. Barone, B. Mennucci, G. A. Petersson, H. Nakatsuji, M. Caricato, X. Li, H. P. Hratchian, A. F. Izmaylov, J. Bloino, G. Zheng, J. L. Sonnenberg, M. Hada, M. Ehara, K. Toyota, R. Fukuda, J. Hasegawa, M. Ishida, T. Nakajima, Y. Honda, O. Kitao, H. Nakai, T. Vreven, J. A. Montgomery, Jr., J. E. Peralta, F. Ogliaro, M. Bearpark, J. J. Heyd, E. Brothers, K. N. Kudin, V. N. Staroverov, R. Kobayashi, J. Normand, K. Raghavachari, A. Rendell, J. C. Burant, S. S. Iyengar, J. Tomasi, M. Cossi, N. Rega, J. M. Millam, M. Klene, J. E. Knox, J. B. Cross, V. Bakken, C. Adamo, J. Jaramillo, R. Gomperts, R. E. Stratmann, O. Yazyev, A. J. Austin, R. Cammi, C. Pomelli, J. W. Ochterski, R. L. Martin, K. Morokuma, V. G. Zakrzewski, G. A. Voth, P. Salvador, J. J. Dannenberg, S. Dapprich, A. D. Daniels, O¨. Farkas, J. B. Foresman, J. V. Ortiz, J. Cioslowski and D. J. Fox, Gaussian 09, Revision D.01, Gaussian, Inc., Wallingford CT, 2009.
46. (a) R. Bauernschmitt and R. Ahlrichs, *Chem. Phys. Lett.*, 1996, **256**, 454-464;(b) R. E. Stratmann, G. E. Scuseria and M. J. Frisch, *J. Chem. Phys.*, 1998, **109**, 8218; (c) M. E. Casida, C. Jamorski, K. C. Casida and D. R. Salahub, *J. Chem. Phys.*, 1998, **108**, 4439-4449.
47. (a) V. Barone and M. Cossi, *J. Phys. Chem.* A, 1998, **102**, 1995-2001; (b) M. Cossi and V. Barone, *J. Chem. Phys.*, 2001, **115**, 4708-4717; (c) M. Cossi, N. Rega, G. Scalmani and V. Barone, *J. Comput. Chem.*, 2003, **24**, 669-681.
48. N. M. O'Boyle, A. L. Tenderholt, K. M. Langner, *J. Comput. Chem.*, 2008, **29**, 839-845.
49. M. Sirajuddin, S. Ali and A. Badshah, *J. Photochem. Photobiol.*, B, 2013, **124**, 1-19.
50. S. Dasari and A. K. Patra, *Dalton Trans*., 2015, **44**, 19844–19855.
51. (a) M. Kumar, G. Kumar, N. K. Mogha, R. Jain, F. Hussain and D. T. Masram, *Spectrochim. Acta*, 2019, **212**, 94–104; (b) M. Kumar, N. K. Mogha, G. Kumar, F. Hussain and D. T. Masram, *Inorg. Chim. Acta*, 2019, **490**, 144–154.
52. (a) F. Kratz, *J Control Release*., 2008, **132**, 171-183; (b) B. Demoro, R. F. De Almeida, F. Marques, C. P. Matos, L. Otero, J. C. Pessoa, I. Santos, A. Rodríguez, V. Moreno, J. Lorenzo and D. Gambino, *Dalton Trans.*, 2013, **42**, 7131-7146. (c) V. D. Suryawanshi, L. S. Walekar, A. H. Gore, P. V. Anbhule and G. B. Kolekar, *J. Pharm. Anal*., 2016, **6**, 56–63
53. (a) A. K. Pramanik, D. Sarkar and T. K. Mondal, *Polyhedron*, 2015, **102**, 32-40; (b) S. Jana, A. K. Pramanik, C. K. Manna and T. K. Mondal, *Polyhedron*, 2015, **150**, 118-125;

(c) A. Das, M. Saha, S. Mandal, S. Das, K. D. Saha and T. K. Mondal, *New J. Chem.*, 2023, **47**, 4931-4943.

54. P. Kalaivani, R. Prabhakaran, P. Poornima, F. Dallemer, K. Vijayalakshmi, V. Vijaya Padma and K. Natarajan, *Organometallics*, 2012, **31**, 8323–8332.
55. T. Sathiya Kamatchi, P. Kalaivani, P. Poornima, V. Vijaya Padma, F. R. Fronczek and K. Natarajan, *RSC Adv*., 2014, **4**, 2004–2022.
56. F. Basuli, S. M. Peng and S. Bhattacharya, *Inorg. Chem.*, 2001, **40**, 1126–1133.
57. R. Ramachandran, G. Prakash, S. Selvamurugan, P. Viswanathamurthi, J. G. Malecki and V. Ramkumar, *Dalton Trans*., 2014, **43**, 7889–7902.
58. P. Roy, R. Naskar, C. K. Manna and T. K. Mondal, *J. Mol. Struct.*, 2019, 1198, 126932.
59. A. Wolfe, G. H. Shimer and T. Meehan, *Biochemistry*, 1987, **26**, 6392.
60. (a) G. Kalaiarasi, S. R. J. Rajkumar, S. Dharani, F. R. Fronczek, M. M. Nadar and R. Prabhakaran, *New J. Chem.*, 2018, **42**, 336-354; (b) G. Devagi, F. Reyhaneh, F. Dallemer, R. Jayakumar, P. Kalaivani and R. Prabhakaran, *New J. Chem.*, 2017, **41**, 8620-8636.
61. K. Jeyalakshmi, J. Haribabu, N. S. P. Bhuvanesh and R. Karvembu, *Dalton Trans*., 2016, **45**, 12518–12531.
62. E. Jayanthi, S. Kalaiselvi, V. Vijaya Padma, N. S. P. Bhuvanesh and N. Dharmaraj, *Dalton Trans*., 2016, **45**, 1693–1707.
63. A. M. Pyle, J. P. Rehmann, R. Meshoyrer, C. V. Kumar, N. J. Turro and J. K. Barton, *J. Am. Chem. Soc*., 1989, **111**, 3051–3058.
64. O. Stern and M. Volmer, *Z. Phys.*, 1919, **20**, 183‑188.
65. B. K. Kundu, S. N. Upadhyay, N. Sinha, R. Ganguly, I. Grabchev, S. Pakhira and S. Mukhopadhyay, *Dalton Trans.*, 2022, **51**, 3937-3953.
66. S. Satyanarayana, J. C. Dabrowiak, J. B. Chaires, *Biochemistry*, 1992, **31**, 9319–9324.
67. (a) L. Haque, S. Bhuiya, R. Tiwari, A. B. Pradhan, S. Das, *RSC Adv.* **6** (2016) 83551. (b) Y. Wang, G. Lin, J. Hong, T. Lu, L. Li, N. Okabe, M. Odoko, *Inorg. Chim. Acta*, 2009, **362**, 377–384. (c) M. Kumar, G. Kumar, N. K. Mogha, R. Jain, F. Hussain and D. T. Masram, *Spectrochim. Acta*, 2019, **212**, 94–104. (d) M. Kumar, N. K. Mogha, G. Kumar, F. Hussain and D. T. Masram, *Inorg. Chim. Acta*, 2019, **490**, 144–154.
68. A. B. Pradhan, L. Haque, S. Bhuiya, S. Das, *RSC Adv*., 2015, **5**, 10219–10230.
69. S. De, S. R. Chaudhuri, A. Panda, G. R. Jadhav, R. S. Kumar, P. Manohar, N. Ramesh, A. Mondal, A. Moorthy, S. Banerjee and P. Paira, *New J. Chem.*, 2019, **43**, 3291-3302.
70. P. Vijayan, P. Viswanathamurthi, P. Sugumar, M. N. Ponnuswamy, M. D. Balakumaran, P. T. Kalaichelvan, K. Velmurugan, R. Nandhakumar and R. J. Butcher, *Inorg. Chem. Front.*, 2015, **2**, 620-639.

71. (a) K. Karami, S. Hashemi, J. Lipkowski, F. Mardani, A. A. Momtazi-borojeni and Z. M. Lighvan, *Appl. Organomet. Chem*., 2017, **31**, 3740; (b) X. F. Zhao, Y. Ouyang, Y. Z. Liu, Q. J. Su, H. Tian, C. Z. Xie and J. Y. Xu, *New J. Chem*., 2014, **38**, 955-965.
72. S. Deepa and A. K. Mishra, *J. Pharm. Biomed. Anal*., 2005, **38**, 556‑563.
73. D. Senthil Raja, N. S. P. Bhuvanesh and K. Natarajan, *Dalton Trans*., 2012, **41**, 4365–4377.
74. J. N. Miller, *Proc. Anal. Div. Chem. Soc*., 1979, **16**, 203–208.
75. S. Mukhopadhyay, R. K. Gupta, R. P. Paitandi, N. K. Rana, G. Sharma, B. Koch, L. K. Rana, M. S. Hundal and D. S. Pandey, *Organometallics*, 2015, **34**, 4491–4506;
76. F. F. Tian, F. L. Jiang and X. L. Han, *J. Phys. Chem. B*, 2010, **114**, 14842–14853
77. (a) S. Rubino, R. Busà, A. Attanzio, R. Alduina, V. Di Stefano, M. A. Girasolo, S. Orecchio and L. Tesoriere, *Bioorg. Med. Chem*., 2017, **25**, 2378-2386; (b) N. Miklášová, E. Fischer-Fodor, P. Lönnecke, C. I. Tomuleasa, P. Virag, M. P. Schrepler, R. Mikláš, L. S. Dumitrescu and E. Hey-Hawkins, *Eur. J. Med. Chem.*, 2012, **49**, 41-47; (c) S. Rubino, V. Di Stefano, A. Attanzio, L. Tesoriere, M. A. Girasolo, F. Nicolò, G. Bruno, S. Orecchio and G.C. Stocco, *Inorg. Chim. Acta*, 2014, **418**, 112-118; (d) L. Masaryk, P. Zoufalý, K. Słoczyńska, E. Zahradniková, D. Milde, P. Koczurkiewicz-Adamczyk and P. Štarha, *Inorg. Chim. Acta*, 2022, **536**, 120891; (e) L. Niu, G. Ren, T. Hou, X. Shen and D. Zhu, *Inorg. Chem. Commun.*, 2021, **130**, 108737.
78. (a) V. Rajendran and M. V. Jain, *Cancer Stem Cells: Methods and Protocols*, 2018, 89-95; (b) C. Guzman, M. Bagga, A. Kaur, J. Westermarck and D. Abankwa, *PloS one*, 2014, **9**, 92444.
79. I. Schmid, C. Uittenbogaart and B. D. Jamieson, *Nat. Protoc.*, 2007, **2**, 187-190.
80. S. Kasibhatla, G. P. Amarante-Mendes, D. Finucane, T. Brunner, E. Bossy-Wetzel and D. R. Green, *Cold Spring Harb. Protoc.*, 2006, **3**, 4493.
81. K. Liu, P. C. Liu, R. Liu and X. Wu, *Med. Sci. Monit. Basic Res.*, 2015, **21**, 15.
82. C. Ciniglia, G. Pinto, C. Sansone and A. Pollio, *Allelopathy J.*, 2010, **26**, 301-308.

CHAPTER-VI

Synthesis, characterization, DNA/Protein binding study and anticancer activity of novel tricarbonyl Re(I) complexes with ONS donor azo-thioether ligands

Abstract

In this article, two new Rhenium(I) tricarbonyl complexes of the formula $[Re(CO)_3(L^1/L^2)]$ (**1/2**) were fabricated and thoroughly characterized by diverse spectroscopic techniques. The crystal structures of the complexes were confirmed by single crystal X-ray diffraction analysis and it disclosed the distorted octahedral geometry around the central metal ions. A theoretical approach on optimization structures, HOMO-LUMO energy gap and time-dependent density functional theory (TDDFT) was carried out to support the experimental observations. The DNA binding ability of complexes with calf thymus DNA was investigated by UV-Vis absorption spectroscopy and fluorescence spectroscopy. Furthermore, viscosity studies executed on the interaction of complexes with CT-DNA revealed the fact that the complexes bind by intercalation. The BSA protein binding studies have been observed by quenching of tryptophan and tyrosine residues in the presence of complexes and the quenching mechanism was established to be static. The changes in the microenvironmental and structural properties of BSA are scrutinised by circular dichroism, synchronous and 3D fluorescence study. Additionally, the *in vitro* cytotoxicity of the complexes against human breast epithelial adenocarcinoma cell line MCF-7 and human breast epithelial cell line (used as normal cell line) MCF-10A were explored by using the MTT assay.

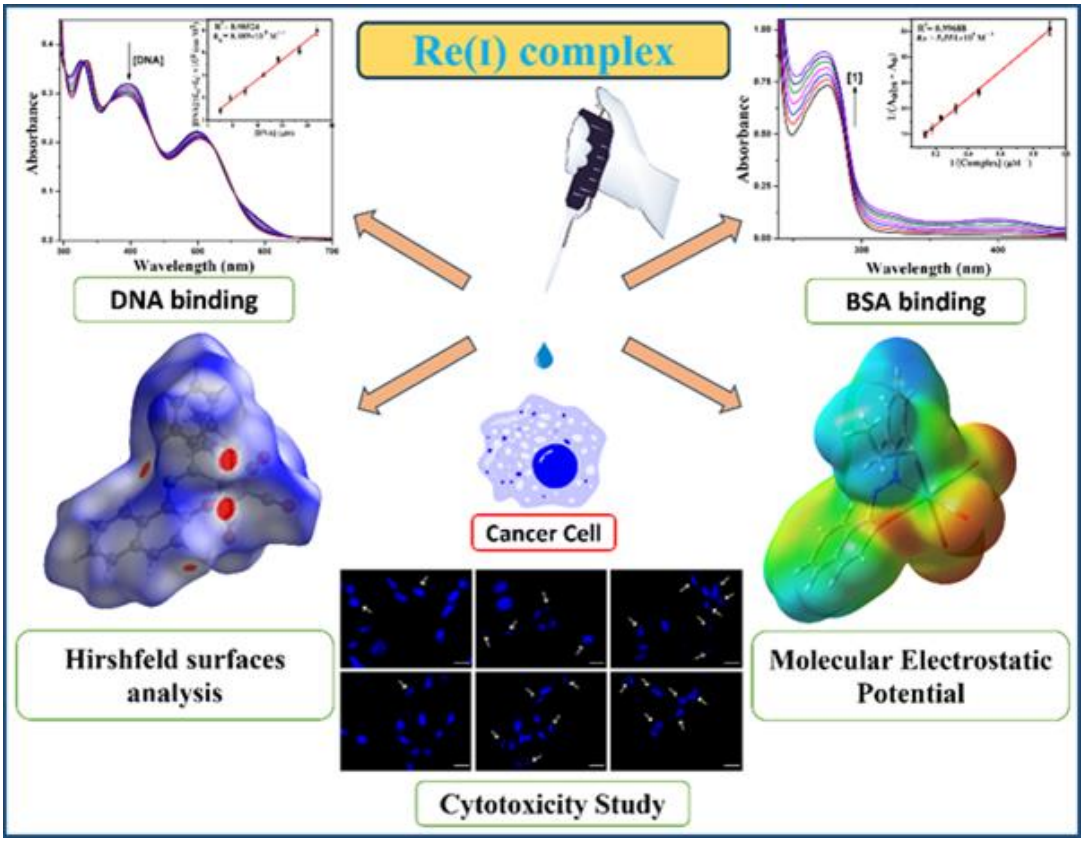

VI.1. Introduction

Cancer is the one of the primary reasons of death globally according to the World Health Organization (WHO). Although the mortality rates are elevating fast but a major section of cancers can be healed through surgery, radiotherapy and chemotherapy depending on the category of cancer.[1,2] Cisplatin, carboplatin and oxaliplatin are accepted as platinum-based anticancer drugs worldwide.[3] However, severe side effects of these platinum drugs along with tumor resistance to them have now turned out to be a difficulty.[4] Hence several non-platinum metals have been manufactured that are equivalent in action to cisplatin along with comparatively lesser side effects. Among them, rhenium(I) complexes have drawn much attention owing to their distinctive anticancer mechanisms. Additionally, recently an array of tricarbonylrhenium(I) complexes have been scrutinized for their pharmacological and radiopharmaceutical applications.[5-11] The complexes of rhenium are much recognized to be kinetically inert owing to the d^6 electronic configuration of the rhenium(I) core in an octahedral field. Thus, despite carbon monoxide toxicity because of its strong affinity for haemoglobin, elevated stability of substitution of the firmly bound CO ligands under physiological and ambient conditions has been confirmed for numerous fac-$[Re(CO)_3]^+$ complexes in aqueous solution and in the human plasma.[12-14]

Additionally, the task of ligands is critical in scheming metal-based anticancer agents as they can control the metal uptake, trafficking, utility and excretion in biological systems. They can also alter their properties such as solubility, lipophilicity and stability of the complex.[11,15] Aromatic azo compounds are unique and multifarious ligands that can coordinate with a variety of transition metals and also it has several flexible donors of combined hard/soft oxygen/nitrogen-sulfur atoms. Aside from their usual colouring function, azo compounds have also been stated to have anticancer, antibacterial, antiviral, antiseptic, antifungal and cytotoxic activities. [16-18]

DNA is the principal intracellular goal of an antitumor agent.[19] Complex can act together with DNA via these following three non-covalent modes: intercalation, groove binding interaction and electrostatic interaction between negatively charged DNA phosphate residue and positively charged species.[20,21] In order to determine the mode and level of binding capability of complexes to DNA, both the coordination geometry of the metal ion and the planarity of ligand have significant functions.[22] Hence, the interaction study of the metal complexes with DNA poses immense significance for the fabrication of novel drugs and their application. Furthermore, the interaction of metal complexes with albumins may propose helpful structural statistics that shows clearly the fact that whether a drug mechanism

is therapeutic enough or not. Antitumor medicines are regularly delivered to cellular targets via proteins.[23,24] Bovine serum albumin (BSA) is an attractive macromolecule mainly used in biophysical and biochemical research among serum albumins owing to the structural homology with human serum albumin and noteworthy ligand-binding features.[25-27]

In this paper we have designed and synthesized Re(I) complexes (Scheme VI.1) having general formula, $[Re(CO)_3(L^1/L^2)]$ (**1/2**) with ONS donor azo-thioether ligands and characterized both of them by using a variety of spectroscopic techniques like NMR, IR, Mass, UV-Vis as well as single crystal X-ray diffraction study. The structural optimization, calculated energy difference of HOMO-LUMO, calculated different reactivity descriptors and TD-DFT analysis were executed with the aid of DFT to get an insight into the electronic structure of the complexes about the reactivity and structural property. In the end, the binding properties of these complexes toward calf thymus DNA (CT-DNA) and bovine serum albumin (BSA) are investigated with the help of absorption and fluorescence spectroscopy. *In vitro* cytotoxicity of these fabricated complexes was tested on human breast epithelial adenocarcinoma cell line (MCF-7) and human breast epithelial cell line (MCF-10A) using MTT assay. To establish discriminating effect of these complexes, they were treated on cancer cells as well as normal cells under the same experimental conditions.

VI.2. Experimental

VI.2.1. Materials and methods

All the reagents and solvents were purchased of highest commercial grade and used without any further purification. Acetylacetone, 2-naphthol, 2-(methylthio)aniline, 2-(ethylthio)aniline and $Re(CO)_5Br$ were purchased from Sigma-Aldrich. The ligands (HL^1 and HL^2) were prepared according to standard literature procedures.[28,29] Tri(hydroxylmethyl)aminomethane (Tris-HCl), Ethidium bromide (EB), calf thymus DNA(CT-DNA) and bovine serum albumin (BSA) were obtained from Sigma Aldrich chemical company. Earle's MEM (#Cat. No: 41500034), DMEM/Ham's F-12 (#Cat. No: 11320033), Fetal Bovine Serum (#Cat. No: 10438026), Trypsin-EDTA (#Cat. No: 25200072) and Antibiotic-Antimycotic (#Cat. No: 15240062) were procured from Gibco. MTT [3-(4,5-Dimethylthiazol-2-yl)-2,5-Diphenyltetrazolium Bromide] (#Cat. No: 475989), 37 % Formaldehyde (#Cat. No: 104003), DMSO (#Cat. No: 102952) and Glycerol (#Cat. No: 818709) were taken from Merck. Hoechst 33528 Stain (#Cat. No: 14530) and Methanol (#Cat. No: 34860) were brought from Sigma Aldrich. All compounds were subsequently used without any further rounds of purification.

Elemental analyses (C, H, N) were performed on a 2400 Series-II CHN analyzer, Perkin Elmer, USA. Waters (Xevo G2 Q-TOF) mass spectrometer was used to record mass spectra of the ligand and complexes. IR spectra were run as KBr pellets on a RX-1 PerkinElmer spectrometer in the 4000–400 cm^{-1} region. ^{1}H-NMR spectra of ligand and complexes were recorded in $CDCl_3$ with TMS as the internal standard on a Bruker (AC) 300 MHz FT-NMR spectrometer. PerkinElmer Lambda 750 spectrophotometer was used for study the binding interactions of complexes with CT-DNA and BSA. The emission spectra were recorded by using Shimadzu RF-6000 fluorescence spectrophotometer at room temperature (298 K). Viscometric measurements were performed using an Ostwald viscometer placing it in a thermostated water bath at 25^0C and flow time was measured with a digital stopwatch. Circular dichroism (CD) studies were made on a JASCO spectropolarimeter (model J815, Jasco International Co., Japan) equipped with a thermalprogrammer (model PFD-425L/15) and temperature controller using a 1cm path length rectangular quartz cuvette.

VI.2.2. Preparation of complexes

VI.2.2.1. Synthesis of Re(I) complex, $[Re(CO)_3L^1]$ (1)

At first, 0.050 g (0.123 mmol) $Re(CO)_5Br$ was dissolved in 10 mL acetonitrile. To this solution, 10 mL acetonitrile solution of previously synthesized ligand HL^1 (0.038 g, 0.123 mmol) was added and refluxed for 8 h. As a result of this reaction, a red coloured solution appeared which was filtered and evaporated to dryness. A red coloured solid product appeared and single red colored crystals of the complex was obtained by slow diffusion of n-hexane into DCM solution. Yield, 0.059 g (83%)

Anal. Calc. for $C_{21}H_{15}N_2O_4SRe$: C, 43.67; H, 2.62; N, 4.85. Found: C, 43.54; H, 2.44; N, 4.55. IR (KBr, cm^{-1}): 3058, 2975, 2935 υ(C-H); 2018, 1929, 1892 υ(CO). ^{1}H NMR (300 MHz, $CDCl_3$): δ 8.16-8.10 (m, 2H), 7.70-7.36 (m, 7H), 6.99 (d, J = 6.9 Hz, 1H), 2.75-2.54 (m, 2H), 1.18 (t, J=7.3Hz, 3H). HRMS: calculated for $C_{21}H_{15}N_2O_4SRe$ $[M+H]^+$ (m/z): 579.0388; found: 579.0363.

VI.2.2.2. Synthesis of Re(I) complex, $[Re(CO)_3L^2]$ (2)

Complex **2** was synthesized by a similar method like complex **1** using $Re(CO)_5Br$ (0.050 g, 0.123 mmol) and HL^2 (0.031 g, 0.123 mmol) as a ligand. Finally yellow-colored crystals of the complex was obtained by slow diffusion of n-hexane into DCM solution. Yield, 0.052 g (81%).

Anal. Calc. for $C_{15}H_{13}N_2O_5SRe$: C, 34.68; H, 2.52; N, 5.39. Found: C, 34.45; H, 2.37; N, 5.25. IR (KBr, cm^{-1}): 3004, 2977, 2929 υ(C-H); 2020, 1924, 1889 υ(CO), 1656 υ(C=O). ^1H NMR (300 MHz, $CDCl_3$): δ 7.89 (d, J=7.9 Hz, 1H), 7.67-7.35 (m, 3H), 2.58 (s, 3H), 2.53 (s, 3H), 2.19 (s, 3H). HRMS: calculated for $C_{15}H_{13}N_2O_5SRe$ $[M+H]^+$ (m/z): 521.0181; found: 520.7710.

VI.2.3. Crystal structure determination and refinement

Crystallographic data collections were performed with an automated Bruker AXS D8 Quest CMOS diffractometer using graphite monochromated Mo-Kα (λ=0.71073Å) radiation by the ω scan method. The structures were solved by direct method and refinements were carried out by full-matrix least-squares techniques on F^2 using the SHELX-2016. All the data were corrected for Lorentz and polarization effects and multi-scan absorption corrections were applied using SHELXTL program package.[30] Anisotropic displacement parameters included for all non-hydrogen atoms, while all hydrogen atoms were placed geometrically and refined by using riding model.

VI.2.4. Computational method

All geometry optimization and energy computations were performed using density functional theory (DFT) with the B3LYP level of theory.[31] LanL2DZ[32] basis set with effective core potential was employed for Re atoms while for the other elements the basis set 6-31G(d)[33] were considered for calculations. The vibrational frequency calculations were performed to ensure that the optimized geometries represented the local minimum on the potential energy surface and there were only positive Eigen values. Gaussian09 program package[34] was employed to visualize geometry optimized structures and to calculate the minimum energy structure. The calculated electronic density contour plots for frontier molecular orbitals were plotted by using the GaussView, Version 5 visualization program. Solvent effects play an important role in the electronic structure of the complexes. The time-dependent density functional theory (TD-DFT)[35] calculations were performed at the same level of theory using the conductor-like polarizable continuum model (CPCM)[36] to introduce the effect of DMSO as a solvent. The fractional contributions of various groups to each molecular orbital were calculated using GaussSum.[37]

VI.2.5. Hirshfeld Surface Analysis of complexes 1 and 2

In order to visualize the intermolecular interactions, prevailing in the crystal, Molecular Hirshfeld surfaces (HS)[38] and the associated 2D-fingerprint[39] plots of complex **1** and **2** were

calculated using Crystal Explorer 17.5 software.[40] Bond lengths to hydrogen atoms were automatically set to standard values, while the structural input CIF. files of the crystals **1** and **2** were read into the software for calculations. For each point on the Hirshfeld isosurface, two distances *d*e, the distance from the point to the nearest nucleus external to the surface and *d*i, the distance to the nearest nucleus internal to the surface, are defined. The normalized contact distance (d_{norm}) based on d_e and d_i is given by the equation (Eq. VI.1).

$$d_{norm} = \frac{(d_i - r_i^{vdw})}{r_i^{vdw}} + \frac{(d_e - r_e^{vdw})}{r_e^{vdw}} \qquad \text{(Eq. VI.1)}$$

where, r_i^{vdw} and r_e^{vdw} are the van der Waals radii of the atoms. The value of d_{norm} is negative or positive depending on intermolecular contacts being shorter or longer than the van der Waals separations.

Graphical plots of the molecular Hirshfeld surfaces mapped with d_{norm} uses a red-white-blue colour scheme, where bright red spots highlight shorter contacts, white areas represent contacts around the van der Waals separation, and blue regions are devoid of close contacts. To visualize the molecular moiety, transparent mapped surfaces are usually shown. For a given crystal structure and set of spherical atomic electron densities, the Hirshfeld surface is unique and thus it suggests the possibility of gaining additional insight into the intermolecular interaction of molecular crystals. 2D Fingerprint plot resolved into different contacts contributed to the total Hirshfeld surface area of the complexes **1** and **2**.

VI.2.6. DNA binding studies

VI.2.6.1. Absorption spectroscopic studies

The DNA binding ability of complex **1** and **2** has been evaluated by absorption as well as emission spectroscopy. The interaction of the complexes with CT-DNA was performed by using Tris-HCl buffer solution having pH 7.2. The concentration of CT-DNA was determined from its absorption intensity at 260nm by employing an extinction coefficient of 6600 $M^{-1}cm^{-1}$.[41] The UV absorbance at 260 and 280 nm of the CT-DNA solution gave a ratio in the range of 1.8 to 1.9, indicating that the DNA was satisfactorily free from protein molecules. The absorption spectra of the complexes at a constant concentration were recorded in presence of different concentrations of CT-DNA and a noteworthy change in absorption values was observed.

VI.2.6.2. Ethidium bromide displacement experiments

The competitive binding interactions of the complexes were investigated by fluorescence spectroscopy method in order to find out whether the compound can displace EB from its CT-DNA-EB system. The CT-DNA-EB complex was initially prepared by adding 15 μM EB and 30 μM CT-DNA in Tris– HCl/NaCl buffer solution (pH = 7.4). Ethidium bromide (EB) displacement experiments were done by successive addition of the complexes into the Tris-HCl buffer solution of CT-DNA-EB complex.[42] After successive addition of the metal complexes, the change in fluorescence intensity at 612 nm were monitored (excitation wavelength 540 nm).

VI.2.6.3. DNA viscosity measurements

The viscosity of the CT-DNA solutions (35.2 μM) was measured in the presence of increasing amounts of the complexes using an Ostwald viscometer placing it in a thermostated water bath at 25.0 °C. Flow time was measured with a digital stopwatch and each sample was measured three times, then the average flow time was calculated. Viscosity values were calculated from the observed flow time of DNA-containing solutions (t) corrected for the flow time of buffer alone (t_0), $\eta = (t - t_0)/ t_0$. The data is reported as $(\eta / \eta_0)^{1/3}$ versus the ratio of the concentration of the complex to CT-DNA (R = [compound]/[CT-DNA]), where η is the viscosity of CT-DNA in the presence of the compound and η_0 is the viscosity of CT-DNA solution alone.[43]

VI.2.7.1. Protein binding studies

BSA (bovine serum albumin) is the most abundant plasma protein present in the circulatory system, which plays a vital role for the distribution and transportation of metal ions, hormones, nutrients, and drug molecules to the specific organs or tissues in the body.[44] The binding ability of complexes with BSA was performed with the help of UV-Vis spectroscopic titration and fluorescence emission quenching methods. The BSA stock solution was prepared using 500 mM phosphate buffer saline (PBS) at pH 7.4 and stored in the dark at 4°C for further use. The concentration of BSA was measured by taking absorbance at 280 nm in UV-Vis spectra (molar extinction coefficient 66,400 M^{-1} cm^{-1}). The stock solution of complexes was prepared in DMSO medium. The absorption spectra of BSA (10 μM) were recorded after gradual addition of complexes at room temperature for calculation of binding constants and binding modes. In fluorescence experiment, tryptophan fluorescence of BSA was recorded in the range 290–450 nm at an excitation wavelength of 280 nm using a slit width of 5 nm. Quenching of emission intensity at ~336 nm for BSA was monitored with

subsequent addition of metal complex. The synchronous fluorescence spectra were also captured in the same instrument in the range of 270-380 nm by scanning the excitation and emission monochromators simultaneously. Different wavelength interval ($\Delta\lambda = \lambda_{em} - \lambda_{ex}$) of $\Delta\lambda$ = 15 nm and $\Delta\lambda$ = 60 nm were set to study the spectrum behavior of tyrosine (Tyr) and tryptophan (Trp) residues of BSA. 3D fluorescence spectroscopy is used to know about the fluorescence of chromophore and also the conformational changes of protein macromolecules by measuring the change of fluorescence intensity in the presence of complexes. The 3D fluorescence spectra of BSA (5 μM) with and without the complexes **1** and **2** were recorded in the wavelength range of 200-400 nm for excitation and 200-500 nm for emission.

VI.2.7.2. Circular dichroism measurements

Circular dichroism (CD) spectra were obtained employing JASCO (J-815) spectropolarimeter at 298 K using a quartz cuvette of 1 cm cell path length. The spectra were recorded in far UV region (200–250 nm) for BSA in presence and absence of copper complexes **1** and **2**. Concentration of BSA was kept constant at 1 μM while varying the concentration of added complexes **1** and **2**. The CD results were expressed in terms of the mean residual ellipticity (MRE) in deg cm^2 $dmol^{-1}$ according to the following equation (Eq. VI.2)[45]

$$MRE = \frac{Observed\ CD\ (mdeg)}{10 C_p n l} \qquad \text{(Eq. VI.2)}$$

Here, C_p represents the molar concentration of the protein, *n* stands for the number of amino acid residues (583 for BSA) and *l* is the path length of the cell (1 cm). The α-helical (%) contents of the free and bound BSA were calculated from the mean MRE values at 208 nm using the following equation (Eq. VI.3)[46]

$$\alpha - helix\ (\%) = \frac{[-MRE_{208} - 4000]}{[33000 - 4000]} \times 100 \qquad \text{(Eq. VI.3)}$$

MRE_{208} is the MRE value observed at 208 nm, 4000 is the MRE of the β-form and random coil conformation at 208 nm, and 33000 is the MRE value of a pure α-helix at 208 nm.

VI.2.7.3. Förster Resonance Energy Transfer (FRET)

The value of R_0 was calculated using the euation (Eq. VI.4)

$$R_0 = 0.2018\left\{[K^2\Phi_D\eta^{-4}J(\lambda)]^{1/6}\right\}\text{Å} \qquad \text{(Eq. VI.4)}$$

where the orientation factor between the emission dipole of the donor and the absorption dipole of the acceptor κ^2 is taken as 2/3, the fluorescence quantum yield of the donor ϕ_D is 0.118, the refractive index of the medium (η) is 1.33, and $J(\lambda)$ is the extent of spectral overlap of donor (BSA) emission and the acceptor (complex) absorption spectra.[47] The value of $J(\lambda)$ can be calculated using the equation (Eq. VI.5)[48]

$$J(\lambda) = \int_0^\infty \bar{I}_D(\lambda)\varepsilon_A(\lambda)\lambda^4 d\lambda \quad M^{-1}cm^{-1}nm^4 \qquad \text{(Eq. VI.5)}$$

Where, $\bar{I}_D(\lambda)$ denotes the normalized fluorescence emission of the donor BSA at the wavelength λ, and $\varepsilon_A(\lambda)$ represents the molar extinction coefficient of the acceptor metal complex at the wavelength λ.

VI.2.8. Biological Studies

VI.2.8.1. Cell lines and Culture condition

Human breast epithelial adenocarcinoma cell line MCF-7 and Human breast epithelial cell line (used as normal cell line) MCF-10A were purchased from NCCS Pune, India. Earle's MEM medium was used to culture MCF-7 cells whereas DMEM/Ham's F-12 medium was used to culture MCF-10A cells were cultured in. Earle's MEM medium was supplemented with 10% FBS and 1% Antibiotic and Antimycotic (Anti-Anti. Cells were maintained in the humidified incubator with 5% CO_2 and 37^0 C. During passage, Trypsin-EDTA was used to detach the adherent cells. All biological experiments were performed after three passages.

VI.2.8.2. Cytotoxicity assay

The cytotoxic effects of complexes **1** and **2** against MCF-7 and MCF-10A cells, were evaluated by MTT assay based on our previously standardized lab protocol.[49] Briefly, in 96 well-plates, 1 × 10^4 cells/well were plated and incubated for 24 h, then treated with complexes **1** and **2** at a range of 1.56 μM to 100 μM and again incubated for 24 h. Thereafter, 5 mg/ml MTT solution was added to each well (100 μl) for 3 h. Finally, DMSO-Methanol (1:1) was added to each well (100 μl) and quantified by taking absorbance at 570 nm in a microtiter plate-reader (Spectramax i3x). The percentage of cell viabilities at various concentration were determined using the following formula:

Percentage (%) Cell viability = [(A_{570} of treated cells) - background) / (A_{570} of untreated cells) - background)] × 100

VI.2.8.3. Clonogenic Assay

The colony formation ability of MCF-7 cells against complexes **1** and **2** were evaluated by Clonogenic assay based on our previously standardized lab protocol.[49] Briefly, 500 MCF-7 cells/well were plated and incubated for 24 h, then treated with two complex **1** concentrations (1/2 of IC_{50} Value: 5.06 µM and IC_{50} Value: 10.12 µM) and two complex **2** concentrations (1/2 of IC_{50} Value: 7.62 µM and IC_{50} Value: 15.24 µM) and again incubated for 24 h. After 24 h, for the cell fixation and staining, methanol and 0.05% Crystal violet stain were used. After staining, wells were subsequently washed with 1X PBS 2-3 times. Finally, all the images were captured. During observation, the relative colony numbers were counted using the Image J Software.

VI.2.8.4. Wound Healing Assay

The cell migration potential of MCF-7 cells against complexes **1** and **2** were evaluated by Wound healing assay based on our previously standardized lab protocol.[50] Briefly, 2×10^5 MCF-7 cells/well were plated in a serum free media to minimize the cellular proliferation. After 24 h of incubation, a scratch was drawn with a 200 µl sterile pipette tip followed by 1X PBS wash. Thereafter, cells were treated with two complex **1** concentrations (1/2 of IC_{50} Value: 5.06 µM and IC_{50} Value: 10.12 µM) and two complex **2** concentrations (1/2 of IC_{50} Value: 7.62 µM and IC_{50} Value: 15.24 µM) and again incubated for 24 h. Finally, all the images were captured using phase contrast microscope (Olympus) in three different time intervals: T0 defines just after the treatment, T24 defines after 24 h of incubation and T48 defines after 48 h of incubation. The wound areas on three different time intervals were evaluated using the Image J Software.

VI.2.8.5. Nuclear Fragmentation Assay for Apoptosis Detection

The nuclear fragmentation of MCF-7 cells against complexes **1** and **2** were evaluated by Nuclear fragmentation assay using Hoechst 33258 stain based on our previously standardized lab protocol.[51] Briefly, 1×10^5 MCF-7 cells/well were plated on sterile coverslips and incubated for 24 h, then treated with two complex **1** concentrations (1/2 of IC_{50} Value: 5.06 µM and IC_{50} Value: 10.12 µM) and two complex **2** concentrations (1/2 of IC_{50} Value: 7.62 µM and IC_{50} Value: 15.24 µM) and again incubated for 24 h. After 24 h, for the cell fixation and staining, 4% formaldehyde and Hoechst 33258 stain were used. After staining, cells were

subsequently washed with 1X PBS and the coverslips were mounted in glycerol. Finally, nuclear morphologies were evaluated using the fluorescent microscope (Olympus).

VI.2.8.6. Statistical Analysis

All the statistical analysis were performed using the GraphPad Prism 8.0.2 Software. All the experiments were repeated independently thrice and the data were calculated as Mean ± SD. One way ANOVA was performed to calculate the significant difference between the treated groups and untreated control group where the $P < 0.05$ was considered statistical significant. Using Chou-Talalay's method in the CompuSyn Software, all the Inhibitory Concentration (IC_{50}) values were calculated.

VI.3. Results and discussion

VI.3.1. Synthesis and formulation

The synthetic route used for the preparation of the new Rhenium(I) tricarbonyl complexes is depicted in Scheme VI.1. The novel complexes **1** and **2** were synthesized via refluxing the equimolar amount of ligand [HL^1 / HL^2] with the Re(I) precursor [$Re(CO)_5Br$]. Both the complexes were thoroughly characterized by the help of a range of spectroscopic techniques and the structures of complexes **1** and **2** were confirmed by single crystal X-ray crystallographic studies.

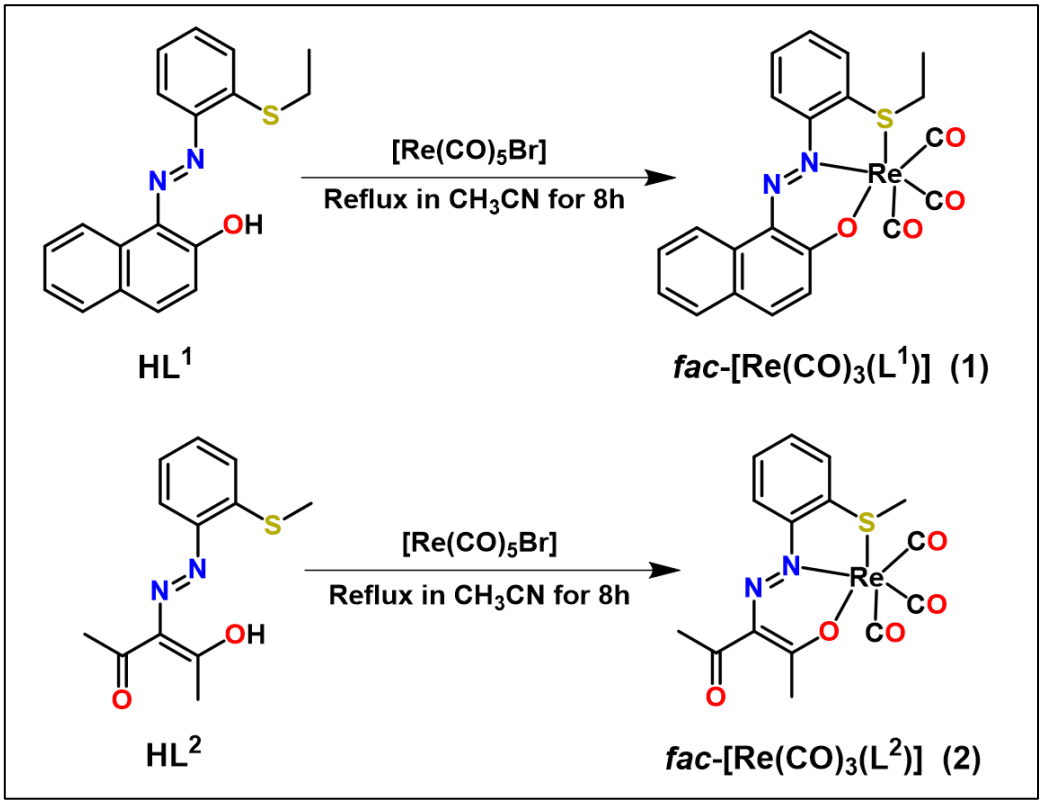

Scheme VI.1. Synthetic scheme for [$Re(CO)_3(L^1)$] (**1**) and [$Re(CO)_3(L^2)$] (**2**).

VI.3.2. Spectral characterization

IR spectra of the complexes reveal characteristic carbonyl stretching peak at 2020-1889 cm^{-1} (Fig. VI.1), which validates the presence of three carbonyl groups in rhenium metal complexes. The CO stretching frequencies of the metal complexes are less than the stretching frequency of free CO.[52] This is owing to the fact that CO group participates in $d\pi(Re)\rightarrow\pi^*(CO)$ back, which results in the increase in bond strength of Re-CO and decrease in bond strength of CO. Moreover, the ketonic stretching of complex **2** is noticed at 1656 cm^{-1}.[53] ^{1}H-NMR spectra of the complexes showed that the peak corresponding to O-H proton of the free ligand vanishes suggesting the coordination of ligand to the metal ions through phenolic oxygen atom. For complex **1**, the $–CH_2$ protons of $–CH_2CH_3$ moiety emerge as multiplate at 2.75-2.54 ppm probably because of the two different type (diastereotopic) of $–CH_2$ protons (Fig. VI.2 and Fig. VI.3). Mass spectrum of $[Re(CO)_3L^1]$ (**1**) shows m/z peak corresponding to $[M+H]^+$ at 579.0363 (Fig. VI.4) while $[Re(CO)_3L^2]$ (**2**) exhibits m/z peak corresponds to $[M+H]^+$ at 520.7710 (Fig. VI.5).

UV-Vis spectrum of the complexes **1** and **2** in DMSO are shown in Fig. VI.6. The absorption spectra of complex **1** disclose moderately strong low energy band at 501 nm. In addition, high energy bands are noticed at 396 and 327 nm. The electronic absorption spectra of complex **2** displays low energy peaks at 402 nm and high energy bands are appeared at 284 nm.

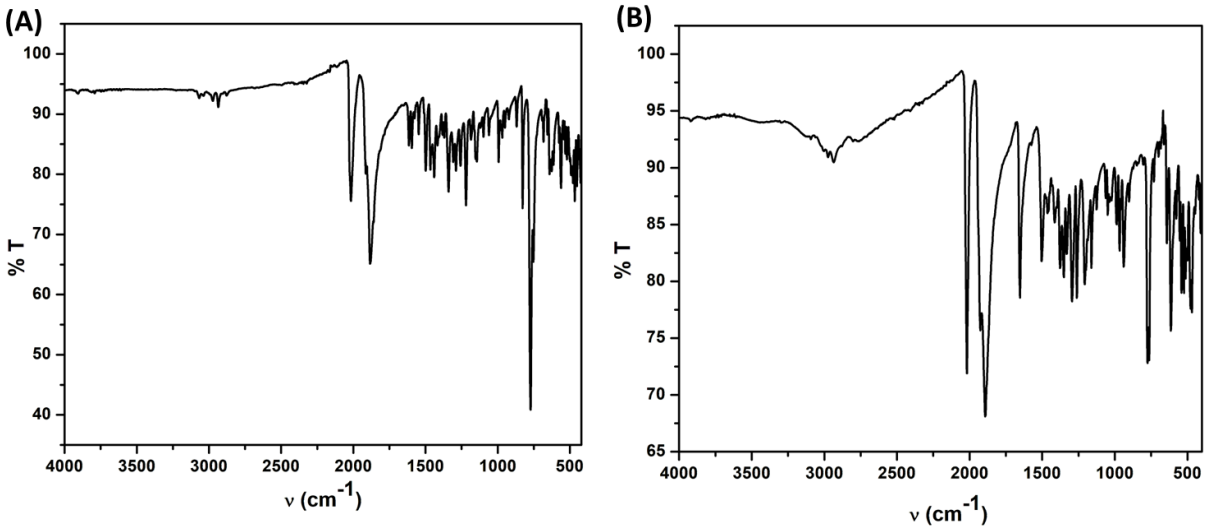

Fig. VI.1. IR spectrum of complex **1 (**A) and complex **2** (B).

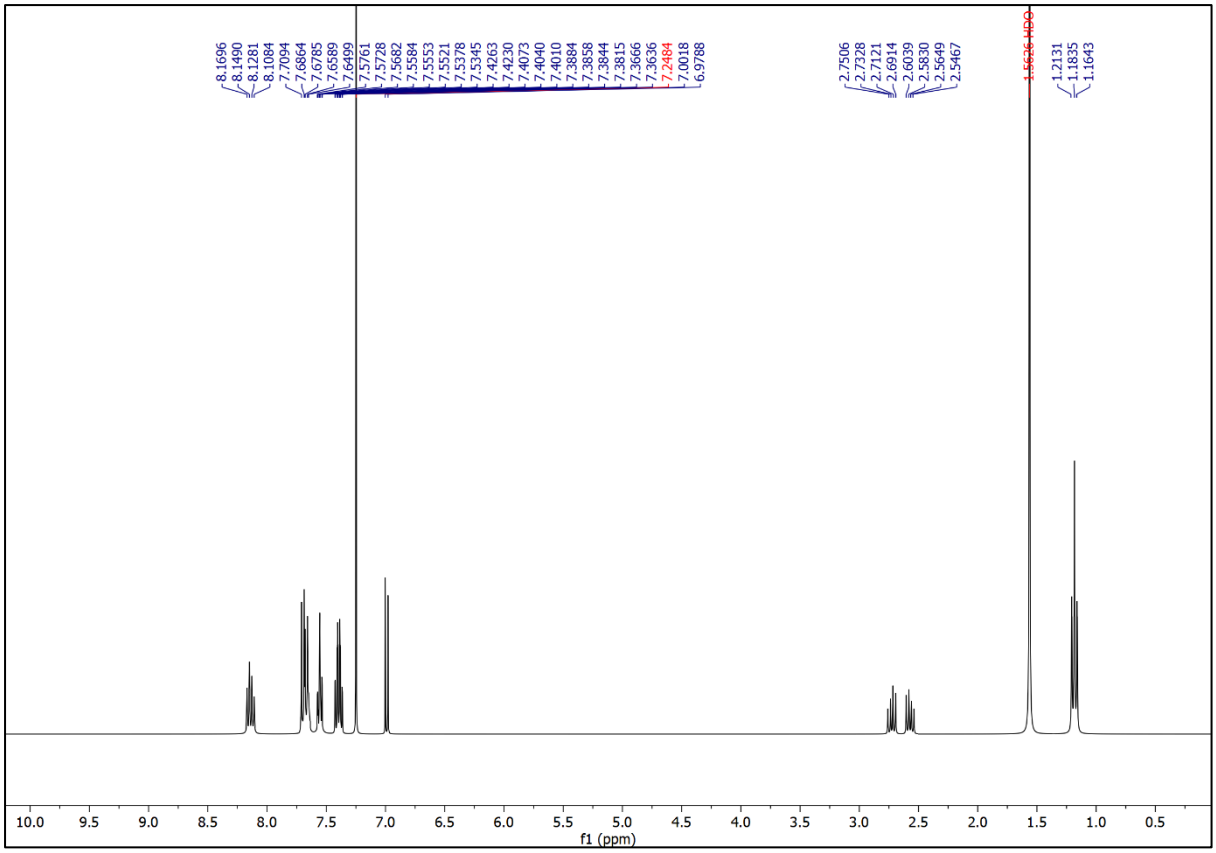

Fig. VI.2. ^{1}H-NMR spectrum of complex **1** in $CDCl_3$

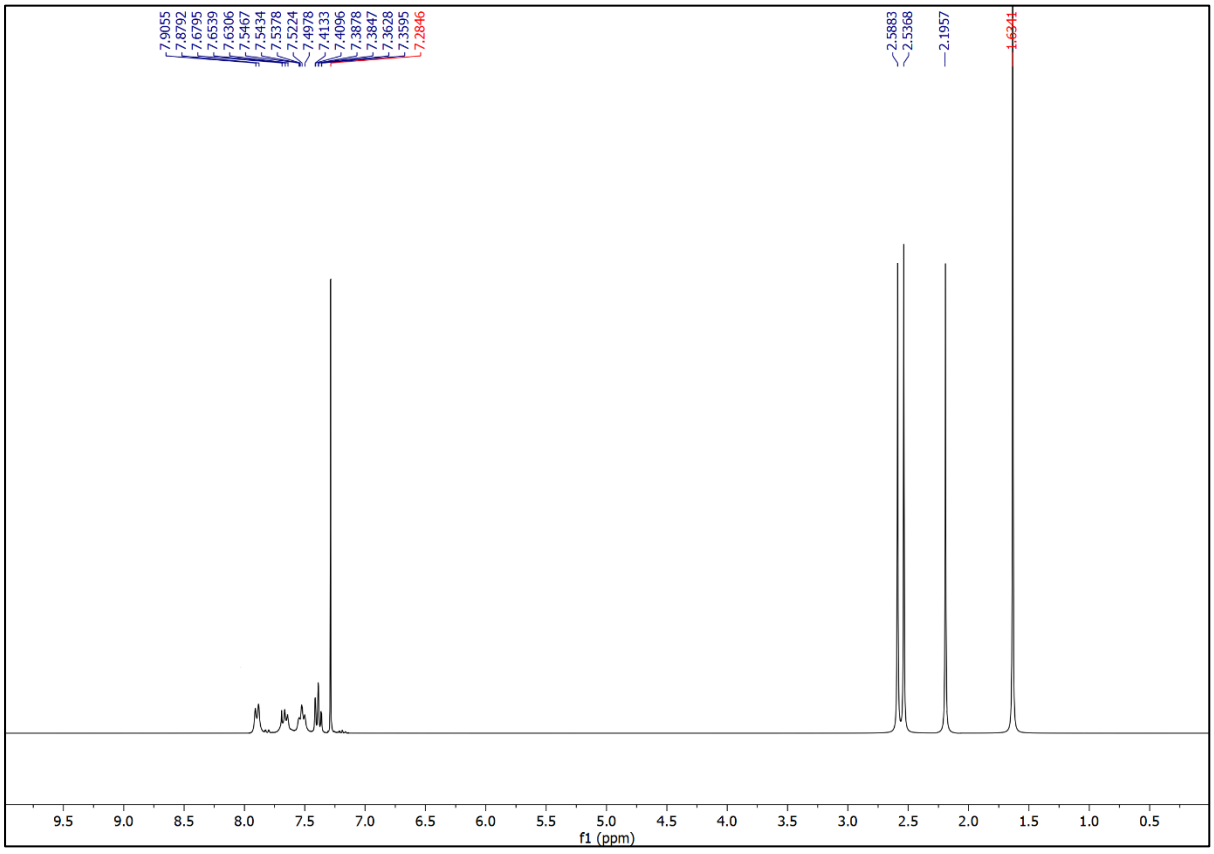

Fig. VI.3. ^{1}H-NMR spectrum of complex **2** in $CDCl_3$

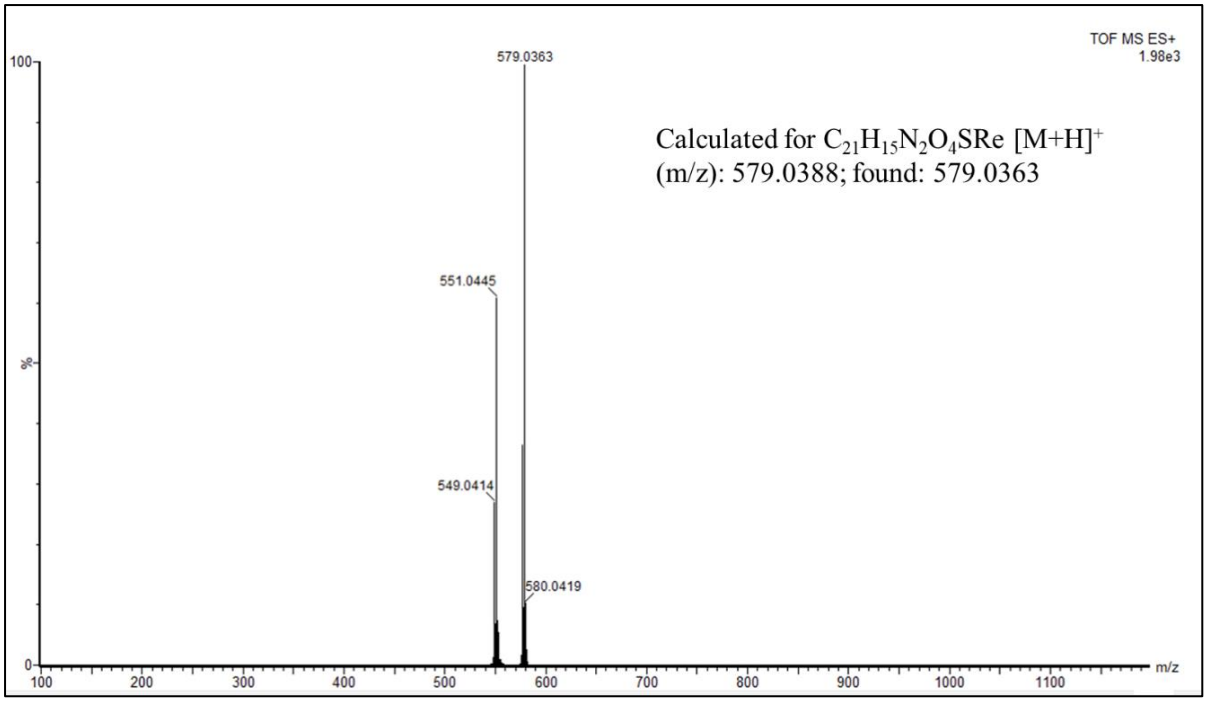

Fig. VI.4. HRMS spectrum of complex **1.**

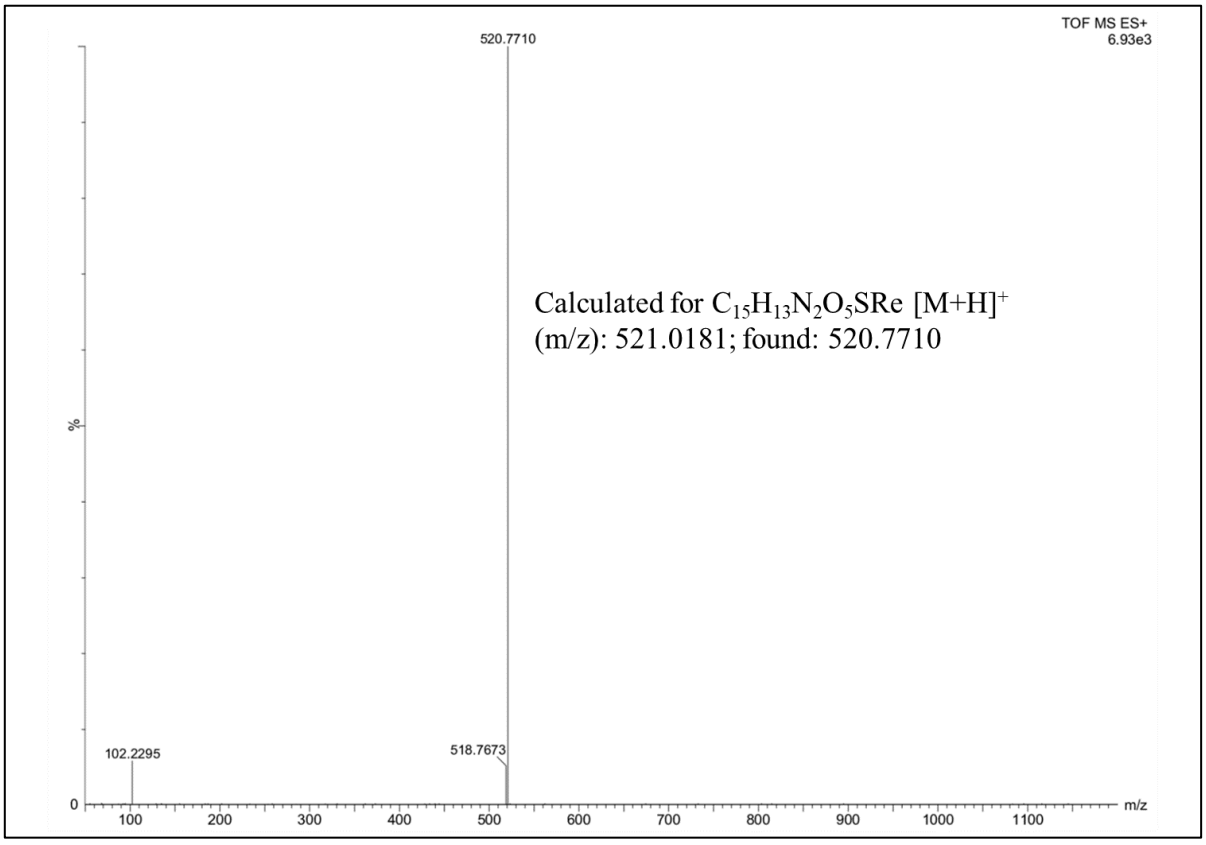

Fig. VI.5. HRMS spectrum of complex **2**

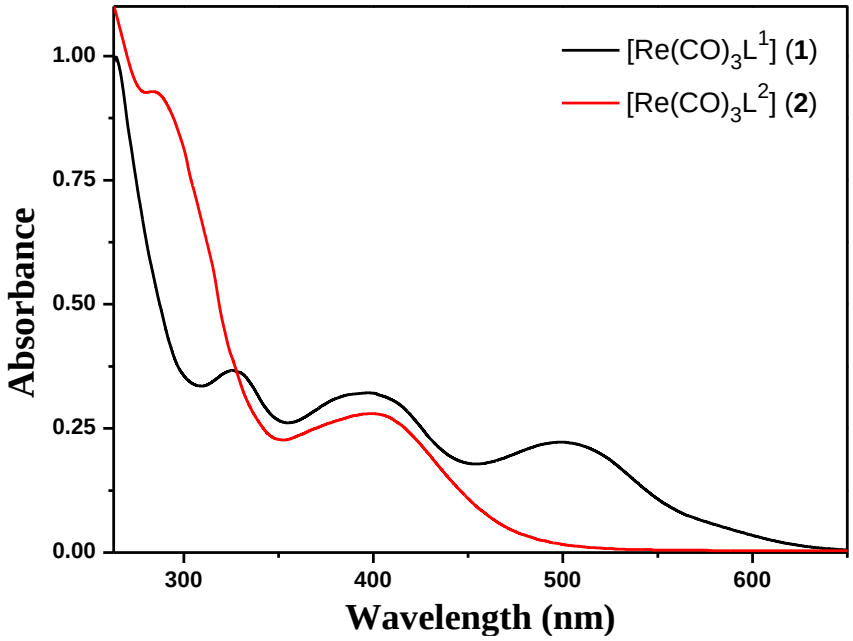

Fig. VI.6. UV-Vis spectra of $[Re(CO)_3(L^1)]$ (**1**) and $[Re(CO)_3(L^2)]$ (**2**) in DMSO.

VI.3.3. Crystallographic study

The molecular structures of the complexes have been confirmed by the single crystal X-ray diffraction method. The single crystal X-ray diffraction study discloses that both the complexes are crystallized in a monoclinic crystal system with the space group *P21/c*. The ORTEP plots of the complexes **1** and **2** along with the atom numbering scheme are shown in Fig. VI.7. The summary of the data collection and the refinement parameters have been incorporated in Table VI.1. Selected inter atomic bond lengths and bond angles of the complexes are summarized in Table VI.2. The bond parameters of the complexes imply a distorted octahedral geometry around the metal ions. The O, N, S pincer type of ligands coordinated with central metal ions through phenolic-O, azo-N and thioether-S atoms, creating a five and six membered chelate rings with a bite angle N(1)-Re(1)-S(1) of 76.26(7)^o , O(4)-Re(1)-N(1) of 78.22(9)^o for complex **1** and 77.67(10)^o, 76.95(12)^o for complex **2** respectively. The three remaining positions are occupied by the carbon atom of the carbonyl group with a fac arrangement. The five and six membered chelate bite angles are considerably deviated from the ideal octahedron, signifying noteworthy distortion in octahedral geometry of the two complexes. The azo bond distances (N1-N2) are found to be 1.277(3) Å and 1.288(5) Å in **1** and **2** respectively.[54] The observed bond distances of complexes **1** and **2** such as Re(1)-N(1) [2.128-2.147 Å], Re(1)-O(4) [2.117-2.142 Å], Re(1)-S(1) [2.4788-2.4928 Å] and Re(1)-C(CO) [1.907-1.937 Å] are noticed to be comparable to the other reported tricarbonyl Re(I) complexes.[55]

Table VI.1. Crystallographic data and refinement parameters of complexes **1** and **2.**

Complex	$[Re(CO)_3(L^1)]$ (**1**)	$[Re(CO)_3(L^2)]$ (**2**)
Formula	C21 H15 N2 O4 Re S	C15 H13 N2 O5 Re S
Formula Weight	577.61	519.53
Crystal System	*monoclinic*	*monoclinic*
Space group	*P 21/c*	*P 21/c*
a, b, c [Å]	12.3197(13), 18.6903(19), 9.6299(11)	6.7789(3), 28.8370(12), 9.0488(4)
α [°]	90	90
β [°]	111.997(3)	106.4660(10)
γ [°]	90	90
V [$Å^3$]	2056.0(4)	1696.34(13)
Z	4	4
D(calc) [g/cm^3]	1.866	2.034
Mu(MoKa)[mm^{-1}]	6.041	7.313
F(000)	1112	992
Temperature (K)	273(2)	293(2)
Radiation [Å]	0.71073	0.71073
θ(Min-Max) [°]	1.783- 27.533	3.163- 27.160
Dataset (h; k; l)	-16 to 15; -24 to 24; -12 to 12	-8 to 8, -36 to 37, -11 to 11
R, wR_2	0.0241, 0.0559	0.0284, 0.0703
Goodness of fit(S)	1.077	1.116

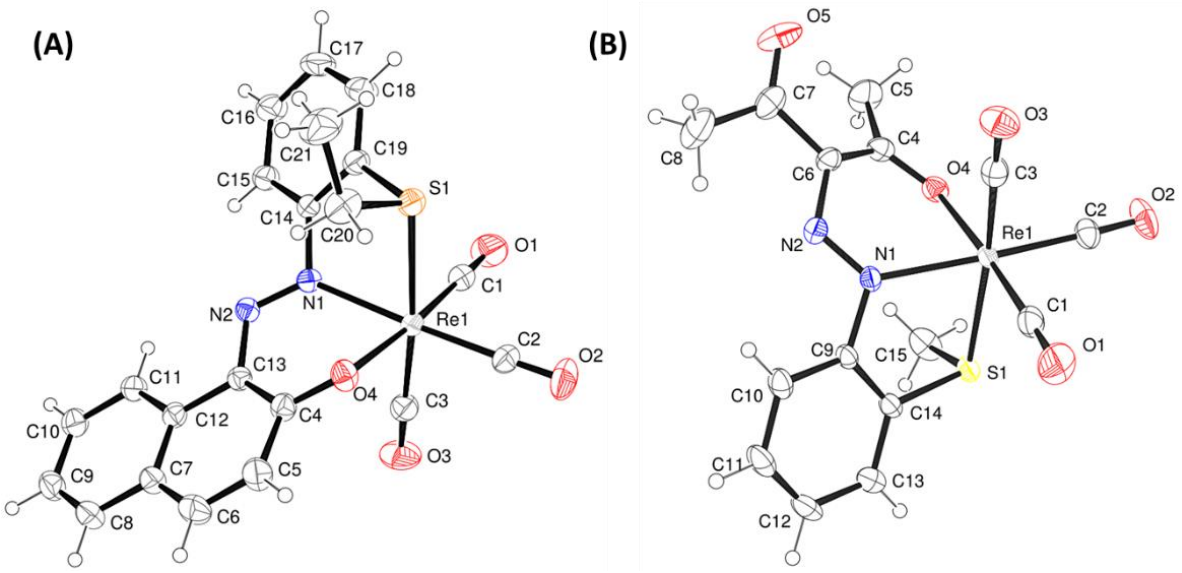

Fig. VI.7. ORTEP plot of complex **1** (A) and complex **2** (B) with 35% ellipsoidal probability.

Table VI.2. Selected X-ray and calculated bond distances and angles of complexes **1** and **2**.

Bonds(Å)	$[Re(CO)_3(L^1)]$		$[Re(CO)_3(L^2)]$	
	X-ray	Calc.	X-ray	Calc.
Re(1)-C(1)	1.908(3)	1.93698	1.907(5)	1.93441
Re(1)-C(2)	1.917(4)	1.95265	1.935(5)	1.95467
Re(1)-C(3)	1.928(4)	1.94214	1.937(5)	1.94321
Re(1)-O(4)	2.117(2)	2.16476	2.142(3)	2.18069
Re(1)-N(1)	2.147(2)	2.18577	2.128(3)	2.17945
Re(1)-S(1)	2.4928(9)	2.56448	2.4788(11)	2.56459
Angles (°)				
C(1)-Re(1)-C(2)	87.80(15)	90.53267	89.4(2)	90.44079
C(1)-Re(1)-C(3)	90.05(15)	89.62770	86.9(2)	89.60812
C(2)-Re(1)-C(3)	89.41(16)	90.51229	89.40(19)	90.76929
C(1)-Re(1)-O(4)	174.44(12)	174.79741	175.87(17)	174.78385
C(2)-Re(1)-O(4)	97.77(12)	94.65501	94.69(17)	94.59264
C(3)-Re(1)-O(4)	89.87(12)	89.93208	92.35(16)	88.95781
C(1)-Re(1)-N(1)	96.27(13)	97.87299	99.07(17)	98.60111
C(2)-Re(1)-N(1)	172.50(14)	168.42935	170.41(17)	167.94610
C(3)-Re(1)-N(1)	96.86(13)	97.44666	95.54(17)	97.21075
O(4)-Re(1)-N(1)	78.22(9)	77.04586	76.95(12)	76.61106
C(1)-Re(1)-S(1)	87.21(11)	86.95429	87.08(16)	86.58329
C(2)-Re(1)-S(1)	97.72(12)	96.84292	98.38(14)	97.07671
C(3)-Re(1)-S(1)	172.25(11)	171.91210	170.10(14)	171.29717
O(4)-Re(1)-S(1)	92.16(8)	92.80750	93.10(9)	94.13968
N(1)-Re(1)-S(1)	76.26(7)	75.79495	77.67(10)	75.66513

VI.3.4. DFT and TDDFT calculations

Recently, a theoretical approach naming density functional theory (DFT) study has been used to get an insight of the structural properties of the molecules before thorough exploration of drug designing and development.[56] DFT calculation was executed for the structural optimization, HOMO-LUMO energy calculation of the complexes which are significant for their structural elucidation, binding mode and biochemical activity.[57] Calculated bond distances and bond angles of the complexes are summed up in Table VI.2.

The calculated geometric parameters are convincingly well reproducing the X-ray crystal structures data. Contour plots of selected molecular orbitals for both the complexes **1** and **2** are shown in Fig. VI.8 and Fig. VI.9 respectively. Energy and compositions of selected molecular orbitals are incorporated in Table VI.3 and Table VI.4 respectively. The HOMO and LUMO energies were used to calculate global reactivity parameters such as ionisation potential (I), electron affinity (A), electronegativity (χ), chemical hardness (η), chemical potential (μ) and electrophilicity index (ω).[58] All the calculated reactivity parameters are listed in Table VI.5. The calculated energy gaps between the HOMO and LUMO are 2.83 eV and 3.42 eV for Complex **1** and **2** respectively. The calculated HOMO-LUMO energy gaps of the complexes are considerably smaller than their corresponding free ligands (Fig. VI.10), suggesting that the complexes are kinetically more reactive toward receptor biomacromolecules like DNA and BSA than the free ligands.

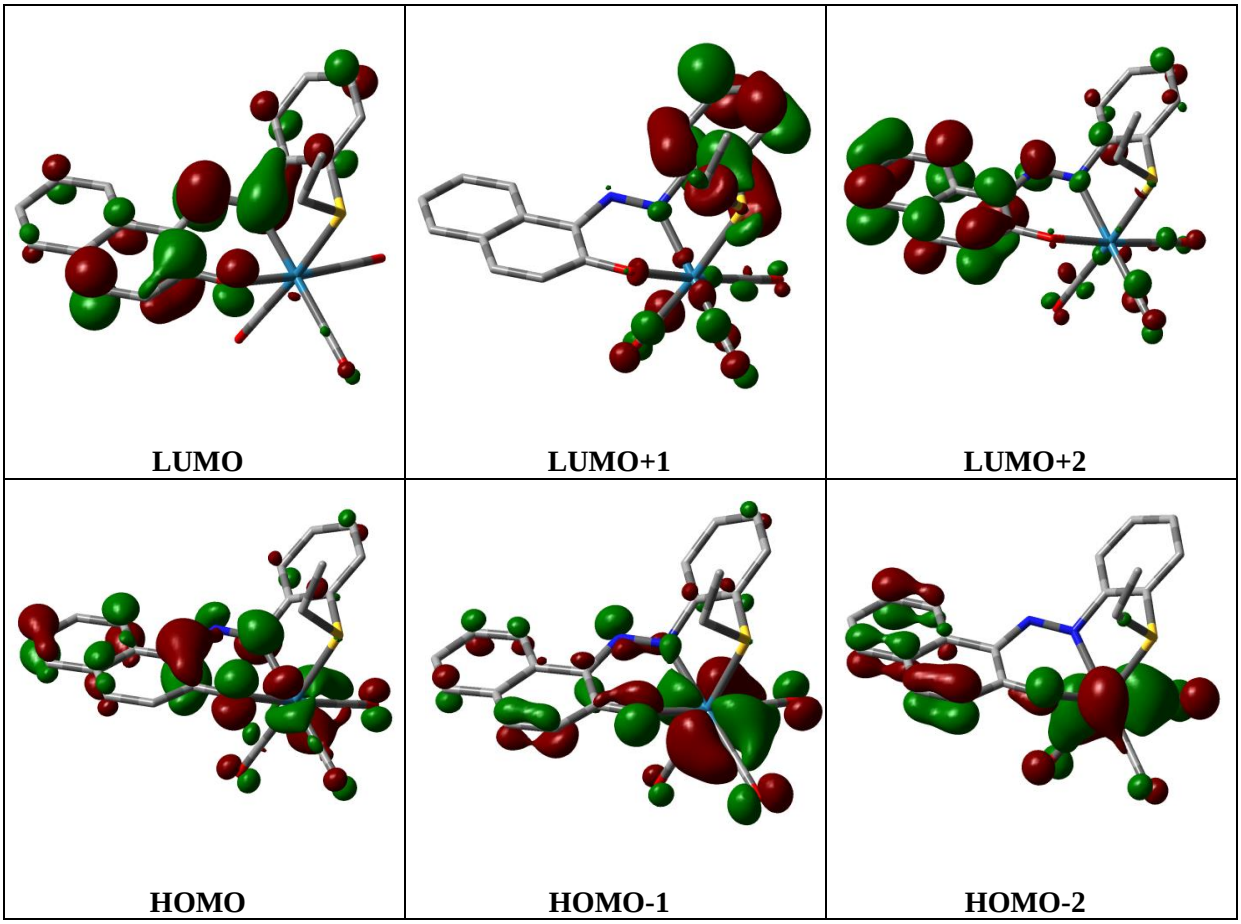

Fig. VI.8. Contour plots of some selected molecular orbital of complex **1.**

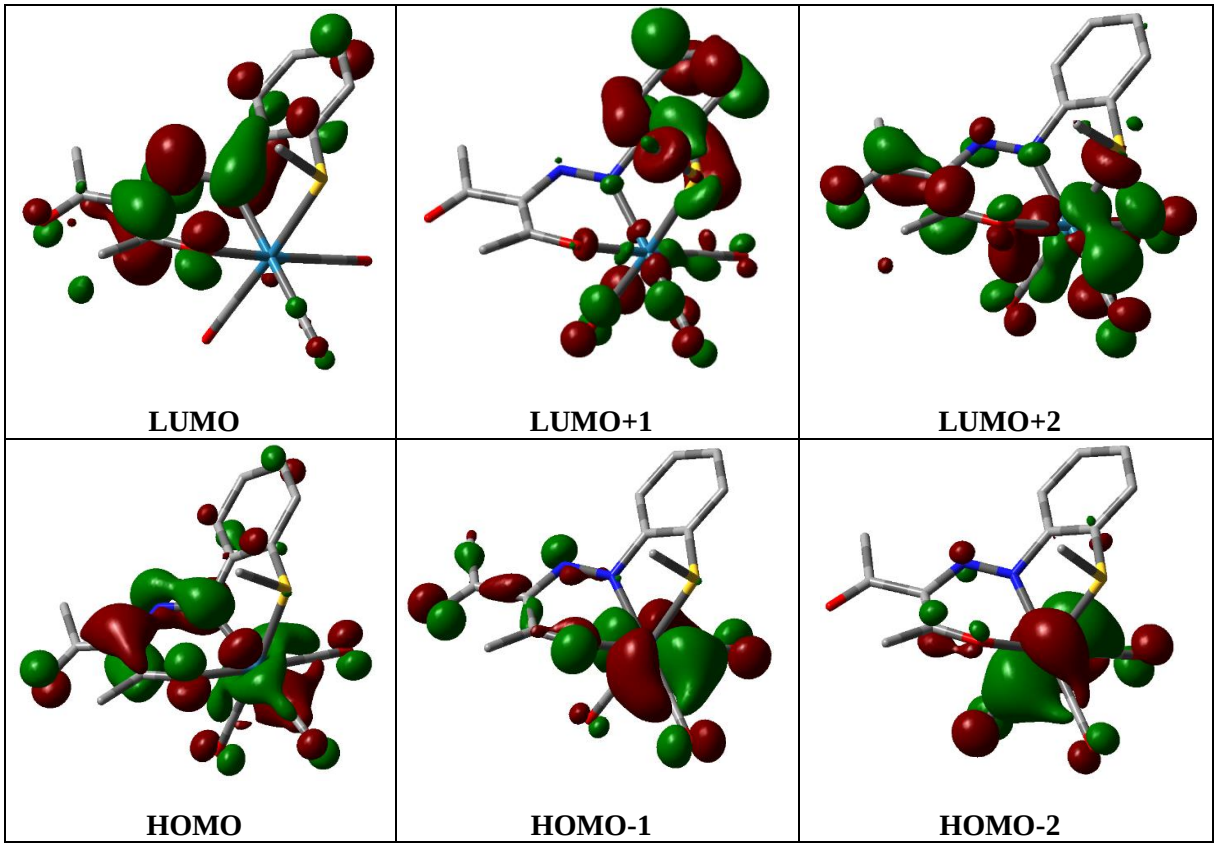

Fig. VI.9. Contour plots of some selected molecular orbital of complex **2.**

Table VI.3. Energy and % of composition of some selected molecular orbitals of complex **1.**

MO	Energy	% of composition		
		Re	L^1	CO
LUMO+5	-0.32	05	72	22
LUMO+4	-0.62	23	38	39
LUMO+3	-0.82	25	40	35
LUMO+2	-0.95	06	85	09
LUMO+1	-1.28	10	76	13
LUMO	-2.64	02	96	02
HOMO	-5.47	17	72	11
HOMO-1	-6.11	44	36	20
HOMO-2	-6.15	46	34	20
HOMO-3	-6.51	49	31	20
HOMO-4	-6.61	27	63	10
HOMO-5	-7.05	07	89	04
HOMO-6	-7.28	03	95	02
HOMO-7	-7.62	02	97	01
HOMO-8	-8.10	10	85	05
HOMO-9	-8.25	04	94	02
HOMO-10	-8.48	03	96	01

Table VI.4. Energy and % of composition of some selected molecular orbitals of complex **2.**

MO	Energy	% of composition		
		Re	L^2	CO
LUMO+5	-0.47	05	70	26
LUMO+4	-0.83	20	46	34
LUMO+3	-0.94	07	79	14
LUMO+2	-1.09	27	38	34
LUMO+1	-1.47	13	70	17
LUMO	-2.47	02	95	03
HOMO	-5.89	23	62	15
HOMO-1	-6.37	52	25	23
HOMO-2	-6.59	64	11	25
HOMO-3	-6.65	11	85	04
HOMO-4	-6.94	41	43	16
HOMO-5	-7.45	03	93	04
HOMO-6	-7.77	02	97	01
HOMO-7	-8.18	05	92	03
HOMO-8	-8.38	09	85	06
HOMO-9	-8.86	08	89	03
HOMO-10	-9.61	00	99	00

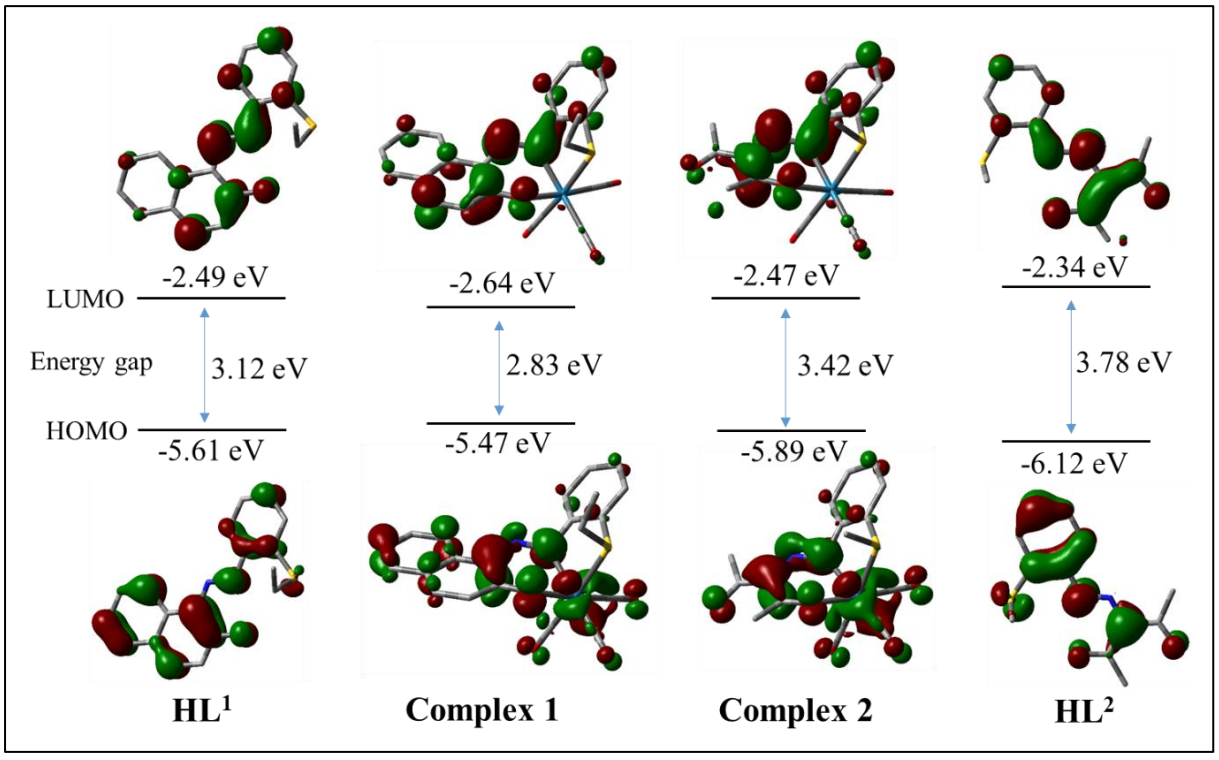

Fig. VI.10. Frontier molecular orbitals of ligands and complexes **1**, **2** and their HOMO–LUMO energy gaps.

Table VI.5. Global reactivity descriptors for complex **1** and **2**.

S. No	Physical property	Formula used	Complex **1**	Complex **2**
1	Ionization Potential (I)	$I = -E_{HOMO}$	5.47 eV	5.89 eV
2	Electron Affinity (A)	$A = -E_{LUMO}$	2.64 eV	2.47 eV
3	Electronegativity (χ)	$\chi = (I+A)/2$	4.05 eV	4.18 eV
4	Chemical Hardness (η)	$\eta = (I-A)$	2.83	3.42
5	Chemical Potential (μ)	$\mu = -(I+A)/2$	-4.05	-4.18
6	Chemical Softness (S)	$S = 1/\eta$	0.353	0.292
7	Electrophilicity Index (ω)	$\omega = \mu^2/2\eta$	2.898	2.554

The theoretical TD-DFT study is a helpful simulation technique, used to correlate and compare the simulated structural property of the complexes with the experimental UV-Vis spectrum.[59] The UV-Vis spectrum of the complex **1** displays an absorption band with λ_{max} at 501 nm, 396 nm and 327 nm which are very close to TD-DFT simulated peak at around 526 nm, 414 nm and 317 nm (Fig. VI.11A). These peaks correspond to the HOMO → LUMO transition, HOMO-1 → LUMO transition and HOMO-6 → LUMO transitions respectively. The complex **2** shows the electronic spectrum with λ_{max} at 402 nm and 284 nm, which are very close to TD-DFT simulated peak positions at 443 nm and 297 nm (Fig. VI.11 B). These peaks correspond to the HOMO → LUMO transition and HOMO-5 → LUMO transition. The corresponding energy of vital peaks, the oscillator strength, and the major transition are listed in Table VI.6.

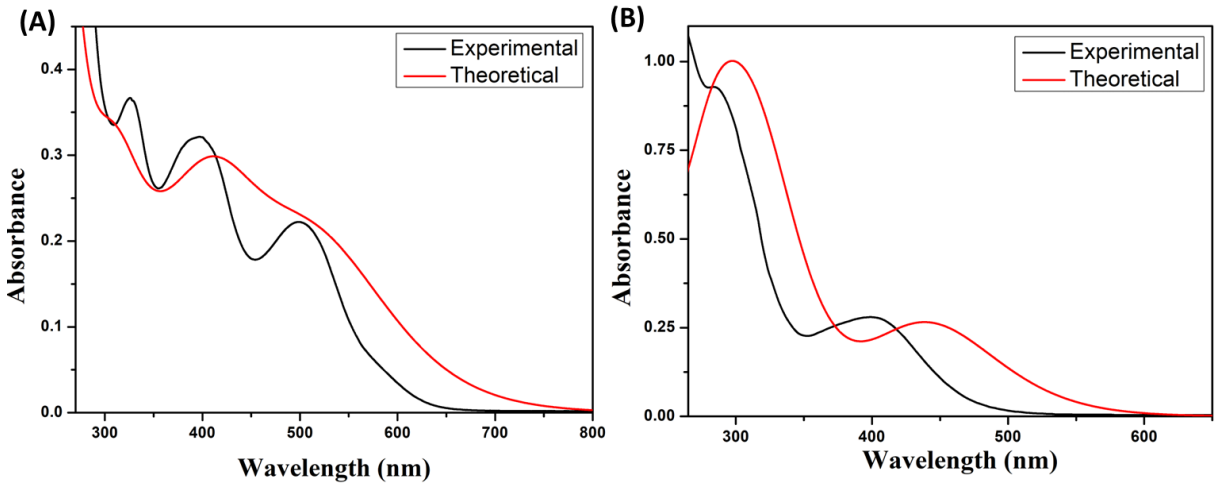

Fig. VI.11. Experimental (black) and TD-DFT simulated (red) UV-Vis spectra of complexes **1** (A) and **2** (B).

Table VI.6. Vertical electronic transition calculated by TDDFT/CPCM method of complex **1** and complex **2.**

Comp	λ (nm)	E (eV)	Osc. Strength (f)	Key excitations	Character	$\lambda_{expt.}$ (nm)
1	526.32	2.3557	0.1551	(96%) HOMO→LUMO	ILCT/ MLCT	501
	414.37	2.9494	0.1659	(50%) HOMO-1→LUMO	ILCT/ MLCT	396
	317.24	3.9082	0.1113	(87%) HOMO-6→LUMO	ILCT	327
2	443.76	2.7939	0.1017	(92%) HOMO→LUMO	ILCT/ MLCT	402
	297.89	3.9374	0.1713	(55%) HOMO-5→LUMO	ILCT	284

VI.3.5. Molecular Electrostatic Potential (MEP)

The molecular electrostatic potential (MEP) prediction is a theoretical constructive technique to expose the visual understanding of molecular shape, electron density, relative polarity, electrophilic-nucleophilic sites and molecular interaction. The molecular electrostatic potential (MEP) surface was computed at the B3LYP/6-31G(d) level of theory from optimized geometry to anticipate the reactive sites in the metal complexes. Different colours are utilized to specify diverse electrostatic potential values at the surface. The red-orange, green and blue colour represents the zone of most negative electrostatic potential, zero electrostatic potential and most positive electrostatic potential respectively. The magnitude of electrostatic potential increases in order as red < orange < yellow < green < cyan < blue.[60,61] The negative regions (red) of MEP correspond to the nucleophilic nature whereas the positive regions (blue) correspond to the electrophilic nature. The colour code of MEP maps for complex **1** and **2** are shown in Fig. VI.12. The negative electrostatic potential regions are chiefly located around the electronegative oxygen atoms, whereas positive electrostatic potential areas are relatively defused and mainly noticed on the ligand moiety. On the whole, neutral green regions are prevailing in both the complexes originating from carbon atom skeletons. The intermolecular interactions of the complexes with DNA and BSA can be envisaged based on the regional potential molecular behaviour and the location of the active sites.

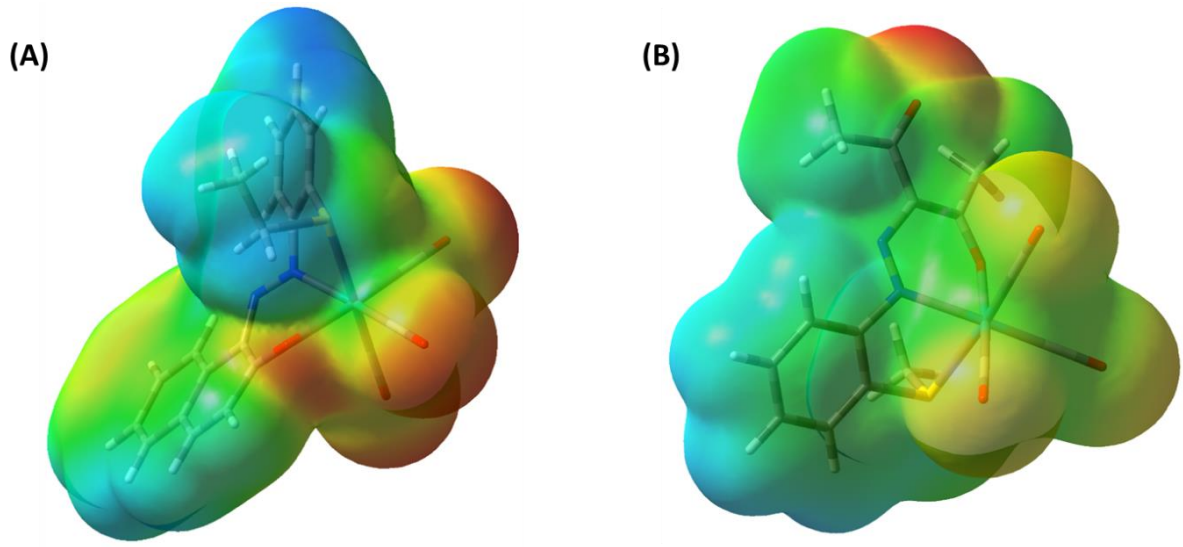

Fig. VI.12. Molecular electrostatic potential (MEP) map of the complex **1** (A) and complex **2** (B).

VI.3.6. Hirshfeld surface (HS) analysis

Hirshfeld surfaces analysis is very important in the study of the packing modes and intermolecular interactions in the molecular crystals.[62] The HS of complexes **1** and **2** mapped over dnorm (in the range of -0.05 to 1.2Å), shape index (range of -1.0 to 1.0 Å), and curvedness (range of -4.0 to 4.0 Å) are shown in Fig. VI.13. The Hirshfeld surface plotted over dnorm can be applied to demonstrate strong H-bonding as well as H-bonding interactions utilizing different colors.[63] This surface contains three colors, red, white, and blue. The red color corresponds to the interatomic contacts for which the distance between the atoms is less than the sum of van der Waals radii of atoms involved. The blue regions around the atoms signify that the distance between the atoms is greater than the sum of the van der Waals radii of the atoms involved. A white spot will be present on the HS if the distance between the atoms is equal to the sum of van der Waals radii of the atoms involved. The presence of π···π interactions in the titled compounds is confirmed by the adjacent red and blue triangles over the shape-index of the HS. Hirshfeld surface mapped on a curvedness map designates the planar arrangement of the molecules.

All the available contacts are summarized in a 2D fingerprint plot as discrete spikes (Fig. VI.14, Fig. VI.15 and Fig. VI.16 respectively). Decomposition of the fingerprint plot permits us to emphasize all the accessible interactions (H···H, H···C/C···H, H···N/N···H, H···O/O···H, C···O/O···C, H···S/S···H) in the complexes and their relative contribution to the total HS. The H···O/O···H contacts are principal in the complexes with the relative contributions being

34.1% and 39.7% for complex **1** and **2** respectively. This is in harmony with the high proportion of hydrogen and oxygen atoms in the structure.

The HS study points towards the crucial job of H-atom contacts and the broad array of H···(C/N/O)/ (C/N/O)···H interactions in establishing the crystal packing. However, the complex can cooperate with other molecules due to van der Waals and hydrogen bonding interactions in the crystal. These types of interactions are involved in numerous protein-small molecule interactions. This fact stimulated us to execute an interaction study to explore the effects of the substances on BSA and CT-DNA more thoroughly.[64]

	d_{norm}	Shape index	Curvedness
1	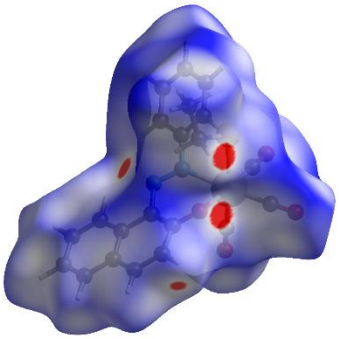	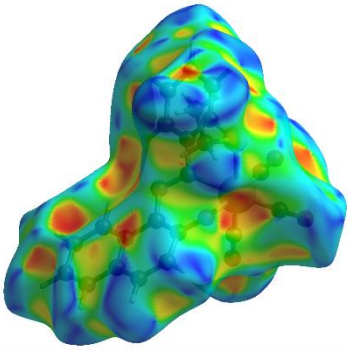	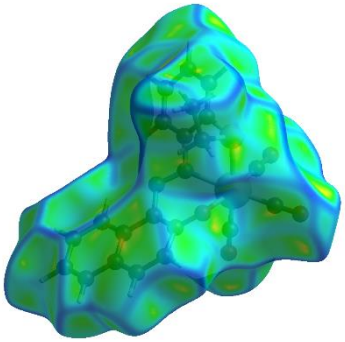
2	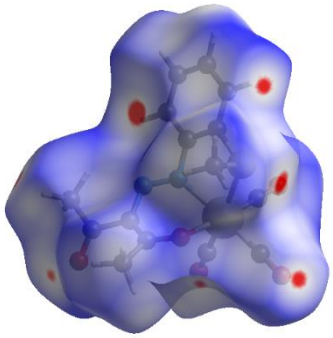	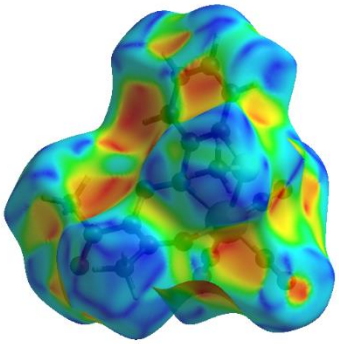	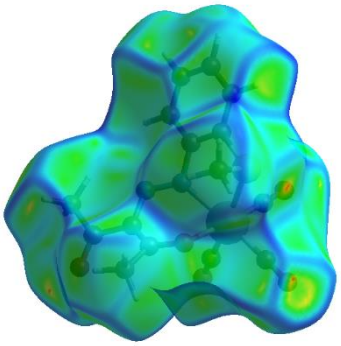

Fig. VI.13. Hirshfeld surfaces mapped with dnorm (left side), shape index (middle) and curvedness (right side).

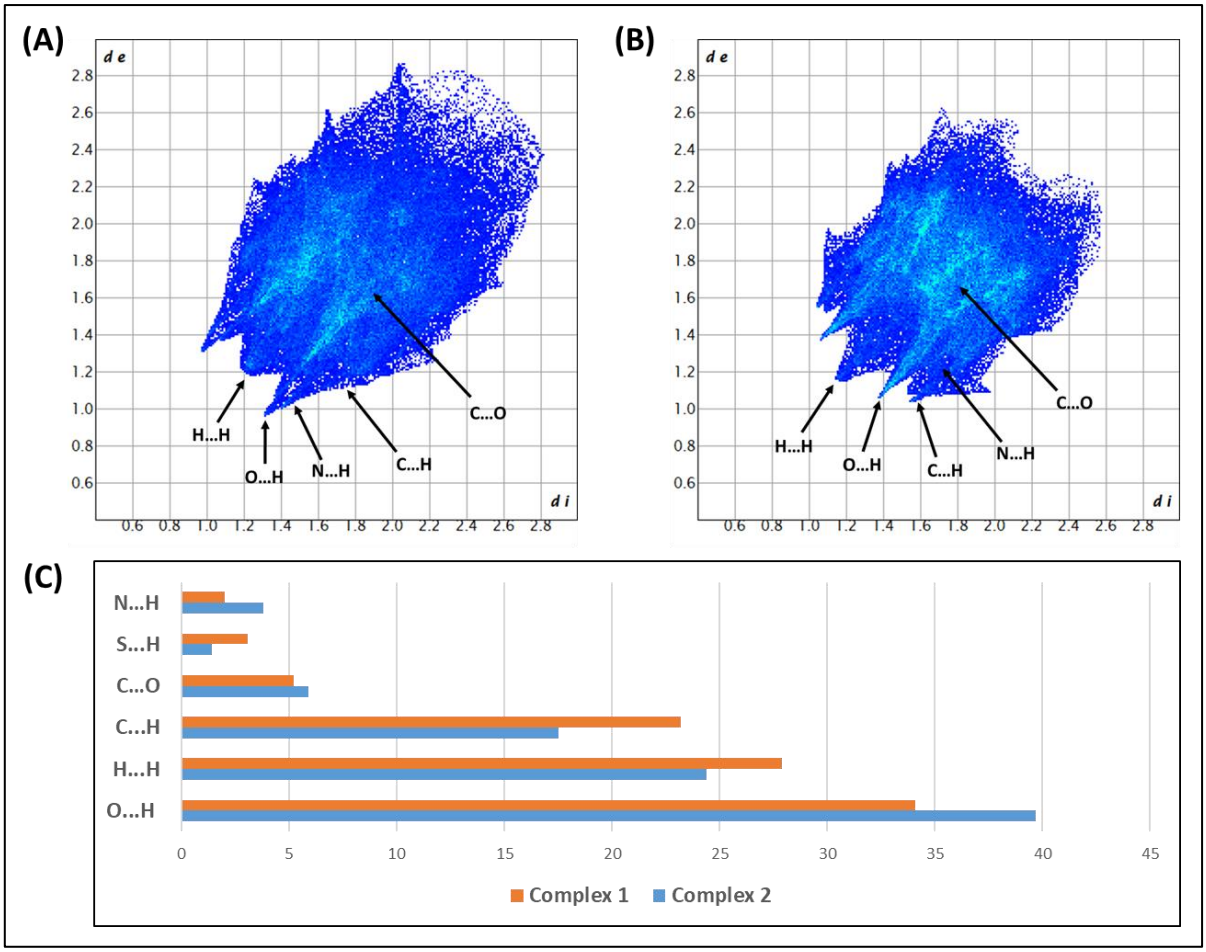

Fig. VI.14. 2D-Fingerprint plot (full) and relative contributions of various intermolecular interactions to the Hirshfeld surface area of complex **1** (A) and **2** (B). (C) Quantitative comparison of contributions (%) of various intermolecular interactions prevailing in complexes **1** and **2**.

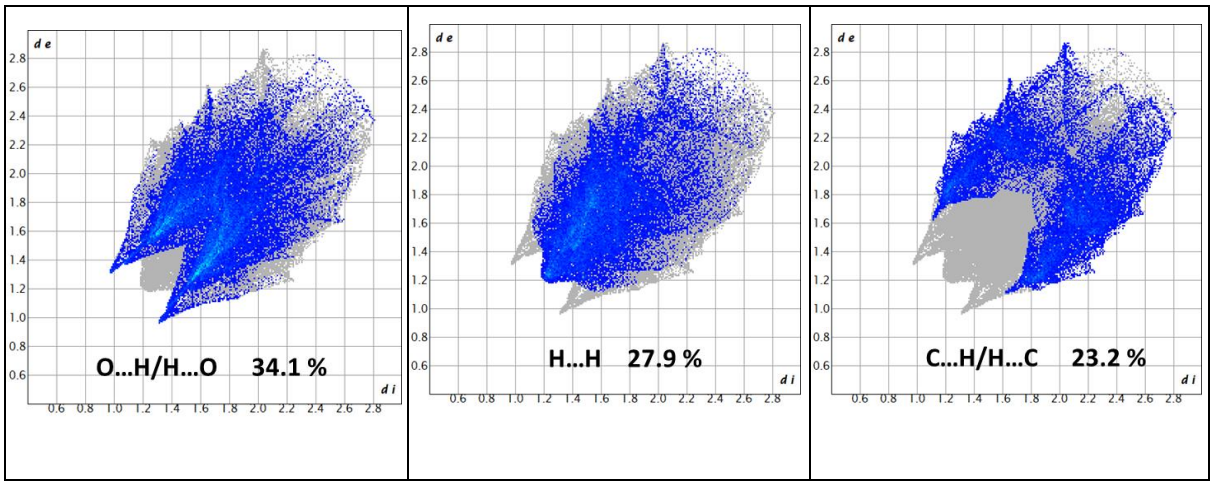

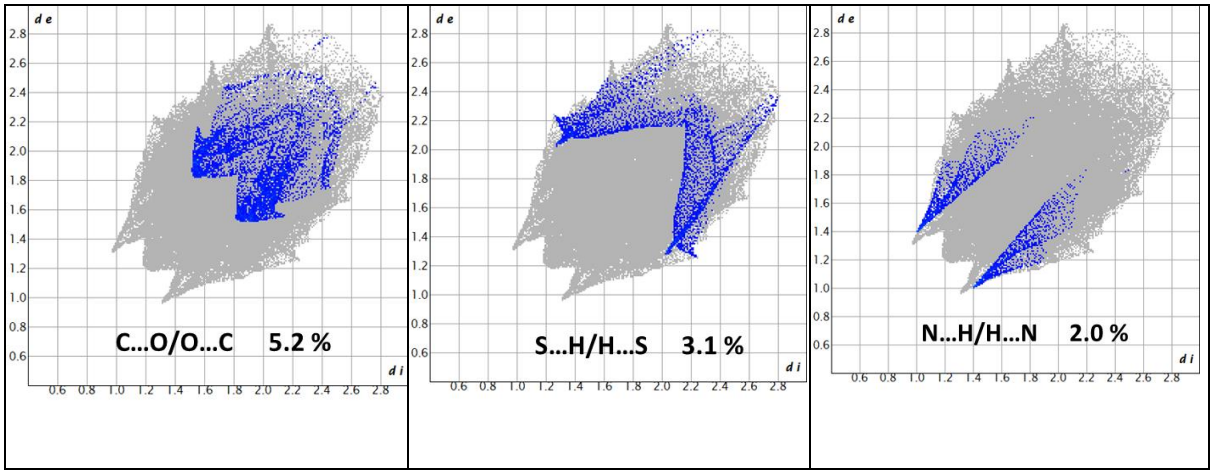

Fig. VI.15. 2D Fingerprint plot resolved into different contacts contributed to the total Hirshfeld surface area of the complex **1.**

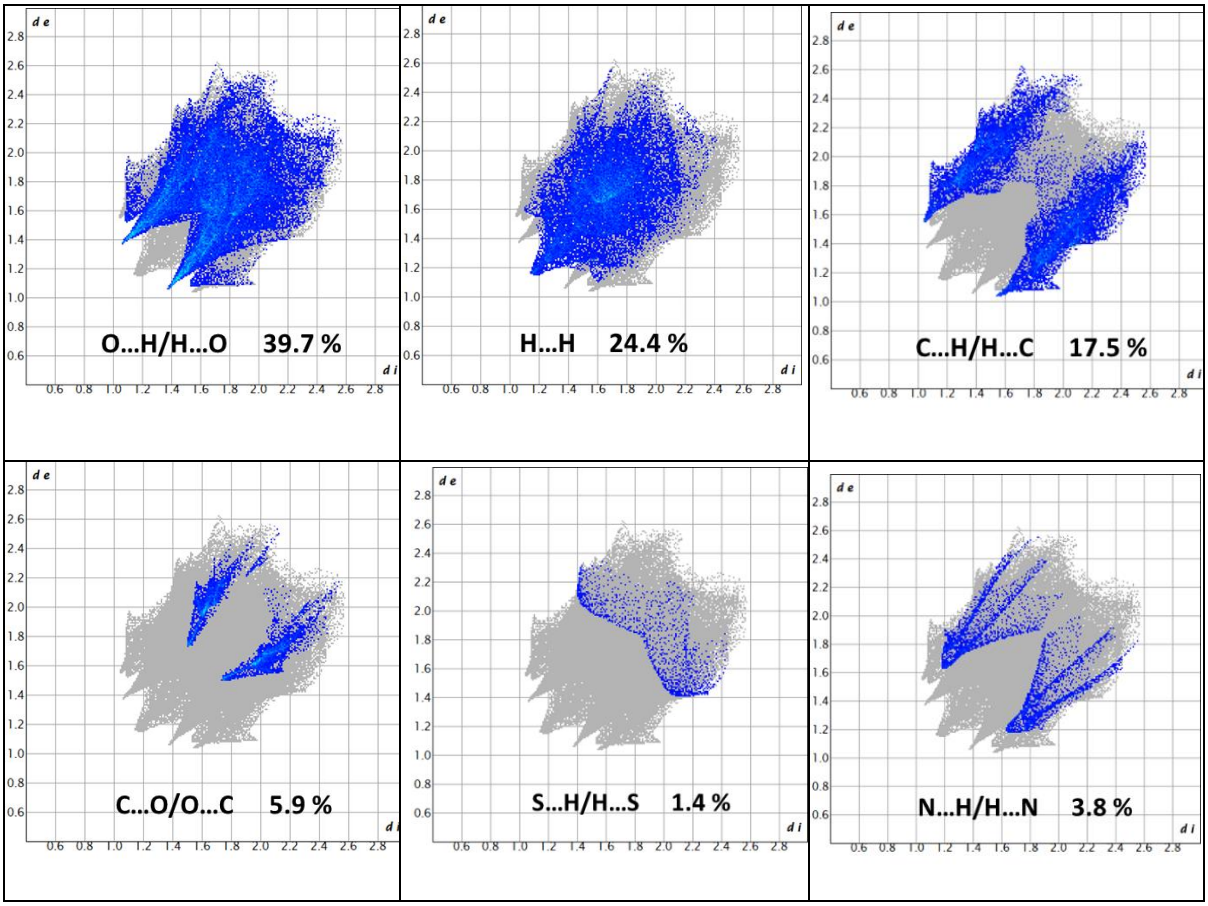

Fig. VI.16. 2D Fingerprint plot resolved into different contacts contributed to the total Hirshfeld surface area of the complex **2.**

VI.3.7. DNA binding studies

DNA is the most likely target site for the metal based anticancer drugs. In order to understand the anticancer capacity of these rhenium-based complexes, it is essential to estimate the binding abilities of the complexes with CT DNA using absorption and emission spectroscopy.[65]

VI.3.7.1. UV-vis method

The binding mode and strength of the complexes with CT-DNA were inspected by using the UV-Vis method. UV-Vis titration is a very recognized method used to study the interaction of a compound with DNA. The UV-visible absorption spectra for the complexes **1** and **2** in the absence and presence of calf thymus DNA (CT-DNA) are displayed in Fig. VI.17. The addition of CT-DNA to the complexes displayed only hypochromism signifying that the complexes are likely bound to CT-DNA through intercalative mode.[66] The noticed hypochromism is owing to the stacking interaction between the aromatic chromophores of the complexes and DNA base pairs consistent with the intercalative mode of binding. To determine relative binding strength of the complexes with CT-DNA, the intrinsic binding constants (K_b) were calculated by plotting [DNA]/($\varepsilon_a - \varepsilon_f$) vs. [DNA] from the spectral titration data with the aid of the Wolfe-Shimer equation (Eq. VI.6).[67]

$$\frac{[DNA]}{(\varepsilon a - \varepsilon f)} = \frac{[DNA]}{(\varepsilon b - \varepsilon f)} + \frac{1}{Kb(\varepsilon b - \varepsilon f)} \qquad \text{(Eq. VI.6)}$$

Where, [DNA] is the concentration of CT-DNA and ε_a is the apparent extinction coefficient of the complex at a given DNA concentration, ε_f and ε_b are the extinction coefficients of the complex in free solution and when fully bound to CT-DNA respectively. The plot of [DNA]/($\varepsilon_a - \varepsilon_f$) *vs.* [DNA] provides a straight line with slope and intercept equal to 1/($\varepsilon_b - \varepsilon_f$) and 1/[$K_b$($\varepsilon_b - \varepsilon_f$)] respectively. The values of K_b were calculated from the ratio of the slope to the intercept.

The intrinsic binding constant (K_b) values are shown in Table VI.7. The K_b values are calculated to be $8.489(\pm0.07)\times10^4\ M^{-1}$ and $7.283(\pm0.06)\times10^4\ M^{-1}$ for complexes **1** and **2** respectively. Even though, results of the absorption spectral studies display that the complexes bind to DNA through intercalation, the authentic binding mode requires to be proved by some additional experiments.

The stability of the complex DNA adducts were discovered by the binding constant values whilst an evaluation of the spontaneity of a complex towards DNA binding was given by using the equation (Eq. VI.7).

$$\Delta G = - RT \ln K_b \qquad \text{(Eq. VI.7)}$$

The free energies for the complexes (listed in Table VI.7) were negative which signified the spontaneity of compound-DNA interaction.

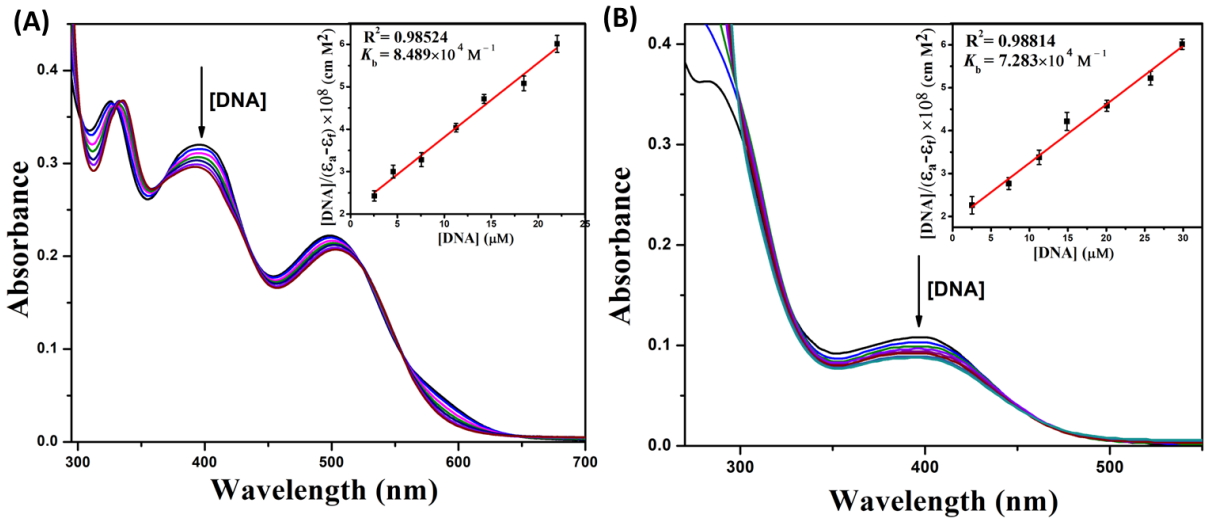

Fig. VI.17. Change in absorption spectra of the complex **1** (A) and **2** (B) in Tris–HCl/NaCl buffer with the gradual addition of CT DNA. Inset: Plot of [DNA]/(ε_a – ε_f) vs. [DNA].

VI.3.7.2. Ethidium bromide (EB) displacement experiment

An ethidium bromide (EB) fluorescence displacement experiment was executed to validate the intercalative mode of the binding between the complexes and CT-DNA. EB is a planar cationic dye that is broadly used as a responsive fluorescence probe for native DNA. In the presence of DNA, EB emits intense fluorescent light, owing to its powerful intercalation between adjacent DNA base pairs. The displacement technique depends on a decrease of this fluorescence which eventually results from the displacement of EB from the DNA sequence by a quencher. The quenching occurs because of the reduction of the number of binding sites on the DNA that are accessible to EB. The method consequently offers indirect proof for an intercalative binding mode.[68] The degree of fluorescence quenching may also be utilized to verify the extent of binding between the quencher and DNA. Here the accumulation of complexes to CT-DNA pre-treated with EB results in a huge amount of decease in emission

intensities with a red shift, demonstrating that the complexes compete with EB for the binding sites of DNA (Fig. VI.18). Quenching data were scrutinized according to the following Stern-Volmer equation (Eq. VI.8).[69]

$$\frac{F_0}{F} = 1 + K_{sv}[Q] \qquad \text{(Eq. VI.8)}$$

Where F_0 and F are the fluorescence intensities of the CT-DNA solutions in the absence and presence of the complexes, respectively. K_{sv} is the Stern-Volmer quenching constant and [Q] is the concentration of complex. The K_{sv} values are obtained from the slope of the plot of F_0/F versus [Q] and are found to be $7.831(\pm0.04)\times10^4$ M^{-1} and $7.655(\pm0.05)\times10^4$ M^{-1} for **1** and **2** respectively.

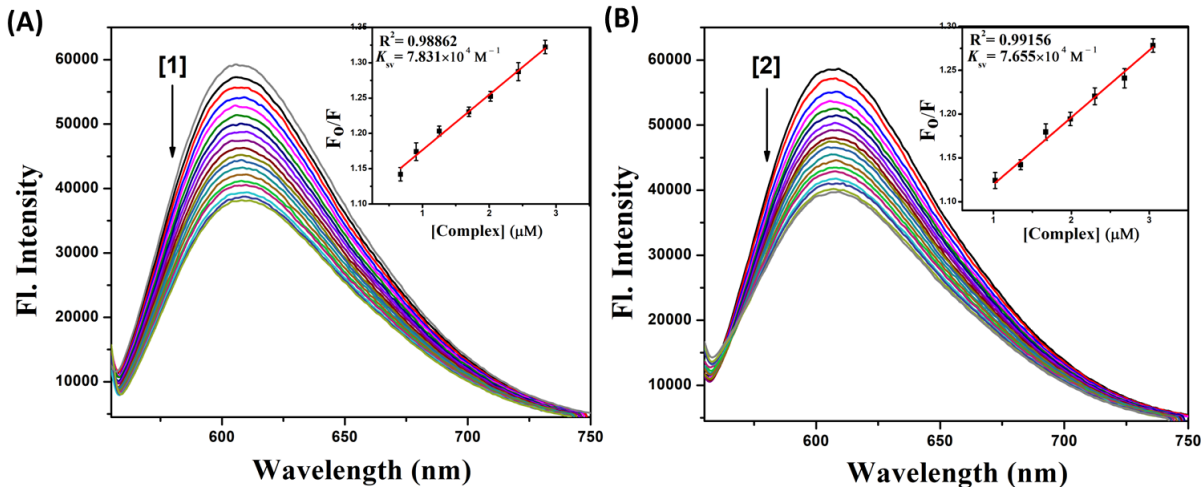

Fig. VI.18. Emission spectra (λ_{ex} = 540 nm) of EB-CT-DNA in presence of increasing concentrations of the complexes **1** (A) and **2** (B). Inset: Plots of emission intensity F_0/F vs. [complex].

Table VI.7. Binding constants (K_b) and Stern-Volmer constants (K_{SV}) values for the interaction of complexes **1** and **2** with CT-DNA.

Compound	UV Method	Fluorescence Method	ΔG (KJ.mol^{-1})
	K_b ($\times10^4$) (M^{-1})	K_{sv} ($\times10^4$) (M^{-1})	
EB-CT-DNA + 1	8.489 ± 0.07	7.831 ± 0.04	- 28.12
EB-CT-DNA + 2	7.283 ± 0.06	7.655 ± 0.05	- 27.74

VI.3.7.3. Viscosity Measurements

Viscosity measurements are susceptible to changes in length of DNA which are considered as one of the least indefinite and most significant tests of a DNA binding study in solution which actually offers strong evidence for the DNA binding mode of complexes. Lengthening of DNA helix happens on intercalation as base pairs are detached to accommodate the binding of complexes guiding to an increase in DNA viscosity.[70] On the other hand, electrostatic or groove binders do not hamper the CT-DNA structure and also do not modify the viscosity of the CT-DNA solution drastically.[71] The effects of the complexes on the viscosity of CT-DNA are displayed in the (Fig. VI.19). The values of $(\eta / \eta_0)^{1/3}$ were plotted against R (R = [complex]/[CT-DNA]), where η and η_0 are the relative viscosities of DNA in presence and absence of the complex respectively. The viscosity of CT-DNA increased progressively with the increment of the complexes, similar to that of the usual intercalator EB.[72] The capability of the complexes to enhance the viscosity of DNA follows the order EB >**1**>**2**. From the results of the viscosity experiments, it is confirmed that the complexes intercalate into the DNA base pairs which is already ascertained through absorption and fluorescence spectroscopic studies.

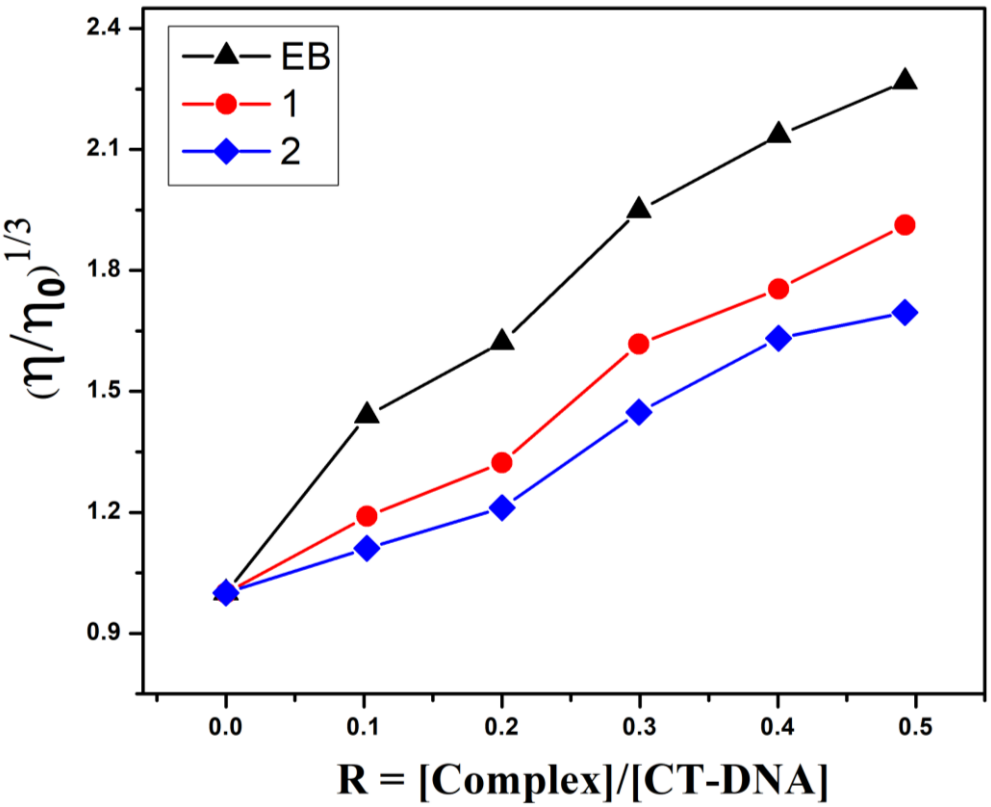

Fig. VI.19. Relative viscosity of CT-DNA interacting with complexes **1**, **2** and EB.

VI.3.8. Protein binding studies

The interactions of drugs with plasma proteins, predominantly with serum albumin are very vital for exploration as binding these proteins may direct to a loss or a progress of the biological properties of the drugs or it can also endow researchers with paths for drug transportation. Herein, bovine serum albumin (BSA) was used as an appropriate model to explore the binding affinity and interaction mechanism of the metal complex.[73]

VI.3.8.1. Absorption spectral studies

UV-visible absorption spectroscopy is a useful technique to differentiate between static and dynamic quenching depending upon the absorption spectra of BSA in presence of the complexes. Dynamic quenching refers to a procedure in which the fluorophore and the quencher meet during the brief existence of the excited state. Static quenching refers to the fluorophore-quencher complex construction in the ground state.[74] Electronic absorption spectra of BSA (10 μM in PBS at pH 7.4) were recorded in the range of 240-450 nm in presence of different concentration of complex which is displayed in the Fig. VI.20. BSA has a characteristic absorption band at 280 nm. From Fig. VI.20 it is apparent that the absorption intensity of BSA steadily increases along with the blue shift in the wavelength, signifying static type of fluorophore–quencher mechanism between BSA and complexes.[75] The association constants (K_a) for the interaction of complexes with BSA were calculated using the Benesi-Hildebrand equation (Eq. VI.9).

$$\frac{1}{A_{obs}-A_0} = \frac{1}{A_c-A_0} + \frac{1}{K_a(A_c-A_0)[complex]} \qquad \text{(Eq. VI.9)}$$

Where A_{obs} is the observed absorbance (at 280 nm) of the solution having various concentrations of the complex, A_0 and A_c are the absorbance of BSA only and of BSA with the complex. The apparent association constants (K_a) were calculated from the plot of $1/(A_{obs}-A_0)$ vs 1/[complex] (Fig. VI.20 inset) and were found to be $5.551(\pm0.05)\times10^4$ M^{-1} and $5.260(\pm0.06)\times10^4 M^{-1}$ for the complexes **1** and **2** respectively. These values are comparable to reported value.[76]

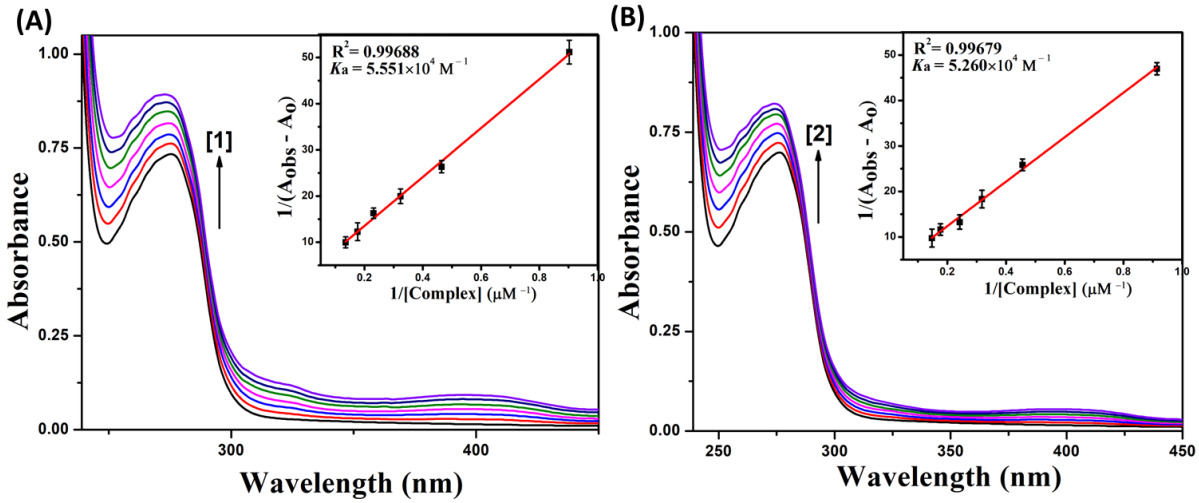

Fig. VI.20. Change in absorption spectra of BSA with the gradual addition of complex **1** (A) and complex **2** (B). Inset: Plot of $1/(A_{obs}-A_0)$ vs 1/[complex].

VI.3.8.2. Fluorescence quenching studies

The fluorescence spectrum of BSA was explored upon the steady addition of the complex to acquire more information on the binding of the complexes with BSA. BSA contains three fluorophores, namely, tryptophan, tyrosine and phenylalanine. But the intrinsic fluorescence of BSA is chiefly due to the presence of tryptophan alone as phenyl alanine has a very low quantum yield and the fluorescence of tyrosine is almost entirely quenched if it is ionized or near an amino group, a carbonyl group, or a tryptophan residue. In case of protein conformational transitions, subunit associations, substrate binding or denaturation the responses in the changes in the emission spectra of tryptophan are common. The interaction between the metal complexes and BSA were estimated by studying the fluorescence emission spectra of BSA with and without the metal complex (Fig. VI.21). On rising the concentration of complexes, a steady decrease in the fluorescence intensity was observed. It is primarily due to the buried active sites in the protein in hydrophobic surroundings.[77] These results recommended a specific interaction of the complexes with the BSA protein.

The linear Stern–Volmer equation (Eq. VI.8) is usually employed to illustrate the quenching mechanism between the complex and BSA. The Stern-Volmer quenching constant values (K_{sv}) calculated from the plot of F_0/F vs [Q] (Fig. VI.21 inset) in respect to complexes **1** and **2** were observed to be $4.803(\pm0.06)\times10^4$ M^{-1} and $4.225(\pm0.04)\times10^4$ M^{-1}. The high K_{sv} values designate that complexes show good fluorescence quenching ability. Furthermore, the quenching rate constant (Kq) of the complexes were noticed to be in the range of 4.80–4.22 × 10^{12} M^{-1} s^{-1}, following the equation $K\text{q} = K_{sv}/\tau_o$ (τ_o refers to the lifetime of the fluorophore

without the quencher with an average value of 10^{-8} s). Since the obtained *K*q value is greater than the value recommended in dynamic quenching (2×10^{10} M^{-1} s^{-1}), the preferred quenching process is static through the formation of a complex.[78]

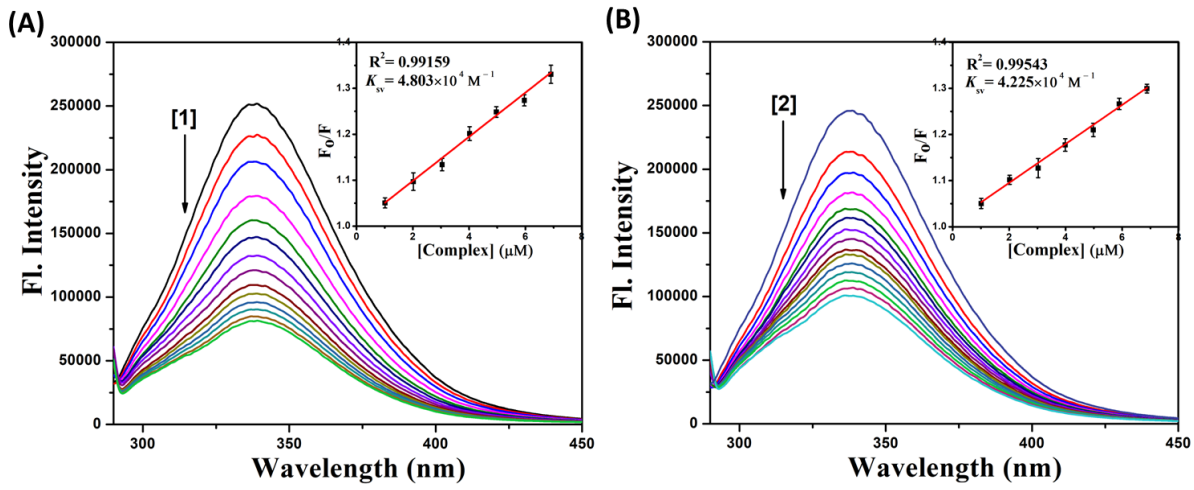

Fig. VI.21. Emission spectra (λ_{ex} = 280 nm) of BSA in presence of increasing concentrations of the complexes **1** (A) and **2** (B). Inset: Plots of emission intensity F_0/F vs. [complex].

VI.3.8.3. Binding constant and binding sites

For Base on the Scatchard equation (Eq. VI.10), the binding constant and the number of binding sites can be estimated.

$$log \frac{(F_0 - F)}{F} = log\ K_b + nlog[complex] \qquad \text{(Eq. VI.10)}$$

Where K_b is the binding constant of complex with BSA and *n* is the number of binding sites. The binding constant (K_b) and the binding sites (*n*) have been achieved from the intercept and slope of the curve of log [(F_o-*F*)/*F*] versus log [complex] (Fig. VI.22). Based on the plot, calculated values of binding constant (K_b) for the complexes **1** and **2** are 3.768(±0.07)×10^4 M^{-1} and 3.372(±0.06)×10^4 M^{-1} and binding sites (*n*) are 0.997(±0.03) and 0.968(±0.02) respectively. The binding constant (K_b) values clearly stated that the synthesized complexes have powerful binding affinity with the serum albumins. The attained binding site values *n* (~1) evidently confirm the existence of a single binding site on BSA protein for the complex.

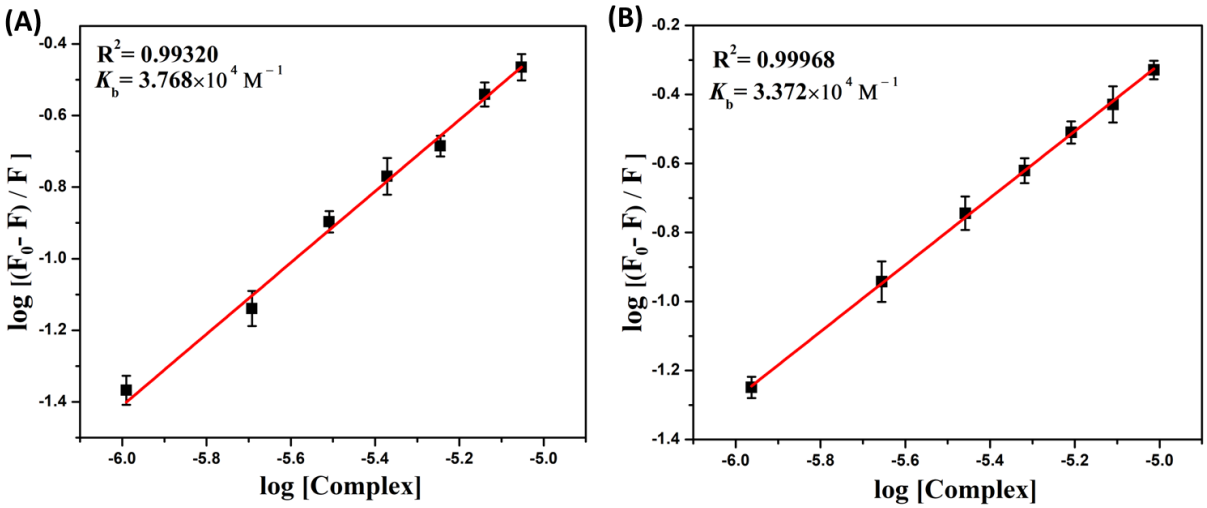

Fig. VI.22. Plot of log [(F_o-F)/F] versus log [complex] of complex **1** (A) and complex **2** (B).

Table VI.8. Protein apparent association constant (K_a), binding constant (K_b), quenching constant (K_{sv}) and number of binding sites (n) for the interaction of complexes **1** and **2** with BSA.

Compound	UV Method	Fluorescence Method		
	K_a ($\times 10^4$) (M^{-1})	K_b ($\times 10^4$) (M^{-1})	K_{sv} ($\times 10^4$) (M^{-1})	n
BSA + **1**	5.551 ± 0.05	3.768 ± 0.07	4.803 ± 0.06	0.997 ± 0.03
BSA + **2**	5.260 ± 0.06	3.372 ± 0.06	4.225 ± 0.04	0.968 ± 0.02

VI.3.8.4. Synchronous fluorescence spectroscopic studies

The synchronous fluorescence spectra provide information on the conformational alteration of the protein molecular microenvironment, predominantly in the surrounding area of the fluorophore moieties of BSA.[79] According to Miller,[80] in synchronous fluorescence spectroscopy, the differentiation between the excitation and emission wavelength ($\Delta\lambda = \lambda_{em} - \lambda_{ex}$) designates the nature of the chromophores in the spectra. In case of $\Delta\lambda$ value being 15 nm, the synchronous fluorescence spectra of BSA are characteristics of tyrosine residue, whereas the larger $\Delta\lambda$ value of 60 nm indicates to the characteristics of tryptophan residue.[81] The maximum emission wavelength of tryptophan and tyrosine residues in the protein molecule is associated to the polarity of their environment. Changes in protein conformation can be made by changes of the maximum emission wavelengths. The synchronous fluorescence spectra of BSA on the addition of complexes studied at $\Delta\lambda$ = 15 nm and $\Delta\lambda$ = 60 nm are revealed in Fig. VI.23 and Fig. VI.24 respectively. The fluorescence intensity of both tryptophan and tyrosine displayed a decrease in intensity. On the other hand, the emission wavelength of the tryptophan residues is noticed to show a blue shift. In the synchronous fluorescence spectra of BSA at $\Delta\lambda$ = 15, a small decrease in the fluorescence intensity of

BSA at 301 nm is observed on addition of the complexes to the solution of BSA. But, in the synchronous fluorescence spectra of BSA at $\Delta\lambda$ = 60, the addition of the complexes to the solution of BSA causes a major decrease in the fluorescence intensity of BSA at 343 nm, along with a red shift. It discloses that the binding around the tryptophan residues was toughened. The results evidently point towards the fact that both the complexes bind to the active sites of the protein which results in a conformational change in the secondary structure of the protein, thereby making them potential molecules for biological applications.

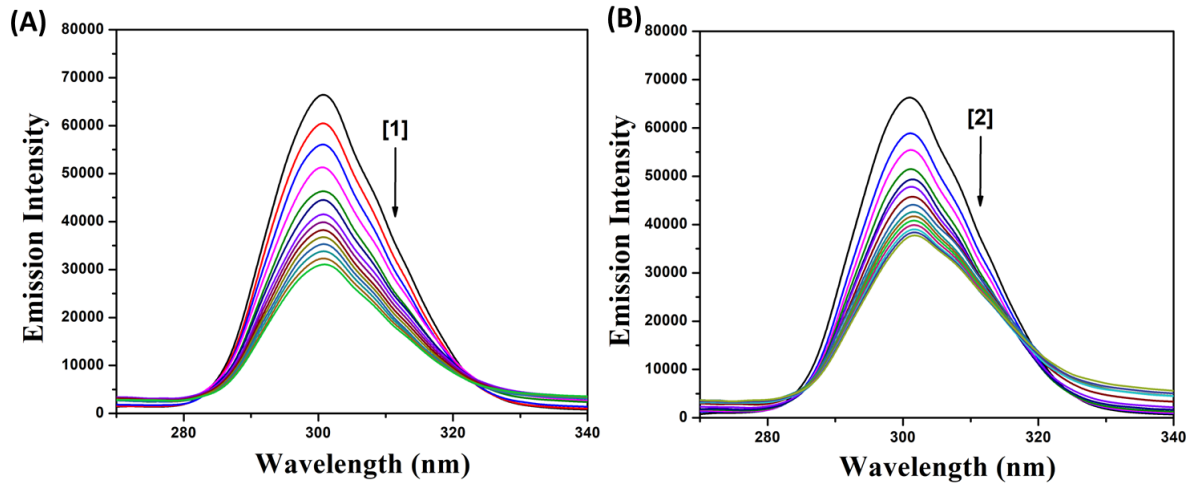

Fig. VI.23. The synchronous spectra of BSA in the presence of increasing amounts of the complexes **1** (A) and **2** (B) at a wavelength difference of $\Delta\lambda$ = 15 nm. The arrow shows the emission intensity changes upon an increase in the concentration of the complexes.

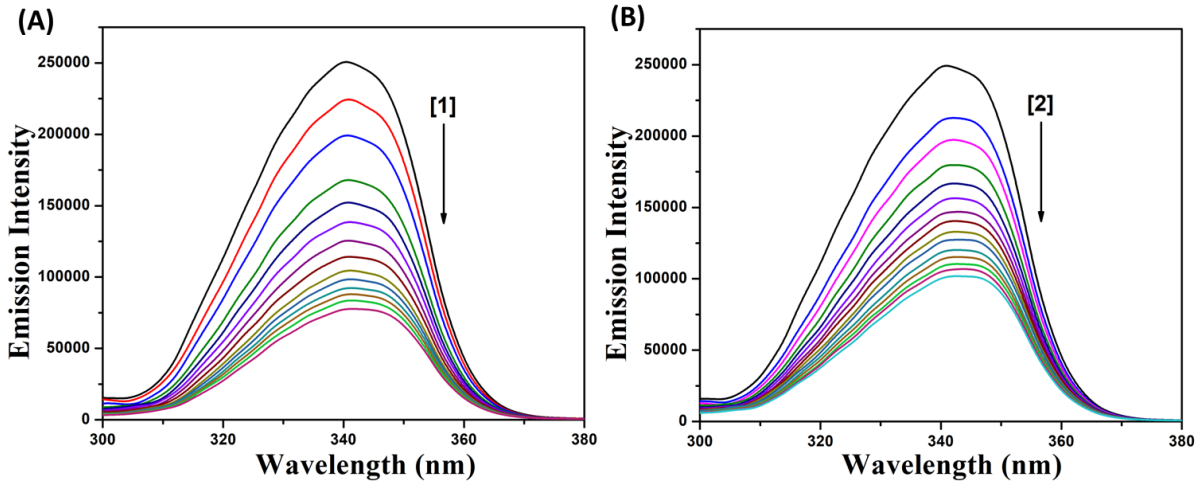

Fig. VI.24. The synchronous spectra of BSA in the presence of increasing amounts of the complexes **1** (A) and **2** (B) at a wavelength difference of $\Delta\lambda$ = 60 nm. The arrow shows the emission intensity changes upon an increase in the concentration of the complexes.

VI.3.8.5. Three-dimensional fluorescence spectra analysis

The analysis of conformational changes of BSA by three-dimensional fluorescence spectra is a potent technique for binding interactions with BSA. The alterations noticed in 3D emission spectra and their associated contour diagrams of BSA in the absence and presence of complexes are disclosed in Fig. VI.25. The first-order Rayleigh scattering peak ($\lambda_{em}= \lambda_{ex}$) and second-order Rayleigh scattering peak ($\lambda_{em}= 2\lambda_{ex}$) are referred to as peak 'c' and 'd' respectively. The very strong peak 'a' depicts the spectral behavior of the Trp and Tyr residues in proteins while another peak 'b' primarily reveals the properties of the polypeptide backbone structures.[82] The emission intensity of Rayleigh scattering peak enhanced on addition of the complex to BSA. This is because of the development of fluorophore-quencher complex between BSA and complexes which enlarged the diameter of the macromolecule and improved the scattering effect. But the fluorescence intensity of peak 'a' and 'b' decrease sharply in the presence of complexes. This result demonstrated that the binding of the complexes to BSA stimulates molecular microenvironment and conformational changes in protein.

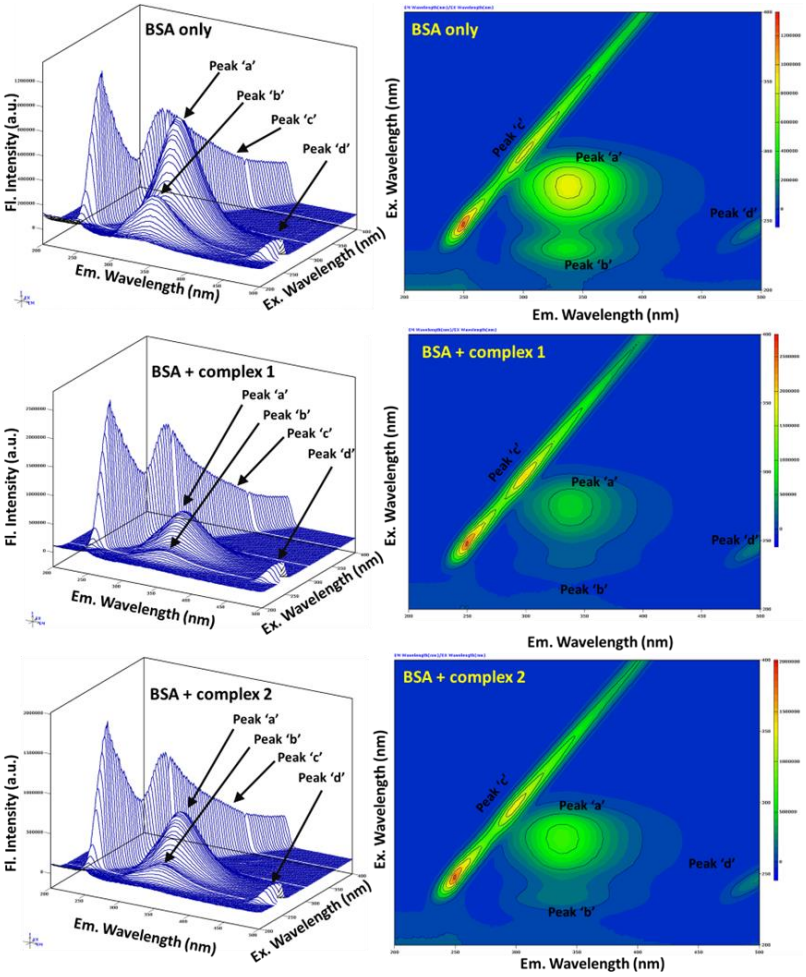

Fig. VI.25. Three-dimensional fluorescence spectra of BSA in the absence and presence of complexes **1** and **2.**

VI.3.8.6. Transfer of energy from BSA to the complexes

Förster resonance energy transfer (FRET) is a non-radiative spectroscopic method that can be utilized to observe the relative orientation and proximity of the fluorophores.[83] It can also be used to quantify the distance dependent energy transfer efficiency (*E*) between the donor and acceptor. Whenever the overlap between the fluorescence emission spectrum of the donor and the UV-Vis absorption spectrum of the acceptor is sufficient, the effective energy transfer from a protein residue (donor) to a complex (acceptor) takes place. The energy transfer efficiency (*E*) can be acquired using the following equation (Eq. VI.11).[84]

$$E = \frac{R_0^6}{R_0^6 + r^6} = 1 - \frac{F}{F_0} \qquad \text{(Eq. VI.11)}$$

where F and F_0 signify the fluorescence intensity of BSA in presence and absence of the complexes, r is the acceptor-donor distance and R_0 is the critical distance when the transfer efficiency is 50%. The $J(\lambda)$ value can be calculated by integrating the overlapped portion of the normalized donor emission spectrum of BSA with the molar extinction coefficient spectrum of acceptor complexes as shown in Fig. VI.26 (yellow shaded area for complexes **1** and **2**). All values of FRET parameters were determined and are summarized in Table VI.9.

For productive energy transfer between BSA and complexes, the donor-acceptor distance (r) should be in the order of 2-8 nm. The statistics (r = 3.70–3.77 nm) clearly state that energy transfer is greatly viable for complex **1** and **2**. Moreover, the r value follows the relationship $0.5R_0 < r < 1.5R_0$, which agrees with the occurrence of static quenching interactions between BSA and complexes.[85] The findings also specifies that the effectiveness of energy transfer (E) for complexes follows the pattern complex **1** > complex **2**.

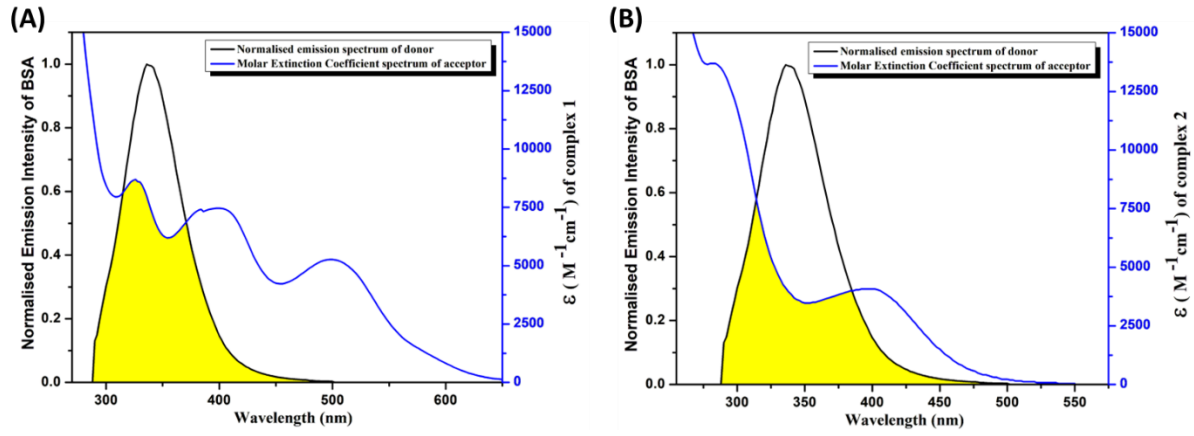

Fig. VI.26. Spectral overlap (yellow shaded area) of the normalized emission spectrum of BSA in PBS buffer (donor) with the molar extinction coefficient of complexes **1** (A) and **2** (B) (acceptor) in DMSO.

Table VI.9. parameters obtained from energy transfer between BSA and complexes **1** and **2**.

Complex	$J(\lambda)$ ($M^{-1}cm^{-1}nm^4$)	R_0 (nm)	E	r (nm)
1	3.60×10^{15}	4.27	0.6785	3.77
2	2.22×10^{15}	3.94	0.5907	3.70

VI.3.8.7. Circular dichroism spectral measurement

To further investigate about whether complexes **1** and **2** can cause a conformational change in BSA protein, circular dichroism (CD) experiments were executed at room temperature. CD is an essential technique for determining changes in protein secondary structures during protein-drug interaction.[86] Thus, the CD spectra of BSA with or without complexes were recorded. At physiological pH, free BSA shows two strong negative bands in the far UV region at 208 nm (π-π* transition) and 219 nm (n-π* transition), which are characteristic of the α-helical structure of BSA.[87] Such bands are perceived to be greatly sensitive to the binding of drugs. The reason is that the intermolecular forces accountable for sustaining the secondary structures can be rehabilitated and activate a conformational modification of the protein. Therefore, the separate addition of complexes **1** and **2** to BSA solution in different molar ratios resulted in a decrease in these negative band intensities without any noteworthy shifting of the peaks. Fig. VI.27 show the CD spectra of BSA at physiological pH and in a variety of molar ratios of protein to drug (1 : 0, 1 : 1, 1 : 3, 1 : 5). These results visibly imply that the binding of our synthesized complexes with BSAs led to a modification in the secondary structure of these proteins.[88] The observed results were represented in terms of mean residue ellipticity (MRE at 208 nm deg cm^2 $dmol^{-1}$).

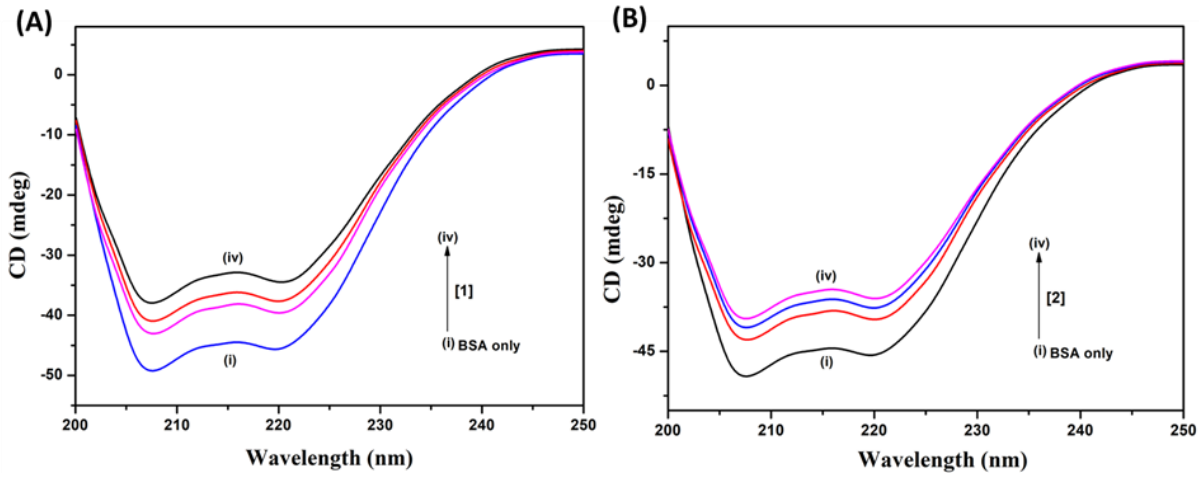

Fig. VI.27. CD spectrum of BSA with different molar ratios of complexes **1** (A) and **2** (B).

The α-helix content of BSA for different BSA: complex ratios are 45.94% (1 : 0); 37.27% for **1** and 37.69.67% for **2** (1 : 1); 34.74% for **1** and 35.16% for **2** (1 : 3); and 30.87% for **1** and 33.34% for **2** (1:5). The calculated results revealed a decrease of α-helix content from the native BSA. It was evident that both of the complexes helped in altering the shape of BSA and reduced the stability of the α-helix. The effect of complex **1** on BSA conformation was stronger than the complex **2** under indistinguishable conditions.

VI.3.9. *In-vitro* Cytotoxicity Study

VI.3.9.1. Cell viability assay

The cytotoxic effect of complexes **1** and **2** against MCF-7 and MCF-10A cells were evaluated by the MTT [3-(4,5-Dimethylthiazol-2-yl)-2,5-Diphenyltetrazolium Bromide] reduction to formazan crystals.[89,90] After 24 h of plating, MCF-7 and MCF-10A cells were treated with complexes **1** and **2** at a range of 1.56 μM to 100 μM for 24 h. From the absorbance values, the relative cell viabilities were counted by using the earlier described formula and results were precisely shown in Fig. VI.28 and Fig. VI.29 respectively. Using the Chou-Talalay's method, all the IC_{50} values were calculated in CompuSyn Software. From the IC_{50} values, listed in Table VI.10, it was found that in case of MCF-7 cells, the IC_{50} values of complex **1** and **2** was 10.12 μM and 15.24 μM respectively which signifies complex **1** has higher cytotoxic potential than complex **2** against the breast epithelial adenocarcinoma cells. However, in case of MCF-10A cells, the IC_{50} values of both the complexes was 138.51 μM and 135.57 μM respectively which signifies both the complexes have very less cytotoxic potential against normal breast epithelial cells.

Table VI.10. Inhibitory Concentration (IC_{50}) values of complex **1** and **2** compounds against both breast epithelial adenocarcinoma cells (MCF-7) and normal breast epithelial cells (MCF-10A) using Chou-Talalay's method in CompuSyn Software.

Compounds	**IC_{50} Values** (μM)	
	MCF-7 cells	MCF-10A cells
Complex 1	10.12	138.51
Complex 2	15.24	135.57
Cisplatin	16.7	31.5

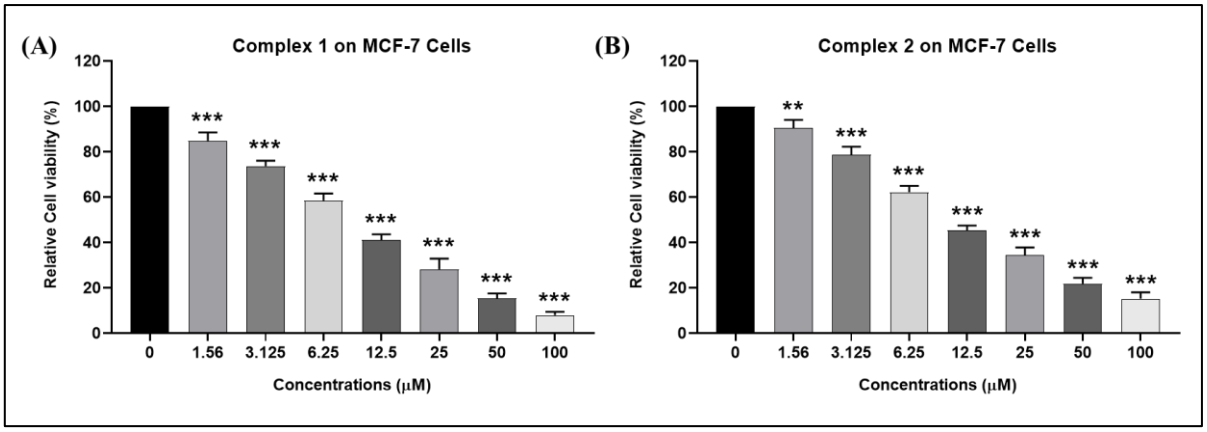

Fig. VI.28. Cell cytotoxicity assay. **(A)-(B)** Bar diagrams represent cell cytotoxicity study of Complex **1** and Complex **2** with different concentrations (at a range of 1.56 μM - 100 μM) against human breast epithelial adenocarcinoma (MCF-7) cells. All the experiments were performed independently thrice and the data were calculated as Mean ± SD where *P < 0.05, **P < 0.01, ***P < 0.001.

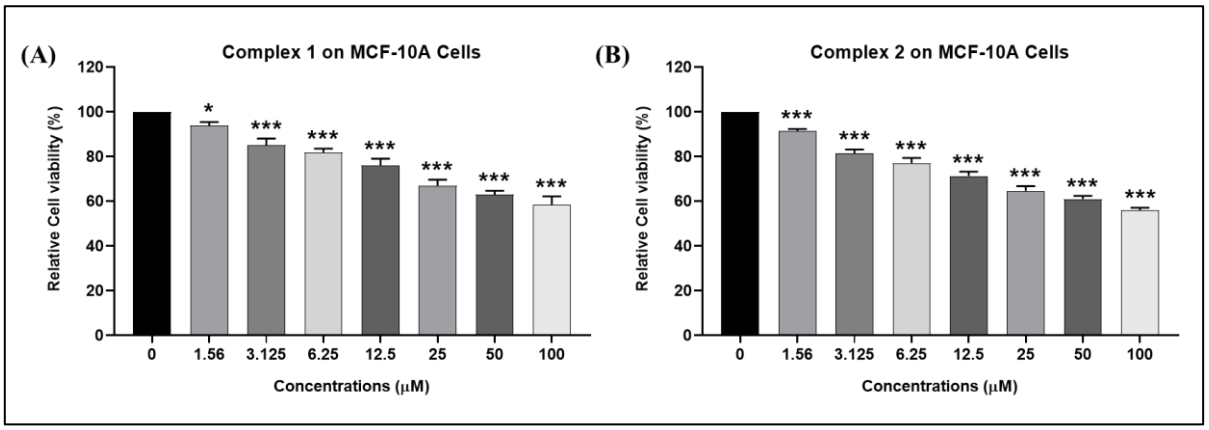

Fig. VI.29. Bar diagrams represent cell cytotoxicity study of Complex **1** (A) and Complex **2** (B) with different concentrations against human normal breast epithelial (MCF-10A) cells.

VI.3.9.2. Clonogenic Assay

The formation of colonies signifies independent survival of cancer cells.[91] Based on their clonogenic survival, the anti-proliferative potential of complexes**1** and **2** against MCF-7 cells, were evaluated. After 24 h of plating, MCF-7 cells were treated with two complex **1** concentrations (1/2 of IC_{50} Value: 5.06 μM and IC_{50} Value: 10.12 μM) and two complex **2** concentrations (1/2 of IC_{50} Value: 7.62 μM and IC_{50} Value: 15.24 μM) and again incubated for 24 h. All the images were captured using a digital camera, shown in Fig. VI.30. The colonies were counted in both control and treated wells using the Image J Software. From the calculated data, it was found that number of colonies were gradually decreased relative to

control group by increasing the concentrations of both the complexes which indicates that both compounds have significant anti-proliferative potential *in-vitro*.

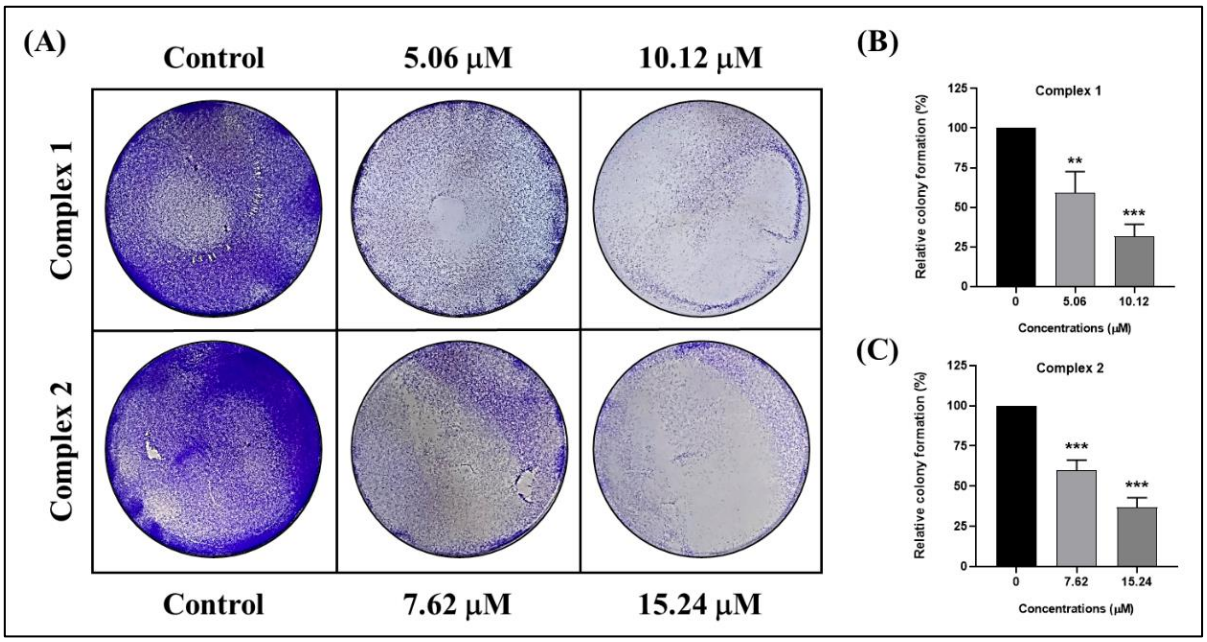

Fig. VI.30. Clonogenic assay. **(A)** Images represent the colony formation ability of human breast epithelial adenocarcinoma (MCF-7) cells against two Complex **1** concentrations (1/2 of IC_{50} Value: 5.06 µM and IC_{50} Value: 10.12 µM) and two Complex **2** concentrations (1/2 of IC_{50} Value: 7.62 µM and IC_{50} Value: 15.24 µM). **(B)-(C)** Bar diagrams represent the relative colony formation (%) of human breast epithelial adenocarcinoma (MCF-7) cells against Complex **1** and Complex **2**. All the experiments were performed independently thrice and the data were calculated as Mean ± SD where *P < 0.05, **P < 0.01, ***P < 0.001.

VI.3.9.3. Wound Healing Assay

The wound healing capabilities of cancer cells signifies the migration potential of cancer cells. Based on the percentage (%) wound closure in different time intervals, the anti-migratory potential of complexes **1** and **2** against MCF-7 cells, were evaluated.[92,93] After 24 h of plating, MCF-7 cells were treated with two complex **1** concentrations (1/2 of IC_{50} Value: 5.06 µM and IC_{50} Value: 10.12 µM) and two complex **2** concentrations (1/2 of IC_{50} Value: 7.62 µM and IC_{50} Value: 15.24 µM) and again incubated for 24 h. All the images were captured using a phase contrast microscope (Olympus) in three different time intervals: T0, T24 and T48, shown in Fig. VI.31. The percentage (%) wound closure in different time intervals were calculated using the Image J Software. From the calculated data, it was found that the percentage (%) wound healing were gradually decreased relative to control group by

increasing the concentrations of both the complexes which indicates that both compounds have significant anti-migratory potential *in-vitro*.

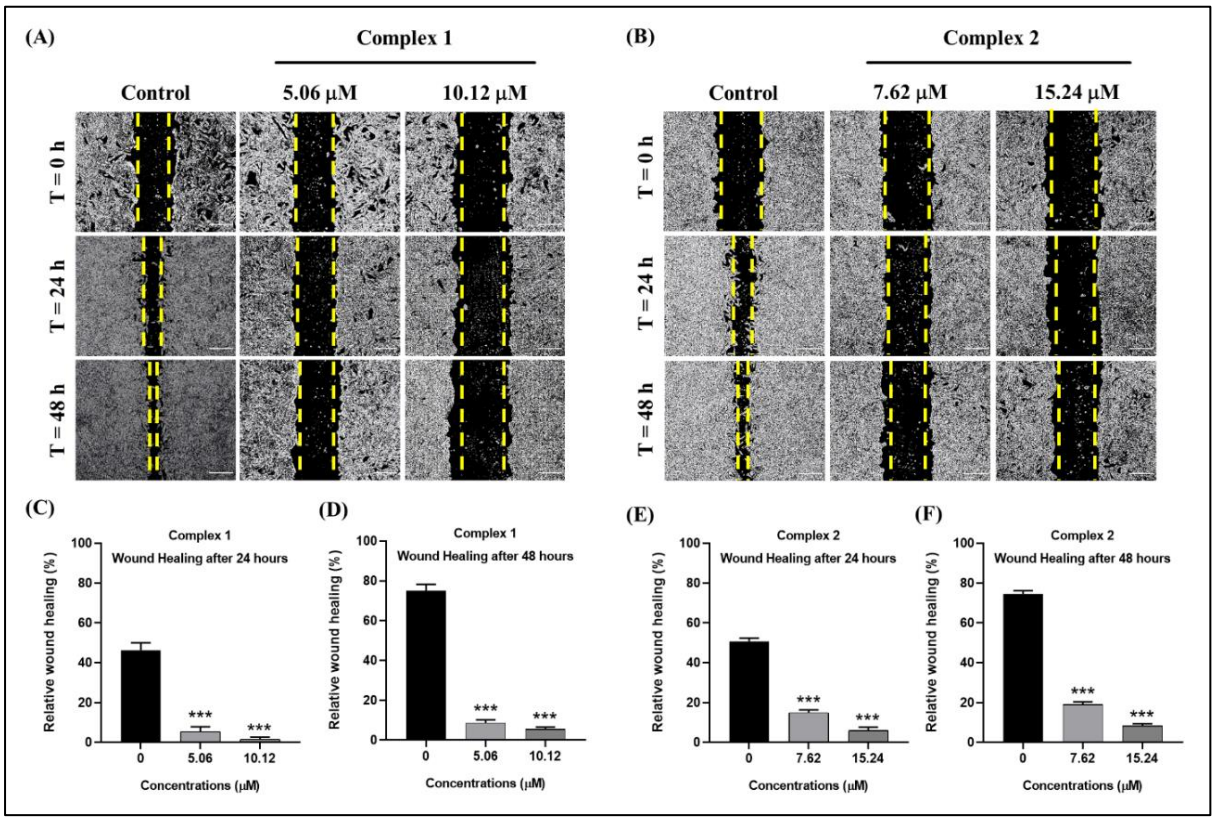

Fig. VI.31. Wound healing assay. **(A)-(B)** Images represent the cell migration ability of human breast epithelial adenocarcinoma (MCF-7) cells against two Complex **1** concentrations (1/2 of IC_{50} Value: 5.06 µM and IC_{50} Value: 10.12 µM) and two Complex **2** concentrations (1/2 of IC_{50} Value: 7.62 µM and IC_{50} Value: 15.24 µM) at three different time intervals: T0 (just after the treatment), T24 (after 24 h of incubation) and T48 (after 48 h of incubation). Magnification 4X. **(C)-(D)** Bar diagrams represent the relative wound healing (%) of human breast epithelial adenocarcinoma (MCF-7) cells against Complex **1** after 24 h and 48 h of incubation. **(E)-(F)** Bar diagrams represent the relative wound healing (%) of human breast epithelial adenocarcinoma (MCF-7) cells against Complex **2** after 24 h and 48 h of incubation. All the experiments were performed independently thrice and the data were calculated as Mean ± SD where *P < 0.05, **P < 0.01, ***P < 0.001.

VI.3.9.4. Nuclear Fragmentation Assay for Apoptosis Detection

To evaluate the changes in nuclear morphology which validates the apoptosis status of the cancer cells, nuclear fragmentation assay was done. Briefly, Hoechst 33258 stain can bind with DNA to check nuclear shrinkage, chromatin condensation and apoptotic body formation by blue fluorescence emission.[94] After 24 h of plating, MCF-7 cells were treated with two complex **1** concentrations (1/2 of IC_{50} Value: 5.06 µM and IC_{50} Value: 10.12 µM) and two

complex **2** concentrations (1/2 of IC_{50} Value: 7.62 µM and IC_{50} Value: 15.24 µM) and again incubated for 24 h. All the images were captured using the fluorescent microscope (Olympus), shown in Fig. VI.32. From the observed data, it was found that the number of nuclear fragmentations were significantly increased relative to the control group by increasing the concentrations of both the complexes which indicates that both compounds have significant apoptotic potential *in-vitro*.

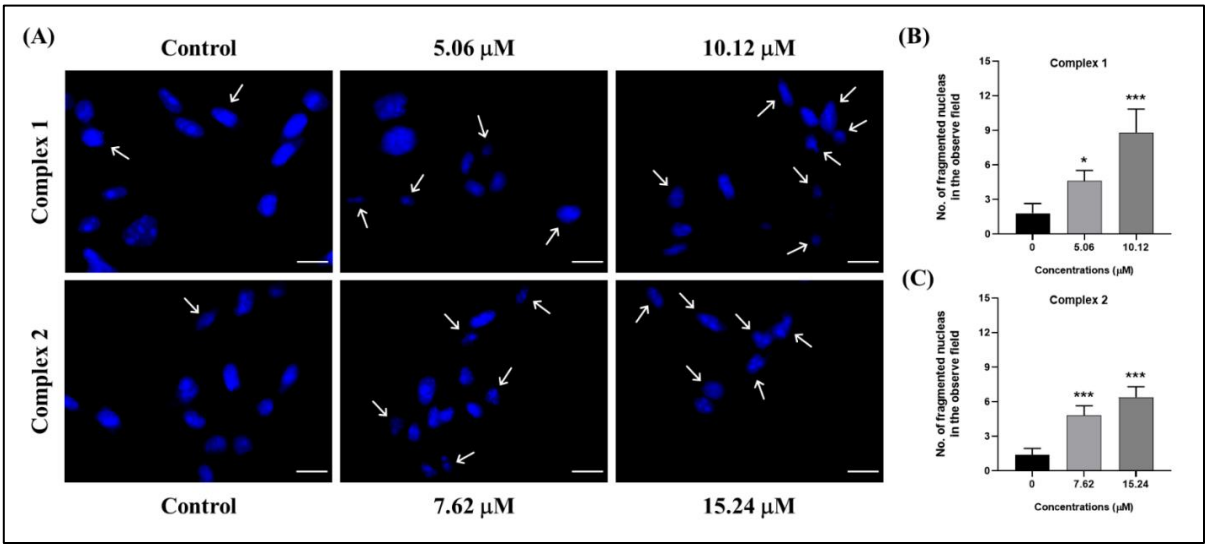

Fig. VI.32. Nuclear fragmentation assay. (A) Images represent the nuclear fragmentations of human breast epithelial adenocarcinoma (MCF-7) cells against two Complex **1** concentrations (1/2 of IC_{50} Value: 5.06 µM and IC_{50} Value: 10.12 µM) and two Complex **2** concentrations (1/2 of IC_{50} Value: 7.62 µM and IC_{50} Value: 15.24 µM). Magnification 100X. (B)-(C) Bar diagrams represent the number of fragmented nuclei in the observed field of human breast epithelial adenocarcinoma (MCF-7) cells against Complex **1** and Complex **2**. All the experiments were performed independently thrice and the data were calculated as Mean ± SD where *P < 0.05, **P < 0.01, ***P < 0.001.

VI.4. Conclusions

So herein two new Rhenium(I) tricarbonyl complexes of the general formula $[Re(CO)_3(L^1/L^2)]$ (**1/2**) were successfully fabricated and thoroughly characterized by analytical and spectral techniques (IR, UV/visible, ^{1}H NMR and ESI-MS). The XRD study showed that the geometries of these complexes are slightly distorted from regular octahedral geometry around the metal centre. The theoretical exploration on their structural optimization, HOMO-LUMO energy and calculated different reactivity descriptors by the DFT study presented an overview of their reactivity which have more or less similar activity. Also, TD-DFT generated electronic transitions were in good agreement with the experimentally resolved UV-vis spectra of the complexes. The molecular electrostatic

potential (MEP) surface of the complexes clearly depicted the reactive region available for interactions. The electrophilicity index of complex **1** displayed a little bit higher value suggesting a higher affinity toward DNA and BSA. The DNA binding ability of the complexes examined by absorption and fluorescence spectral techniques revealed an intercalative interaction between complexes and CT-DNA. Further, the binding abilities of the complexes with BSA also observed by absorption and fluorescence spectroscopy and revealed the presence of static quenching. Both the complexes display noteworthy cytotoxicity against the cancer cell lines with the IC_{50} values ranging from 10.12 to 15.24 μM and show potential selectivity to non-tumorigenic normal cells. More significantly, complex **1** exhibited powerful anticancer activity against MCF-7 cancer cell lines better than complex **2**. The main chemical and biological conclusion of this study have confirmed that the complexes can definitely demonstrate activity in human cancer cells in vitro in a logical range of concentrations thereby signifying that these complexes are very capable candidates as antitumor reagents. On the basis of the aforementioned results, our synthesized rhenium(I) complexes can be additionally explored using in vivo models.

VI.5. References

1. F. Bray, J. Ferlay, I. Soerjomataram, R. L. Siegel, L. A. Torre and A. Jemal, *CA Cancer J. Clin.*, 2018, **68**, 394-424.
2. R. L. Siegel, K. D. Miller, H. E. Fuchs and A. Jemal, *CA Cancer J. Clin*., 2021, **71**, 7-33.
3. X. Chen, Y. Wu, H. Dong, C. Y. Zhang and Y. Zhang, *Curr. Mol. Med.*, 2013, **13**, 1603-1612.
4. L. Galluzzi, L. Senovilla, I. Vitale, J. Michels, I. Martins, O. Kepp, M. Castedo and G. Kroemer, *Oncogene*, 2012, **31**, 1869-1883.
5. (a) A. Palmioli, A. Aliprandi, D. Septiadi, M. Mauro, A. Bernardi, L. De Cola and M. Panigati, *Org. Biomol. Chem.*, 2017, **15**, 1686-1699; (b) P. K. K. Leung, L. C. C. Lee, T. K. Y. Ip, H. W. Liu, S. M. Yiu, N. P. Lee and K. K. W. Lo, *Chem. Commun.*, 2021, **57**, 11256-11259; (c) W. Wang, Y. K. Yan, T. A. Hor, J. J. Vittal, J. R. Wheaton and I. H. Hall, *Polyhedron*, 2002, **21**, 1991-1999.
6. (a) T. Kanagasundaram, C. S. Kramer, E. Boros and K. Kopka, *Dalton Trans.*, 2020, **49**, 7294-7298; (b) J. Zhang, J. J. Vittal, W. Henderson, J. R. Wheaton, I. H. Hall, T. A. Hor and Y. K. Yan, *J. Organomet. Chem.*, 2002, **650,** 123-132.
7. J. Ho, W. Y. Lee, K. J. T. Koh, P. P. F. Lee and Y. K. Yan, *J. Inorg. Biochem.*, 2013, **119**, 10-20.

8. (a) S. C. Marker, A. P. King, S. Granja, B. Vaughn, J. J. Woods, E. Boros and J. J. Wilson, *Inorg. Chem.,* 2020, **59**, 10285-10303; (b) S. C. Marker, A. P. King, R. V. Swanda, B. Vaughn, E. Boros, S. B. Qian and J. J. Wilson, *Angew. Chem.,* 2020, **59**, 13391-13400.
9. (a) K. M. Knopf, B. L. Murphy, S. N. MacMillan, J. M. Baskin, M. P. Barr, E. Boros and J. J. Wilson, *J. Am. Chem. Soc.,* 2017, **139,** 14302-14314; (b) C. C. Konkankit, A. P. King, K. M. Knopf, T. L. Southard and J. J. Wilson, *ACS Med. Chem. Lett.,* 2019, **10,** 822-827.
10. (a) C. C. Konkankit, A. P. King, K. M. Knopf, T. L. Southard and J. J. Wilson, *ACS Med. Chem. Lett.,* 2019, **10**, 822-827; (b) G. Gasser, A. Pinto, S. Neumann, A. M. Sosniak, M. Seitz, K. Merz, R. Heumann and N. Metzler-Nolte, *Dalton Trans.,* 2012, **41**, 2304-2313; (c) A. Leonidova and G. Gasser, *ACS Chem. Biol.,* 2014, **9**, 2180-2193.
11. (a) A. Leonidova, V. Pierroz, R. Rubbiani, Y. Lan, A. G. Schmitz, A. Kaech, R. K. Sigel, S. Ferrari and G. Gasser, *Chem. Sci.,* 2014, **5**, 4044-4056; (b) R. R. Ye, B. C. Chen, J. J. Lu, X. R. Ma and R. T. Li, *J. Inorg.Biochem.,* 2021, **223**, 111537; (c) J. Delasoie, A. Pavic, N. Voutier, S. Vojnovic, A. Crochet, J. Nikodinovic-Runic and F. Zobi, *Eur. J. Med. Chem.,* 2020, **204**, 112583.
12. R. Foresti, M. G. Bani-Hani and R. Motterlini, *Intensive Care Med.,* 2008, **34**, 649-658.
13. E. Kianfar, C. Schäfer, M. R. Lornejad-Schäfer, E. Portenkirchner and G. Knör, *Inorg. Chim. Acta*., 2015, **435**, 174-177.
14. C. V. Garcia, G. L. Parrilha, B. L. Rodrigues, S. F. Teixeira, R. A. de Azevedo, A. K. Ferreira and H. Beraldo, *New J. Chem.,* 2016, **40**, 7379-7387.
15. I. Romero-Canelon and P. J. Sadler, *Inorg. Chem.,* 2013, **52,** 12276-12291.
16. (a) W. H. Mahmoud, F. N. Sayed and G. G. Mohamed, *Appl. Organomet. Chem.,* 2016, **30**, 959-973; (b) W. H. Mahmoud, F. N. Sayed and G. G. Mohamed, *Appl. Organomet. Chem.,* 2018, **32**, 4347.
17. R. G. Deghadi, W. H. Mahmoud and G. G. Mohamed, *Appl. Organomet. Chem.,* 2020, **34**, 5883.
18. M. A. I. Al-Gaber, H. M. Abd El-Lateef, M. M. Khalaf, S. Shaaban, M. Shawky, G. G. Mohamed, A. Abdou, M. Gouda and A. M. Abu-Dief, *Mater*., 2023, **16**, 897.
19. (a) J. Madureira, C. I. Ramos, M. Marques, C. Maia, B. de Sousa, L. Campino, M. G. Santana-Marques and N. Farrell, *Inorg. Chem.,* 2013**, 52**, 8881-8894; (b) M. Stiborova and E. Frei, *Curr. Med. Chem.,* 2014, **21**, 575-591; (c) J. Poljaková, T. Eckschlager, J. Hraběta, J. Hřebačková, S. Smutný, E. Frei, V. Martínek, R. Kizek and M. Stiborová, *Biochem. Pharmacol.,* 2009, **77**, 1466-1479.
20. (a) L. Andrezálová and Z. Országhová, *J. Inorg. Biochem.,* 2021, **225**, 111624; (b) B. J. Pages, D. L. Ang, E. P. Wright and J. R. Aldrich-Wright, *Dalton Trans.,* 2015, **44**, 3505 -3526.
21. (a) A. Kellett, Z. Molphy, C. Slator, V. McKee and N. P. Farrell, *Chem. Soc. Rev*., 2019, **48**, 971-988; (b) C. Selvaraj and S. K. Singh, *Curr. Pharm. Des.,* 2018, **24**, 3739-3757.

22. (a) P. Jaividhya, R. Dhivya, M. A. Akbarsha and M. Palaniandavar, *J. Inorg. Biochem.*, 2012, **114**, 94-105; (b) V. Rajendiran, R. Karthik, M. Palaniandavar, H. Stoeckli-Evans, V. S. Periasamy, M. A. Akbarsha, B. S. Srinag and H. Krishnamurthy, *Inorg. Chem.*, 2007, **46**, 8208-8221.
23. (a) V. P. Torchilin and A. N. Lukyanov, *Drug Discov. Today*, 2003, **8**, 259-266; (b) E. Ruoslahti, *Adv. Drug Deliv. Rev.*, 2017, **110**, 3-12.
24. (a) S. Dissanayake, W. A. Denny, S. Gamage and V. Sarojini, *J. Control Release*, 2017, **250**, 62-76; (b) X. Liu, F. Wu, Y. Ji and L. Yin, *Bioconjug. Chem.*, 2018, **30**, 305-324.
25. Y. Rahman, S. Afrin and M. Tabish, *Arch. Biochem. Biophys.*, 2018, **652**, 27-37.
26. (a) M. Akram, F. Ansari and I. A. Bhat, *J. Mol. Liq.*, 2019, **276**, 519-528; (b) A. Precupas, R. Sandu, A. R. Leonties, D. F. Anghel and V. T. Popa, *New J Chem*., 2017, **41**, 15003-15015.
27. Q. Jiao, W. Zhang, Y. Jiang, L. Jiang, X. Chen and B. Liu, *Front. Chem.*, 2019, **7**, 840.
28. (a) P. Roy, R. Naskar, C. K. Manna and T. K. Mondal, *J. Mol. Struct.*, 2019, **1198**, 126932; (b) S. Acharya, A. Kejriwal, A. N. Biswas, P. Das, D. N. Neogi and P. Bandyopadhyay, *Polyhedron*, 2012, **38**, 50-57.
29. M. K. Paira, T. K. Mondal, E. López-Torres, J. Ribas and C. Sinha, *Polyhedron*, 2010, **29**, 3147-3156.
30. (a) G. M. Sheldrick, A*cta Crystallogr. C Struct. Chem*., 2015, **71**, 3-8.; (b) G. M. Sheldrick, *Acta Crystallogr*. *A: Found. Adv*. 2015, **71**, 3-8.
31. (a) A. D. Becke, *J. Chem. Phys*., 1992, **96**, 2155-2160; (b) L. Pandey, C. Doiron, J. S. Sears and J. L. Brédas, *Phys. Chem. Chem. Phys.*, 2012, **14**, 14243-14248.
32. (a) P. J. Hay and W. R. Wadt, *J. Chem. Phys*., 1985, **82**, 270-283; (b) P. J. Hay and W. R. Wadt, *J. Chem. Phys*., 1985, **82**, 299-310.
33. (a) W. J. Hehre, R. Ditchfield and J. A. Pople, *J. Chem. Phys*., 1972, **56**, 2257-2261.
34. M. J. Frisch, G. W. Trucks, H. B. Schlegel, G. E. Scuseria, M. A. Robb, J. R. Cheeseman, G. Scalmani, V. Barone, B. Mennucci, G. A. Petersson and H. Nakatsuji, *Gaussian Inc Wallingford.*, 2009.
35. (a) R. Peverati and D. G. Truhlar, *Phys. Chem. Chem. Phys.*, 2012, **14**, 11363-11370; (b) M. E. Casida, C. Jamorski, K. C. Casida and D. R. Salahub, *J. Chem. Phys*., 1998, **108**, 4439-4449.
36. (a) V. Barone and M. Cossi, *J. Phys. Chem*. A., 1998, **102**, 1995-2001; (b) M. Cossi and V. Barone, *J. Chem. Phys*., 2001, **115**, 4708-4717; (c) M. Cossi, N. Rega, G. Scalmani and V. Barone, *J. Comput. Chem*., 2003, **24**, 669-681
37. N. M. O'boyle, A. L. Tenderholt and K. M. Langner, *J. Comput. Chem.*, 2008, **29**, 839-845.
38. (a) M. A. Spackman and D. Jayatilaka, *Cryst. Eng. Comm*., **11**, 19-32; (b) H. F. Clausen, M. S. Chevallier, M. A. Spackman and B. B. Iversen, *New J. Chem*., 2009, **34**, 193-199.
39. (a) A. L. Rohl, M. Moret, W. Kaminsky, K. Claborn, J. J. McKinnon and B. Kahr, *Cryst. Growth Des*. 2008, **8**, 4517-4525; (b) A. Parkin, G. Barr, W. Dong, C. J. Gilmore, D.

Jayatilaka, J. J. McKinnon, M. A. Spackman and C. C. Wilson, *Cryst. Eng. Comm*., 2007, **9**, 648-652.

40. (a) C. F. Mackenzie, P. R. Spackman, D. Jayatilaka and M. A. Spackman, *IUCrJ*., 2017, **4**, 575-587; (b) P. R. Spackman, M. J. Turner, J. J. McKinnon, S. K. Wolff, D. J. Grimwood, D. Jayatilaka and M. A. Spackman, *J. Appl. Crystallogr*., 2021, **54**, 1006-1011.
41. M. E. Reichmann, S. A. Rice, C. A. Thomas and P. Doty, *J Am Chem Soc*., 1954, **76**, 3047-3053.
42. S. Dasari and A. K. Patra, *Dalton Trans.*, 2015, **44**, 19844-19855.
43. (a) M. Kumar, G. Kumar, N. K. Mogha, R. Jain, F. Hussain and D. T. Masram, *Spectrochim. Acta A Mol. Biomol. Spectrosc*., 2019, **212**, 94-104; (b) M. Kumar, N. K. Mogha, G. Kumar, F. Hussain and D. T. Masram, *Inorg. Chim. Acta*., 2019, **490**, 144-154.
44. (a) F. Kratz, *J. of controlled release*., 2008, **132**, 171-183; (b) B. Demoro, R. F. De Almeida, F. Marques, C. P. Matos, L. Otero, J. C. Pessoa, I. Santos, A. Rodríguez, V. Moreno, J. Lorenzo and D. Gambino, *Dalton Trans*., 2013, **42**, 7131-7146; (c) V. D. Suryawanshi, L. S. Walekar, A. H. Gore, P. V. Anbhule and G. B. Kolekar, *J. Pharm. Anal*., 2016, **6**, 56-63.
45. (a) M. Kumar, G. Kumar, K. M. Dadure and D. T. Masram, *New J. Chem*., 2019, **43**, 15462-15481; (b) Y. Rahman, S. Afrin, M. A. Isa, S. Ahmed and M. Tabish, *J. Biomol. Struct. Dyn*., 2019.
46. H. Gao, L. Lei, J. Liu, Q. Kong, X. Chen and Z. Hu, *J. Photochem. Photobiol. A: Chem*., 2004, **167**, 213-221.
47. A. Banerjee, M. Mohanty, S. Lima, R. Samanta, E. Garribba, T. Sasamori and R. Dinda, *New J.Chem*., 2020, **44**, 10946-10963.
48. S. U. Parsekar, P. Velankanni, S. Sridhar, P. Haldar, N. A. Mate, A. Banerjee, P. S. Antharjanam, A. P. Koley and M. Kumar, *Dalton Trans*., 2020, **49**, 2947-2965.
49. P. Mukherjee, S. Guha, G. Das, A. Samui and S. K. Sahu, *J. Photochem. Photobiol. A: Chem.*, 2023, 114907.
50. M. G. F. Guefack, D. Talukdar, R. Mukherjee, S. Guha, D. Mitra, D. Saha, G. Das, F. Damen, V. Kuete and N. Murmu, *J. Ethnopharmacol*., 2024, **319**, 117093.
51. M. Siva, K. Das, S. Guha, S. Sivagnanam, G. Das, A. Saha, A. Stewart, B. Maity and P. Das, *ACS Appl. Bio Mater*., 2023.
52. (a) T. L. Brown and D. J. Darensbourg, *Inorg. Chem.*, 1967, **6**, 971-977; (b) P. S. Braterman, R. Bau and H. D. Kaesz, *Inorg. Chem.*, 1967, **6**, 2097-2102.
53. (a) M. K. Paira, T. K. Mondal, D. Ojha, A. M. Slawin, E. R. Tiekink, A. Samanta and C. Sinha, *Inorganica Chim. Acta.*, 2011, **370**, 175-186; (b) S. Biswas, D. Sarkar, P. Roy and T. K. Mondal, *Polyhedron*, 2017, **131**, 1-7.
54. S. Acharya, A. Kejriwal, A. N. Biswas, P. Das, D. N. Neogi and P. Bandyopadhyay, *Inorganica Chim. Acta*., 2013, **394**, 757-764.

55. (a) P. Roy, D. Sarkar, P. Ghosh, R. Naskar, N. Murmu and T. K. Mondal, *Polyhedron*, 2019, **161**, 154-160; (b) M. S. Jana, A. K. Pramanik, S. Kundu and T. K. Mondal, *Polyhedron*, 2012, **40**, 46-52; (c) A. K. Pramanik, M. S. Jana, S. Kundu and T. K. Mondal, *J. Mol. Struct.*, 2012, **1017,** 19-25.
56. (a) I. B. Obot, D. D. Macdonald and Z. M. Gasem, *Corros. Sci.*, 2015, **99**, 1-30: (b) D. K. Verma, R. Aslam, J. Aslam, M. A. Quraishi, E. E. Ebenso and C. Verma, *J. Mol. Struct.*, 2021, **1236**, 130294.
57. A. Thamarai, R. Vadamalar, M. Raja, S. Muthu, B. Narayana, P. Ramesh, R. Raj Muhamed, S. Sevvanthi and S. Aayisha, *Spectrochim. Acta A Mol. Biomol. Spectrosc.*, 2020**, 226**, 117609.
58. (a) V. Choudhary, A. Bhatt, D. Dash and N. Sharma, *J. Comput. Chem.*, 2019, **40**, 2354-2363; (b) M. Miar, A. Shiroudi, K. Pourshamsian, A. R. Oliaey and F. Hatamjafari, *J. Chem. Res.*, 2021, **45**, 147-158.
59. A. G. Martynov, J. Mack, A. K. May, T. Nyokong, Y, G. Gorbunova and A. Y. Tsivadze, *ACS omega*, 2019, **4**, 7265-7284.
60. M. S. A. Abdel-Mottaleb and S. N. Ali, *Int. J. Photoenergy*, 2016.
61. (a) M. K. Chaudhary, A. Srivastava, K. K. Singh, P. Tandon and B. D. Joshi, *Comput. Theor. Chem.*, 2020, **1191**, 113031; (b) M. Feizi-Dehnayebi, E. Dehghanian and H. Mansouri-Torshizi, *J. Mol. Struct.*, 2021, **1240,** 130535.
62. (a) P. R. Spackman, M. J. Turner, J. J. McKinnon, S. K. Wolff, D. J. Grimwood, D. Jayatilaka and M. A. Spackman, *J. Appl. Crystallogr.*, 2021, **54**, 1006-1011; (b) S. L. Tan, M. M. Jotani and E. R. Tiekink, *Acta Crystallogr. E: Crystallogr.*, 2019, **75**, 308-318.
63. (a) A. Fatima, G. Khanum, A. Sharma, K. Garima, S. Savita, I. Verma, N. Siddiqui and S. Javed, *J. Mol. Struct.*, 2022, **1249**, 131571; (b) A. Fatima, M. Singh, N. Agarwal, I. Verma, R. J. Butcher, N. Siddiqui and S. Javed, *J. Mol. Liq.*, 2021, **343**, 117549.
64. (a) M. Bashir, A. A. Dar and I. Yousuf, *ACS omega*., 2023, **8**, 3026-3042; (b) S. Mandal, R. Naskar, A. S. Mondal, B. Bera and T. K. Mondal, *Dalton Trans.*, 2023, **52,** 5983-5998.
65. (a) L. C. C. Lee, K. K. Leung and K. K. W. Lo, *Dalton Trans.*, 2017, **46**, 16357-16380; (b) Q. Qi, Q. Wang, Y. Li, D. Z. Silva, M. E. L. Ruiz, R. Ouyang, B. Liu and Y. Miao, *mol.*, 2023. **28**, 2733.
66. (a) U. Das, S. Shanavas, A. H. Nagendra, B. Kar, N. Roy, S. Vardhan, S. K. Sahoo, D. Panda, B. Bose and P. Paira, *Appl. Bio Mater.*, 2023, **6**, 410-424; (b) C. C. Konkankit, S. C. Marker, K. M. Knopf and J. J. Wilson, *Dalton Trans.*, 2018, **47**, 9934-9974.
67. A. Wolfe, G. H. Shimer Jr and T. Meehan, *Biochem.*, 1987, **26**, 6392-6396.
68. (a) F. L. Thorp-Greenwood, M. P. Coogan, L. Mishra, N. Kumari, G. Rai and S. Saripella, *New J. Chem.*, 2012, **36**, 64-72; (b) A. Das, M. Saha, S. Mandal, S. Das, K. D. Saha and T. K. Mondal, *New J. Chem.*, 2023, **47**, 4931-4943.
69. (a) J. R. Lakowicz, ed., *Principles of fluorescence spectroscopy*, 2006; (b) D. J. Desilets, P. T. Kissinger and F. E. Lytle, *Anal. Chem.*, 1987, **59**, 1244-1246.

70. (a) L. Haque, S. Bhuiya, R. Tiwari, A. B. Pradhan and S. Das, *RSC Adv.*, 2016, **6**, 83551-83562; (b) Y. Wang, G. Lin, J. Hong, T. Lu, L. Li, N. Okabe and M. Odoko, *Inorganica Chim. Acta*, 2009, **362**, 377-384; (c) M. Kumar, G. Kumar, N. K. Mogha, R. Jain, F. Hussain and D. T. Masram, *Spectrochim. Acta A Mol. Biomol. Spectrosc.*, 2019, **212**, 94-104; (d) M. Kumar, N. K. Mogha, G. Kumar, F. Hussain and D. T. Masram, *Inorganica Chim. Acta*, 2019. **490**, 144-154.
71. (a) A. B. Pradhan, L. Haque, S. Bhuiya and S. Das, *RSC Adv.*, 2015, **5**, 10219-10230; (b) A. B. Pradhan, L. Haque, S. Bhuiya, A. Ganguly and S. Das, *J. Phys. Chem. B*, 2015, **119,** 6916-6929.
72. (a) S. De, S. R. Chaudhuri, A. Panda, G. R. Jadhav, R. S. Kumar, P. Manohar, N. Ramesh, A. Mondal, A. Moorthy, S. Banerjee and P. Paira, *New J. Chem.*, 2019, **43**, 3291-3302; (b) K. Nagaraj and S. Arunachalam, *Int. J. Biol. Macromol.*, 2013, **62,** 273-280.
73. (a) G. Lambrinidis, T. Vallianatou and A. Tsantili-Kakoulidou, *Adv. Drug Deliv. Rev.*, 2015, **86**, 27-45; (b) Y. Yuan, S. Chang, Z. Zhang, Z. Li, S. Li, P. Xie, W. P. Yau, H. Lin, W. Cai, Y. Zhang and X. Xiang, *Chemom. Intell. Lab. Syst.*, 2020, **199,** 103962; (c) N. A. Kratochwil, W. Huber, F. Müller, M. Kansy and P. R. Gerber, *Biochem. Pharmacol.*, 2002, **64**, 1355-1374.
74. (a) P. R. Callis, *J. Mol. Struct.*, 2014, **1077**, 14-21; (b) A. Sharma, J. Enderlein and M. Kumbhakar, *J. Phys. Chem., Lett.*, 2017, **8**, 5821-5826.
75. (a) B. K. Kundu, S. N. Upadhyay, N. Sinha, R. Ganguly, I. Grabchev, S. Pakhira and S. Mukhopadhyay, *Dalton Trans*., 2022, **51**, 3937-3953; (b) S. Pandit and S. Kundu, *Colloids Surf. A: Physicochem. Eng. Asp.*, 2021, **628**, 127253.
76. (a) J. Bhuvaneswari, A. K. Fathima and S. Rajagopal, *J. Photochem. Photobiol. A: Chem.*, 2012, **227**, 38-44; (b) G. Balakrishnan, T. Rajendran, K. S. Murugan, M. Ganesan, V. K. Sivasubramanian and S. Rajagopal, *J. Lumin.*, 2019, ***205***, 51-60; (c) K. P. Frin and V. M. Nascimento, *J. Braz. Chem. Soc.*, 2016, **27,** 179-185; (c) A. Das, S. Mandal, R. Mukherjee, R. Naskar, N. Murmu and T. K. Mondal, *New J. Chem.*, 2023, **47**, 17359-17372.
77. (a) K. Karami, S. Hashemi, J. Lipkowski, F. Mardani, A. A. Momtazi-borojeni and Z. M. Lighvan, *Appl. Organomet. Chem.*, 2017, **31**, 3740; (b) D. G. Isom, C. A. Castañeda, B. R. Cannon, P. D. Velu and E. B. García-Moreno, *Proc. Natl. Acad. Sci.*, 2010, **107**, 16096-16100.
78. (a) Y. Xiang and F. Wu *Spectrochim. Acta A Mol. Biomol. Spectrosc*., 2010, **77,** 430-436: (b) P. Acharya, R. Maity, A. Kuila, T. Maity, S. Maity, N. Sepay and B. C. Samanta, *Appl. Organomet. Chem*., 2022, **36**, 6640.
79. D. S. Raja, N. S. Bhuvanesh and K. Natarajan, *Dalton Trans.*, 2012, **41**, 4365-4377.
80. J. N. Miller, *J. Pharm. Biomed. Anal.*, 1983, **1,** 525-535.
81. M. Makarska-Bialokoz and A. Lipke, *J. Mol. Liq.*, 2019, **276**, 595-604.
82. (a) S. Mukhopadhyay, R. K. Gupta, R. P. Paitandi, N. K. Rana, G. Sharma, B. Koch, L. K. Rana, M. S. Hundal and D. S. Pandey, *Organomet.*, 2015, **34**, 4491-4506; (b) F. F. Tian, F. L.

Jiang, X. L. Han, C. Xiang, Y. S. Ge, J. H. Li, Y. Zhang, R. Li, X. L. Ding and Y. Liu, *Phys. Chem. B.*, 2010, **114**, 14842-14853.

83. J. R. Lakowicz, *Principles of Fluorescence Spectroscopy, 3rd edition*, 2006.
84. A. Banerjee, M. Mohanty, S. Lima, R. Samanta, E. Garribba, T. Sasamori and R. Dinda, *New J. Chem.*, 2020, **44**, 10946-10963.
85. (a) G. Sahu, A. Banerjee, R. Samanta, M. Mohanty, S. Lima, E. R. Tiekink and R. Dinda, *Inorg. Chem.*, 2021, **60**, 15291-15309; (b) T. A. Wani, A. H. Bakheit, S. Zargar, M. A. Hamidaddin and I. A. Darwish, *PLoS One*., 2017, **12,** 0176015; (c) F. Jalilehvand, A. E. Garcia, P. Niksirat, Y. Z. Finfrock and B. S. Gelfand, *J. Inorg. Biochem.*, 2021, **224**, 111556.
86. (a) M. Kumar, G. Kumar and D. T. Masram, *New J. Chem.*, 2020, **44**, 8595-8613; (b) Z. Chen, S. Zhang, Z. Zhu and Y. Zhang, *New J. Chem.*, 2017, **41**, 6340-6348.
87. (a) Z. Tian, L. Tian, M. Shi, S. Zhao, S. Guo, W. Luo, C. Wang and Z. Tian, *J. Photochem. Photobiol. B Biol.*, 2020, **209**, 111917; (b) A. Precupas, A. R. Leonties, A. Neacsu, R. Sandu and V. T. Popa, *New J. Chem.*, 2019, **43**, 3891-3898.
88. X. Long, Y. F. Zeng, Y. Liu, Y. Liu, T. Li, L. Liao and Y. Guo, *RSC Adv.*, 2018, **8**, 31201-31212.
89. D. C. Francisco, P. Peddi, J. M. Hair, B. A. Flood, A. M. Cecil, P. T. Kalogerinis, G. Sigounas and A. G. Georgakilas, *Free Radic. Biol. Med.*, 2008, **44**, 558-569.
90. (a) R. Yang, H. Hanwell, J. Zhang, R. Tsao and K. A. Meckling, *J. Agric. Food Chem.*, 2011, **59**, 13328-13336; (b) T. C. Hsieh, E. K. Wijeratne, J. Y. Liang, A. L. Gunatilaka and J. M. Wu, *Biochem. Biophys. Res. Commun.*, 2005, **337**, 224-231.
91. (a) H. Rafehi, C. Orlowski, G. T. Georgiadis, K. Ververis, A. El-Osta and T. C. Karagiannis, *Radiat. Oncol.*, 2012, **7**, 1-6.
92. E. Bertran, E. Crosas-Molist, P. Sancho, L. Caja, J. Lopez-Luque, E. Navarro, G. Egea, R. Lastra, T. Serrano, E. Ramos and I. Fabregat, *J. Hepatol.*, 2013, **58**, 2032-2044.
93. (a) N. K. Saxena, D. Sharma, X. Ding, S. Lin, F. Marra, D. Merlin and F. A. Anania, *Cancer Res.*, 2007, **67**, 2497-2507; (b) M. J. Hsieh, C. W. Lin, S. F. Yang, M. K. Chen and H. L. Chiou, *Br. J. Pharmacol.*, 2014, **171**, 3037-3050.
94. (a) N. Atale, S. Gupta, U. C. S. Yadav and V. Rani, *J. Microsc.*, 2014, **255**, 7-19; (b) P. Majtnerova, J. Capek, F. Petira, J. Handl and T. Rousar, *Sci. Rep.*, 2021, **11**, 11921.

Jiang, X. L. Han, C. Xiang, Y. S. Ge, J. H. Li, Y. Zhang, R. Li, X. L. Ding and Y. Liu, *Phys. Chem. B.*, 2010, **114**, 14842-14853.

83. J. R. Lakowicz, *Principles of Fluorescence Spectroscopy, 3rd edition*, 2006.
84. A. Banerjee, M. Mohanty, S. Lima, R. Samanta, E. Garribba, T. Sasamori and R. Dinda, *New J. Chem.*, 2020, **44**, 10946-10963.
85. (a) G. Sahu, A. Banerjee, R. Samanta, M. Mohanty, S. Lima, E. R. Tiekink and R. Dinda, *Inorg. Chem.*, 2021, **60**, 15291-15309; (b) T. A. Wani, A. H. Bakheit, S. Zargar, M. A. Hamidaddin and I. A. Darwish, *PLoS One*., 2017, **12,** 0176015; (c) F. Jalilehvand, A. E. Garcia, P. Niksirat, Y. Z. Finfrock and B. S. Gelfand, *J. Inorg. Biochem.*, 2021, **224**, 111556.
86. (a) M. Kumar, G. Kumar and D. T. Masram, *New J. Chem.*, 2020, **44**, 8595-8613; (b) Z. Chen, S. Zhang, Z. Zhu and Y. Zhang, *New J. Chem.*, 2017, **41**, 6340-6348.
87. (a) Z. Tian, L. Tian, M. Shi, S. Zhao, S. Guo, W. Luo, C. Wang and Z. Tian, *J. Photochem. Photobiol. B Biol.*, 2020, **209**, 111917; (b) A. Precupas, A. R. Leonties, A. Neacsu, R. Sandu and V. T. Popa, *New J. Chem.*, 2019, **43**, 3891-3898.
88. X. Long, Y. F. Zeng, Y. Liu, Y. Liu, T. Li, L. Liao and Y. Guo, *RSC Adv.*, 2018, **8**, 31201-31212.
89. D. C. Francisco, P. Peddi, J. M. Hair, B. A. Flood, A. M. Cecil, P. T. Kalogerinis, G. Sigounas and A. G. Georgakilas, *Free Radic. Biol. Med.*, 2008, **44**, 558-569.
90. (a) R. Yang, H. Hanwell, J. Zhang, R. Tsao and K. A. Meckling, *J. Agric. Food Chem.*, 2011, **59**, 13328-13336; (b) T. C. Hsieh, E. K. Wijeratne, J. Y. Liang, A. L. Gunatilaka and J. M. Wu, *Biochem. Biophys. Res. Commun.*, 2005, **337**, 224-231.
91. (a) H. Rafehi, C. Orlowski, G. T. Georgiadis, K. Ververis, A. El-Osta and T. C. Karagiannis, *Radiat. Oncol.*, 2012, **7**, 1-6.
92. E. Bertran, E. Crosas-Molist, P. Sancho, L. Caja, J. Lopez-Luque, E. Navarro, G. Egea, R. Lastra, T. Serrano, E. Ramos and I. Fabregat, *J. Hepatol.*, 2013, **58**, 2032-2044.
93. (a) N. K. Saxena, D. Sharma, X. Ding, S. Lin, F. Marra, D. Merlin and F. A. Anania, *Cancer Res.*, 2007, **67**, 2497-2507; (b) M. J. Hsieh, C. W. Lin, S. F. Yang, M. K. Chen and H. L. Chiou, *Br. J. Pharmacol.*, 2014, **171**, 3037-3050.
94. (a) N. Atale, S. Gupta, U. C. S. Yadav and V. Rani, *J. Microsc.*, 2014, **255**, 7-19; (b) P. Majtnerova, J. Capek, F. Petira, J. Handl and T. Rousar, *Sci. Rep.*, 2021, **11**, 11921.

LIST OF PUBLICATIONS

1. Synthesis of Ru(II) cyclometallated complexes via C(aryl)-S bond activation: X-ray structure, DNA/BSA protein binding and antiproliferative activity.
   A. Das, S. Mandal, R. Mukherjee, R. Naskar, N. Murmu and T. K. Mondal*, *New Journal of Chemistry*, 2023, 47, 17359-17372.
2. New palladium(II) and platinum(II) complexes with an ONS donor azo-thioether pincer ligand: synthesis, characterization, protein binding study and in vitro cytotoxicity.
   A. Das, M. Saha**,** S. Mandal, S. Das, K. Das Saha and T. K. Mondal*, *New Journal of Chemistry*, 2023, 47, 4931-4943.
3. Adaptable Biomolecule-Interactive Dual Colorimetric Chemosensor for Cu^{2+} and Pd^{2+}: Insight from Crystal Structure, Photophysical Investigations, Real-Time Sampling, and Molecular Logic Circuits.
   S. Mandal, **A. Das,** A. Biswas, A. Halder, D. Mondal and T. K. Mondal*, *Crystal Growth & Design*, 2024, 24, 1051-1067.
4. A novel carbazole-benzothiazole-based chemodosimeter for the chromogenic and fluorogenic recognition of CN^{-}.
   A. Maji, A. Biswas, **A. Das**, S. Gharami, K. Aicha and T. K. Mondal*, *New Journal of Chemistry*, 2023, 47, 11557-11564.
5. A biphenyl thiosemicarbazide based fluorogenic chemosensor for selective recognition of Cd^{2+}: application in cell bioimaging.
   A. Biswas, D. Mitra, R. Naskar, A. Maji, **A. Das**, N. Murmu and T. K. Mondal*, *Analytical Methods*, 2023, 15, 2745-2754.
6. Synthesis of a new benzoate bridged NNO tethered copper(II) complex: Exploration of its bio, catalytic and anticancer activities.
   S. Mandal, R. Naskar, R. Mukherjee, A. Sau Mondal, **A. Das** and Nabendu Murmu, T. K. Mondal*, *New Journal of Chemistry*, 2023, 47, 15267-15282.
7. A new “turn-on” molecular switch for idiosyncratic detection of Al3+ ion along with its application in live cell imaging.
   A. Biswas, R. Naskar, D. Mitra, **A. Das**, S. Gharami, N. Murmu and T. K. Mondal*, *New Journal of Chemistry*, 2022, 46, 21968-21975.

8. A new palladium(II) phosphino complex with ONS donor Schiff base ligand: Synthesis, characterization and catalytic activity towards Suzuki-Miyaura cross-coupling reaction.

C. K. Manna, R. Naskar, B. Bera, **A. Das**, T. K. Mondal*, *Journal of Molecular Structure*, 2021, 1237, 130322.

9. Synthesis of thiolato bridged dimeric rhodium(III) triphenylphosphine complex via C-S bond cleavage: X-ray structure, DFT computation and catalytic evaluation towards transfer hydrogenation of ketones.

S. Biswas, C. K. Manna, R. Naskar, **A. Das**, and T. K. Mondal*, *Inorganica Chimica Acta*, 2021, 515, 120096.

NJC

ROYAL SOCIETY OF CHEMISTRY

PAPER

View Article Online
View Journal | View Issue

Cite this: *New J. Chem.*, 2023, **47**, 4931

New palladium(II) and platinum(II) complexes with an ONS donor azo-thioether pincer ligand: synthesis, characterization, protein binding study and *in vitro* cytotoxicity†

Akash Das,[a] Moumita Saha,[b] Subrata Mandal,[a] Sanjib Das,[b] Krishna Das Saha *[b] and Tapan K. Mondal *[a]

Received 21st January 2023,
Accepted 5th February 2023

DOI: 10.1039/d3nj00334e

rsc.li/njc

New Pd(II) and Pt(II) complexes, [Pd(L)Cl] (**1**) and [Pt(L)Cl] (**2**), with an O,N,S donor azo-thioether pincer ligand (HL) are synthesized and thoroughly characterized by spectroscopic techniques. X-Ray structures of the complexes revealed the distorted square planar geometry around the central metal ions. Electronic structures and spectral properties are interpreted by DFT and TDDFT calculations. Interaction of the complexes with CT-DNA and BSA proteins is studied by absorption and fluorescence methods. Fluorescence titration revealed that the complexes strongly quench DNA bound ethidium bromide (EB) as well as the intrinsic fluorescence of BSA protein through static quenching. The high binding constants (K_b) obtained from the DNA binding studies promoted *in vitro* cytotoxicity assays of the complexes in various human cancer cell lines (colon cancer cell line HCT116, lung cancer cell line A549 and liver cancer cell line HepG2). The half maximal inhibitory concentrations (IC_{50}) of complexes **1** and **2** are found to be less compared to cisplatin.

1. Introduction

Cancer is undoubtedly one of the foremost health concerns in our society and serves as a principal target in the field of medicinal chemistry.[1] While searching for antitumor drugs among metal complexes, the invention of cisplatin occurred during the period from 1960 to 1970. Cisplatin is one of the most potent chemotherapy drugs extensively used for cancer treatment.[2,3] Despite its clinical accomplishments for the past 40 years in the treatment of certain tumors, it has many disagreeable side effects such as nausea, nephrotoxicity, ototoxicity, tumor resistance, neurotoxicity, bone and back pain, weakness, blood clots, fatigue and hair loss.[4] These severe side effects caused by cisplatin and its analogues carboplatin and oxaliplatin offer an incentive for the breakthrough of novel platinum-based complexes bearing multidentate ligands which are alternative to cisplatin with higher potency, higher cancer cell selectivity and lower resistance. Therefore, a noteworthy number of different platinum complexes were fabricated with the aim to prevail over the disadvantages of cisplatin.[5–8] Also due to the similarity between the coordination geometry of Pd(II) and Pt(II), non-platinum metal-based compounds such as palladium(II) complexes are being used for cancer treatment. Thus, the design of new palladium based anti-cancer drugs is very vital for effectual and proficient use as chemotherapeutic agents.[9–14] However, a disadvantage of the palladium-based drugs is the fact that the aquation and ligand-exchange rates of Pd(II) complexes are about 10^5 times faster than those of the Pt(II)Pt(II) analogues.[15] The higher reactivity of Pd(II) could avert the metal based drugs to reach their target DNA by favouring interactions with other donor species present in the bloodstream, boosting their toxicity and deteriorating their therapeutic potential. Thus, in order to fabricate improved and competitive palladium complex-based anticancer agents, a fitting choice of ligand is of the essence.[16,17] The coordinated ligands play a significant role in the anticancer activity of metal containing antitumor drugs as they can adjust key parameters such as reactivity and lipophilicity. In recent times, several Pd(II) complexes have been designed and studied against various types of cancer cells and some of them demonstrate highly capable biological activity *in vitro*, which is most notably preferable over cisplatin.[18–24]

Azo compounds are intriguing substances that have demonstrated a variety of applications, including in food technology,

[a] *Department of Chemistry, Jadavpur University, Kolkata, 700032, India. E-mail: tapank.mondal@jadavpuruniversity.in*
[b] *Cancer Biology & Inflammatory Disorder Division, CSIR-Indian Institute of Chemical Biology, Kolkata, 700032, India. E-mail: krishna@iicb.res.in*

† Electronic supplementary information (ESI) available: NMR, IR and HRMS of all new compounds, X-ray structure analysis, DFT calculation *etc.* CCDC 2178572 and 2178573. For ESI and crystallographic data in CIF or other electronic format see DOI: https://doi.org/10.1039/d3nj00334e

NJC

ROYAL SOCIETY OF CHEMISTRY

PAPER

View Article Online
View Journal | View Issue

Cite this: *New J. Chem.*, 2023, **47**, 17359

Synthesis of Ru(II) cyclometallated complexes *via* C(aryl)–S bond activation: X-ray structure, DNA/BSA protein binding and antiproliferative activity†

Akash Das,[a] Subrata Mandal,[a] Rimi Mukherjee,[b] Rahul Naskar,[a] Nabendu Murmu[b] and Tapan K. Mondal *[a]

As a contribution to the development of new ruthenium complexes with pharmacologically interesting properties, two new cyclometallated ruthenium(II) carbonyl complexes of the general formula [Ru(L^1/L^2)(CO)(PPh_3)$_2$] (**1/2**) were synthesized and characterized using analytical and spectral techniques (IR, UV/visible, ^{1}H NMR and ESI-MS). The crystal structures of complexes (**1** and **2**) were confirmed by X-ray crystallography, which indicated CNO tridentate coordination of the ligands through C(aryl)–S bond activation. The electronic structures and spectral properties of complexes **1** and **2** were interpreted by DFT and TDDFT calculations. The binding ability of the Ru(II) complexes with calf thymus DNA (CT DNA) and bovine serum albumin (BSA) has been explored by absorption and emission titration methods. A good binding affinity with DNA was observed with an intercalative binding mode, which was further confirmed by EB displacement and viscosity measurement studies. The BSA protein binding studies have been monitored by quenching of tryptophan and tyrosine residues in the presence of complexes and the quenching mechanism was found to be static. Synchronous and 3D fluorescence spectroscopy studies were carried out to validate the micro environmental changes in BSA. In addition, the *in vitro* cytotoxicity of the ligands and complexes against the human breast cancer cell line (MCF-7), human lung cancer cell line (A549), triple negative breast cancer cell line (MDA-MB-231) and gastric adenocarcinoma cell line (AGS) was investigated by using the MTT assay and the IC_{50} values of the complexes towards MCF-7 cell lines were found to be even less compared to cisplatin.

Received 24th May 2023,
Accepted 17th August 2023

DOI: 10.1039/d3nj02391e

rsc.li/njc

1. Introduction

Despite tremendous breakthroughs in the previous fifty years, cancer remains one of the major causes of mortality worldwide.[1,2] Chemotherapy, the administration of cytotoxic chemical agents, remains the most common cancer treatment method, along with surgical excision and radiotherapy.[3–5] Rosenberg's serendipitous discovery of cisplatin as a powerful anticancer agent in 1965, and subsequent clearance for clinical usage, propelled chemotherapy to the forefront of cancer treatment for common tumours such as testicular, ovarian, colorectal, *etc.*[6–8] 0Additionally, this has sparked interest in the creation of numerous generations of platin medications, including carboplatin,[9] oxaliplatin[10] and nedaplatin[11] which are now widely accepted in clinical settings. Although cisplatin and its analogues have been the mainstay of therapeutic medications for cancer therapy globally, these FDA-approved Pt(II) drugs face significant challenges due to their significant, inescapable adverse effects, including nephrotoxicity, hair loss, blood clots, high toxicity and multi-drug resistance.[12–15] So, an urgent need for the development of some alternative drugs that can address the aforementioned flaws comes into the picture. Ruthenium(II/III)-based anticancer medicines have emerged as appealing alternatives to Pt(II)-based anticancer agents over the years.[16] Some of the significant developments in this field include the beginning of clinical trials for NAMI-A ([ImH][*trans*-$RuCl_4$(DMSO-S)(Im)], where Im = imidazole and DMSO-S = sulphur bound dimethylsulfoxide), and KP1019 ([IndH][*trans*-$RuCl_4(Ind)_2$]) as Ru(III)-based anticancer drug candidates.[17–20] However, NAMI-A's low therapeutic index and KP1019's poor solubility precluded their entry into phase II clinical studies.[21–23] Nonetheless, this early achievement spurred a lot of interest in Ru(II/III) complexes as viable chemotherapeutics, laying a new road map in the field of anti-cancer metallodrugs beyond Pt(II) complexes. Ru-based complexes have rich physiochemical

[a] *Department of Chemistry, Jadavpur University, Kolkata-700032, India. E-mail: tapank.mondal@jadavpuruniversity.in*
[b] *Department of Signal Transduction and Biogenic Amines (STBA), Chittaranjan National Cancer Institute, Kolkata-700026, India*

† Electronic supplementary information (ESI) available: NMR, IR and HRMS of all new compounds, X-ray structure analysis, DFT calculation *etc.* CCDC 2262838 and 2262839. For ESI and crystallographic data in CIF or other electronic format see DOI: https://doi.org/10.1039/d3nj02391e

CRYSTAL GROWTH & DESIGN

pubs.acs.org/crystal

Article

Adaptable Biomolecule-Interactive Dual Colorimetric Chemosensor for Cu^{2+} and Pd^{2+}: Insight from Crystal Structure, Photophysical Investigations, Real-Time Sampling, and Molecular Logic Circuits

Subrata Mandal, Akash Das, Amitav Biswas, Arpan Halder, Dibyendu Mondal, and Tapan K. Mondal*

Cite This: *Cryst. Growth Des.* 2024, 24, 1051−1067

Read Online

ACCESS | Metrics & More | Article Recommendations | Supporting Information

ABSTRACT: Considering the crisis of single probes for the simultaneous colorimetric detection of both Cu^{2+} and Pd^{2+} metal ions, which are toxic to living organisms even in trace amounts, in this communication, we report the facile synthesis and characterization, including single-crystal X-ray diffraction (SCXRD), of a single molecular probe (E)-3-((2-(methylthio)phenyl)diazenyl)-[1,1′-biphenyl]-4-ol (**TABH**). **TABH** is bioactive and avidly interacts with biomolecules such as BSA protein and CT DNA, as evidenced by spectrofluorometric and photometric tests. The probe is also proficient in the selective and swift colorimetric sensing of Cu^{2+} and Pd^{2+} ions in ACN/H_2O (4/1 v/v, pH = 7.2) medium over other metal ions. The sensor's ability to selectively bind the analytes is demonstrated by a noticeable color shift from yellow to reddish brown for Cu^{2+} and violet for Pd^{2+}, which is clearly visible to the human eye. A detailed investigation of the recognition mechanism using Job's plot, ^1H nuclear magnetic resonance (NMR), infrared (IR) analysis, electrospray ionization (ESI) mass analysis, and density functional theory (DFT) calculations confirmed a 1:1 binding stoichiometry for both ions. Furthermore, the chemosensor exhibits a strong association affinity (7.61×10^4 and 1.42×10^5 M^{-1} for Cu^{2+} and Pd^{2+}, respectively) and a low detection limit (54.8 and 5.32 nM for Cu^{2+} and Pd^{2+}, respectively). Binding data and absorption studies revealed that Pd^{2+} had a higher affinity for the probe than Cu^{2+}. This makes it simple for Pd^{2+} to replace Cu^{2+} in the [**TAB-Cu**$^{2+}$] complex, increasing Pd^{2+}'s differential selectivity over Cu^{2+}. Cu^{2+} sensing is reversible with the addition of both ethylenediaminetetraacetic acid (EDTA) and triphenylphosphine (PPh_3), whereas Pd^{2+} sensing is exclusively reversible with the presence of PPh_3 only. The sensing activities were also investigated with molecular logic operations of AND, OR, and NOT gates. In addition, the chemoprobe proved to be effective in identifying Cu^{2+} and Pd^{2+} in actual water samples. It was then converted into test strips, creating a portable device for on-site analysis and testing.

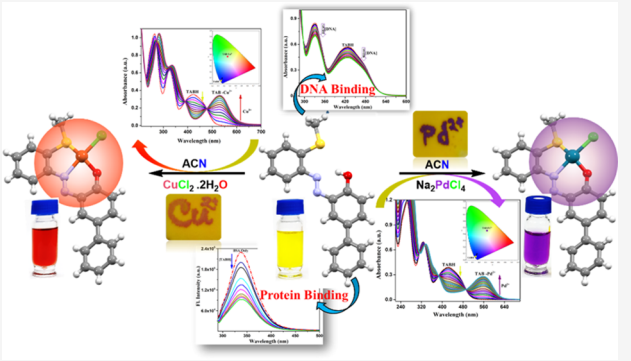

INTRODUCTION

The industrial boom of the 21st century, particularly the extensive expansion of chemical businesses and mining projects around the world, has harmed Mother Earth, endangering a variety of living things.[1,2] Although heavy metals play an important part in human metabolic activities, excessive consumption can lead to serious health concerns.[3−5] As a result, recognizing and sensitively detecting heavy metals as well as transition metal ions such as cadmium, mercury, lead, copper, and palladium are of great contemporary excitement and have garnered a lot of attention recently in chemistry, biology, and environmental research.[6−8] The Cu^{2+} ion is the third (after iron and zinc) prevalent necessary trace element in living beings.[9,10] A large number of fundamental physiological and pathological processes, including the maintenance of nerves and blood vessels, the production of red blood cells, the formation of bone and connective tissues, iron absorption, signal transduction, free radical detoxification, and dioxygen transport, depend on Cu^{2+}. Tyrosinase, cytochrome c oxidase, and superoxide dismutase all use it as an important cofactor.[11−13] Additionally, copper is widely utilized in a variety of industrial applications, including wiring, etching, electroplating, and metal polishing; thus, it is no surprise that industrial effluent contains higher quantities of copper.[14] Though beneficial, the copper ion at an excessive concentration is very toxic for living organisms. Excess intake of it can trigger severe neurodegenerative diseases such as Alzheimer's, Menke's, Parkinson's, and Wilson's diseases as well as gastrointestinal issues like vomiting, headaches, weakness, and diarrhea.[15−18] In contrast, the precious platinum group metal (PGM) palladium is utilized extensively in a variety of

Received: September 10, 2023
Revised: January 10, 2024
Accepted: January 11, 2024
Published: January 27, 2024

NJC

ROYAL SOCIETY OF CHEMISTRY

PAPER

View Article Online
View Journal | View Issue

Cite this: *New J. Chem.*, 2023, **47**, 11557

A novel carbazole-benzothiazole-based chemodosimeter for the chromogenic and fluorogenic recognition of CN^-†

Atanu Maji, Amitav Biswas, Akash Das, Saswati Gharami, Krishnendu Aich and Tapan K. Mondal *

Received 11th March 2023,
Accepted 17th May 2023

DOI: 10.1039/d3nj01157g

rsc.li/njc

A novel colorimetric and fluorescent sensing probe, (*E*)-3-(4-(9H-carbazol-9-yl)phenyl)-2-(benzo[*d*]thiazol-2-yl)acrylonitrile (CBTA), was synthesized and characterized by spectroscopic techniques. CBTA displayed "turn off" fluorescence in the presence of cyanide with a higher selectivity than that of others anions such as Br^-, Cl^-, I^-, NO_3^-, SO_4^{2-}, SCN^-, CO_3^{2-}, N_3^-, OH^-, HCO_3^-, $H_2PO_4^-$, HPO_4^{2-}, F^-, ACO^-, and PO_4^{3-} in a DMSO : H_2O medium (40 : 60, v/v, HEPES buffer, pH = 7.2). The "turn off" fluorescence response mechanism can be attributed to the intra-molecular charge transfer (ICT) process, which is blocked by the nucleophilic attack of cyanide ions at the cyano vinyl group of the probe. The LOD was found to be 3.57×10^{-8} M. The interaction involved behind the sensing of cyanide was investigated by Job's plot analysis, ^{1}H-NMR, and mass spectroscopic studies. DFT and TDDFT were also employed to verify the experimental outcomes. Moreover, the test strip experiment provides a wide application prospect of the receptor for detecting poisonous cyanide in the environment and biological system.

Introduction

The development of a new molecular probe for the detection of anions is of great interest because of their vital roles in a wide range of medicines, catalysis, life science, and environment.[1] Additionally, food safety issues and water pollution by poisonous anions have drawn attention with the development of science and technology nowadays.[2–6] Cyanide is one of the most well-known toxic anions, even at a lower concentration, which can be lethal to human beings, animals, and environment. Cyanide is currently extensively used in many industrial processes such as electroplating, petrochemicals, photography, steel production, gold mining, metallurgy, and the synthesis of resign and fibre due to its critical role in multi-functional reactions.[7] World Health Organization (WHO) stipulates that the permissible acceptable concentration of cyanide in drinking water is 1.9×10^{-6} mol L^{-1}.[8] By the way, cyanide is present in some insects, fruits, seeds, and roots where it is released through the hydrolysis process of cyanogenic glycosides.[9–14] Cyanide binds to the iron ion in cytochrome *c* oxidase, blocks the electron transport in metabolism, and inhibits the production of ATP in cells, making the biological system inefficient to provide sufficient energy to the heart, central nervous system and other vital organs ultimately.[15,16] Considering the above-mentioned fact, the development of simple, efficient and rapid detection tools with high selectivity and sensitivity towards cyanide is an ongoing hot topic to prevent the harmful effect in the human body from contaminated food and environment.

To date, fluorescent molecular probes capable of detecting CN^- have been reported based on fluorescence resonance energy transfer (FRET),[17–19] intra-molecular charge transfer (ICT),[20,21] twisted intra-molecular charge transfer (TICT),[22] excited state intra-molecular proton transfer (ESIPT),[23,24] and photo-induced electron transfer (PET).[25,26] Recently, several groups have reported detection methods by utilizing the nucleophilic addition reaction of cyanide directly involved in the development of covalent bond formation and showed anti-interference ability and high selectivity.[27–38] Compared with the traditional sophisticated analytical tools such as spectrophotometry, voltammetry, chromatography, and potentiometric methods, optical molecular probes based on colorimetric and fluorometric responses towards CN^- are of great preference in virtue of their convenience, simplicity, tenability, low cost, high selectivity and rapid response.[39] Particularly, a naked-eye optical sensor is very much impressive. Since the Tang *et al.* discovery of the AIE phenomenon in 2001, several research groups have been published a growing number of AIE active

Department of Chemistry, Jadavpur University, Kolkata-700032, India.
E-mail: tapank.mondal@jadavpuruniversity.in

† Electronic supplementary information (ESI) available: NMR and MS of all new compounds, limit of detection determination, quantum yield calculation. See DOI: https://doi.org/10.1039/d3nj01157g

Analytical Methods

ROYAL SOCIETY OF CHEMISTRY

PAPER

View Article Online
View Journal | View Issue

Cite this: *Anal. Methods*, 2023, **15**, 2745

A biphenyl thiosemicarbazide based fluorogenic chemosensor for selective recognition of Cd^{2+}: application in cell bioimaging†

Amitav Biswas,[a] Debarpan Mitra,[b] Rahul Naskar,[a] Atanu Maji,[a] Akash Das,[a] Nabendu Murmu[b] and Tapan Kumar Mondal *[a]

A diversified biphenyl thiosemicarbazide based chemosensor (HBMC) has been fabricated and reported for the specific detection of Cd^{2+} in a MeOH : H_2O (4 : 1) solution. We observed a chromogenic change from colorless to light yellow colour, and it showed a "turn-on" fluorogenic change from non fluorescent to blooming cyan colour. In fluorometric titration a sharp "turn-on" emission for Cd^{2+} was observed with a ~16 fold increase in fluorescence intensity value at 496 nm by incremental addition of Cd^{2+} ions in the MeOH : H_2O (4 : 1) solution. The reversibility of the chemosensor (HBMC) was confirmed by a sequential addition of the EDTA solution. Again the binding stoichiometry of HBMC with Cd^{2+} was found to be 2 : 1, as confirmed by Job's plot analysis and HRMS spectra of the HBMC–Cd^{2+} complex. The mechanism for Cd^{2+} sensing in MeOH : H_2O (4 : 1) is based upon the inhibition of C=N isomerization and ESIPT process and simultaneously turning on the CHEF (chelation enhanced fluorescence) process. The limit of detection for Cd^{2+} was found to be in the order of 10^{-8} (M), which implies that HBMC is an efficient probe to detect Cd^{2+} at the microscopic level. A reusability study was performed and on-sight detection of cadmium ions by the chemosensor (HBMC) was established by dip-stick experiment. *In vitro* detection of Cd^{2+} in human breast cancer cells (MDA-MB-231) by HBMC discloses its cell permeability and biocompatible nature. Computational studies (DFT and TDDFT) with the probe HBMC and HBMC–Cd^{2+} complex were also performed.

Received 16th March 2023
Accepted 10th May 2023

DOI: 10.1039/d3ay00403a

rsc.li/methods

Introduction

With reference to human health and the environmental system, discriminative detection of heavy and toxic metal ions is one of the most noteworthy aspects in the field of chemosensors. Among those heavy metal ions Cd^{2+} tops the list in relation to its hazardous nature and detrimental effects.[1] Due to the irreversible damage caused by its use in the fields of batteries, smelting, mining, pigments, metallurgy, and fertilizers it has become a hazardous global pollutant.[2–5] Hence due to its outrageous use, it has triggered an inescapable contamination of our soil, water, food, and air.[6–8] Simultaneously living organisms and human health are also being threatened by the excessive use of cadmium.[9] Mainly through water or air, food and inhalation of cigarette smoke, humans are exposed to cadmium.[10] The toxicity level of cadmium is so soaring that the US Environmental Protection Agency (EPA) and Agency for Toxic Substances and Disease Registry have listed this toxic heavy metal as the seventh on the Top 20 Hazardous Substances Priority List,[11] while the WHO (World Health Organization) has given an enforceable drinking water standard for cadmium of 3 ppb to prevent kidney related diseases.[12] This continuous short and long term cadmium exposure of humans causes different disorders, resulting in lung, breast and prostate cancer.[13–15] Therefore the International Agency for Research on Cancer (IARC) has categorized cadmium compounds as carcinogens of category I.[16] The abnormal concentration of cadmium also causes damage to several organs such as the brain, kidneys, bones, and gastrointestinal tract and has increased the risk of cardiovascular disease.[17–20] Renal and adipose tissue dysfunctions and calcium metabolism are also factors caused by excessive cadmium intake.[21–24] However, the mechanism involved in the uptake of Cd^{2+} by cellular and environmental systems and Cd^{2+} carcinogenesis remains obscured.[25–27] Therefore developing a reliable technique to detect Cd^{2+} in environmental systems is an absolute necessity. However there are several techniques such as atomic absorption/emission spectroscopy (AAS/AES), inductively coupled plasma mass spectrometry (ICP-MS), inductively coupled plasma atomic emission spectroscopy (ICP-AES), and anodic stripping voltammetric analysis, but these techniques

[a]*Department: Chemistry, Jadavpur University, Kolkata-700032, India. E-mail: tapank.mondal@jadavpuruniversity.in*

[b]*Department of Signal Transduction and Biogenic Amines (STBA), Chittaranjan National Cancer Institute, Kolkata-700026, India*

† Electronic supplementary information (ESI) available. See DOI: https://doi.org/10.1039/d3ay00403a

NJC

ROYAL SOCIETY OF CHEMISTRY

PAPER

View Article Online
View Journal | View Issue

Cite this: *New J. Chem.*, 2023, **47**, 15267

Synthesis of a new benzoate bridged NNO tethered copper(II) complex: exploration of its bio, catalytic and anticancer activities†

Subrata Mandal,[a] Rahul Naskar,[a] Rimi Mukherjee,[b] Apurba Sau Mondal,[a] Akash Das,[a] Nabendu Murmu[b] and Tapan K. Mondal *[a]

Considering the pervasive and multifarious impact of copper ions in different biological processes, this research effort covers the one-pot easy synthesis, characterization details (spectroscopic, X-ray structure and quantum calculation including DFT and TD DFT), Hirshfeld surface computation, and bio, catalytic and anticancer activities of a benzoate bridging NNO tethered homo-binuclear copper complex of the formulation $[(CuL)_2(PhCOO)](ClO_4)$ (**1**). The bio-catalytic activities of **1** have been evaluated spectrophotometrically during the aerial oxidation of 3,5-di-*tert*-butylcatechol (3,5-DTBC) and 2-aminophenol (OAPH) in acetonitrile. Using spectro-photo and fluorometric titration, it has been found that complex **1** binds avidly to CT DNA and BSA protein (binding propensities of $\sim 10^5$ M^{-1}). The data from circular dichroism (CD) and viscosity testing indicate that it binds to DNA intercalatively. The static quenching of BSA's endogenous fluorescence is demonstrated by fluorescence life time titration using **1**, which is further verified by a temperature-dependent quenching analysis. Synchronous spectroscopic tests combined with CD and 3D fluorescence spectra of BSA in the presence of **1** support the protein's structural modifications around the Trp-residue. Relevant thermodynamic parameters (ΔH, ΔS and ΔG) and FRET distances between the pair (BSA and **1**) were also estimated. Finally, the MTT colorimetric technique was used to measure **1**'s cytotoxic activities against a range of malignant and non-cancerous cell lines. **1** exhibits specific cytotoxicity against MCF-7 (human breast cancer) exclusively (IC_{50} = 9.53 ± 2.5 μM at 24 h) with an apoptotic mechanism of cell death, as validated by Hoechst and AO/EB staining.

Received 19th April 2023,
Accepted 19th July 2023

DOI: 10.1039/d3nj01806g

rsc.li/njc

Introduction

It is advantageous and environmentally sustainable to use molecular oxygen to oxidize a variety of organic molecules because it generates no hazardous byproducts.[1–3] Unfortunately, under ambient conditions, molecular oxygen's triplet spin creates kinetic inertness towards such oxidation. Nevertheless, metalloenzymes of various transition metals facilitate the spin-forbidden interaction between dioxygen and organic matter in numerous biological reactions[4–10] by changing the spin state of molecular oxygen from triplet to singlet. In this context, copper-containing metalloenzymes are common in nature and are essential for the physiological activation of oxygen.[11–17] Catechol oxidase[14–17] and phenoxazinone synthase,[22] naturally present in ***Streptomyces antibioticus*** bacteria, are two renowned multi-copper oxidases that are involved exclusively in oxygen-mediated oxidation of *o*-diphenols (catechols)[18–21] and *o*-aminophenol. As soon as the crystal structure of catecholase[24] and phenoxazinone synthase[22a] came into the picture, it drew the attention of people, especially synthetic inorganic and bio-inorganic chemists, all over the world to design bio-inspired small molecules that could match the structural characteristics of metalloenzymes' active sites.

Tridentate NNO Schiff base ligands have become an incredibly adaptable class of molecules in making copper complexes as they are multifarious, redox active, low toxicity and generally mimic the structure of the active sites in copper proteins.[23–28] As a result of their electronic and steric characteristics, the copper centre adopts varied geometries and coordination numbers, producing complexes with intriguing features. These complexes are used in redox activities, O_2 transport,[29] catalysis,[30–32]

[a] *Department of Chemistry, Jadavpur University, Kolkata- 700032, India. E-mail: tapank.mondal@jadavpuruniversity.in*
[b] *Department of Signal Transduction and Biogenic Amines (STBA), Chittaranjan National Cancer Institute, Kolkata- 700026, India*

† Electronic supplementary information (ESI) available: Experimental details of the synthesis and characterization (FT-IR, UV-Vis, Fluorescence and ESI-mass spectra) of complex **1**, X-ray structure and Hirshfeld surface analysis, DFT calculation, enzyme-like activities, plots of DNA/protein binding studies and anticancer activity, *etc.* CCDC 2251584 for complex **1**. For ESI and crystallographic data in CIF or other electronic format see DOI: https://doi.org/10.1039/d3nj01806g

NJC

ROYAL SOCIETY OF CHEMISTRY

PAPER

View Article Online
View Journal | View Issue

Cite this: *New J. Chem.*, 2022, **46**, 21968

A new "turn-on" molecular switch for idiosyncratic detection of Al^{3+} ion along with its application in live cell imaging†

Amitav Biswas,[a] Rahul Naskar,[a] Debarpan Mitra,[b] Akash Das,[a] Saswati Gharami,[a] Nabendu Murmu[b] and Tapan Kumar Mondal *[a]

Received 14th July 2022,
Accepted 21st October 2022

DOI: 10.1039/d2nj03481f

rsc.li/njc

A highly sensitive, reversible, reusable and fluorogenic "turn-on" probe (HBTC) is fabricated for the sole detection of Al^{3+}. On incremental addition of Al^{3+} in a solution of HBTC in ACN : H_2O (4 : 1), a sharp "turn-on" emission enhancement is observed at 480 nm. The reversibility of the probe (HBTC) was displayed on the addition of F^- solution. The detection limit is found to be of the order of 10^{-9} M which suggests that HBTC can detect Al^{3+} at a very minute level. The mechanism for Al^{3+} detection in ACN : H_2O (4 : 1) is attributed to forbidding C=N isomerization and ESIPT process simultaneously turning on the chelation-enhanced fluorescence process. The reusability and real-time application of the probe are also studied. Bioimaging study reveals that HBTC can detect Al^{3+} in human breast cancer cells (MDA-MB-231). Electronic structure of the probe is explained by density functional theory.

Introduction

Nowadays undue use of ionic pollutants in industry and the farming sector has become a menace to the environment.[1,2] Hence rapid and accurate detection of those ions has become a promising part in the research field in modern times. It is well known that aluminium is the most abundant metallic element in earth's crust. And it has become an integrated part of daily lifestyle such as in drinking water supplies, utensils, packaging of foods, powder, cosmetic products, processed dairy products, cookware, bleached flour, component of medicine, medicine storage containers and manufacturing of cars.[3–7] The WHO (World Health Organization) stated that the average consumption of Al^{3+} in the human body through several ways is about 3–10 mg per kg per day and the maximum recommended limit Al-contaminated water is 7.42 μM.[8–10] Although it has negative effects on both biological and environment systems, it is extensively used on a daily basis. The central nervous system is deeply affected by overexposure of Al.[11] Abnormal concentration of Al in the human body is related to many neurological disorders including Alzheimer's disease, Parkinson's disease and dementia.[12–14] On the other hand, regular intake of Al beyond permissible limits causes bone disease, damage in the gastrointestinal tract, encephalopathy, microcytic hypochromic anaemia, myopathy, bone softening, impaired lung function, fibrosis and chronic renal failure.[15–18] Therefore, it is imperative to develop probes that can detect and track aluminium ions with high sensitivity using minimal resources and under biological conditions. Among different sensing tools for detection of such kinds of environmental hazardous metal, fluorescence-based chemosensors are considered to be efficient for specifically detecting target analytes.[19] Different mechanisms like excited-state intra-/intermolecular proton transfer (ESIPT), chelation-enhanced fluorescence (CHEF), metal–ligand charge transfer, photoinduced electron/energy transfer, fluorescence resonance energy transfer, intramolecular charge transfer, and –C=N– isomerisation are considered to be the reason for chemosensing processes.[20,21] A strong oxidising site is preferred for the CHEF process, through which a radiative process gets turn on.[22] Comparing with different transition metal ions, chemosensors detecting solely Al^{3+} are limited, due to poor coordination power, strong hydration enthalpy and lack of spectroscopic characteristics.[23,24] Being a hard acid, Al^{3+} always prefers to bind hard centres like N and O donor sites. Schiff bases possess excellent coordinating capabilities, showing different biological activities and have potential analytical application.[25,26] Hence, development of probes with such binding sites causing metal–ligand CHEF is an interesting approach due to a fluorescence "turn-on" mechanism on interaction with a guest.

Recently in 2021, Singh *et al.* reported a silatrane-based Schiff base-functionalized probe which can detect Al^{3+} ions

[a] *Department of Chemistry, Jadavpur University, Kolkata, 700032, India. E-mail: tapank.mondal@jadavpuruniversity.in*
[b] *Department of Signal Transduction and Biogenic Amines (STBA), Chittaranjan National Cancer Institute, Kolkata, 700026, India*

† Electronic supplementary information (ESI) available. See DOI: https://doi.org/10.1039/d2nj03481f

Journal of Molecular Structure 1237 (2021) 130322

Contents lists available at ScienceDirect

Journal of Molecular Structure

journal homepage: www.elsevier.com/locate/molstr

A new palladium(II) phosphino complex with ONS donor Schiff base ligand: Synthesis, characterization and catalytic activity towards Suzuki-Miyaura cross-coupling reaction

Chandan Kumar Manna, Rahul Naskar, Biswajit Bera, Akash Das, Tapan Kumar Mondal*

Department of Chemistry, Inorganic Chemistry Section, Jadavpur University, Kolkata, 700032, India

ARTICLE INFO

Article history:
Received 14 December 2020
Revised 5 March 2021
Accepted 15 March 2021
Available online 26 March 2021

Keywords:
Palladium(II) phosphino complex
ONS donor Schiff base ligand
X-ray structure
DFT computation
Suzuki-Miyaura cross coupling

ABSTRACT

New palladium(II) phosphino complex, $[Pd(PPh_3)(L)](ClO_4)$ (**1**) with thioether containing ONS donor Schiff base ligand (HL) is synthesized by the reaction of HL with sodium tetrachloropalladate (Na_2PdCl_4) and PPh_3. The complex is thoroughly characterized by several spectroscopic techniques. The square planar geometry of the complex is confirmed by single crystal X-ray crystallography. Cyclic voltammetric study in acetonitrile exhibits ligand based irreversible oxidation and reduction peaks at +1.18 V and -1.25 V respectively versus Ag/AgCl reference electrode. Electronic structure and UV-vis spectrum of the complex are interpreted by DFT and TDDFT calculations. Catalytic property of the complex towards Suzuki-Miyaura cross coupling reactions is explored and excellent catalytic conversions (86-97%) are observed with various substituted aryl halides and phenylboronic acid at 100 °C.

1. Introduction

Since the first report of palladium-catalyzed Suzuki-Miyaura C-C cross-coupling reaction in 1979 [1,2], it is used as the most efficient and effective method for the synthesis of a wide variety of biaryl compounds, used in pharmaceutical applications and various chemical industries [3-6]. The efficiency of catalytic cross-coupling reactions is significantly varied with the ligand environment around the palladium center [7-10]. Moreover, palladium(0/II) phosphine complexes are known to be the most efficient catalysts for C-C cross coupling reactions [11-17]. Several palladium(II) triphenylphosphine-Schiff base complexes are also reported to be effective catalysts towards Suzuki-Miyaura cross-coupling reaction [18-20]. Again, the chemistry of transition metal complexes with ONS donor ligand are extensively studied because of their potential use in industrial and synthetic processes such as catalysis, photochemistry, and biological systems [21-25]. So far, several palladium(II) complexes with tridentate ONS donor ligands are synthesized, characterized and explored their catalytic and biological activities [26-28]. Palladium(II) complexes with ONS donor Schiff base ligands are successfully utilized as effective catalyst towards Suzuki-Miyaura cross-coupling reactions [29-33]. Herein, we report the synthesis of a new palladium(II) triphenylphosphine complex, $[Pd(PPh_3)(L)](ClO_4)$ (**1**) with ONS based thioether containing Schiff base ligand (HL). Structure of the complex is confirmed by single crystal X-ray diffraction method. Electronic structure and redox properties are interpreted by DFT studies. The complex is proved to be an efficient catalyst in Suzuki-Miyaura cross-coupling reactions of phenyl boronic acid with various aryl halides.

2. Experimental

2.1. Material and methods

All the reagents and solvents were purchased from commercial sources and were used as received. 3,5-Dichlorosalicyldehyde, 2-aminothiophenol, triphenyl phosphine and Na_2PdCl_4 were purchased from Sigma Aldrich. 2-(Ethylthio)aniline was synthesized following the reported method [34].

Microanalyses (C, H, N) data were obtained using a PerkinElmer Series-II CHN-2400 CHNS/O elemental analyzer. Electronic spectra were measured on a Lambda 750 PerkinElmer spectrophotometer in dichloromethane. IR spectra were recorded on a RX-1 PerkinElmer spectrometer in the range of 4000–400 cm^{-1} with the samples in the form of KBr pellets. HRMS mass spectra were recorded on a Waters (Xevo G2 Q-TOF) mass spectrometer. ^{1}H-NMR spectra were recorded in $CDCl_3$ on a Bruker (AC) 300 MHz

* Corresponding author.
E-mail address: tapank.mondal@jadavpuruniversity.in (T.K. Mondal).

https://doi.org/10.1016/j.molstruc.2021.130322
0022-2860/

Inorganica Chimica Acta 515 (2021) 120096

Contents lists available at ScienceDirect

Inorganica Chimica Acta

journal homepage: www.elsevier.com/locate/ica

Synthesis of new rhodium(III) complex by benzylic C—S bond cleavage of thioether containing NNS donor Schiff base ligand: Investigation of catalytic activity towards transfer hydrogenation of ketones

Sujan Biswas, Chandan Kumar Manna, Rahul Naskar, Akash Das, Tapan Kumar Mondal *

Inorganic Chemistry Section, Department of Chemistry, Jadavpur University, Kolkata 700032, India

ARTICLE INFO

Keywords:
Rhodium(III) complex
C—S bond cleavage
Electrochemistry
Transfer hydrogenation of ketones
DFT computation

ABSTRACT

A new rhodium(III)-triphenylphosphine mixed ligand complex, $[Rh(PPh_3)(L)Cl_2]$ (**1**) is synthesized by benzylic C—S bond cleavage of **L**-CH_2Ph ligand (where, **L**-CH_2Ph = 2-(benzylthio)-N-(pyridin-2-ylmethylene)aniline). The complex is thoroughly characterized by several spectroscopic techniques. Geometry of the complex is confirmed by single crystal X-ray crystallography. Electronic structure, redox properties, absorption and emission properties of the complex were studied. DFT and TDDFT calculations were carried out to interpret the electronic structure and absorption properties of the complex respectively. The synthesized Rh(III) complex was tested as catalyst towards transfer hydrogenation reaction of ketones in ^{i}PrOH and an excellent catalytic conversion was observed under mild conditions.

1. Introduction

It is well-known that C—S bonds can be activated by transition metals to form novel sulfur compounds or sulfide complexes [1–3] and this process is extensively studied for the last few decades due to its importance in industry [4–6]. Recently, transition-metal mediated C—S bond activation and cleavage is applied in diverse bioorganic and synthetic chemistry [7,8]. Moreover, transition metals mediated C—S bond activation along with the transformation processes are of stimulating interest from the perspective of synthetic, mechanistic as well as catalytic aspects [9–11]. Transition metal mediated cleavage of both C(aryl)-S and C(alkyl)-S bonds are extensively studied. Hanton et al. reported Cl^- triggered facile C(alkyl)-S cleavage of thioether moiety in platinum(II) complex [12]. Goswami et al. reported the effect of reaction temperature and $d\pi(M) \rightarrow \pi(N{=}N)$ on C(alkyl)-S cleavage in platinum(II)-thioether complex [13]. Pramanik et al. explored the C(alkyl)-S cleavage in Rh(III) and Ir(III) complexes in presence of excess PPh_3 [14,15]. In recent years, Biswas et al. reported the activation of both C(aryl)-S and C(alkyl)-S bonds to form cyclometalates and metal-thiolato complexes respectively of group 9 metals [16]. In our previous works, we have reported the synthesis of Pd(II), Ru(II) and Rh(III) complexes by metal induced C(alkyl)-S and C(aryl)-S bond scission of thioether containing ligand systems [17–20]. Herein, we have synthesized a new Rh(III)-triphenylphosphine complex supported by a tridentate pyridine-imine-thiolato ligand backbone *via* benzylic C—S bond cleavage of the thioether ligand, **L**-CH_2Ph (where, **L**-CH_2Ph = 2-(benzylthio)-N-(pyridin-2-ylmethylene)aniline). It's worth to mention here that the benzylic group plays an important role to cleavage of the C—S bond for the present case. In our previous work, no C—S bond scission was observed and a S(Me)-Rh coordination mode was found under the similar reaction conditions [21].

On the other hand, transfer hydrogenation of ketone to the corresponding alcohol is one of the most important fundamental subjects in modern synthetic chemistry [22,23] and is a convenient method to reduce carbonyl compounds without the use of hazardous hydrogen gas or moisture-sensitive hydride reagents [24–27]. Moreover, the transfer hydrogenation of ketones is widely accepted in industry as a cost-effective way for the production of a number of hydroxylated organic products [28]. Over the last few decades, significant effort on hydrogenation is given on the use of ruthenium, rhodium and iridium catalysts [29–31]. In view of the significant contribution of rhodium complexes towards catalysis, herein we have also explored the catalytic efficiency of the synthesized Rh(III) complex, $[Rh(PPh_3)(L)Cl_2]$ (**1**) towards transfer hydrogenation of ketones in ^{i}PrOH.

* Corresponding author.
E-mail address: tapank.mondal@jadavpuruniversity.in (T. Kumar Mondal).

https://doi.org/10.1016/j.ica.2020.120096
Received 17 July 2020; Received in revised form 18 October 2020; Accepted 19 October 2020
Available online 22 October 2020